NASA CONTRACTOR
REPORT

NASA CR-2702

EFFECTS OF FORWARD VELOCITY ON TURBULENT JET MIXING NOISE

Prepared by
LOCKHEED-GEORGIA COMPANY
Marietta, Ga. 30063
for Lewis Research Center

NATIONAL AERONAUTICS AND SPACE ADMINISTRATION • WASHINGTON, D. C. • JULY 1976

1. Report No. NASA CR-2702	2. Government Accession No.	3. Recipient's Catalog No.
4. Title and Subtitle EFFECTS OF FORWARD VELOCITY ON TURBULENT JET MIXING NOISE		5. Report Date JULY, 1976
		6. Performing Organization Code
7. Author(s)		8. Performing Organization Report No. None
9. Performing Organization Name and Address Lockheed-Georgia Company Marietta, Georg 30063		10. Work Unit No.
		11. Contract or Grant No. NAS3-18540
12. Sponsoring Agency Name and Address National Aeronautics and Space Administration Washington, D.C. 20546		13. Type of Report and Period Covered Contractor Report
		14. Sponsoring Agency Code

15. Supplementary Notes

16. Abstract

The effects of forward motion on the characteristics of turbulent mixing noise from jets were investigated by conducting flight simulation experiments in an anechoic free jet facility. The tests were conducted over a broad range of model and free jet velocities. The resulting scaling laws, after facility corrections were applied, were in close agreement with scaling laws derived from theoretical and semiempirical considerations. Additionally, measurements of the flow structure of jets were made in a wind tunnel by using a laser-velocimeter. These tests were conducted to describe the effects of velocity ratio and jet exit Mach number on the development of a jet in a coflowing stream. These turbulence measurements and a simplified Lighthill radiation model were used in making predictions of the variation in radiated noise at 90° to the jet axis with velocity ratio. Finally, the influence of forward motion on flow-acoustic interactions was examined through a reinterpretation of the "static" numerical solutions to the Lilley equation. Outside the cone of silence, the Lilley equation radiation levels change with forward motion in a way that could be calculated, to a good approximation, with a geometric acoustics analytic result.

17. Key Words (Suggested by Author(s)) Jet noise; Free jets; Wind tunnels; Flight effects; Laser velocimetry; Forward velocity effects; Lilley equation	18. Distribution Statement Unclassified - unlimited STAR Category 71		
19. Security Classif. (of this report) Unclassified	20. Security Classif. (of this page) Unclassified	21. No. of Pages 406	22. Price* $11.00

CONTENTS

CONTENTS (Cont'd)

CONTENTS (Cont'd)

v

1. INTRODUCTION

The noise generated by a jet exhaust has been studied in great detail, both theoretically and experimentally, since the development of jet engines thirty years ago. This work has been devoted to the prediction, understanding, and reduction of jet noise. It has now become possible to predict the noise of a jet quite accurately, and in fact, the theory to substantiate and explain these predictions is now available for a static jet.

In recent years U. S. government regulations have made it mandatory to control the noise of aircraft operating from U. S. airports. As a result of these regulations, it is necessary to include aircraft noise as a design constraint in new aircraft projects. To emphasize the severity of the jet noise problem for high performance jet engines, the noise of the Concorde has been recorded as being some 20 - 25 dBA higher than that from the new generation wide-body transport aircraft (which meet the FAA noise regulations by a narrow margin). Assuming that these reports on Concorde noise levels are accurate, then quite obviously the problem of noise due to jet engine operation is critical, since the Concorde may not be permitted to operate from many of the world's major airports.

When noise is considered as an aircraft design parameter, not only are the characteristics of the basic jet of concern, but the effects of aircraft configuration and operation must also be properly accounted for in noise predictions. In this regard, aircraft forward motion is found to be a significant parameter controlling the generation of jet noise. When aircraft forward velocity considerations were first introduced, it was assumed that the relative velocity between the jet exhaust and the aircraft forward velocity would be the controlling parameter for jet noise generation. Indeed, this seems to be the case when the noise of jets is studied in ground-based forward motion simulation facilities, such as wind tunnels. However, in the past few years, as a result of intensive study of jet noise suppressor performance in actual flight tests, it has been observed that jet noise does not scale on relative velocity raised to a fixed exponent for either conical nozzles or suppressors. In addition, jet noise trends from conical and suppressor nozzles as measured in flight simulation facilities are not observed in actual flight tests. This is a matter of great concern since suppressors which have been optimized in static tests or in flight simulation facilities fall far short of expectations in actual flight tests (ref. 1).

As a result of the major significance of flight velocity on jet noise and the apparent inconsistency between jet noise trends observed in actual flight and in flight simulation facilities, NASA Lewis Research Laboratory decided to embark on a study of the problems of understanding the generation, propagation, and measurement of exhaust-generated noise from jets in flight. The work described in this report represents a contracted study of the fundamental aspects controlling the generation, propagation, and measurement of noise from a conical jet in forward flight.

More specifically, the primary objective of this program was to obtain a fundamental study of the problems involved in either theoretically predicting or empirically extrapolating the jet noise field (from both subsonic and supersonic exhausts) received on the ground from an aircraft flying overhead in typical takeoff and landing approach patterns. Such prediction or extrapolation would be made from static ground tests both with and without relative velocity effects on the nozzle configuration. The ultimate goal of this program was to make detailed recommendations based on the studies conducted under the following four specific tasks, for a possible follow-on program.

Task 1: Literature Survey and Preliminary Investigation
Task 2: Acoustic Propagation Effects
Task 3: Source Alteration Effects
Task 4: Investigation of Verification Techniques

The first task involved a compilation and assessment of the existing literature on jet noise flight effects and related subjects. This was completed early in the program, and a literature survey report was submitted for NASA's internal use. The remainder of the program comprised a basic study of the generation and radiation of noise from jets in flight. In addition, the problems of measurement of noise from aircraft in flight were studied in some detail.

The intent of this contract was that it act as a program definition phase for more comprehensive work to follow. This intent has been met, and in several areas, new data and theory are presented which lead to definitive conclusions regarding the generation of noise of jets in flight.

This report is compiled in three major sections which describe the technical work accomplished in this contract. A synopsis of the technical work described in these three sections is given in Section 5.

Contributors to the work presented in this report are Robert H. Burrin, Christopher L. Morfey, Philip J. Morris, C. Benton Reid, H. K. Tanna, Brian J. Tester, and M. Clay Whiffen.

2

2. INFLIGHT SIMULATION EXPERIMENTS ON JET NOISE

2.1 OBSERVED EFFECTS OF FORWARD MOTION ON JET NOISE

During the initial period of intensive research on jet noise and the development of jet noise suppressors in the 1950's and early 1960's, the effect of aircraft motion on the source (the "relative velocity" effect) was considered, and the reduction in noise level at peak polar angle was duly noted. Attempts were made to describe this reduction by using the relative velocity rather than the absolute jet velocity in noise estimation procedures. It was observed, however, that this did not fully agree with the measured results, and a further term was introduced by Greatrex (ref. 5) and Coles (ref. 6) in an attempt to allow for an increase in noise generation due to elongation of the jet mixing region which was known to take place in flight. During this period, some theoretical work was carried out by Ffowcs Williams which included the effects of aircraft motion (ref. 7); however, this does not appear to have been widely used.

It is probably correct that, although many flight tests were made and compared with static results, most of these were of a developmental nature rather than being oriented toward engine research purposes. Hence, only peak levels were required, and the more fundamental aspects of comparing the directivities and spectral shapes in detail were rarely dealt with. In these early investigations, the effects of ground reflection were certainly not well considered, and atmospheric attenuation data were ill-defined. Also, the standard frequency analysis system was at that time in octave bands, which would obscure important differences that may exist between static and flight spectra.

The corrections usually applied to static acoustic test data to theoretically convert the results to the moving source or inflight results relative to a stationary observer are (a) a Doppler shift in frequency, (b) a change in filter band level due to change in Doppler-shifted center frequency, and (c) a so-called dynamic effect or convective amplification due to source motion relative to the fixed observer.

Corrections for effects (a) and (b) have been given by Mangiarotty and Turner (ref. 8). The source motion effect (often referred to as the dynamic effect in the past) was derived by Ffowcs Williams (ref. 7). The effects of relative velocity on the source strengths and on radiation efficiency through flow/acoustic interactions have not been determined. In the SAE prediction method (ref. 9), the noise generated by a jet in motion is simply taken to be equal to that of a static jet with exhaust velocity equal to the relative velocity of the moving jet (jet velocity minus forward speed of the jet).

Recent Measurements and Observations

A considerable amount of noise measurements, both from model-scale configurations operated in the inflight simulation mode and from full-scale

flight tests, has been published, but the majority of these studies have been concentrated on various suppressor nozzle configurations [Coles, *et al*, (ref. 10); Brausch (ref. 11); Burley and Karabinus (ref. 12); Hoch and Hawkins (ref. 13); Von Glahn, *et al*, (ref. 14); Burley and Johns (ref. 15); Burley, *et al*, (ref. 16); Chamberlain (ref. 17); Von Glahn and Goodykoontz (ref. 18); Burley and Head (ref. 19); Gubkina and Mel'nikov (ref. 20); Von Glahn, *et al*, (ref. 21); Brooks and Woodrow (ref. 22); Bushell (ref. 1); Cocking and Bryce (ref. 23)]. Data on the basic conical (or convergent) nozzle are, therefore, rather scarce. Furthermore, there is considerable disagreement between the results of various investigations, and the situation is quite inconclusive at the present time. The use of the corrections given above does not explain the differences measured between inflight and static tests. Several factors can be suggested which play very important roles in producing widely varying and misleading conclusions in such experimental programs. In particular, these are internal or extraneous noise sources in the rig or the engine under test; geometry of the configuration under test (which must influence the flow properties in the shear layer of the jet); improper account of the effects of environmental factors; and finally, inaccurate and/or inadequate techniques for the acquisition and analysis of the noise data.

The discovery of the importance of internal core noise or "tailpipe" noise under static conditions on many of the test vehicles gave an explanation of why the expected relative velocity effects may not be observed in flight. This was that the tailpipe noise sources would dominate the inflight noise and there is no obvious reason why noise from these sources should fall with forward velocity. As a result, many of the earlier measurements carried out to study the effects of forward motion on jet noise, from both conical and suppression nozzles, have been invalidated.

However, further investigation has shown that in the jet velocity regimes where internal noise would not be *thought* to dominate even in flight, the changes of the measured noise characteristics (in particular, the field shape) with jet and aircraft velocity, are not consistent. Even the shock-associated noise level at 90° to the jet axis is found to be increased in flight, contrary to the theoretical suggestion that dynamic effects or convective amplification due to aircraft motion should be zero or negligible at this angle. Therefore, it is clear that further understanding of the characteristics of jet noise is required under flight conditions.

Inspection of the more recent full-scale flight results [Hoch and Hawkins (ref. 13), Brooks and Woodrow (ref. 22), and Bushell (ref. 1)] and comparison with static test data reveal that, although a "relative velocity" reduction in turbulent mixing noise is observed close to the downstream jet axis in flight, no general reduction is observed around the complete field. Indeed, the observations range from small reductions in the rear arc to actual amplifications of the noise in the forward quadrant; the level in the forward arc rises with aircraft speed instead of falling as a simple relative velocity effect would predict. In contrast, results from the inflight simulation experiments at model scale conducted by NGTE (ref. 23) and NASA-Lewis (ref. 21), indicate that noise reductions with forward velocity are

4

present around the complete field, and in general, the magnitude of the relative velocity effect increases as the observer moves from the forward arc towards the downstream jet axis. This fundamental discrepancy between the inflight simulation results and the full-scale flight experiments is illustrated qualitatively in Figure 2.1. The changes in OASPL with forward motion can also be displayed conveniently as a relative velocity (jet velocity minus forward speed) dependence. This is shown in Figure 2.2, where the inflight effects are expressed quantitatively in terms of the relative velocity exponent, m.

To summarize, it is clear that there are significant differences between the inflight effects as observed from flight tests and those from model-scale inflight simulation experiments. These discrepancies need to be resolved before the flight simulation techniques can be used as a long-term research tool to obtain a fundamental understanding of forward velocity effects on jet noise. A significant effort in the present program has been directed toward this problem, as will become apparent in the later parts of this report.

2.2   FLIGHT SIMULATION TECHNIQUES

In the preceding section, published inflight effects on jet noise, derived from facilities which simulate forward motion, were briefly introduced without mentioning any specific simulation concept. The purpose of this section is to present brief descriptions of various flight simulation methods that are either in use or gaining increasing interest at the present time. But before this is done, it is perhaps worthwhile to summarize the problems involved with actual flight tests.

2.2.1 Full-Scale Flight Testing

Full-scale flight testing is a direct method giving the required noise measurements with no intermediate steps or recourse to theory. However, the cost associated with any comprehensive flight test program is prohibitive, and there are several disadvantages which are difficult to overcome:

(1)   The internal noise sources are almost always significant in a full-scale engine, and their contribution to the total sound field must be established and, if necessary, adequately suppressed to levels well below the unsilenced jet noise so that no significant contamination occurs when the magnitudes of turbulent mixing noise decrease in flight.

(2)   The envelope or test window of jet operating conditions (exhaust velocity and temperature) and flight speed is usually restricted in a flight test program.

(3)   The sound generated by the jet exhaust flow has to propagate through a complex inhomogeneous environment on its way to the ground-based
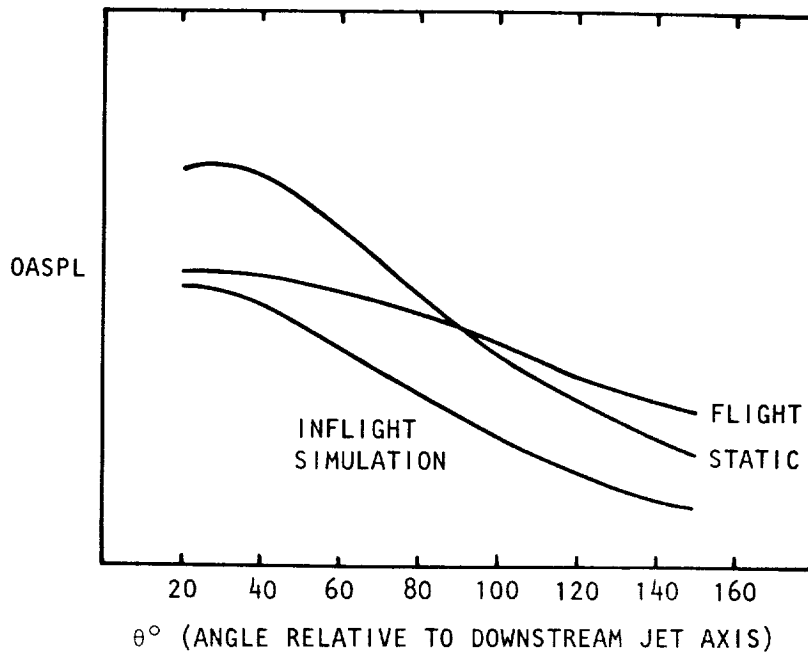
Figure 2.1 Qualitative illustration of inflight
effects on jet noise.
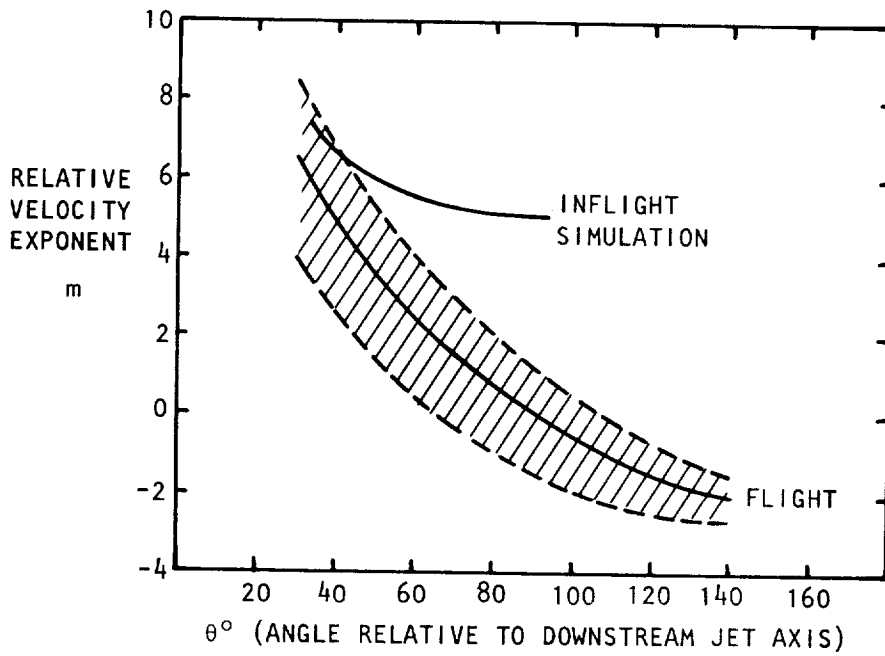
Figure 2.2 Quantitative illustration of inflight
effects on jet noise.

6

observer, and many of the phenomena associated with propagation of sound through a real atmosphere have yet to be understood and properly quantified.

(4) The acquisition of flyover noise data and the correction procedure necessary to yield free-field data is extremely complicated. It involves statistical averaging of nonstationary acoustic data, accurate determination of aircraft position and speed, proper account of ground reflection, and accurate atmospheric absorption corrections. These aspects of flyover data acquisition are discussed in detail in Appendix 2A of this report.

In view of the above difficulties associated with flight testing, several methods for investigating inflight effects on jet noise have evolved in recent years. The four most promising types of flight simulation facilities are:

(1) jet mounted on a ground based moving vehicle

(2) jet mounted at the end of a rotating arm (a spinning rig),

(3) stationary jet in a large-scale acoustically-treated wind tunnel, and

(4) stationary jet immersed in a larger surrounding jet (a free-jet facility).

Each of these has its own merits as well as facility oriented problems, and these are discussed briefly below.

2.2.2 Ground-Based Moving Vehicle

Investigation of inflight effects on jet noise by mounting the engine configuration on a ground-based vehicle, which can be translated at constant speed, appears attractive at first sight since the relative motion between a moving source and a stationary observer can be simulated exactly. Two examples of such a facility are the high speed train and the rocket powered sled. However, these facilities are accompanied by problems which are similar to those encountered in aircraft flyover noise measurements.

2.2.3 Spinning Rig

The use of a spinning rig, where the model-scale jet exhaust is mounted at the end of a rigid arm that rotates at constant speed, also provides an exact relative motion simulation. The main advantages of this method are that the costs involved are much smaller than flyover testing and the atmospheric propagation effects are diminished by an order of magnitude since the propagation distances are smaller. However, there are severe technical problems associated in operating such a facility. In particular, because the angular position of the moving jet source relative to fixed microphones is changing rapidly, the problems associated with noise data acquisition and reduction are very complicated. It should also be noted that even if the contamination from internal noise sources and

rig-generated self noise can be reduced to acceptable levels, the undesirable effects of centrifugal forces in producing distortion of the jet flow have yet to be established.

2.2.4 Large-Scale Anechoic Wind Tunnel

The step from static testing in relatively idealized test facilities to full-scale flight testing is large. Therefore, a very useful intermediate step can be provided by operating the jet configuration under examination in a wind tunnel, in which the effect of forward motion is produced by the tunnel air flow.

A comprehensive review of the use of wind tunnels for acoustic and aerodynamic measurements in the inflight simulation mode, and current research aimed at the design and operation of large wind tunnels, has been published recently by AGARD (ref. 24, 25, and 26).

Aerodynamic measurements on a moving configuration do not appear very practical, but can be achieved relatively easily in a wind tunnel environment. The acoustic measurements can be achieved by making the test section anechoic, although the costs required to modify any large-scale tunnel, such as the NASA-Ames 12.2 m x 24.4 m facility, to obtain acceptable background noise levels and to minimize wall reflections, are high. In addition, operating costs are considerable for comprehensive evaluation of inflight effects on jet noise.

Simulation of aircraft motion in such a manner is attractive in that a model rig free from internal noise can be set up and tested in a controlled anechoic environment. The jet operating conditions and the tunnel speed can be controlled independently. In addition, the measurements are carried out in essentially a static (steady state) environment. However, the quality of acoustic measurements is highly dependent upon having a quiet means of propulsion for the tunnel and in developing microphones which are insensitive to the air flow across them. The noise levels induced by air flow over the microphones placed within the tunnel flow are usually high, and therefore preclude any meaningful measurements at reasonably high tunnel velocities of interest.

A minor disadvantage of this technique is the lack of a true relative velocity effect between source and observer, unless the microphone is traversed past the nozzle at the moving stream velocity. However, the effects of forward motion on jet structure as well as changes in noise characteristics for an observer moving with the jet can be established. The translation of acoustic data from a wind tunnel facility to the fly-over situation can be achieved far more readily within the bounds of existing theoretical expertise.

2.2.5 Free-Jet Anechoic Wind Tunnel

This flight simulation method removes many of the limitations of conventional wind tunnels for acoustic testing. The aircraft forward motion in

8

a free-jet or open-jet facility is simulated by immersing the primary jet exhaust configuration in a larger surrounding jet. The microphones are placed in the far field outside the free jet flow, and the complete test section is enclosed in an anechoic chamber to provide a free-field environment. In addition to retaining other advantages of a large-scale wind tunnel, a carefully designed free-jet facility is also capable of providing low background noise levels. Furthermore, the cost associated with operating these facilities is minimal in comparison to the large wind tunnels.

However, since the sound generated by the model jet has to propagate through the shear layer of the free jet before it reaches the microphones, this facility does introduce additional problems which have to be overcome. These are (1) refraction by mean velocity gradients, and (2) scattering by turbulence in the free-jet mixing layer. The refraction phenomenon gives rise to a change in the amplitude of the incident wave as well as a modification in the raypath angle. Corrections for these amplitude and angle changes therefore need to be established, and these can be obtained theoretically and/or experimentally. Detailed description of the correction procedure, derived during the present program, is given in Section 3.1.3. As regards the effects of turbulence scattering in a free-jet facility, all qualitative evidence available to date suggests that this is not an important effect. However, further work is required to produce quantitative results on this phenomenon. This scattering effect is discussed in some detail in the later parts of this report.

Having presented an overview of the various flight simulation facilities that can be utilized to study the effects of forward motion on jet noise, the inflight simulation experiments that were conducted in the present program are described in the following subsections. The experiments were conducted in the Lockheed Anechoic Free-Jet Facility, which is described next.

2.3   ANECHOIC FREE-JET FACILITY

2.3.1   Facility Description

An existing anechoic chamber was modified utilizing as many other existing pieces of hardware as possible. Prior to the construction of the full scale facility, a one-fifth scale model was built to confirm various aerodynamic performance concepts and to aid in the design of the free-jet working section as well as the shape of the collector.

The basic anechoic room was 3.4 m (long) by 3.4 m (wide) by 5.2 m (high) between wedge tips. The interior was lined with fiberglas anechoic wedges which provided a 99% echo-free environment at all frequencies above 100 Hertz. The chamber was completely isolated from the rest of the acoustics laboratory since it was mounted on massive springs. A spring-tensioned

cable floor, suspended from the walls, provided easy access to the interior of the chamber for instrumentation calibration and test section changes.

A planview schematic of the complete facility is shown in Figure 2.3. Starting from the left, air was drawn into the intake, through the honeycomb and screens to the contraction, across the anechoic room to the collector, through the diffuser, the two right angle corners with turning vanes, through the duct silencers to the transition section. The facility was powered by the jet ejector, whose exhaust and entrainment flows were diffused through the 17.1 m long muffler/diffuser section on the right of Figure 2.3.

The intake/contraction section was an existing part of a research smoke tunnel, and the ejector/diffuser section formed the major part of a now de-activated inlet noise absorption test facility adjacent to the research complex. The ready availability of this power source prompted its incorporation into the free jet facility design rather than a fan.

Because of the high noise levels generated by the 8.6 cm diameter jet ejector, being operated at pressure ratios up to 8 in order to induce flows through the working section of up to 75 m/s, a significant amount of acoustic treatment was necessary between the ejector and the anechoic room. The design criterion adopted was to assume that the total noise generated by the ejector, propagated upstream to the collector and then radiated spherically to the microphone measuring stations within the room. The amount of attenuation provided by the duct was required to be sufficient to reduce the ejector noise at the microphones to levels at least 10 dB below the lowest noise levels to be measured in the test program over the entire frequency range of interest. Of course, this acoustic treatment had to be traded off against aerodynamic performance, the aim being to achieve at least 60 m/s free jet velocity.

To achieve this noise criterion, the tunnel between the collector inside the room and the ejector intake was constructed from 1.27 cm plywood inner and outer walls separated by wooden studs. The cavities in the floor, walls, and roof were all filled with a total of 21,000 kg. of dry sand to minimize the flanking (or structure borne) transmission of sound from the ejector. The duct was lined throughout with 15.2 cm. of 32 kg/m^3 density polyurethane foam. Acoustically treated turning vanes were installed in both right angle bends and 2.1 m long, low aerodynamic loss, IAC (Industrial Acoustics Company) quiet duct silencers were installed downstream of the second turn.

The intake shown in Figure 2.4 is approximately 2.03 m x 2.84 m and the contraction provides a working section area 0.76 m x 1.07 m, the latter dimensions being vertical. In order to perform adequate directivity measurements of noise generated by the model jets placed inside the free jet, a minimum working section length of 2.9 m was required. This allowed measurements to be made in the range 30° - 90° from the downstream jet axis. The microphone arc, centered at the nozzle exit plane, had a radius of 2.74 m (54 nozzle diameters for 5.08 cm. diameter nozzles) and was placed outside the free jet flow.

10

MICROPHONES LOCATED ON 2.74 M RADIUS BELOW
WORKING SECTION CENTERLINE
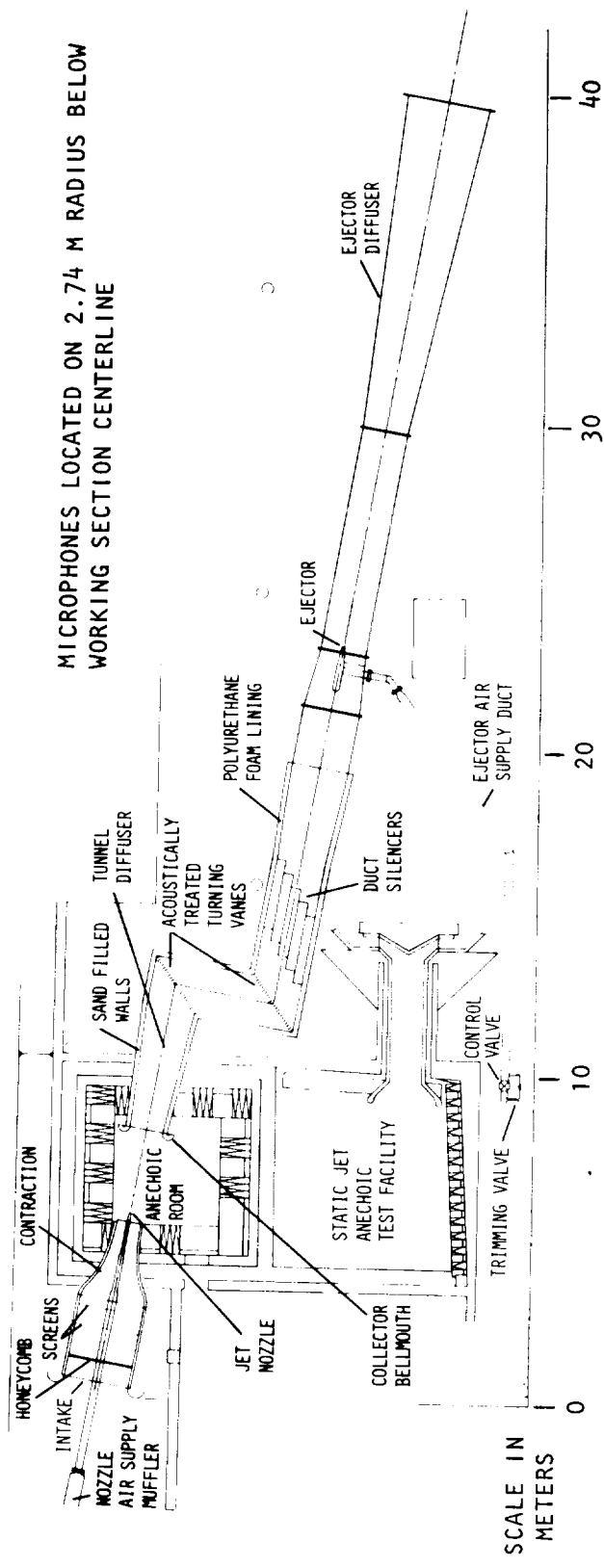
Figure 2.3 Planview schematic of anechoic free-jet facility.
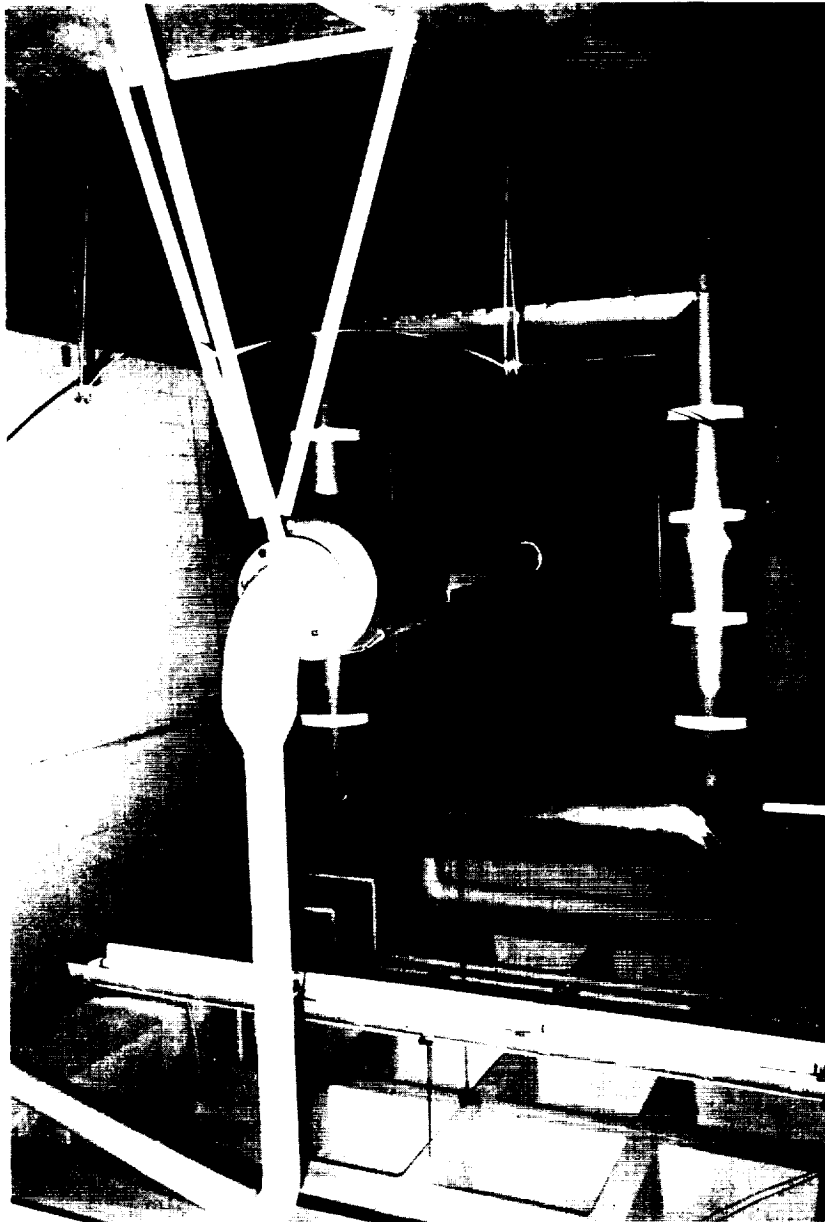
Figure 2.4   Anechoic free-jet intake and model jet air supply.

12

The free jet centerline was oriented at an angle of 10° from the closest room wall to allow for free jet spread without having to trim existing room wedges. The tunnel diffuser entrance was 1.12 m x 1.42 m and diffused to 1.52 m x 1.83 m in a length of almost 6.10 m. The distance between the turns was about 3.05 m and the total length of lined duct from collector to ejector intake was about 15.5 m. The total installation was aligned axially using a low power laser.

The air supply to the jet ejector originated from the main 2.07 x 10⁶ N/m² compressor which supplied air to all research center facilities. Ejector air was controlled by a 15.2 cm. Fisher valve, with a 5.1 cm. Annin valve in parallel for low free jet velocities and fine tuning at higher velocities. The ejector ducting was 25.4 cm. pipe over the majority of its length but reduced to 20.8 cm just prior to the pylon mount. The ejector air supply ducting and diffuser are shown in Figure 2.5.

For each of installation and minimum blockage (and therefore minimum flow disturbance) in the working section, the air supply ducting for the model jet was installed axially in the intake/contraction section rather than through a swept pylon mounted on the anechoic room wall. The ducting was designed to avoid any flow separation within the accelerating free jet flow in the contraction section, a totally welded construction being adopted for this purpose. The ducting was aligned by using a low power laser, placed at the end of the collector/diffuser and aimed along the free jet centerline, thus ensuring that the model jet flow would exhaust axially in the free stream. The cold air supply was regulated by a 5.1 cm. Annin automatically controlled valve. A Lockheed-built muffler, and an IAC (Industrial Acoustics Company) PRV2 muffler, were connected in series to reduce upstream valve noise to sufficiently low levels so as not to contaminate any measurements to be made in the room. The IAC muffler is shown in Figures 2.3 and 2.4. Downstream of the muffler was a 20.3 cm. diameter plenum 6.1 m. long, followed by a 1.8 m length of 15.2 cm pipe, and finally, approximately 0.91 m of 10.2 cm pipe faired with the 15.2 cm. section to preclude any outer flow separations. The nozzles were attached to the end of the 10.2 cm. pipe, setting the exit plane approximately 30 cm. beyond the end of the free jet contraction.

Four nozzles were specially made for use in this facility, and in the wind tunnel (described in paragraph 4.2.2): A convergent nozzle and three convergent-divergent nozzles designed by the method of characteristics, to operate nominally at Mach numbers of 1.4, 1.7, and 2.0. They were turned from aluminum bar stock, the external shape being a straight taper from 11.4 cm. O/D to 5.1 cm. O/D over a length of 27.9 cm. to mate smoothly with the faired 10.2 cm. I/D air supply pipe, once again to preclude the possibility of flow separation. The nozzles were attached with six countersunk screws around the circumference at the 10.2 cm. end. The four nozzles are shown in Figure 2.6, together with the cross-sectional drawing of the M = 1.7 nozzle.

Nozzle performance was evaluated by a simple shadowgraph system. Unfortunately, the facility used in these tests could not be operated at the ʼressure ratio required for the Mach 2.0 nozzle, but the M = 1.4 and 1.7 ʼʑles were tested to determine the pressure ratios for optimum shock-free

Figure 2.5   Anechoic free-jet facility ejector diffuser
and air supply ducting.

Figure 2.6 5.08 Cm. diameter jet nozzle configuration.

15

performance. Figure 2.7 shows a series of three shadowgraph photographs for each of these nozzles, indicating that the nozzle Mach numbers for optimum performance were 1.37 and 1.67 at pressure ratios of 3.06 and 4.73, respectively.

2.3.2 Aerodynamic Performance Evaluation Tests

2.3.2.1 Flow visualization tests. Initial tests were performed in the anechoic chamber using a smoke generator and a tufted wand to ascertain visually several important characteristics of the free jet flow in the working section and flow induced in the surrounding areas of the room.

These tests indicated that the jet appeared to be stable throughout its length. There was no discernable snaking or deflection due to the proximity of the closest wall or the ceiling. The jet had no tendency whatsoever to attach to either of these areas, presumably due to the effectiveness of the uneven surface of the anechoic wedges. Stagnation on the collector bell-mouth was regularly disposed around the periphery, and no separation was detected inside the diffuser.

In the chamber itself, outside of the free jet flow, the induced veloc-ities were quite small, everywhere a good deal less than 10% of the tunnel velocity. The highest velocities, approaching 10% of the tunnel velocity, were noted in the standing vortex around the collector bellmouth. The only microphone likely to be affected by this flow was located beneath the collector at 30° to the downstream axis.

2.3.2.2 Flow surveys using a specially built pressure probe rake. A series of initial calibration tests were carried out using a specially de-signed pressure probe rake. This rake could be positioned at any axial station between the free jet exit plane (at the end of the contraction) and the collector bellmouth. It was an easy task to manually perform vertical traverses with the rake at selected axial stations.

The rake itself was made from a 1.22 m length of 7 cm x .12 cm stream-lined steel tube. It was supported by brackets at its extremities and drilled at 2.54 cm intervals along its entire length to accommodate 3.18 mm probes. In this way, the pressure probes could be arrayed differently for each axial station as necessary. Up to 16 total pressure probes and 5 static pressure probes were utilized during the test surveys. A second order curve was fitted to the readings of the five static pressure probes, distributed along the rake, and the room static pressure at the edges of the free jet to determine the static pressure at each of the total pressure probe locations.

Surveys were made at the exit plane of the contraction and then at 0.56, 1.12, 1.67, and 2.24 m downstream. The surveys at each station were made from the upper to the lower extremities of the free jet, and the spacing of the measurements was chosen accordingly. The rake, positioned at 0.56 m axially, is shown in Figure 2.8. In addition, piezometer pressures were recorded in the settling chamber of the intake prior to the contraction, and

16

M = 1.24

$P_R/P_O = 2.56$

M = 1.37

$P_R/P_O = 3.06$

M = 1.48

$P_R/P_O = 3.55$
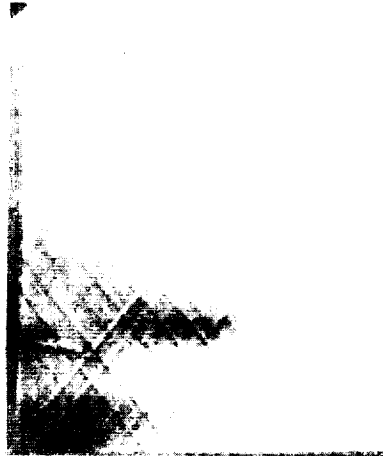
M = 1.63

$P_R/P_O = 4.47$

M = 1.67

$P_R/R_O = 4.73$

M = 1.70

$P_R/P_O = 4.96$

Figure 2.7 Shadowgraph calibration photographs of Mach 1.4 and Mach 1.7 nozzles.
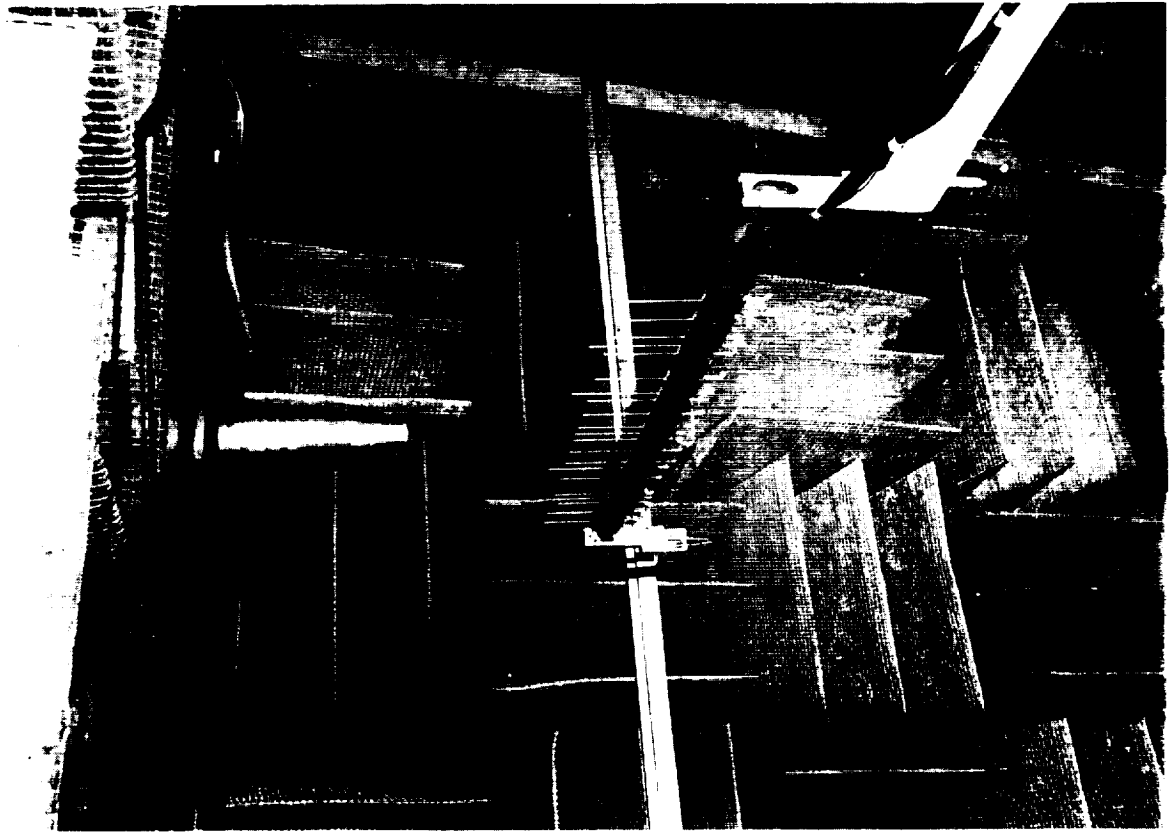
Figure 2.8 Rake for aerodynamic calibration of free-jet.

10.2 cm upstream of the exit plane. (The static measurement points were located one in each side and one in top and bottom surfaces connected to the same manometer tube with identical lengths of tubing.) The measurements were made using a portable multitube manometer especially made for the purpose. The rake probes were connected in such a way as to display the jet shape on the manometer. A 35 mm camera was set up in front of the manometer and a photograph taken at each measurement position. A typical print of the manometer display is shown in Figure 2.9.

Figure 2.10 shows a three-dimensional plot of the potential core edge (defined here as the 98% velocity point) for a tunnel velocity of 61 m/s.

The mean dynamic pressure at the jet exit-plane was computed for the potential core. The mean excluded the boundary layer areas of the contraction section and the centrally-positioned model jet nozzle air supply ducting. The area included in the averaging is shown cross hatched in Figure 2.11, which also shows the positions of the total and static pressure probes.

HP-65 computer programs were written for on-the-spot evaluation of tunnel conditions from piezometer, temperature and barometric data, and conversely, the piezometer differential necessary for a required tunnel velocity to facilitate test condition setup.

Figure 2.12 shows curves of variation of free jet nominal velocity, ejector weight flow, and the ratio of tunnel to ejector weight flow, with ejector pressure ratio.

2.3.2.3 Conclusion. The aerodynamic performance evaluation tests carried out showed that the facility could be confidently used for model scale investigations of the effects of aircraft motion on jet noise. There were no problems associated with free jet stability, collector/diffuser performance, flow separation in the intake/contraction or excessive air flow circulation in the room. Continuous tests could be carried out at free jet velocities up to 70 m/s. Although free jet velocities up to 75 m/s were possible, limitations of available supply air mass flow precluded the simultaneous operation of the 5.08 cm model jets.

2.3.3 Acoustic Performance Evaluation Tests

In order to confirm the acoustic design criteria and to ensure the accuracy of the subsequent jet noise measurements, the anechoic free-jet facility was subjected to rigorous performance evaluation tests, and the results are presented below.

2.3.3.1 Anechoic quality of facility. The first series of calibration tests were designed to evaluate the anechoic quality of the facility and to ensure that the proposed microphone distance of 2.74 m (54 nozzle diameters) was in the acoustic far field. An audio driver unit placed at the nozzle exit location was used as the sound source (i.e., point source) and the intensity vs. distance plots were obtained with a traversing microphone

DISPLAY OF FREE JET PROFILE
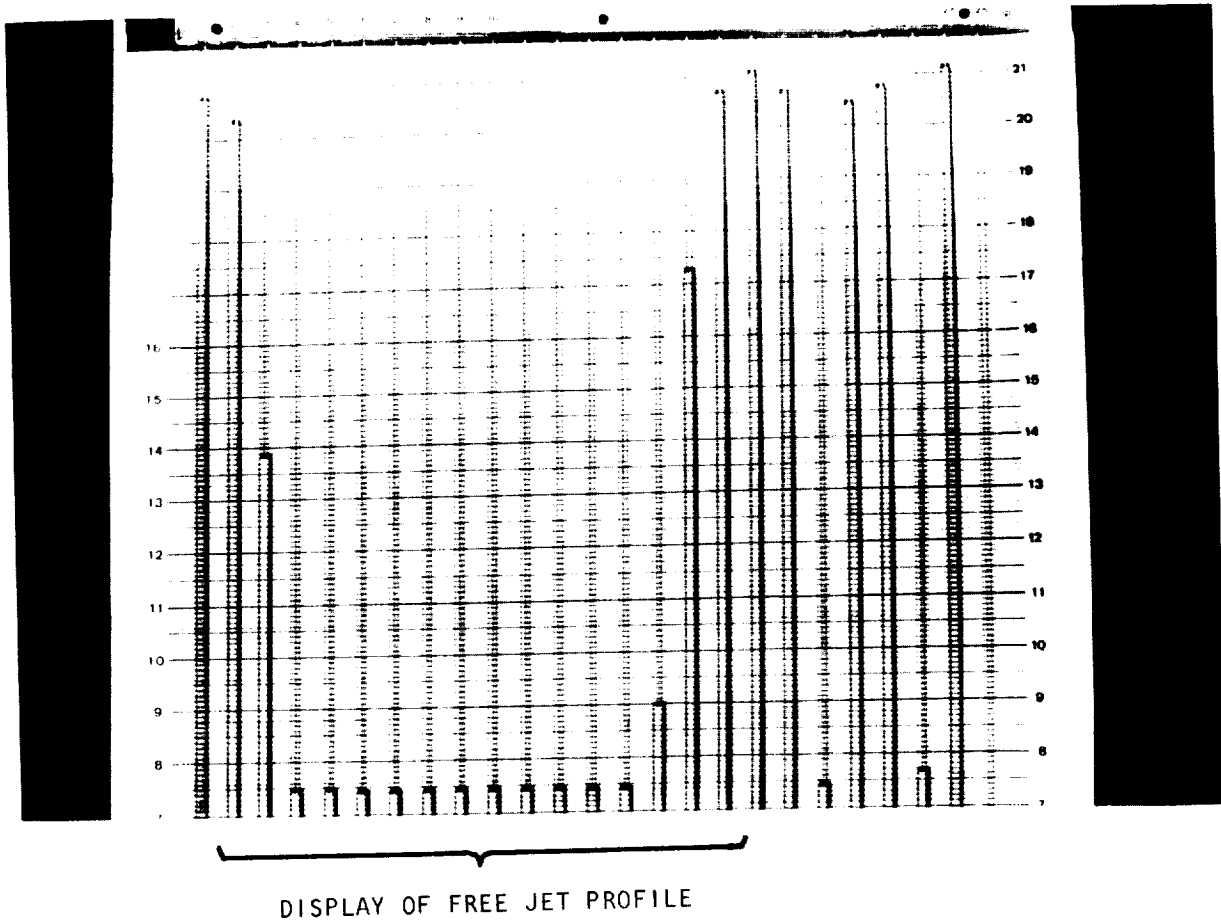
Figure 2.9 Multitube manometer showing free-jet velocity profile.

20

$V_T = 61.0$ M/S

FREE JET EXIT PLANE
0.76 M x 1.07 M

POTENTIAL CORE
DEFINED AS
98% VELOCITY PROFILE

2.24

1.68

1.12

0.56

0

METERS
DOWNSTREAM
FROM EXIT
PLANE
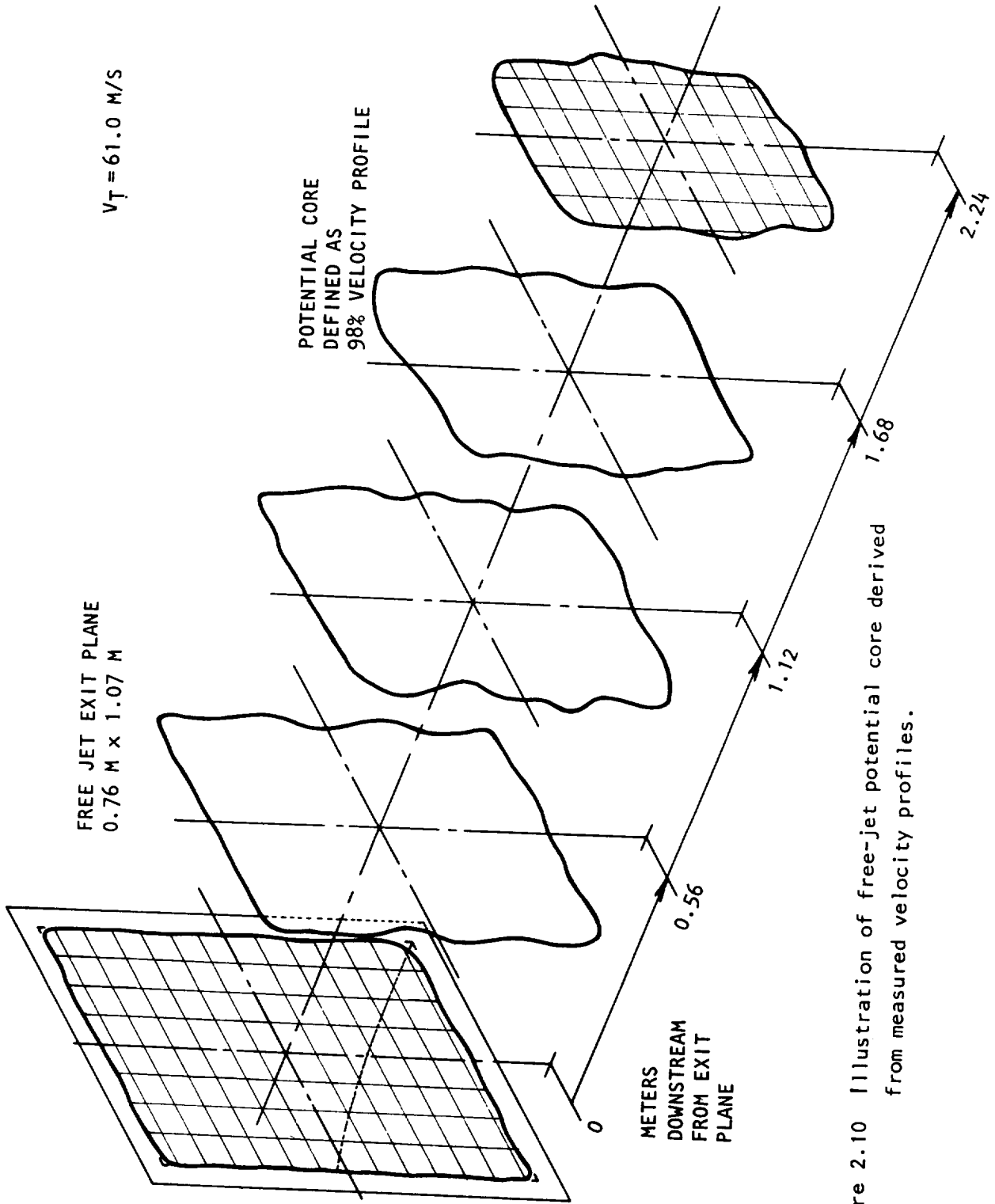
Figure 2.10   Illustration of free-jet potential core derived
from measured velocity profiles.

21

Figure 2.11   Positions of total and static
                pressure probes for free-jet
                exit plane calibration.
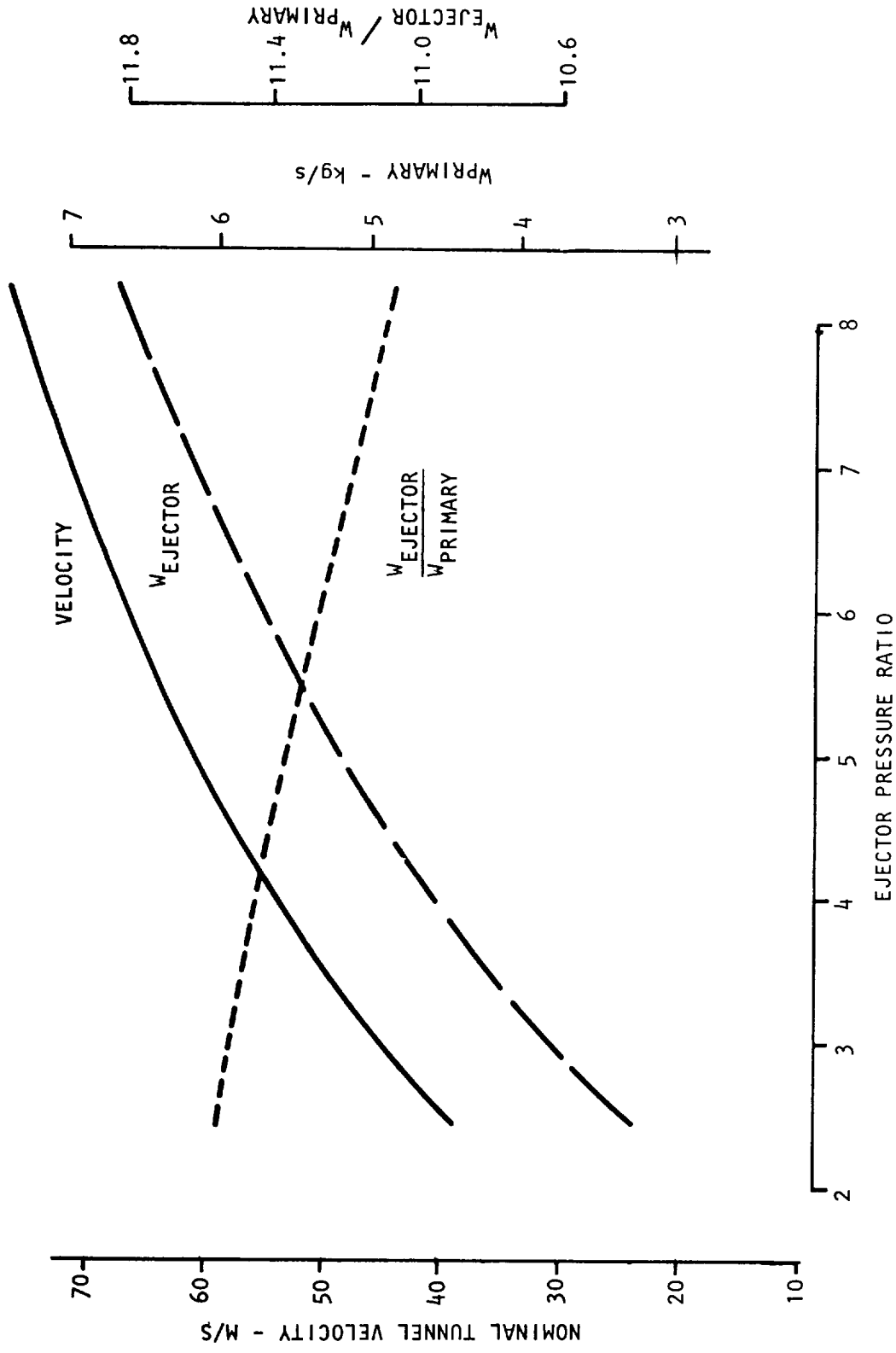
Figure 2.12 Anechoic free-jet facility ejector performance curves.

arrangement. The microphone was traversed along three different directions (30°, 60° and 90° to the downstream jet axis), and for each of these traverses, measurements were made of the SPL fall-off as a function of distance, both for a pure tone noise source and for a one-third octave filtered white noise source. Along each of these traverses, the results for discrete frequency excitation were slightly inferior to the results for filtered one-third octave excitation. However, the results along the three directions from the sound source were essentially similar. A typical set of the intensity-distance plots at various frequencies is presented in Figure 2.13. It can be seen from this figure that the anechoic quality of the facility was acceptable down to a frequency of approximately 200 Hz, and that at a distance of 2.74 m, the microphone was in the acoustic far field at all frequencies (above 200 Hz) of interest.

2.3.3.2 Background and electronic instrumentation noise. The background (or ambient noise in the anechoic room was measured with a 12.7 mm. B&K microphone (Type 4133), which had a dynamic range of 32 to 160 dB. The microphone was located in the center of the room, directly under the free-jet test section at a distance of approximately 3 m from the test section center line, which corresponded roughly to the 60° measurement position in the jet noise test program. The resulting background-plus-instrumentation noise spectra at various free-jet (or tunnel) velocities, V_T, are presented in Figure 2.14.

It should be noted that the total noise floor in the subsequent experimental program also contains a contribution from the complete instrumentation system used in the data acquisition and reduction process. The magnitude of this instrumentation (electronic) noise contamination unfortunately varies from one spectrum to another, depending upon the settings selected. The results from the test program (raw data) should therefore be scrutinized carefully, and all spectra or parts of spectra, which are obviously seen to be contaminated by the total background and measuring instrumentation system noise, should be rejected in the analysis of the results. This important aspect is elaborated further in Section 2.4.

2.3.3.3 Rig internal noise tests. The "acoustic cleanliness" or internal noise tests were conducted to produce evidence for the lack of any significant contamination, in the measurement arena, from noise sources which are normally present upstream of the nozzle exit plane. In the first instance, the tests described below were conducted with only the IAC muffler in position. It was found that the internal noise contamination was rather high, and further silencing of upstream valve noise was necessary. This was achieved successfully by connecting the Lockheed-built muffler (used in other research programs) in series with the IAC muffler. The tests described below refer to this configuration, which was used in the subsequent jet noise experimental program.

The internal noise tests, with zero tunnel velocity, were carried out with the basic instrumentation system, consisting of 12.7 mm. B&K microphones, a 1/3-octave analyzer and a level recorder, so that the instrumentation noise was kept to a minimum. In order to establish the magnitude of

24
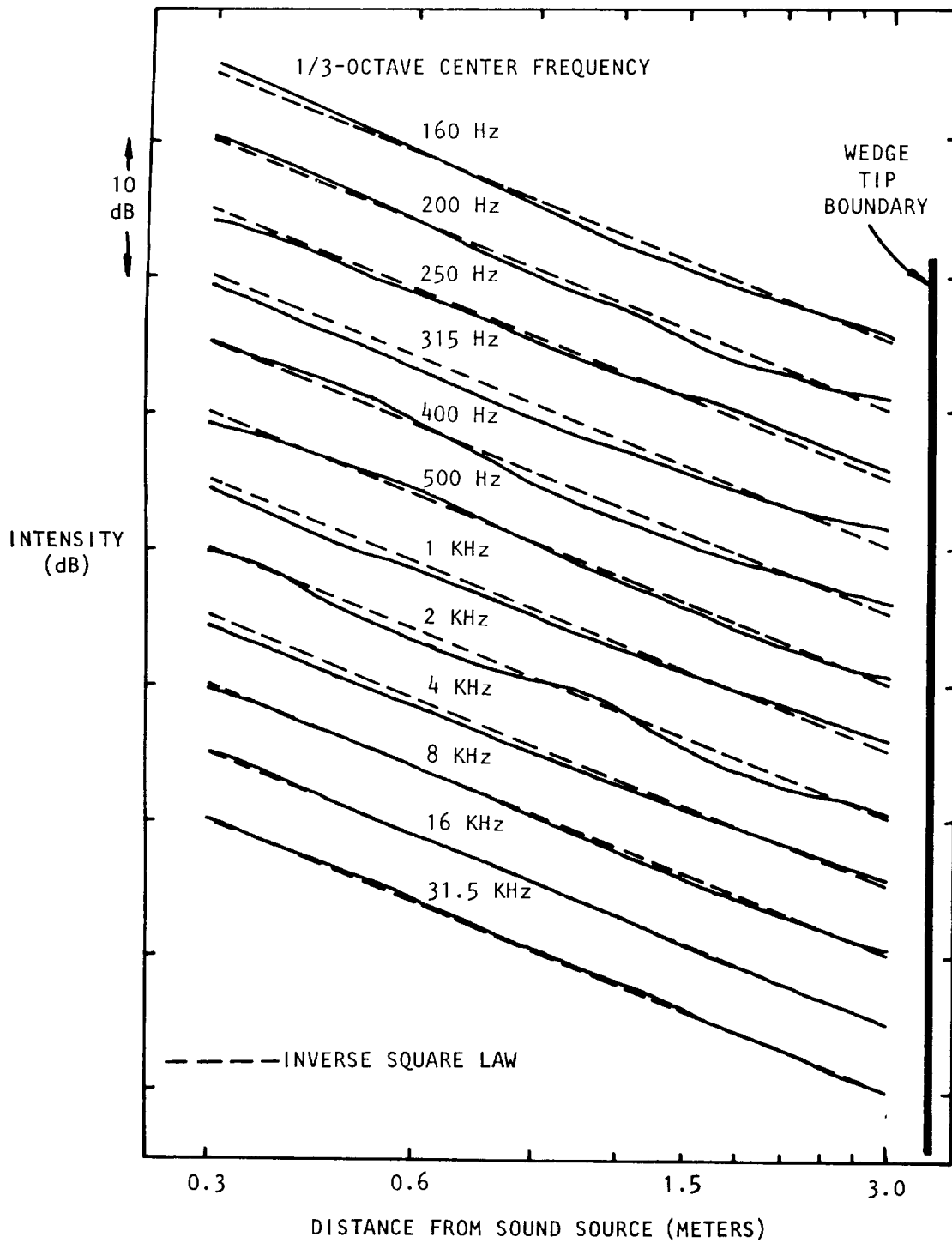
Figure 2.13 Intensity-distance plots with point sound source.
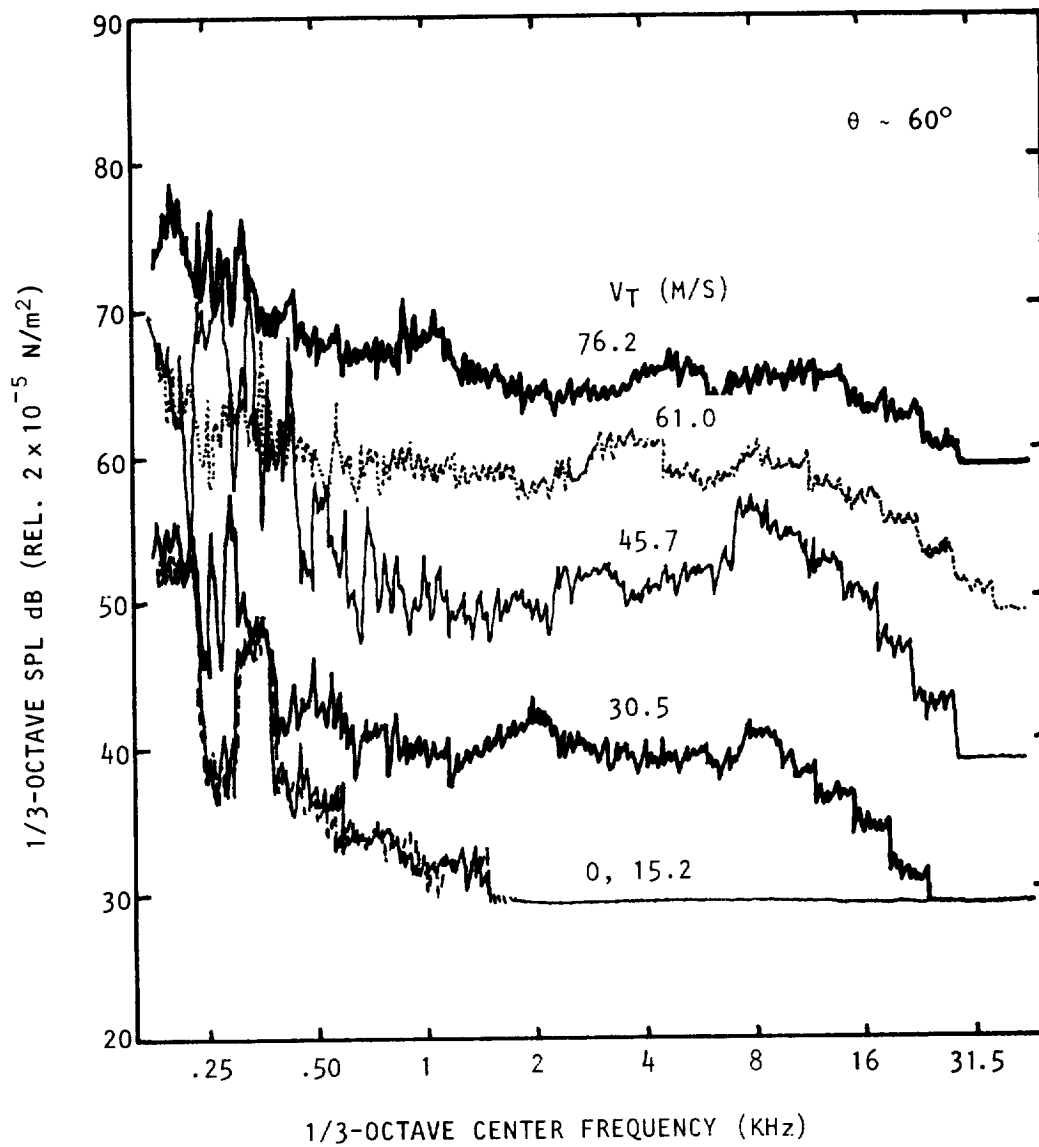
Figure 2.14   Background + instrumentation noise spectra at various
tunnel velocities (B&K instrumentation). (Microphone
at approximately 60° location.)

the internally generated noise at a low value of jet exit velocity ratio ($V_J/a_O = 0.32$, cold), a systematic study was carried out and a typical set of results at approximately 60° to the jet axis is presented in Figure 2.15. The background/instrumentation noise is given by spectrum A in this figure. Spectrum B represents the turbulent mixing noise for the 5.08 cm diameter cold jet at $V_J/a_O = 0.32$. The internal noise for this jet operation condition was estimated by increasing the nozzle diameter to 10.2 cm and keeping the mass flow through the pipework constant. The jet velocity was therefore reduced by a factor of four, and from the relationship

$$I \propto d^2 V_J^8$$

for the turbulent mixing noise, it could be calculated that the mixing noise would be 42 dB down in this case, while the internal noise would be essentially unaltered. The resulting spectrum C shown in Figure 2.15, therefore represents the combined background/instrumentation/internal noise contribution and it can be seen that it is much lower in magnitude than the corresponding mixing noise spectrum B. Further indirect evidence for the absence of internal noise contamination is presented in Figure 2.16, where it can be seen that the spectra at four values of jet velocity in the range from $V_J/a_O = 0.32$ to 0.6 do conform to a clean stacking pattern relative to one another as expected.

In conclusion, it can be safely stated that the internally generated noise from the facility was *not* significant at least down to $V_J/a_O = 0.32$. All data for $V_J/a_O > 0.32$ obtained from this jet noise rig represented true turbulent mixing noise, unaffected by internal noise. The low velocity data would, however, be influenced by background and instrumentation noise as discussed previously, and this should be taken into account in the data selection process.

2.3.4 Point Source Tests

In theory, a tremendous amount of information can be gained from point source tests. In particular, in the anechoic free-jet facility, point source tests can be very useful in both calibration and basic research testing. For the purpose of calibration, the point source is useful in locating room reflections and in determining the limits of the absorption qualities of the anechoic room for no flow testing. In evaluating the effects of the free-jet on the acoustic characteristics of the room, the point source tests are necessary for determining changes in basic source directivity, source efficiency and shear layer reflection characteristics. From a more fundamental viewpoint, point source tests are quite useful in a free-jet facility, in particular, for determining (1) the effects of the shear layer on source directivity and amplitude in the far field, (2) the effects of free-jet mixing region turbulence scattering, and (3) the change in ray angle resulting from transmission through the shear layer (by determining the phase front normal direction).

All of the above mentioned tests should be conducted prior to or in conjunction with jet noise tests to aid in interpretation of the test

		V_J/a_0
A	BACKGROUND + INSTRUMENTATION NOISE	
B	MIXING NOISE	0.32
C	BACKGROUND + INSTRUMENTATION + INTERNAL NOISE	0.32 (EFFECTIVE)
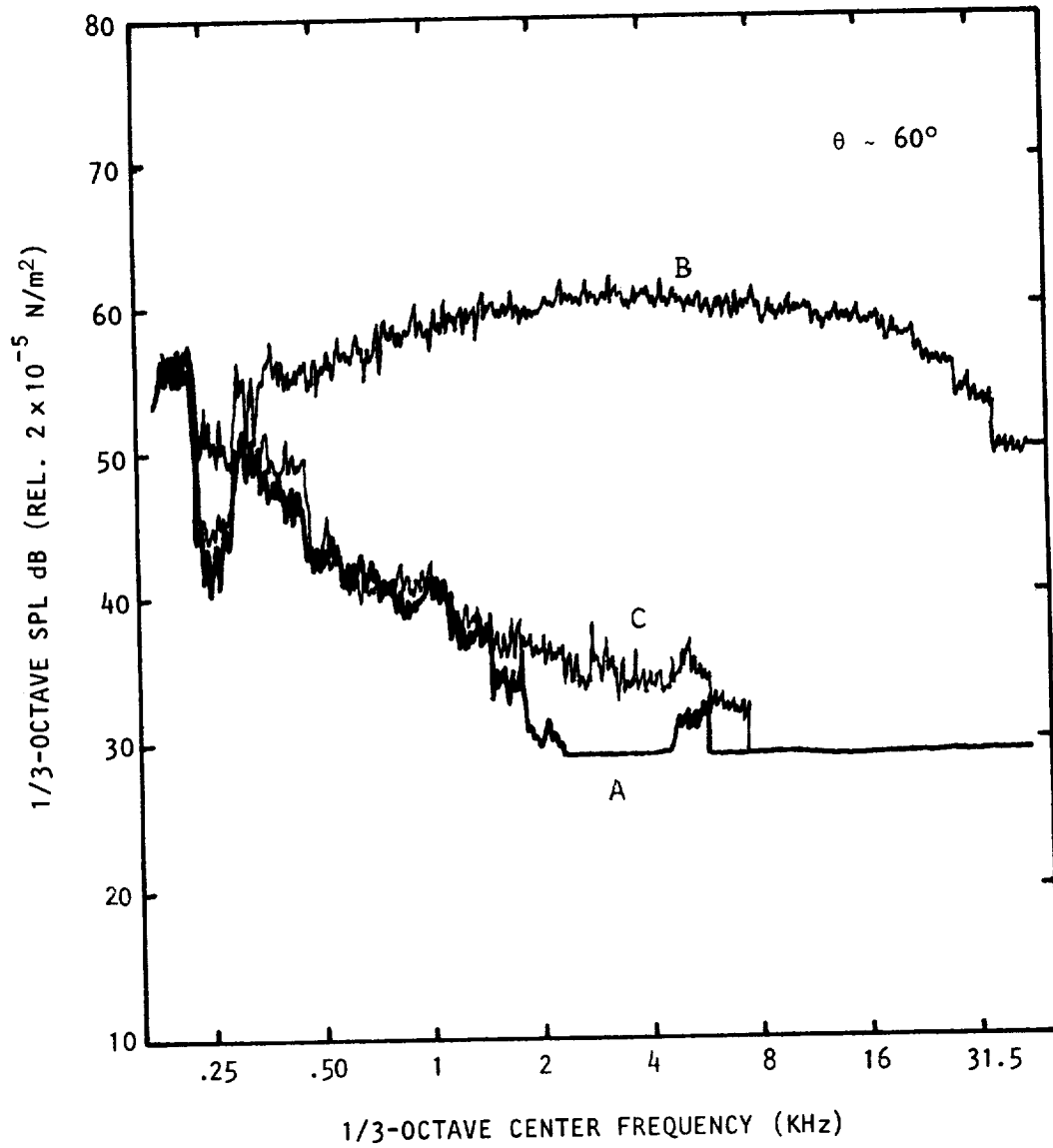
Figure 2.15   Rig internal noise tests with IAC + Lockheed mufflers ($\theta \sim 60°$).

28
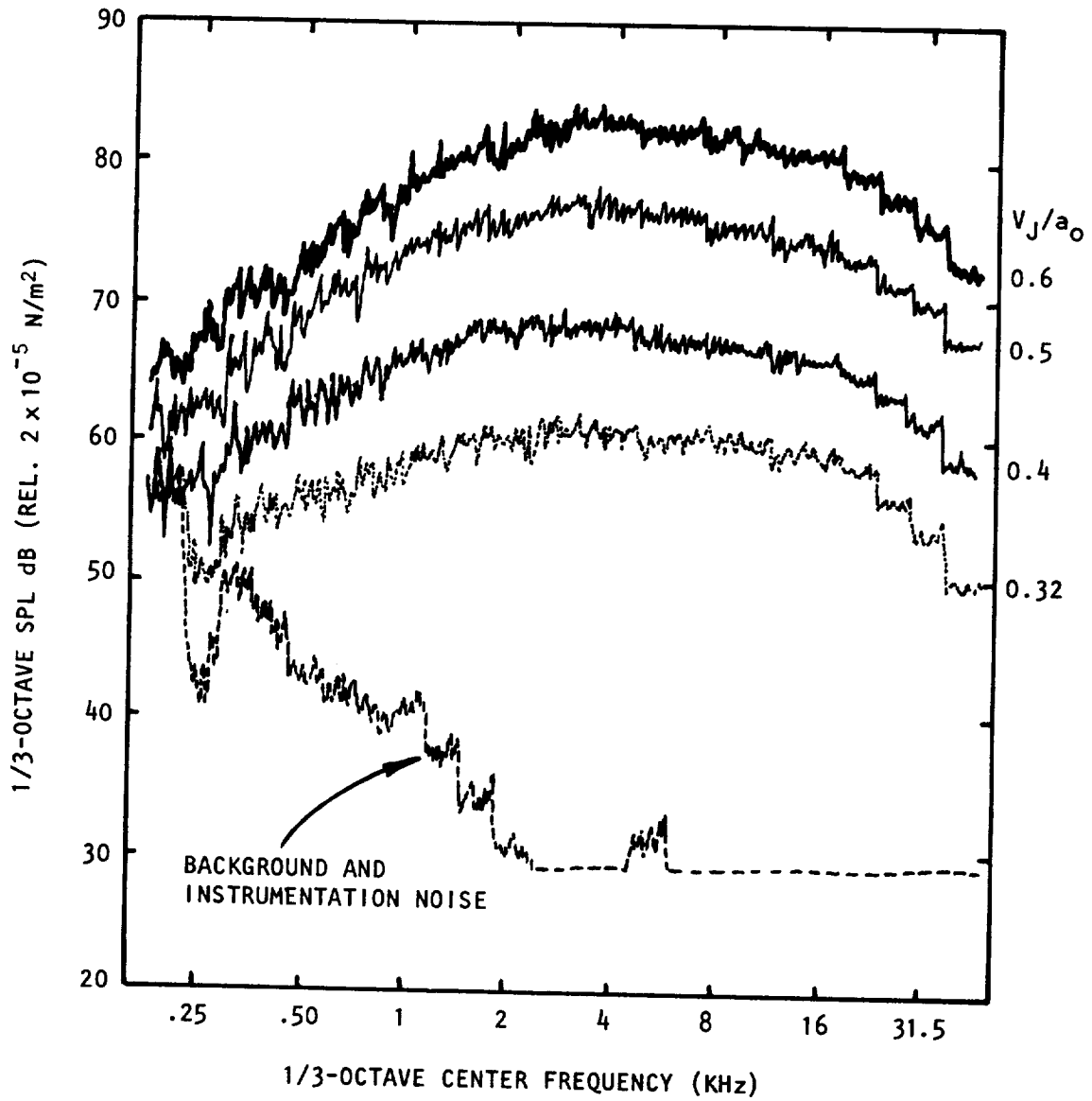
Figure 2.16   Spectra at various V_J/a_o with IAC + Lockheed mufflers ($\theta \sim 60°$).

results and to provide experimental values or confirm theoretical values for the amplitude and angle corrections. However, a fairly major effort is required to conduct some of the more useful tests and no provision was made for extensive point source testing in this program.

Some preliminary point source tests were conducted with the goal of determining basic source directivity in the flow, amplitude of source reflection at the free-jet shear layer, the far-field amplitude and directivity, and the effect of the free-jet mixing region turbulence on scattering of sound from the source. The "point" source is shown in Figure 2.17. The sound was generated by a commercially available 100-watt audio driver unit and propagated through an inverse conical horn section through the right angle bend to the 0.64 cm diameter opening. Output levels of approximately 115 dB at 1 m from the opening could be obtained from 1 KHz to 5 KHz. The source exit point was located as shown in Figure 2.18 at an axial location of 20.3 cm. from the free-jet exit plane.

The first test conducted was a near-field radial traverse for the purpose of determining the order of magnitude of internal reflections from the shear layer at 90°. Because of differences between the free-jet results and inflight data, especially at 90°, it was hypothesized that free-jet corrections at 90°, which assume no internal reflections for waves normal to the mixing layer, might be incorrect due either to free-jet divergence or finite axial velocity gradients in the mixing region.

The traverse mechanism is shown in Figure 2.17. The microphone was equipped with a probe with a right angle bend. The sound signal was sensed through static pressure ports. Microphone position was detected by a potentiometer which drove the X-axis of an X-Y recorder. A typical output is shown in Figure 2.19 for four frequencies. The measured amplitude vs. distance from the source shown in Figure 2.19 is compared with inverse square law for discrete frequency excitation. It is obvious that near the source, direct radiation is dominating the sound pressure signal and an inverse square law behavior is observed. However, at a distance some 25 cm. from the source, reflections from the exposed free-jet lip have a considerable influence. This problem was not given further consideration since, as stated in section 2.3.3, it did not exist for broadband noise and also it did not preclude determination of internal reflections from the free-jet shear layer, which was the primary objective of this particular test. However, because of the strong reflections near the lip line, the source was positioned at 10.2 cm. from the lip line in order to change the angle of the unwanted reflection and increase the source amplitude at the mixing layer interface. A typical result is shown in Figure 2.20 for 2500 and 3150 Hz. The solid line is for no-flow, the dashed line for 30.5 m/s and the dotted line for 61.0 m/s. The source amplitude remained unchanged during these tests. While at 61.0 m/s there were minor perturbations near the free-jet lip line, these perturbations were linked to a measurement problem rather than a reflection. In the mixing region, the probe microphone sensed high broadband turbulent pressure fluctuations, and as a result of non-normal unsteady impingement on the static ports, self-noise was generated. The ability of the narrow band filters to remove this broadband component of noise was inadequate in the mixing regions; thus the measurement was a sum of discrete plus random.

30

DRIVE
MOTOR

LINEAR
POTENTIOMETER
FOR POSITION
READOUT

PULLEY

DRIVE
CABLE

MICROPHONE
SUPPORT
CABLE

TRAVERSING
MICROPHONE
PROBE

POINT
SOURCE
PROBE

ACOUSTIC
DRIVER
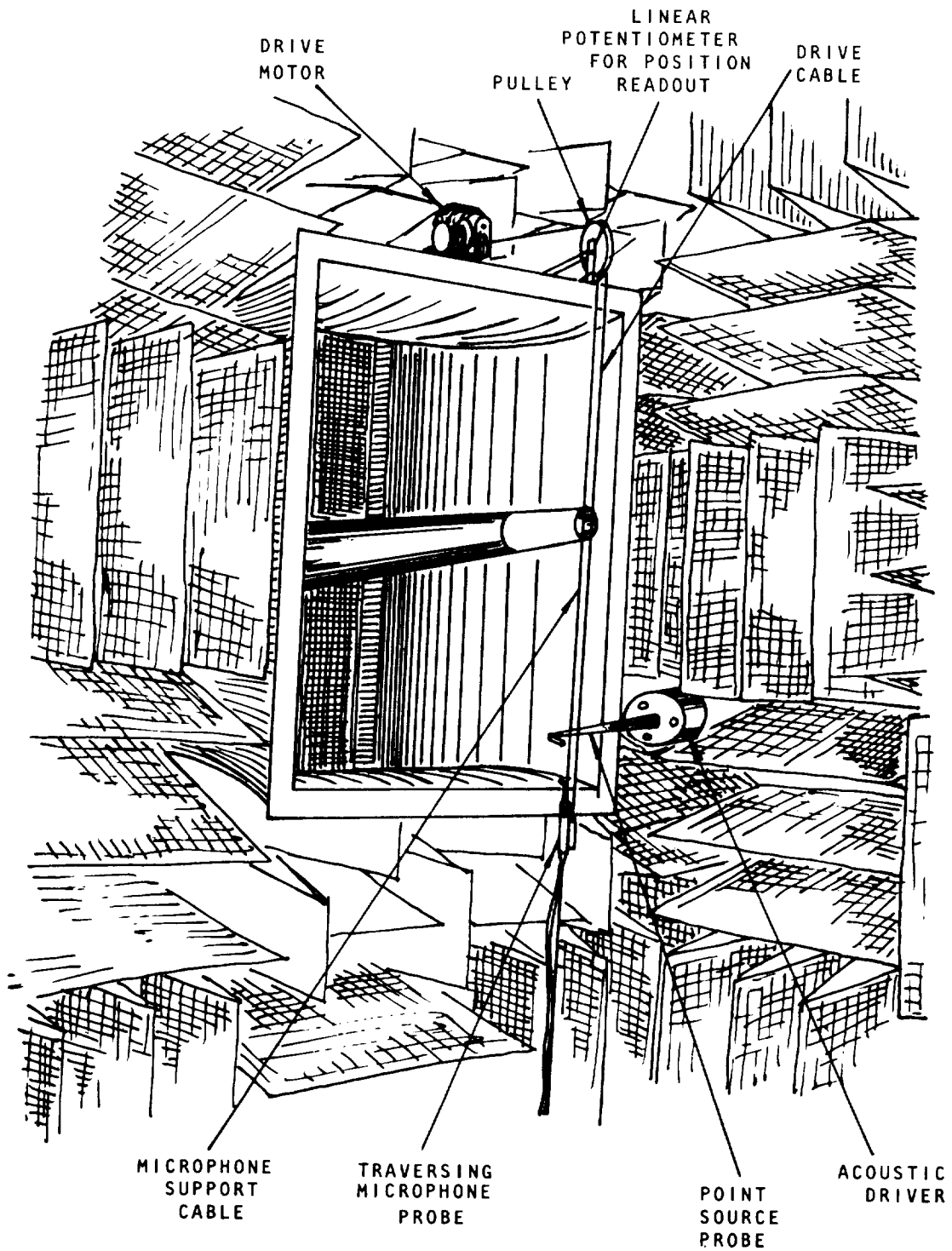
Figure 2.17   Sketch of point source and microphone traversing
mechanism located in free jet.
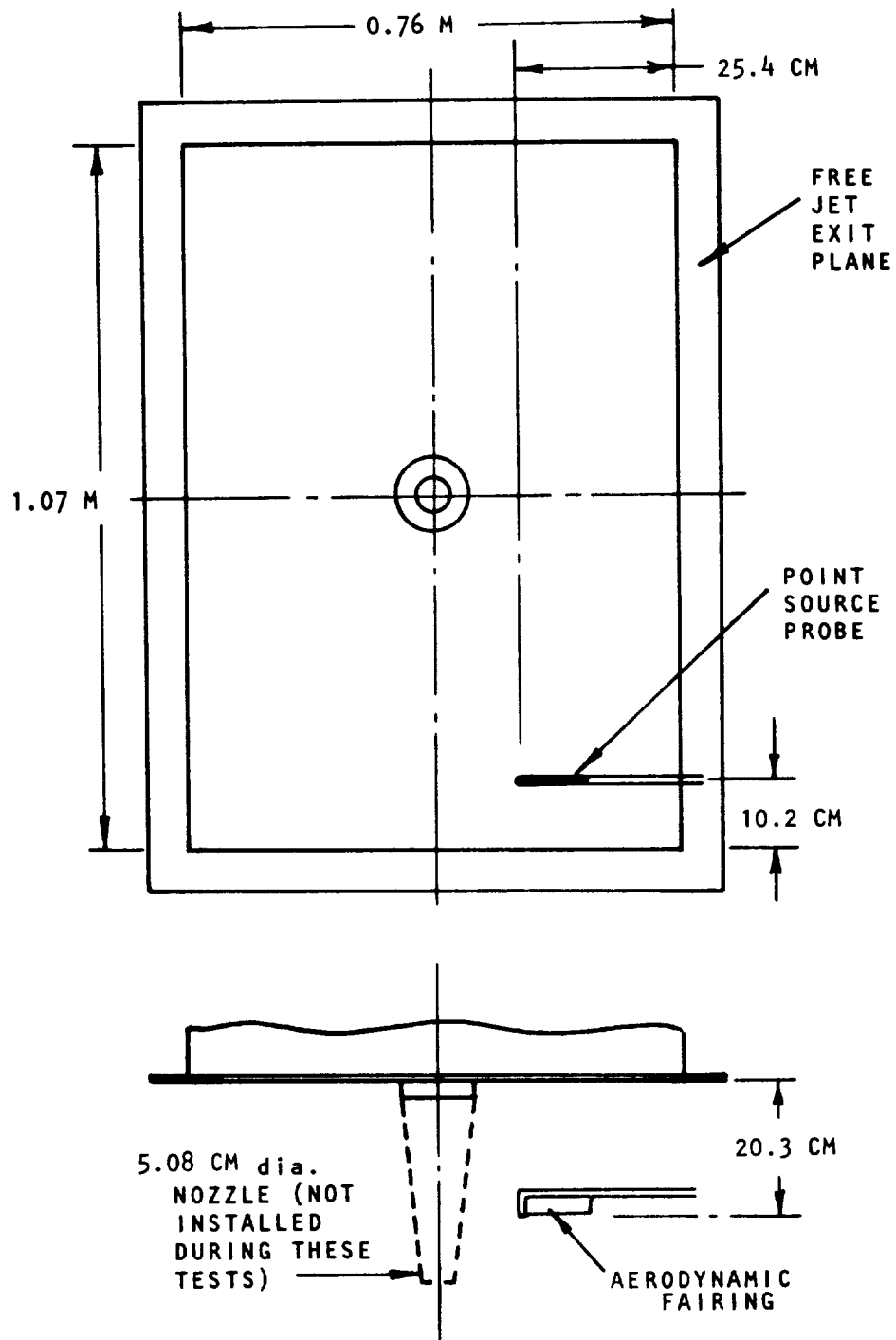
Figure 2.18 Schematic showing location of point source.
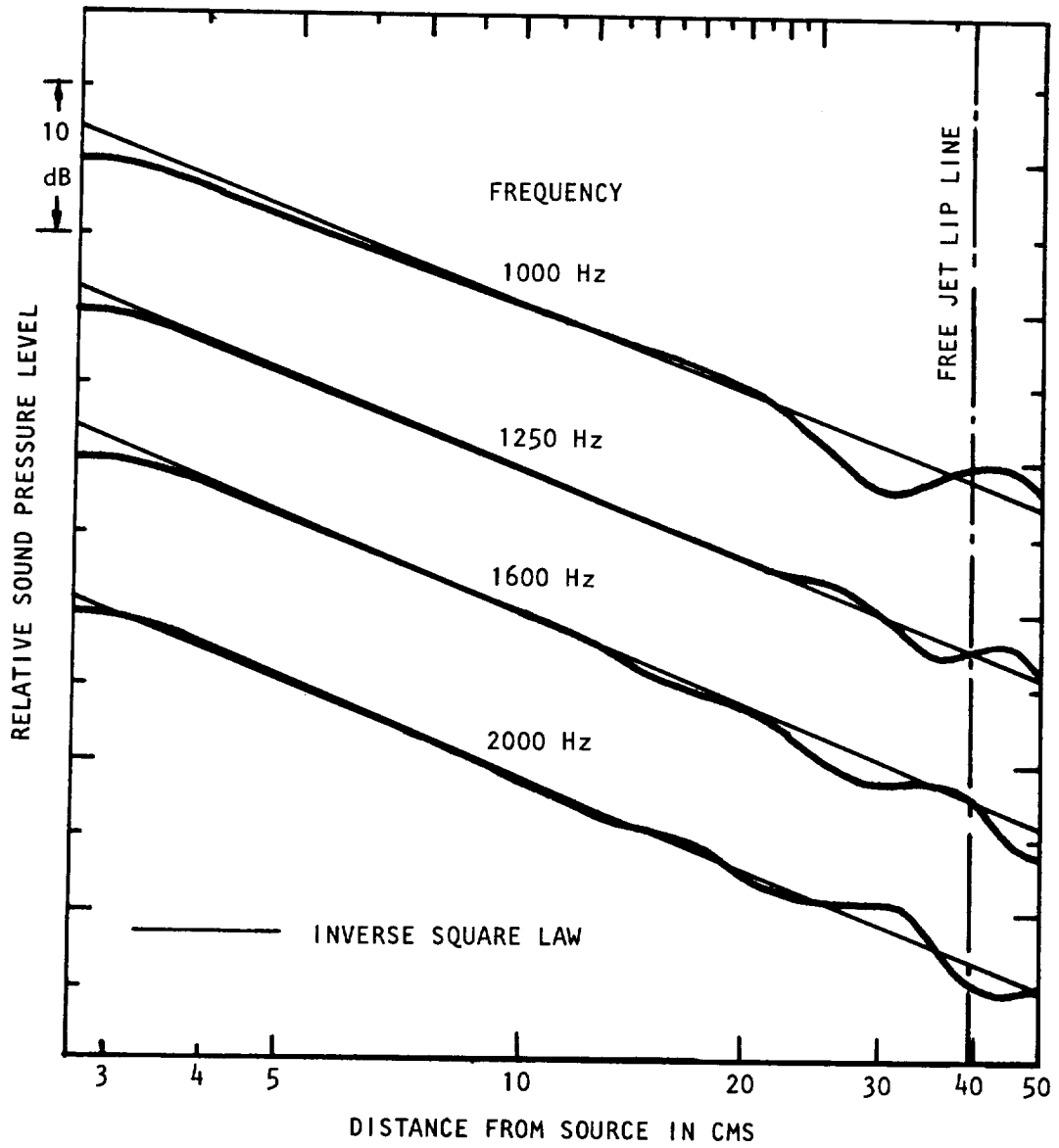
Figure 2.19 Variation of SPL with distance from point source
for discrete frequency excitation.
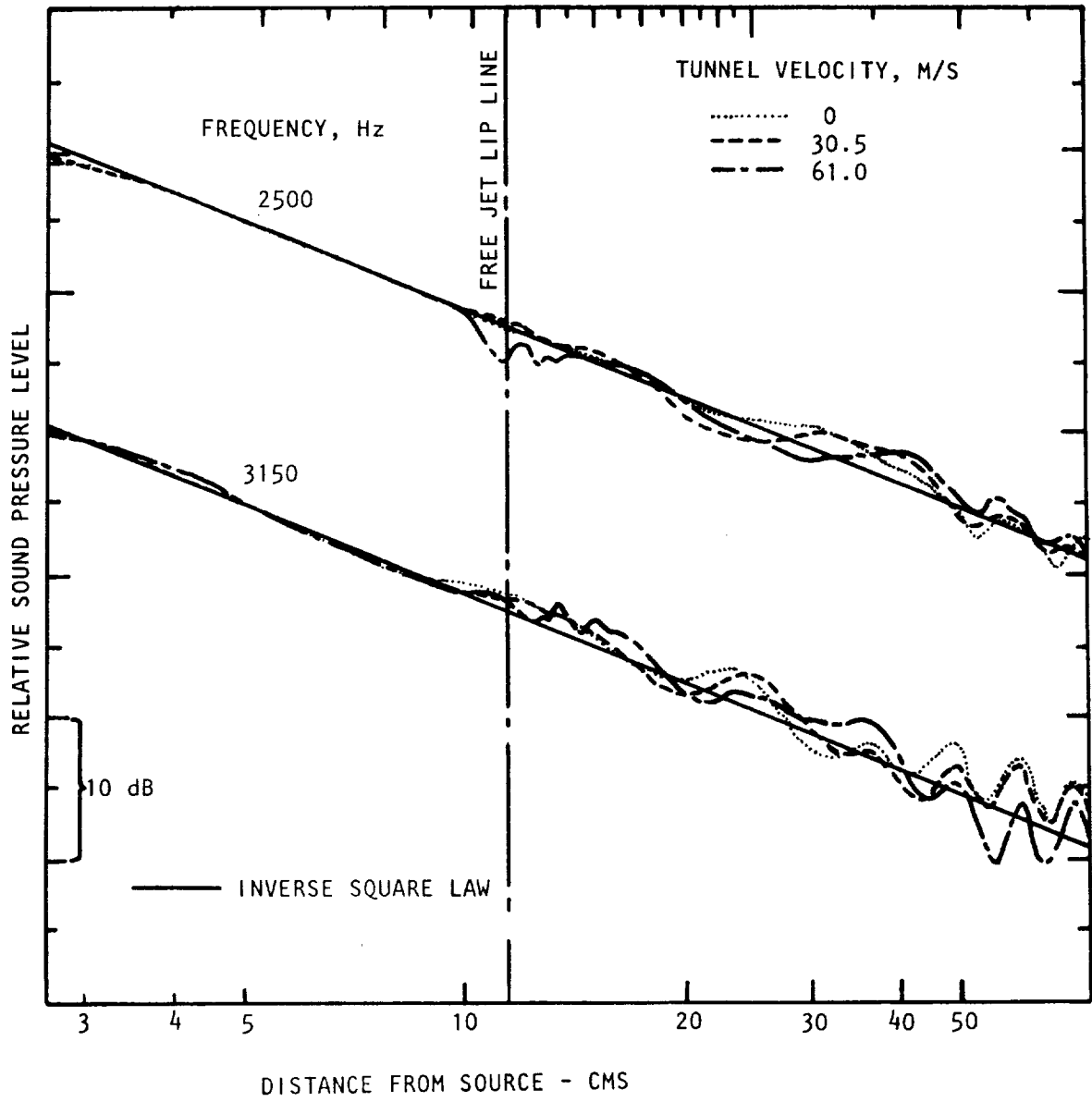
Figure 2.20   Effect of free-jet velocity and source frequency on
sound transmission through free-jet shear layer.

34

If, however, the data were examined on either side of the mixing region, some general observations could be made. First, no detectable internal reflections were observed. On the outside, some small variations in level, admittedly influenced by a reflected wave field, were detected. Due to the surface reflection problem, no specific conclusion could be derived for this region. Thus, the only significant conclusion gleaned from this test was that internal reflections at the 90° angle were not a problem, as expected from the vortex sheet model.

Another potential problem with free-jet forward flight effects testing is the scattering of sound, generated within the potential flow region, as it propagates through turbulent eddies in the mixing layer. This problem has been analyzed by Mani (ref. 27), who looked at the change in directivity for a highly directive source. He showed considerable diffusion in the far field sound pressure directivity for frequencies as low as $\omega_0 r_s/a_0 = 4$ where in this case r_s was the radius of the source region. The magnitude of diffusive scattering was controlled by the parameter DR where R was the far-field radius and D was a diffusion constant which is defined as 1/4 of the mean square angular deviation of the ray, per unit length of the ray path, due to scattering. The diffusion constant is shown, for high frequency, to be approximately represented by

$$DR = M_t^2 \ (\omega_0 R/a_0) \ f(\omega_0 L/a_0)$$

where M_t is the turbulent Mach number and $f(\omega_0 L/a_0)$ is inversely related to the length scale of turbulence.

For values of $DR = 10^{-2}$ and 5×10^{-2} at frequencies $\omega_0 r_s/a_0 = 4$ and 8, the calculated diffusion is very significant and in some cases a very peaky angular distribution is diffused to the extent that it nearly appears to have originated from a point monopole. Thus, the diffusion or turbulent scattering problem is one which deserves attention in free-jet acoustic studies.

Another approach at examining the turbulent scattering problem considers spectral broadening of an original discrete frequency signal. As the discrete tone wavefront propagates through the turbulent eddies, the speed of propagation of the wave varies. This random variation in propagation speed along the wavefront results in a narrow-band random modulation in the amplitude and phase of the signal which manifests itself as spectral broadening. Many studies have been conducted in this area of research [Rudd (ref. 28), Brown and Clifford (ref. 29)]; however, experimental data on free-jet facilities have not been available until recently. Foley and Paterson (ref. 30) discuss a test in the United Aircraft anechoic free-jet facility. They display a test result for a 24,000 Hz signal propagating through the shear layer of their free-jet facility for 61.0 m/s tunnel velocity. Spectral broadening in this instance appears to be fairly significant although no quantification is given. They state that the effect is not significant until the wavelength is less than the integral scale of turbulence.

Because of source limitations it was not possible to conduct scattering tests above 5000 Hz. The source directivity was essentially spherical at that frequency, thus an examination of angular diffusion was not possible.

35

However, an examination of the frequency spectrum in the far-field was undertaken with and without flow. The spectrum was examined through a 2 Hz narrow band filter. A typical result at 5000 Hz and 52.5° angle to the jet axis is shown in Figure 2.21, first for no flow and then at 61.0 m/s tunnel velocity, for a source positioned 10.2 cm above the lip line and 20.3 cm downstream. At 20.3 cm. in this facility, the integral scale of turbulence corresponded approximately to wavelengths of 1.3 cm to 3.8 cm or frequencies of 8000 Hz to 24,000 Hz at the position where the ray propagated through the mixing layer. Examination of the two narrow band spectra shows that there is no detectable difference and in fact further examination shows that the spectral shape is that of the 2 Hz filter.

Thus, it can be confirmed that at wavelengths greater than the scale of turbulence, spectral broadening is not a problem in free-jet facilities. Further work is required, however, for higher frequencies.

2.4 EXPERIMENTAL PROGRAM AND PROCEDURE

The influence of forward motion on unheated jet exhaust noise was examined in the present program by measuring the turbulent mixing noise in the far field from three 5.08 cm diameter nozzles, operated in the anechoic free-jet facility. The free jet to nozzle area ratio was 400. The nozzles employed were the $M = 1$ convergent nozzle, and the $M = 1.4$ and 1.7 convergent-divergent nozzles. In order to avoid the contamination of data from shock-associated noise, these latter were operated at their design pressure ratios only. Nine microphones were placed on an arc of radius 2.74 m $(R/d = 54)$, centered at the nozzle exit plane. The measurement angles were $\theta_m = 30° (7\frac{1}{2}°)$ 90° relative to the downstream jet axis.

The experimental program was carefully planned to yield results at (1) constant jet efflux velocity (V_J/a_o) with varying tunnel velocity (V_T/a_o), and (2) constant tunnel velocity with varying primary jet velocity. Forty test conditions (combinations of V_J/a_o and V_T/a_o) were initially chosen. The *nominal* values of jet exit velocity and tunnel velocity were

$$V_J/a_o = 0.4, \ 0.5, \ 0.6, \ 0.7, \ 0.8, \ 0.9, \ 1.17 \text{ and } 1.345 \text{ (8 values)};$$

$$V_T/a_o = \text{minimum}, \ 0.05, \ 0.10, \ 0.15 \text{ and } 0.20 \text{ (5 values)}.$$

The minimum tunnel velocity, V_{TO}, is defined as the tunnel velocity which is provided by the ejector action of the primary jet in the absence of any additional velocity supplied by the facility ejector itself. Its magnitude, therefore, increases as V_J/a_o increases.

For each combination of V_J/a_o and V_T/a_o, the static pressure ratio p_R/p_T was determined by using the analysis developed in Appendix 2B. The values of various parameters defining the test conditions are tabulated in detail at the beginning of Appendix 2C.

36

NO TUNNEL FLOW

dB RE. PEAK VALUE

$V_T = 61.0$ M/S
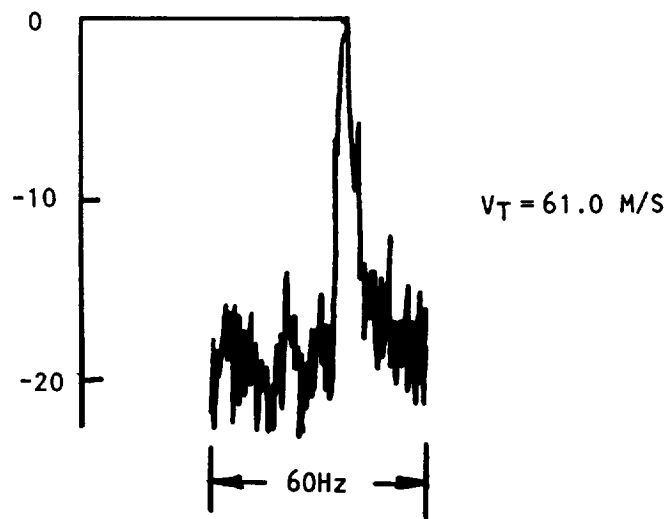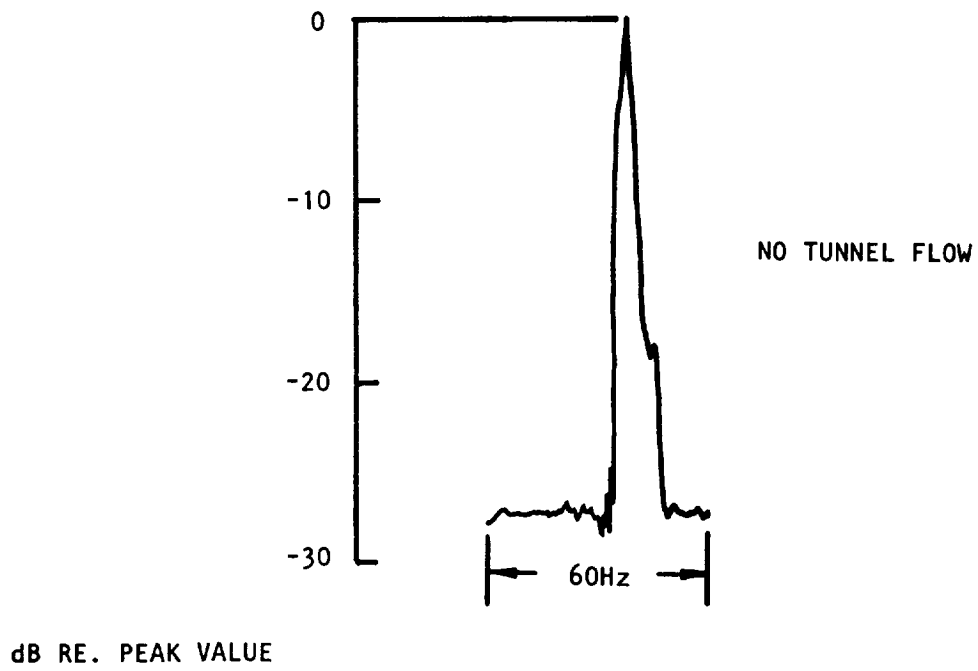
Figure 2.21 Effect of propagation through shear layer
on spectrum shape of discrete tone source
of 5000 Hz discrete frequency for narrow
band (2 Hz filter) spectra measured in
far-field at 52.5° to jet axis.

2.4.1 Test Procedure

The quantities to be measured in setting up the test conditions are defined in the sketch shown in Figure 2.22. In order to set the experiment at the desired combination of V_J/a_o and V_T/a_o (for the convergent nozzle) or M_J and V_T/a_o (for the two con-div nozzles), the following sequence was adopted:

Tunnel:

1. Specify V_T/a_o
2. Read p_o, T_o
3. Calculate a_o (= a_T)
4. Calculate V_T
5. Compute $(p_1 - p_T)$ using tunnel calibration computer program on HP-65
6. Set tunnel at $(p_1 - p_T)$ to obtain desired V_T/a_o

Jet:

7. Specify V_J/a_o or M_J
8. Compute p_R/p_T using relationships derived in Appendix 2B
9. Read p_T
10. Calculate p_R
11. Set jet at p_R to obtain desired V_J/a_o or M_J
12. Check if $(p_1 - p_T)$ has altered, and adjust if necessary.

During each test, all pressure and temperature measurements were recorded; subsequent to the test program, these measurements were used to compute the exact jet and tunnel operating conditions, which are tabulated in Appendix 2C, for every test conducted.

2.4.2 Data Acquisition

In the present experimental program, nine 12.7 mm. B&K microphones Type 4133 with FET cathode followers Type 2619 were mounted on the microphone arc at $7\frac{1}{2}°$ intervals from $30°$ to $90°$ to the downstream jet axis. The responses were recorded simultaneously on a 14-channel Honeywell FM tape recorder at 305 cm/s. In order to obtain the 1/3-octave spectrum from 200 Hz to 40 KHz using a Hewlett-Packard real time 1/3-octave audio spectrum analyzer, the tape speed was reduced to 76.25 cm/s on playback. The 1/3-octave levels were then recorded on an incremental tape recorder for subsequent detailed analysis using a data reduction program developed for use on the Univac 418 digital computer. This program incorporated the microphone frequency
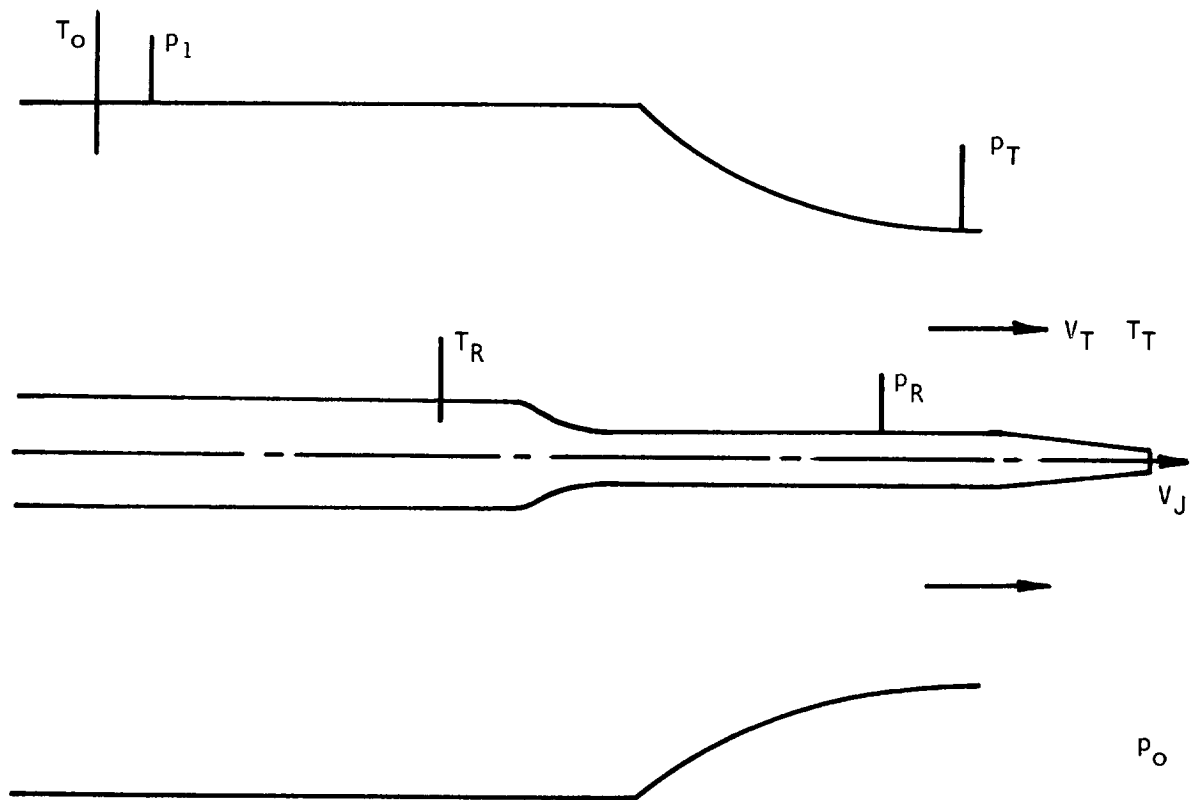
ASSUMPTION: $T_R = T_o = T_T \rightarrow a_o = a_T$

MEASUREMENTS:

T_o	TUNNEL INTAKE TEMPERATURE
T_R	UPSTREAM (OR PLENUM) JET TEMPERATURE
P_1	TUNNEL INTAKE STATIC PRESSURE (PIEZOMETER)
P_T	TUNNEL NOZZLE STATIC PRESSURE (PIEZOMETER)
P_R	UPSTREAM (OR PLENUM) STATIC PRESSURE
P_o	AMBIENT PRESSURE IN ANECHOIC ROOM

Figure 2.22 Measurements for setting test conditions.

response corrections and atmospheric absorption corrections. The results were finally displayed in the form of tabulated one-third octave band sound pressure levels over the frequency range from 200 Hz to 40 KHz, and the overall levels were also computed over this frequency range.

2.4.3 Data Quality

All acoustic data acquired in the present experimental program were carefully scrutinized in order to ensure that the results which are selected for detailed analysis would not be contaminated to any significant extent by contributions from any other noise sources. The data from the entire test program are given in Appendix 2C for future reference. In using these data, the following points *must* be considered at all times:

(1) There is no significant contamination from rig internal noise sources, as established in Section 2.3.3.

(2) The two major sources of extraneous noise are the tunnel background noise and the measuring instrumentation electronic noise. As expected, the influence of these sources is maximum for low V_J/a_0, high V_T/a_0 test conditions. In general, when present, the effect of background noise is noticeable at low frequencies, whereas the presence of instrumentation noise results in a slight lift in the spectrum levels at the high frequency end.

(3) Although the supersonic nozzle calibration tests (shadowgraph tests) revealed no significant shock pattern in the jet flow at design pressure ratios for all nozzles, close examination of the acoustic data indicates that in the case of the $M = 1.4$ nozzle, the spectra are slightly contaminated by shock-associated noise at the higher frequencies. This indicates slight imperfections in the machining of the nozzle contour.

(4) At high tunnel velocities, the spectra measured by the $\theta_m = 30°$ microphone are affected by the air-flow generated noise over this microphone as described in Section 2.3.2.1.

(5) The spectra measured at $\theta_m = 75°$ contain a slight ripple due to room reflection, which was not detected in the earlier acoustic calibration tests. However, this effect is consistently present, and therefore it does not influence the final conclusions derived from the data analysis.

The results which are presented in the rest of this report are essentially free from any of the above limitations; hence, any conclusions or scaling laws derived from them are considered to be accurate.

One further point regarding data presentation needs to be made here. Although the measured spectra contain minor variations in level about the mean variation from one 1/3-octave band to the next, the spectra presented in this report are shown as continuous spectra, purely for convenience. A typical example, showing the actual measured 1/3-octave band levels and the corresponding continuous spectrum, is presented in Figure 2.23. It can be observed that the presentation of data in this fashion takes no unjustifiable liberty, and indeed it simplifies the spectrum plot considerably,

40

$V_J/a_o = 0.9$
$V_T/a_o = 0.15$
$\theta_m = 60°$

1/3 OCTAVE CENTER FREQUENCY

1/3-OCTAVE SPL — dB (REL. 2×10^{-5} N/m^2)
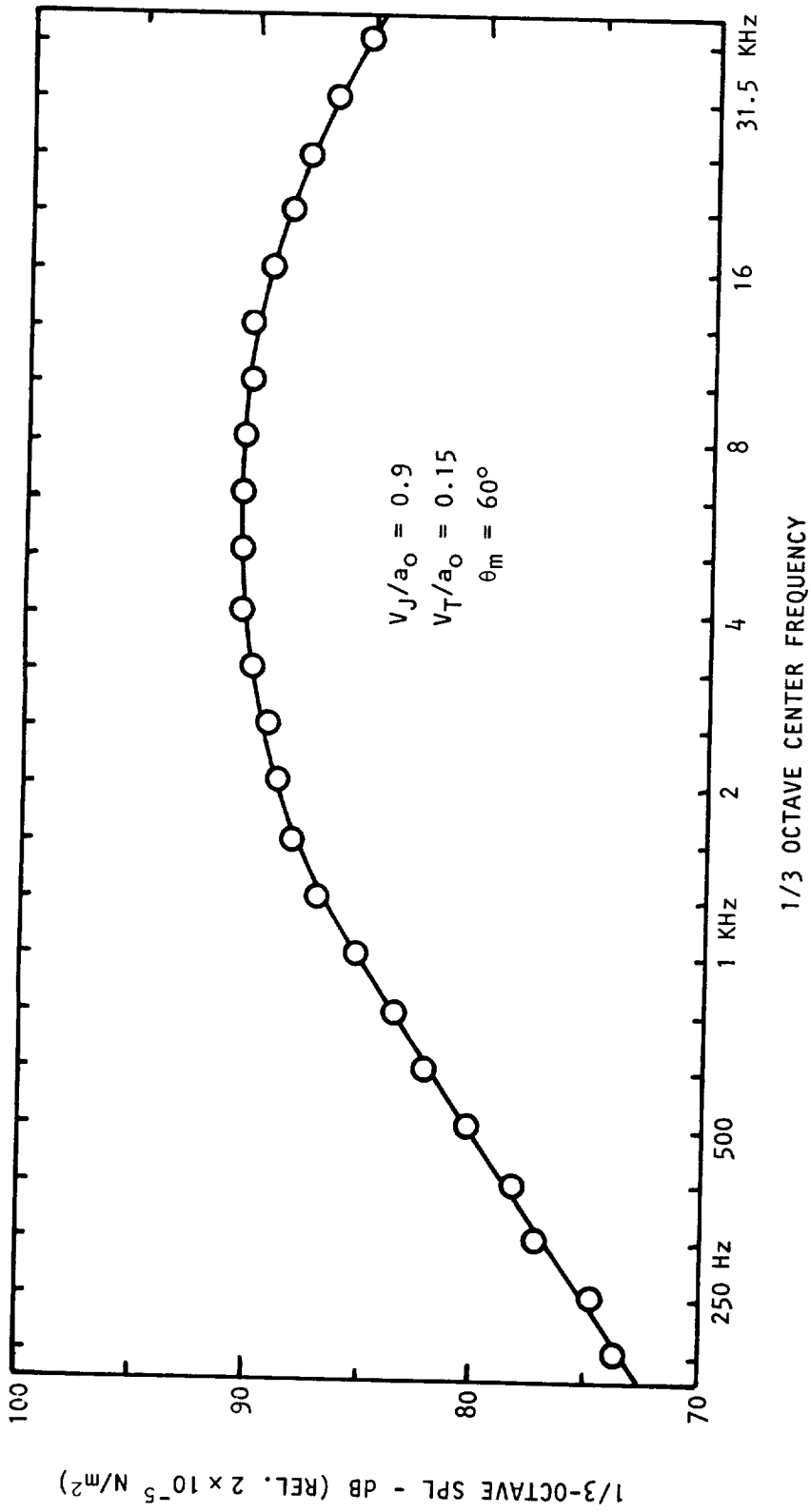
Figure 2.23 Typical spectrum smoothing.

especially when it is necessary to plot several closely spaced spectra on the same figure.

2.5   MEASURED (OR UNCORRECTED) RESULTS

The turbulent mixing noise results from the inflight simulation experiments, conducted in the anechoic free-jet facility, are first presented without applying any facility corrections. These corrections were mentioned briefly earlier, and their magnitudes as well as the correction procedure are derived in the present program in Section 3.1. The corresponding corrected results will be presented and discussed in the next section. The major effects of forward motion on the directivity and spectral characteristics of turbulent mixing noise, derived from the uncorrected results are discussed below.

2.5.1   Overall SPL Results

The influence of tunnel velocity (V_T/a_0) on the directivity of overall SPL at various jet efflux velocities (V_J/a_0) in the wide range from $V_J/a_0 = 0.4$ to 1.345 is shown systematically in Figure 2.24. It should be noted that the angle θ_m is the *measurement* angle relative to the downstream jet axis, and not the *emission* angle. For a fixed measurement angle θ_m, the angle at which sound was emitted from the jet, θ_e, varies as the tunnel velocity is varied. Conversely, in order to examine the changes in noise radiated at a fixed emission angle θ_e with increasing tunnel velocity, the measurement angle θ_m must be varied appropriately. The relationships between these two angles form a part of the correction procedure that will be described in section 3.1.

The directivities shown in Figure 2.24 contain remarkably little scatter. For a fixed value of jet velocity V_J/a_0, the directivities at increasing tunnel velocities appear virtually parallel at first sight. This observation agrees qualitatively with the results of the free-jet experiments conducted at NASA-Lewis (ref. 21). However, a closer examination also reveals that, in general, the reductions in OASPL with forward velocity are slightly angular dependent, being a little higher as the measurement angle approaches the jet axis.

In order to provide a quantitative description of the reductions in OASPL at all measurement angles considered, the results were correlated on the relative velocity $(V_{REL} = V_J - V_T)$ basis, as follows.

The overall intensity of turbulent mixing noise at measurement angle θ_m can be written to scale according to

$$I(\theta_m) \propto V_{REL}^m \, V_J^n \, , \tag{2-1}$$

where the exponents m and n are functions of θ_m. The corresponding OASPL is therefore given by

42
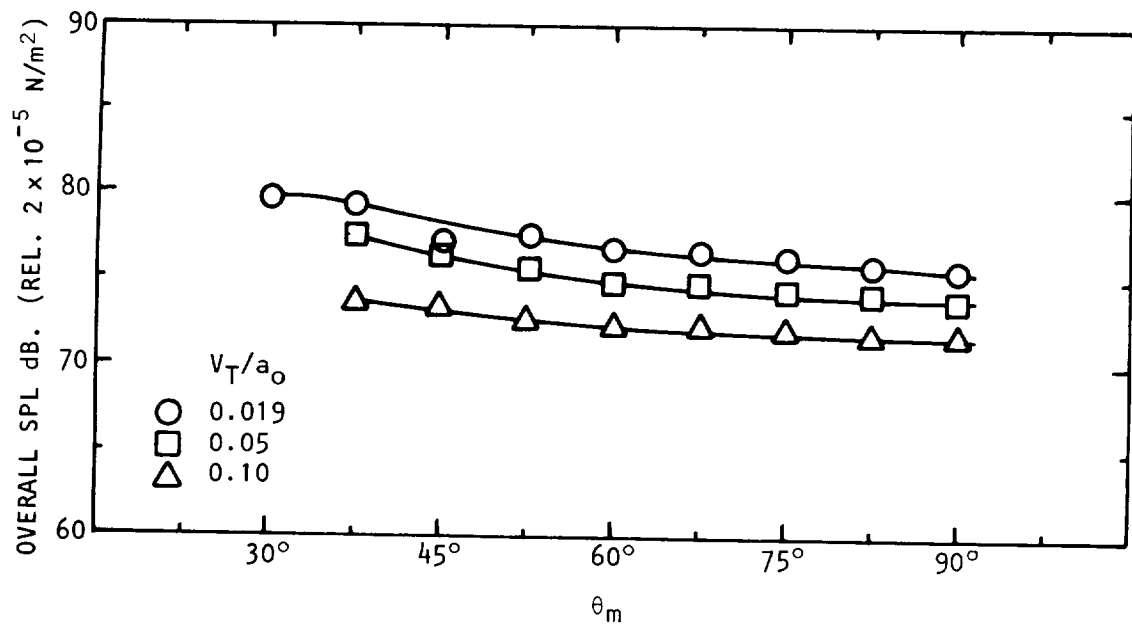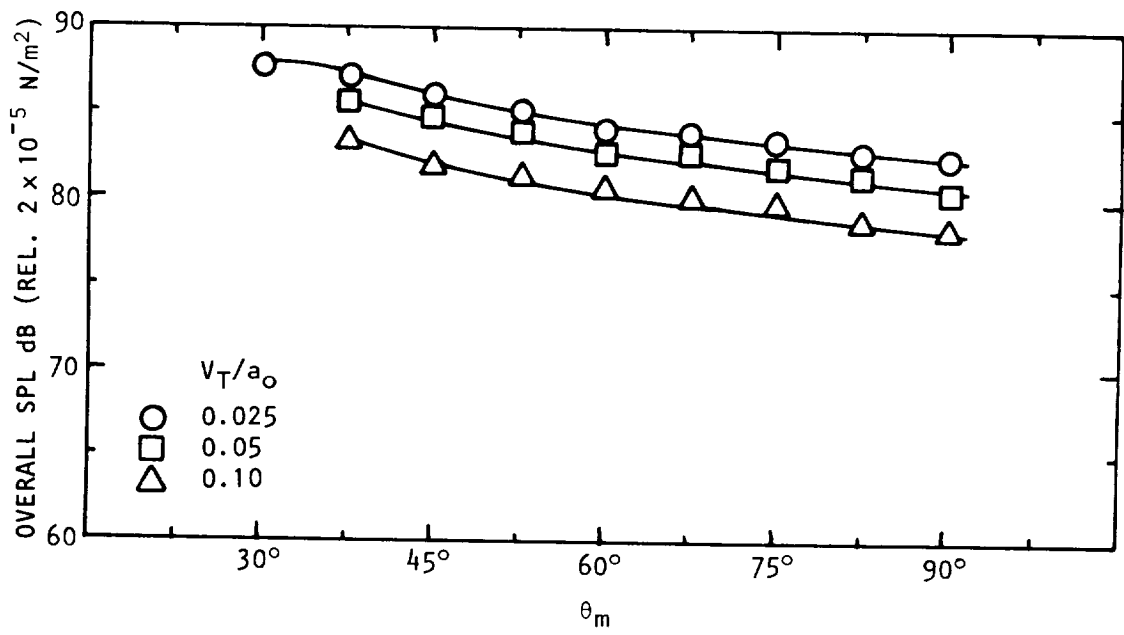
Figure 2.24 Effect of tunnel velocity on the directivity of measured (uncorrected) overall SPL at various jet exit velocities.

(c) $V_J/a_o = 0.6$
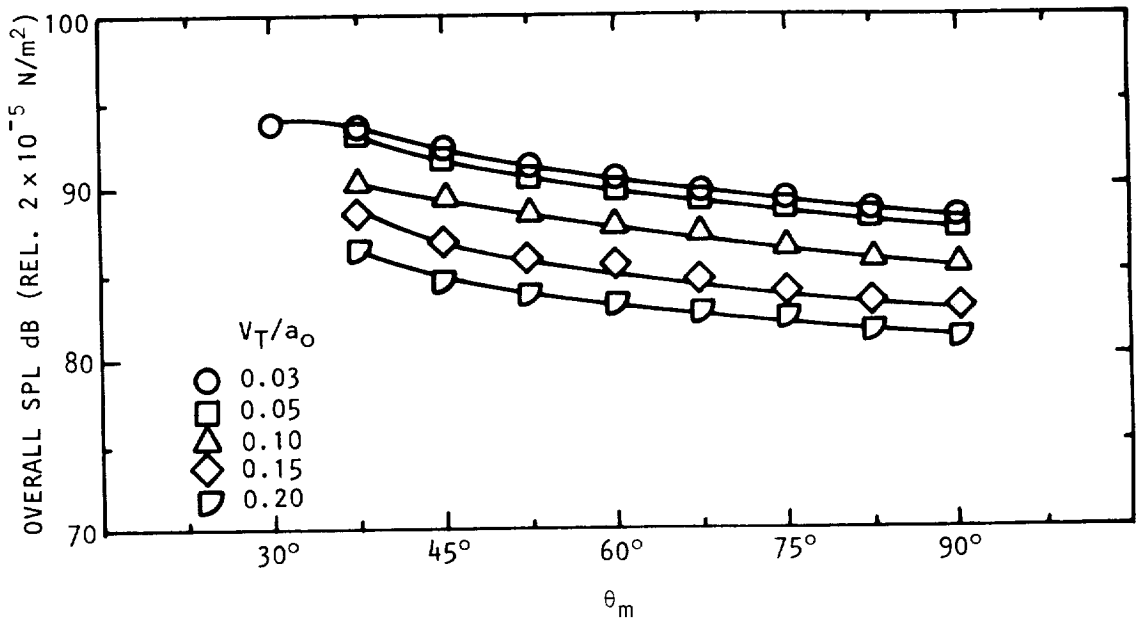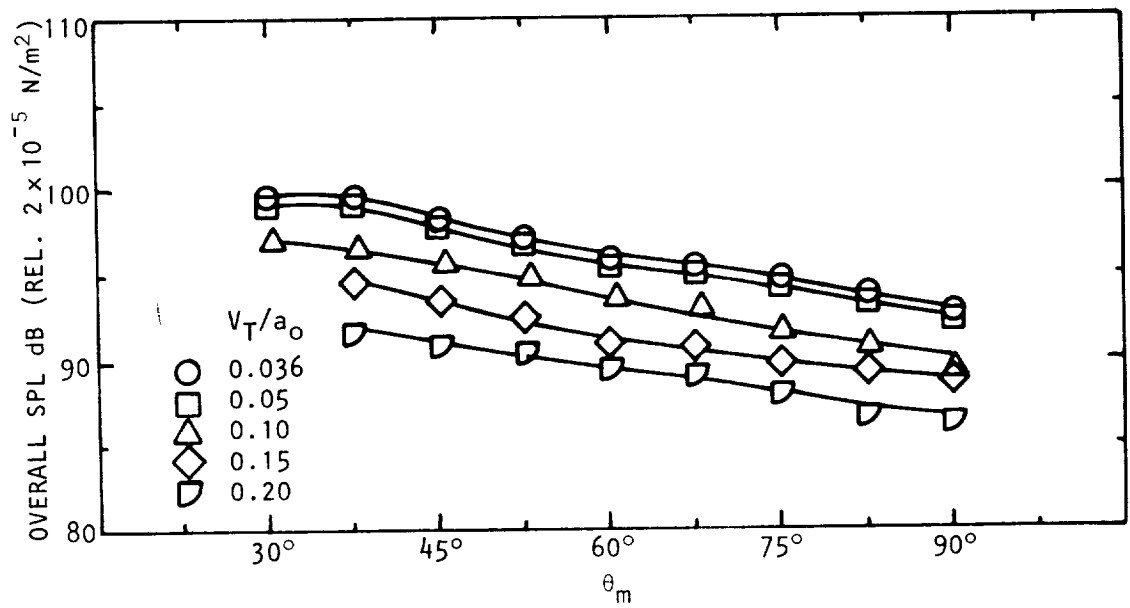
(d) $V_J/a_o = 0.7$

Figure 2.24 Continued.

(e) $V_J/a_o = 0.8$
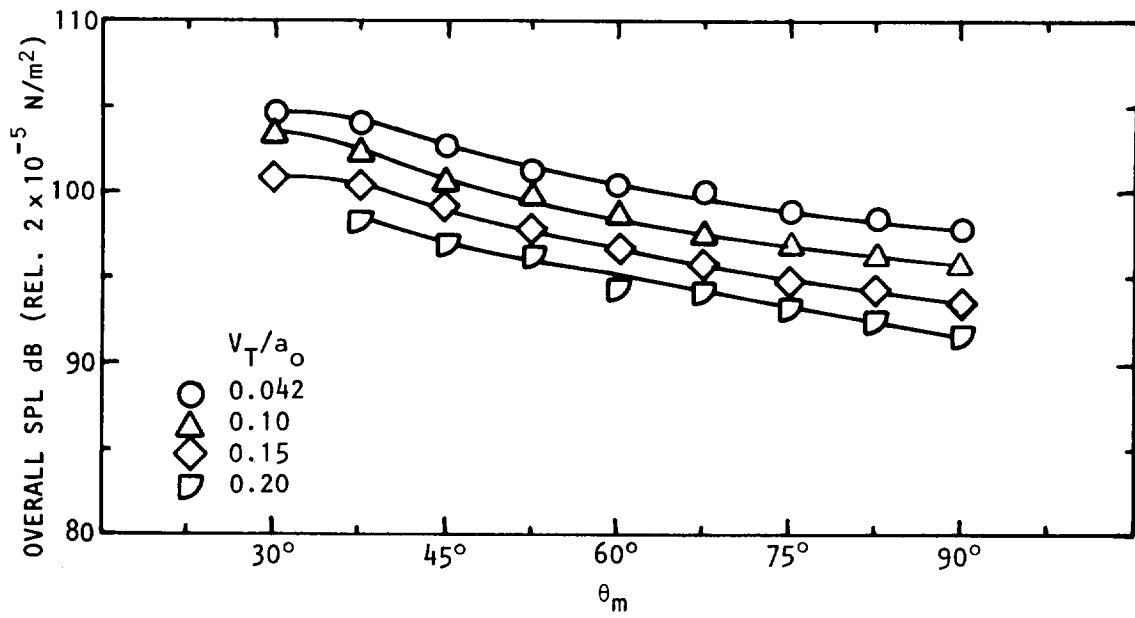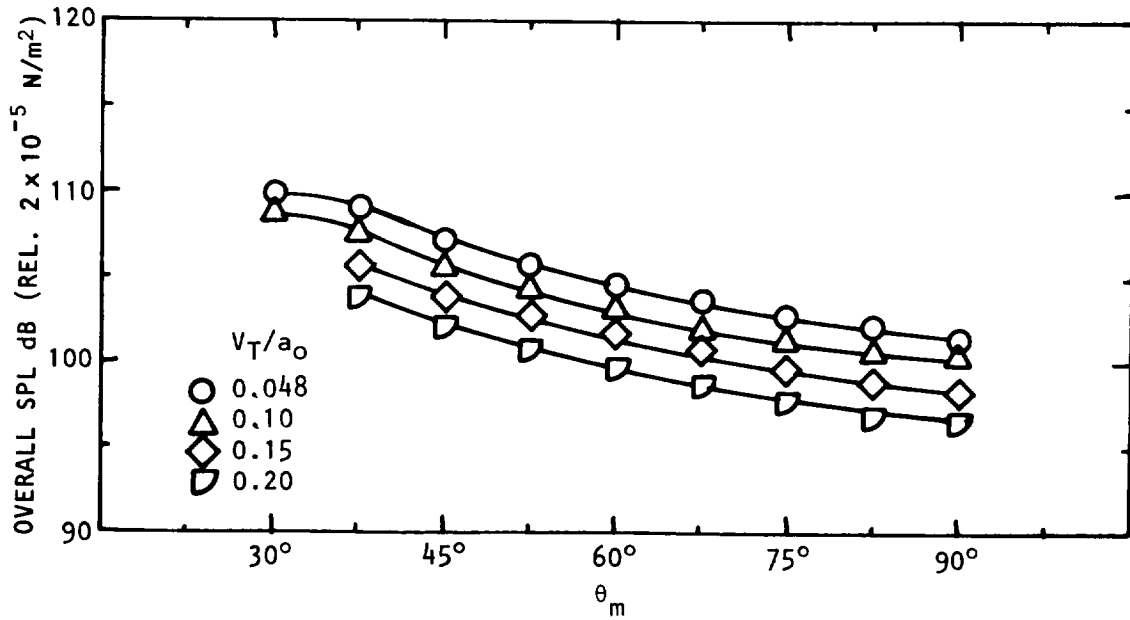
(f) $V_J/a_o = 0.9$

Figure 2.24 Continued.

(g) $V_J/a_o = 1.345$
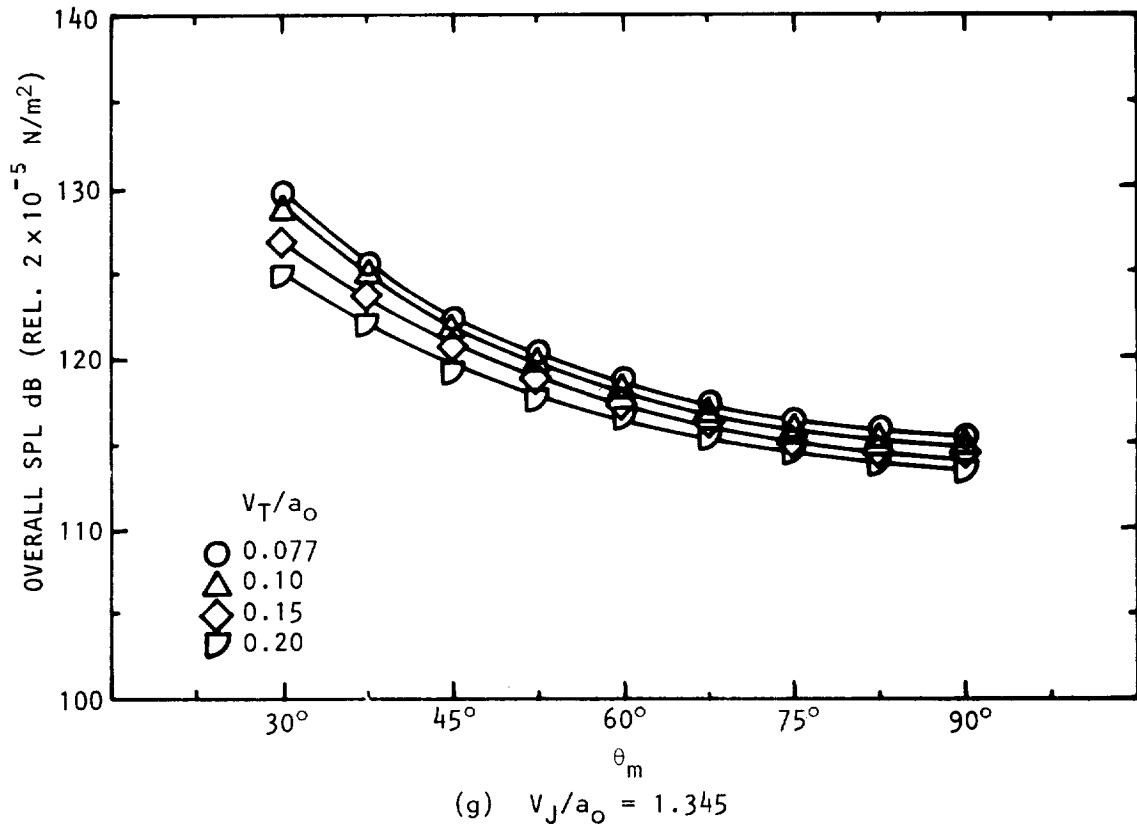
Figure 2.24 Concluded.

$$OASPL(\theta_m) \propto 10 \; \log_{10} \; [V_{REL}^m \; V_J^n] \; . \tag{2-2}$$

From the above scaling relationship, the reduction in OASPL from minimum tunnel velocity (V_{TO}) to any other tunnel velocity (V_T) can be written as

$$\Delta OASPL(\theta_m) = 10 \; \log_{10} \left| \frac{V_J - V_{TO}}{V_J - V_T} \right|^m \; . \tag{2-3}$$

The relative velocity exponent m is simply the slope of a graph which displays values of measured $\Delta OASPL$ as a function of the velocity parameter $10 \; \log_{10} \; [(V_J - V_{TO})/V_{REL}]$.

The measured overall noise reductions at all angles are plotted against the velocity parameter in Figure 2.25, and the relative velocity exponent line is drawn through the experimental points at each angle θ_m. The magnitude of the scatter is well within the bounds of the experimental accuracy, except at $\theta_m = 30°$, where, as mentioned previously, the air flow over the microphone produced undesirable pressure fluctuations in some cases.

Finally, the variation of the relative velocity exponent m with measurement angle θ_m is presented in Figure 2.26. Also shown in this figure are the values obtained from the free-jet experiments reported by Von Glahn, *et al* (ref. 21). It should be noted that the concept of relative velocity exponent does not provide any physical insight into the inflight effects on jet noise, except at 90° to the jet axis. It is used here merely to illustrate the good agreement between the present results and those from other free-jet experiments. The small differences seen in the figure are to be expected in view of the differences in the two facilities used.

2.5.2 1/3-Octave Spectral Results

The influence of tunnel velocity on the one-third octave spectra at three measurement angles ($\theta_m = 90°$, 60° and 37.5°) throughout the jet velocity range are shown in Figures 2.27, 2.28, and 2.29. The number of spectra presented in these figures is sufficient to provide a complete picture. It is recalled that some of the spectra do not span the entire frequency range from 200 Hz to 40 KHz due to reasons outlined earlier; that is, only those parts of the spectra which are not contaminated to any significant extent by background and/or instrumentation noise are considered.

At the measurement angle of 90°, the reductions in sound pressure levels with increasing tunnel velocity throughout the frequency range are consistent, resulting in virtually parallel spectra at a fixed value of V_J/a_0. It will be shown later that at this measurement angle, the values of corresponding emission angles at various tunnel velocities are not very different. Therefore, the observed reductions in the spectrum levels at $\theta_m = 90°$ provide a good indication of the changes in equivalent source strength with forward velocity. This reduction in source strength appears to be fairly independent of frequency. On the other hand, it is misleading to derive any conclusions
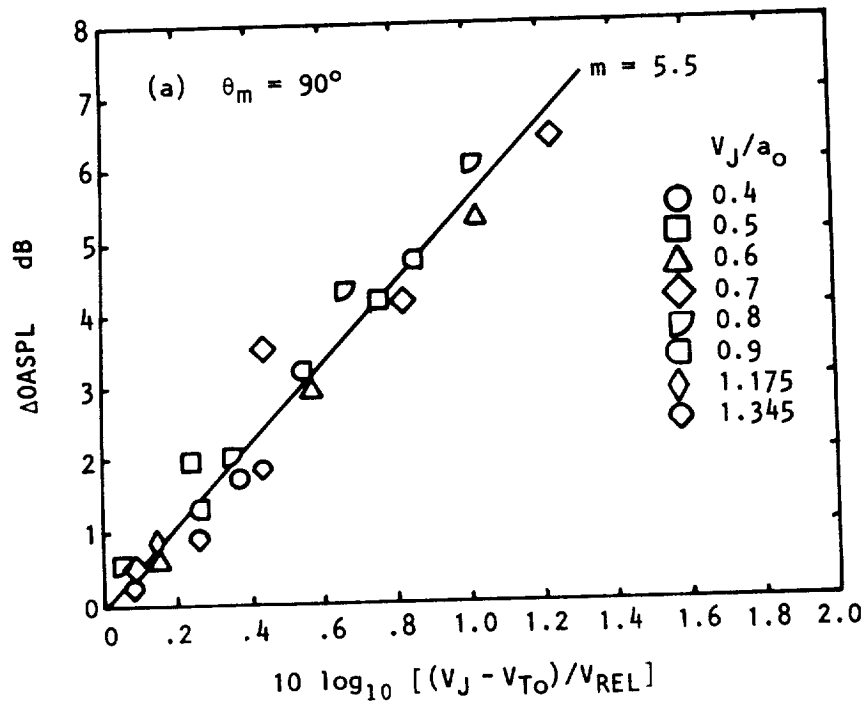
Figure 2.25   Relative velocity scaling of measured
(uncorrected) overall SPL reductions
at various measurement angles.
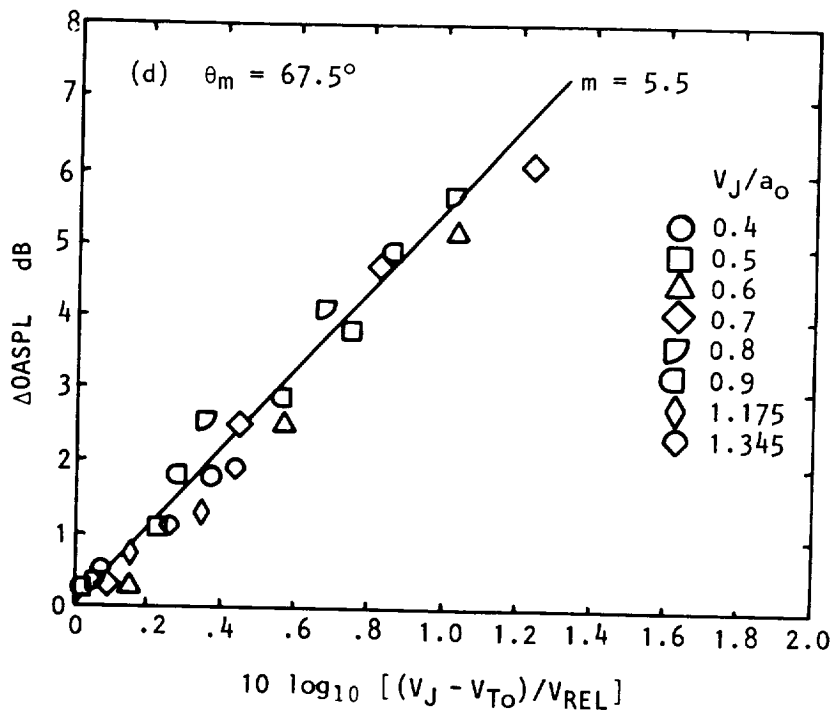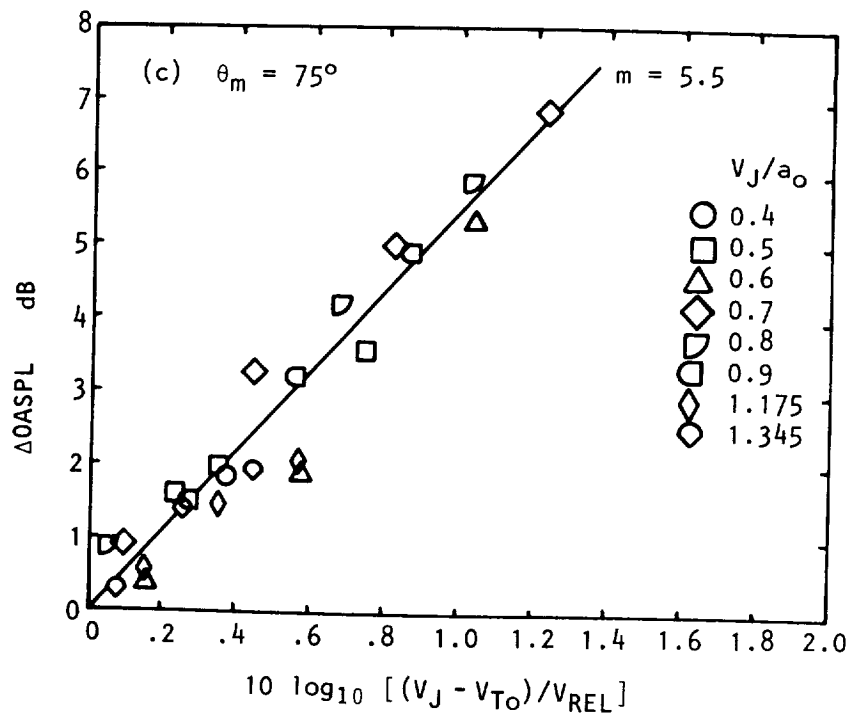
Figure 2.25 Continued.
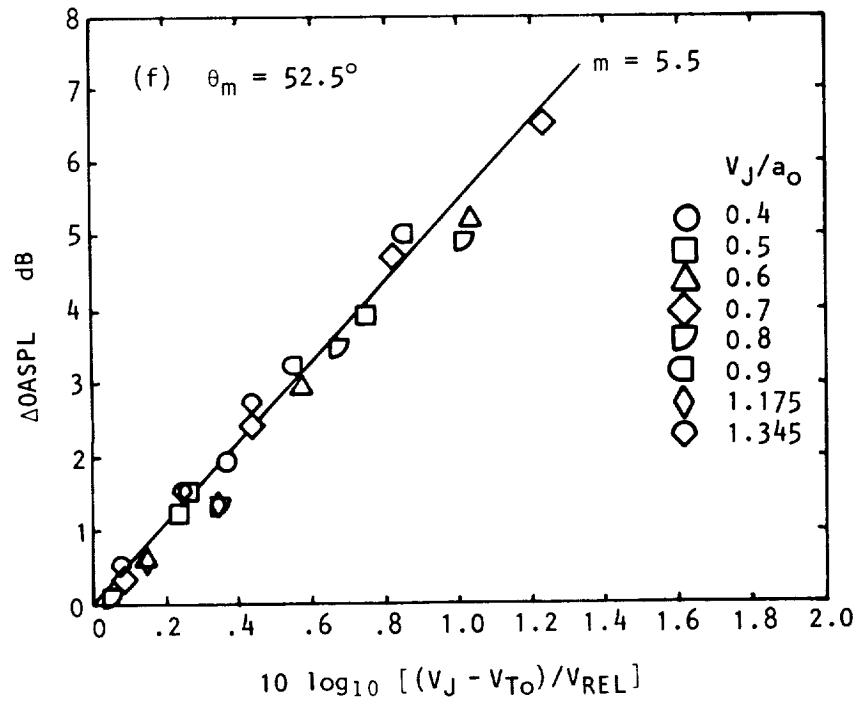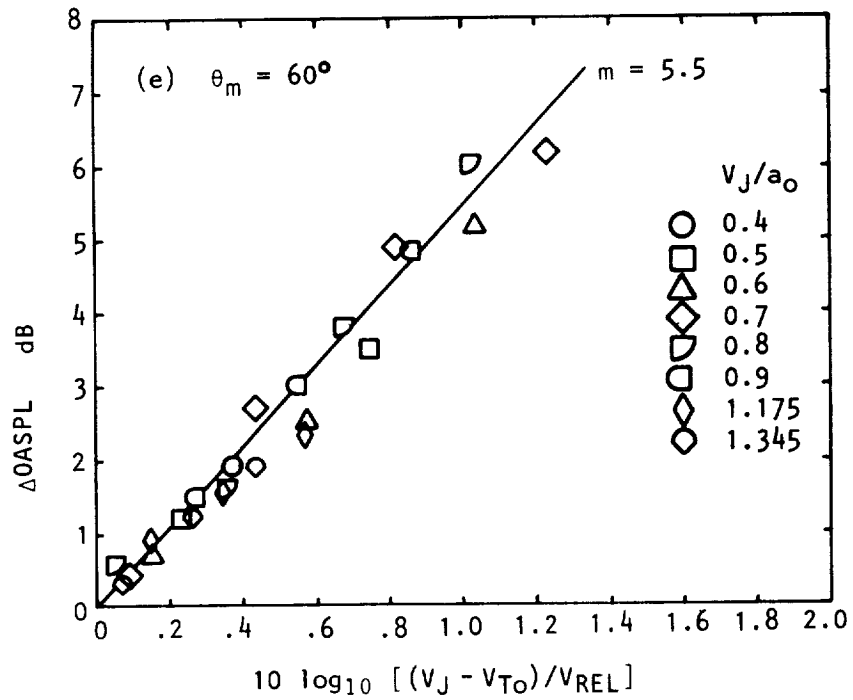
Figure 2.25 Continued.
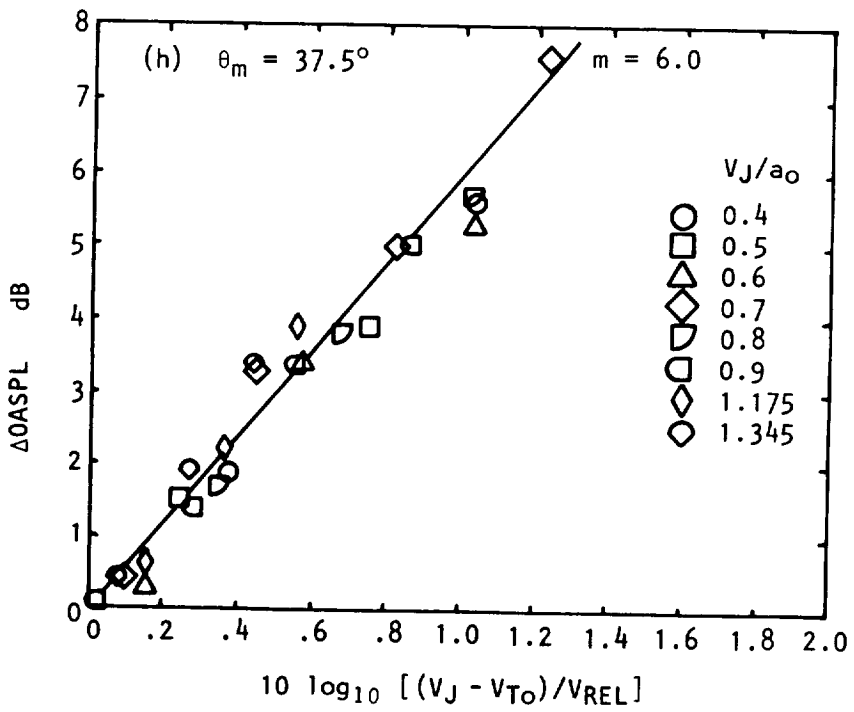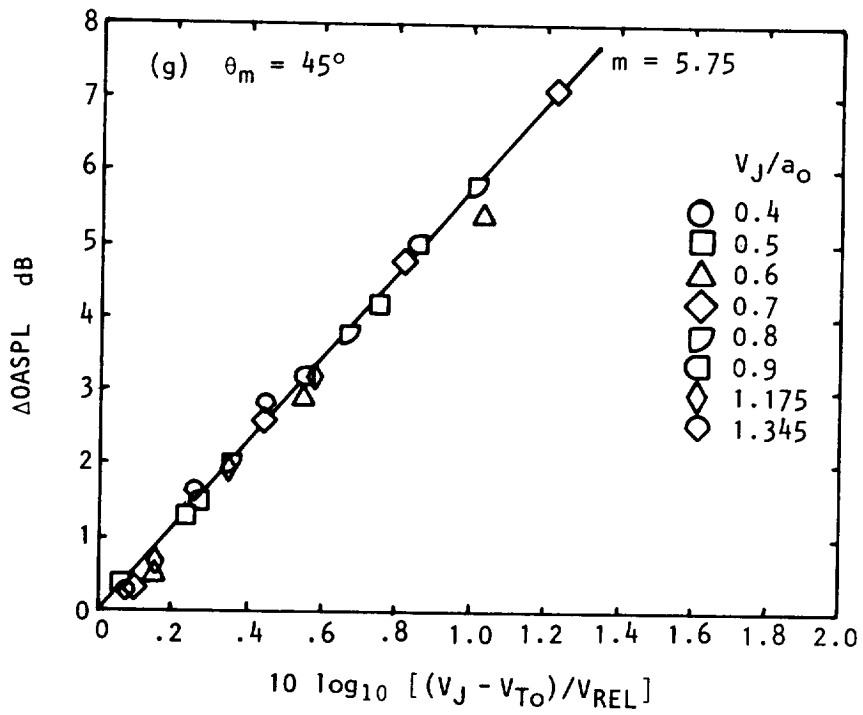
Figure 2.25 Continued.
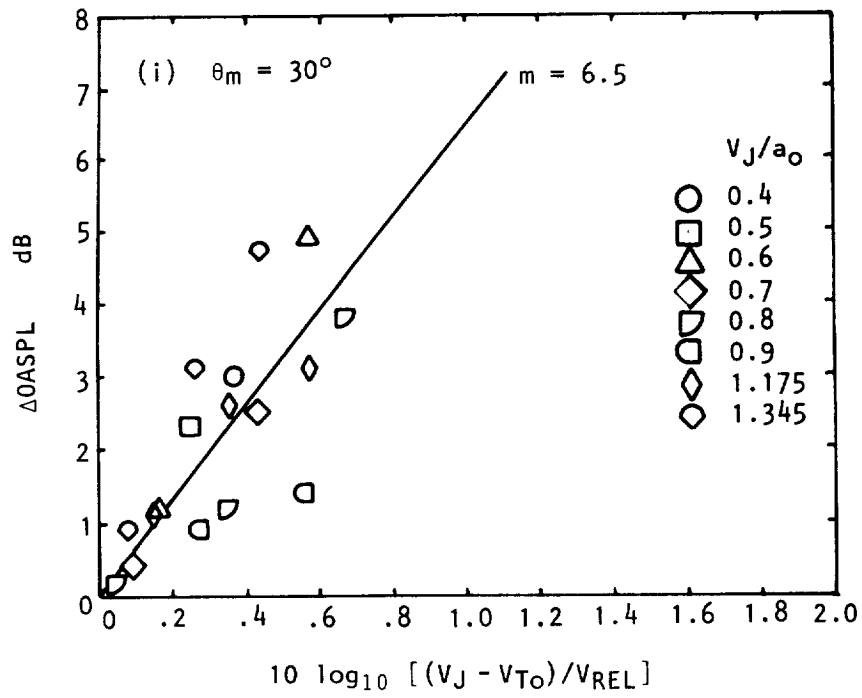
Figure 2.25 Concluded.
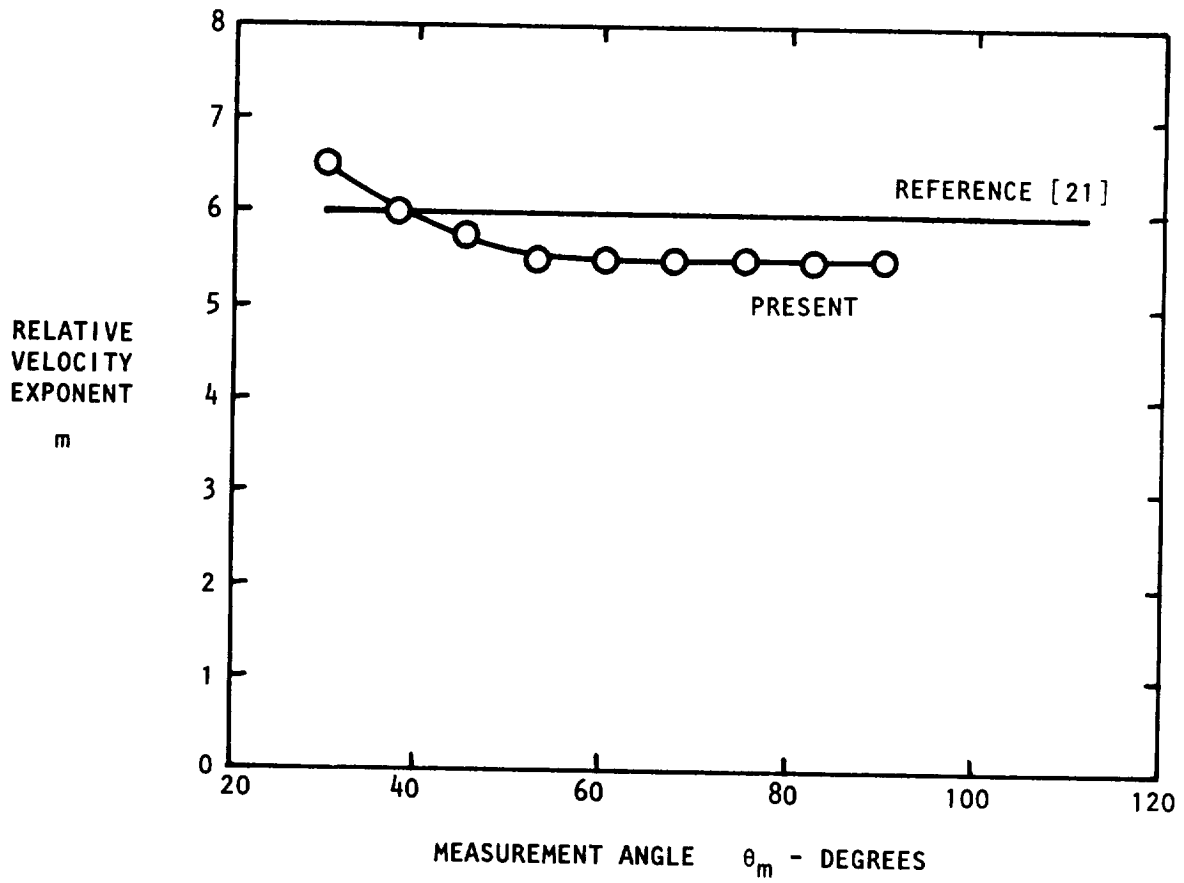
Figure 2.26 Relative velocity exponent from measured
(uncorrected) overall SPL results.
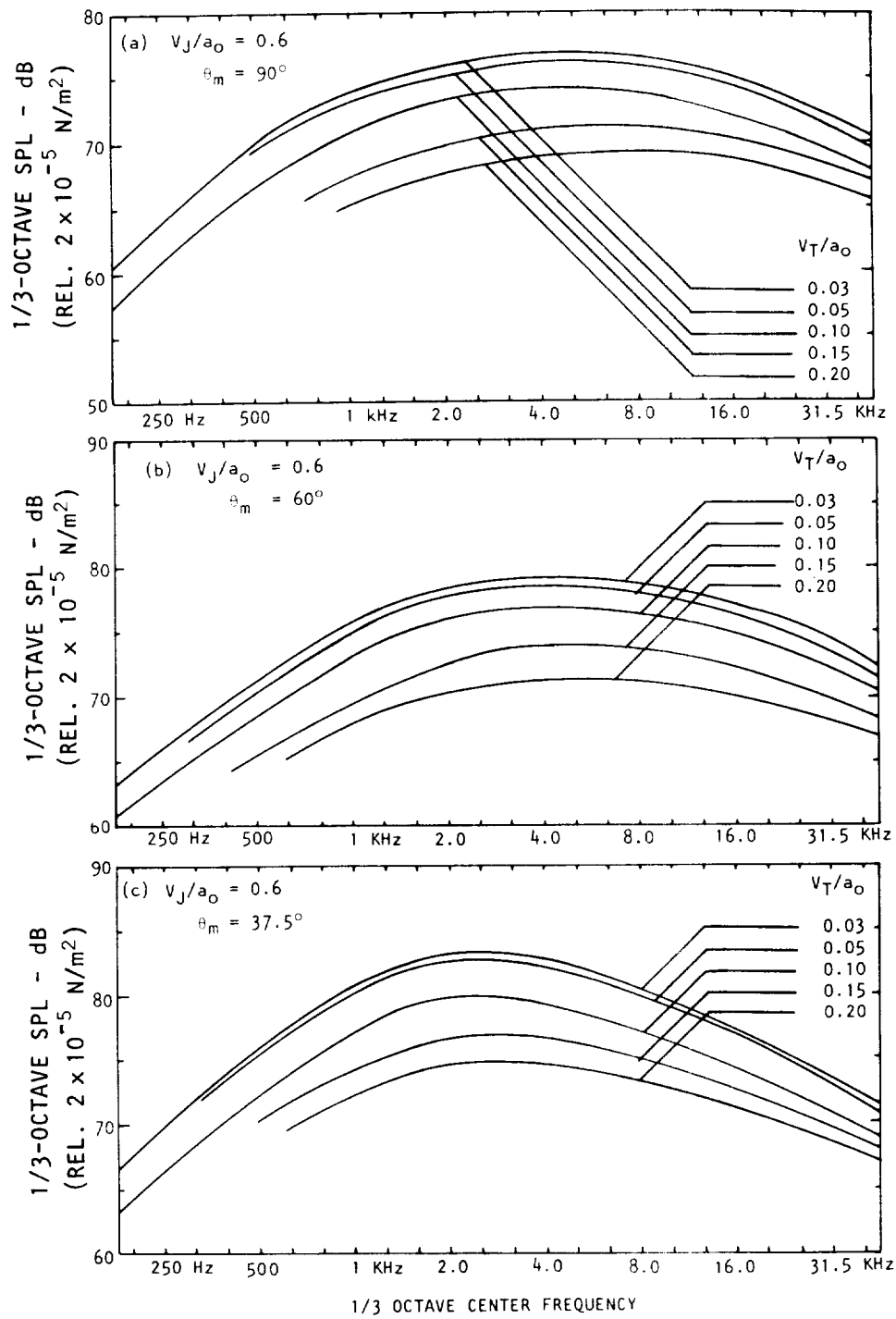
Figure 2.27 Effect of tunnel velocity on measured
(uncorrected) spectra at low jet
velocity ($V_J/a_o = 0.6$).
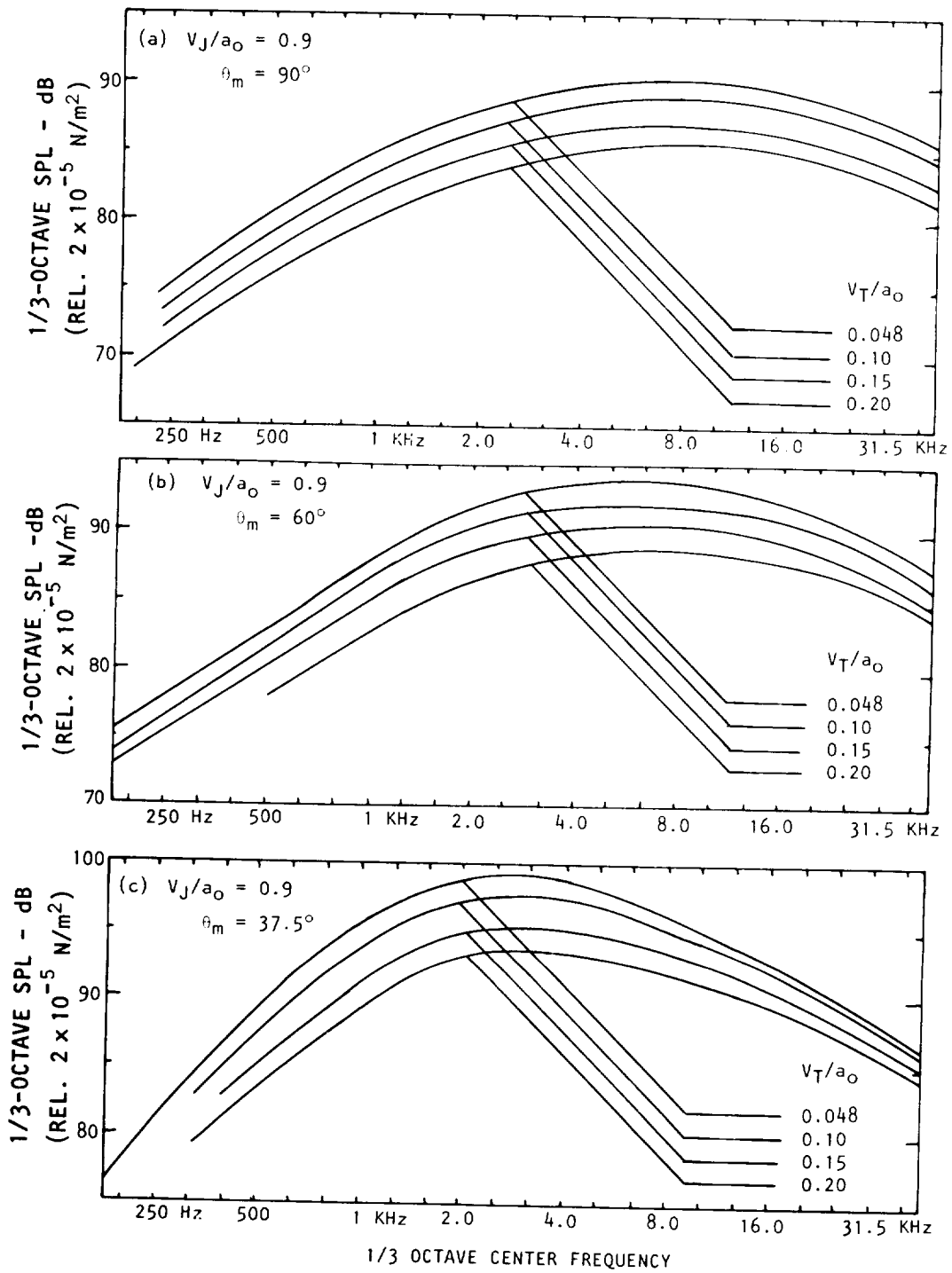
Figure 2.28 Effect of tunnel velocity on measured (uncorrected) spectra at medium jet velocity ($V_J/a_o = 0.9$).
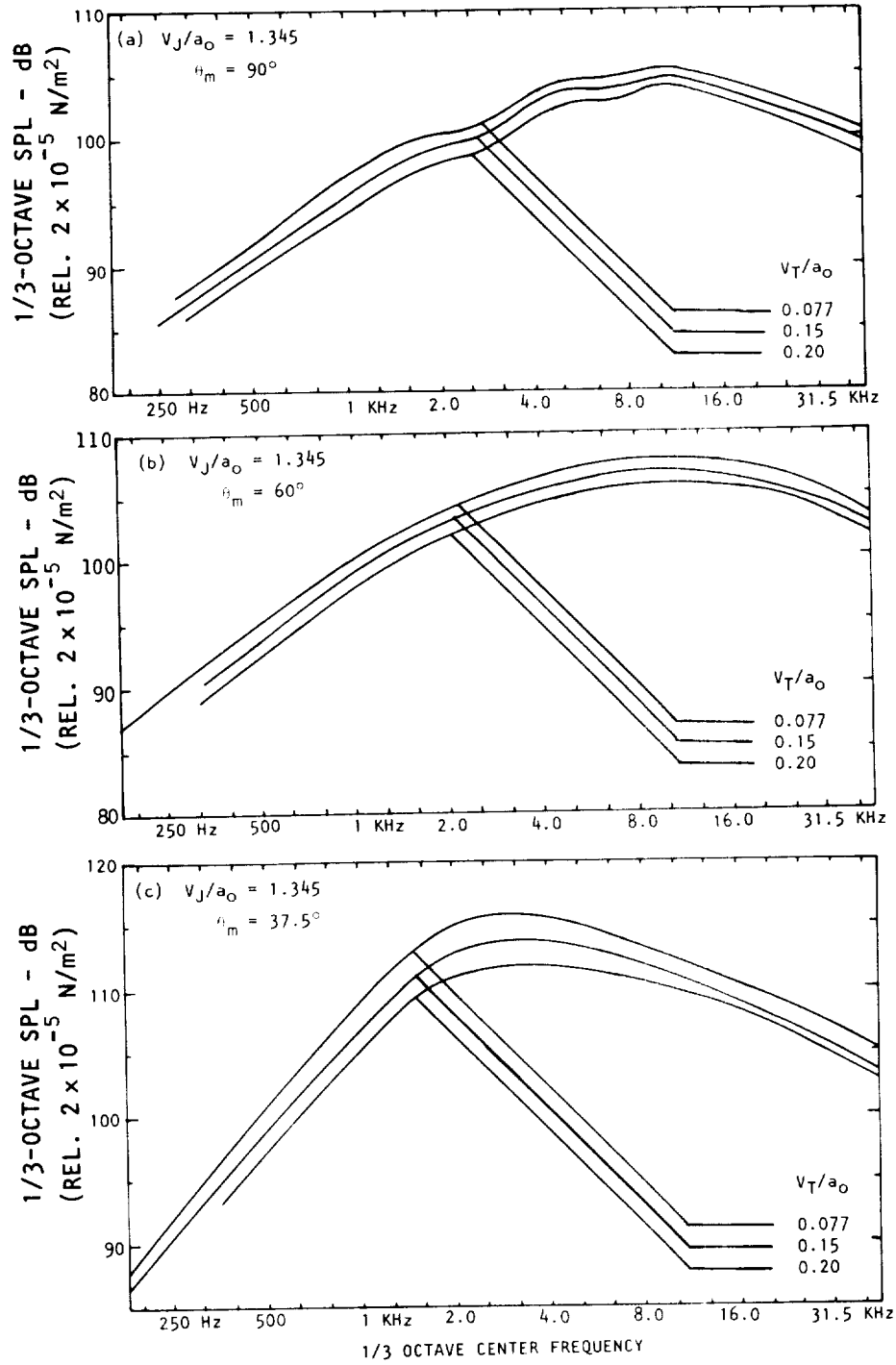
Figure 2.29 Effect of tunnel velocity on measured (uncorrected) spectra at high jet velocity ($V_J/a_o = 1.345$).

at this stage from the measured spectra at angles other than 90° to the jet axis, since the emission angle corresponding to a fixed measurement angle could vary significantly with varying tunnel velocity. The spectra at $\theta_m = 60°$ and 37.5° are presented here purely for future reference. As a general observation, however, we may note in passing that at small measurement angles, the reduction in sound pressure levels with increasing tunnel velocity is frequency dependent, and the magnitudes of these reductions decrease progressively as the observed frequency increases beyond the peak frequency.

It remains to be seen how the spectral characteristics observed above from the uncorrected results are modified by the facility corrections. This aspect is examined in the following section.

2.6 CORRECTED RESULTS

In the previous section, the effects of forward motion on the directivity and spectral characteristics of jet mixing noise were examined in a a preliminary manner where the measured results were not corrected for any of the complications introduced by testing the model jet in a larger co-flowing stream, with the microphones placed outside in a stationary medium. An adequate understanding and accurate quantification of these facility corrections are vital to the success of a free-jet facility in simulating forward velocity effects on jet noise. Considerable effort in the present program was directed towards this aspect of inflight simulation, and the complete details of various phenomena involved, together with a systematic data correction procedure, are given in section 3.1 of this report. In essence, the correction procedure takes proper account of source distribution effects in a jet flow, the downstream convection of sound waves by the tunnel flow, and the refraction of sound caused by the free-jet shear layer. The refraction effect causes a change in the ray path angle and a change in the sound pressure amplitude as the sound waves propagate through the shear layer. The correction procedure incorporates all these effects in a realistic manner, and using the measured or uncorrected results at fixed measurement angles, θ_m, it yields results corrected to constant emission angles, θ_e, for an observer moving with the jet.

In the present program, the measured results at three jet exit velocities ($V_J/a_o = 0.6$, 0.9 and 1.345) were subjected to the correction procedure, and the corresponding corrected results at fixed emission angles are presented in this section. The spectral results are examined first.

2.6.1 Corrected 1/3 -Octave Spectra

The corrected one-third octave spectra corresponding to the measured spectra discussed in the previous section are presented in Figures 2.30, 2.31, and 2.32, for $V_J/a_o = 0.6$, 0.9, and 1.345, respectively. In order to obtain the corrected spectrum at some emission angle, θ_e, the measured spectra have to go through an interpolation procedure, both in frequency and
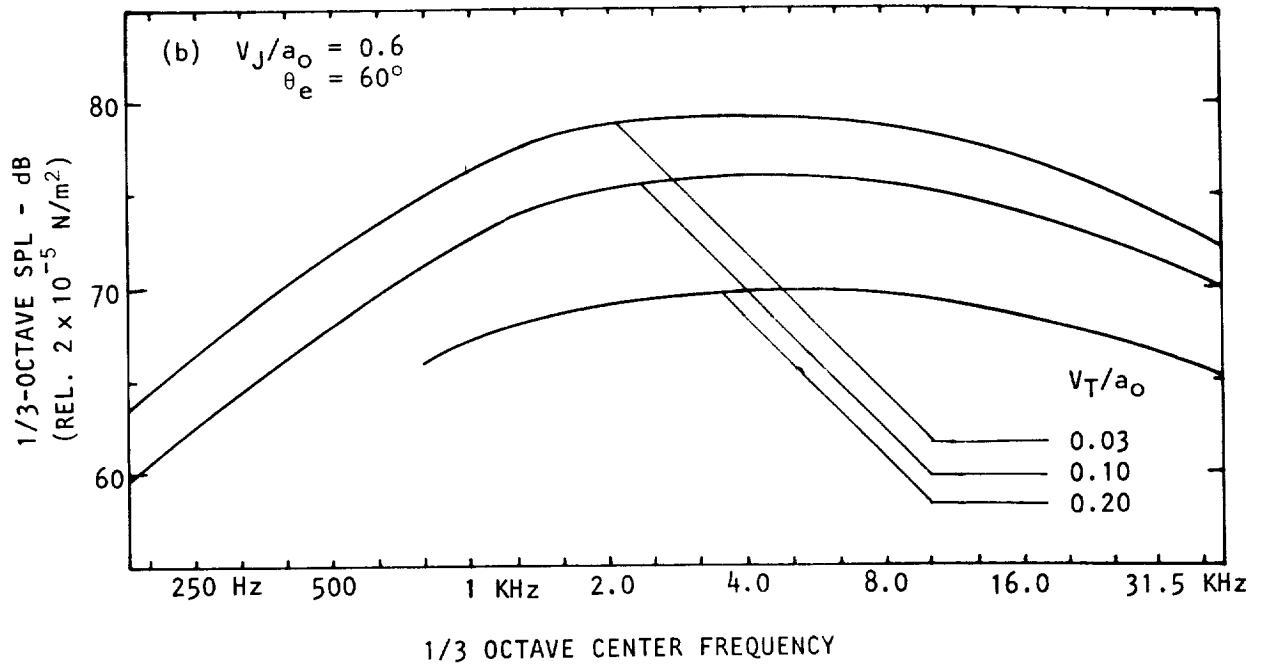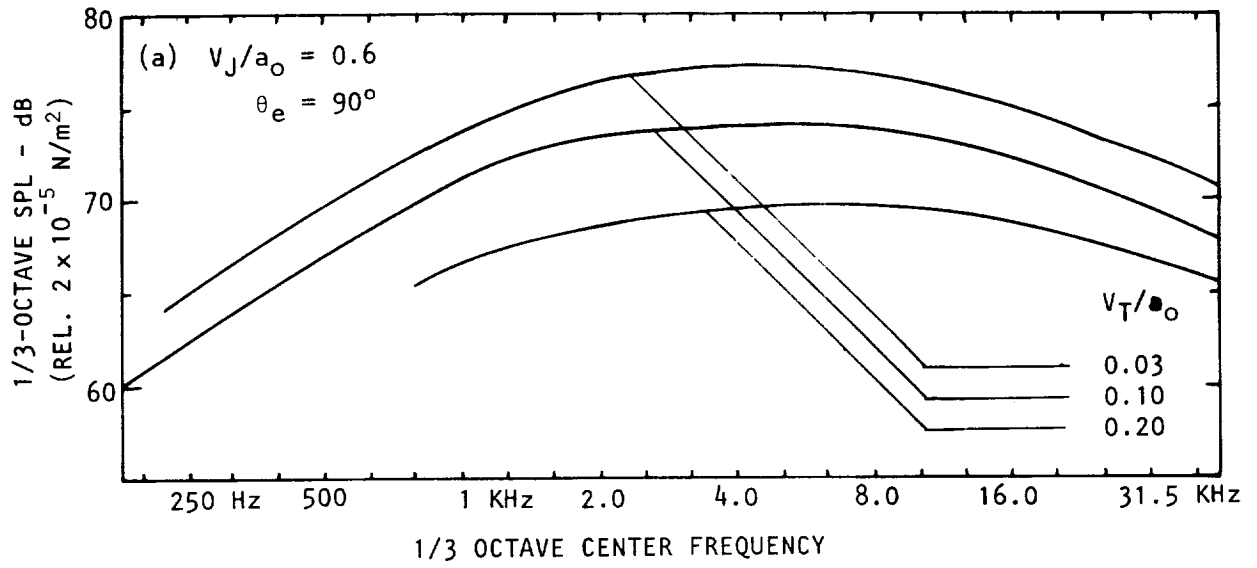
Figure 2.30   Effect of tunnel velocity on corrected spectra
at low jet velocity ($V_J/a_o = 0.6$).

58
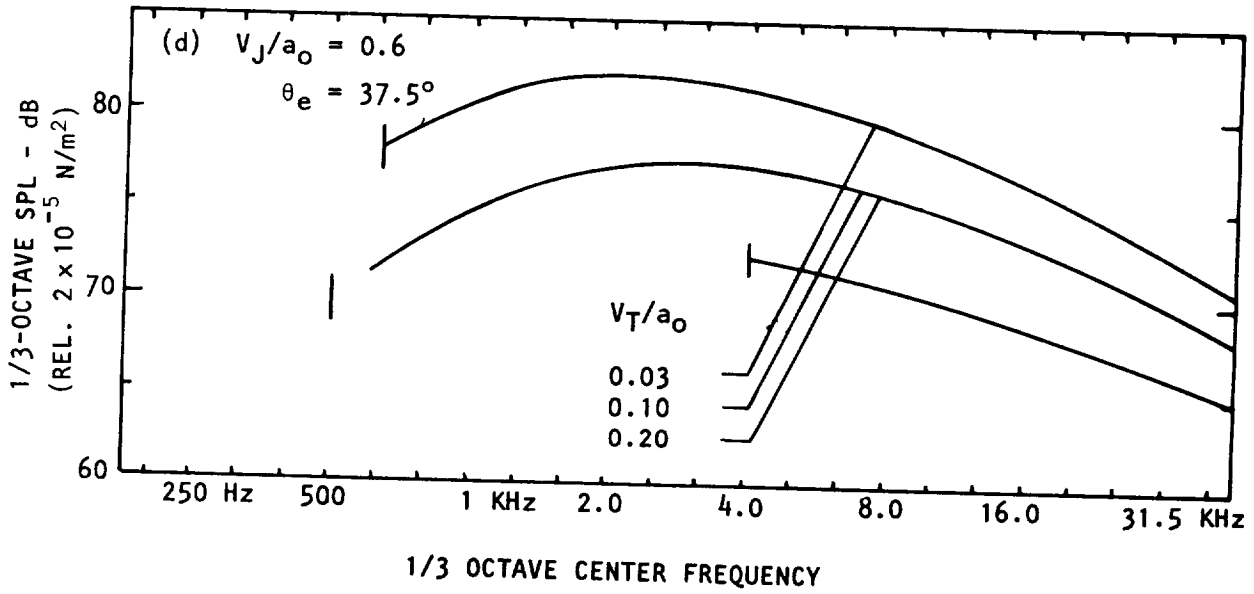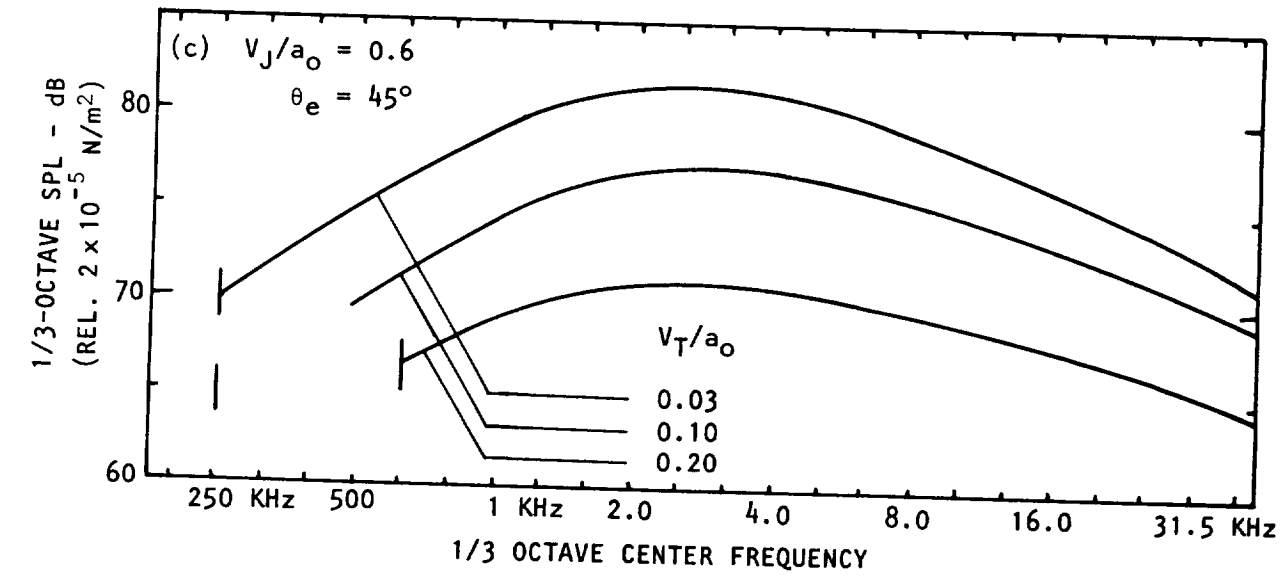
Figure 2.30   Concluded.
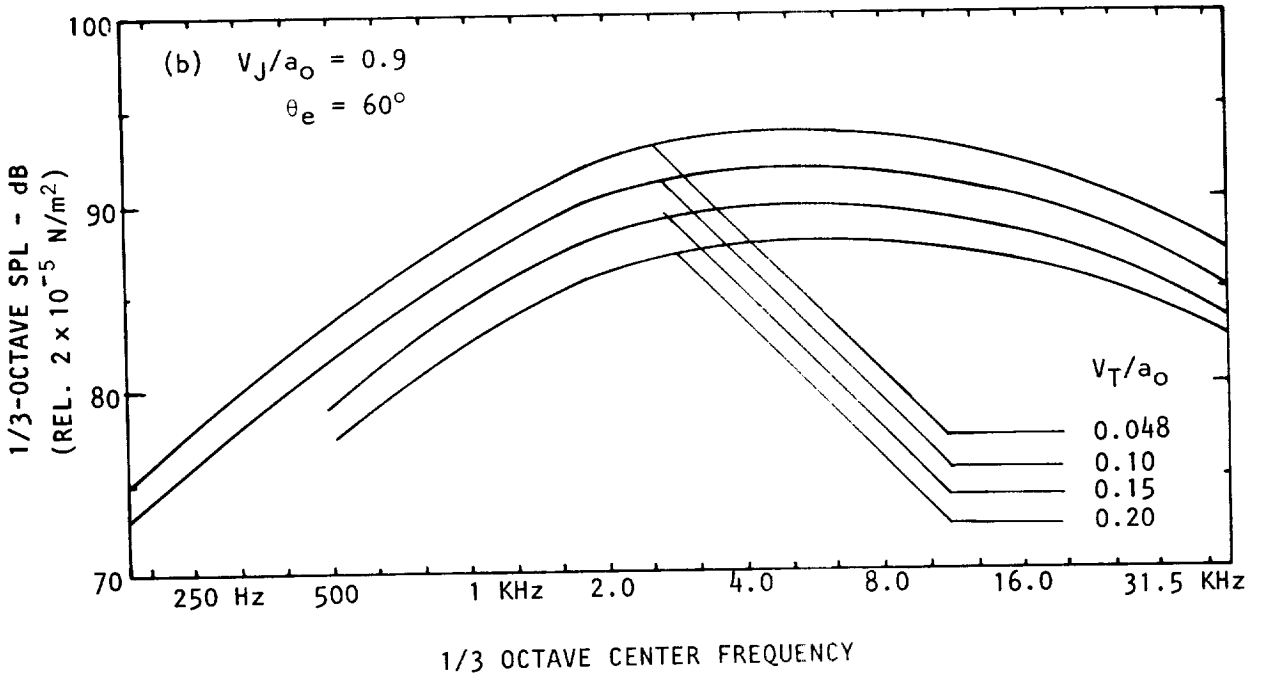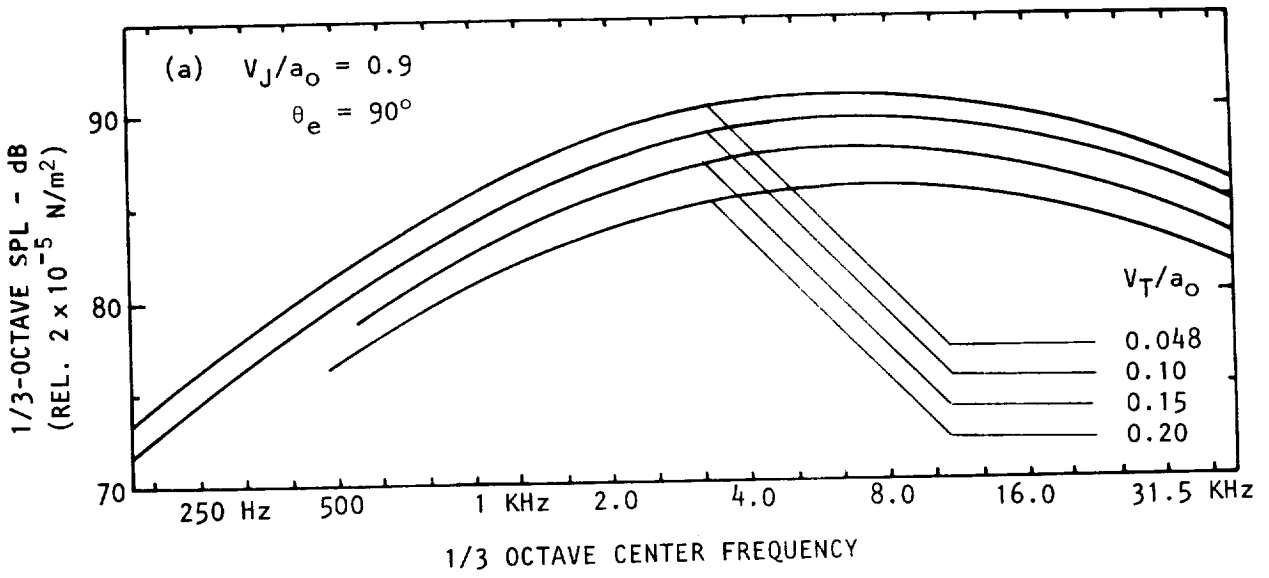
Figure 2.31   Effect of tunnel velocity on corrected spectra
at medium jet velocity ($V_J/a_O = 0.9$).

60

(c) $V_J/a_o = 0.9$
    $\theta_e = 45°$

1/3-OCTAVE SPL - dB
(REL. 2×10^{-5} N/m^2)

100

90

80

V_T/a_o

0.048
0.10
0.15
0.20

250 Hz   500   1 KHz   2.0   4.0   8.0   16.0   31.5 KHz

1/3 OCTAVE CENTER FREQUENCY

(d) $V_J/a_o = 0.9$
    $\theta_e = 37.5°$

1/3-OCTAVE SPL - dB
(REL. 2×10^{-5} N/m^2)

100

90

80

V_T/a_o

0.048
0.10
0.15
0.20

250 Hz   500   1 KHz   2.0   4.0   8.0   16.0   31.5 KHz

1/3 OCTAVE CENTER FREQUENCY
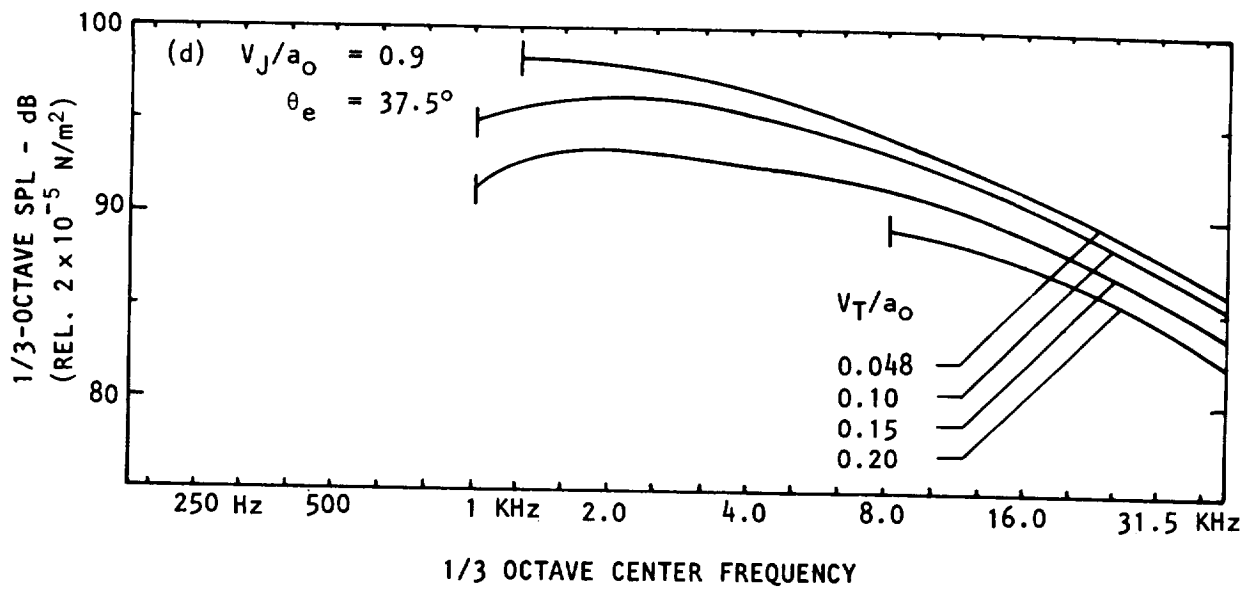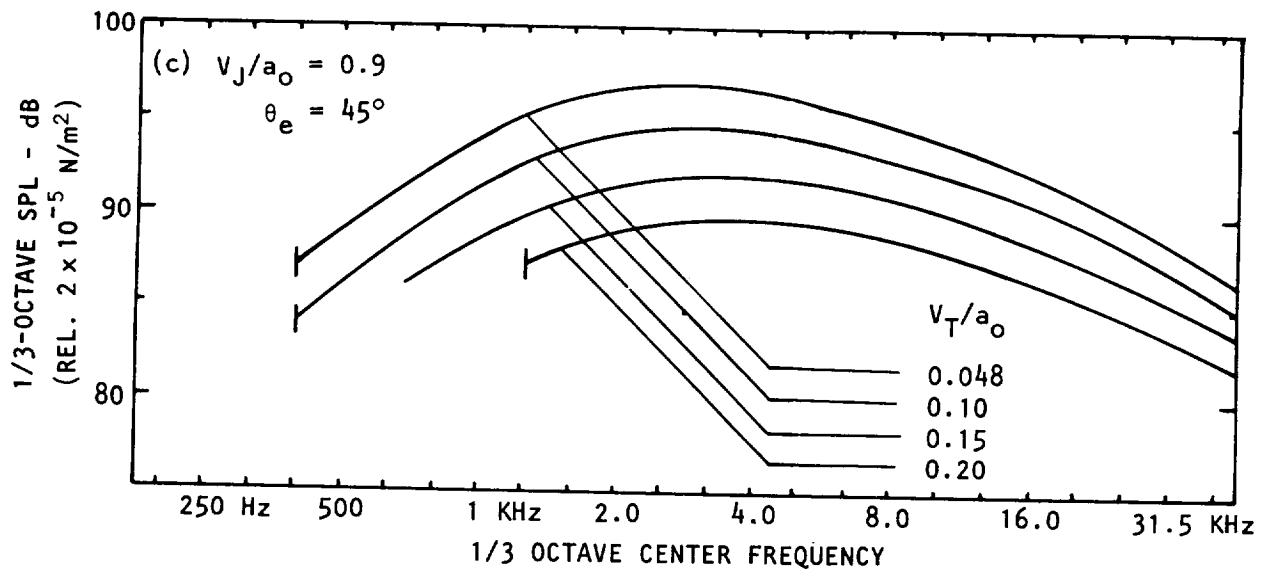
Figure 2.31 Concluded.

61
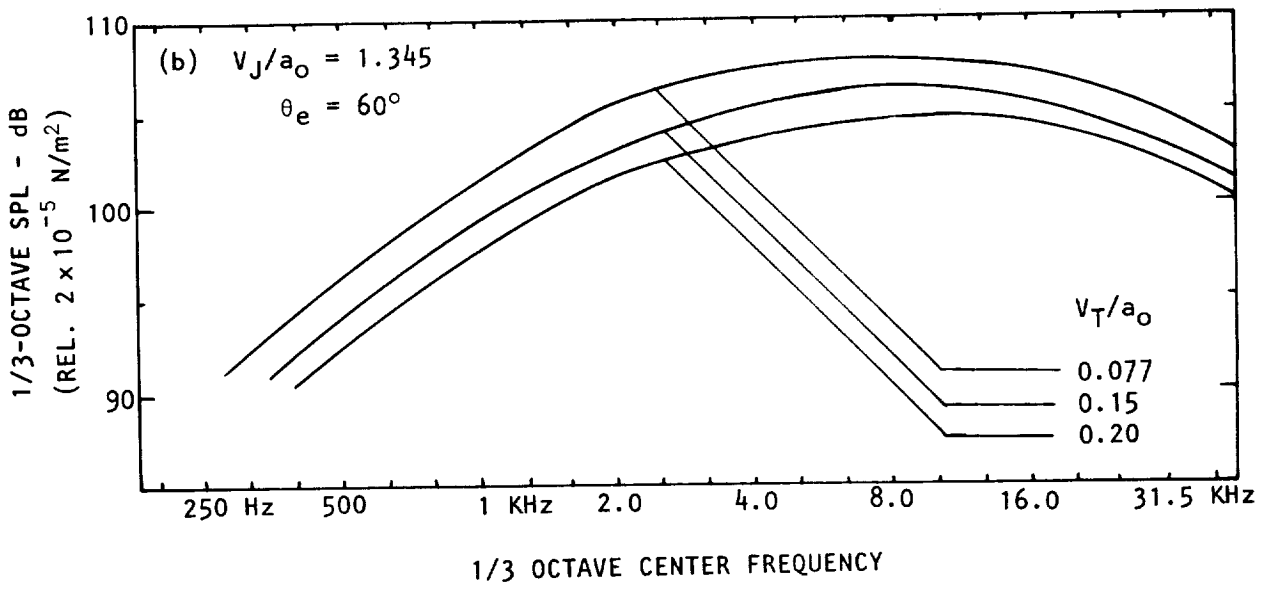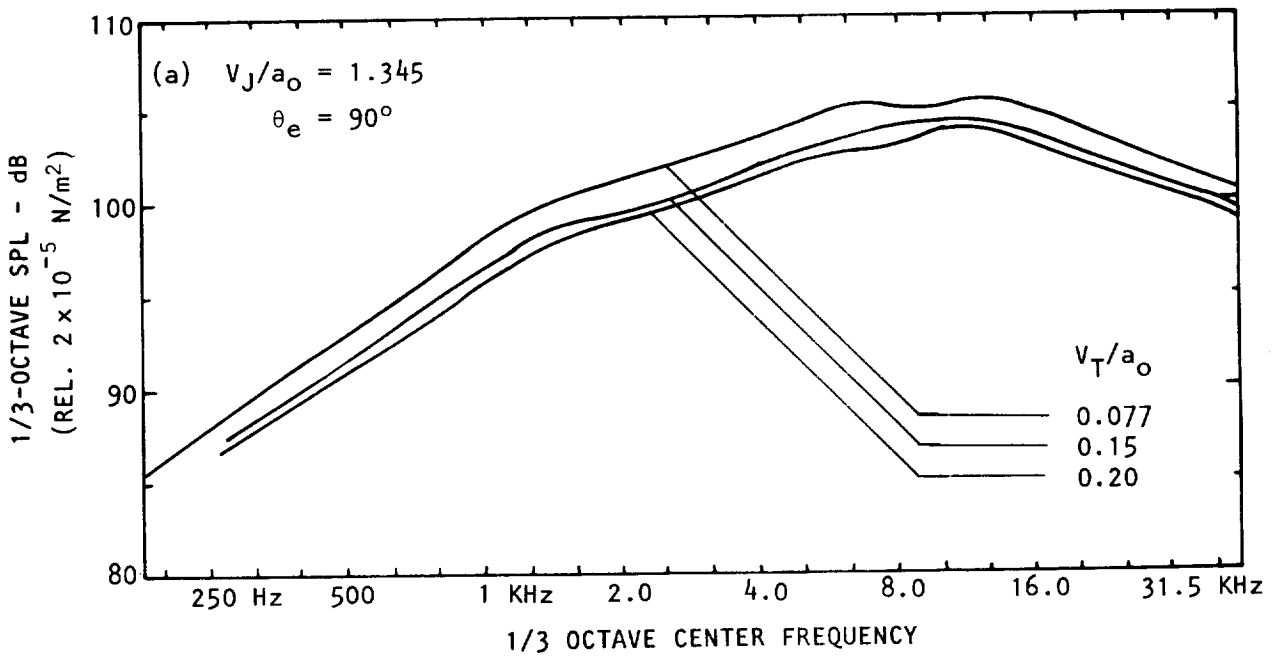
Figure 2.32   Effect of tunnel velocity on corrected spectra
at high jet velocity (V_J/a_o = 1.345).
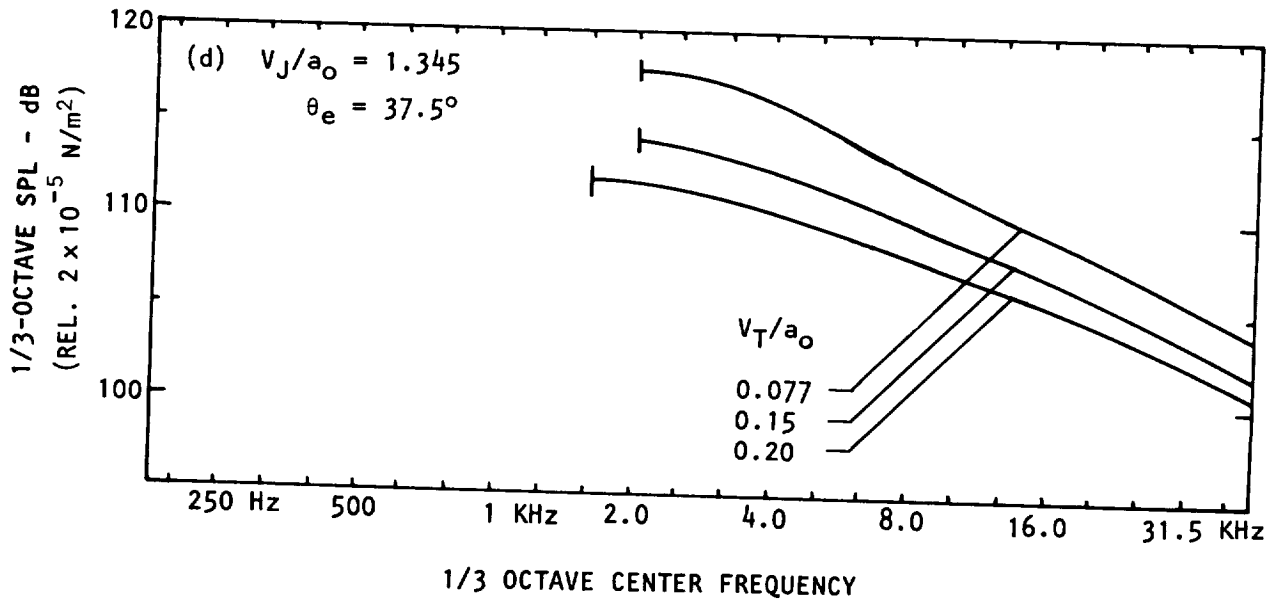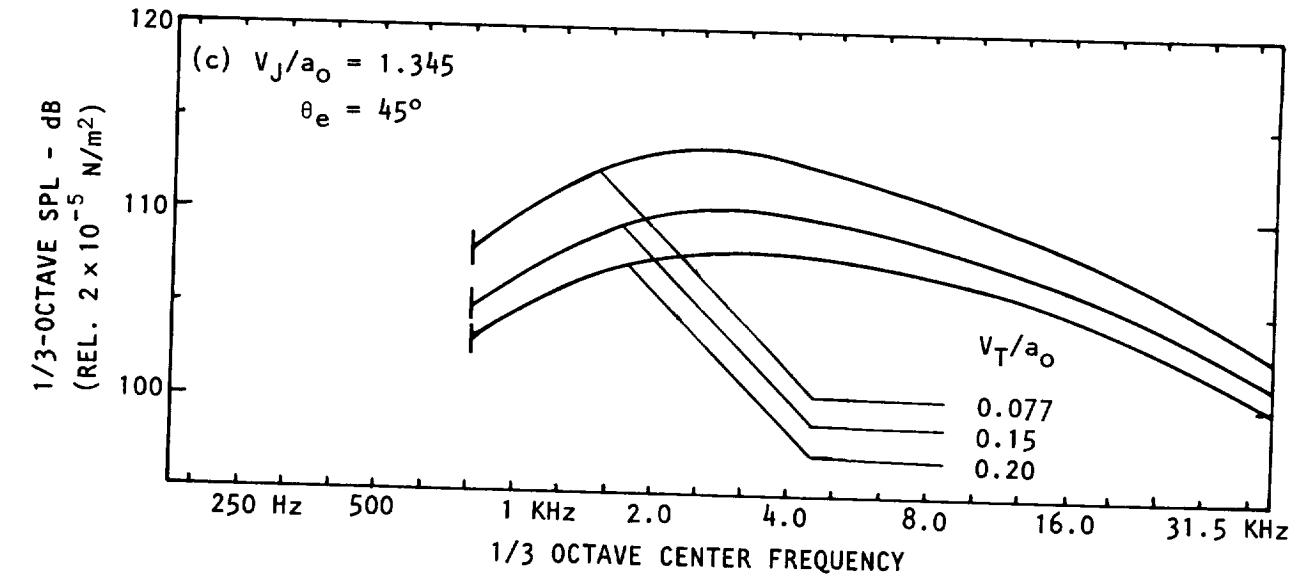
Figure 2.32 Concluded.

in angle, as will be described in section 3.1. At low frequencies and low θ_e, this procedure requires measured values at angles θ_m smaller than those used in the experimental program, and hence, the corrected spectra at low θ_e have a lower limiting frequency; it is not possible to obtain corrected levels at frequencies lower than this limiting frequency. In the spectra presented in the figures, the lower limiting frequency, when present, is identified by a vertical line in most cases.

The general features exhibited by the corrected spectra at constant emission angles (θ_e) are qualitatively similar to those exhibited by the measured spectra at constant measurement angles (θ_m). However, there are some quantitative differences. At $\theta_e = 90°$, the flow (or refraction) corrections at all tunnel velocities and frequencies are found to be negligible. The reductions in 1/3-octave levels with increasing tunnel velocity are virtually identical to those noted previously at $\theta_m = 90°$, although the absolute levels at all tunnel velocities are a little higher due to the source location corrections. In contrast, at smaller emission angles, the shear layer refraction corrections do become significant. Their magnitudes increase as the tunnel velocity increases. The consequence of this effect is that the reductions obtained from corrected spectra at constant θ_e are larger than the reductions observed in uncorrected spectra at the same value of constant θ_m. In other words, at low emission angles, the relative velocity effect is larger for the corrected results than for the corresponding uncorrected results at the same values of measurement angles. The reductions in corrected noise levels with tunnel velocity were scaled on the relative velocity basis, as done previously for the uncorrected results, and the findings are described in the following section.

2.6.2 Corrected Overall SPL Results

The overall sound pressure levels for the corrected spectra were obtained by summing the levels in various 1/3-octave bands. The summation was carried out over the frequency range from 1 KHz to 40 KHz due to the lower frequency limit imposed by the correction procedure, as mentioned above.

The effect of tunnel velocity V_T/a_0 on the directivity of corrected overall SPL at $V_J/a_0 = 0.6$, 0.9 and 1.345 is shown in Figure 2.33. It should be remembered that the effect of forward motion is examined here at constant emission angles, and therefore represents a true static-to-flight comparison for an observer moving with the jet nozzle. The effect of forward motion is seen to provide a significant noise reduction at all emission angles considered here. The magnitudes of the reductions increase slightly as the observer moves from $\theta_e = 90°$ towards the downstream jet axis.

In order to obtain the relative velocity exponent m for the corrected results, the OASPL reductions at all emission angles were plotted against the velocity parameter $10 \log_{10} [(V_J - V_{TO})/V_{REL}]$ as described before, and the results are shown in Figure 2.34. Since the amount of data subjected to the facility corrections was limited within the scope of the present program, the number of data points in the figure, through which the slope representing exponent m is plotted, is unfortunately limited. Nevertheless, the final

64

(a) $V_J/a_o = 0.6$
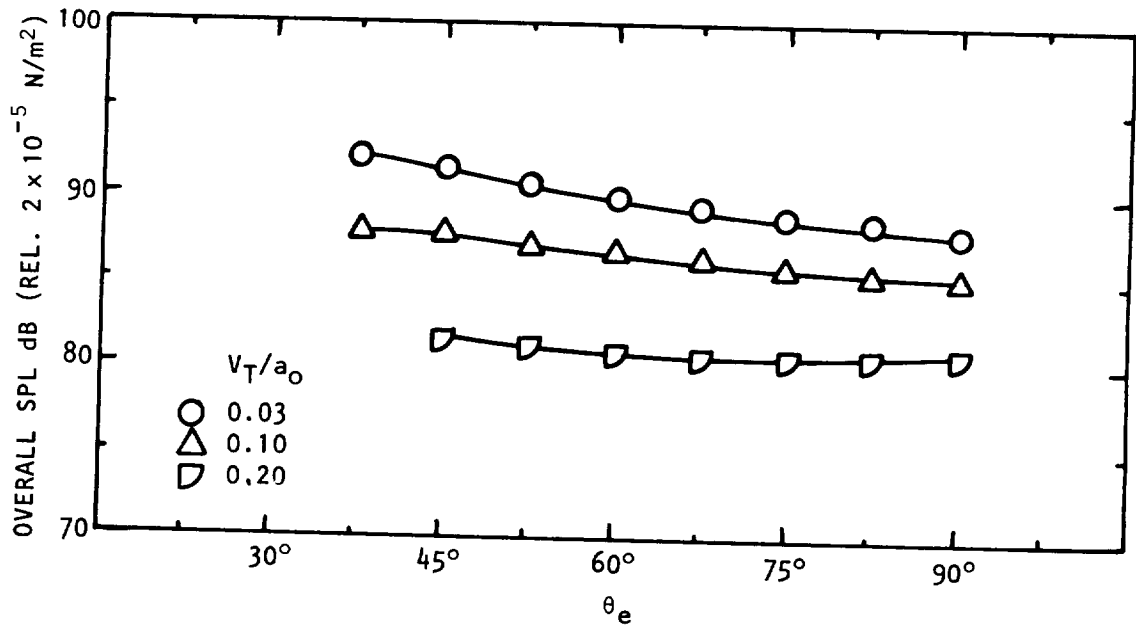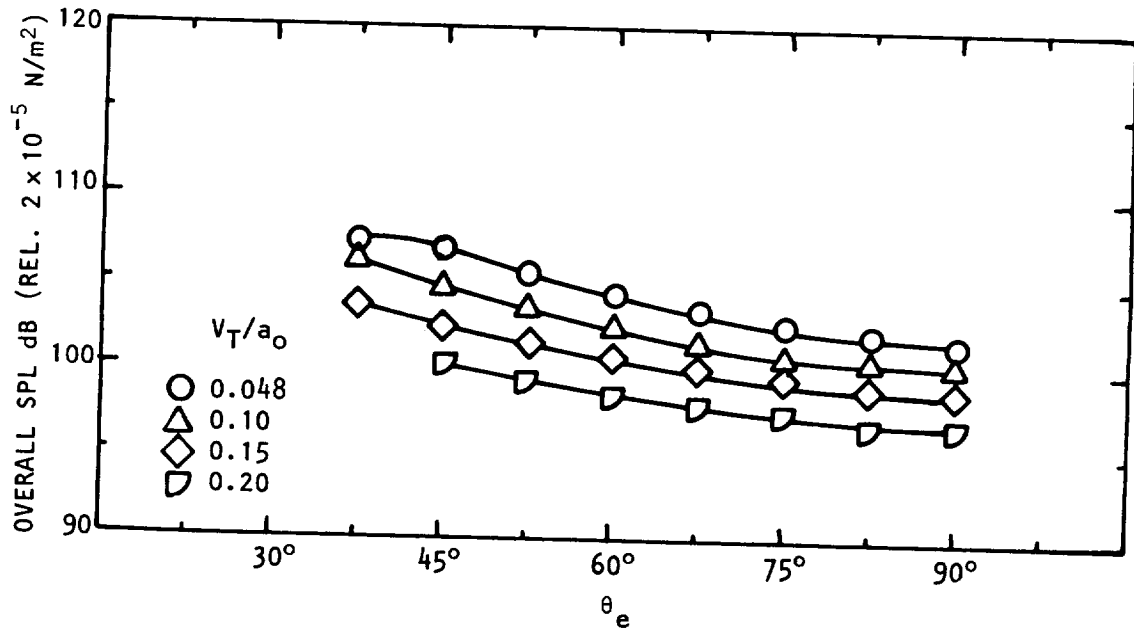

(b) $V_J/a_o = 0.9$

Figure 2.33 Effect of tunnel velocity on the directivity of corrected overall SPL at various jet exit velocities.
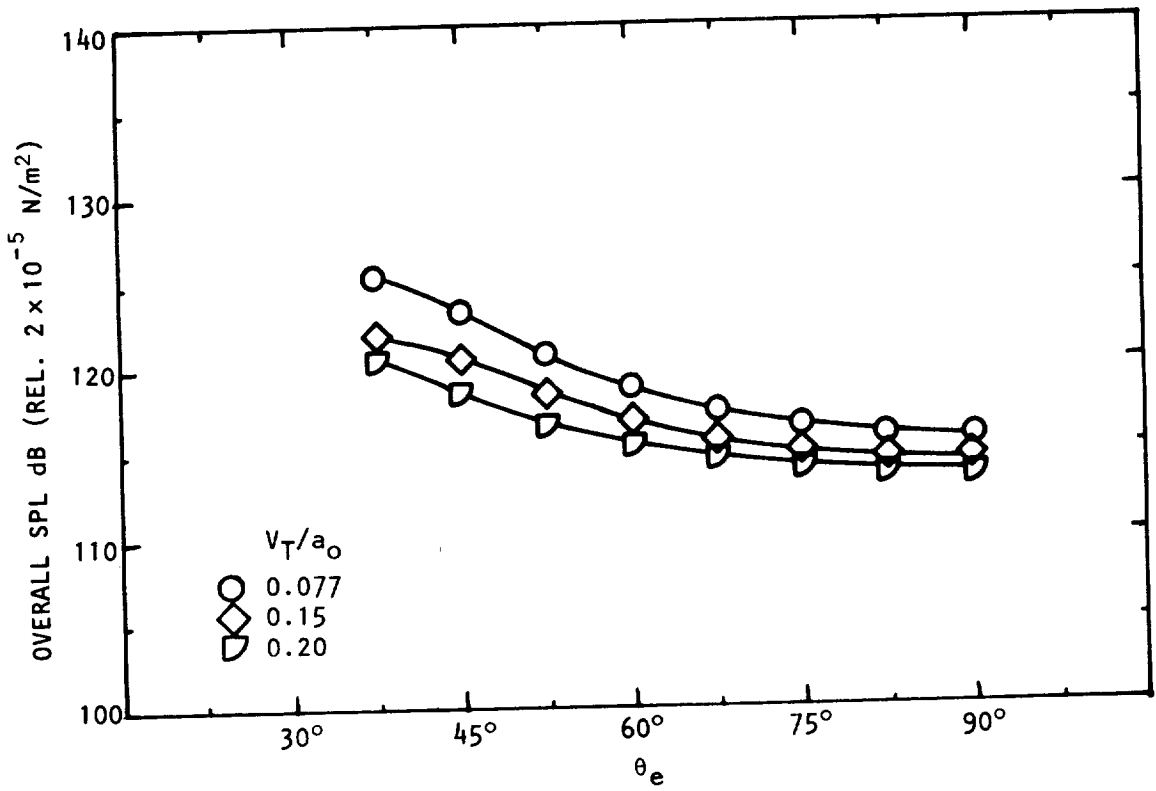
(c) $V_J/a_o = 1.345$

Figure 2.33 Concluded.
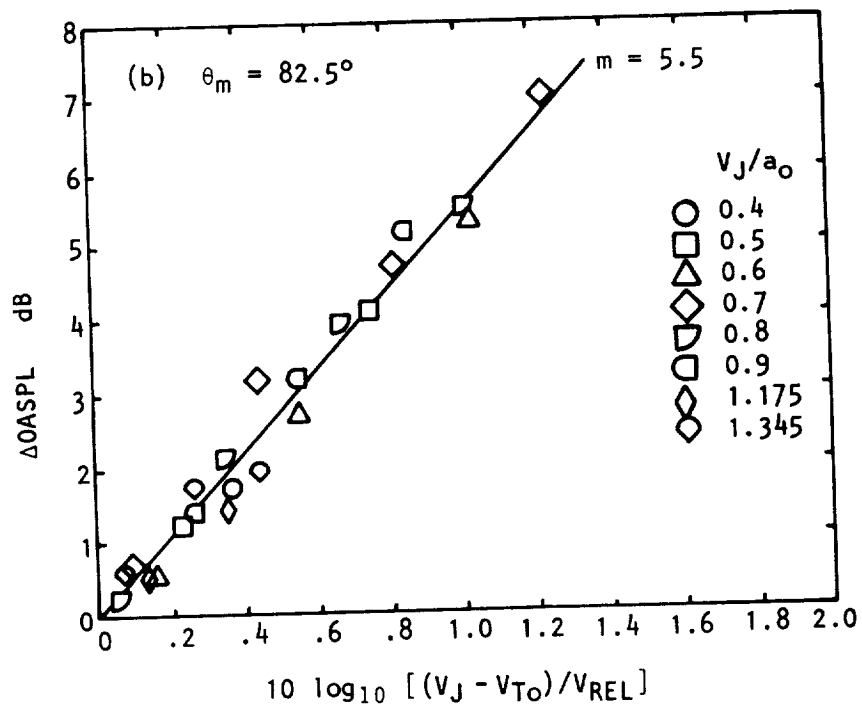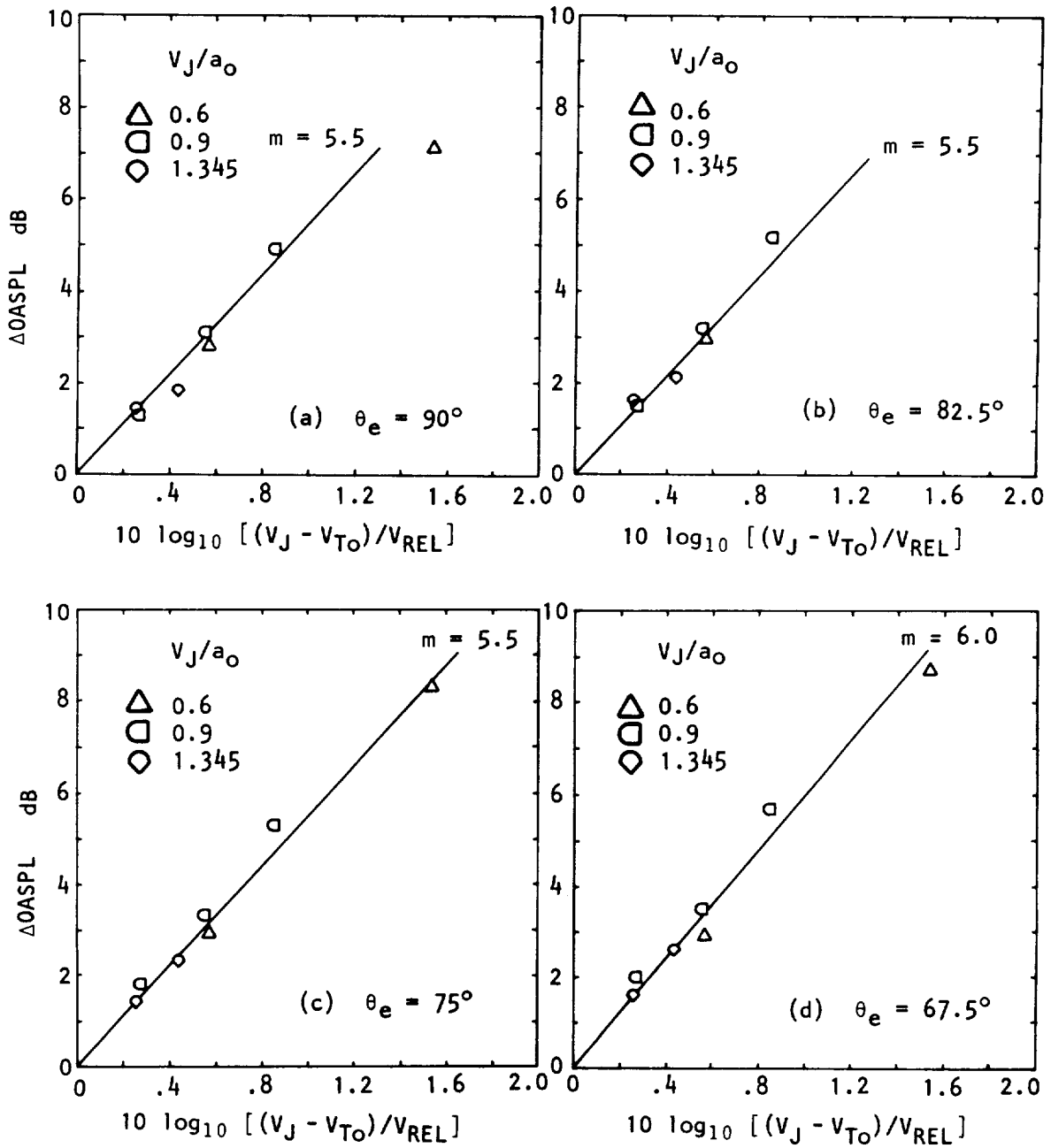
Figure 2.34   Relative velocity scaling of corrected overall
SPL reductions at various emission angles.

67
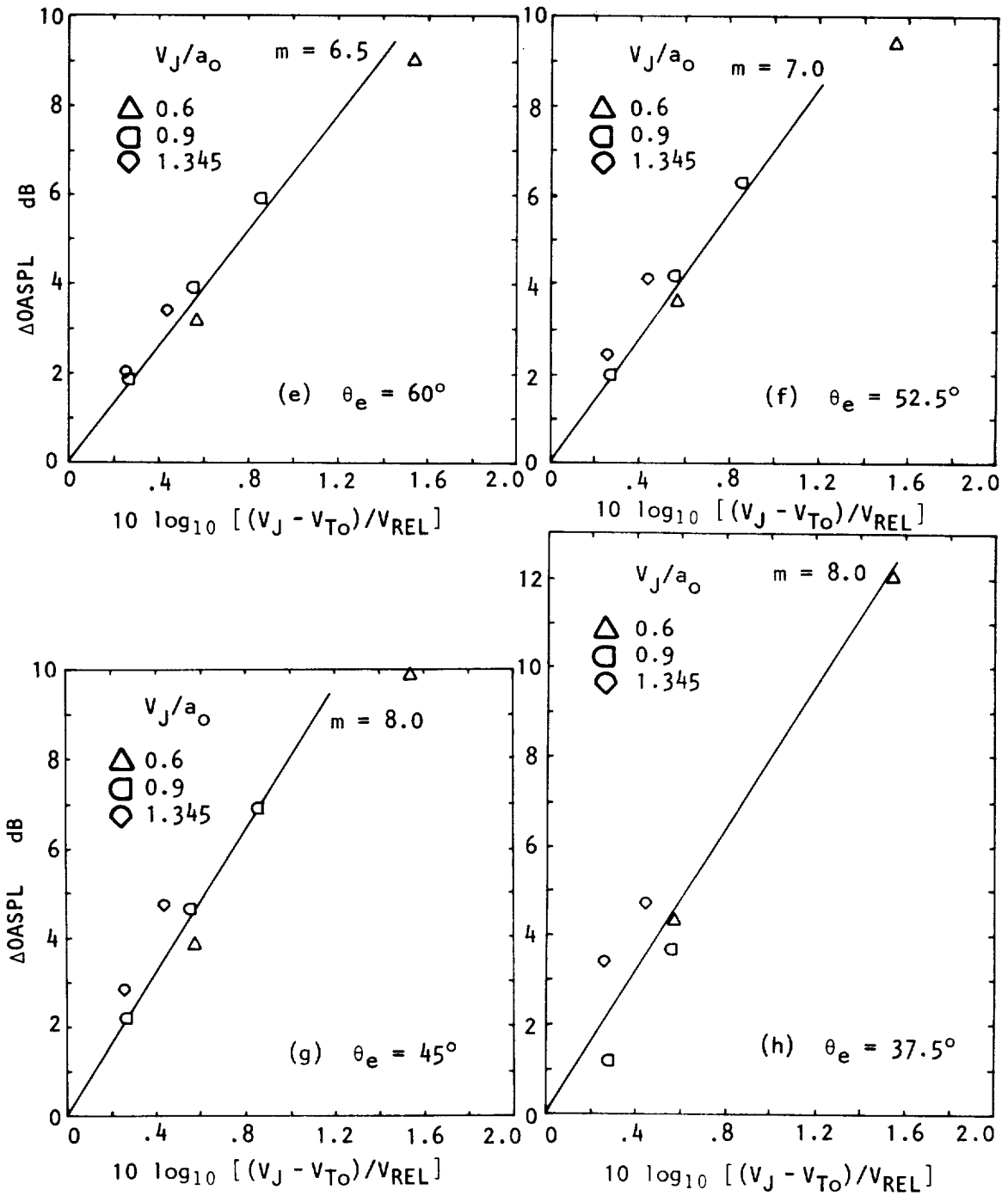
Figure 2.34   Concluded.

results are considered to be fairly accurate. At 90° to the jet axis, the overall intensity is proportional to 5.5 powers of the relative velocity, a result which is closely in agreement with the scaling laws derived from jet flow measurements in Section 4.

Finally, the variation of resulting relative velocity exponent m with emission angle θ_e is plotted in Figure 2.35. For comparison, the exponent values obtained in Section 2.5 from uncorrected data are also shown in this figure. In order to compare the forward velocity effects on jet noise obtained from the present experiments with the results of other investigations, the latter are also included in the figure. In particular, the published inflight effects studies considered here are (1) the free-jet experiments conducted by NASA-Lewis (ref. 21), (2) the wind tunnel experiments conducted by NGTE (ref. 23), and (3) the full-scale flight results reported by Rolls-Royce (ref. 1). Figure 2.35 thus provides a simplified overview of the inflight effects on jet noise on the relative velocity basis from all types of facilities. The major facts and implications can now be discussed in some detail.

(1) The first major observation can be derived by comparing the relative velocity exponents obtained in the present experiments from the corrected data and the uncorrected data. The facility corrections, designed to convert results from a free-jet simulation to a corresponding wind tunnel simulation, are negligible at 90° to the jet axis, but produce a significant difference at lower angles in the rearward arc.

(2) In the NGTE wind tunnel experiments, the procedure for deriving the relative velocity exponent m included the so-called dynamic effect correction (i.e., an amplification due to relative motion between tunnel flow and stationary jet), which was not included so far in the present data manipulations. In order to obtain a true comparison with the NGTE results, this correction was also applied to the present results by using

$$\underset{\substack{\text{with} \\ \text{dynamic} \\ \text{correction}}}{\Delta OASPL(\theta_e)} = \underset{\substack{\text{without} \\ \text{dynamic} \\ \text{correction}}}{\Delta OASPL(\theta_e)} - 10 \log_{10}\left\{\frac{1 + M_T\cos\theta_e}{1 + M_{TO}\cos\theta_e}\right\} \qquad (2\text{-}4)$$

where

$$\underset{\substack{\text{without} \\ \text{dynamic} \\ \text{correction}}}{\Delta OASPL(\theta_e)} = 10 \log_{10}\left\{\frac{V_J - V_{TO}}{V_J - V_T}\right\}^m \qquad (2\text{-}5)$$

The overall SPL reductions with dynamic corrections are therefore lower than the overall SPL reductions without dynamic corrections. They were correlated
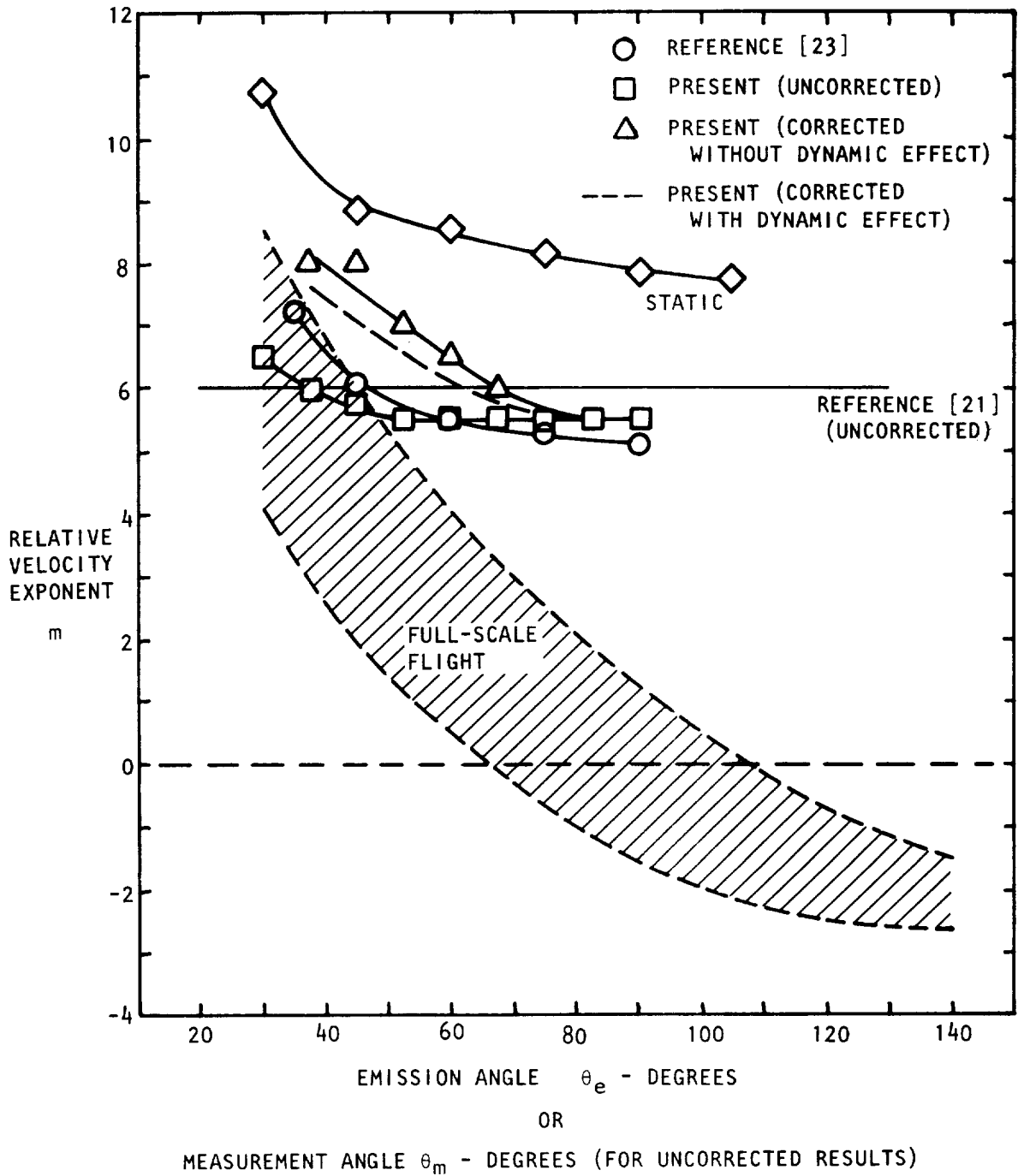
Figure 2.35 Comparison of relative velocity exponents from various
inflight simulation experiments and flight tests.

on the relative velocity basis at each emission angle θ_e, and the resulting relative velocity exponent values are given by the broken curve in Figure 2.35. It can be seen that the effect of this dynamic correction is zero at $\theta_e = 90°$, and the magnitude of the effect increases as θ_e decreases.

Comparison of these modified exponents with the corresponding NGTE results in Figure 2.35 shows that the agreement is good at all emission angles. The small differences are perhaps to be expected for two reasons: (a) the present results were corrected to take proper account of realistic source location, whereas no such correction was applied to the NGTE results (where the sources were assumed to be located at the nozzle exit plane); (b) the microphones in the NGTE tests were placed at a sideline distance of twenty-two nozzle diameters from the jet axis, which is not large enough to provide results that approach true far-field radiation characteristics.

The good agreement between the results of the present free-jet experiments, carefully corrected to yield results which would be expected from a corresponding wind tunnel simulation, and the results from the NGTE wind tunnel experiments, which utilized a large test section to nozzle area ratio (~5000), provides three important implications: (a) the effect of turbulence scattering in a free-jet mixing layer, which was not included in the data correction procedure, does not appear to be significant; for if it was significant, then the agreement between the free-jet experiments and the wind tunnel experiments, where the scattering problem does not arise, would not be as good as we see here; (b) the free jet to nozzle area ratio of 400 used in the present experiments appears to be adequate for accurate evaluation of inflight effects on jet noise characteristics; (c) a free-jet facility is capable of simulating many of the inflight effects on jet noise, providing adequate and accurate facility corrections are applied to the measured results.

(3) Finally, the comparison of relative velocity exponents from inflight simulation experiments with the envelope of exponents obtained from full-scale flight results is rather discouraging. At low angles to the jet exhaust, it appears that the flight simulation results are in reasonable agreement with the actual flight results. At larger angles, however, the reductions in noise levels with forward motion observed in the model simulation experiments are larger than those measured in flight tests. At $\theta_e = 90°$, there is little or no change in the flyover noise levels, whereas the free-jet experiments indicate significant noise reductions which scale on the 5.5 powers of the relative velocity.

The obvious question to be raised at this stage is, what is the reason for this discrepancy between the flight simulation results and the full-scale aircraft flyover results? The first possibility stems from the fact that in the present experiments, although the jet velocity regime was simulated adequately, the effect of jet heating was not considered; in contrast, all flyover results are obtained from heated jet flows. Hence, an exact comparison for matching jet operating conditions should be carried out after obtaining results from heated flight simulation experiments. Having stated this, however, the acoustic scaling laws from heated jets, derived in Appendix 4C, suggest that although this possibility will bridge the gap

between model simulation and flight results considerably, it might not be able to provide the complete explanation.

In attempting to resolve this discrepancy further, it is readily admitted that there *are* subtle differences in the two sets of experiments: in the flight simulation tests, there is no relative motion between the source and the observer, whereas in the flyover tests, the noise source is being convected relative to a stationary observer. However, further considerations also show that none of the features associated with source motion (for example, eddy convection velocity effects, source acceleration effects, etc.) will affect the results at 90° to the direction of motion. It must therefore be concluded that the flight results considered so far may not represent pure turbulent mixing noise, and are likely to be contaminated by engine internal or other noise sources.

2.6.3 Prediction of Static-to-Flight Noise Reduction

We have previously alluded to the point that although the concept of relative velocity exponent is very convenient in semi-empirical correlation schemes, it does not provide any physical explanation of static to flight noise reductions, except at 90° to the jet axis where it is a measure of the changes in equivalent source strength. Hence, an attempt was made to correlate the measured (*with* facility corrections) OASPL reductions at all emission angles in terms of a theoretical result for convective amplification due to eddy convection, derived in Section 3.

The starting point for the theoretical correlation formula is that the intensity at $\theta_e = 90°$ is proportional to $V_{REL}^{5.5}$. The intensity at any other emission angle θ_e is then given by adding the eddy convective amplification and jet motion amplification (resulting from the relative motion between tunnel flow and stationary jet) to this basic dependence, which is the source alteration effect. The overall SPL can therefore be expressed as

$$OASPL(\theta_e) \propto 10 \; \log_{10} \left[(V_J - V_T)^{5.5} \; (CA_{V_J} - V_T) \left\{ \frac{1}{1 + M_T \cos\theta_e} \right\} \right], \qquad (2\text{-}6)$$

where CA is the eddy convective amplification given by

$$CA = \frac{(1 - M_c \cos\theta_e)^6}{\{(1 - M_c \cos\theta_e)^2 + \alpha^2 M_c^2\}^{9/2}}, \qquad (2\text{-}7)$$

and the subscript $V_J - V_T$ denotes the velocity at which the eddy convection Mach number M_c is to be evaluated. This convective amplification result is derived from geometric acoustics in Section 3, and is valid outside the zone of silence. The reduction in OASPL from minimum tunnel velocity, V_{TO}, to any other tunnel velocity, V_T, can be written as

$$\Delta OASPL(\theta_e) = 10 \log_{10} \left[\left| \frac{V_J - V_{TO}}{V_J - V_T} \right|^{5.5} \left| \frac{CA_{V_J} - V_{TO}}{CA_{V_J} - V_T} \right| \left\{ \frac{1 + M_T \cos\theta_e}{1 + M_{TO}\cos\theta_e} \right\} \right]. \quad (2\text{-}8)$$

In using equations (2-7) and (2-8), the eddy convection velocity was assumed to be 0.67 times the applicable relative velocity, and α was taken to be 0.3. Although these values are consistent with the values obtained from static jet flow measurements by several investigators, their magnitudes for jets in a co-flowing stream need to be derived experimentally.

For all measured (with facility corrections) OASPL reductions, the corresponding theoretical OASPL reductions were calculated, and the comparison of results at all emission angles θ_e (including 90°) greater than the cone of silence angles θ_c, where θ_c is given by

$$\theta_c = \cos^{-1} \frac{1}{1 + 0.67 \left| \frac{V_J}{a_0} - \frac{V_T}{a_0} \right|}, \quad (2\text{-}9)$$

is shown in Figure 2.36.

The calculated noise reductions are in close agreement with the measured (with facility corrections) noise reductions, the majority of the points agreeing within ±1/2 dB.

The good agreement observed here provides an important indirect implication. The calculation formula used here is basically similar to the formula used by NGTE; although there are significant physical differences between the two, the numerical differences over the range of V_J/a_0 considered here are not significant. The fact that both the wind tunnel results and the free-jet results correlate well with the prediction formulae suggests that the corrected results from the present free-jet experiments are compatible with the results obtained from the wind tunnel experiments. This provides further indirect evidence to our previous conclusion that a free-jet facility is very suitable for a fundamental study of forward motion effects on jet noise.

2.7 SUMMARY AND CONCLUSIONS

The effects of forward motion on the characteristics (both directivity and spectral) of turbulent mixing noise from jet exhausts were examined by conducting inflight simulation experiments in the Lockheed anechoic free-jet facility. The highlights of the experimental program and the major conclusions are as follows:

(1) The facility was capable of providing tunnel velocities up to 75 m/s with a test section of 0.76 m x 1.07 m. Prior to the jet noise experiments, the facility was subjected to detailed aerodynamic and acoustic performance evaluation tests.
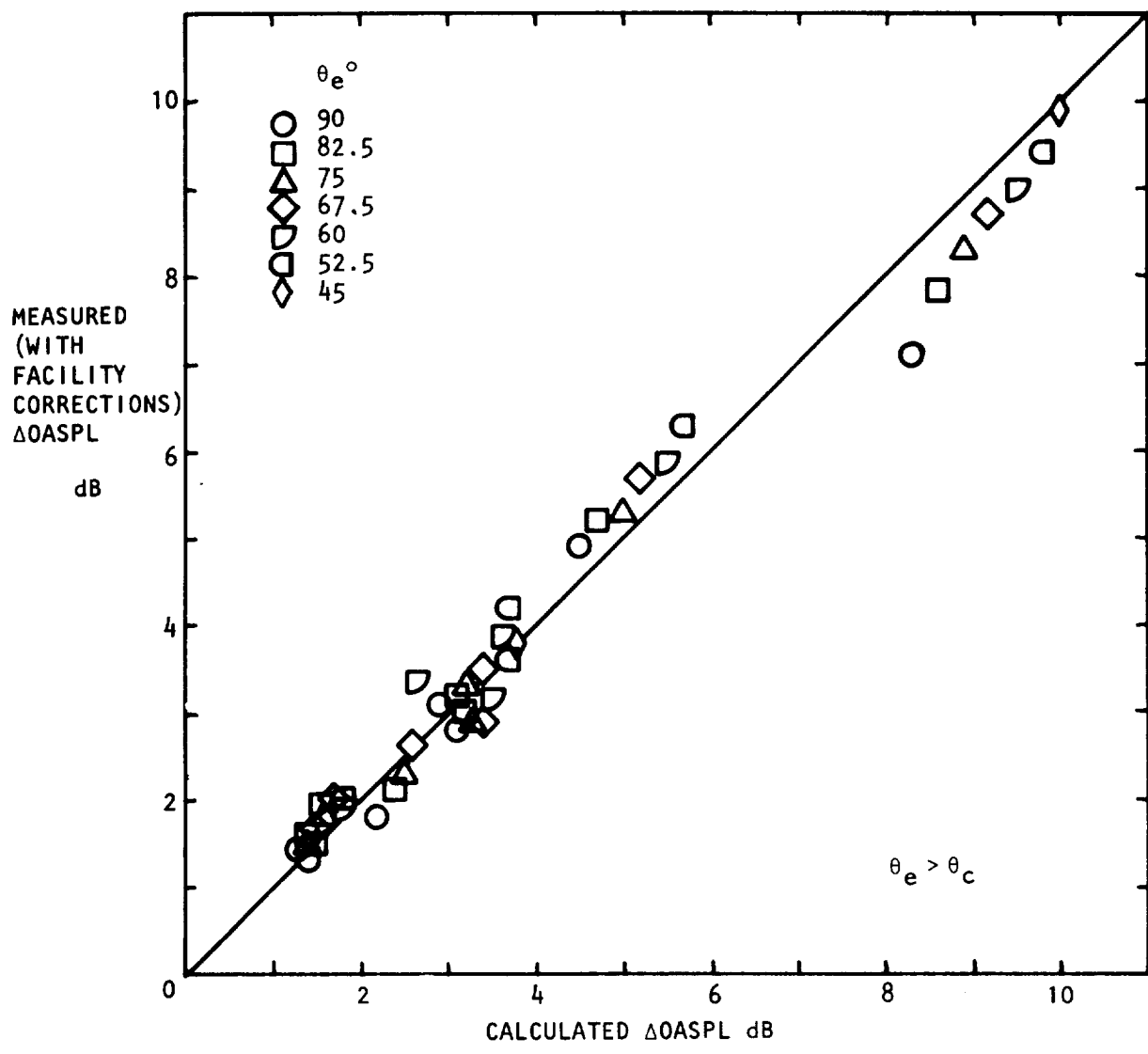
Figure 2.36   Comparison of measured (with facility corrections) OASPL reductions with calculated OASPL reductions.

74

(2) The aerodynamic performance tests revealed that there were no problems associated with free-jet stability, and the air flow circulation velocities in the anechoic chamber were acceptable.

(3) The acoustic performance tests established that (a) the facility was anechoic for frequencies down to 200 Hz, (b) the facility background noise in the measurement arena was low, and (c) the jet noise results would not be contaminated by rig internal noise at least down to $V_J/a_0 = 0.32$.

(4) Limited calibration experiments using a point source established that in the frequency range from 1 KHz to 5 KHz, no detectable internal reflections in the free-jet test section were observed for tunnel velocities up to 61.0 m/s. It was also confirmed that at these frequencies, the effect of turbulence scattering in a free-jet facility was not significant. These point source experiments need to be extended to higher frequencies.

(5) In the jet noise experimental program, the free-jet to nozzle area ratio[+] was 400. The nozzles (diameter = 5.08 cm.) employed were M = 1 convergent nozzle, and M = 1.4, 1.7 convergent-divergent nozzles. The measurement angles were $\theta_m = 30°$ ($7\frac{1}{2}°$) $90°$ relative to the downstream jet axis, and the microphones were placed at 54 nozzle diameters. Acoustic measurements were conducted at forty different test conditions (combinations of V_J/a_0 and V_T/a_0); eight values of jet exit velocity were chosen in the range $0.4 \le V_J/a_0 \le 1.345$, and the tunnel velocity was varied up to $V_T/a_0 = 0.2$. All acoustic data were carefully scrutinized prior to detailed analysis, and all data likely to be contaminated by extraneous noise sources (background/instrumentation/shock noise) were not utilized.

(6) The uncorrected results (i.e., data to which no facility corrections were applied) were found to be in good agreement with the results from published free-jet experiments.

(7) The measured results were subjected to a systematic data correction procedure, which was derived in the present program, and which converted the results from a free-jet facility to the corresponding results that would be obtained in a large-scale wind tunnel simulation. In essence, the correction procedure took proper account of source distribution effects in a jet flow, the downstream convection of sound waves by the tunnel flow, and the refraction of sound caused by the free-jet shear layer. Using the measured or uncorrected results at fixed measurement angles, θ_m, the procedure finally yielded results corrected to constant emission angles, θ_e, for an observer moving with the jet nozzle.

(8) In general, the magnitudes of the facility corrections were negligible at 90° to the jet axis, but produced a significant effect at low angles in the rearward arc.

(9) At $\theta_e = 90°$, the effect of tunnel velocity on the corrected spectra was virtually independent of frequency, and the spectra at various tunnel velocities were nearly parallel. This implied constant reduction in equivalent source strength at all frequencies. At smaller angles to the downstream

---

[+]See Footnote on page 76.

jet axis, the noise reductions with forward velocity were slightly frequency dependent; at $\theta_e \sim 40°$, the magnitudes of these reductions decreased slightly, but consistently, as the frequency increased.

(10) The corrected overall SPL results indicated that the magnitudes of the inflight noise reductions increased as the observer moved from $\theta_e = 90°$ toward the downstream jet axis. The reductions at all emission angles were scaled on the relative velocity (jet velocity minus tunnel velocity) basis. At $\theta_e = 90°$, the overall intensity was found to be proportional to 5.5 powers of the relative velocity, a result which agreed closely with the theoretical velocity dependence, $I \propto V_{REL}^6$, that is derived purely from source alteration considerations in Appendix 4C.

(11) Comparison of the relative velocity exponents m, obtained from the present corrected results, with the exponent values obtained in the NGTE wind tunnel experiments (where the test section to nozzle area ratio was 5000), showed that the agreement was good at all emission angles.⁺ From this comparison, it is concluded that (a) the effect of scattering caused by turbulence in the free-jet mixing layer did not appear to be significant; (b) the free jet to nozzle area ratio of 400 used in the present experiments was adequate for accurate evaluation of inflight effects on jet noise, and (c) a free-jet facility is capable of simulating most of the inflight effects on jet noise, providing adequate and accurate facility corrections are applied to the measured results.

(12) The comparison of results from inflight simulation experiments with full-scale flight results shows that although the agreement is reasonable at low angles to the jet exhaust, there are significant discrepancies at larger angles. At $\theta_e = 90°$, there is little or no change in the flyover noise levels, whereas the free-jet experiments indicate significant noise reductions. All attempts to explain this discrepancy in terms of source motion (relative to a fixed observer) effects lead to the conclusion that the flyover results at 90° will not be affected. It is therefore concluded that the flight results considered here may not represent pure turbulent mixing noise, but are likely to be contaminated significantly by engine internal or other noise sources. It is recommended that the "acoustic cleanliness" of all flight results be examined thoroughly, both for existing flight data as well as any future flight test results.

(13) Finally, a theoretical formula for the prediction of inflight noise reductions at emission angles outside the so-called zone of silence was presented, and the correlation between calculated and measured OASPL reductions was obtained to an accuracy of ±1/2 dB.

⁺*The area ratio of 400 in the present free-jet experiments is based on the nozzle exit area for the 5.08 cm. diameter primary jet, and is not based on the cross-sectional area of the 10.2 cm. upstream air supply pipe. This is justified, since there is no flow separation over the outer surface of the jet nozzle. For a suppressor nozzle configuration, however, it may not be possible to consider the area ratio in this manner. In particular, for highly segmented nozzles, the area ratio should not be based on the effective area at the nozzle exit plane. In such cases, it is necessary to examine the spread rate of the jet flow in order to ensure correct aerodynamic simulation.*

3. ACOUSTIC PROPAGATION THEORY

In a scientific investigation of the effects of forward motion on jet exhaust noise from aircraft, the many-faceted role of acoustic propagation theory is crystallized in the central problem of *flight simulation*; that is, to specify the features required of flight simulation facilities and then to relate acoustic measurements from real flight simulation facilities with those taken under flight test conditions.

In order to do this it is necessary, first, to define idealized models of the facilities and flight test conditions. With highly idealized models, basic features can be identified and fundamental relations can be established in a straightforward way; then the models can be made progressively more realistic, in a step-by-step fashion, so that the influence and significance of each real effect can be assessed in a logical manner.

An "overview" type investigation that would assess the influence of all known, real sound propagation effects under flight and simulated flight con-ditions (e.g. turbulence scattering, ground reflections) is clearly desirable. However, when the investigation is severely limited by temporal and/or finan-cial constraints, a choice should be made between a necessarily superficial "overview" study and an "in depth" investigation focused on one or two of the more important aspects of the problem. The investigation described in this chapter is of the latter type.

In section 3.1 the most basic idealized models of a flight test condi-tion and a flight simulation facility are defined and the acoustic propaga-tion features of two (static) practical realizations of the ideal flight simulation facility are described. In one of these, the free-jet facility, acoustic propagation through the free-jet shear layer is studied in consider-able detail with the aid of geometric acoustics theory. This, in conjunction with a semi-empirical model of axial source distributions in the primary jet, leads to a simple correction procedure that converts free-jet measured acoustic data to estimated flight data. Most of the detailed aspects of this work is described in Appendices 3A through 3F.

In section 3.2 attention is focused upon the influence of forward motion on the so-called flow-acoustic interactions; that is, the interactions that occur as sound escapes from a source region in a highly sheared mean flow field *and* the diffraction, or refraction, of the sound wave as it propagates out of the *primary* jet flow into the radiation field. The most realistic description of those effects are provided by numerical solutions to the Lilley equation; the interpretation of those solutions is extended to include forward motion effects. Some numerical solutions to the Lilley equation are presented to illustrate how flow-acoustic *alteration* effects outside the cone of silence can be calculated to a good approximation with a completely analytic expression. The flow-acoustic interaction effects are incorporated into an overall jet noise model which includes the so-called dynamic effect and the Doppler factor that is a function of the eddy convection velocity relative to the stationary observer under flight conditions.

77

3.1 ACOUSTIC THEORY FOR FLIGHT SIMULATION FACILITIES

3.1.1 The Ideal Flight (IF) Condition

The Ideal Flight condition is shown in Figure 3.1. The acoustic source—the aircraft exhaust — moves with a uniform speed, V_A, along a straight and level flight path in an infinite atmosphere, i.e. the ground surface or reflections and scattering from the ground surface are absent. (Similarly, the aircraft itself is assumed to be acoustically transparent.) The speed of sound and mean density a_0, ρ_0, of the atmosphere are uniform everywhere and the atmosphere is entirely at rest (apart from the motion due to the sound wave itself). The atmosphere is also ideal in the sense that the sound wave is not attenuated except through spherical divergence.

In Figure 3.1 the aircraft is shown in two positions; the first, in Figure 3.1a, corresponds to a time $t = t_e$, at which a partiuclar sound pulse (or small portion of the pressure-time history of the actual, continuously radiated signal) is emitted. At this emission time the observer/aircraft angle and distance are denoted θ_e and R_r. The second position, in Figure 3.1b, is at a later time, when that pulse has travelled the distance R_r to the observer at the speed of sound, a_0. At this reception time the observer/aircraft angle and distance are denoted ψ and R_ψ.

The relation between θ_e and ψ can be derived by working in terms of the pulse travel time, $\hat{t}$, where

$$\hat{t} = R_r/a_0 \qquad (3-1)$$

as indicated in Figure 3.2. The result

$$\cot \psi = \frac{V_A + a_0\cos\theta_e}{a_0 \sin\theta_e} = \frac{M_A + \cos\theta_e}{\sin\theta_e} \qquad (3-2)$$

is equivalent to that given by Ribner (ref. 31), i.e.

$$\cos\theta_e = \frac{\cos\psi - M_A \{1 - M_A^2\sin^2\psi\}^{\frac{1}{2}}}{\{1 - M_A^2\sin^2\psi\}^{\frac{1}{2}} - M_A\cos\psi} \qquad (3-3)$$

or

$$\cos\theta_e = \cos\psi \{1 - M_A^2\sin^2\psi\}^{\frac{1}{2}} - M_A\sin^2\psi. \qquad (3-4)$$

The difference between the emission and reception angles, $\theta_e - \psi$, is shown as a function of ψ in Figure 3.3a, for five values of M_A. The maximum difference occurs when the reception angle is equal to $90°$.

The relation between emission and reception distances R_r, R_ψ follows from the geometry sketched in Figure 3.2

78

AIRCRAFT POSITION AT
EMISSION TIME $t = t_e$

V_A

FLIGHT
PATH

θ_e

UNIFORM ATMOSPHERE
ρ_o, a_o

R_r
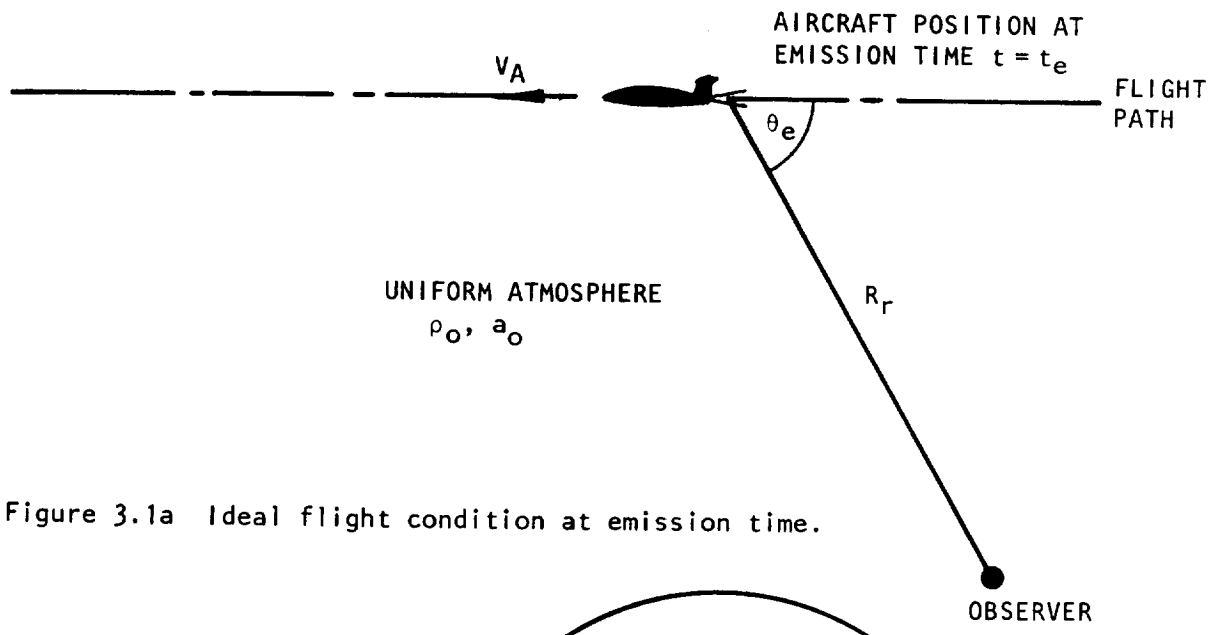
Figure 3.1a   Ideal flight condition at emission time.

OBSERVER

AIRCRAFT POSITION AT
RECEPTION TIME
$t = t_e + R_r/a_o$

V_a

FLIGH
PATH

ψ

θ_e

R_r

R_ψ

UNIFORM
ATMOSPHERE ρ_o, a_o

OBSERVER
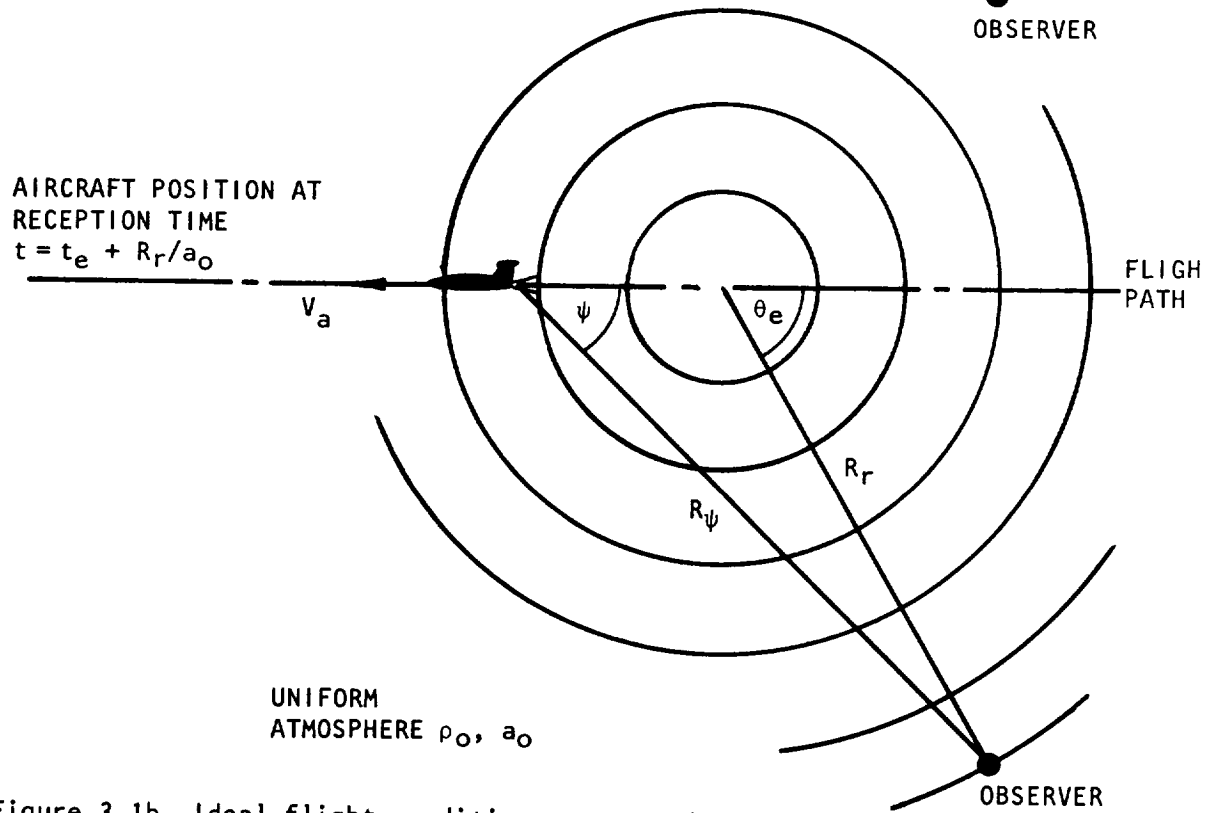
Figure 3.1b   Ideal flight condition at reception time.

79
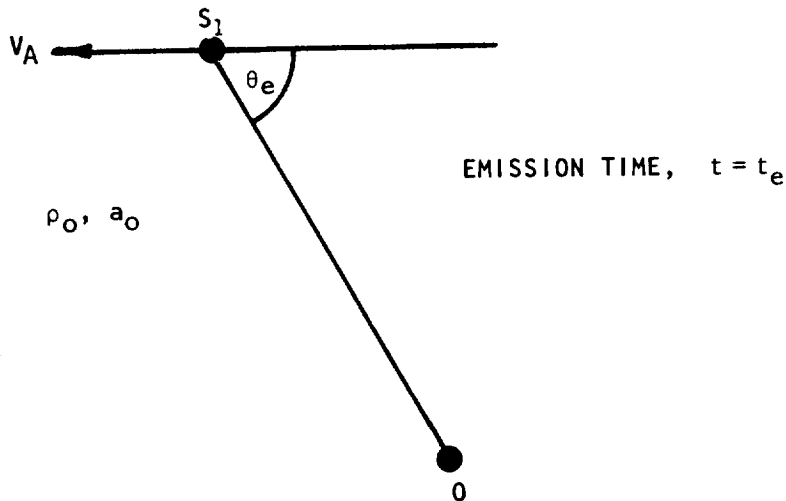
Figure 3.2a   Ideal flight condition geometry at emission time.
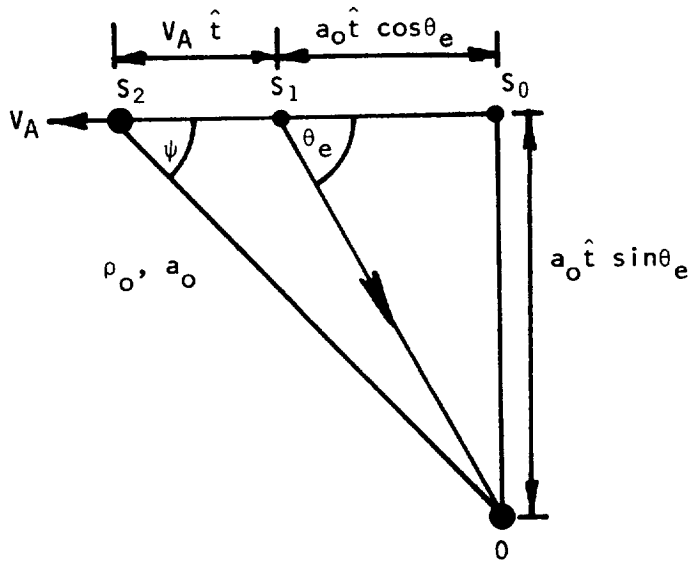
RECEPTION TIME, $t = t_e + \hat{t}$
$(\hat{t} = R_r/a_o)$

DISTANCES: $S_1 0 = a_o \hat{t}$
$S_1 S_2 = V_A \hat{t}$

$\therefore \cot \psi = \dfrac{S_2 S_o}{S_o 0} = \dfrac{V_A + a_o \cos\theta_e}{a_o \sin\theta_e}$

Figure 3.2b   Ideal flight condition geometry at reception time.
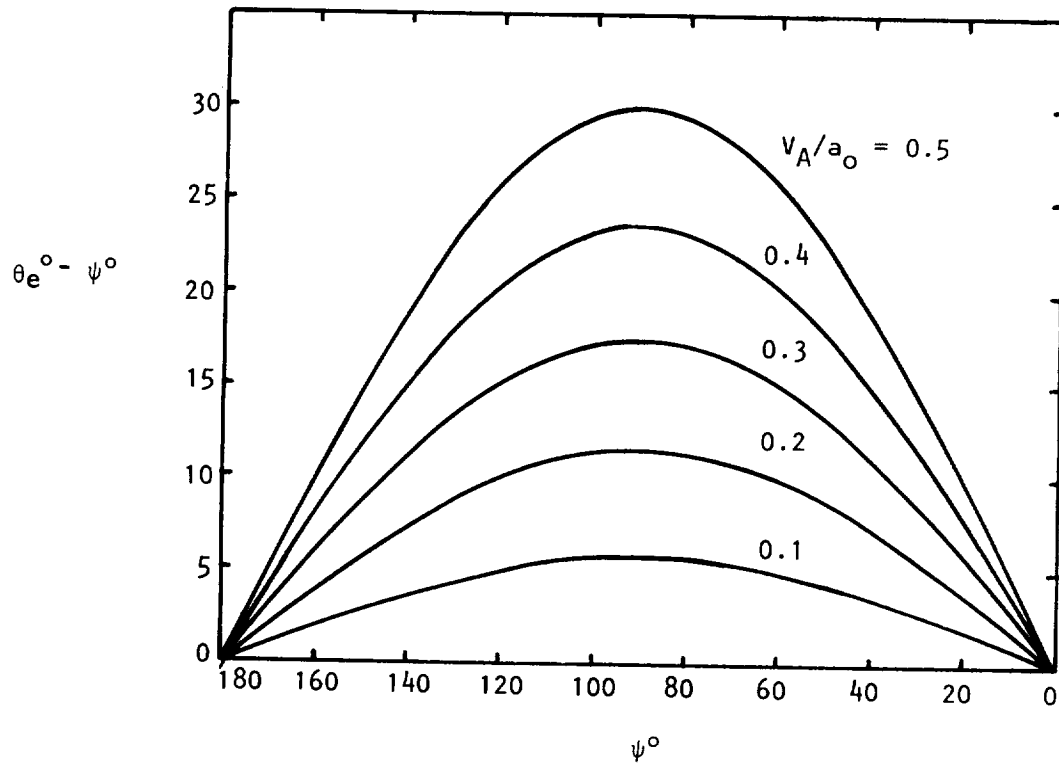
Figure 3.3a   Variation of emission-reception angle difference, $\theta_e - \psi$, with reception angle, ψ, for several aircraft Mach numbers $M_A = V_A/a_o$.
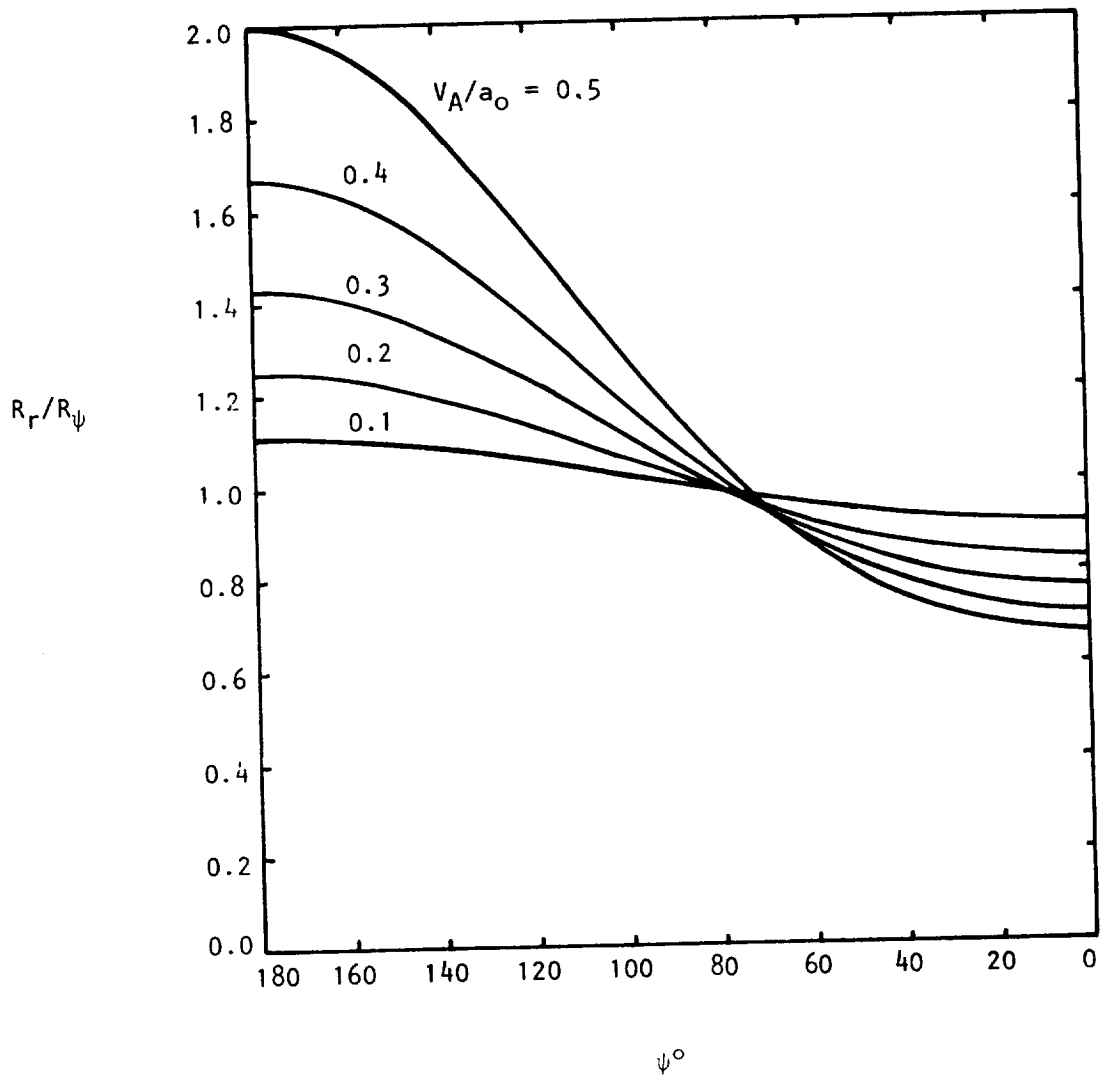
Figure 3.3b   Variation of emission/reception radius ratio, $R_r/R\psi$, with reception angle, ψ, for several aircraft Mach numbers $M_A = V_A/a_o$.

$$R_r/R_\psi = \{1 + M_A^2 + 2M_A \cos\theta_e\}^{-\frac{1}{2}} \tag{3-5}$$

or equivalently, according to Ribner (ref. 31)

$$R_r/R_\psi = (1 - M_A^2 \sin^2\psi)^{\frac{1}{2}}/(1 + M_A \cos\theta_e) . \tag{3-6}$$

This ratio is evaluated in Figure 3.3b for the range of parameter values used in Figure 3.3a.

In the next section this Ideal Flight condition is transformed to a frame of reference in which both the aircraft and observer are at rest.

3.1.2 The Ideal Wind Tunnel (IWT)

The transformation of the Ideal Flight condition, described in the previous section, to a frame of reference in which both acoustic source and observer or microphone are at rest, is carried out in two steps. Starting with the IF condition at reception time, as shown in Figure 3.4a, the first step is to set the microphone in motion so that it occupies the same position *at* reception time but is moving with the same speed and direction as the aircraft, as shown in Figure 3.4b. The moving microphone measures the same acoustic pressure amplitudes as the stationary one but over a modified time period; a pulse detected over a time period Δt_0 by the stationary microphone is detected by the moving microphone over the modified time period $\Delta t = \Delta t_0 D_0$ where

$$D_0 = \{1 + V_A \cos\theta_e/a_0\}^{-1} . \tag{3-7}$$

Hence, in general, the microphones measure the same mean square pressures and the same proportional bandwidth mean square pressures — at different frequencies related by the Doppler factor D_0. That is, if the stationary microphone measures a pressure power spectral density (psd) P_0 at frequency ω_0 and the moving microphone measures a pressure psd P at frequency ω then

$$\omega_0 \cdot P_0(\omega_0) = \omega \cdot P(\omega) \tag{3-8}$$

where

$$\omega_0 = \omega D_0 . \tag{3-9}$$

The second step is simply a Galilean coordinate transformation to the frame of reference that moves with the aircraft and microphone. This does not change the stationary-moving microphone measurement relations given above. However, it does mean that the atmospheric medium now moves with a uniform speed V_A in this new reference frame, as shown in Figure 3.4c. This is referred to here as the "Ideal Wind Tunnel" (IWT): "Ideal" because the "cross section" is infinite and the flow velocity is absolutely uniform and parallel (equal in magnitude to the uniform aircraft speed). Also, of
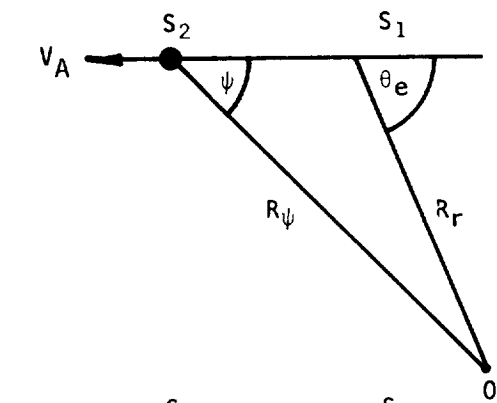
(a) Ideal flight condition at reception time.
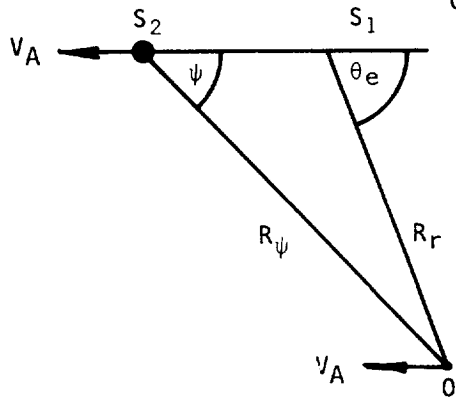
(b) Ideal flight condition at reception time with co-moving microphone (velocity $-V_A$) so that it occupies position 0 at the reception time $t = t_e + R_r/a_o$.
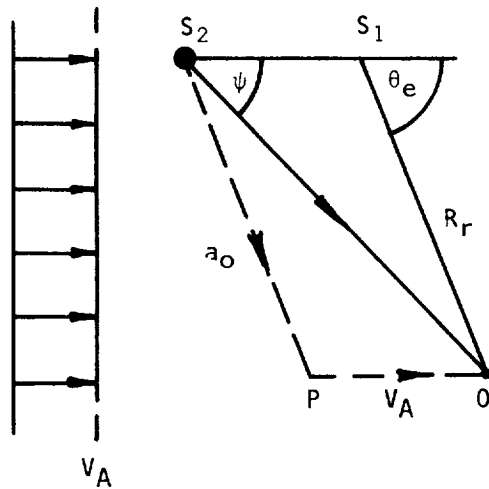
(c) Ideal flight condition at reception time in a co-moving reference frame such that both source and microphone are at rest; now atmospheric medium moves, with uniform velocity V_A - "Ideal Wind Tunnel."

Figure 3.4 The three stages in the transformation from the ideal flight condition to the ideal wind tunnel.

course, the ideal properties of the atmosphere in the IF condition carry over to this new reference frame.

In the IWT the sound pulse emitted by the source at position S_2 propagates along the ray path S_20. The direction and speed of the pulse are still given by θ_e and a_0 *relative to the flow* as shown in Figure 3.4c. The angle θ_e is now the wavenormal angle and R_r is the distance travelled by the ray in the wavenormal direction; ψ is the ray angle. These quantities are denoted by θ_T, R_{rT} and ψ_T in the real wind tunnel or free-jet context. However, it should be emphasized that in principle they are identical, i.e. $\theta_e = \theta_T$, $R_r = R_{rT}$, $\psi = \psi_T$ except that it will be necessary to define more carefully the origin of the polar coordinates R_{rT}, θ_T in the free-jet configuration.

3.1.3 The Real Wind Tunnel and Free-Jet Flight Simulation Facilities: Data Correction to IWT Conditions

The two practical realizations of the IWT are the real wind tunnel and the free-jet; an example of the latter is described in Section 2. For convenience, a real wind tunnel flight simulation facility is defined as one in which the source and microphones are both located within the flow, and a free-jet facility as one in which the microphones are located outside the flow. Both facilities differ, in principle, from the desired IWT facility in that the outer boundary of the uniform flow is a finite distance from the source. The presence of that boundary may influence the source if sufficiently close on the wavelength scale (ref. 23). This effect is not considered here in detail; for the present it is assumed that over the frequency range of interest (1 - 40 KHz) and with the source-boundary separation distance of ~20" in the Lockheed facility, this effect can be neglected.

The outer boundary of the uniform flow may also reflect/scatter sound that may cause significant interference with the direct radiation at microphone locations in the real wind tunnel. In the free-jet facility, the direct radiation undergoes transmission, refraction and scattering effects as it propagates through the free-jet shear layer. The resulting radiation levels at the microphone locations outside the flow may differ considerably from the (required) direct radiation existing within the flow. Internal reflection in either type of facility are not thought to be important, in fact, it will be argued that usually conditions are such that sound propagation within the free-jet shear layer can be described by geometric acoustics. Then, by definition there are *no* reflections and the transmission and refraction processes can be calculated with fairly well established analytical models. Turbulence scattering effects are not considered here since the limited experimental results presented in Section 2 suggest that this is an unimportant effect in the present context.

One other problem in flight simulation is that a restriction can arise on the maximum source-microphone distance(s) such that consistent scaling of this distance is not possible. Thus, for example, a separation distance of one hundred jet nozzle diameters or more may be used in a flight test,

but only twenty diameters might be possible in a real wind tunnel due to its finite cross-section. Since the jet mixing noise source is distributed axially, reduction in the microphone-jet nozzle separation will result in a progressive distortion in the measured directivity pattern relative to that measured at large or true far-field distances.

In what follows the emphasis is upon the free-jet facility and how theoretical and empirical models have been utilized to estimate corrections that convert measured data to estimated, true far-field IWT data. The actual corrected or estimated IWT data is given in Section 2 along with the basic free-jet measured data.

A detailed description of the models and correction procedures is given in Appendices 3A - 3F. In Appendix 3A theoretical expressions are developed, based upon geometric acoustics, for the radiation from various types of source distributions (simple, quadrupole; volume acceleration, volume displacement; at rest, convected; compact, noncompact) when the source distribution is immersed in a parallel, stratified, sheared flow. Appendix 3B deals with the more general case of wave acoustics propagation in an infinite, parallel, stratified sheared flow, mainly in connection with the Lilley equation solutions described in section 3.2. Thus, Appendices 3A and 3B are not exclusively concerned with the correction procedure and models, but they provide a general introduction and lay the foundation for the theoretical work in this section.

The mean flow model used in Appendices 3A and 3B is stratified; that is, the mean flow properties vary only with the transverse coordinate. Thus, a ray may propagate a significant distance in the flow direction, but the axial mean velocity, for example, is not allowed to vary in that direction as it does in a real jet flow. Appendix 3C describes an investigation in which that restriction is relaxed, but it is shown that axial variations and gradients have a negligible influence on the refraction of sound rays by the free-jet shear layer. That is, a *stratified* flow model *is* adequate for present purposes and the ray paths may be drawn as if the shear layer has been replaced by a vortex sheet at the free-jet lip-line. On the other hand, the theory of Appendices 3A - 3C rests entirely on the assumption that the sound propagation is governed by the laws of geometric acoustics (GA). A qualitative justification of that assumption is given in Appendix 3C; detailed quantitative information on the accuracy of GA for infinite stratified sheared flow models of the primary jet are being obtained from Lilley equation solutions under an on-going USAF/DOT contract. A complete Lilley equation study should be undertaken of radiation from quadrupole sources at realistic locations in a primary jet that is surrounded by a (finite cross section) free-jet, in order to assess the accuracy of the present geometric acoustics approach.

With the results of Appendix 3C the rest of the GA correction procedure is straightforward. In Appendix 3D, a simple but adequate model is given for the effective axial location of the jet noise sources as a function of frequency or Strouhal number. In Appendix 3E the GA energy conservation law is used to relate measured acoustic pressures outside the free-jet with the

86

(required) acoustic pressures inside the uniform, potential core region of the free-jet. The actual correction procedure is then described in Appendix 3F.

3.2 THEORETICAL FLIGHT ALTERATION EFFECTS ON FLOW-ACOUSTIC INTERACTIONS

Theoretical flight alteration effects on flow-acoustic interactions in the geometric acoustics limit can be calculated outside the cone of silence from the analytic expressions given in Appendix 3A. For example, equation (3A-15) with equation (3A-26) can be written as

$$\omega_o P_o(\omega_o) \propto D_o D_{s,rel}^2 / D_{m,rel}^5 \qquad \text{(3-10)}$$

(volume acceleration source, denoted in subsequent analysis by $\nu = 1$)

if

$$- a_o/(a_s - V_{s,rel}) < \cos\theta_e < a_o/(a_s + V_{s,rel}) \qquad \text{(3-11)}$$

where

$$V_{s,rel} = V_s - V_A \qquad \text{(3-12)}$$

$$D_{s,rel} = 1 - V_{s,rel} \cos\theta_e/a_o \qquad \text{(3-13)}$$

$$D_{m,rel} = [\{1 - (V_c - V_A) \cos\theta_e/a_o\}^2 + \{(V_{el}^2 - V_{et}^2)/a_o^2\} \cos^2\theta_e$$

$$+ D_{s,rel}^2 \, V_{et}^2/a_s^2]^{\frac{1}{2}} \qquad \text{(3-14)}$$

$$D_o = \{1 + V_A \cos\theta_e/a_o\}^{-1}$$

and V_s is the mean axial fluid velocity at the typical source position; that is, the *directivity* of the IF (or IWT) proportional bandwidth mean square pressure radiated by a volume acceleration quadrupole distribution is altered by forward motion in three ways, through:

(a) the dynamic effect (D_o factor),

(b) the eddy convection alteration effect ($V_c \rightarrow V_c - V_A$), and

(c) the flow-acoustic alteration effect ($D_s \rightarrow D_{s,rel}$)

The first two effects are well established features of Ribner's (ref. 31) or Ffowcs Williams' (ref. 7) extension of the Lighthill jet mixing noise analogy model. It should be noted that the so-called dynamic effect can also

appear in the Ideal Wind Tunnel directivity expression where the observer is stationary with respect to the nozzle. (Here V_T has been replaced by V_A). In general, flow-acoustic alteration effects are described by numerical solutions to Lilley's equation which, in effect, replace the geometric acoustics analytic result (given above, for example); essentially this means that the flow-acoustic interaction factor $D^2_{s,rel}$ is replaced by the so-called flow factor $F^{(1)}_{rel}(\omega_0)$, as outlined in Appendix 3B. Lilley's equation solutions are regarded as more realistic than GA results in describing flow-acoustic interactions although in many practical cases differences between the two are small. This is indeed the case, outside the cone of silence, when axial source locations are chosen according to the model described in Appendix 3D, and this will be illustrated with examples given below.

The GA result given by equation (3-10) refers to a volume acceleration source distribution; the corresponding volume displacement result is

$$\omega_0 P_0(\omega_0) \propto D_0 \, D^6_{s,rel}/D^9_{m,rel} \quad \text{(volume displacement} \atop \text{source denoted by } \nu = 3) \qquad (3\text{-}15)$$

In a recent paper (ref. 32) Tester and Morfey have presented arguments in favor of the displacement type of source, at least for modeling jet mixing noise with Lilley's equation. Thus numerical solutions given before are confined to this type of source [the flow factor has the superscript $(\nu) = (3)$] although throughout Appendices A and B and elsewhere in this section analytical results are given for both types of source since the volume acceleration source has the same frequency dependence as that of classical Lighthill quadrupole source distribution and therefore remains of considerable interest.

To summarize the utilization of Lilley equation results, the numerical solutions to that equation define a value for the flow factor $F_{rel}(\omega_0)$ or $F(\omega)$, the ratio of the far-field radiation intensity to its value without the mean flow (e.g. $V_s = V_A$ or $V_s = V_A = 0$) the source strength being held constant. The flow factor $F_{rel}(\omega_0)$ is used in the IF reference frame context,

$$\omega_0 P_0(\omega_0) \propto F^{(\nu)}_{rel}(\omega_0) \, D_0/D^{2\nu+3}_{m,rel}, \qquad (3\text{-}16)$$

and $F(\omega)$ in the IWT reference frame contexts

$$\omega P(\omega) \propto F^{(\nu)}(\omega)/D^{2\nu+3}_m . \qquad (3\text{-}17)$$

Thus, although the proportional bandwidth mean square pressures are identical, the modified Doppler factors representing convective amplification due to source motion are different in each case and the dynamic effect factor is excluded from the IWT expression; hence the flow factors are not identical. The IWT modified Doppler factor $D_m = \omega_m/\omega$ is given by equation (3A-19) or (3B-1) (in which the transverse wavenumber scaling velocities, $V_{e2} = V_{e3} = V_{et}$, are neglected)

88

$$\omega_m^2 = (\omega - k_1 \, V_{c1})^2 + k_1^2 \, V_{e1}^2 = \omega^2 D_m^2 \tag{3-18}$$

The wavenumber k_1 is first defined in the IF frame

$$k_1 = (\omega_0/a_0) \cos\theta_e \tag{3-19}$$

and is invariant under the Galilean transformation to the IWT frame. Thus D_m can be written as

$$D_m = \{(1 - D_0 \, V_{c1} \cos\theta_e/a_0)^2 + D_0^2 \, (V_{e1}\cos\theta_e/a_0)^2\}^{\frac{1}{2}} \tag{3-20}$$

The appropriate modified Doppler factor for the IF frame, $D_{m,rel}$, is simply

$$D_{m,rel} = D_m/D_0$$

$$= [\{1 - (V_{c1} - V_0) \cos\theta_e/a_0\}^2 + \{V_{e1} \cos\theta_e/a_0\}^2]^{\frac{1}{2}} \tag{3-21}$$

where now the eddy convection velocity appears in a "relative to observer form" [as it does in the Ribner (ref. 31) or Ffowcs Williams (ref. 7) results].

In the following section the relation between the two different flow factors is given and the choice of reference frame (in which the Lilley equation has been solved) is discussed.

3.2.1 Choice of Reference Frame for Lilley Equation Solutions

In Appendix 3B the relation between the Lilley equation flow factor in the ideal flight and wind tunnel reference frames, F_{rel}, F is given as

$$F^{(3)}(\omega) = F_{rel}^{(3)}(\omega_0) \, D_0^{10} \qquad \text{(volume displacement source)} \tag{3-22}$$

$$F^{(1)}(\omega) = F_{rel}^{(1)}(\omega_0) \, D_0^6 \qquad \text{(volume acceleration source)} \tag{3-23}$$

where

$$D_0 = \omega_0/\omega = (1 + V_A\cos\theta_e/a_0)^{-1}.$$

In the IWT reference frame the flow factor $F(\omega)$ is modified by the presence of the co-flowing stream (see Figure 3.5) of velocity $V = V_A$. In the IF reference frame, $F_{rel}(\omega_0)$ changes in response to the reduction in the mean velocity, e.g. from V_J to $V_J - V_A = V_{J,rel}$. With the simple relation given above conversion from one reference frame to the other is straightforward and flow factor results can be generated in either reference frame. Here the IF frame is chosen since the flow profile is identical to that in the
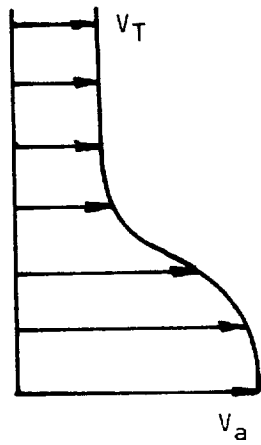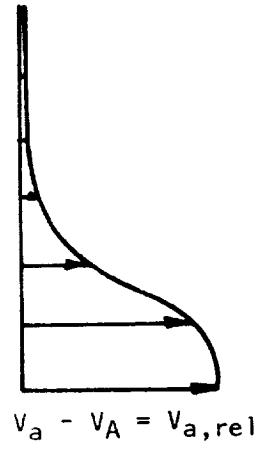
(a)   Ideal wind tunnel.   (b)   Ideal flight.

Figure 3.5   Typical mean flow profiles for the Lilley equation
            in each reference frame: (a) ideal wind tunnel,
            (b) ideal flight.

static case, for which the Lilley equation solution method was originally developed, but with the velocity profile reduced by the forward speed, V_A. Thus, it has not been necessary to modify in any way the solution method. That method has been fully described in a recent paper by Tester and Morfey (ref. 33), which also includes a selection of numerical results and some comparisons with measured static jet noise directivity data.

3.2.2 Definition of Parameters

However, the results given in references (32) and (33) are not in a sufficiently complete or suitable form for the present investigation. Of major interest here is the variation of calculated flow-acoustic interaction effects with forward motion, i.e. with, say, variation of centerline velocity, $V_{a,rel} = V_a - V_A$; the absolute centerline velocity is denoted V_a since solutions for the fully developed region of the jet flow where $V_a \neq V_J$ are included in this study.

The frequency parameter is the modified Strouhal number S_m where

$$S_m = S \ D_{m,rel} \tag{3-24}$$

$$S = f_o d / V_{J,rel} \qquad (f_o = \omega_o / 2\pi) \tag{3-25}$$

$$D_{m,rel} = \{D^2_{s,rel} \ [1 + \alpha_1^2 (V_{a,rel}/a_o)^2] + (\beta_1^2 - \alpha_1^2) \ (V_{a,rel} \cos\theta_e/a_o)^2\}^{\frac{1}{2}} \tag{3-26}$$

$$D_{s,rel} = \{1 + (V_s - V_A) \cos\theta_s/a_o\}^{-1} \tag{3-27}$$

$$\alpha_1 = 0.2, \ \beta_1 = 0.4 \tag{3-28}$$

$$(V_s - V_A) = 0.6 \ (V_a - V_A). \tag{3-29}$$

This isothermal form of the modified Doppler factor follows from equation (3A-23) (in Appendix 3A) and the assumption that the wavenumber scaling velocities V_{e1}, V_{et} are proportional to $V_{a,rel}$; the values of α_1, β_1 were obtained by Szewczyk and Morfey (ref. 34) from their purely geometric acoustics analysis of Lockheed *static* jet mixing noise data (refs. 35, 36). They also deduced that $V_c \pm V_s \pm 0.6 \ V_J$ and this result, together with the α_1, β_1 results, have been used here for the flight case without any quantitative justification. Actually it has been established in further work, as yet incomplete, that the precise form of this modified Doppler factor is not critical in this theoretical exercise and that $D_{s,rel}$ could be used in place of $D_{m,rel}$ in equation (3-24). The exact value of $V_c = V_s$ itself is also not critical provided that the wavenormal angle θ_s within the *primary* jet is held constant where

$$\cos\theta_e = \cos\theta_s \cdot D_{s,rel}. \tag{3-30}$$

In the following numerical results, error function velocity profiles have been used which correspond, nominally, to actual profiles at the axial locations of 1 and 4 diameters in the intial mixing region of an axisymmetric jet. In addition, an "inverse exponential squared" profile has been used to represent the transition and fully developed regions. Each profile is defined by the ratio of its vorticity thickness, δ_ω, and the radius, r_1, at which the mean velocity is 66.3% of its centerline value.

3.2.3 Numerical Results

At the nominal one diameter axial location $(\delta_\omega/r_1 = .26)$, Lilley equation flow factor results are shown in Figure 3.6 for $\theta_s = 60°$ and modified Strouhal numbers $S_m = 1.0$, 2.0 and 4.0. According to the simple law described in Appendix 3D, the one diameter location is equal to the effective axial location for $S_m = 5$ radiation. Thus, radiation at Strouhal numbers less than this tend to originate further downstream. The results in Figure 3.6 show quite clearly that radiation at Strouhal numbers greater than $S_m = 4$ differ from the geometric acoustics limit by less than 1/2 dB.

At the nominal four diameter axial location for $\theta_s = 60°$ and $S_m = 0.5$, 1.0 and 2.0, the flow factor results shown in Figure 3.7 obey a similar trend. This axial location corresponds to the effective one for $S_m \doteq 1.0$ radiation and here the difference between wave and geometric acoustics is less than 1 dB. However, the major trend of interest in these results is that the rate of change of flow factor with $V_{a,rel}$ or slope of the curves in Figures 3.6 and 3.7 is almost identical to that of the analytic geometric acoustics limit over a *wide range* of Strouhal numbers. Therefore, unless the semi-empirical law for effective axial source location variation with Strouhal number is grossly in error for both static and flight conditions, any change in $V_{a,rel}$ (e.g. by a change in aircraft speed, V_A) will bring about a *change* in the Lilley equation flow factor, $F_{rel}^{(3)}(\omega_o)$ which can be closely predicted by the *change* in the GA limit. That limit is given by

$$F_{rel}^{(3)}(\omega_o)\Big|_{GA} = D_{s,rel}^{6} \; ; \tag{3-31}$$

its derivation is briefly described in reference (32). This feature is also exhibited by the results shown in Figure 3.8 for a fully-developed mean velocity profile. In this case, a different Strouhal number is utilized, S_m', where

$$S_m' = (D_{m,rel} \, f_o) \, (2 \, r_1)/V_{a,rel}$$

$$= S_m \, (2 \, r_1/d) \, (V_{J,rel}/V_{a,rel}). \tag{3-32}$$

Since $2 r_1$ is approximately equal to δ_ω for this profile, S_m' is roughly the *local* modified Strouhal number.

$$S_m' \simeq (D_{m,rel} \, f_o) \, \delta_\omega/V_{a,rel} \tag{3-33}$$

92
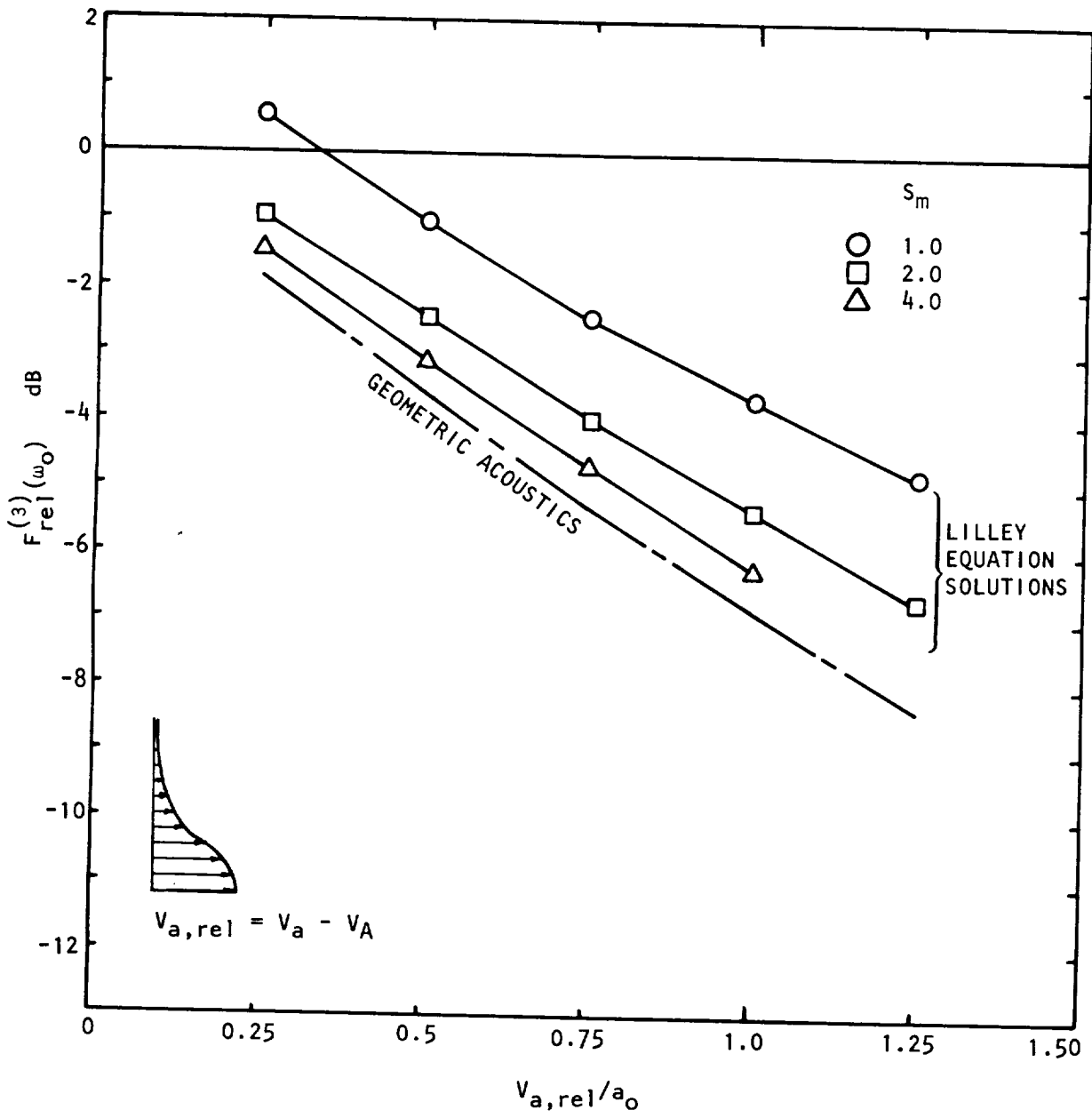
Figure 3.6 Variation of the flow-acoustic interactions factor, $F_{rel}^{(3)}$, with the relative centerline velocity, $V_{a,rel}$, from Lilley equation solutions and from geometric acoustics theory. *Profile: One diameter axial location*, $\delta_\omega/r_1 = 0.26$; $V_a \approx V_J$. *Source emission angle*, $\theta_s = 60°$.
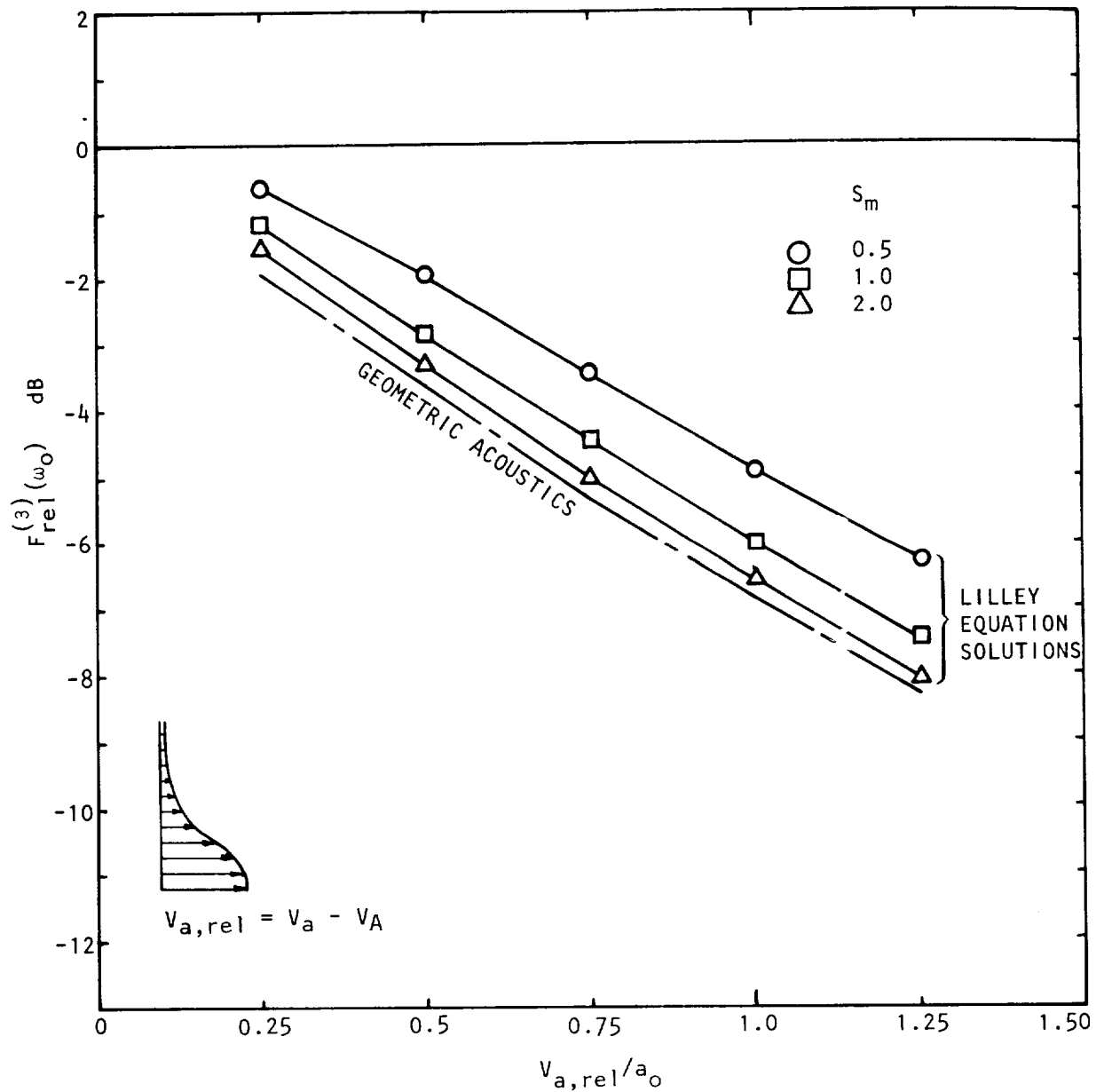
Figure 3.7   Variation of the flow-acoustic interactions factor, $F_{rel}^{(3)}$, with the relative centerline velocity, $V_{a,rel}$, from Lilley equation solutions and geometric acoustics theory. *Profile: Four diameter axial location*, $\delta_\omega/r_1 = 1.05$; $V_a \equiv V_J$. *Source emission angle*, $\theta_s = 60°$.

94
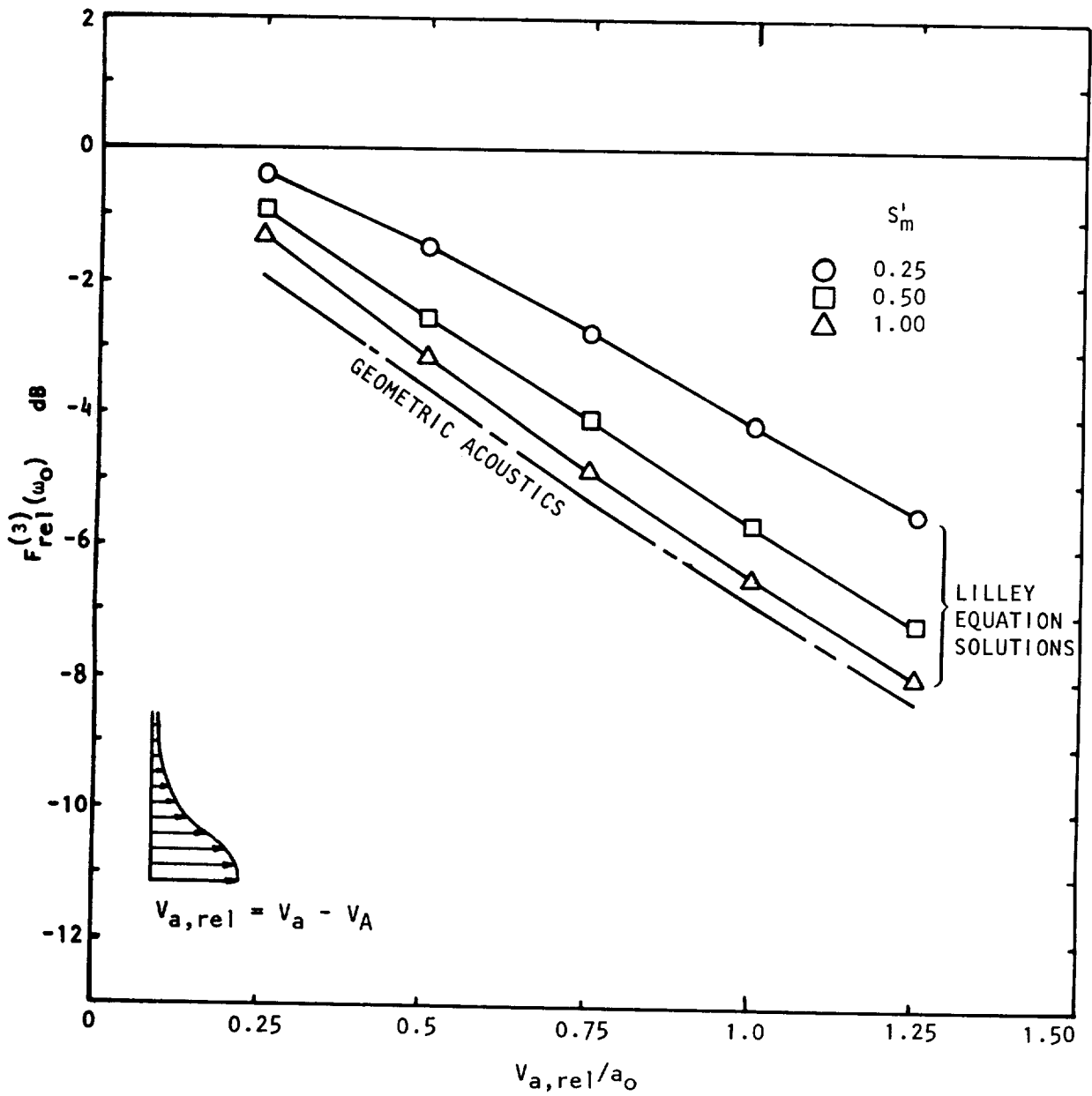
Figure 3.8 Variation of the flow-acoustic interactions factor, $F_{rel}^{(3)}$, with the relative centerline velocity, $V_{a,rel}$, from Lilley equation solutions and geometric acoustics theory. *Profile: Fully developed,* $\delta_\omega/r = 1.82$; $V_a \neq V_J$. *Source emission angle,* $\theta_s = 60°$.

i.e. one based on the local shear layer thickness and the local centerline mean velocity. This takes a value of order unity so that the difference between the Lilley equation flow factors and that given by the GA limit for all S_m values less than unity are small and the slopes are nearly identical.

The main influence of the wavenormal angle θ_s is to modify the differences between Lilley equation and GA flow factors as illustrated in Figure 3.9 for $\theta_s = 30^\circ$; the slopes, however, remain very similar. The variation of θ_e with θ_s is given in Table 3.1.

$(V_{a,rel}/a_o)/\theta_s^\circ$	0	30	60	120
.25	29.6	40.0	62.3	122.7
.50	39.7	46.6	64.2	126.0
.75	46.4	51.4	65.9	130.2
1.00	51.3	55.2	67.4	135.6
1.25	55.2	58.3	68.7	143.1

Table 3.1 Emission angle values, θ_e°, as a function of source emission or wavenormal angle θ_s and $V_{a,rel}/a_o$ with $V_{s,rel} = 0.6\ V_{a,rel}$
$(\cos\theta_e = \cos\theta_s/(1 + V_{s,rel}\ \cos\theta_s/a_o))$.

3.2.4 The Geometric Acoustics Result for Data Correlation Outside the Cone of Silence

It is clear from the preceding results (including Table 3.1) that for moderate changes in $V_{a,rel}$ or λ, at constant θ_s or θ_e, the GA limit can be used, to a good approximation, to calculate estimated forward motion alteration effects on flow-acoustic interactions. From equation (3B-12) (Appendix 3B) and equation (3-31) it follows that changes in directivity at constant Strouhal number in the IWT reference frame can be estimated from the expression

$$D_{s,rel}^6\ D_o/D_{m,rel}^9 \tag{3-34}$$

where

$$D_{s,rel} = 1 - (V_s - V_A)\ \cos\theta_e/a_o$$

$$D_o = (1 + V_A\ \cos\theta_e/a_o)^{-1}$$

and $D_{m,rel}$ can be evaluated with equation (3-26). An alternative form for $D_{m,rel}$, used in Section 2 for data correlation purposes, is

$$D_{m,rel} = \{D_{s,rel}^2 + \alpha^2(V_{c,rel}/a_o)^2\}^{\frac{1}{2}} \tag{3-35}$$

$$(\alpha = 0.3)\ .$$

96
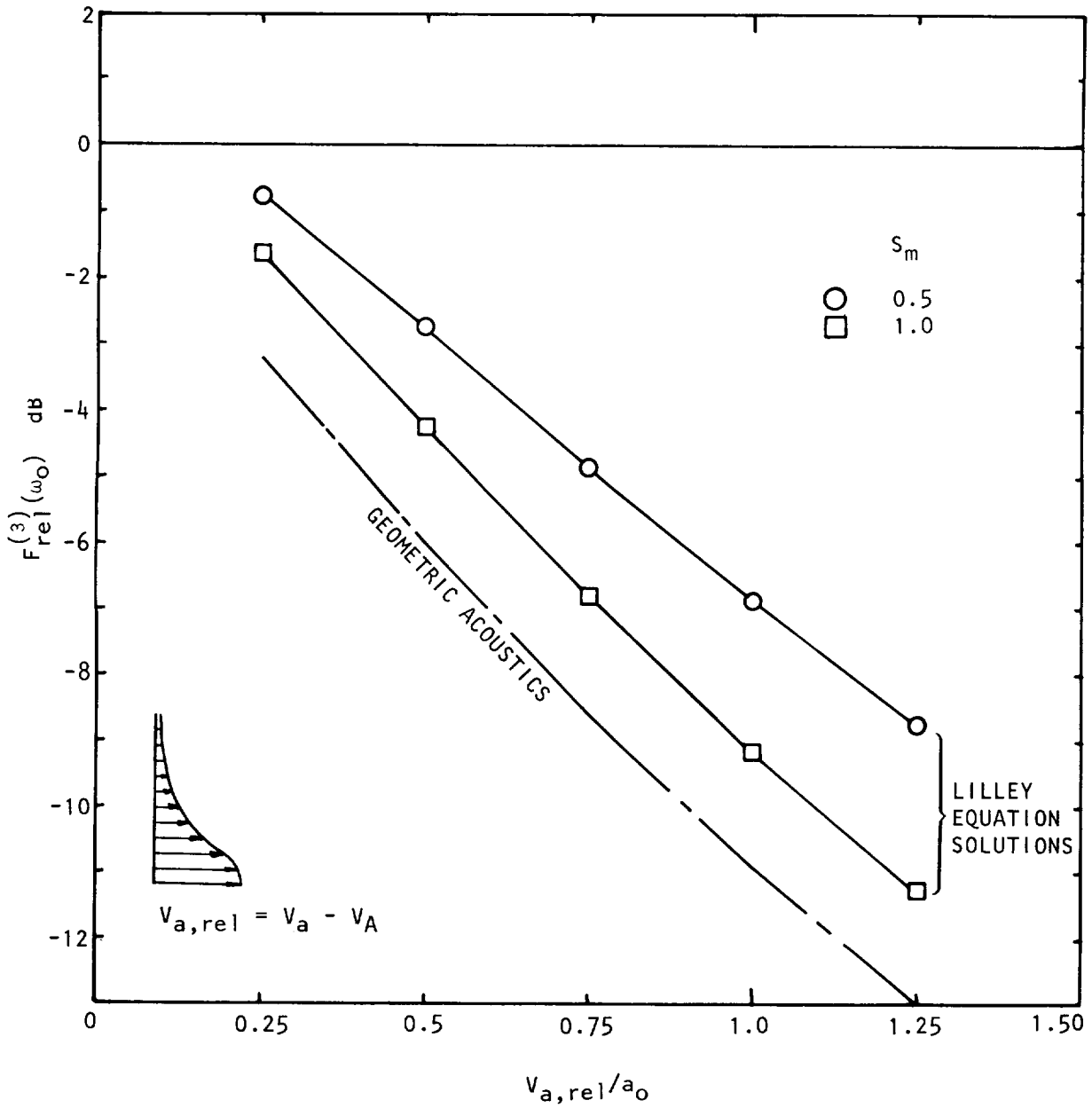
Figure 3.9 Variation of the flow-acoustic interactions factors, $F_{rel}^{(3)}$, with the relative centerline velocity, $V_{a,rel}$, from Lilley equation solutions and geometric acoustics theory. *Profile: Four diameter axial location,* $\delta_\omega/r_1 = 1.05$; $V_a \equiv V_J$. *Source emission angle* $\theta_s = 30°$.

97

There the Doppler factor $D_{s,rel}$ is calculated with

$$V_s - V_A = V_c - V_A = V_{c,rel} = 0.67 \, V_{J,rel}. \tag{3-36}$$

Equation (3-36) is based upon the assumption that the eddy convection velocity, V_c, and the mean flow velocity at the effective source location, V_s, are identical. Also, it implies that the eddy convection velocity changes with forward motion since it can be rewritten as

$$V_c = 0.67 \, V_J + 0.33 \, V_A. \tag{3-37}$$

Neither equation (3-36) nor equation (3-37) are based on any solid evidence, experimental or theoretical; they are simply assumptions which are convenient to use and appear to be reasonable at this time.

The expression (3-34) above has been evaluated and the results compared with overall directivity alteration in the measured data as shown in Figure 2.2. The excellent agreement provides adequate incentive to extend the present investigation to the forward arc, to angles inside the cone of silence and to non-isothermal jets.

5.3 CONCLUSIONS

Detailed conclusions for each of the main investigation areas have been given in the appropriate subsections and appendices; they can be summarized as follows:

(1) It is necessary to define idealized, conceptual models of flight and *simulated* flight conditions in order to highlight the important acoustic features and interrelationships and to specify the basic acoustic features required of flight simulation facilities. In the Ideal Flight (IF) condition emission and reception angles and distances must be distinguished; here their functional relations have also been defined and evaluated. In the Ideal Wind Tunnel (IWT), IF data can be acquired if the distance travelled by the sound wave in the wavenormal direction and the wavenormal angle are both held constant. Then only a Doppler frequency shift needs to be applied to convert data from the IWT to the IF condition. Amplitude "corrections" are not required for the mean square pressure nor for the proportional bandwidth mean square pressure.

(2) In a real wind tunnel flight simulation facility, unwanted reflections and scattering from the outer boundary region of the uniform tunnel flow are probably unimportant. However, the finite area ratio effect and the axial distribution of the turbulent jet mixing noise source should be investigated. The finite area ratio effect should be examined with the aid of Lilley equation solutions for the complete flow field. The axial source distribution effect can be modeled empirically to yield distance and angle corrections for the measured data. Otherwise the ideal and real wind tunnel

are acoustically equivalent if "atmospheric" attenuation effects in the real wind tunnel can be estimated accurately.

(3) Acoustic propagation in the free-jet flight simulation facility has been studied in considerable detail in the geometric acoustics approximation. The approximation can be justified, *qualitatively*, for the present application by an analysis of the Lilley equation in relation to the equation governing geometric acoustics propagation. However, the accuracy of Geometric Acoustics (GA) should be assessed in future work with a quantitative study based upon Lilley equation solutions.

The position and angle of ray paths through the free-jet shear layer have been calculated; the mean flow within the shear layer was allowed to vary axially in a realistic way. The results are nearly identical to those that are calculated with a vortex sheet model of the free-jet flow, over a wide range of parameters. However, the amplitude of the sound along a ray path is governed by the ray tube geometry *and* the law of energy conservation in a ray tube, *not* the transmission of a sound ray by a vortex sheet. Hence, angle and distance corrections that convert free-jet data to estimated Ideal Wind Tunnel data can be based on a standard vortex sheet model while transmission-amplitude corrections should be calculated with the analytic formula derived here.

The complete correction procedure also uses an empirical model of the turbulent mixing noise source axial distribution (as a function of Strouhal number) to calculate additional angle and distance corrections.

(4) The influence of forward motion on flow-acoustic interactions (within the primary jet flow alone) has been examined in the Ideal Flight condition through a re-interpretation of the "static" numerical solutions to the Lilley equation and with geometric acoustics. It has been demonstrated that outside the cone of silence the Lilley equation radiation levels *change* with forward motion in a way that can be calculated, to a good approximation, with the analytic, GA result. When this GA flow-acoustic alteration effect was combined with the standard, theoretical, dynamic and convective amplification alteration effects, the predicted directivity alteration with forward motion was found to be in excellent agreement with measured free-jet data outside the cone of silence. This successful correlation of directivity data justifies an extension of the present work to include forward arc angles, angles inside the cone of silence and non-isothermal primary jet flow.

4. EFFECT OF FORWARD VELOCITY ON THE STRUCTURE OF A TURBULENT JET

4.1 INTRODUCTION

In this chapter of the report, the changes in structure of a round jet caused by variation of free stream velocity will be examined. The work to be described is in three sections. The first section is an experimental investigation, and turbulence measurements of a round jet in a wind tunnel are presented. These measurements are used to provide scaling laws for various characteristic lengths and velocities as functions of velocity ratio and jet Mach number. The second section is a numerical study of the development of a turbulent jet in a moving stream. The results of this analysis are compared with experimental measurements. The third section makes use of the scaling laws derived from the experiments to predict the changes in radiated noise with changes in velocity ratio brought about by alteration of the turbulent jet structure. Several appendices associated with this chapter are also included. These provide a complete tabulation of the velocity measurements and a discussion of the data processing techniques used to analyze the laser velocimeter measurements. A simple analysis is also available to describe the decay of the jet center-line velocity. Finally, an original method, based on the velocity at the dividing streamline, of noise radiation scaling with changes in forward velocity is given.

Before the investigations are described in detail, it is necessary to discuss to what extent the experiments performed simulate the case of a full-scale jet moving through stationary air at a uniform forward velocity. There are two questions which need to be considered. Firstly, whether the stationary jet in a moving stream simulates a moving jet in a stationary stream from the point of view of turbulent structure? Secondly, can the measurements made at model-size be used to predict full-size structure?

The answer to the first question is based simply on a change in reference system. A control volume is considered which surrounds the disturbed flow region around the jet and the axes are fixed relative to the jet exit. So long as the boundary conditions in the jet reference frame are unchanged, the only difference that can exist is due to changes in the equations which govern the fluid motion due to motion of the reference frame. So long as the motion of this reference frame is given by a uniform linear velocity, the forces on a fluid particle remain unchanged. Clearly, this would not be true if the frame of reference fixed with the jet were moving with some angular velocity or a uniform acceleration. Thus, uniform translation of the axes fixed with respect to the jet will not change the fluid motion in that reference frame. It was noted, however, that the boundary conditions must not be changed by motion of this reference frame. This leads to two points. Firstly, the flow is not simulated by a jet into stationary air whose jet exit velocity is equal to the difference in velocity between the original jet and free stream since this transformation

100

has not moved the jet nozzle itself with the appropriate uniform motion of the reference axes. Secondly, the jet development for a jet moving in an infinite quiescent medium is only simulated by a stationary jet in a moving medium if the moving medium is also infinite in extent. This condition was referred to as the "ideal wind tunnel" in section 3. Clearly the real wind tunnel will not satisfy this criterion completely due to the presence of the tunnel walls. This change in boundary conditions manifests itself in a deceleration of the medium and hence the creation of an adverse pressure gradient. However, the degree to which the real wind tunnel changes the flow is a function of the relative dimensions of the tunnel cross-section and the jet. The magnitude of the free-stream pressure gradient will be considered in the experimental study given in section 4.2. It should also be noted that a reference frame fixed with respect to the jet is the obvious choice for a description of the fluid motion since, once the operating conditions have been set, the motion is stationary in this frame. Clearly, the motion is not stationary for a frame of reference moving with the surrounding air.

The second question to be discussed is whether the model size experiments may be scaled to full-size? It has already been noted that the equations for the fluid motion are unaltered by the choice of reference frame, subject to the conditions given above. Thus, in an ideal case the two situations may be scaled with the appropriate use of nondimensional quantities such as the Reynolds number and Mach number, etc. However, the situation is not ideal and a number of factors may influence the scaling. If the question is confined to scaling of a cold model scale air jet to full scale, the changes in the fluid composition or nozzle geometry which would be encountered in a real jet engine do not apply. However, certain conditions are likely to not scale. The wind tunnel free-stream turbulence has a particular amplitude and length scale. This turbulence will influence the jet development tending to enhance the mixing process if the amplitude is large and the scales small. If the atmosphere through which the aircraft is assumed to be flying were completely at rest and the aircraft structure did not create any turbulence in the flow surrounding the jet, there would be an obvious difference between the wind tunnel simulation and the flight case. However, the atmosphere is not still and the aircraft surfaces may influence the air surrounding the jet, though relative levels and scales of the atmospheric turbulence are unlikely to be duplicated in the wind tunnel. Another feature which is unlikely to scale exactly is the turbulence at the jet exit, being a function of the flow configuration upstream of the jet exit. The initial turbulence level is known to influence the jet development.

It can be seen that those factors which prevent identical scaling are in each case due to non-scaling of the boundary conditions. The degree to which these changes may influence the flow in this situation needs examination; however, in gross terms their influence is likely to be overshadowed by the alterations expected when a real jet engine is considered. It is to be concluded then that the turbulent structure of a full-scale jet with forward velocity moving through stationary air may be well simulated by a wind tunnel model jet experiment.

In the next section an experimental study of the effect of a secondary stream on the development of a turbulent jet will be described.

4.2 EXPERIMENTAL INVESTIGATION OF THE EFFECT OF A SECONDARY STREAM ON THE STRUCTURE OF A TURBULENT JET

In the following section an experimental investigation will be described. Measurements of turbulent velocities were made, using a laser velocimeter, in a turbulent jet mounted in a low speed wind tunnel. The variation of the jet development with the change in velocity ratio and jet exit Mach number were examined. Before describing the experimental study, previous investigations of two-stream mixing problems will be discussed.

4.2.1 Summary of Previous Work

There have been few experimental investigations of the mixing of two streams of finite velocity. This has been mostly due to the difficulties in constructing adequate experimental facilities. Those experiments which have been conducted can be divided into five classes. These are:

  (i)   two-dimensional mixing layer,

  (ii) the two-dimensional or plane jet in a moving stream,

  (iii) the round jet in a wind tunnel,

  (iv) the round jet in a free jet facility, and

  (v)   coaxial round jets.

4.2.1.1 The two-dimensional mixing layer. The two-dimensional mixing layer is perhaps the simplest two-stream flow to be examined. Analytically, convenient similarity solutions for the mean velocity have been obtained using an eddy viscosity assumption and this has prompted several experimental investigations. Sabin (ref. 37) used a water channel with movable side walls to examine the effect of pressure gradient on the development of the mixing layer. Velocity ratios between .47 and .66 were obtained for very low flow velocities. Measurements of mean velocity were made and it was concluded that the dimensionless velocity profiles in a similarity coordinate could be expressed as functions of the velocity ratio alone. Yule (ref. 38) made an extensive study of the mixing layer. Two velocity ratios, .3 and .61 were examined. Measurements were made of mean axial velocity, three components of the velocity fluctuations, shear stress and longitudinal and lateral space correlations. The variation of the measured spreading parameter agreed with the measurements of Miles and Shih (ref. 39) and was given by

$$\frac{\sigma}{\sigma_0} = \frac{(1 - \lambda)}{(1 + \lambda)^{\frac{1}{2}}}, \tag{4-1}$$

where σ is the spreading parameter defined by Görtler (ref. 69) and σ_0 is the value of σ for λ, the velocity ratio between the two streams, equal to zero.

102

It should be noted that the data of Sabin (ref. 37) gave a relationship of the form,

$$\frac{\sigma}{\sigma_o} = \frac{(1 - \lambda)}{(1 + \lambda)} \cdot$$

(4-2)

Yule (ref. 38) also noted that the peak value of the nondimensionalized total turbulence intensity, $\bar{q}^2/(\bar{V}_a - \bar{V}_b)^2$, increased with λ. Jones $et\ al$ (ref. 40) also made spatial cross-correlations and calculated the variation of convection velocity across the layer for a primary stream velocity of 30.5 m/s and a secondary velocity of 9.14 m/s. Measurements of intermittency were also made. Brown and Roshko (ref. 41) made measurements using air, nitrogen, and helium. Use of these various gases allowed the effects of velocity ratio and density ratio to be examined separately. It was concluded that a relationship of the form of equation (4-2) could be used to describe the rate of growth of the shear layer. It will be shown in section 4.4 that the behavior of this spreading parameter for small values of λ is important to the prediction of noise radiation. Brown and Roshko (ref. 41) gave a very careful discussion of possible descriptions of this behavior; however, the scatter in the data did not enable one relationship to be preferred over any other. Brown and Roshko (ref. 41) also showed that the change in the growth of the mixing layer due to density differences in two streams of different gases was less than the change due to density differences caused by high speed flow. This latter effect was interpreted as being due to compressibility rather than density difference.

4.2.1.2 The plane jet. The plane jet exhausting into a moving free-stream was examined experimentally by Bradbury (ref. 42). It was shown that departures from self-preservation for small velocity ratios of .07 and .16 were of no significance. Bradbury and Riley (ref. 43) considered a wider range of velocity ratios and concluded that the flow changed from a pure jet flow near the nozzle exit to a self-preserving wake flow far downstream. Weinstein (ref. 44) also examined the plane jet and made mean axial velocity measurements for velocity ratios between .5 and 2.

4.2.1.3 The round jet in a wind tunnel. Curtet and Ricou (ref. 45) and Antonia and Bilger (ref. 46) made measurements of the structure of a round jet in a wind tunnel. The former investigation was principally made to study the effect of the ratio of wind tunnel radius to jet radius on the free stream and jet development. Clearly measurements of this type do not simulate the 'ideal wind tunnel' with an infinite moving stream and the results cannot be used for prediction of forward flight effects. However, the results were used for an experimental comparison by Hill (ref. 47) whose analytical work enables the influence of the tunnel walls to be estimated. Antonia and Bilger's (ref. 46) experiments were for low velocity (28 and 42 m/s) round jets at velocity ratios of .22 and .33. The investigation concentrated on whether assumptions of turbulence similarity could be made far downstream of the jet exit where the flow approached a small deficit wake. They concluded that the flow far downstream depends strongly on the complete past history of the flow and that no turbulence similarity

assumption was possible. Forstall and Shapiro (ref. 2) also made measurements of a round jet in a wind tunnel. Their results will be of considerable interest in this current investigation. Measurements of mean velocity and mass concentration (helium was used in a tracer in the primary jet) were made for low speeds with velocity ratios in the range .2 to .75. On the basis of these measurements the following empirical formulae were proposed.

$$\bar{x}_c = 8 + 24\ \lambda, \tag{4-3}$$

$$\frac{\bar{V}_a - \lambda}{1 - \lambda} = \frac{\bar{x}_c}{\bar{x}} \tag{4-4}$$

$$\bar{r}_{.5} = (\bar{x}/\bar{x}_c)^{1-\lambda}, \tag{4-5}$$

$$\frac{\bar{V}_1 - \lambda}{\bar{V}_a - \lambda} = \frac{1}{2}\left[1 + \cos\frac{\pi\bar{r}}{2\bar{r}_{.5}} \right]. \tag{4-6}$$

Landis and Shapiro (ref. 48) and Pabst (ref. 49) considered the development of a heated air jet exhausting into a moving stream. The measurements by Landis and Shapiro (ref. 48) were of the mean axial velocity and were made for velocity ratios of .333 to .852. Pabst's (ref. 49) measurements are reported in detail by Szablewski (ref. 50). The primary jet velocity in these measurements was 400 m/s and the jet temperature was 300°C. Velocity ratios in the range .045 to .47 were examined. The measurements of mean axial velocity and temperature showed good collapse radially when plotted as $(\bar{V}_1 - \lambda)/(\bar{V}_a - \lambda)$ and $\bar{T}/\bar{T}_a$ against $\bar{r}/\bar{x}$, downstream of the potential core. Von Glahn $et\ al$ (ref. 51) made pitot-static surveys for various nozzle configurations, including a convergent circular nozzle, in a wind tunnel. Primary jet Mach numbers between .45 and 1.02 were used and Mach number ratios of between .1 and .75 were examined. It was concluded that the centerline velocity could be correlated for the various Mach number ratios by plotting $(\bar{V}_a - \lambda)/(1 - \lambda)$ as a function of $[\bar{x}/(2C_n\sqrt{1+M_J})]^b$ where C_n was the effective nozzle coefficient and b was an empirically developed exponent given by,

$$b = 1 + \frac{1}{3}\ [\lambda^2 - 1]^{-1}. \tag{4-7}$$

4.2.1.4 Coaxial Jets. Alpinieri (ref. 52) made measurements of axial mean velocity and concentration for coaxial jets. Hydrogen and carbon dioxide were used as the inner jet gases and the outer jet was of air at 198 m/s. Velocity ratios in the range .8 to 2.13 were considered. The hydrogen temperature was 270 ± 5.5°C and the carbon dioxide temperature was 254 ± 5.5°C Coaxial jet flows have also been studied by Peters $et\ al$ (ref. 53) using hydrogen and air, Fricke and Schorr (ref. 54) using helium and nitrogen and Zawacki and Weinstein (ref. 55) using freon and air. Velocity ratios in these experiments ranged from .12 to 39.5. In each case

axial mean velocity and concentration were measured. Zawacki and Weinstein (ref. 55) also measured the axial turbulence intensity and the mean density. Eggers and Torrence (ref. 56) made pitot static traverses in a coaxial jet with the outer jet exit velocity always greater than the primary jet velocity. Measurements were made for supersonic outer jet velocities and slightly subsonic inner jet velocities.

4.2.1.5 Summary. Several points emerge from this review of previous experimental studies. Because of the relative ease of measurement, the mean axial velocity is the most often measured quantity. Measurements of turbulence intensity have been made in relatively few experiments and these have been limited, by available instrumentation, to low velocities. The main interest in round jets in moving streams appears to have been concentrated in two distinct areas. Firstly, the rate of the decay of the jet centerline axial mean velocity, has been studied. Secondly, the assumptions of similarity and self-preservation have been examined. This has, for the post part, involved measurements downstream of the end of the potential core. Clearly, the following areas are in need of attention:

(1)   the effect of the secondary stream on the initial development of a round jet,

(2)   the variation of turbulence intensity with velocity ratio, and

(3)   the variation of turbulence intensity with jet Mach number.

The progress made toward understanding in these areas will be described in the subsequent sections.

4.2.2   Description of Experimental Facilities

In this section the facilities used for the measurement of the effect of velocity ratio and Mach number on the flow properties of an axisymmetric jet are described.

The wind tunnel used in the experiments, shown in Figure 4-1, was a closed-circuit, single-return, low-speed facility located in the Research Laboratory. The test section was approximately .76 m x 1.09 m with a length of 1.22 meters. The flow was driven by a 1.83 m diameter, 10-bladed, single-stage axial flow fan. The fan was driven by a 3×10^5 Watts, 1200 rpm, synchronous speed induction motor. The fan speed could be varied over the range from 0 to 1150 rpm by means of an eddy-current, coupling-type variable speed unit. Steady state speed regulation was 1/8 of 1 percent. A standard friction brake rated at 1017 Joule braking torque could bring the fan to rest from full speed in less than 15 seconds. The tunnel provided an empty flow velocity capability of 0 to 94.5 m/s.

A nozzle installation is illustrated in the photograph in Figure 4-2. An air duct 20.3 cms. in diameter was installed to supply air through a 5.08 cm. automatically controlled value to the 5.08 cm. diameter nozzles which exhausted axially down the center of the wind tunnel working

PLENUM

NOZZLE   LASER

PLENUM

TUNNEL SCREEN

WORKING SECTION

PYLON

SLOT

8-INCH SUPPLY DUCT

PRESSURE BALANCE DOOR
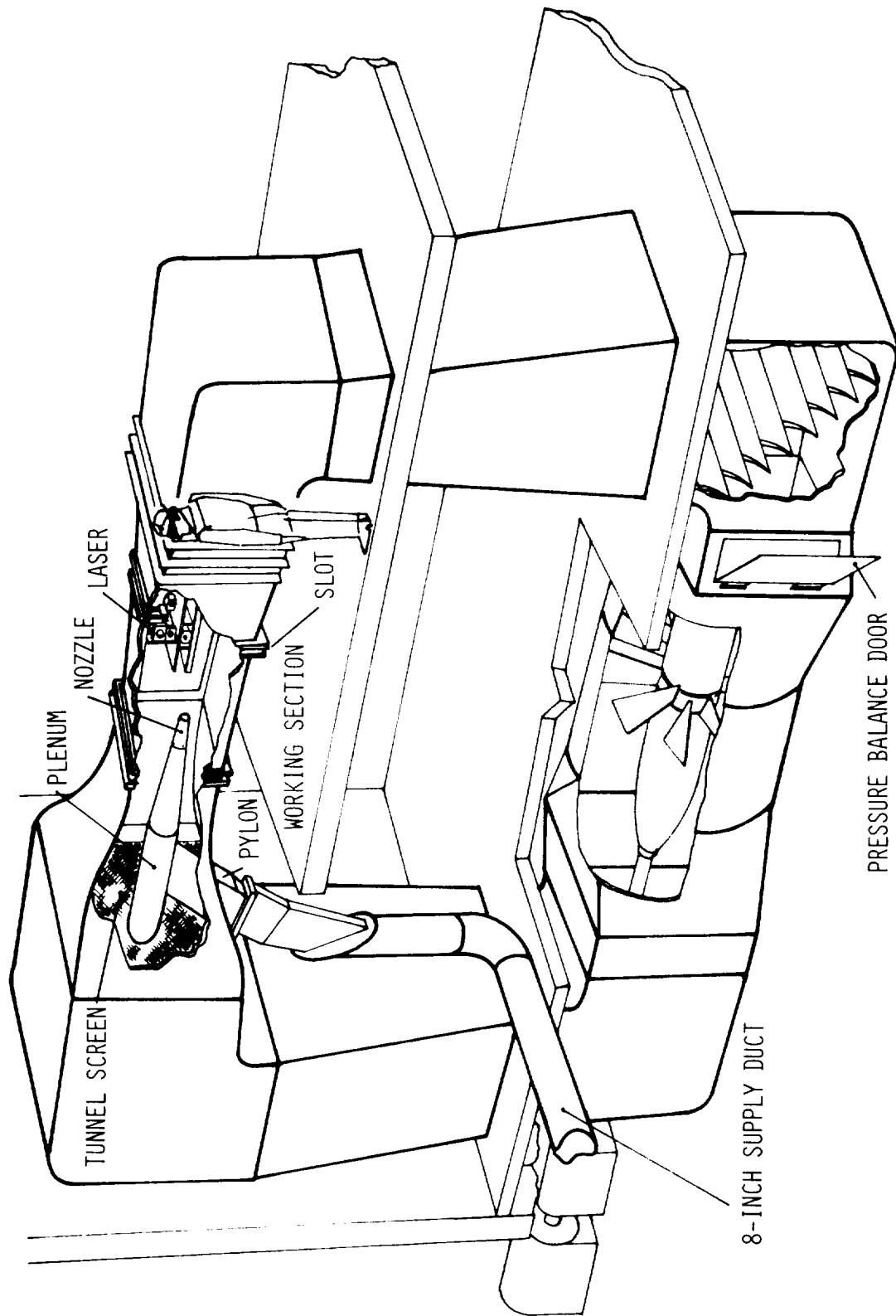
Figure 4.1 Schematic of wind tunnel installation.
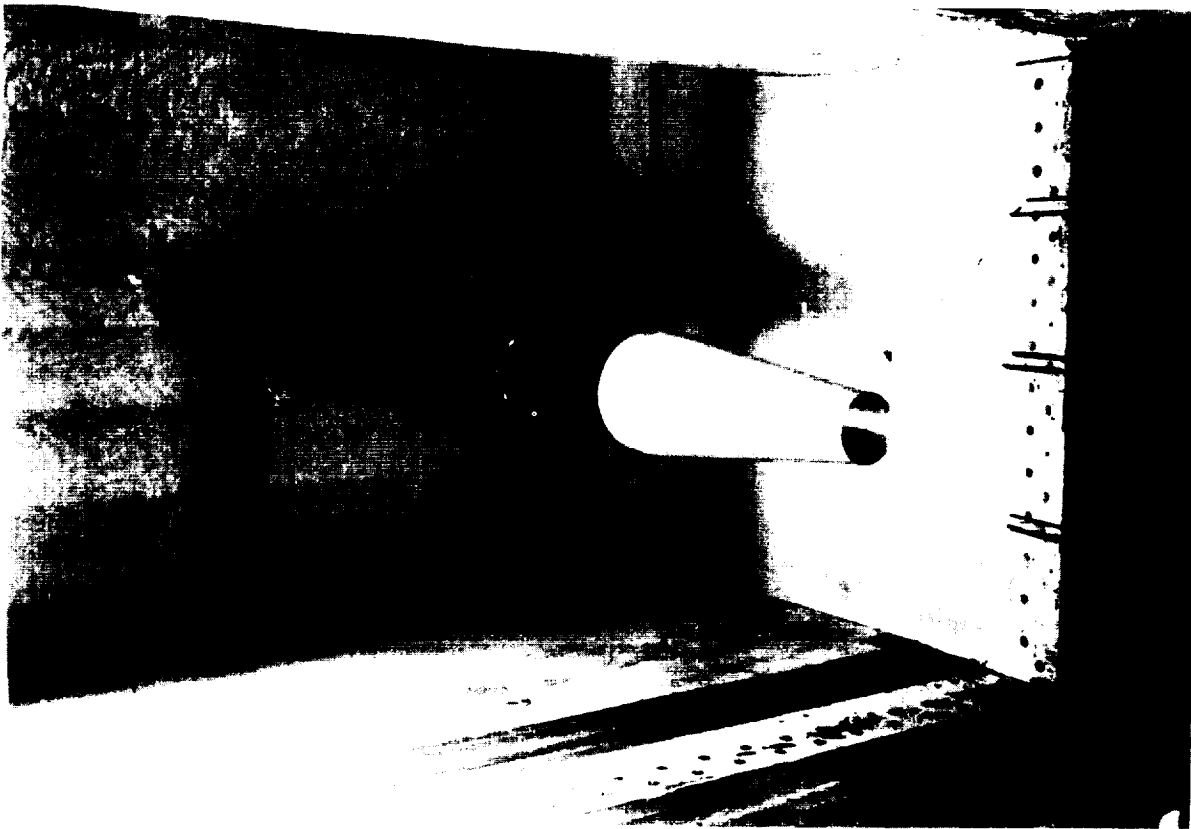
Figure 4.2 Pylon, plenum and nozzle installation.

section. As a result of the proximity of the tunnel screens (shown cross hatched in the schematic) to the metal contraction section just upstream of the working section, access for the air duct and pylon mount system was extremely limited. A rectangular duct was designed with a cross-sectional area equivalent to a 15.2 cm. round duct. This rectangular duct, made from .95 cm. steel plate, formed the basis of the pylon mount which was fitted with wooden leading and trailing edge fairings and contoured with aluminum fill. The airfoil section was a 21% thick zero lift design. A 20.3 cm. diameter nacelle made from standard pipe was mounted on top of the pylon with a wooden bullet upstream fairing as shown. A 5.08 cm. thick section of .32 cm. cell honeycomb was installed in the 20.3 cm. plenum as a flow straightener. A 20.3 cm. to 10.2 cm. reduction was attached to this plenum and smoothly faired to the end of a short length of 10.2 cm. pipe to which the model jet nozzles were attached. This air supply ducting was aligned axially in the tunnel by use of a low power laser mounted at the downstream end of the working section. The nozzle exit plane position was governed by the extent of the optical glass wall through which the laser beams were passed. Because of the limited extent of this glass panel a 22.9 cm. long, 10.2 cm. I/D spacer pipe was made to be inserted just upstream of the nozzle so that a total of 17 diameters of the jet flow could be explored by removal or insertion of the extension. The laser velocimeter, shown schematically in Figure 4.3 and described in detail below, was mounted on a hydraulic table outside the wind tunnel working section providing vertical positioning. Axial positioning was achieved with a lead-screw and way system, similar to that of a center lathe, aligned parallel to the tunnel centerline. Lateral traversing capability was provided in a similar manner.

Slots in the tunnel wall just downstream of the working section were provided to vent the working section to ambient. Since a considerable amount of extra air was to be injected into the tunnel via the jet nozzles, some means of preventing a pressure build-up was needed. This was achieved by providing a "bleeder" door just upstream of the fan as shown in Figure 4.1. The opening or closing of this door was achieved by means of a cable and winch system controlled from the test stand.

The measurement of the mean properties of a turbulent flow has a practical importance, but it is only by measuring the fluctuating components of the flow that it is possible to obtain a better understanding of the mechanism of the turbulent flow and provide justification for any mathematical hypothesis used in representing the motion. Measurements of the time averaged properties of the flow may be achieved by total and static pressure surveys in high velocity and temperature flows. However, measurements of turbulent fluctuations have normally been limited to fairly low speed flows since in these velocity regions the conventional measuring devices, the hot-wire or film anemometer give uncontaminated velocity measurements and are structurally sound. It is only with the development of optical measurement techniques that accurate measurements have been viable in hot or high speed turbulent flows. There are two main advantages in using optical techniques. Firstly, there is no need to insert a probe in the flow which might disturb the flow regime or be physically incapable of withstanding stresses exerted by the

108
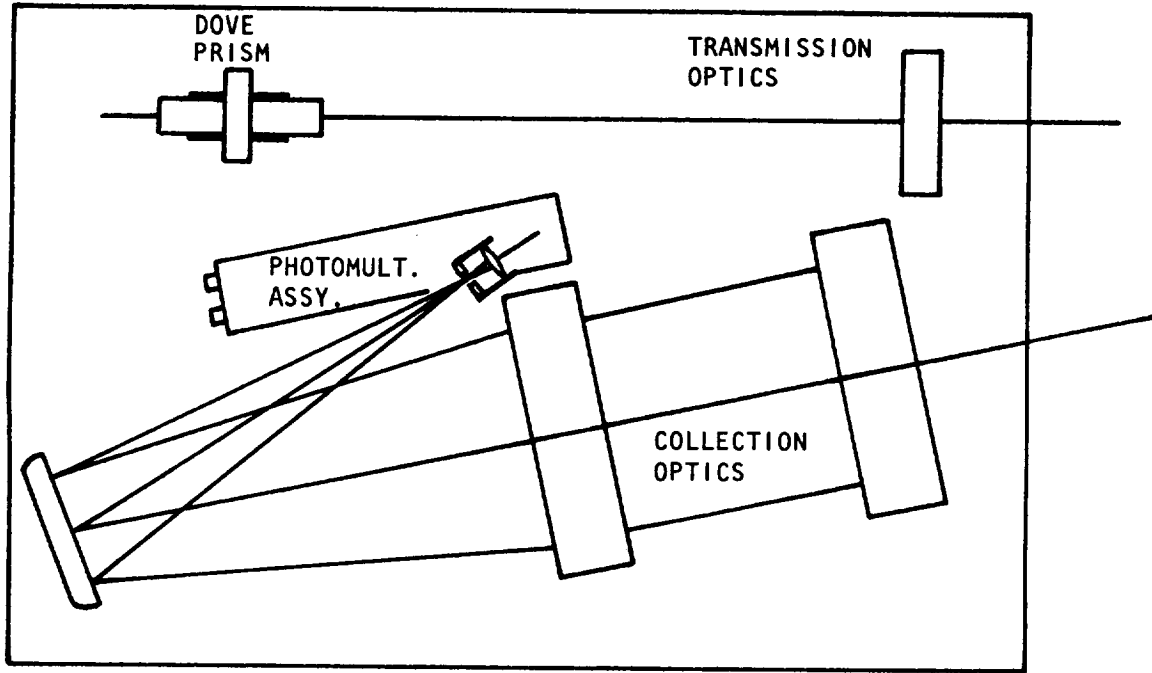
Figure 4.3   Plan view of LV optics platform.

flow. Secondly, an unambiguous measurement of velocity is obtained and measurements can be carried out in regions where the density and temperature may fluctuate.

There are a number of optical techniques for remotely detecting the velocity of particles and these methods are well documented (ref. 67). The approach to be described here, which has been developed by Lockheed-Georgia Company, is based on an interference pattern of light formed in the measurement volume by the intersection of two coherent monochromatic light beams. As a microscopic particle passes through this fringe pattern, light is scattered and detected by a photo-sensor. The detector output signal burst has a frequency depending on the spacing of the interference pattern and the velocity component of the particle normal to the fringes. Since the fringe spacing is set by the geometry of the optics, the normal particle velocity is readily derived from the detector signal frequency.

A detailed account of much of the optics, electronics and data processing used in the current laser velocimeter system is given in references 58 and 59. However, a brief description of the configuration used in these experiments and some modifications that have been made will be described here.

A plan view of the optical configuration is sketched in Figure 4.3 and a photograph of the complete unit is shown in Figure 4.4 . A 4-watt argon laser is mounted beneath the optics platform. The beam splitter/color filter assembly separates the two predominant lines of the argon laser into four beams; two blue and two green. These beams are turned through a dove prism, which allows rotation of the fringe patterns, and are then simultaneously focussed and caused to cross by the transmitting lens. This creates two coincident ellipsoidal measurement volumes. Light scattered by the particles passing through the measurement volume is collected by the receiving optics, mounted beside the transmitting optics, and is fed to a photomultiplier assembly. This assembly filters the collected back-scattered light into blue and green components which are sensed by two photomultiplier tubes. The resulting signals are subsequently processed to provide the particle component velocities.

In this configuration the laser velocimeter is able to provide measurements of two orthogonal components of turbulent velocity as long as the deviation of the instantaneous velocity vector from the axial direction is sufficiently small. Since the angular criterion is not met by the expected velocities in a turbulent jet, these fringe patterns were rotated 45° for the current measurements and only the set of fringes normal to the jet axis were used. This meant that measurements of axial velocity only were made. The angular restriction can be alleviated by movement of the fringes in the measurement volume. This can be achieved by use of a Bragg cell in the beam splitter optics which frequency shifts one color light beam with respect to the other. This optical device has been incorporated in a current laser velocimeter system by Lockheed-Georgia.

110
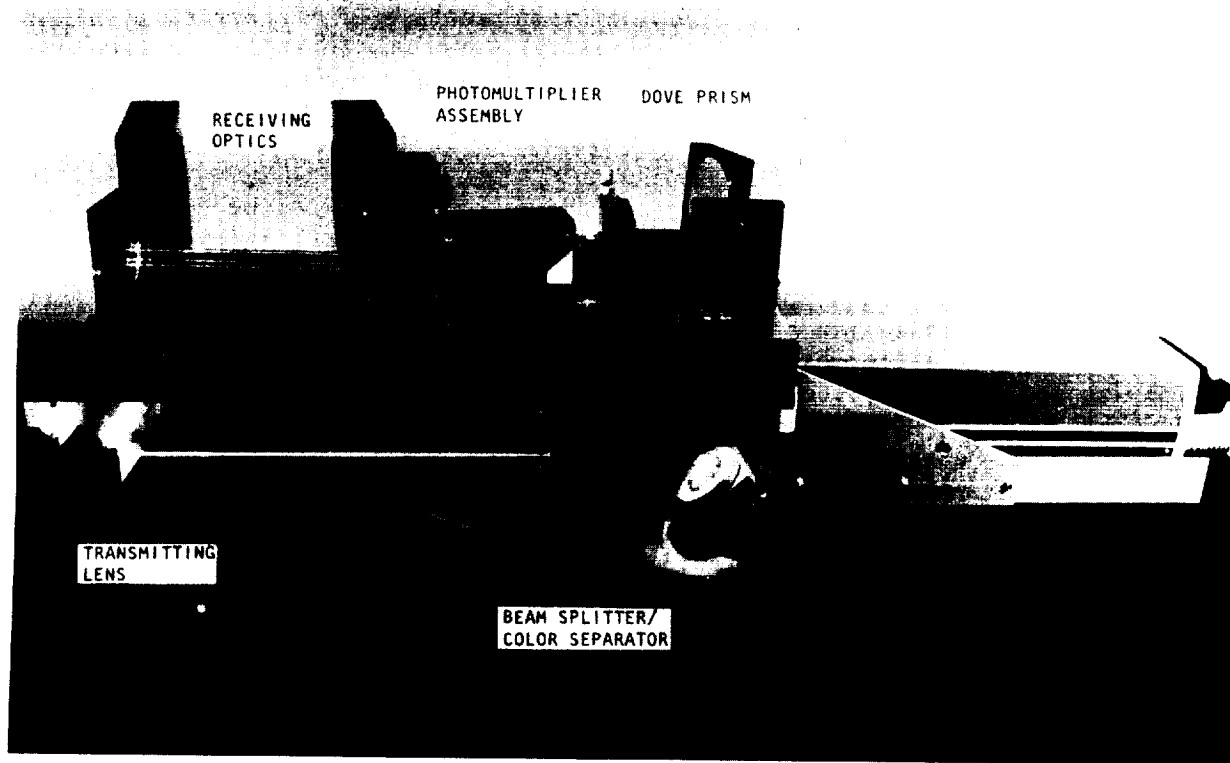
Figure 4.4 LV optical configuration.

A most important aspect of the electronic processor is the data valida-
tion circuitry. The original design, described in reference 58, was based on
a digital comparison of the time for the first four fringe crossings with the
time for the second four as well as an odd ratio comparison, three to five,
of the fringe-crossing time count. Because of the digital nature of the com-
parison, the acceptable time difference varied up to 3% of the period and at
higher frequencies (velocities), where the fringe crossing period is very
small, the accepted error was an increasing percentage of the period. This
error window was found to be unacceptable and a new analog validation system
was constructed. This error window is constant at $\pm 1\%$ over a variable
velocity range of thirty to one. This system was used in the current
measurement program.

In order to obtain satisfactory particles, the flow must be seeded arti-
ficially. It was found to be convenient to use different particles in the jet
flow and the wind tunnel air. The jet air was seeded by introducing aluminum
oxide particles, coated with CAB-O-SIL to reduce agglomeration, into the jet
plenum. The particle size probability distribution peaked at 1 micron with
an upper limit of 3 microns. The wind tunnel flow was seeded using an
aerosol of 1010 hydraulic oil generated by a Laskin nozzle (ref. 60).

4.2.3 Experimental Program and Summary of Measurements

The test conditions were designed to provide the maximum amount of use-
ful data within the limits of the facility and instrumentation. The effects
of two major changes were of interest. Firstly, how does the secondary
stream velocity affect the jet development at fixed jet exit velocity, and
secondly, how does the jet exit Mach number affect the jet development? In
order to answer these two questions the experiments were divided into two
sections. In the first the jet exit velocity was held constant and the wind
tunnel velocity varied. In the second the jet exit Mach number was changed
and the velocity ratio was kept constant. The test program is shown in
Figure 4.5. In order to achieve a large range of velocity ratios and limit
the spacing between the jet operating Mach numbers, the first series of
measurements were carried out at $M_J = .47$ and nominal velocity ratios of .1,
.2, .3, .4 and .5. The second series of measurements were performed at a
fixed velocity ratio of .1 and jet exit Mach numbers of .47, .9, 1.37 and
1.67. The jet air was unheated in all the experiments.

It was anticipated that the general effect of increasing both velocity
ratio and Mach number would be to stretch the jet flow in the axial direc-
tion. In order to obtain a representative set of turbulence measurements in
series I ($M_J = .47$ for various velocity ratios), the following procedure was
adopted. First a jet centerline traverse was carried out to give an indica-
tion of the potential core length, x_c. Radial traverses were then performed
at axial locations x_c, $x_c/2$ and $x_c/4$. Radial traverses were also made at
$x = 81.3$ cm. and $x = 0.51$ cm. These two locations were close to the limits
of the measurement range set by the size of the LV optics and the dimensions
of the working section window described in section 4.2.2.

In order to reach the correct operating velocities in as short a time
as possible, the following procedure was adopted. The correct values of

112
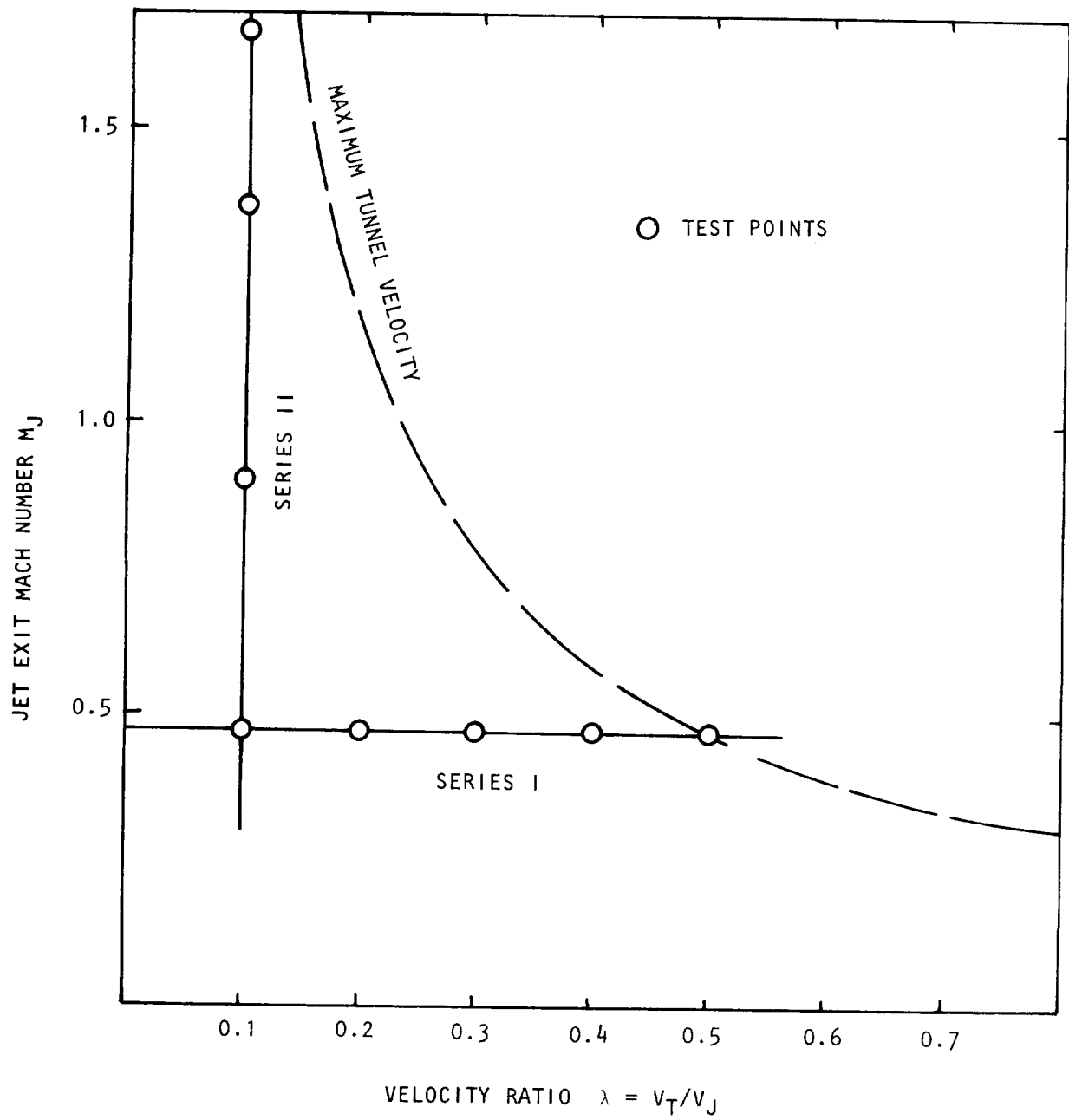
Figure 4.5 Jet turbulence test program.

static pressure ratio and tunnel dynamic pressure were calculated in the manner described in Appendix 2B. The jet and tunnel were simultaneously run up to their correct operating conditions on the assumption of a working section pressure equal to the ambient pressure. A door in the return section of the wind tunnel pressure, which was left open at the beginning of the run-up procedure to prevent pressure build-up in the tunnel as a result of excess mass flow injected by the jet, was then progressively closed until the static pressure in the working section was equal to ambient pressure. Minor adjustments to the tunnel speed and door position then enabled the correct test conditions to be quickly reached.

At the time that a measurement was taken, a magnetic tape was written which recorded each individual velocity and its time of occurrence. Before analyzing the data, it was necessary to process this recorded data. The processing was required to correct for the natural biassing of the velocity data. Since the amount of fluid passing through the measurement volume was proportional to the local fluid velocity then, even if particles were uniformly distributed in the fluid, a bias towards higher velocities occurred. It can be shown (ref. 61) that if there is no dependence between the particle velocity and the particle number density then the true mean velocity is found by taking the reciprocal of the arithmetic mean of the particle periods (time for the particle to cross eight fringes) multiplied by a constant of proportionality. It can also be shown that this biassing effect leads to a weighting of the velocity probability distribution function which is inversely proportional to the velocity. An example of the correction of a sample set of data is given in Appendix 4D. A correction for this weighting of the probability function was made in the data processing, and the moments of the corrected distribution function were calculated giving the mean, standard deviation, skewness and kurtosis. At the same time any obvious noise points which had been validated by the LV processor were removed. A typical example of this procedure is also given in Appendix 4D. The effects of particle size distributions are also discussed in Appendix 4D.

There are two characteristic parameters of the flow which were calculated numerically from the mean velocity profile: the vorticity thickness and the dividing streamline radius. These two parameters as well as the jet half-width, the dividing streamline velocity, and the potential core radius were calculated at the same time. The calculation of the vorticity thickness involved finding the radial derivative of the mean velocity. In order to avoid unrealistic values of this derivative, the velocity profiles were smoothes prior to the calculation.

Since no measurement of temperature in the flow was made, an approximate relationship had to be used between the local mean density and velocity in order to calculate the dividing streamline radius. The dividing streamline radius is defined as the radius at which

$$\int_{o}^{\bar{r}_{ds}} \rho \, V_1 \, r dr = \rho_J \, \frac{V_J}{2} \, r_J^2 ,$$

114

assuming that the velocity and temperature are constant across the jet exit. Using Crocco's relationship based on a Prandtl number of unity, it can be shown that the local mean density is given by

$$\left|\frac{\rho}{\rho_J}\right| = \left|1 + \left(\frac{T_T}{T_J} - 1\right)\frac{(1 - \bar{V}_1)}{(1 - \lambda)} + \frac{(\gamma - 1)}{2} M_J^2 (\bar{V}_1 - \lambda)(1 - \bar{V}_1)\right|^{-1}.$$

Assuming constant total temperature, the jet/tunnel temperature ratio is given by

$$\frac{T_T}{T_J} = 1 + \frac{(\gamma - 1)}{2} M_J^2 (1 - \lambda^2).$$

With the density defined in this manner, the dividing streamline radius was readily calculable.

The velocity measurements will now be described. The analysis of these measurements using various scales will be carried out in section 4.2.4. However, before describing these measurements the influence of the tunnel walls, if any, on the development of the jet will be examined.

The wind tunnel experiment was aimed at reproducing the flow conditions in and around a jet in an infinite stream of constant velocity. However, since the tunnel working section had only finite cross-sectional area, the tunnel walls were expected to influence the jet development. When a jet is confined in a duct, there will be a region in the flow, before the jet boundary reaches the duct walls, where the entrainment of air from the duct flow into the jet is rapid enough to decelerate the freestream and establish a positive axial pressure gradient. The magnitude of this pressure gradient depends on both the ratio of the jet velocity to the duct velocity and the ratio of the jet diameter to the duct diameter. Hill (ref. 47) showed analytically that the behavior of jets confined in constant area ducts can be expressed as a function of only two independent variables, x/r_T and $m/(M\rho)^{\frac{1}{2}}$, where r_T is the radius of the duct, m is the total mass flow per unit area and M is twice the average sum of momentum and pressure forces per unit area (obtained by integrating the momentum equation across the duct and axially). Assuming uniform flow in the jet and duct in the exit plane of the nozzle, the value of $m/(M\rho)^{\frac{1}{2}}$ in the jet exit plane is given, in the notation of this report, by

$$\frac{m}{(M\rho)^{\frac{1}{2}}} = \frac{\lambda + (1 - \lambda)\ (r_J/r_T)^2}{\left(\lambda^2 + 2(1 - \lambda^2)\ (r_J/r_T)^2\right)^{\frac{1}{2}}}$$

In the present experiments the equivalent duct radius to jet radius ratio was 20 to 1. The range of values of $m/(M\rho)^{\frac{1}{2}}$ was between .84 for the lowest velocity ratio and .995 for the case of $\lambda = .5$. Hill's (ref. 47) calculations based on an integral approach show that in the first duct diameter there are some small changes in the duct velocity near the wall for values of

$(m/M\rho)^{\frac{1}{2}}$ of this order. The larger the value of $m/(M\rho)^{\frac{1}{2}}$, the smaller will be the pressure gradient.

Static pressure measurements were made in the tunnel wall for each velocity ratio and jet Mach number (measurements are not available for $M_J = .9$, $\lambda = .1$ due to a computer malfunction). These wall pressure measurements are shown in Figure 4.6 as differences from ambient pressure. Their relative location is a function of the accuracy with which the working section pressure was adjusted to ambient using the method described previously in this section. The maximum static pressure gradients are shown in Figure 4.7. It can be seen that there is little effect on the pressure differences when the jet plenum extension, mentioned in section 4.2.2, is removed. The trend of increasing axial pressure gradient with tunnel velocity is contrary to Hill's predictions. However, the pressure differences are small and Hill dealt with the problem of a circular duct with no wall boundary layers. Also, in the wind tunnel used in these experiments, slots, open to ambient conditions, are found in the tunnel walls at the end of the working section. This would also be expected to vary the pressure gradient from that predicted by Hill. The change in wall pressure was equivalent to a 2% variation in free-stream velocity at the highest tunnel speed and a 1% variation at the lowest tunnel speed. Thus, it can be concluded that for the range of experimental conditions covered, the wind tunnel free stream was a close approximation to an infinite uniform secondary flow.

The variations of the jet centerline axial mean velocity and turbulent intensity for fixed jet Mach number and various velocity ratios are shown in Figures 4.8 and 4.9, respectively. Some basic trends in the data are immediately seen. As the velocity ratio λ increases, so the potential core length of the jet increases, and the rate of decay of the centerline velocity with axial distance decreases. The development of the jet has been slowed with respect to time and since the jet exit velocity is constant the jet development occurs over a region of increased axial extent. The maximum turbulence intensity along the jet centerline also decreases with increasing velocity ratio and the location of the peak moves downstream. All the intensity traverses show a secondary, smaller peak, closer to the jet exit which may have been due to a regular vortex shedding from the jet lip.

The variations of mean velocity and turbulence intensity on the jet centerline for fixed velocity ratio and various jet Mach numbers are shown in Figures 4.10 and 4.11, respectively. Again some basic trends are immediately seen. Increasing the jet Mach number increases the potential core length and decreases the rate of decay of the jet centerline velocity. There also appears to be a clear division between the centerline behavior of the subsonic and supersonic jets. This difference is also seen in the axial behavior of the turbulence intensity. For the subsonic jets, there is very little change in the peak intensity level and only a slight downstream movement of the peak. The maximum turbulence intensity levels for the supersonic jet exit velocities is lower than the subsonic peak values and the location of the peak is further downstream. The secondary peak in the $M_J = .47$ intensity data has disappeared for the higher jet exit velocities. This suggests another possibility, i.e., that the peak was caused by separation at

116
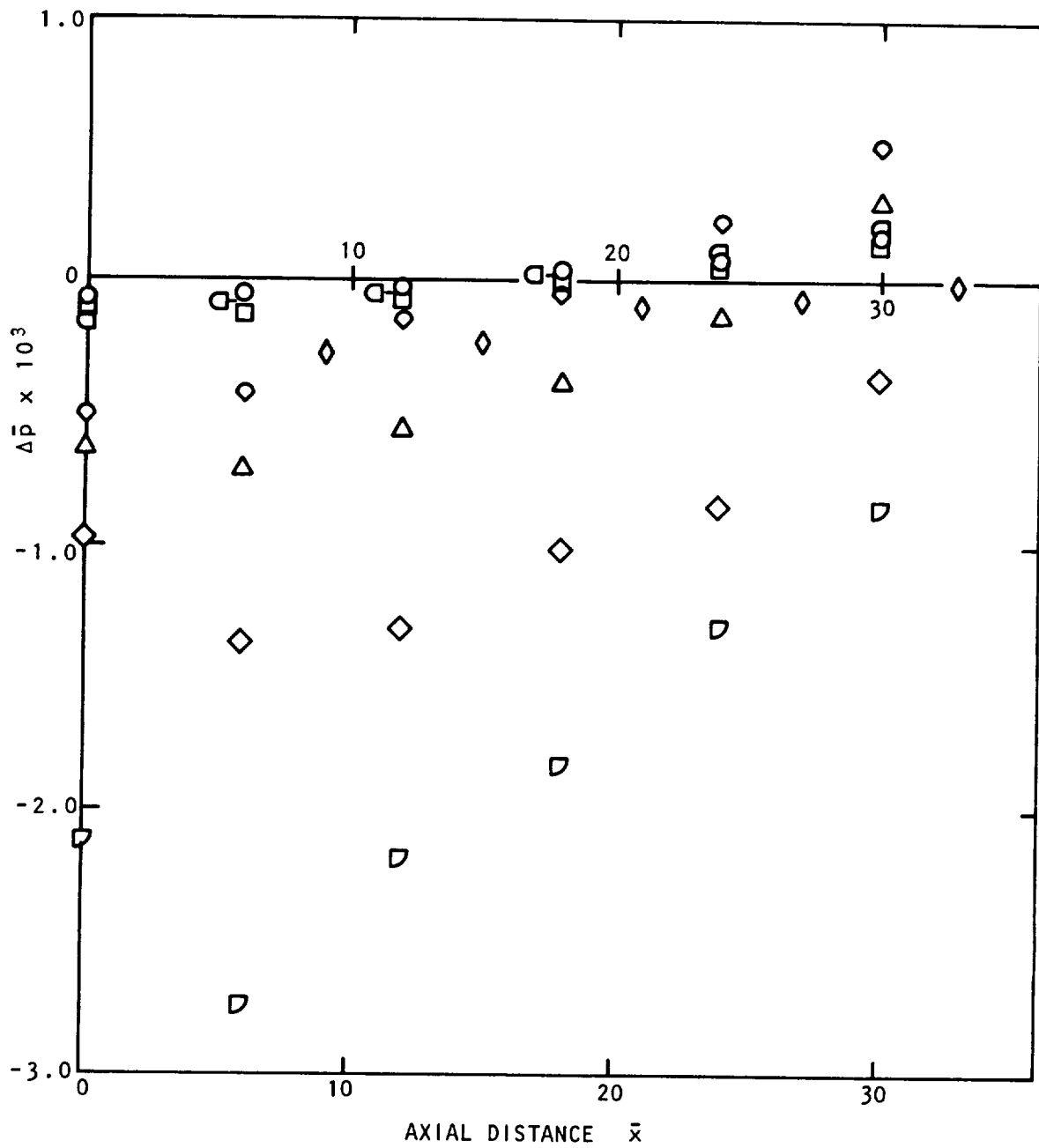
Figure 4.6 Working section wall pressure differences.
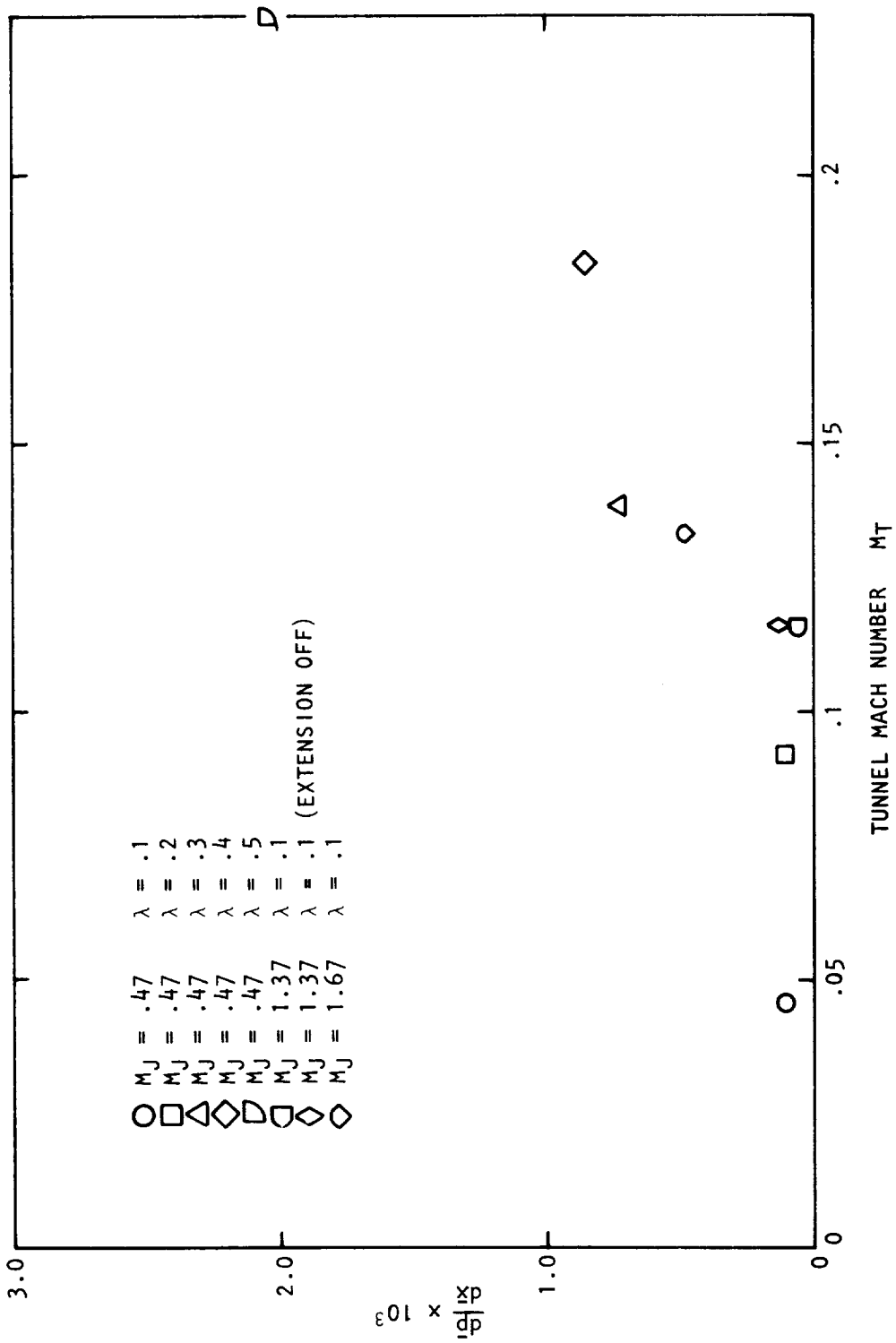
Figure 4.7 Maximum working section pressure gradient as a function of tunnel Mach number.

118
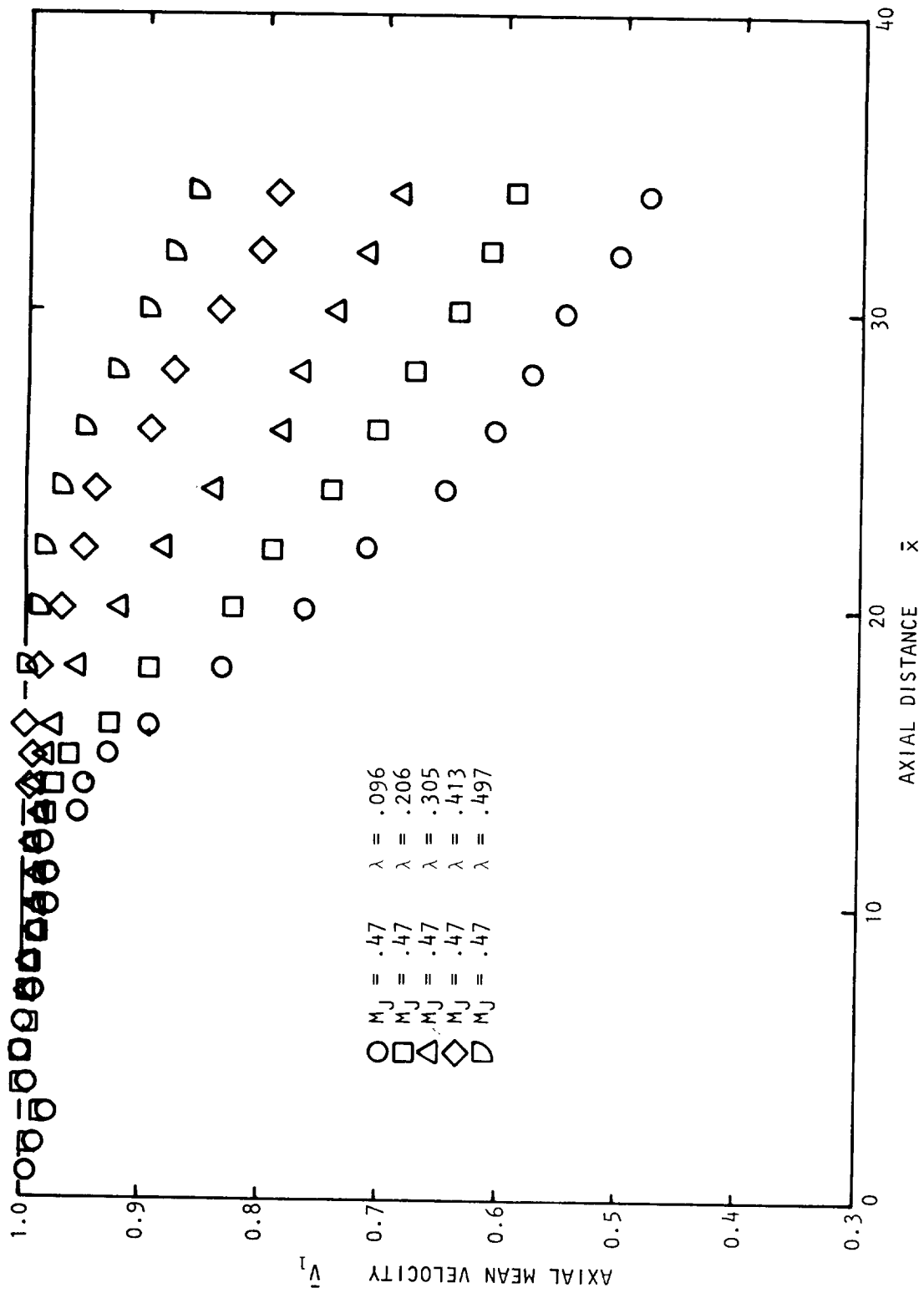
Figure 4.8 Axial mean velocity on jet centerline, $M_J = .47$

AXIAL DISTANCE $\bar{x}$

AXIAL MEAN VELOCITY $\bar{V}_1$

O	$M_J = .47$	$\lambda = .096$
□	$M_J = .47$	$\lambda = .206$
◁	$M_J = .47$	$\lambda = .305$
◇	$M_J = .47$	$\lambda = .413$
D	$M_J = .47$	$\lambda = .497$
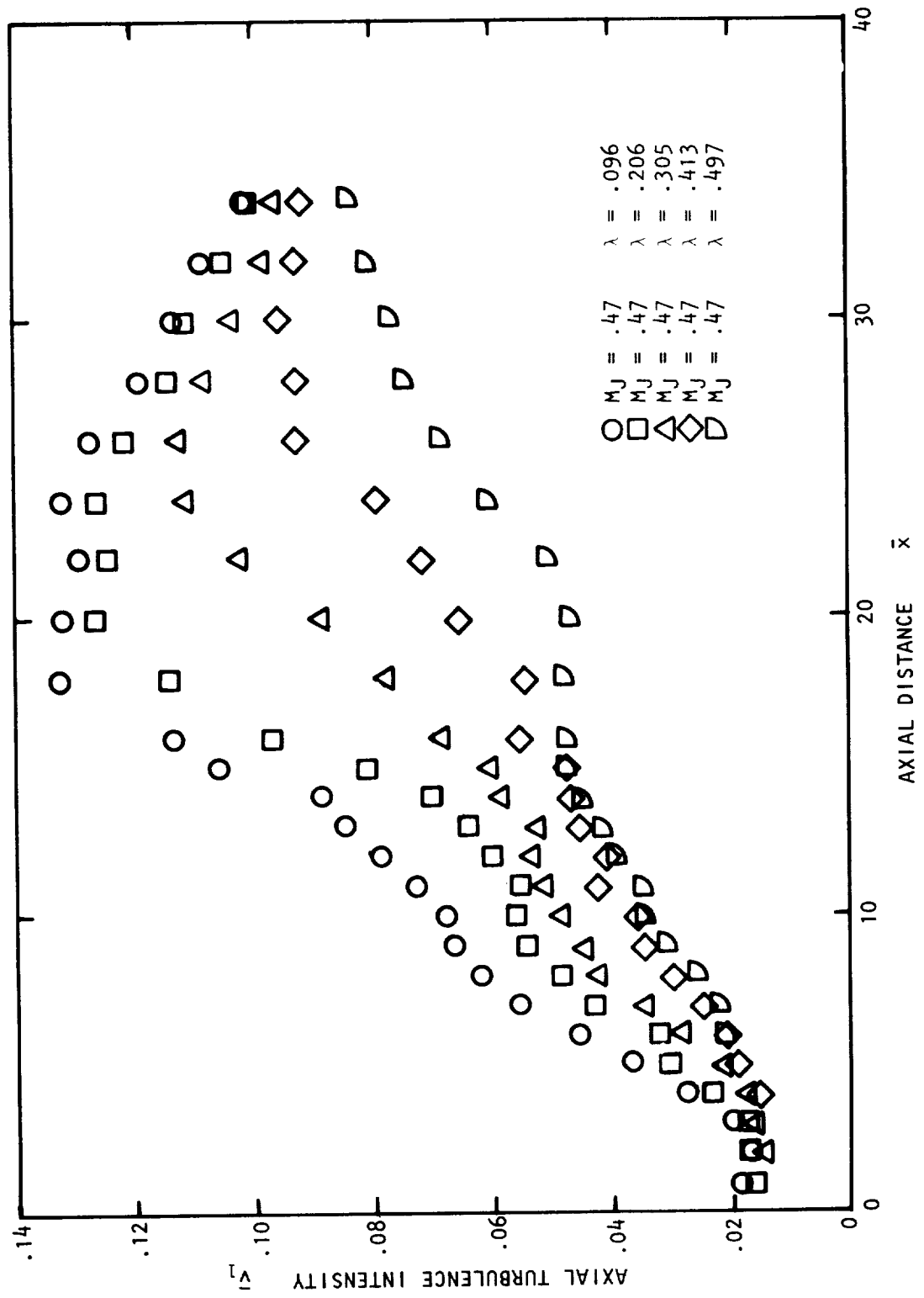
Figure 4.9 Axial turbulence intensity on jet centerline, $M_J = .47$.

○	$M_J = .47$	$\lambda = .096$
□	$M_J = .47$	$\lambda = .206$
◁	$M_J = .47$	$\lambda = .305$
◇	$M_J = .47$	$\lambda = .413$
◻	$M_J = .47$	$\lambda = .497$

AXIAL DISTANCE $\bar{x}$

AXIAL TURBULENCE INTENSITY $\bar{v}_1$

120
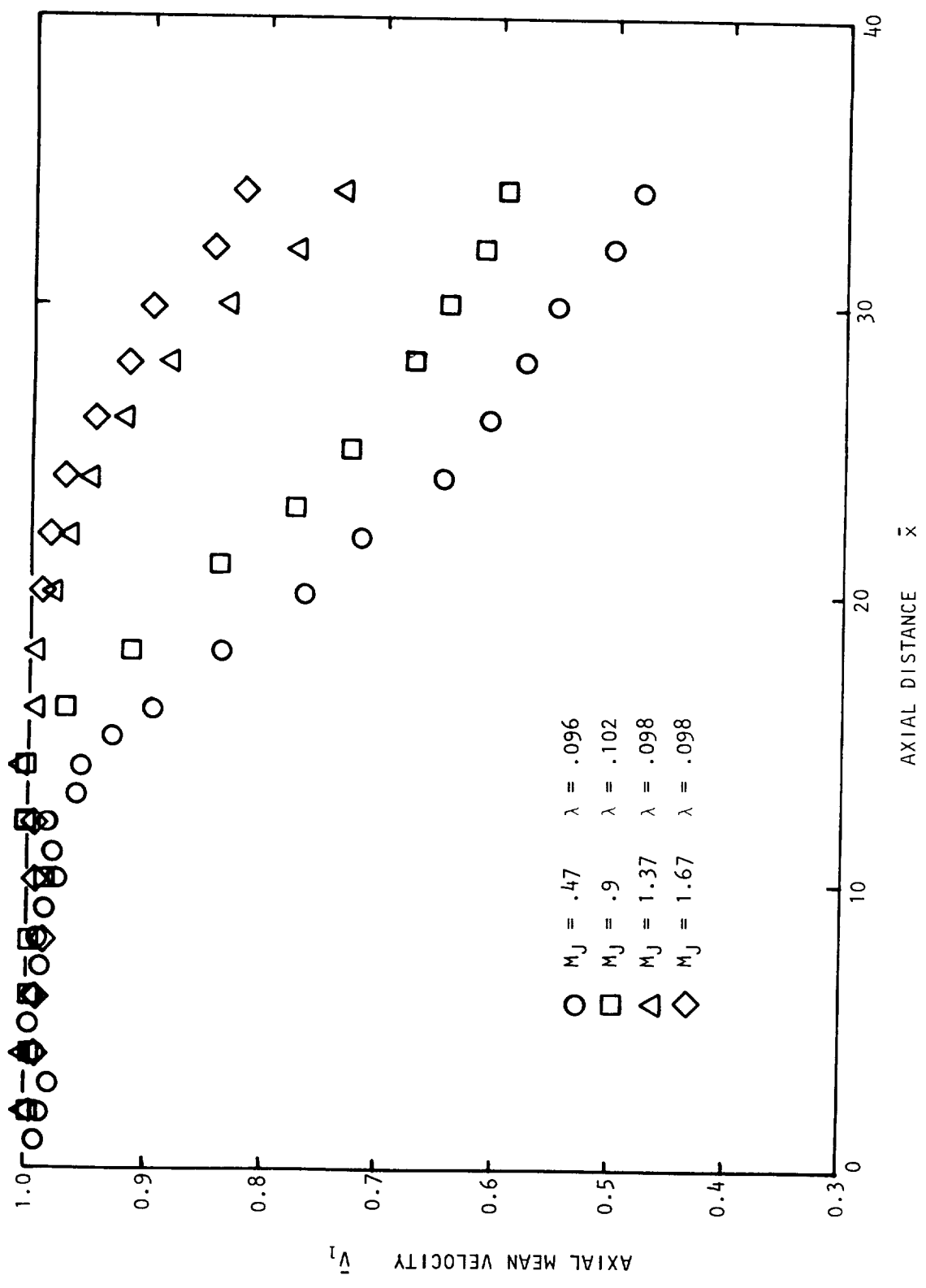
Figure 4.10 Axial mean velocity on jet centerline, λ = .1

AXIAL DISTANCE $\bar{x}$

AXIAL MEAN VELOCITY $\bar{V}_1$

○	M_J = .47	λ = .096
□	M_J = .9	λ = .102
◁	M_J = 1.37	λ = .098
◇	M_J = 1.67	λ = .098

121
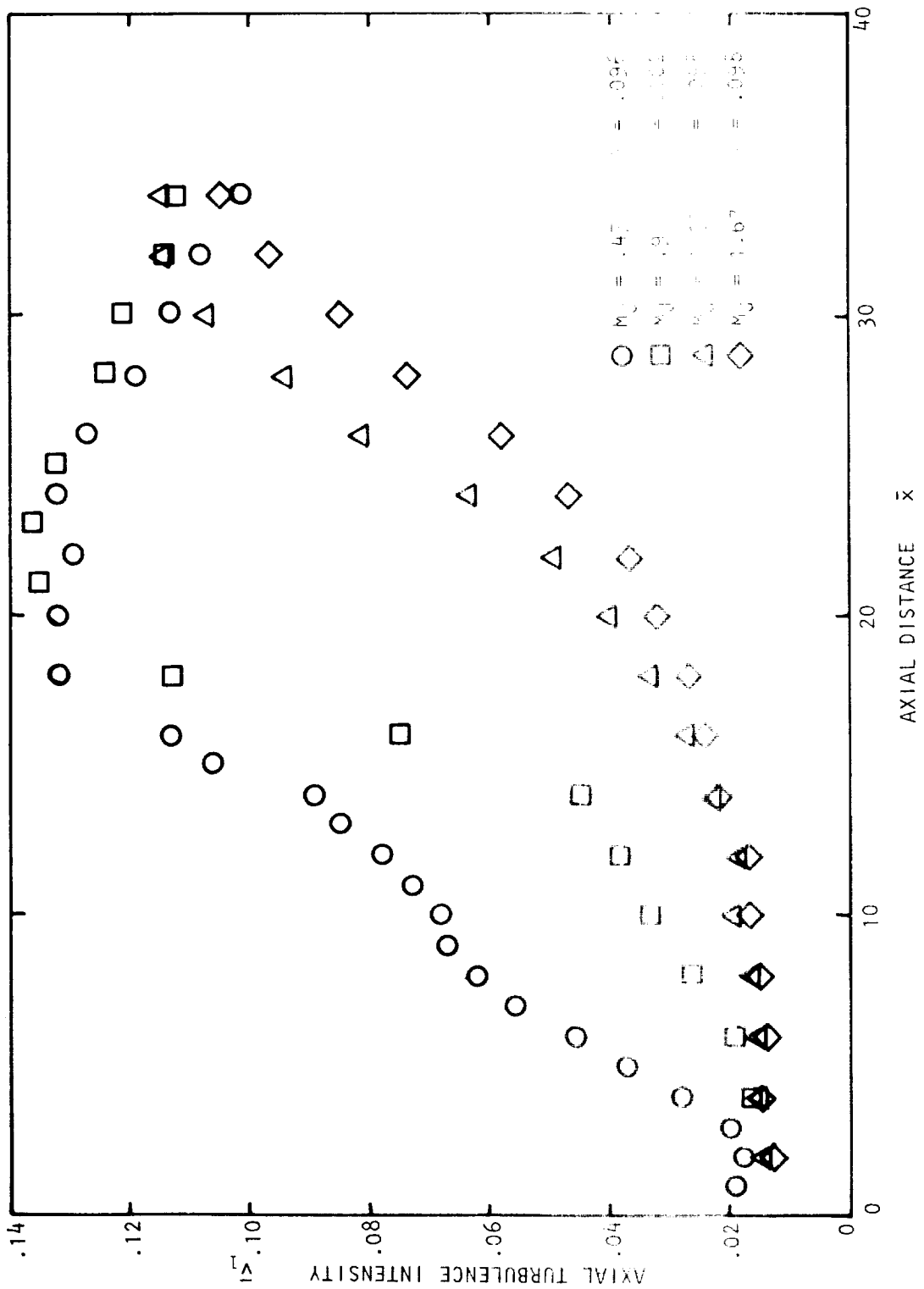
Figure 4.11 Axial turbulence intensity on jet centerline, $\lambda = .1$.

the main air supply valve, where the pressure drop for $M_J = .47$ was from 2×10^6 N/m^2 to 1.6×10^4 N/m^2, causing regular pulsations in the air supply.

It was indicated above that radial traverses were made at various multiples of the estimated potential core length. For the series I tests, ($M_J = .47$, variable λ) the axial locations at which the radial traverses were made are shown in Table I.

MJ	λ (NOMINAL)	AXIAL LOCATIONS OF RADIAL TRAVERSES (RADII)			
.47	.1	3.25	6.5	15	32
.47	.2	3.50	7.0	14	32
.47	.3	3.75	7.5	15	32
.47	.4	4.50	9.0	18	32
.47	.5	5.25	10.5	21	32

TABLE I

The mean velocity profiles and turbulence intensity profiles in the annular mixing region of the jet for $M_J = .47$ and five velocity ratios are shown in Figure 4.12 through 4.21. The corresponding radial mean velocity and turbulence intensity profiles at $\bar{x} = 32$ are shown in Figures 4.22 and 4.23. Initial profiles of mean velocity and turbulence intensity at $\bar{x} = .2$ for $M_J = .47$ and $\lambda = .384$ and .480 are shown in Figures 4.24 and 4.25, respectively. These measurements of mean velocity and turbulence intensity for a fixed jet Mach number and various velocity ratios will be examined in some detail in section 4.2.4. However, several points of explanation and comment will be made here:

(1) The measurements for a velocity ratio of .1 are expected to be the least accurate for several reasons. Firstly, the tunnel speed was hard to keep constant at that low velocity. Secondly, the LV processor, in particular the error circuitry, had to be readjusted for this case to enable velocity measurements to be made at the low speed. From the velocity probability distribution functions, it could be seen that instantaneous velocities well below the tunnel speed were encountered. It is possible that some truncation of the lowest velocities may have occurred.

(2) The radial traverse, for $M_J = .47$ and $\lambda = 1$, was made at $\bar{x} = 15$ rather than $\bar{x} = 13$ due to a positioning error.

(3) The initial velocity profiles were made at $\bar{x} = .2$ rather than $\bar{x} = 0$ for two reasons. Firstly, the two laser beams, which intersect at the measurement point to create a fringe pattern, approach this point at a small but finite angle. The closest location of the jet exit at which a traverse could be made was set by this angle. This is sketched below.

123
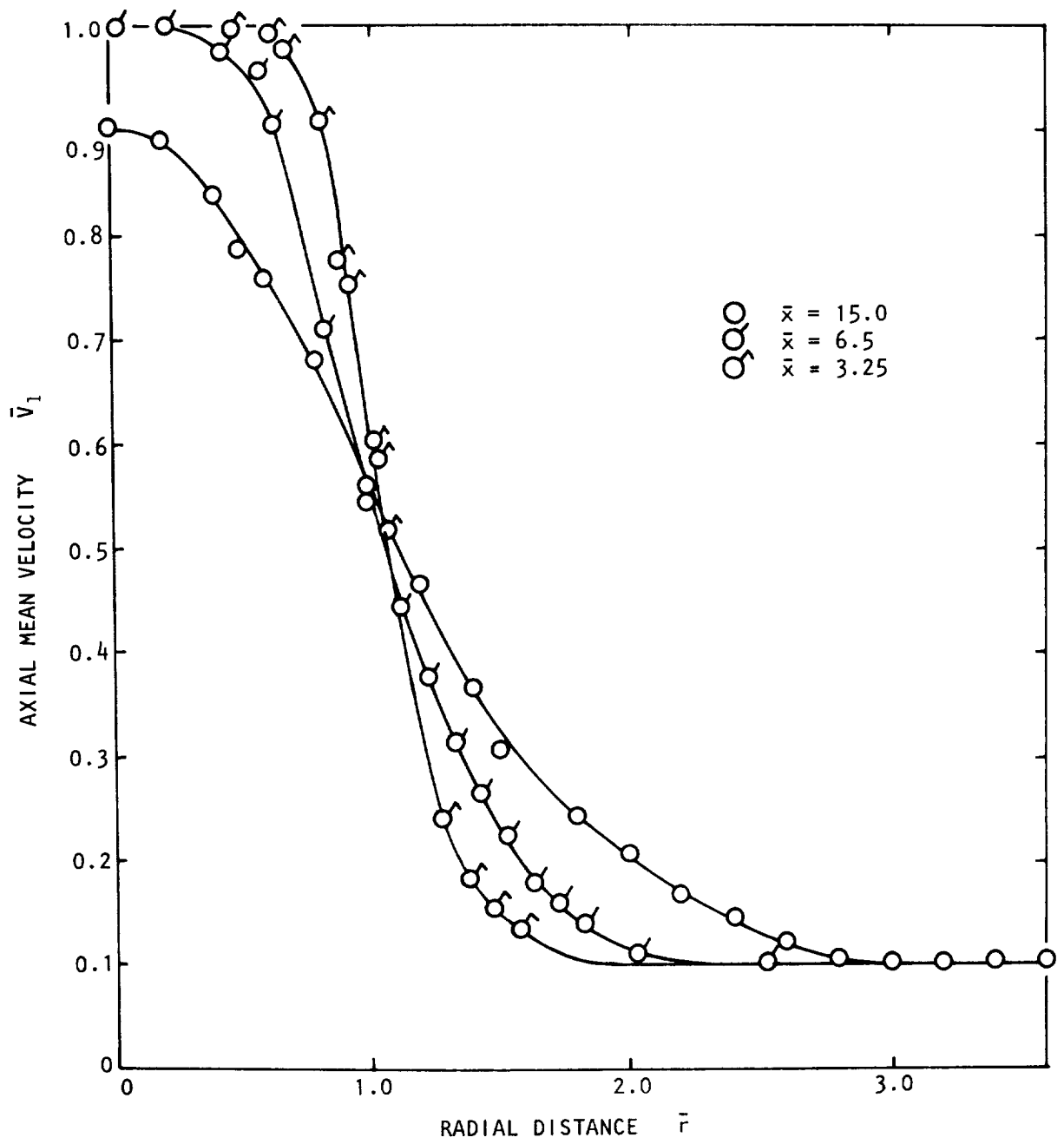
Figure 4.12   Axial mean velocity profiles, $M_J = .47$, $\lambda = .1$.

124
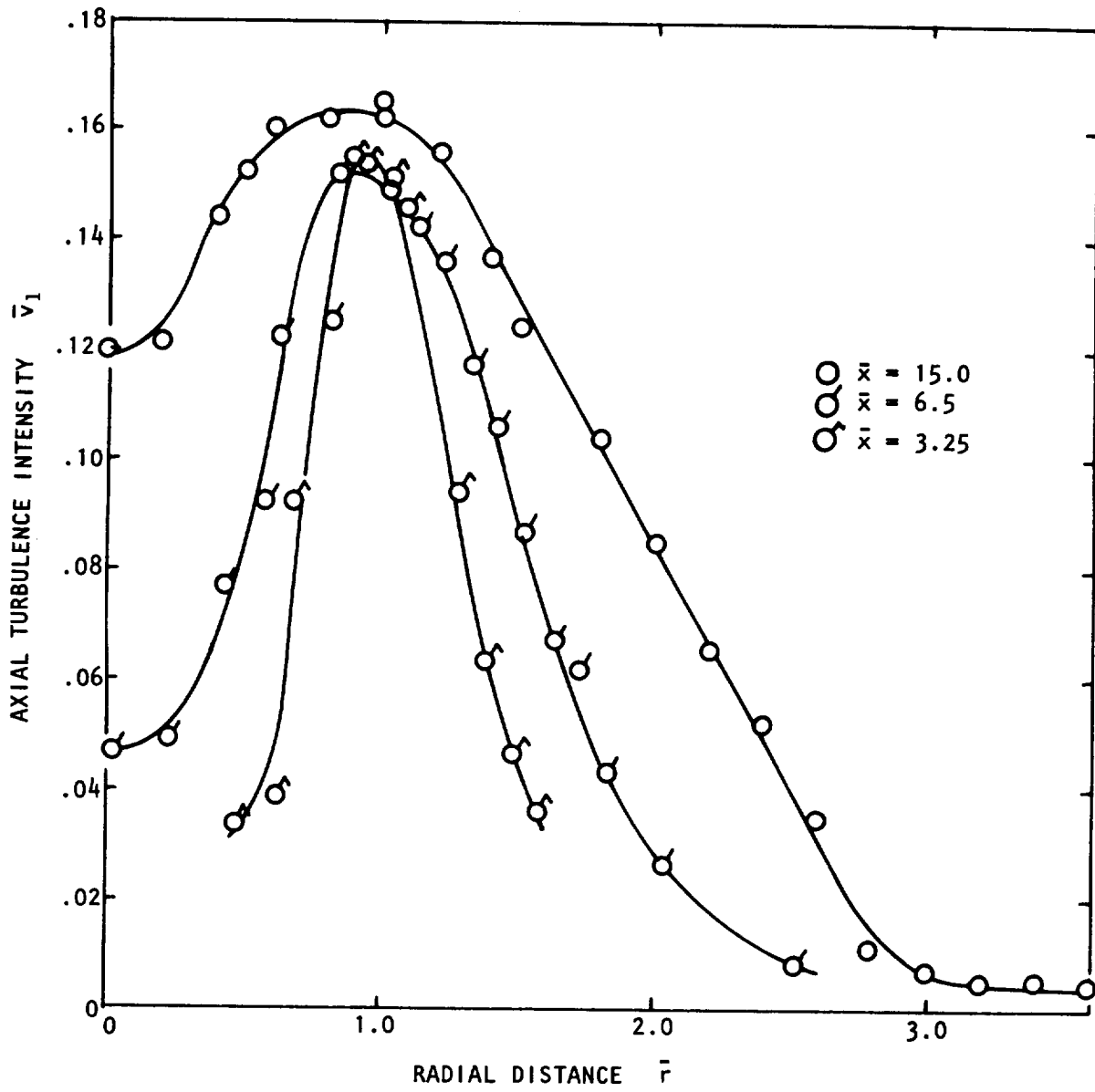
Figure 4.13 Axial turbulence intensity profiles, $M_J = .47$, $\lambda = .1$.
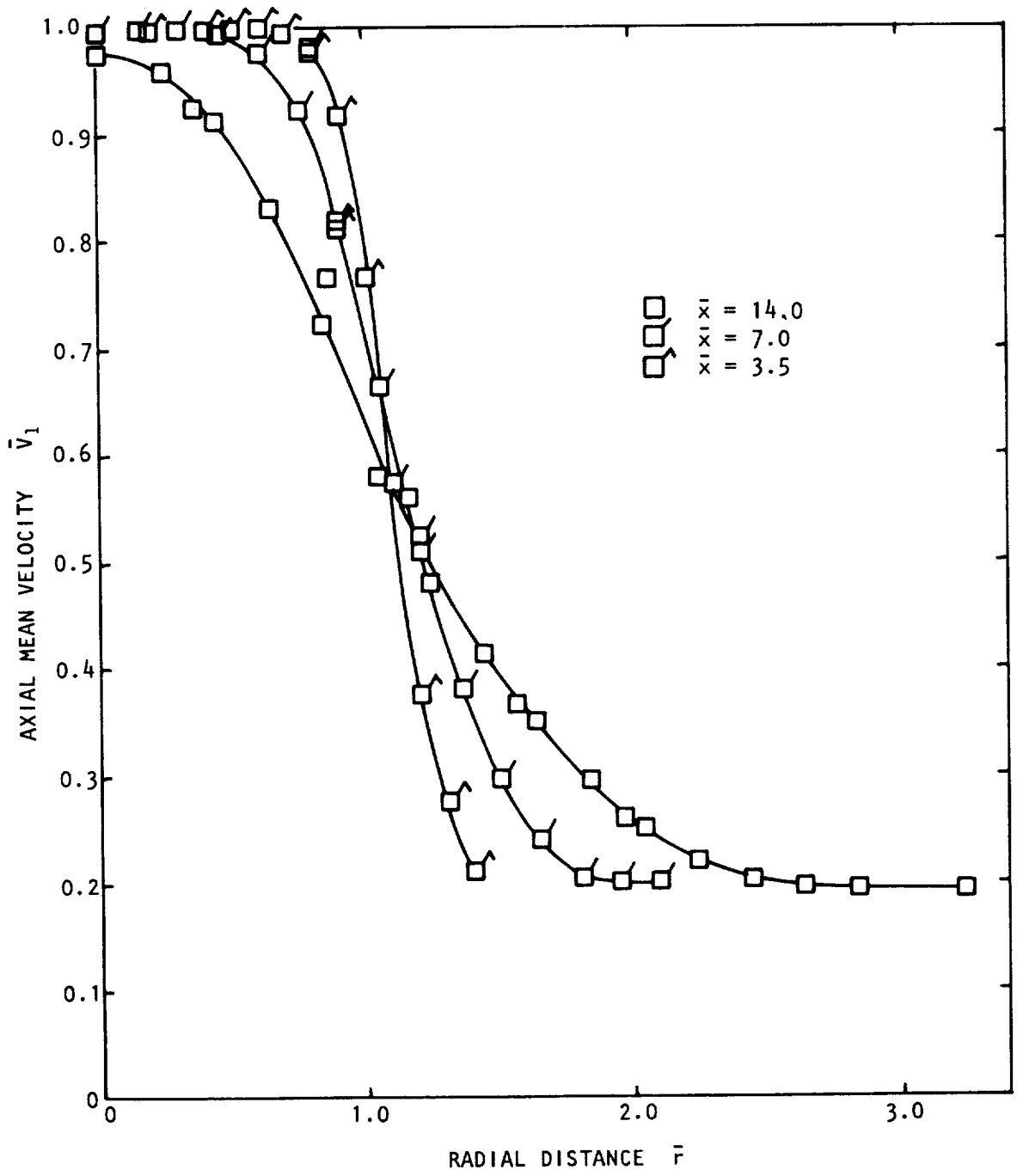
Figure 4.14 Axial mean velocity profiles, M_J = .47, λ = .2 .

Figure 4.15 Axial turbulence intensity profiles, $M_J = .47$, $\lambda = .2$.
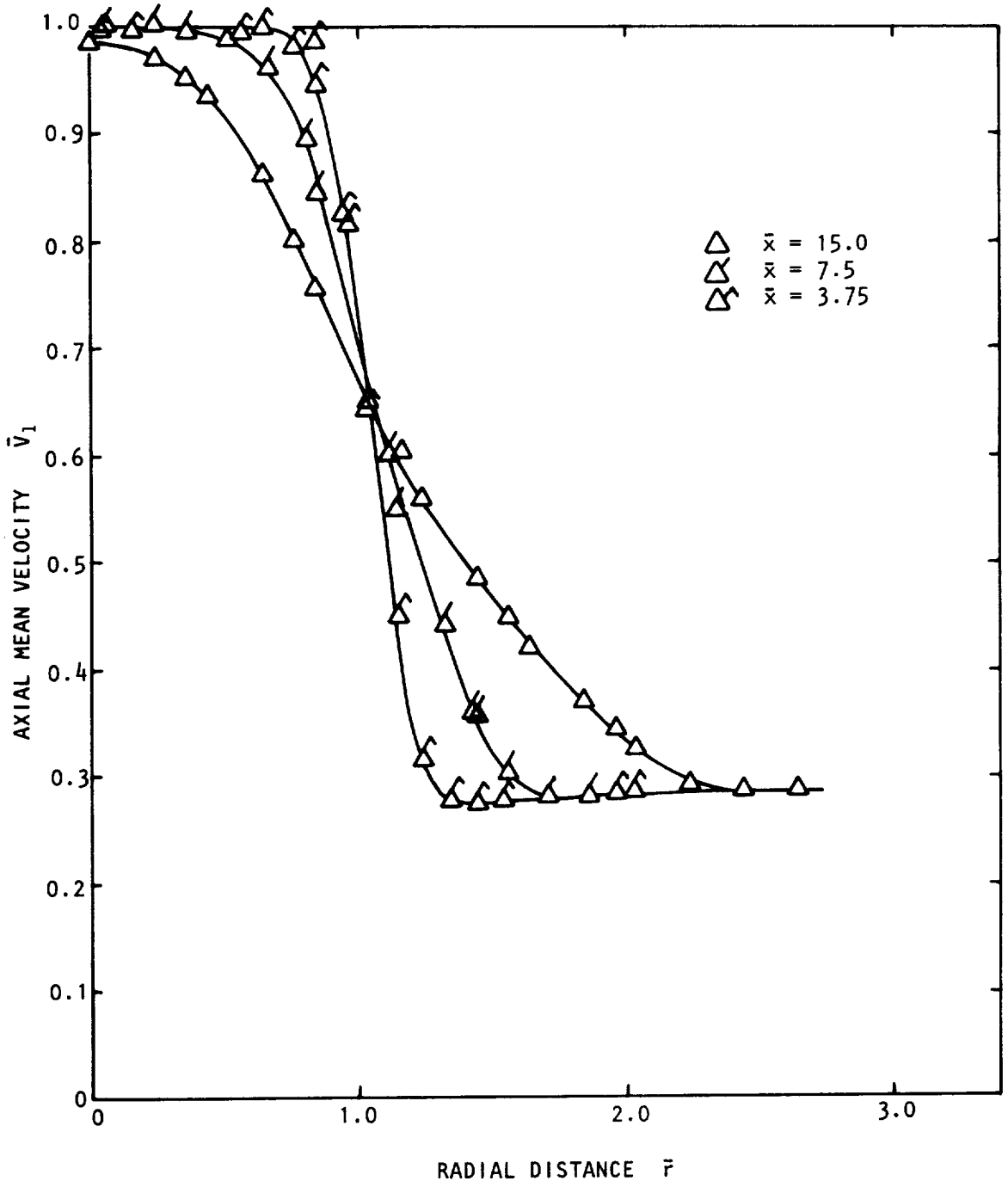
Figure 4.16 Axial mean velocity profiles, $M_J = .47$, $\lambda = .3$.
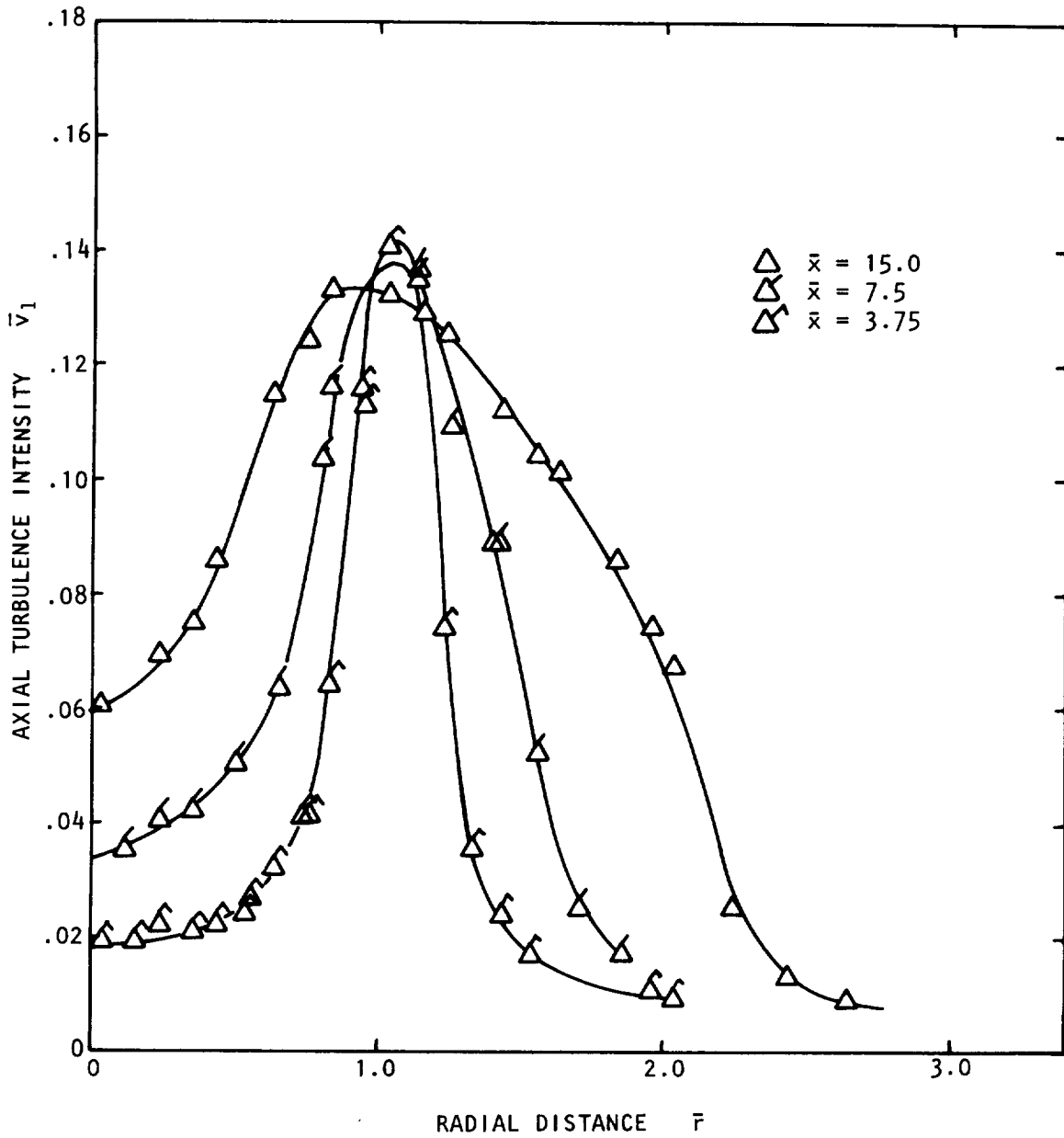
Figure 4.17 Axial turbulence intensity profiles, $M_J = .47$, $\lambda = .3$.
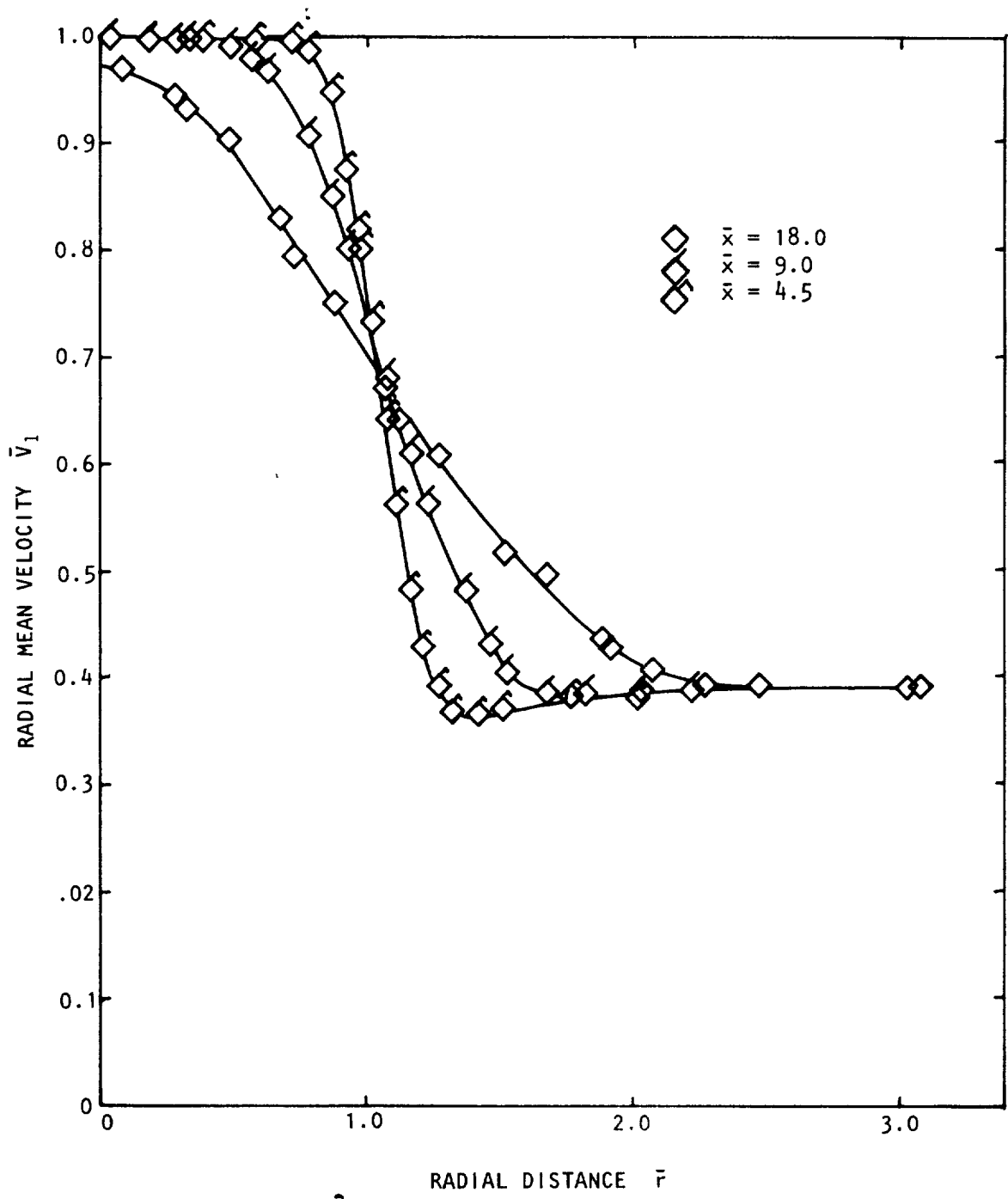
Figure 4.18   Axial mean velocity profiles, $M_J = .47$, $\lambda = .4$.
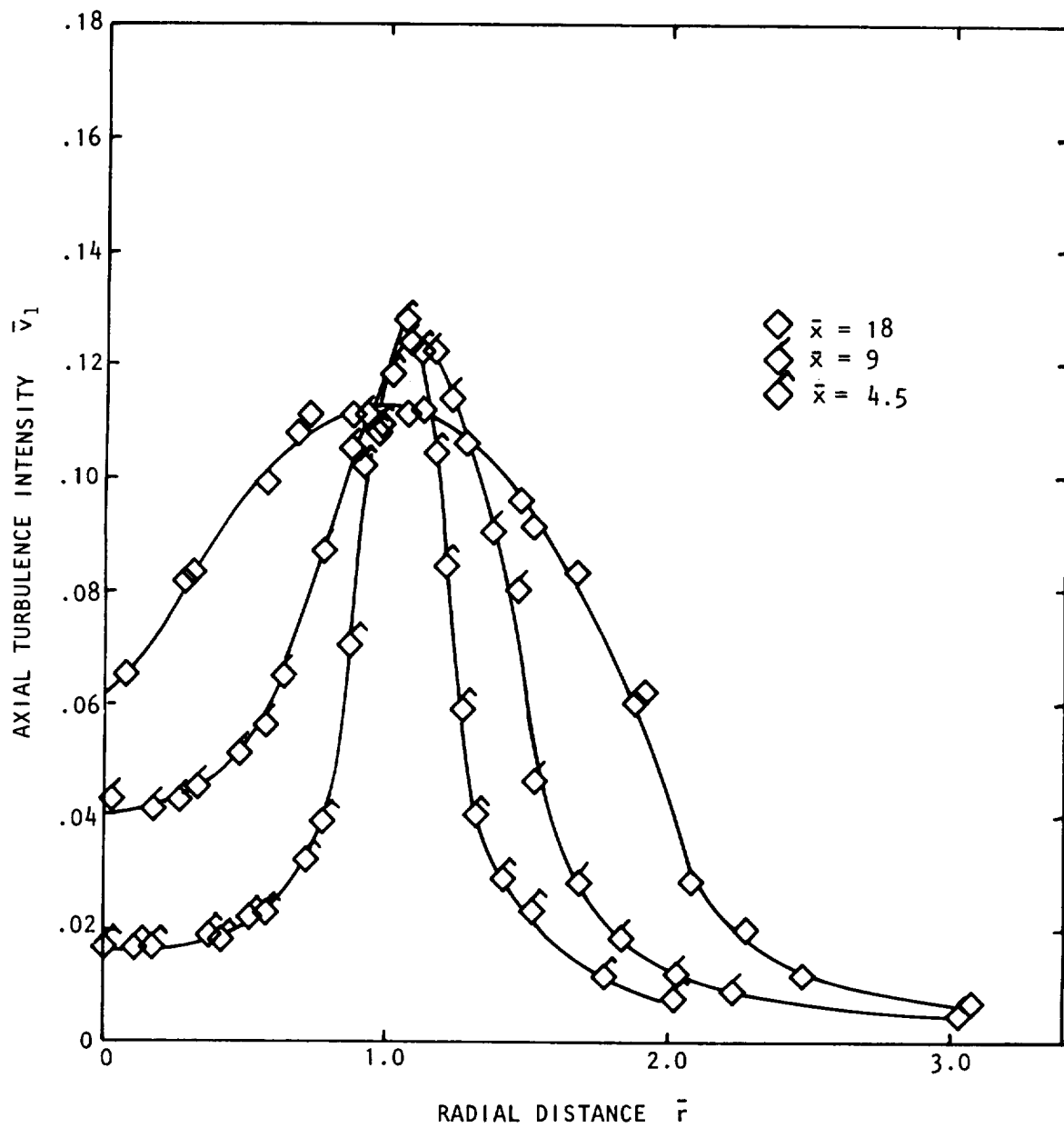
Figure 4.19   Axial turbulence intensity profiles, $M_J = .47$, $\lambda = .4$.
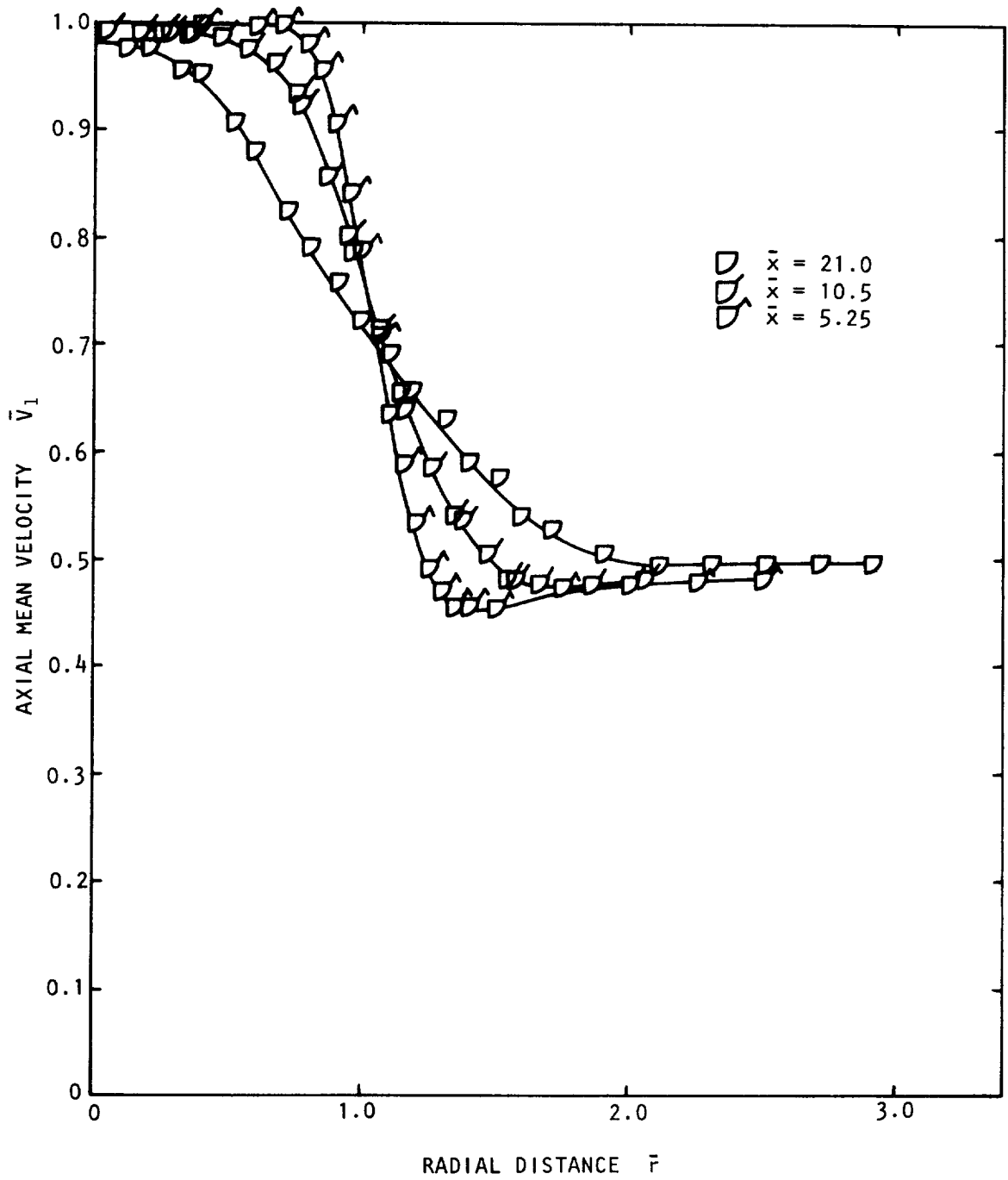
Figure 4.20 Axial mean velocity profiles, $M_J = .47$, $\lambda = .5$.
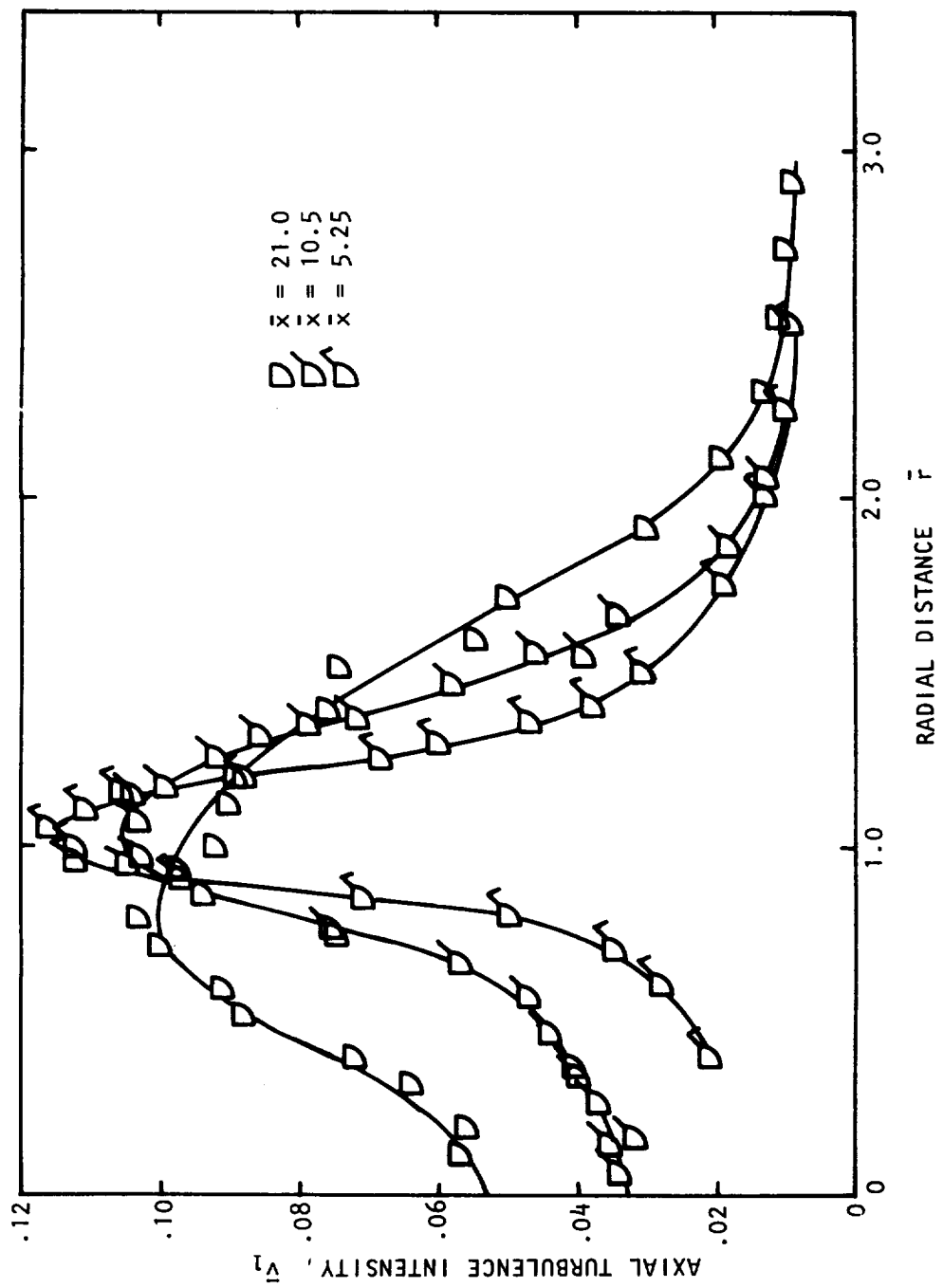
Figure 4.21 Axial turbulence intensity profiles, $M_J = .47$, $\lambda = .5$.

$\bar{x} = 21.0$
$\bar{x} = 10.5$
$\bar{x} = 5.25$

RADIAL DISTANCE $\bar{r}$

AXIAL TURBULENCE INTENSITY, $\bar{v}_1$

133
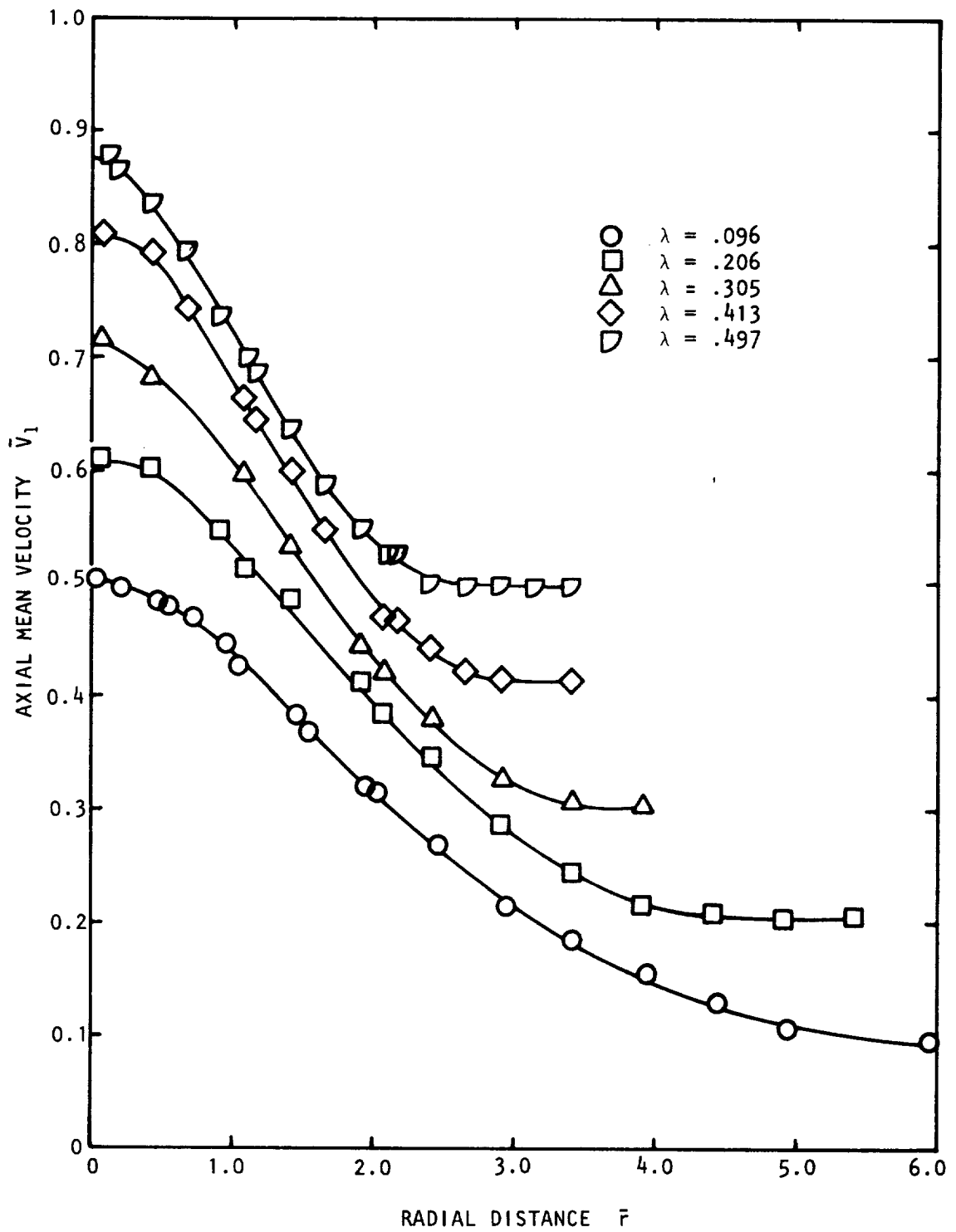
Figure 4.22 Axial mean velocity profiles, $M_J = .47$, $\bar{x} = 32$.
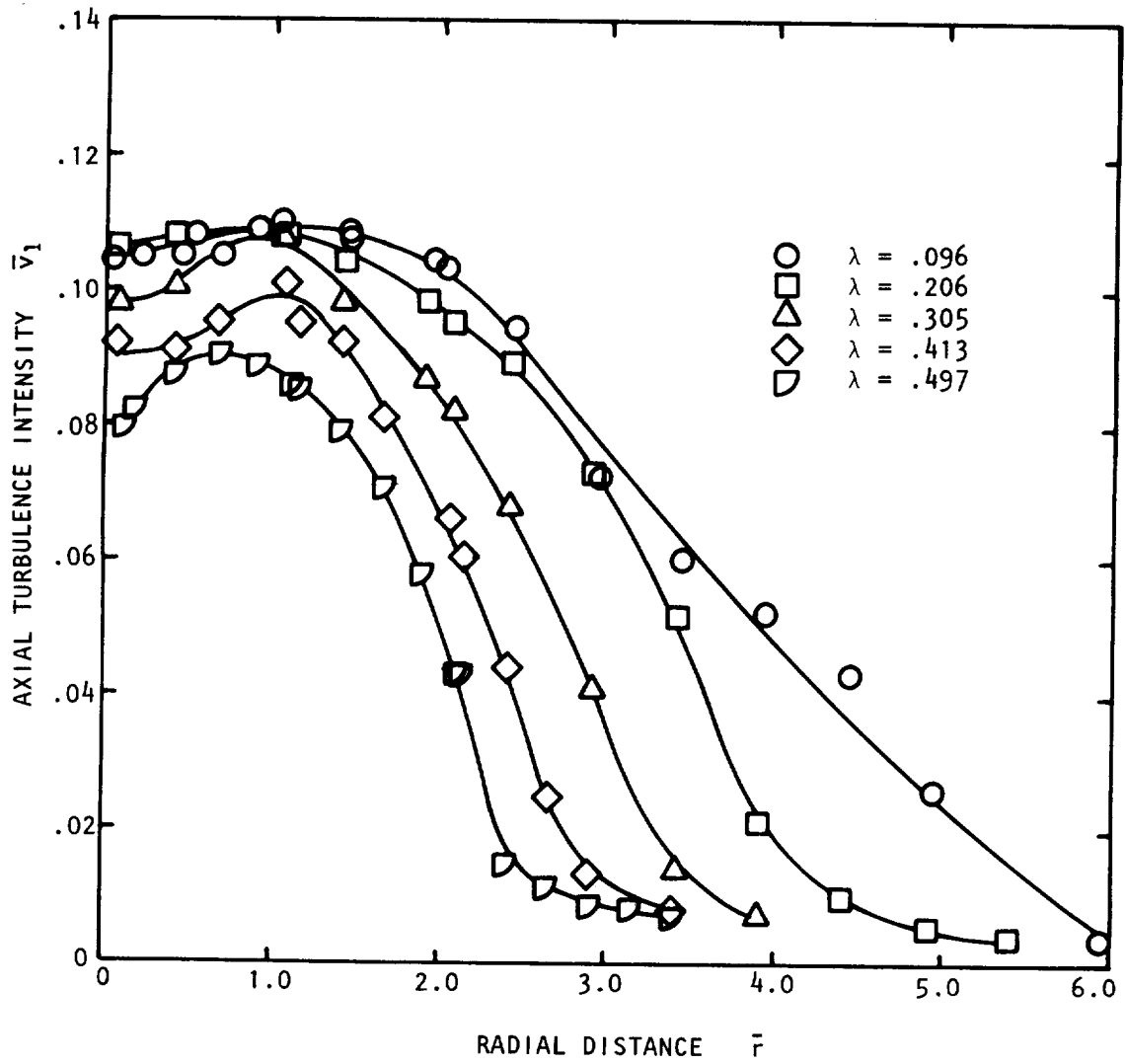
Figure 4.23 Axial turbulence intensity profiles, $M_J = .47$, $\bar{x} = 32$.
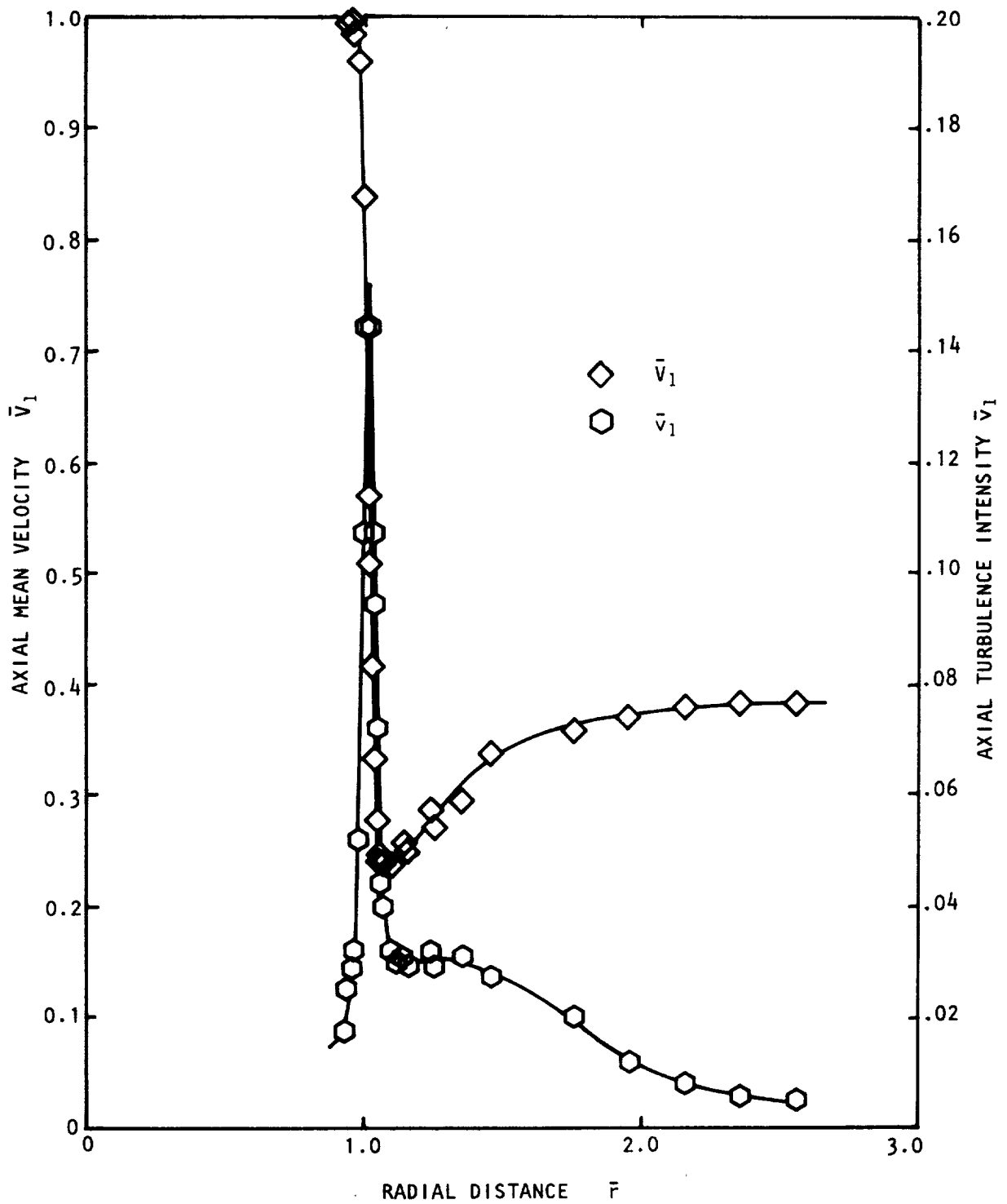
Figure 4.24   Initial velocity profiles, $M_J = .47$, $\lambda = .384$, $\bar{x} = .2$.
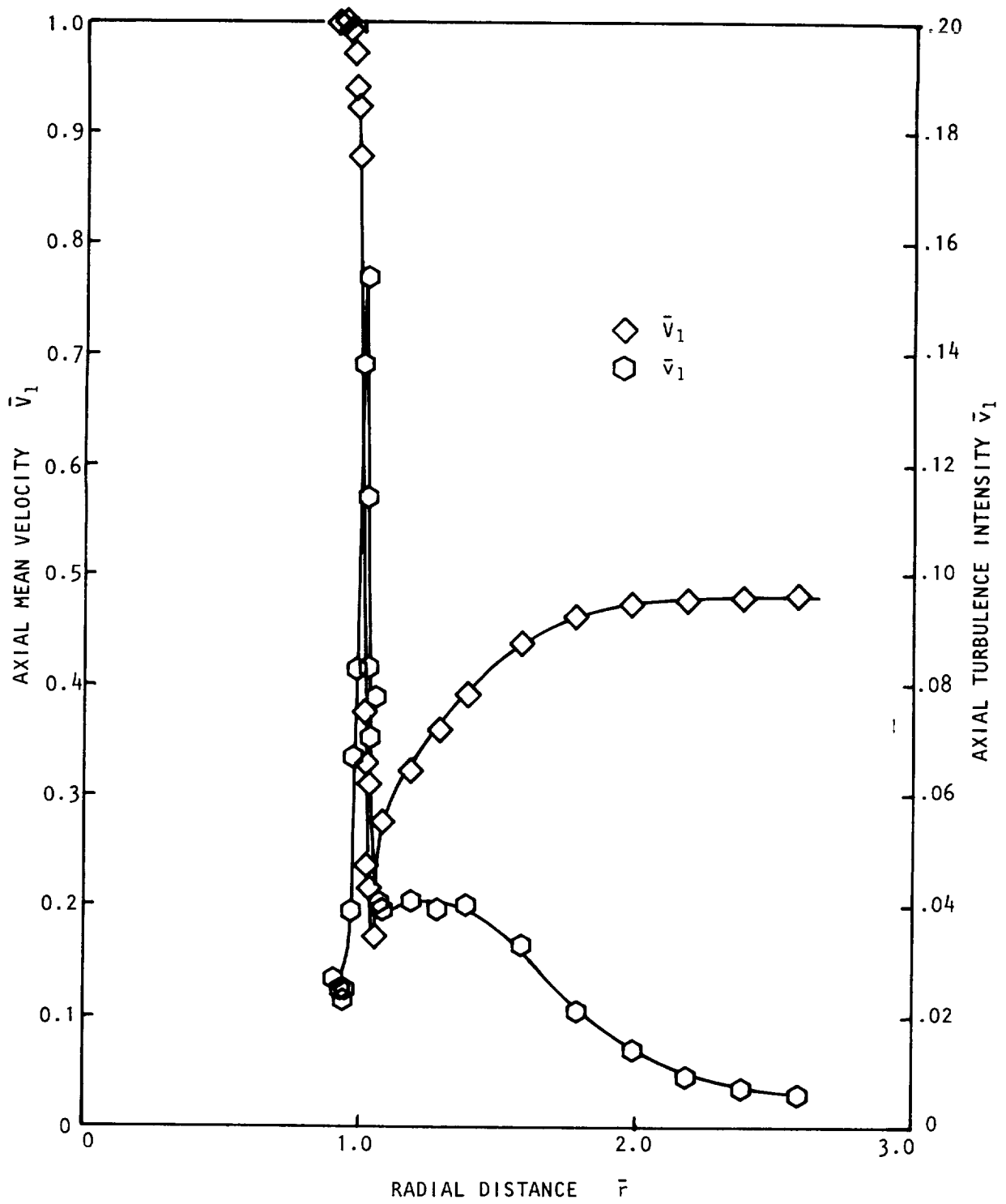
Figure 4.25   Initial velocity profile, $M_J = .47$, $\lambda = .480$, $\bar{x} = .2$.

```
                              ⌐ 0.51 CM.
                              │
                              ▼
LV OPTICS ◄───
                        ┌─────┬─────┐
                        │ PLAN │ VIEW │
```
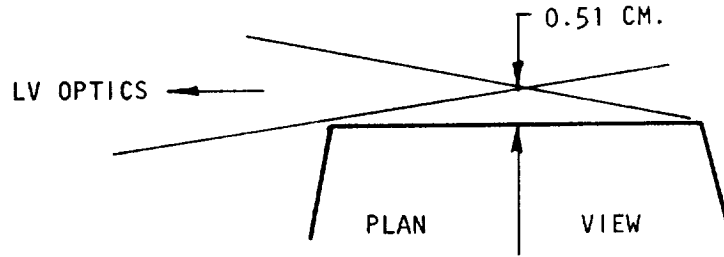
Secondly, since particles only reach a location in the flow from inside the jet or in the wind tunnel, seeding is very uneven in the stagnation region at the lip.

Since the lengths of the potential cores for the series II measurements (fixed velocity ratio, variable Mach number) were expected, in some cases, to stretch beyond the length of the working section, radial traverses in this measurement series were made at fixed distances from the jet exit. The locations were at $\bar{x} = 4$, 8, 16, and 32. The mean velocity and turbulence intensity profiles for $\lambda = .1$ and three jet exit Mach numbers are shown in Figures 4.26 through 4.31. The velocity measurements are tabulated in Appendix 4A.

In the next section the data is reduced on the basis of several scaling parameters.

4.2.4 Characteristic Dimensions and Scaling Parameters

In this section the measured mean velocity and turbulence intensity distributions, described in section 4.2.3, will be used to calculate the variation of several characteristic properties of the flow. These parameters will be subsequently used as scaling parameters for the velocity distributions.

It was noted in the previous section that the effect of increasing the free-stream velocity was to stretch the mixing region in the axial direction. In Appendix 4B the decay of the centerline velocity is shown to follow the relationship

$$\frac{\bar{V}_a - \lambda}{1 - \lambda} = 1 - \exp\left[\frac{1}{2\xi_v}\right] \qquad (4\text{-}1)$$

where
$$\xi_v = .04 \ (1 - .92 \ \lambda) \ \bar{x} - .35. \qquad (4\text{-}2)$$

The data reduced in this manner is shown in Figure 4.32. This leads to an expression for the potential core length, $\bar{x}_c$, of

138
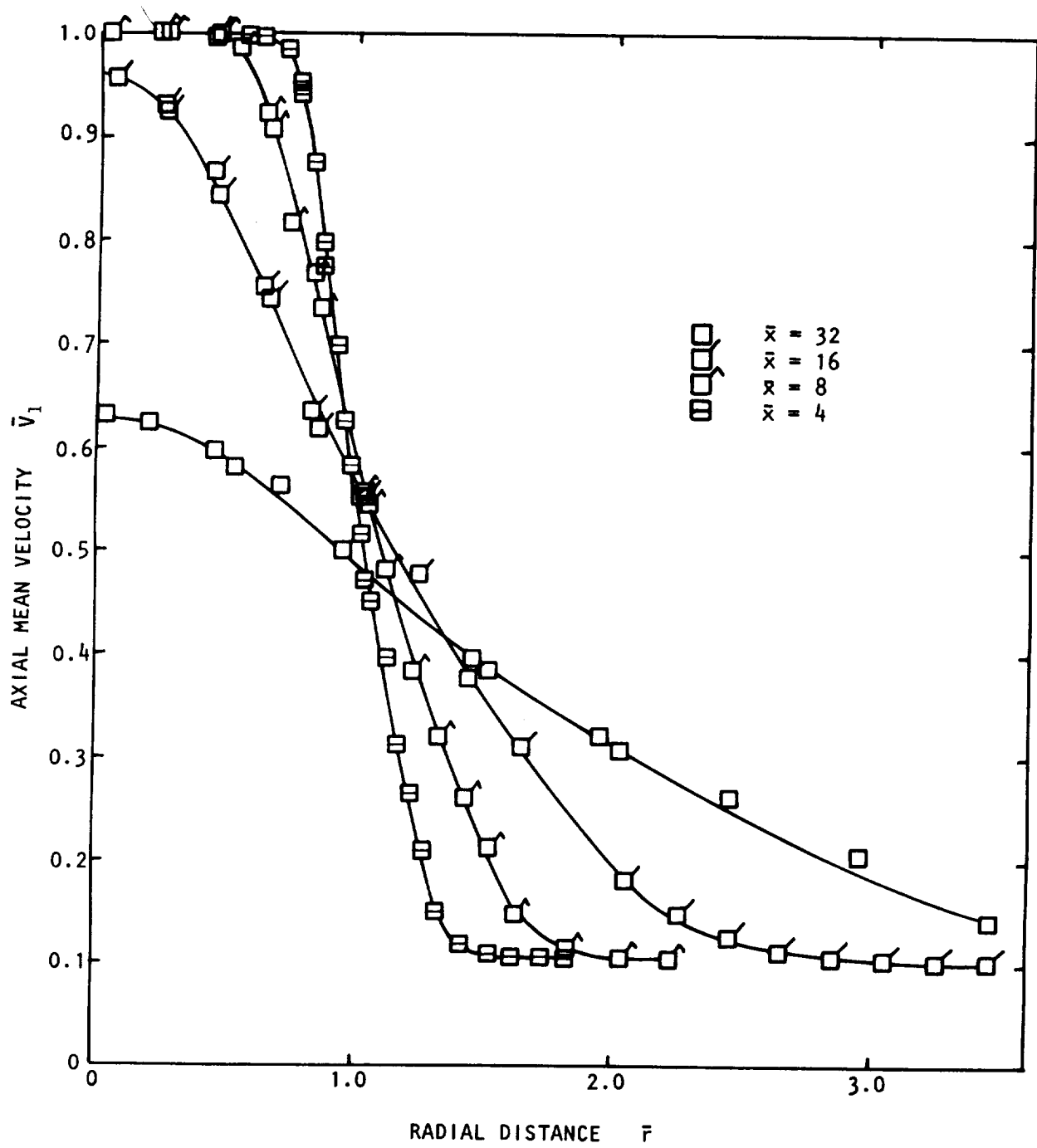
Figure 4.26 Axial mean velocity profiles, $M_J = .9$, $\lambda = .1$.
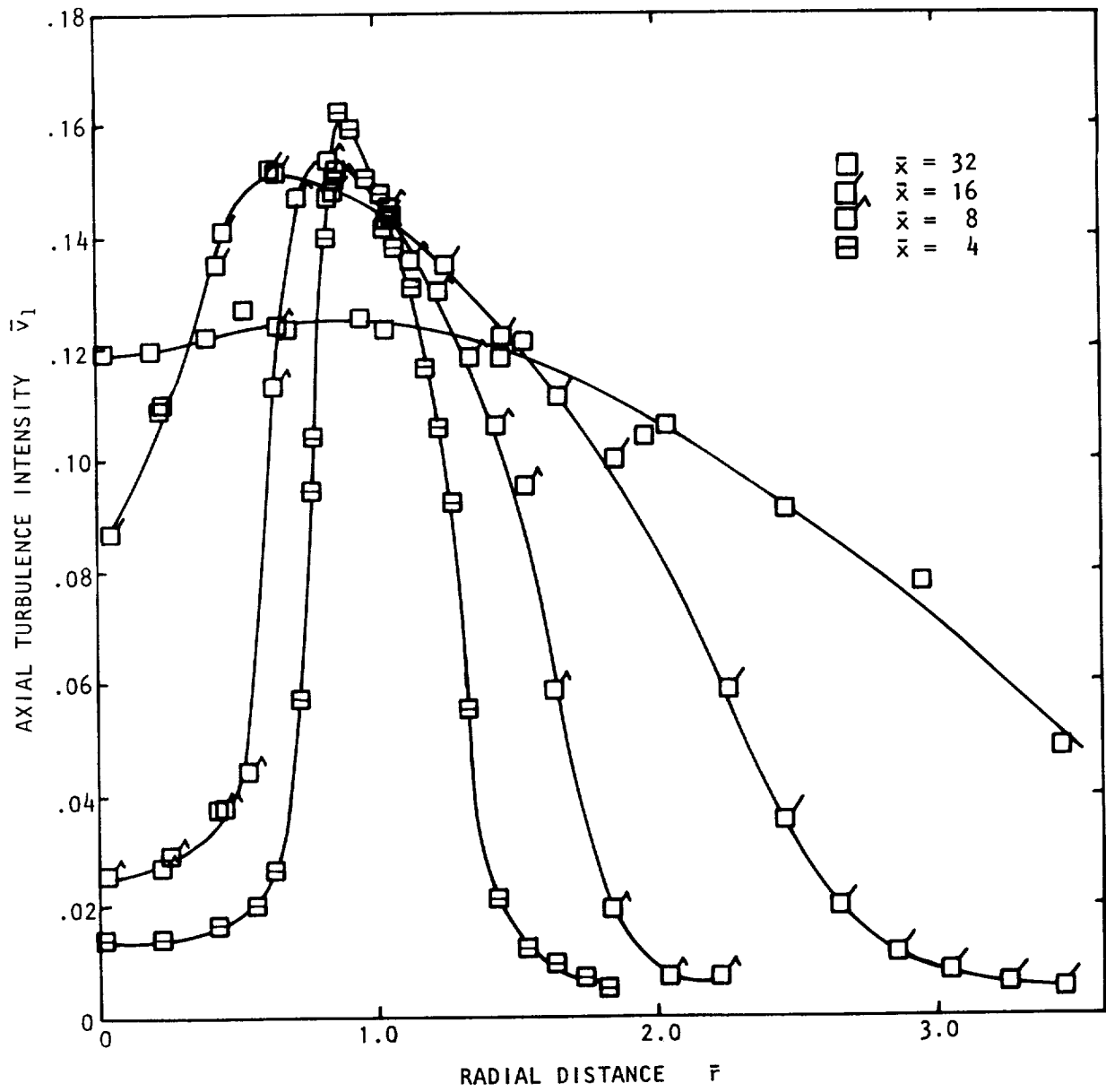
Figure 4.27   Axial turbulence intensity profiles, $M_J + .9$, $\lambda = .1$.

140
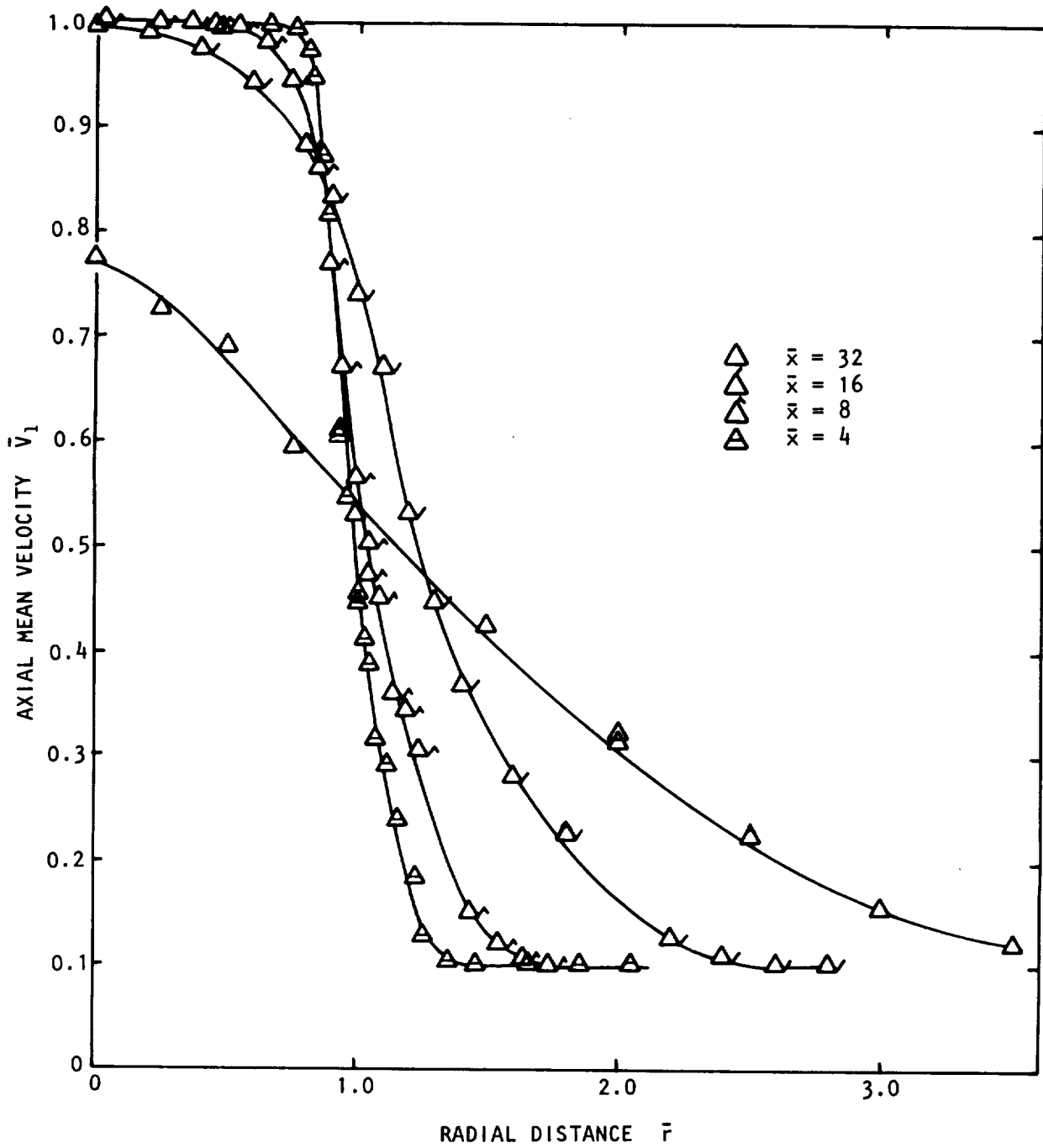
Figure 4.28   Axial mean velocity profiles, $M_J = 1.37$, $\lambda = .1$.
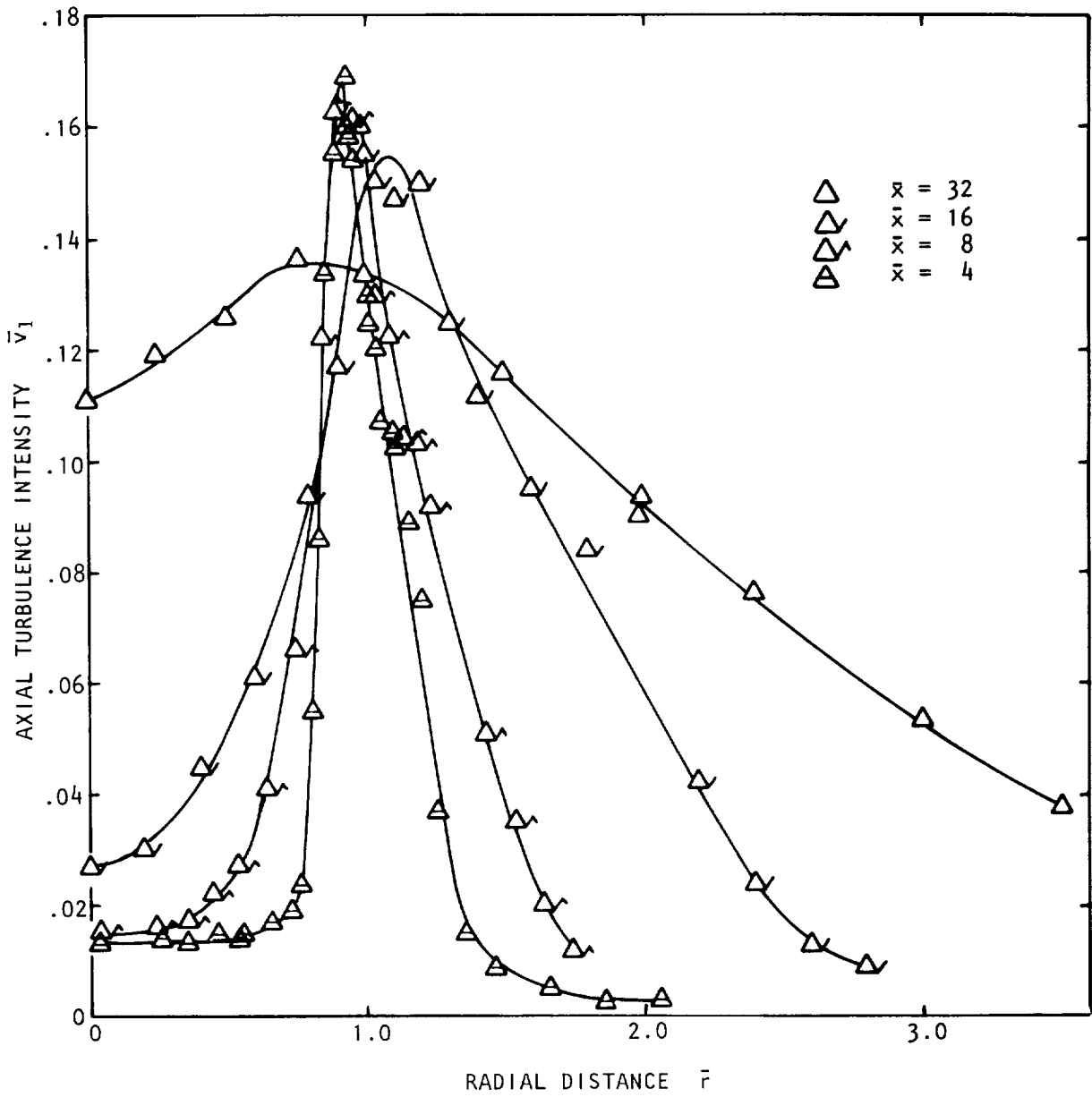
Figure 4.29 Axial turbulence intensity distributions, $M_J = 1.37$, $\lambda = .1$.
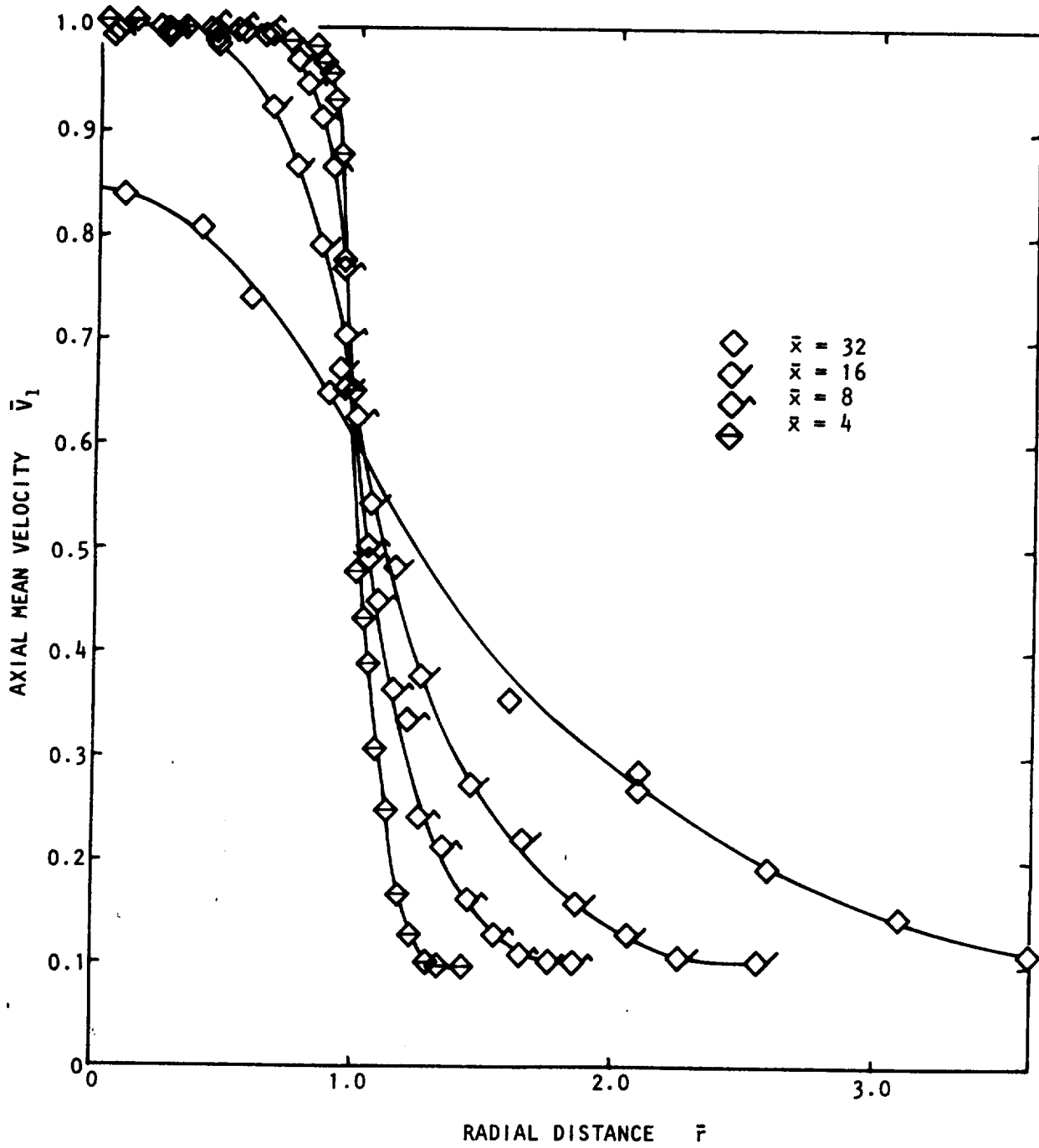
Figure 4.30   Axial mean velocity profiles, $M_J = 1.67$, $\lambda = .1$.
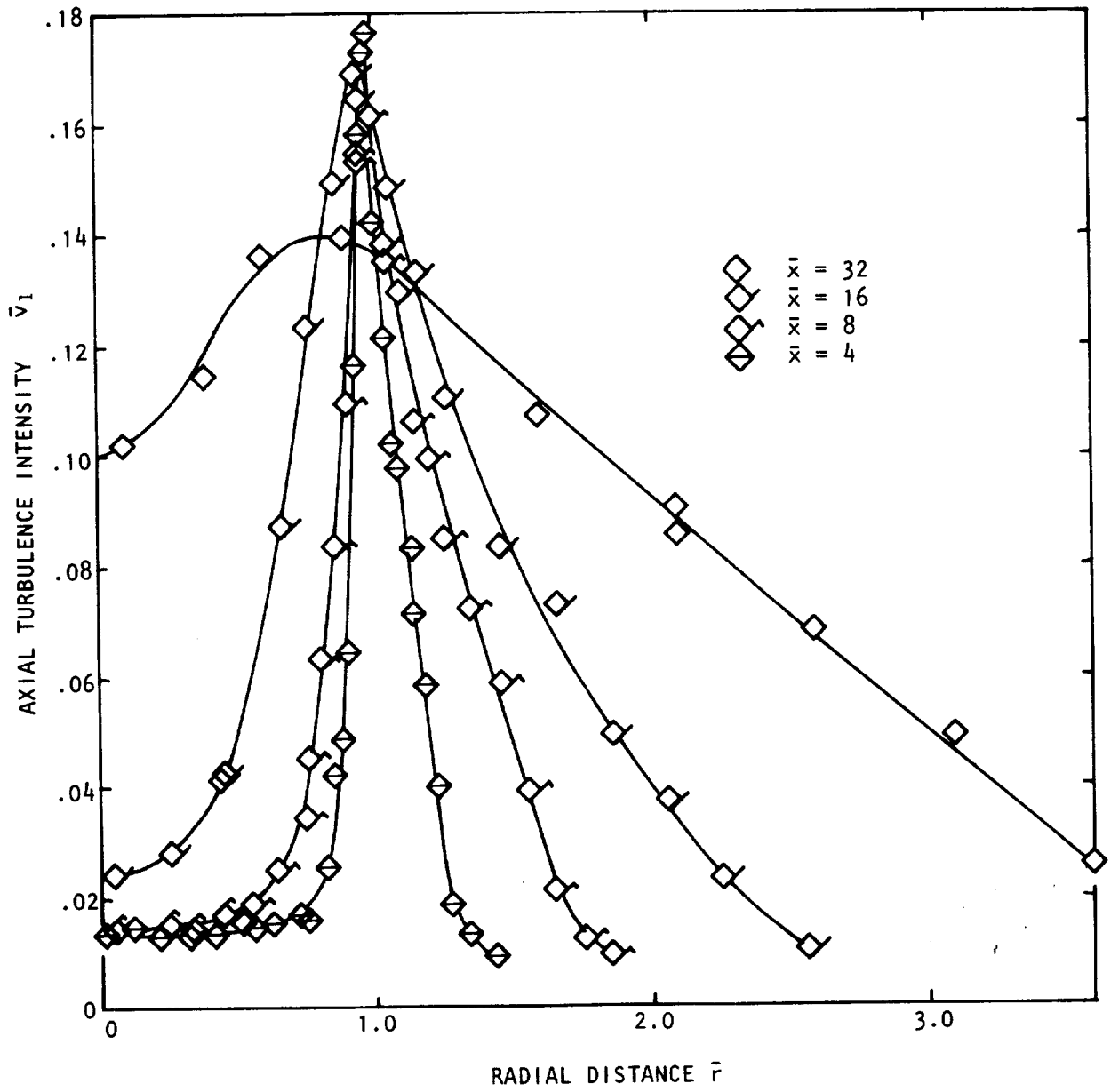
Figure 4.31 Axial turbulence intensity profiles, $M_J = 1.67$, $\lambda = .1$.
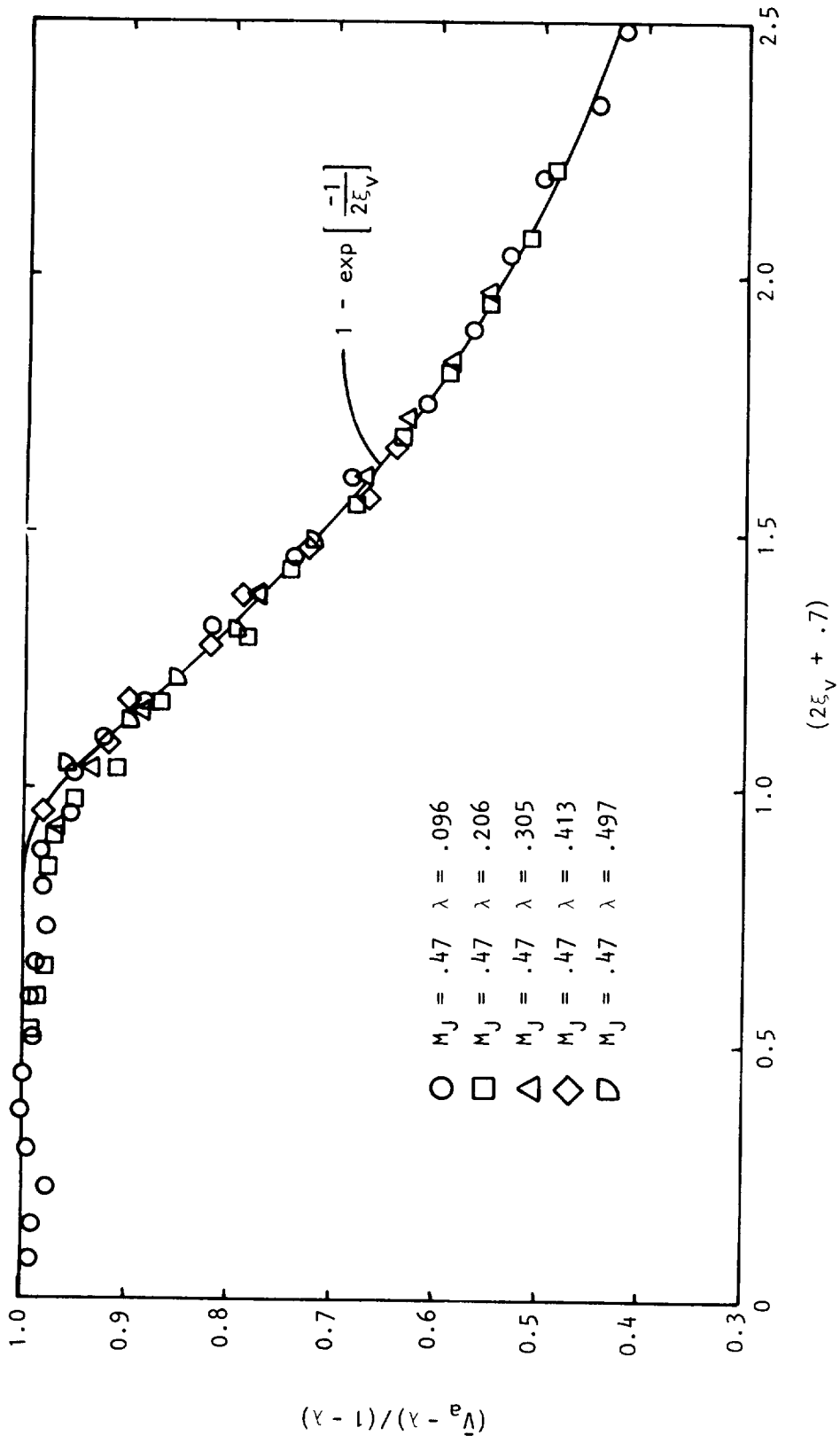
Figure 4.32 Centerline velocity decay, $M_J = .47$.

145

$$\bar{x}_c = 8.77/(1 - .92 \lambda).$$

(4-3)

The empirical form for the variation of $\bar{x}_c$ with λ given by Forstall and Shapiro (ref. 2) was

$$\bar{x}_c = 8 + 24 \lambda.$$

(4-4)

This expression was obtained by fitting an expression of the form

$$\frac{\bar{V}_a - \lambda}{1 - \lambda} \propto \frac{1}{\bar{x}},$$

(4-5)

to their measurements. The same method has been applied to the present measurements and this is shown in Figure 4.33. It can be seen that even for the limited axial extent of the present measurements an expression of the form (4-5) fits the data adequately once a transition from the annular mixing region has been passed. Comparison of the expressions (4-1) and (4-5) shows that the former exhibits no discontinuity in the derivative of the centerline velocity at the end of the potential core whereas the latter does. When $\bar{x} = \bar{x}_c$, $(\bar{V}_a - \lambda)/(1 - \lambda) = 1$, the exponential term in equation (4-1) can be written as $\exp\{-A(\lambda)/(\bar{x} - \bar{x}_c)\}$, where $A(\lambda)$ is readily obtained from equations (4-2) and (4-3). For a fixed velocity ratio the exponential may be expanded for large values of $(\bar{x} - \bar{x}_c)$ giving,

$$\frac{\bar{V}_a - \lambda}{1 - \lambda} \propto \frac{1}{\bar{x} - \bar{x}_c},$$

(4-6)

which is significantly different from expression (4-5). The variation of potential core length as a function of velocity ratio, found by these various methods is shown in Figure 4.34. There is a considerable scatter in Forstall and Shapiro's measurements. However, if equation (4-1) is compared with their measurements of the centerline velocity, there is fair agreement. This is shown in Figure 4.35. Since the empirical constants in equation (4-1) are dependent on the Mach number of the jet, some differences are to be expected.

The variation of the potential core length with Mach number is shown in Figure 4.36. Witze (ref. 3) made use of a two-region turbulence model to predict the development of subsonic and supersonic free jets. The empirical relationships he derived from a large number of experiments are shown in Figure 4.36. Clearly, there is some problem with the predictions for slightly supersonic jet exit velocities. However, the general trends of the current measurements for $\lambda = .1$ and these predictions are in good agreement.

The rate of spreading of the jet is also defined at the axial variation of the jet width. In the present investigation the width of the jet is defined as the vorticity thickness, δ_ω, which is given by

$$\delta_\omega = \frac{\bar{V}_a - \lambda}{(\partial \bar{V}_1 / \partial \bar{r})_{max}}$$

(4-7)
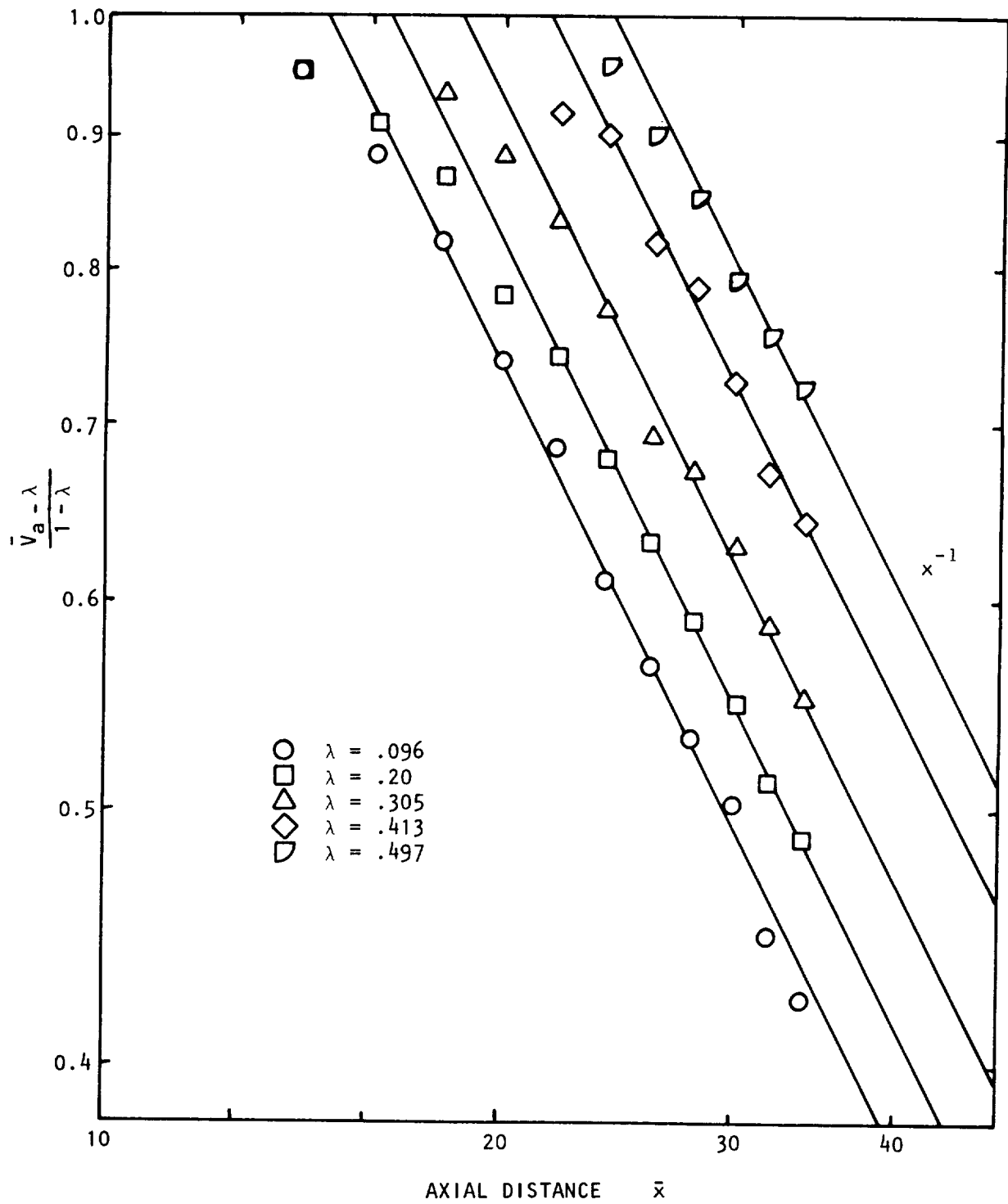
Figure 4.33   Centerline velocity decay, $M_J = .47$.
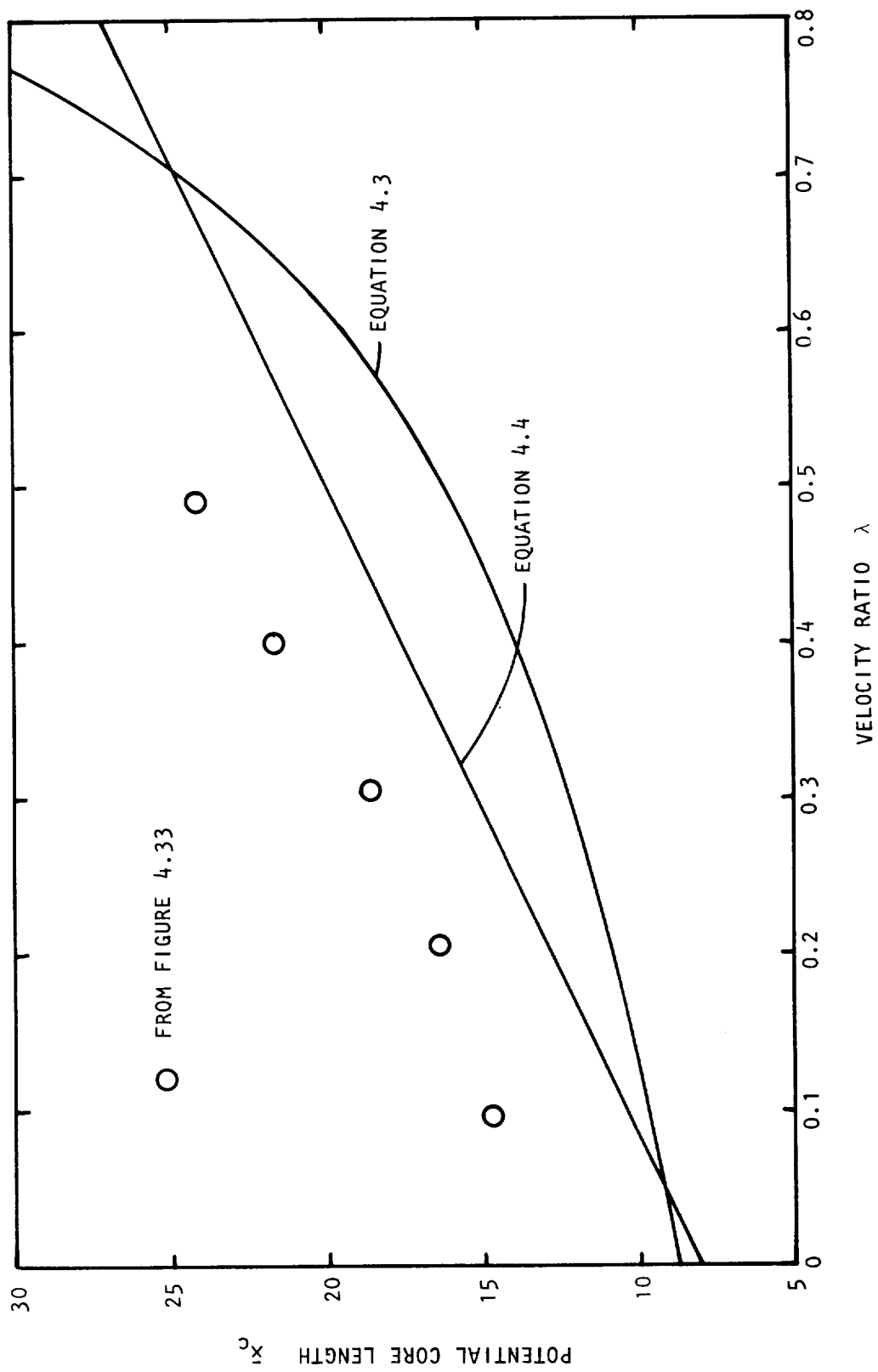
Figure 4.34 Variation of potential core length with velocity rate.
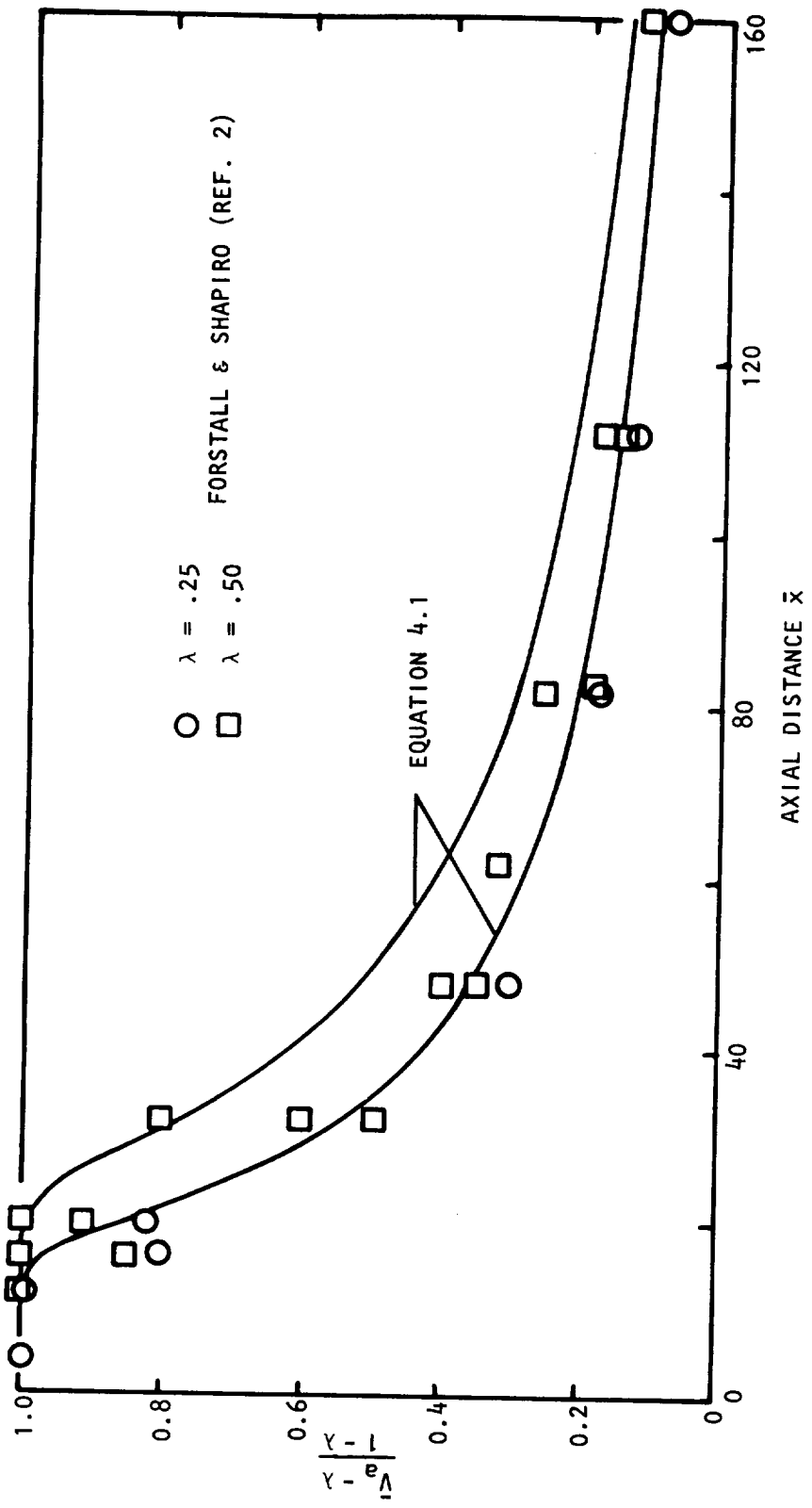
Figure 4.35 Centerline velocity decay.

149
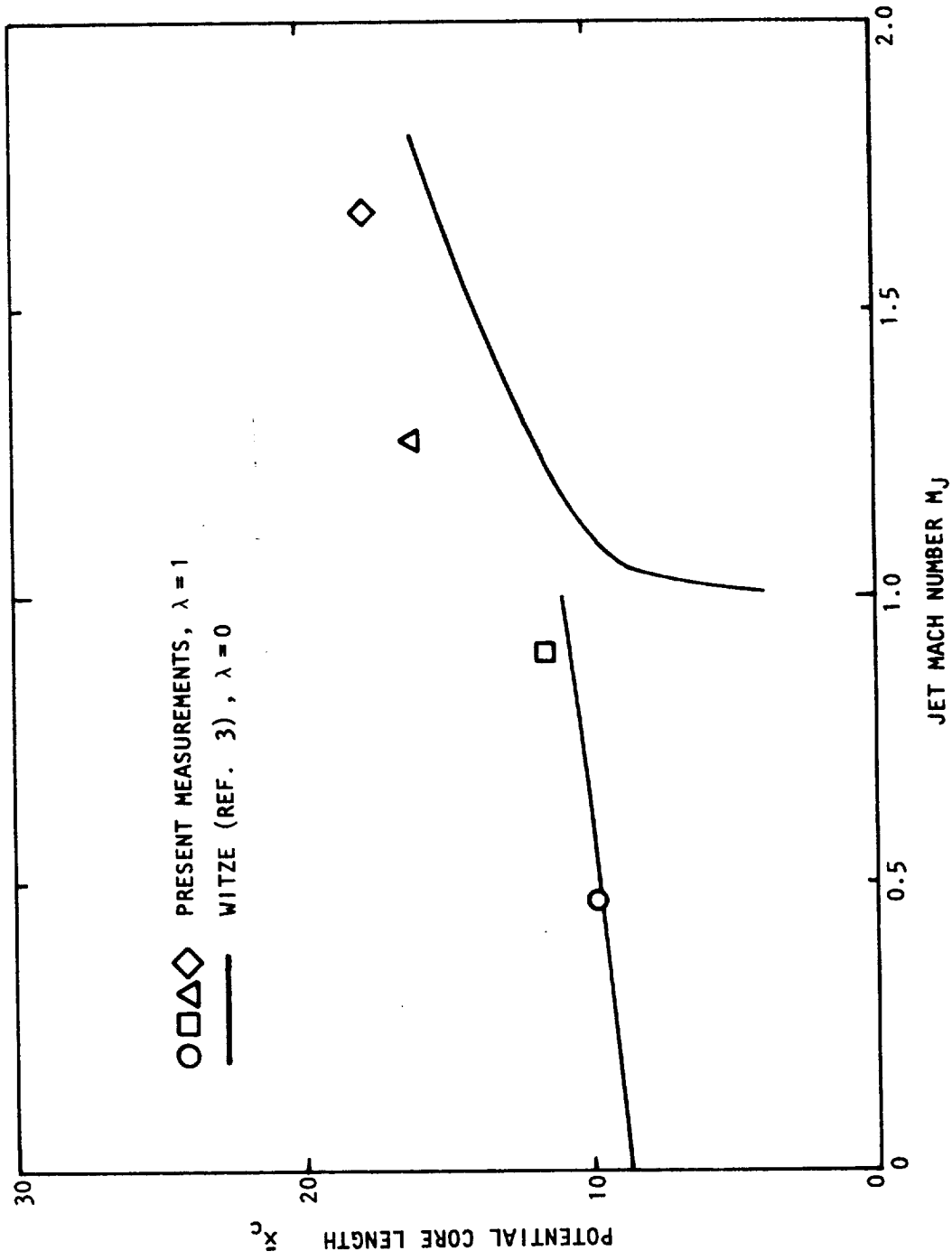
Figure 4.36 Variation of potential core length with Mach number.

150

Brown and Roshko (ref. 41) point out that this definition of thickness is appropriate since the growth of the turbulent jet is governed by the unstable motion induced by the vorticity. It has been found convenient for the purposes of presentation to consider the jet in two separate regions: the annular mixing region up to the end of the potential core and the flow region downstream of the potential core.

It is to be expected that for sufficiently small ratios of vorticity thickness to potential core radius the initial mixing region will spread in the same manner as the two-dimensional mixing region. In fact, the spread rate of the axisymmetric jet agrees closely with that of the two-dimensional mixing region up to the end of the potential core. The variation of $\bar{\delta}_\omega/\bar{x}$ for the two-dimensional mixing region is compared with the present measurements in Figure 4.37. It can be seen that the variation of mixing region thickness with axial distance agrees well for the two flows and can be simply related by

$$\bar{\delta}_\omega = \text{const.} \frac{(1 - \lambda)}{(1 + \lambda)} \bar{x} \qquad (4-8)$$

where Brown and Roshko (ref. 41) give the constant in equation (4-8) a value of .181. Equation (4-8) is also shown in Figure 4.37.

A second parameter which describes the rate of spread of the jet is the dividing streamline radius. This radius was defined in section 4.2.3. The location of the dividing streamline is shown in Figure 4.38 for the annular mixing region for the series I, $M_J = .47$ measurements. The value of the virtual origin of mixing, $\bar{x}_0$, was found to vary between -.5 and 1.5. The calculated location of the dividing streamline as given by Korst and Chow (ref. 67) is also shown. It can be seen that these calculations for the two-dimensional mixing layer indicate a much slower divergence of the dividing streamline. The dividing streamline velocity is shown in Figure 4.39 and is compared with Korst and Chow's calculations. In all cases, except $\lambda = .1$, there is some agreement between the measured values of $\bar{V}_{ds}$ and the calculations for small values of $\bar{x} - \bar{x}_0$. In the axisymmetric jet case, the dividing streamline velocity decreases with axial distance. It should be remembered that, in the two-dimensional case, the mean velocity is similar whereas, in the axisymmetric jet case the mean velocity profile is not similar.

In order to examine the effect of velocity ratio on the rate of growth of the jet downstream of the potential core, it is convenient to examine first the shape of the mean velocity profiles in this region. The local velocity difference normalized by the difference between the centerline velocity and the tunnel velocity is plotted in Figure 4.40 as a function of the radial distance divided by the half-velocity radius. It will be shown that there is a linear relationship between the half-velocity radius and the vorticity thickness so either can be used as the nondimensionalizing quantity. However, it is convenient to use the half velocity radius in the momentum equation below. It can be seen that there is good collapse of the
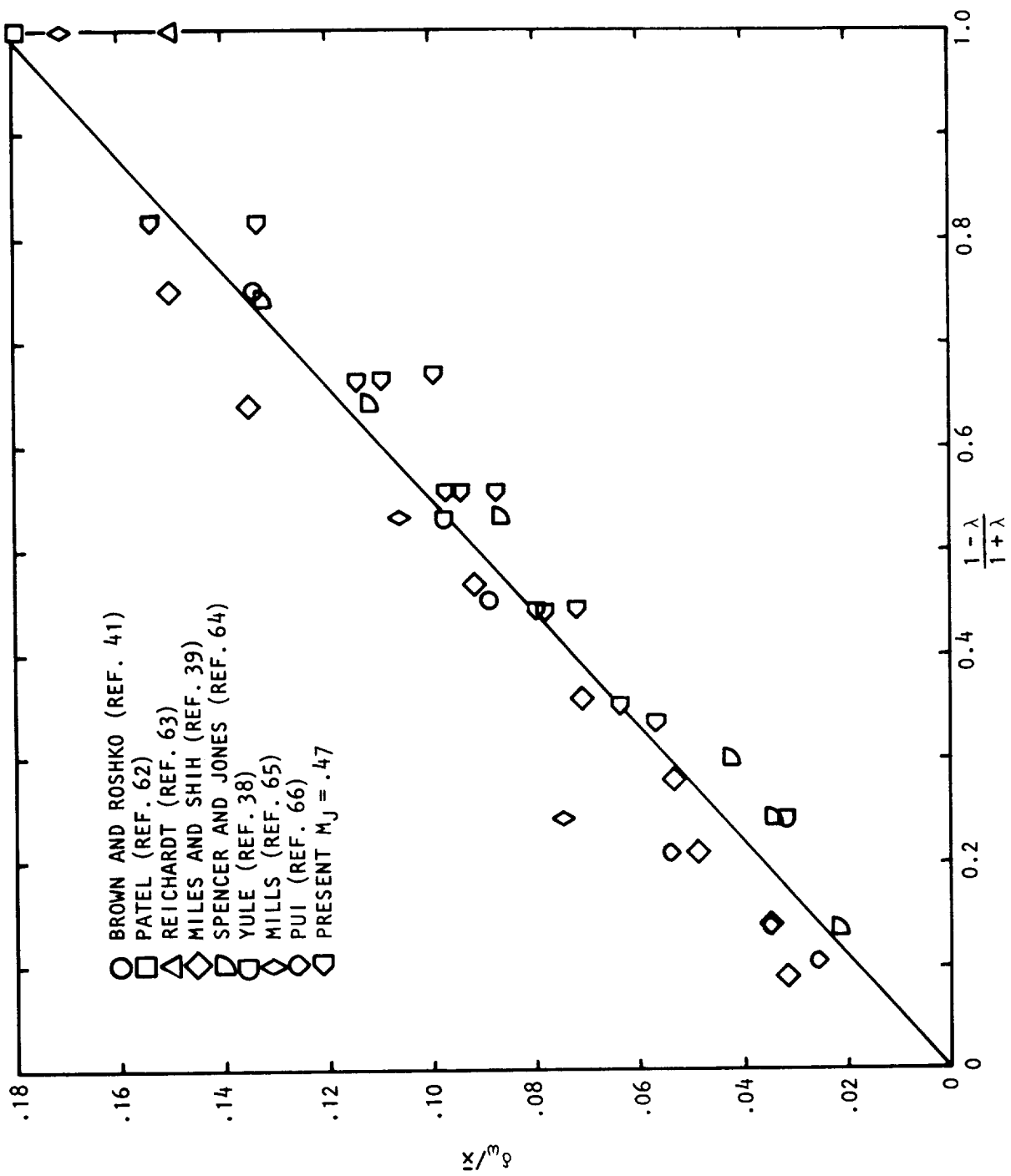
Figure 4.37 Variation of vorticity thickness with velocity ratio.

Legend:
- ○ BROWN AND ROSHKO (REF. 41)
- □ PATEL (REF. 62)
- ◁ REICHARDT (REF. 63)
- ◇ MILES AND SHIH (REF. 39)
- ⬠ SPENCER AND JONES (REF. 64)
- ⬡ YULE (REF. 38)
- ◇ MILLS (REF. 65)
- ◇ PUI (REF. 66)
- ⬡ PRESENT $M_J = .47$

Axis labels: $\dfrac{1-\lambda}{1+\lambda}$ (horizontal), $\delta_\omega/\bar{x}$ (vertical)

152
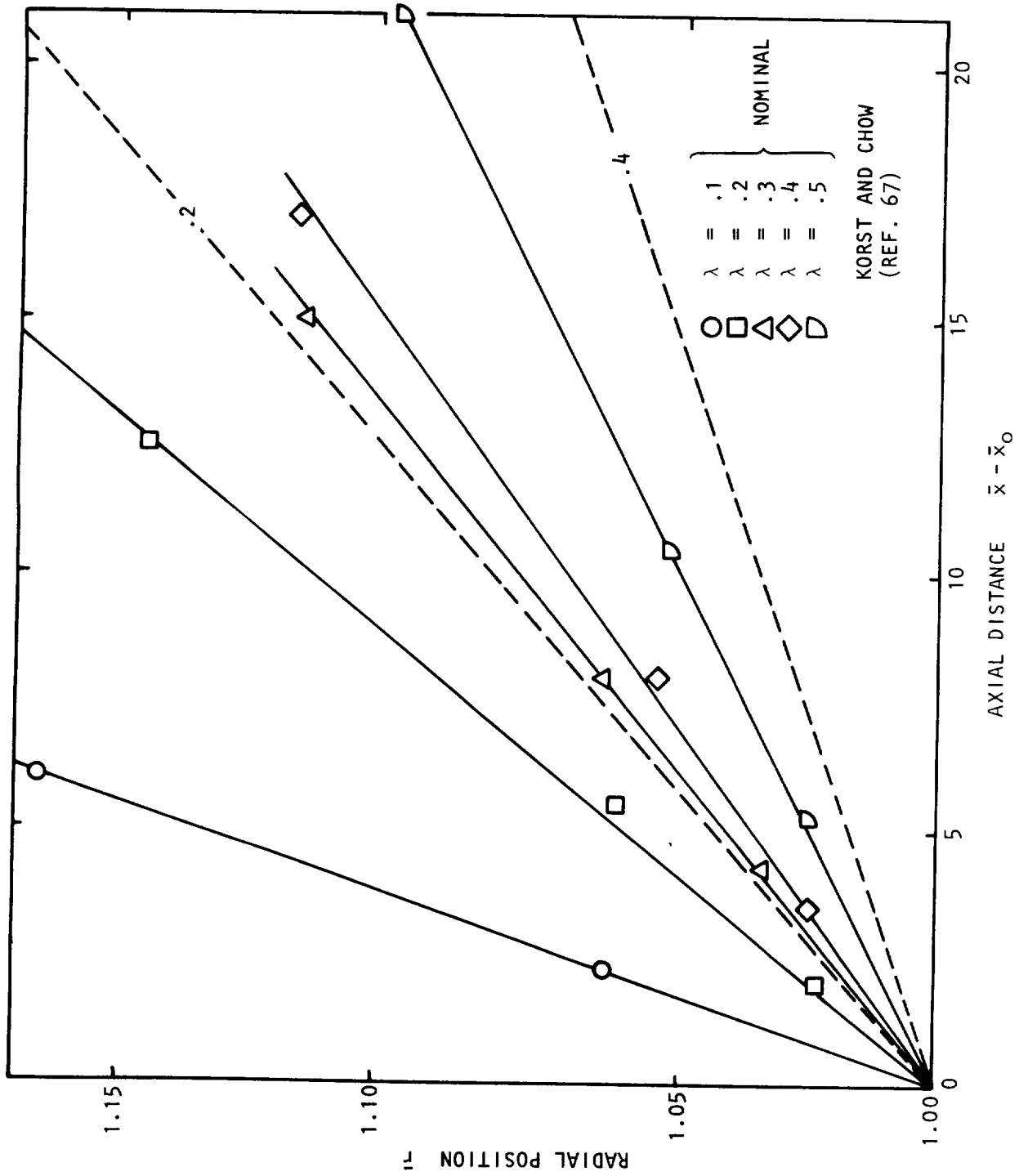
Figure 4.38 Location of the dividing streamline.
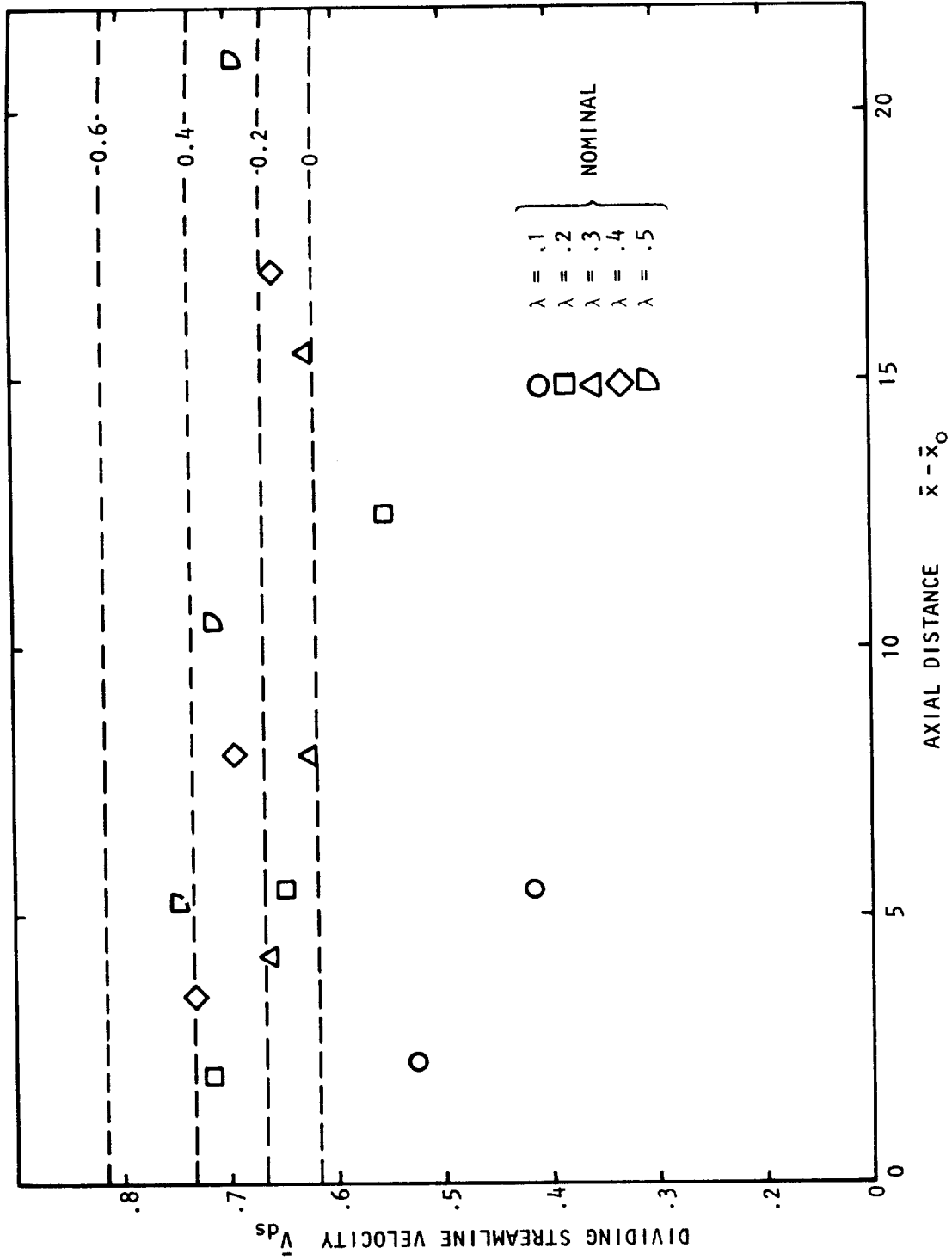
Figure 4.39 Variation of dividing streamline velocity with velocity ratio.
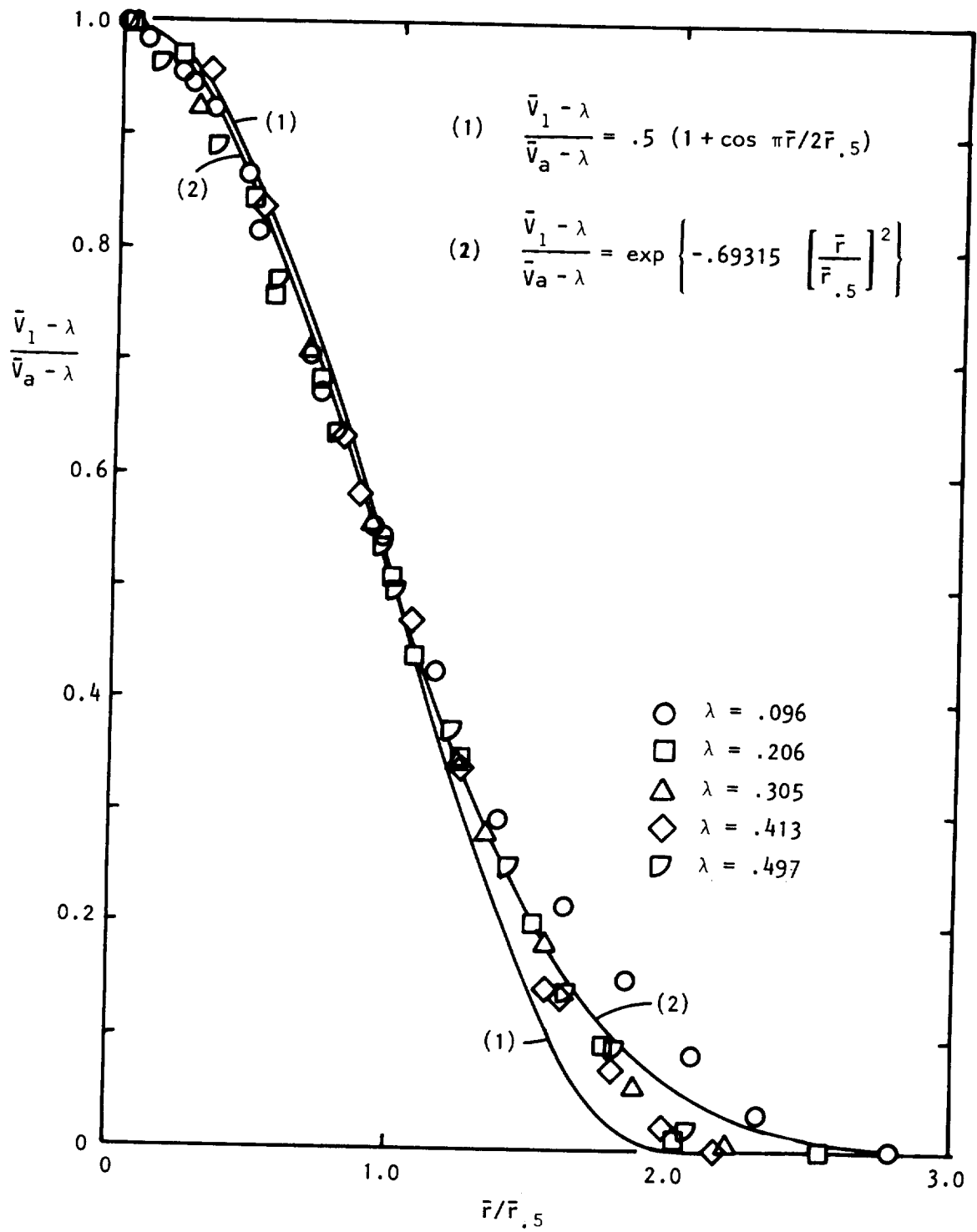
Figure 4.40   Mean flow profiles at $\bar{x} = 32$, $M_J = .47$.

(1) $\dfrac{\bar{V}_1 - \lambda}{\bar{V}_a - \lambda} = .5 \; (1 + \cos \pi\bar{r}/2\bar{r}_{.5})$

(2) $\dfrac{\bar{V}_1 - \lambda}{\bar{V}_a - \lambda} = \exp\left\{ -.69315 \; \left[\dfrac{\bar{r}}{\bar{r}_{.5}}\right]^2 \right\}$

○ $\lambda = .096$
□ $\lambda = .206$
△ $\lambda = .305$
◇ $\lambda = .413$
▽ $\lambda = .497$

data except for the lowest velocity ratio, $\lambda = .096$. Two analytical functions have been shown for comparison. The first is the cosine profile

$$\frac{\bar{V}_1 - \lambda}{\bar{V}_a - \lambda} = \frac{1}{2}\left| 1 + \cos\frac{\pi\bar{r}}{2\bar{r}_{.5}}\right| \quad : \quad \bar{r} \leq 2\bar{r}_{.5} \qquad (4\text{-}9)$$

This is the representation used by Squire and Trouncer (ref. 68). The second function is the error curve

$$\frac{\bar{V}_1 - \lambda}{\bar{V}_a - \lambda} = \exp\left|- .69315\left[\frac{\bar{r}}{\bar{r}_{.5}}\right]^2\right| = \frac{1}{2}^{(\bar{r}/\bar{r}_{.5})^2} \qquad (4\text{-}10)$$

It can be seen that both representations are a good fit to the data over most of the jet. The cosine curve, equation (4-9), will be used in the subsequent analysis.

An expression for the variation of the jet half width as a function of axial distance can now be obtained from a simplified form of the momentum equation. If it is assumed that the tunnel wall radius is sufficiently large in comparison to the jet radius so that there is no induced pressure gradient and the tunnel velocity is constant, then the momentum equation can be integrated to obtain

$$\int_0^{\bar{r}_T} \bar{\rho}\,\bar{V}_1^2\,\bar{r}d\bar{r} = const = \frac{1}{2}\{\bar{\rho}_J + \lambda^2(\bar{r}_T^2 - 1)\}. \qquad (4\text{-}11)$$

Assuming the mean velocity takes the form,

$$\bar{V}_1 = \lambda + (\bar{V}_a - \lambda)\,f(\bar{r}/\bar{r}_{.5}) \qquad (4\text{-}12)$$

and letting $\qquad\qquad \bar{r}/\bar{r}_{.5} = \eta, \qquad\qquad\qquad (4\text{-}13)$

then for the incompressible case, equation (4-11) can be written,

$$\bar{r}_{.5}^2\,\{2(\bar{V}_a - \lambda)\lambda\beta_1 + (\bar{V}_a - \lambda)^2\beta_2\} = \frac{(1 - \lambda^2)}{2} \qquad (4\text{-}14)$$

where

$$\beta_1 = \int_0^{\eta_T} f(\eta)\,\eta d\eta$$

and $\qquad\qquad\qquad\qquad\qquad\qquad\qquad\qquad\qquad\qquad\qquad (4\text{-}15)$

$$\beta_2 = \int_0^{\eta_T} f^2(\eta)\,\eta d\eta$$

156

For a mean velocity profile of the form of equation (4-9), these integrals are given by, $\beta_1 = .595$ and $\beta_2 = .345$. The corresponding values for the profile (4-10) are $\beta_1 = .721$, $\beta_2 = .361$. Hill (ref. 47) used measured free jet velocity profiles to evaluate the integrals and obtained the values: $\beta_1 = .788$ and $\beta_2 = .369$. (The exact values depend on the ratio of the half velocity radius to the radius at the "edge" of the jet). Use will be made in this analysis of the first result corresponding to the cosine profile, equation (4-9). The axial dependence of $(\bar{V}_a - \lambda)$ is given by equation (4-1) so that equation (4-14) becomes,

$$\bar{r}_{.5}^2 = \frac{1}{2} \left\{ \frac{(1 + \lambda)}{2\lambda\beta_1 g(\bar{x}) + (1 - \lambda)\beta_2 g^2(\bar{x})} \right\}, \tag{4-16}$$

where
$$g(\bar{x}) = 1 - \exp\{-1/2\xi_v\}, \tag{4-17}$$

and ξ_v is defined in equation (4-2). The axial variation of $\bar{r}_{.5}$, given by equation (4-16), is shown in Figure 4.41. It was shown earlier in equation (4-6) that $(\bar{V}_a - \lambda)/(1 - \lambda) = g(\bar{x}) \propto A(\lambda)/(\bar{x} - \bar{x}_c)^{-1}$ for large values of $(\bar{x} - \bar{x}_c)$ where $A(\lambda)$ was defined above equation (4-6). For large values of $\bar{x} - \bar{x}_c$ equation (4-6) shows that $g(\bar{x}) \propto (\bar{x} - \bar{x}_c)^{-1}$. This leads to an interesting result for the asymptotic form of (4-16). For λ equal to zero the half-velocity radius is linearly proportional to $(\bar{x} - \bar{x}_c)$. For λ not equal to zero and sufficiently large values of $(x - x_c)$, $\bar{r}_{.5}$ is proportional to the square root of $(\bar{x} - \bar{x}_c)$. Close examination of the asymptotic form of (4-16) shows that the function deviates from a linear growth with $(\bar{x} - \bar{x}_c)$ and approaches the square root dependence depending on the relative magnitudes of $2\lambda\beta_1(\bar{x} - \bar{x}_c)/(1 - \lambda)\beta_2 A(\lambda)$ and unity. The approach to these two limits is shown in Figure 4.41 and the present measurements are also shown to agree with the prediction. Szablewski (ref. 50) used a similar method to that used here. However, the asymptotic dependence is somewhat different, being $\bar{r}_{.5} \propto x^{1/3}$. This result was found by solving a first order differential equation in $\bar{x}$ for the centerline velocity which was obtained from an integral form of the mechanical energy equation with the mean velocity described by a shape function. In fact, Szablewski's asymptotic dependence is more reasonable since it does correspond to the axisymmetric wake flow value. However, for small values of $(\bar{x} - \bar{x}_c)$, particularly close to the end of the potential core, equations (4-16) and (4-17) describe the jet growth more accurately since the expression for $g(\bar{x})$, the centerline velocity, is more accurate than that used by Szablewski. Clearly the accuracy with which the jet width is predicted depends on the accuracy of the centerline velocity prediction.

Since the mean velocity profiles in the developed region of the jet have been shown to have a similar form, the vorticity thickness is to be expected to be linearly proportional to the half velocity radius. The vorticity thickness is plotted against the half velocity radius in Figure 4-42. Also shown are the relationships given by equations (4-9) and (4-10), which give $\bar{\delta}_\omega = 4\bar{r}_{.5}/\pi$ and $\bar{\delta}_\omega = 1.400\bar{r}_{.5}$, respectively. The good agreement between the measurements and the ratio predicted by the error curve indicates that the slope of this function is closer to the measured slopes.
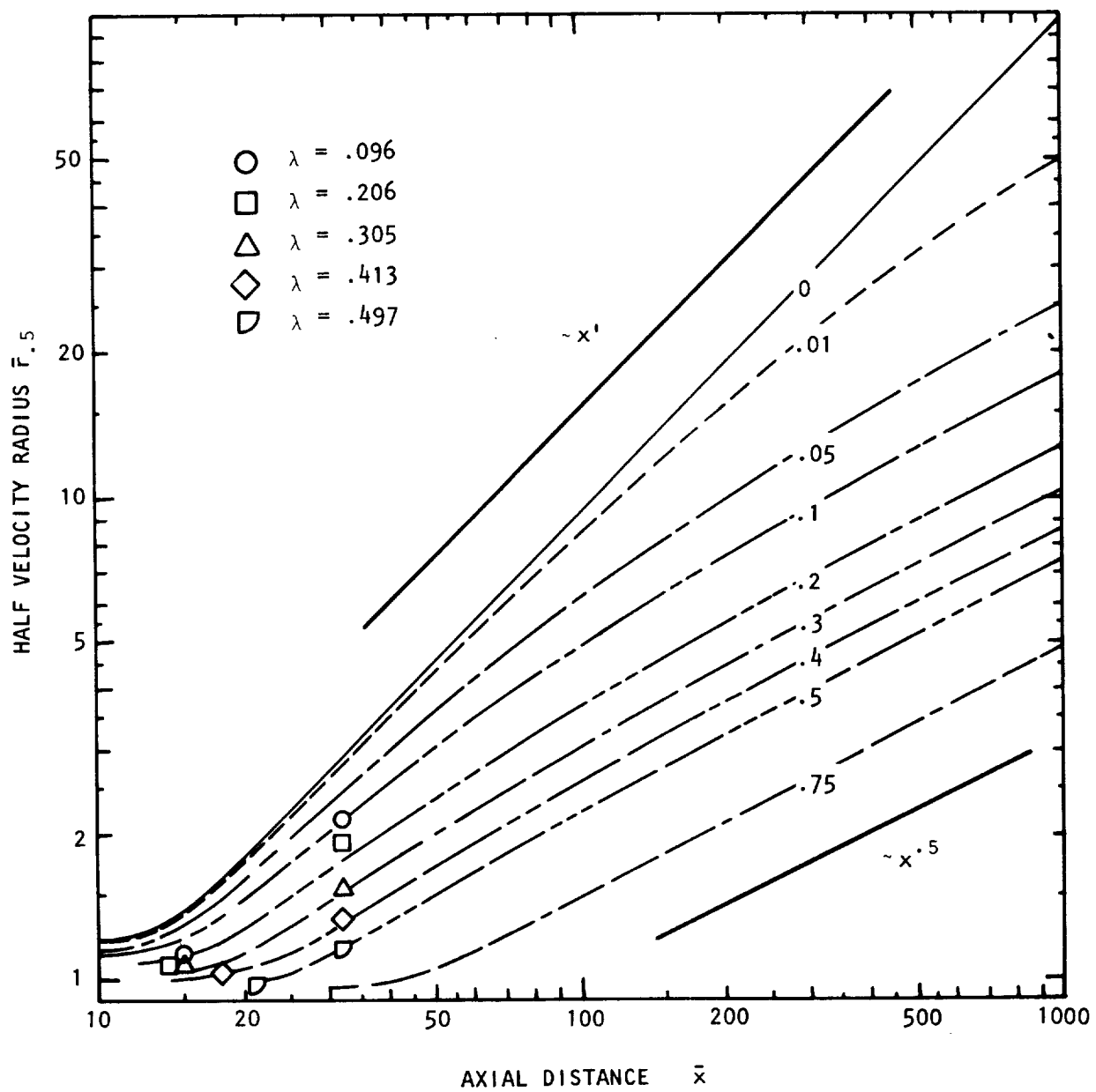
Figure 4.41   Location of half-velocity radius, $M_J = .47$.

158
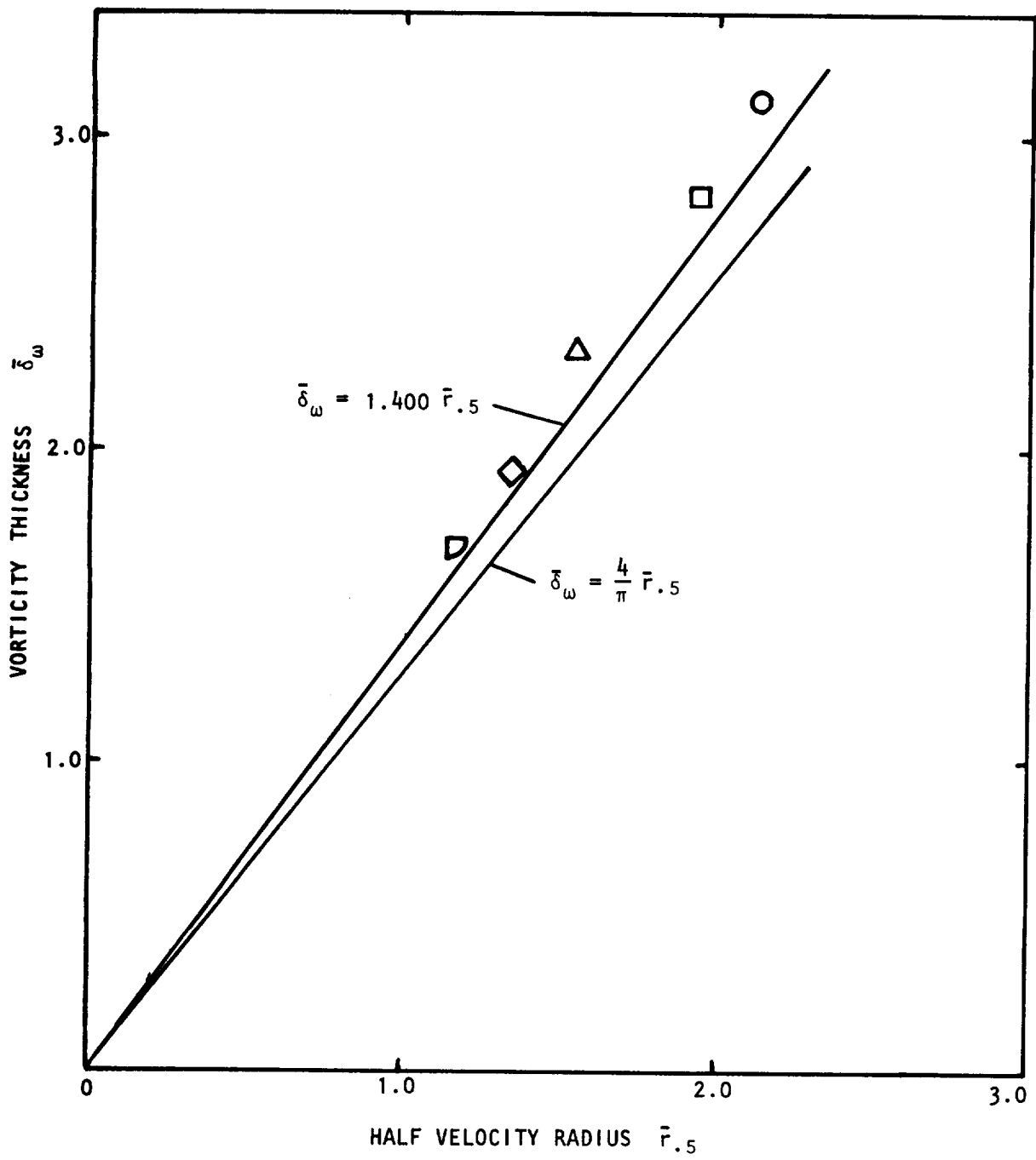
Figure 4.42 Relationship between vorticity thickness and half-velocity radius.

In the annular mixing region the mean velocity profiles can also be collapsed with the appropriate choice of coordinates. This does not apply to the mean profiles which occur in a region of flow establishment, where the wake velocity defect downstream of the jet lip still exists. The mean velocity data in the annular mixing region in the form $(\bar{V}_1 - \lambda)/(\bar{V}_a - \lambda)$ as a function of $(\bar{r} - \bar{r}_{.5})/\bar{\delta}_\omega$ are shown in Figure 4.43. Though $\bar{V}_a$ is equal to one in most cases, some data just downstream of the lip of the potential core has been included. The collapse is seen to be very good. A good fit to the data is given by the expression,

$$\frac{\bar{V}_1 - \lambda}{\bar{V}_a - \lambda} = \frac{1}{2}(1 - \sin 2\eta); \quad -\frac{\pi}{4} \le \eta \le \frac{\pi}{4} \qquad (4\text{-}18)$$

where

$$\eta = \frac{\bar{r} - \bar{r}_{.5}}{\bar{\delta}_\omega} \qquad (4\text{-}19)$$

The simple expression (4-18) has a derivative of -1 at $\eta = 0$ which is a condition enforced on the data by the choice of the vorticity thickness as the local characteristic length.

If the mean velocity profile is described in terms of a shape function and there is no pressure gradient, then two characteristic dimensions of the flow are required to specify the profile locally. These two parameters can be related through the momentum integral equation. Downstream of the potential core the centerline velocity and the half-velocity radius or vorticity thickness are the obvious choices. From equation (4-19) it can be seen that in the annular mixing region, the half-velocity radius and the vorticity thickness have been used. Either of these parameters could have been replaced by the potential core radius. The variation of the half-velocity radius and potential core radius with velocity ratio and axial distance is shown in Figure 4.44. The potential core radius was defined as the radius at which $(\bar{V}_1 - \lambda)/(1 - \lambda) = .98$. An analysis of the axial variation of $\bar{r}_{.5}$ and $\bar{r}_c$, the core radius, can be easily carried out in the same manner as for the developed jet. It is interesting to note that the half-velocity radius appears to decrease with axial distance at some axial locations. This is not inconsistent with the prediction of the half-velocity radius at the end of the potential core given by equation (4-16) as,

$$\bar{r}_{.5}^2 = \frac{1}{2}\left| \frac{1 + \lambda}{2\lambda\beta_1 + (1 - \lambda)\beta_2} \right|, \quad \bar{x} = \bar{x}_c \qquad (4\text{-}19)$$

The solution to this equation is also shown in Figure 4.44. The measurements at the end of the potential core also indicate that for the higher velocity ratios the half-velocity radius does lie within the jet lip line.
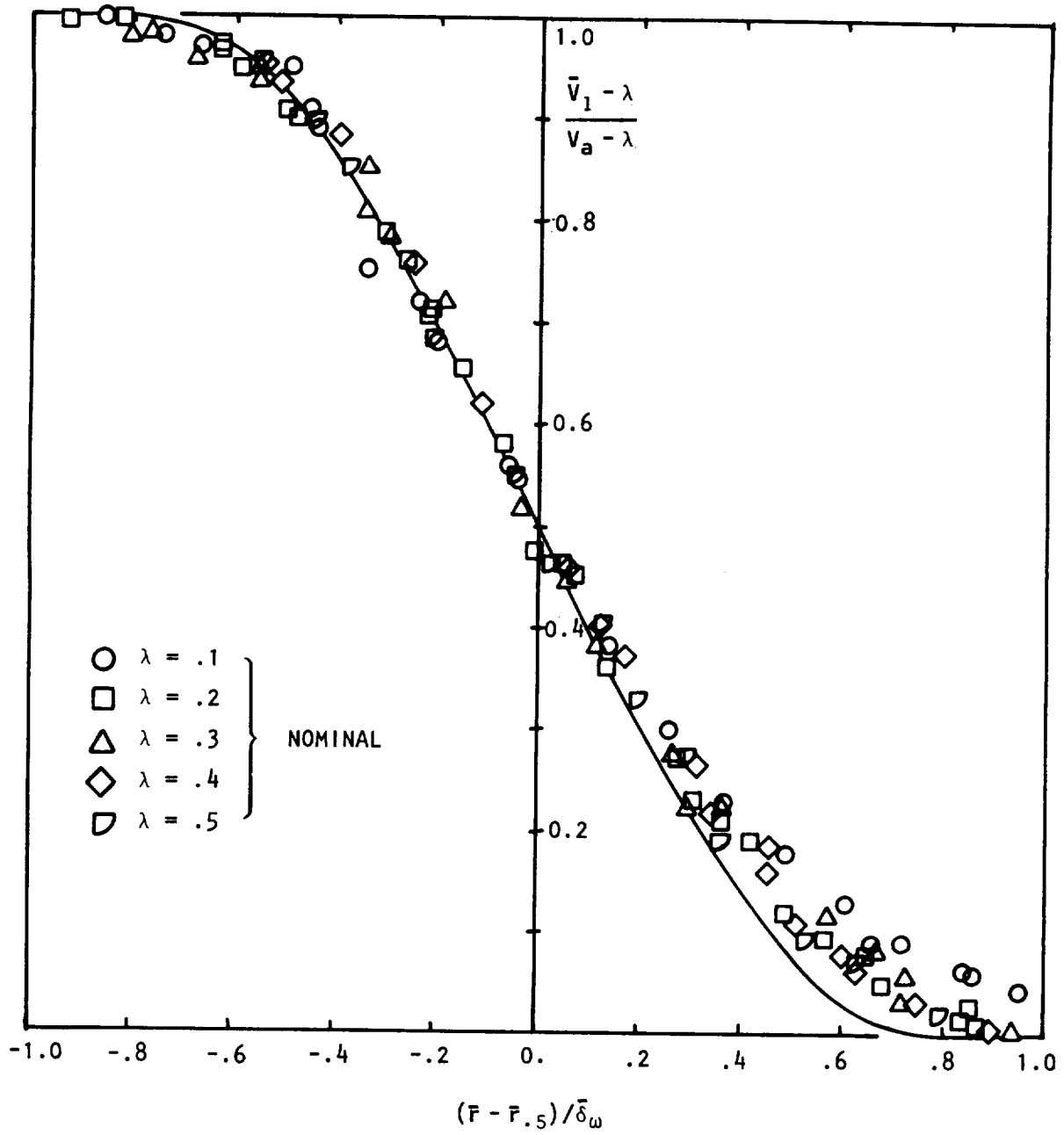
Figure 4.43 Radial distribution of axial velocity in the mixing region, $M_J = .47$.
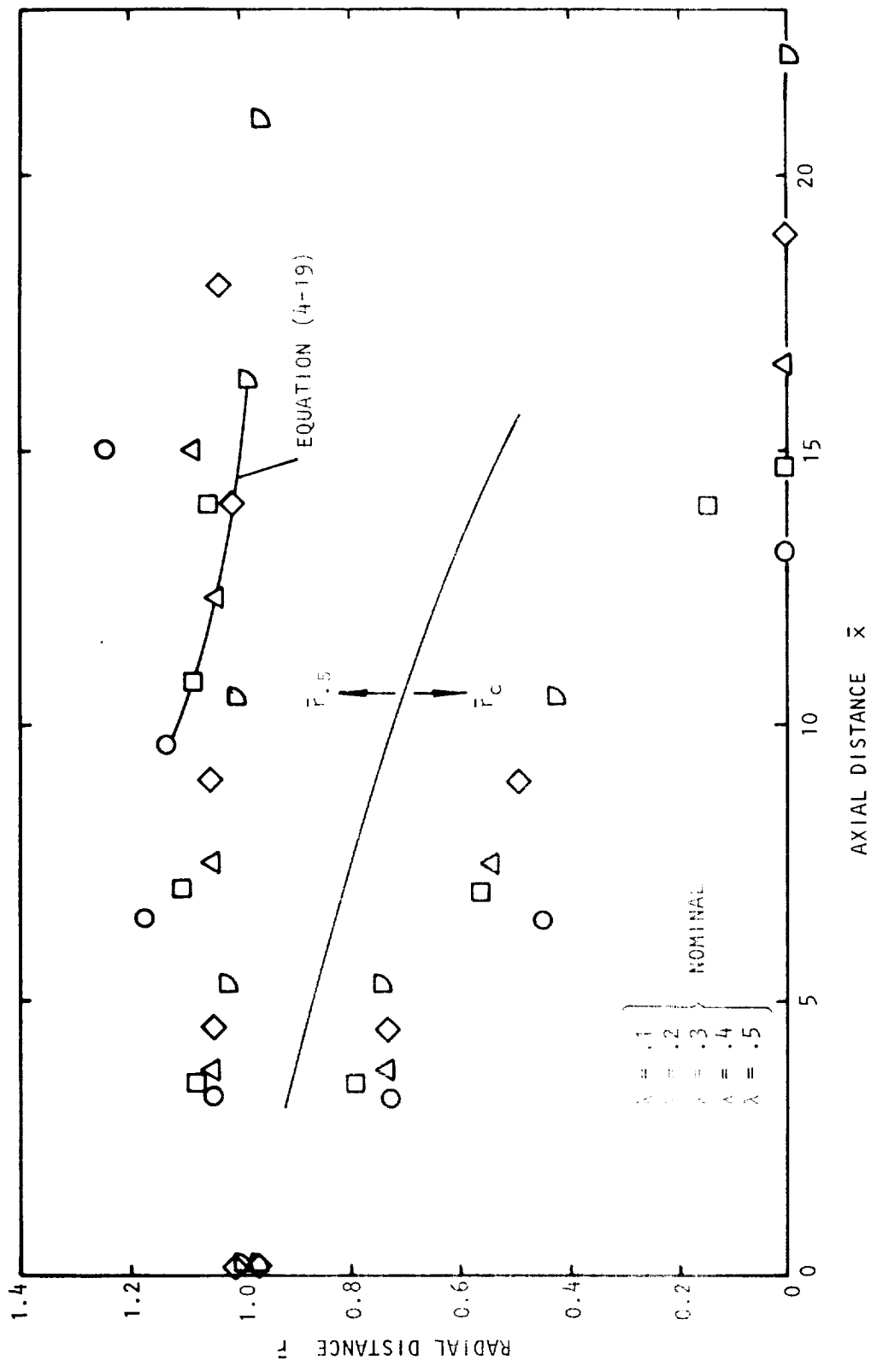
Figure 4.44 Variation of potential core radius and half velocity radius with axial distance.

162

The effect of change in jet Mach number for a fixed velocity ratio is now examined. Equation 4.8 gives the effect of velocity ratio on the growth rate in the annular mixing region for uniform density. In Figure 4.45 the vorticity thickness is plotted as a function of axial distance for λ nominally equal to .1 and various jet Mach numbers. The slope of the lines drawn in Figure 4.45 is called the spreading rate and, following Brown and Roshko (ref. 41), will be denoted by $\bar{\delta}_\omega'$. For the two-dimensional shear layer the spreading rate is related to Görtler's (ref. 69) parameter σ by the relation,

$$\bar{\delta}_\omega' = \pi^{\frac{1}{2}}/\sigma.$$

(4-20)

Brown and Roshko (ref. 41) used an order of magnitude estimation to arrive at the dependence of the spreading angle on the Mach number. This dependence was of the form,

$$\bar{\delta}_\omega' \propto M^{-1} (1 - \lambda)^{\frac{1}{2}},$$

(4-21)

for high Mach numbers. In Figure 4-45 the variation of spreading rate $\bar{\delta}_\omega'$ has been plotted as a function of jet Mach number. Clearly an inverse dependence of the spreading rate on Mach number is evident for both measurements of $\lambda = 0$ and $\lambda = .1$. The data collected by Birch and Eggers (ref. 70) indicates that for subsonic Mach numbers the spreading rate is constant. Thus, it is concluded that the expressions for the spreading rate of the annular mixing region of the jet are:

$$\bar{\delta}_\omega' \propto (1 - \lambda)/(1 + \lambda) \qquad M_J < 1$$

$$\bar{\delta}_\omega' \propto M_J^{-1} (1 - \lambda)/(1 + \lambda) \qquad M_J \geq 1$$

(4-22)

The variation of vorticity thickness at $\bar{x} = 32$ for various Mach numbers is shown in Figure 4-47. Both these results and the measurements in the annular mixing region suggest that for $\lambda = .1$ the Mach number affects the spreading rate like M_J^{-1} for values of M_J greater than .7. However, the data points are too few to suggest any empirical relationship for this breakpoint and in the developed jet the vorticity thickness will be assumed to have the same Mach number dependence as in the annular mixing region, namely

$$\bar{\delta}_\omega \sim M_J^{-1}, \qquad M_J \geq 1.$$

(4-23)

The dividing streamline radius, defined in section 4.2.3, is shown in Figure 4.48. The dividing streamline radius is seen to decrease with increasing axial distance in the supersonic cases in the annular mixing region. The half-velocity radius and the potential core radius are shown in Figure 4.49. The potential core lengths have been calculated using the constants given in Table III and equation (4B-22) of Appendix 4B. Clearly, the initial conditions are varying as a function of Mach number. No corrections for changes in virtual origin have been made.
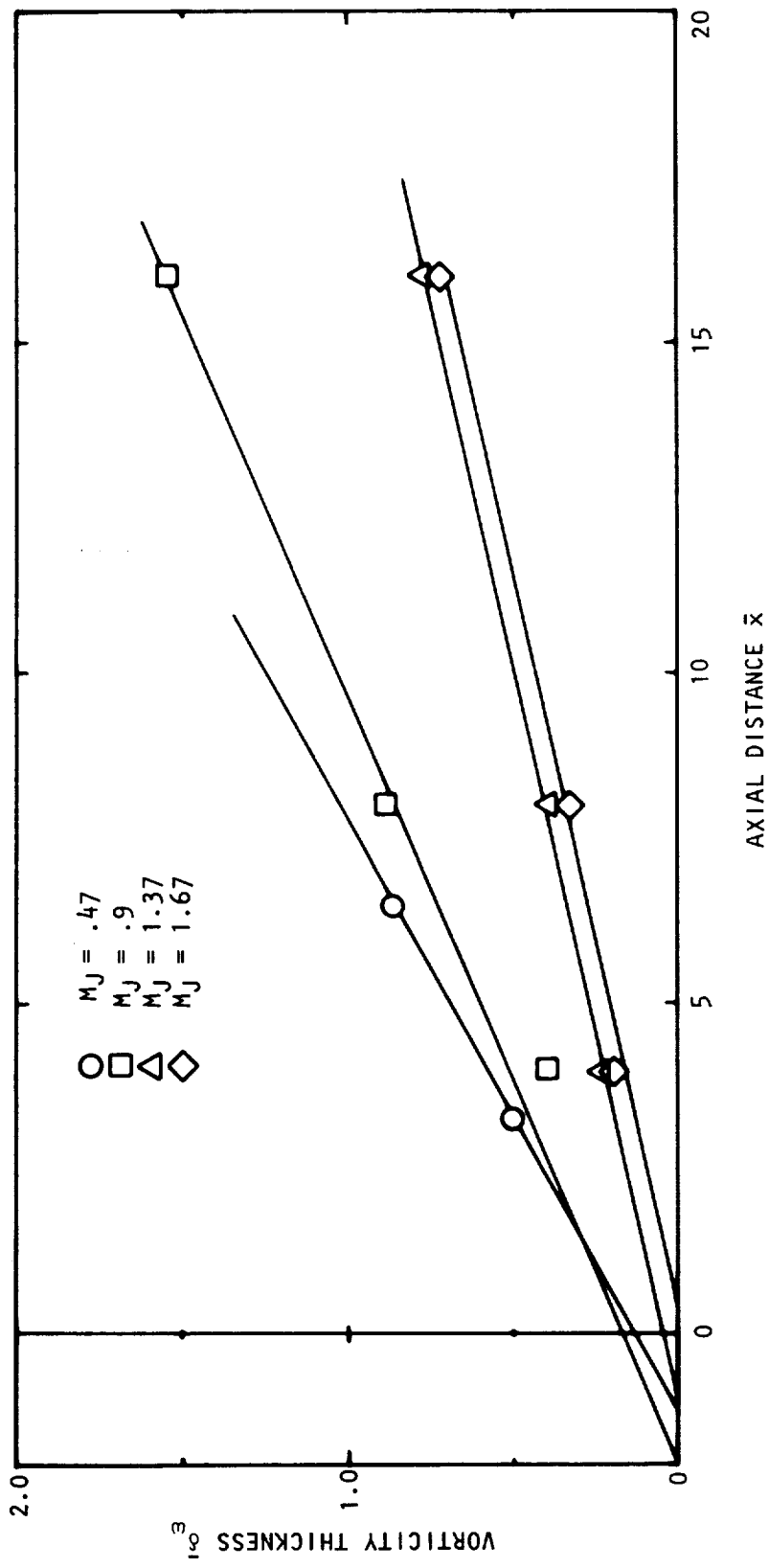
Figure 4.45 Variation of vorticity thickness with Mach number, $\lambda = .1$.

164

Figure 4.46   Variation of spreading rate with Mach number.
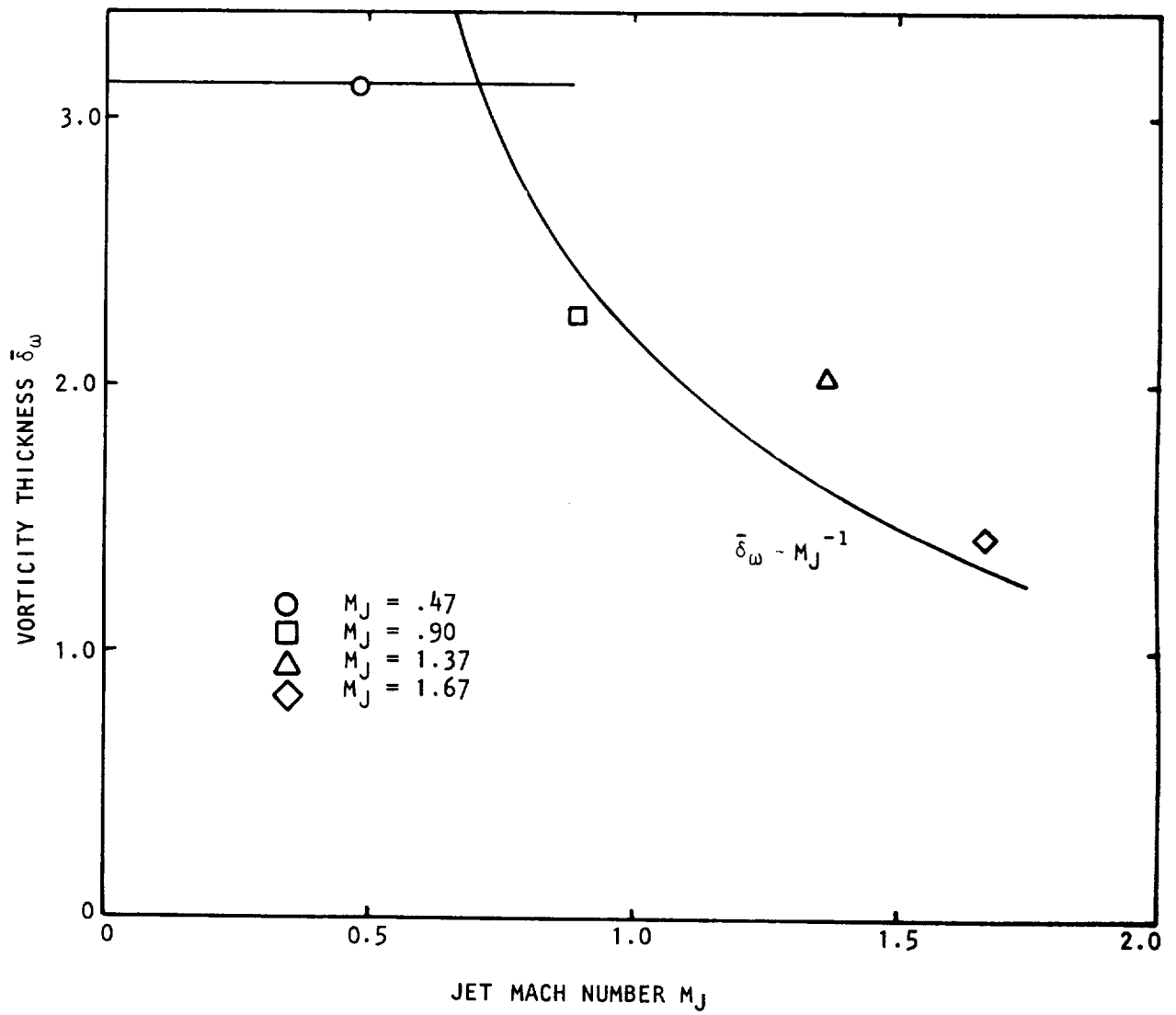
Figure 4.47 Variation of vorticity thickness with Mach number at $\bar{x} = 32$, $\lambda = .1$.
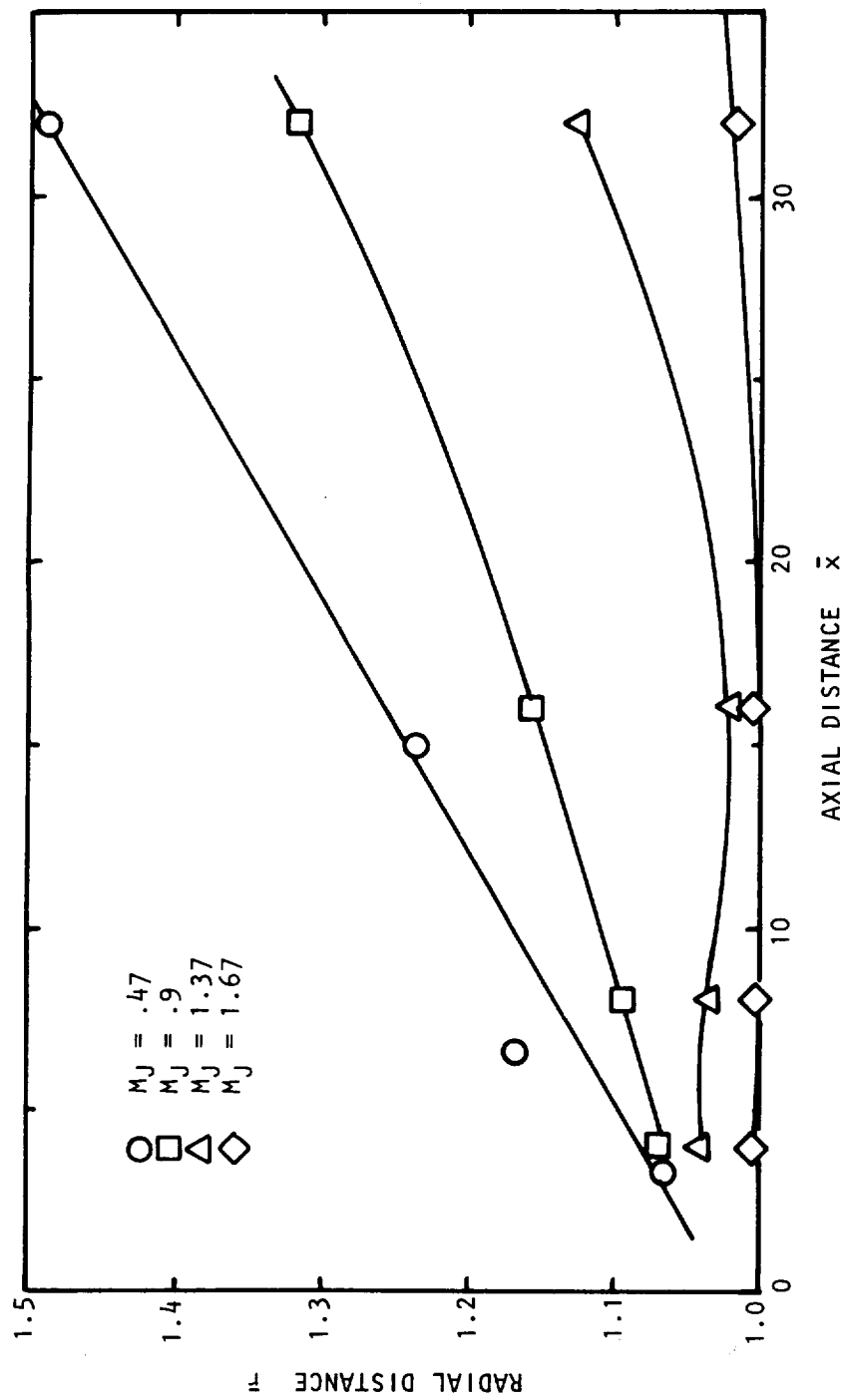
Figure 4.48 Variation of dividing streamline radius with axial distance, $\lambda = .1$.

$M_J = .47$
$M_J = .9$
$M_J = 1.37$
$M_J = 1.67$

AXIAL DISTANCE $\bar{x}$
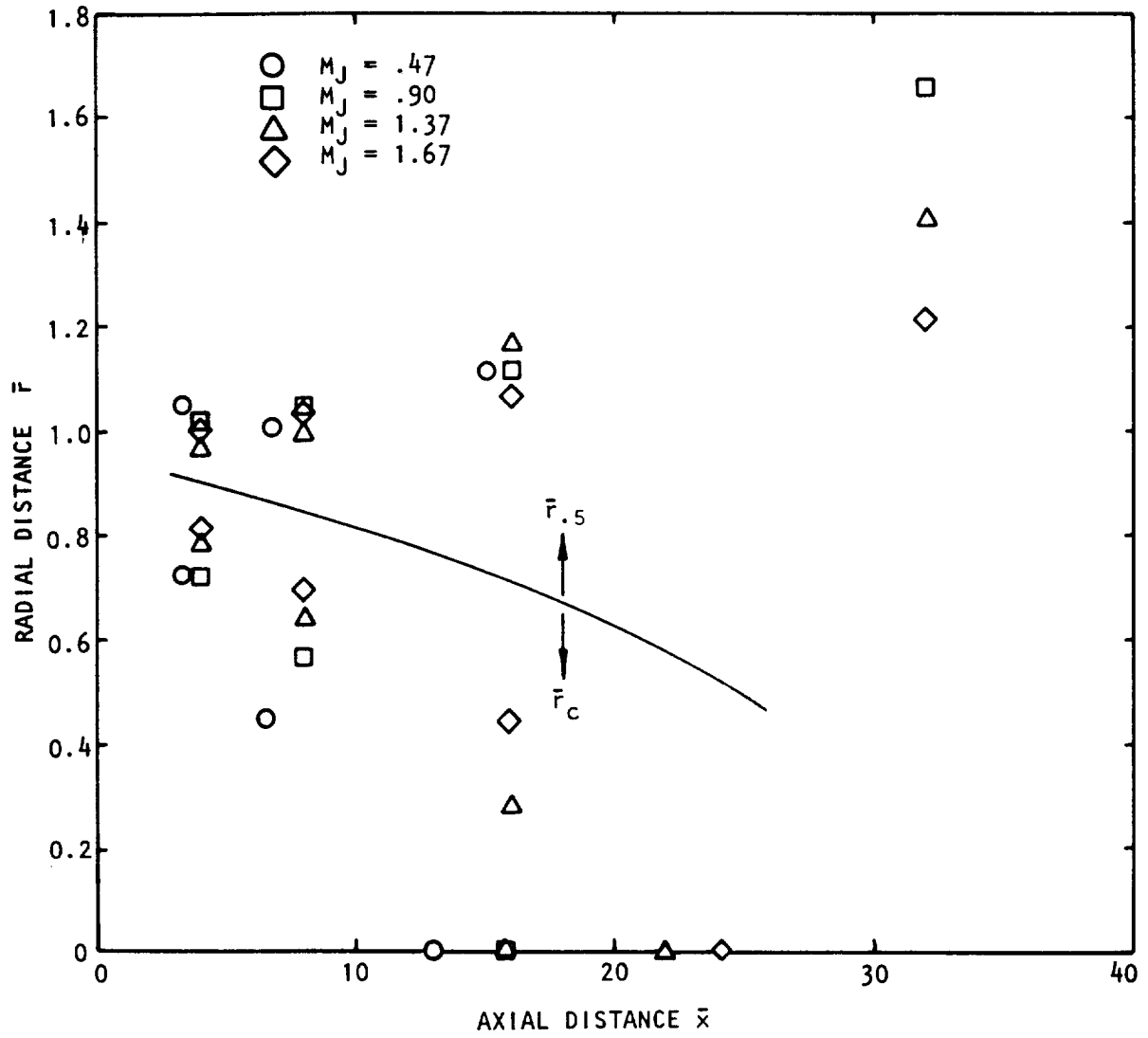
RADIAL DISTANCE $\bar{r}$

Figure 4.49 Variation of half-velocity radius and potential core radius
with axial distance, $\lambda = .1$.

In Figure 4.50 the mean velocity profiles for $\lambda = .1$ and various Mach numbers have been plotted. The profiles for $M_J = .47$ and $M_J = .9$ agree closely and follow a form similar to the profile obtained for various velocity ratios and $M_J = .47$ in Figure 4.42. The corresponding function fit given by equation (4-18) is also shown. However, the data corresponding to the supersonic jet exit conditions, though they agree closely with each other, do not follow the subsonic profiles. This is also the case downstream of the potential core, as is shown in Figure 4.51. The centerline Mach number for $M_J = .47$, .90, and 1.37 is locally subsonic whereas that for $M_J = 1.67$ is locally supersonic. Anderson and Johns (ref. 75) have proposed a turbulence mixing model where the eddy viscosity in the supersonic region was different from that in the subsonic regime. Brown and Roshko (ref. 41) also noted that at high Mach numbers a different model for the eddy viscosity could be used. The value of the eddy viscosity in a model used by Witze (ref. 3) was also found to take different values in subsonic and supersonic regions. This would lead to different profiles depending on the local conditions.

The change in the turbulence level with velocity ratio and Mach number will now be examined. Two possible scaling velocities will be considered. The first is the usual velocity difference and the second is the difference between the jet centerline velocity and the dividing streamline velocity. In Figure 4.52 the maximum axial turbulence intensity is plotted as a function of both these velocity differences. A greater amount of scatter is to be expected in the dividing streamline velocity difference due to the extra computations. A good fit to the data plotted as a function of velocity difference $(\bar{V}_a - \lambda)$ is given by

$$\bar{v}_{1_{max}} = .053 + .118\ (\bar{V}_a - \lambda).\tag{4-24}$$

The effect of Mach number on the maximum axial turbulence intensity is shown in Figure 4.52. It can be seen that the jet Mach number has little effect on the value of $\bar{v}_{1_{max}}$. This confirms Brown and Roshko's supposition that the value of $v_{1_{max}}$ is a function of the velocity difference only.

For the case of an axisymmetric jet the variation of $\bar{v}_{1_{max}}$ with velocity difference for small velocity differences can be inferred from measurements of axisymmetric jets into still air far downstream of the jet exit where the jet centerline velocity is very small. The measurements by Wygnanski and Fiedler (ref. 4) show that by 40 diameters downstream of the jet exit the value of $\bar{v}_{1_{max}}$ is a constant fraction of the centerline velocity, namely

$$\bar{v}_{1_{max}} = .3\ (\bar{V}_a - \lambda)\quad :\quad (\bar{V}_a - \lambda) < .163.\tag{4-25}$$

In Figure 4.54, Wygnanski and Fiedler's and the present measurements of $\bar{v}_{1_{max}}$ have been plotted as a function of $(\bar{V}_a - \lambda)$. It can be seen that the curve can be divided into two regions. The first given by Equation (4-25) and the second given by,

$$\bar{v}_{1_{max}} = .175\ (\bar{V}_a - \lambda)^{.7}\quad (\bar{V}_a - \lambda) > .163.\tag{4-26}$$
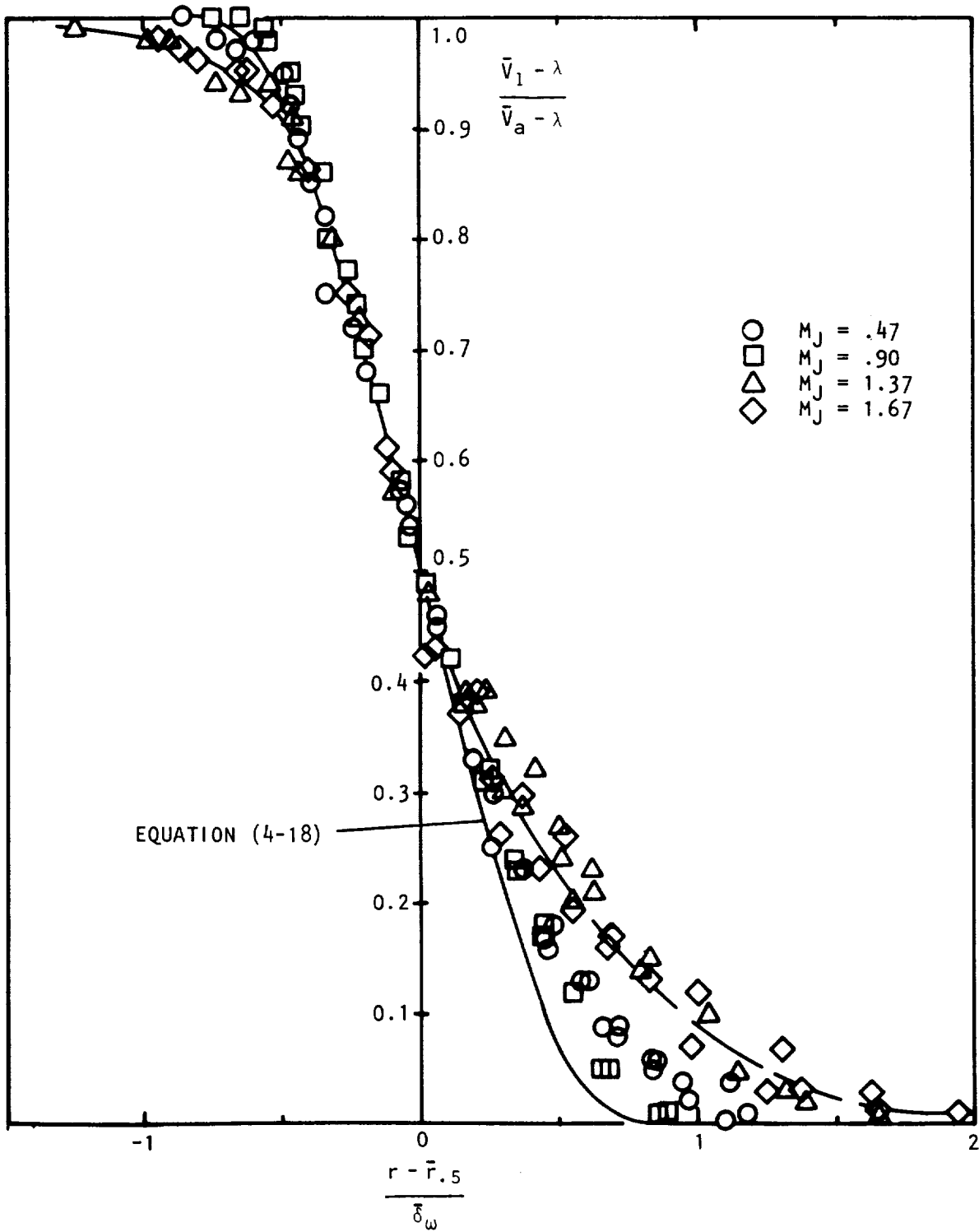
Figure 4.50   Mean velocity profiles in annular mixing region, $\lambda = .1$.
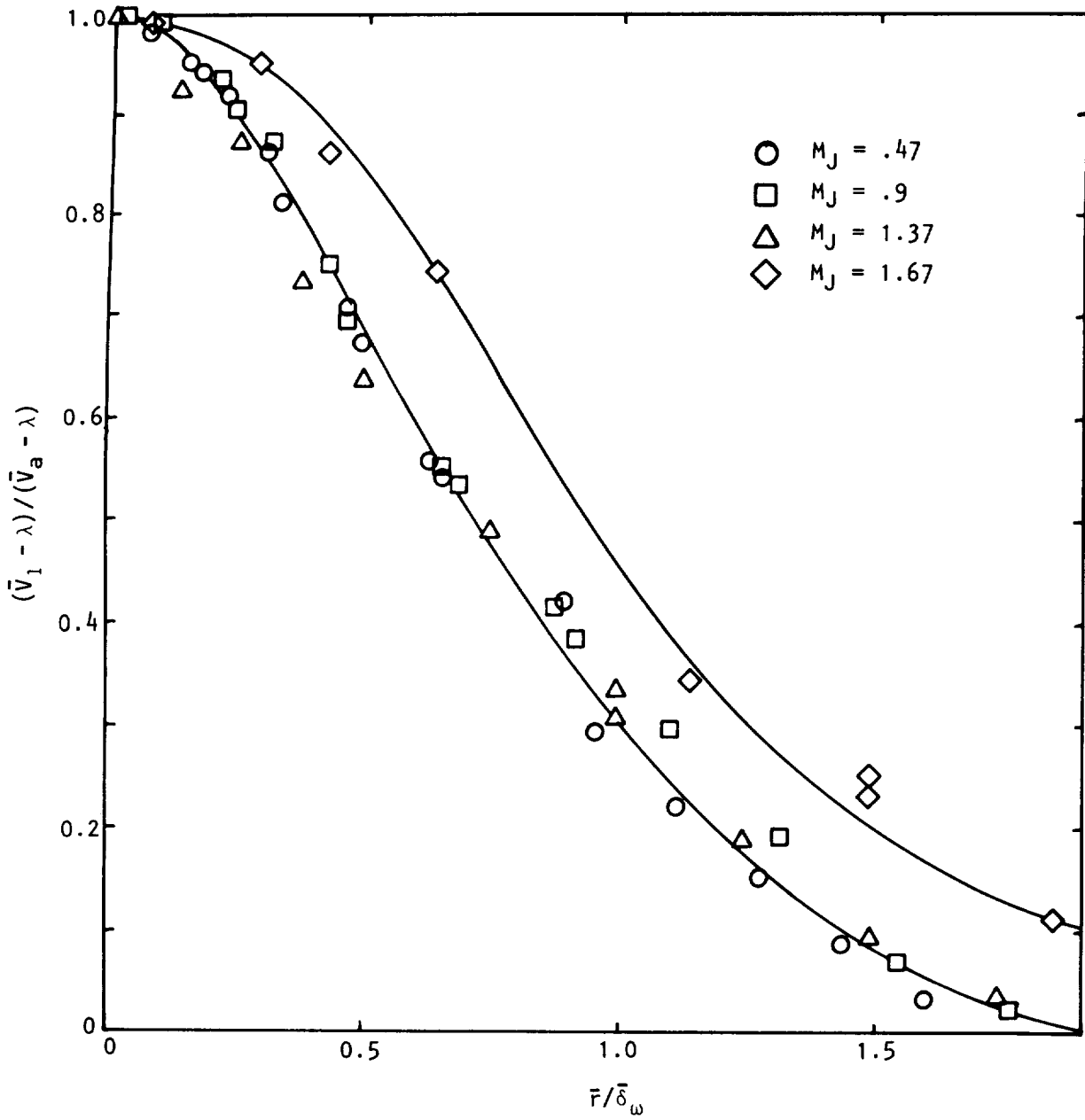
Figure 4.51 Mean velocity profiles at $\bar{x} = 32$, $\lambda = .1$.
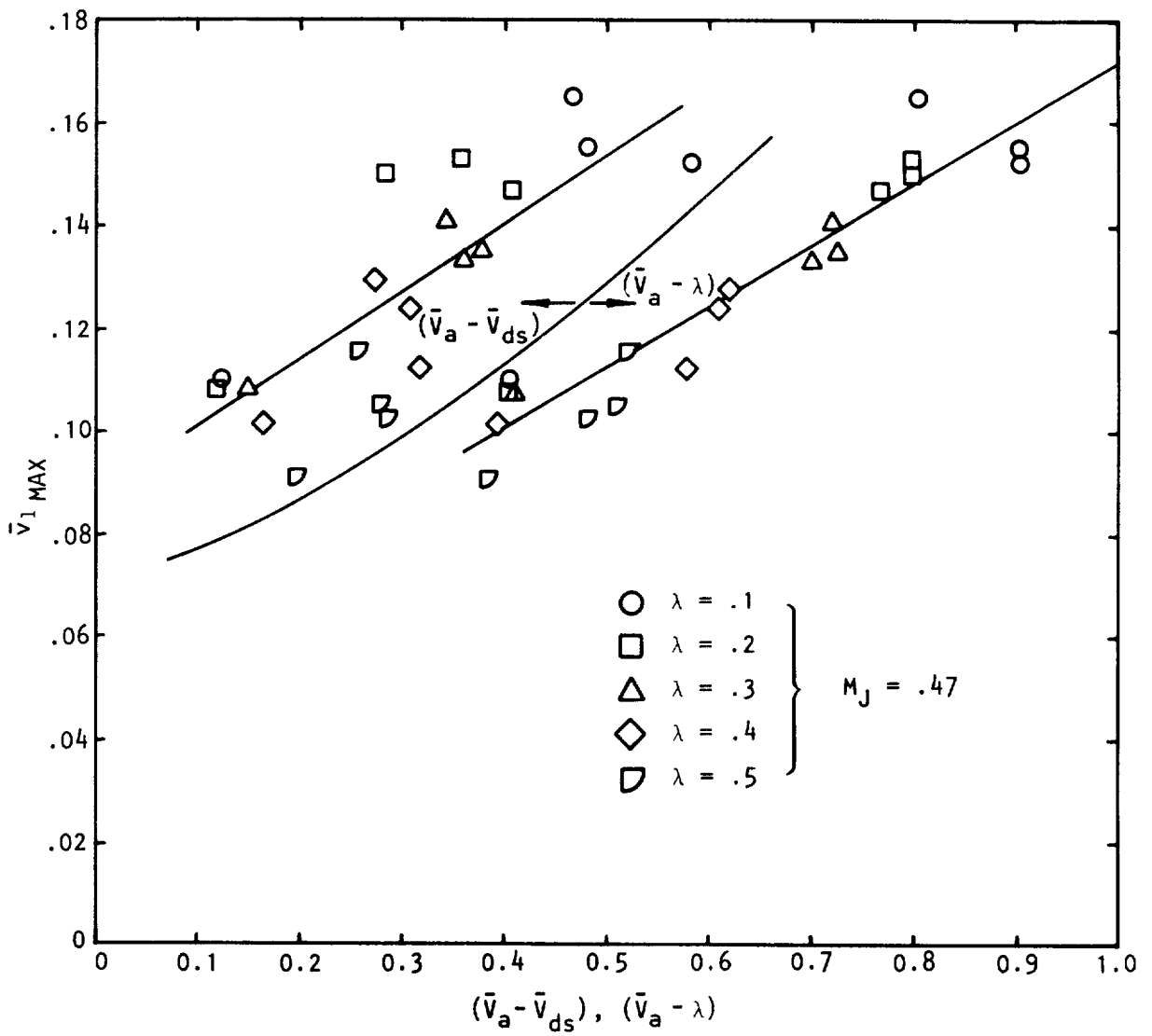
Figure 4.52 Variation of maximum axial turbulence intensity
with velocity difference, MJ.
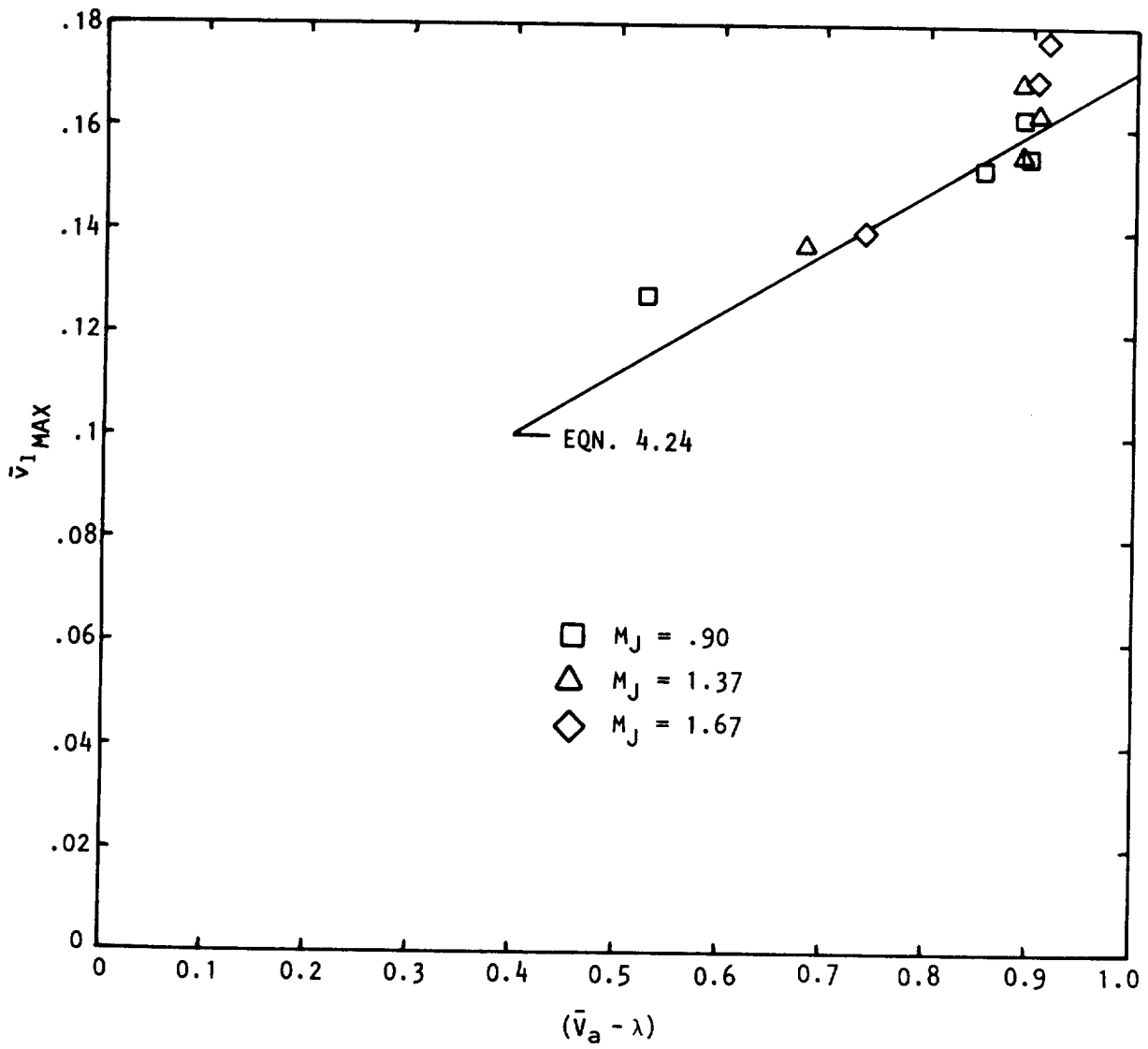
Figure 4.53   Variation of maximum axial turbulence intensity
with Mach number.
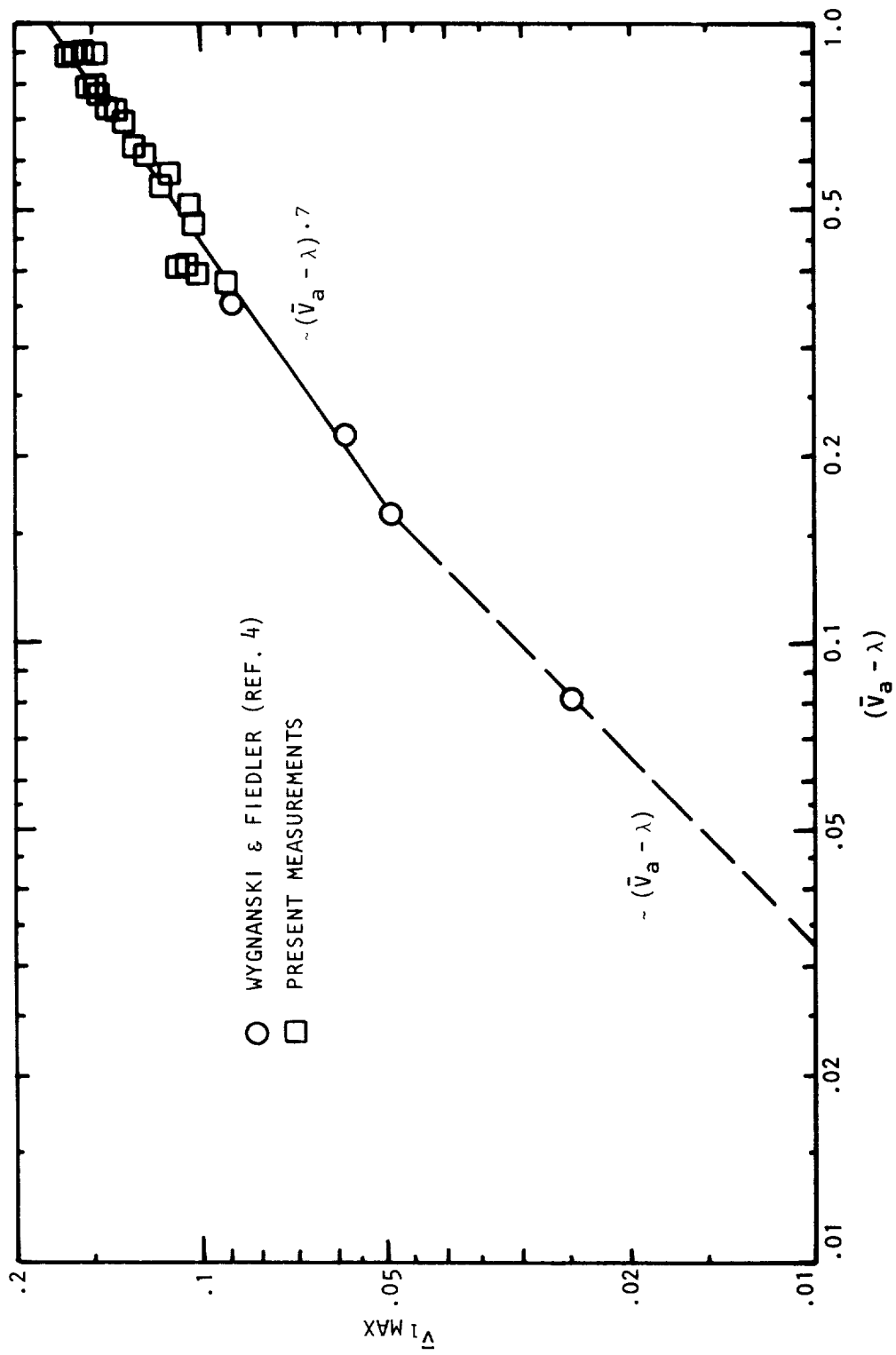
Figure 4.54 Variation of maximum turbulence intensity with velocity difference.

174

The slope of the linear portion of the curve, equation (4-29), and hence the crossover between the two regions will be a function of the shape of the wake generating body. Various asymptotic values of $\bar{v}_1/(\bar{V}_a - \lambda)$ have been noted by Antonia and Bilger (ref. 46).

No measurements have been made of the radial and azimuthal velocity components in the present study. However, it will be assumed that the radial velocity fluctuation is proportional to the rate of spread of the jet and the jet velocity. This assumption is based on obtaining an estimate of the order of magnitude of the covariance $\overline{v_1 v_2}$ from the momentum and continuity equations using, as we have shown above, the relationship between v_1 and the velocity difference. It will be further assumed that the azimuthal velocity fluctuation is related to the other two components by [Townsend, ref. (76)]

$$v_3^2 = (v_1^2 + v_2^2)/2. \qquad (4-27)$$

Thus, the total mean square turbulent velocity is given by,

$$q^2 = 3 \ (v_1^2 + v_2^2)/2. \qquad (4-28)$$

Using the expressions (4-22) for the spreading rate, it can be shown that

$$q^2 = \frac{3}{2} v_1^2 \left\{ 1 + \frac{(1-\lambda)^{.6}}{(1+\lambda)^2} \right\} \qquad M_J < 1, \qquad (4-29)$$

and

$$q^2 = \frac{3}{2} \left\{ 1 + \frac{(1-\lambda)^{.6}}{M^2(1+\lambda)^2} \right\} v_1^2, \qquad M_J \geq 1. \qquad (4-30)$$

In the next section a numerical method for describing the structure of a jet in a moving stream will be discussed.

4.3 NUMERICAL STUDY OF THE EFFECT OF A SECONDARY STREAM ON THE STRUCTURE OF A TURBULENT JET

In this section a well-established numerical technique is applied to the problem of the jet flow in a moving stream. The various analytical and numerical solutions that have been previously used will first be briefly reviewed.

4.3.1 Summary of Previous Work

There are four main classes of approach which have been used to analyze the jet boundary-layer problem. They are:

(i)   similarity analyses,

(ii) integral methods,

(iii) eddy viscosity models, and

(iv) turbulent kinetic energy models.

In most cases these techniques, particularly the more simple analytical methods, have been used to treat special cases of free-shear flow such as the two-dimensional mixing layer or the free jet. However, some of the basic assumptions of each method can be considered to be relevant to the problem of a round jet in a moving stream.

The first method, the similarity analysis, makes the assumption of jet similarity. This does not imply that all components of the flow conform to the rigid definition of self-preservation but simply that the mean flow be similar. These methods have been widely used and are described in the works of Abramovich (ref. 77), Pai (ref. 78), and Schlichting (ref. 79). The mean flow properties are described in terms of a single similarity coordinate which grows with the developing flow. This technique does imply that the local flow has no dependence on the initial conditions and as such, is only applicable in fully-developed regions of the flow where, in the case of jet flow, for example, the conditions at the jet exit no longer affect the jet development. A virtual origin of the flow may also be identified and measured experimentally which accounts for changes in the initial flow conditions.

The second approach, the integral method, has been applied to the case of jets in a co-flowing stream. This general class of analysis uses a form of the boundary layer equation integrated across the jet. This method is used to calculate the downstream development of certain jet scaling parameters, such as the jet width, defined in a number of ways, or the jet center-line velocity. The equations of motion are usually written in terms of a similarity variable, and the shape of the mean velocity profile must be provided. As such, this method has limited usefulness since it is only applicable in regions where the mean flow is similar and it does not calculate the mean velocity profile but rather requires it as an input. Squire and Trouncer (ref. 68) integrated the momentum equation between the jet centerline and a radial location within the flow. The shear stress at this location was evaluated using the mixing length theory. Hill (ref. 47) used a moment-of-momentum integral equation which was obtained, for the axisymmetric jet by multiplying the momentum equation throughout by the square of the similarity coordinate and integrating across the flow. The resulting integrals were evaluated using measured mean velocity profiles of a jet exhausting into still air. Szablewski (ref. 50) also used an integral approach to describe the motion of a heated jet into still air. He assumed that the mean velocity and temperature profiles could be represented by the function, $(1 - \eta^{3/2})^2$, where the definition of η was different for the two properties. Integral methods have also been used by Patel and Newman (ref. 80), Gartshore (ref. 81), Vogel (ref. 82), Bradbury (ref. 42), Bradbury and Riley (ref. 43), and Antonia and Bilger (ref. 46). Except in those works where the shear stress is measured, an assumption is made as to the

relationship between the shear stress and the local mean shear. This is achieved by the adoption of a hypothesis for the eddy viscosity or the turbulent Reynolds number which will be described below. Peters and Phares (ref. 83) used a hybrid integral approach where the integrated turbulent kinetic energy equation was solved simultaneously with the integral equations of the mean flow. The turbulent shear stress was linearly related to the turbulent kinetic energy. It can be seen that though integral methods provide a simple way of determining the development of the shear flow they cannot describe the whole flow region and do not permit calculation of radial flow profiles. An integral approach has been used in section 4.2.4 to describe the relationship between the jet width and the jet centerline velocity downstream of the potential core.

The third class of analytical approach concerns the use of an eddy viscosity model. In the time-averaged boundary layer equations, the terms which present the greatest problems are the time-averaged products of turbulent fluctuations such as the Reynolds shear stresses and the product of velocity and temperature fluctuations which occur in the thermal energy equation. Unless these products are evaluated experimentally, some hypothesis is required which relates them to the mean properties of the flow. Such an hypothesis is that originally proposed by Boussinesq (ref. 84) which is now commonly referred to as the eddy viscosity hypothesis. The eddy viscosity was used to relate the turbulent shear stresses to mean shear in the same manner as the shearing stress in a laminar flow is related to the local rate of strain through the dynamic viscosity of the fluid. However, it is still necessary to relate the eddy viscosity coefficient to properties of the flow. An attempt to do this was made by Prandtl (ref. 85) in his mixing length theory. This relates the kinematic eddy viscosity to the square of a length, whose value must be established for the particular flow problem, multiplied by the modulus of the local mean shear. This meant that the shear stress would be zero at points in the flow where the local mean shear was zero. A second hypothesis was proposed by Prandtl (ref. 86) which stated that the kinematic eddy viscosity was proportional to the width of the mixing region and the maximum difference in the mean velocities of the flow.

Gartshore (ref. 81) used Townsend's (ref. 76) large eddy hypothesis to compute local values of the eddy or turbulent Reynolds number. This method related the change in turbulent Reynolds number from a self-preserving jet to a wake flow through the ratio of the strain rate of the mean flow at some typical station in the outer region of the jet.

There have been many proposed eddy viscosity models of this type for both compressible and incompressible flows. These include those of Kleinstein (ref. 87), Warren (ref. 88), Alpinieri (ref. 89), Ferri *et al* (ref. 90), Witze (ref. 3), and Zelazny *et al* (ref. 91). The solutions obtained using this method agree very well, in each specific case, with the experimental results for the equivalent problem. However, no satisfactory universal constant has been found which binds together all the models. This method is simple to use and does give good agreement with experiments if the appropriate eddy viscosity model can be found for each flow region.

The fourth class of analytical approach is that involving the use of the turbulent energy equation. The use of this equation is once again for the purpose of describing the turbulent shear stresses. It is hypothesized that the turbulent kinetic energy controls the magnitude of the eddy viscosity. This suggestion was originally also due to Prandtl and has since been considered by Glushko (ref. 92), Harlow and Nakayama (ref. 93) Beckwith and Bushnell (ref. 94), Mellor and Herring (ref. 95), and Spalding (ref. 96). In these models the eddy viscosity becomes proportional to the square root of the turbulent kinetic energy. Townsend (ref. 76) made an alternative suggestion in which the shear stress was assumed to be proportional to the turbulent kinetic energy. Bradshaw *et al* (ref. 97) used this hypothesis successfully in the two-dimensional boundary layer. This hypothesis was also the one used in the integral approach of Peters and Phares (ref. 83) described above. The introduction of the turbulent kinetic energy equation does require the specification of a number of relationships which describe the diffusion and dissipation of Reynolds stresses (this is described in detail by Nash and Patel (ref. 98). Harsha and Lee (ref. 99) and Lee and Harsha (ref. 100) have shown that the constant relating shear stress to turbulent kinetic energy applies over a very wide range of jet flows. However, the use of this equation does give the local shear stress a dependence on the upstream history of the flow. The solution of the equations derived can be achieved using a finite difference approach and downstream marching since the equations are parabolic and form an initial value problem. The most comprehensive study of this approach for compressible jets has been carried out by Heck and Ferguson (ref. 101) and Heck and Merkle (ref. 102) which also allows for the presence of shocks in the flow.

The numerical method on which Heck and Merkle (ref. 102) based the turbulent mixing solution was that originated by Patankar and Spalding (ref. 103). The GENMIX programs have been used extensively to solve many turbulent mixing problems. The method is based on the simultaneous solution of a parabolic system of equations and the number of equations used is not limited. Various multiple equation models have been proposed and equations for all the Reynolds stresses $\overline{u_i u_j}$ (ref. 104), the decay rate of turbulence energy and the turbulence energy (ref. 105, 106).

In the next section a two equation model of the turbulence which uses a transport equation for the dissipation rate is described.

4.3.2 Description of the Numerical Method

In a turbulence model which makes use of a conservation equation for the turbulent kinetic energy, it is necessary to provide several empirical relationships. Among these is the definition of the dissipation length which is required to enable the dissipation term in the T.K.E. equation to be evaluated. This length is usually linearly related to the local width of the shear flow and the constant of proportionality varies depending on whether the flow is plane or axisymmetric. The measurements of Antonia and Bilger (ref. 46) indicated that for the axisymmetric jet-wake, there were large changes in the ratio of the dissipation length to local thickness. This suggests that a turbulence model based simply on the kinetic energy

178

equation is not adequate for the problem of a turbulent jet into a moving stream. For this reason a system of equations is solved which includes an equation for both the turbulent kinetic energy and the turbulence energy decay rate.

The analysis and the numerical technique used have been described in great detail by Pantakar and Spalding (ref. 103) and Launder *et al* (ref. 107) and no reiteration will be given here. However, it has been found that the method of defining the initial conditions influences the solution. The method for obtaining these initial conditions from measurements will be discussed here.

In many cases all the initial values of the dependent variables will not have been measured. The parameters to be described are the axial mean velocity, the stagnation enthalpy, the turbulence kinetic energy and the turbulence dissipation rate. Measurements of axial mean velocity are usually available and the stagnation enthalpy can be calculated from these measurements and temperature measurements or by use of a Crocco's relation to obtain the temperature. If measurements of the covariance $<v_1v_2>$ are not available, they can be estimated from the relation

$$<v_1v_2> = \mu_t \; \partial V_1/\partial r \qquad\qquad (4\text{-}31)$$

where μ_t is an assumed eddy viscosity. The turbulence kinetic energy can then be estimated from the relation

$$k = |<v_1v_2>|/.3. \qquad\qquad (4\text{-}32)$$

The energy dissipation rate is used in the definition of the eddy viscosity and this relationship can be inverted to estimate the dissipation rate as

$$\varepsilon = C_\mu \; \frac{\rho k^2}{\mu_t}, \qquad\qquad (4\text{-}33)$$

where C_μ and the remaining empirical constants required for the solution are given by Lauder *et al* (ref. 107).

Using these definitions of the initial values for the dependent variables, the flow field can be obtained by numerical integration of the conservation equations. In the next section some solutions are described and it will be seen that some expertise is required in the choice of initial conditions.

4.3.3 Numerical solutions and data comparisons

In this section two numerical tests will be described. The first is a test case [case 9, (ref. 108)] where the definition of the initial conditions has been given by the authors of the numerical technique. The second case is a use of the solution with the starting conditions taken directly from the current measurements.

179

In the first test case the mean velocity profile was measured. Helium was added as a tracer to the jet flow. The measurements were made by Forstall (ref. 109). The initial turbulent kinetic energy was calculated from the mean velocity data using equations (4-31) and (4-32). The dissipation rate was then found from equation (4-33). The value of μ_t used in the calculation of the initial profile was that used by Launder $et\ al$ (ref. 107) and was given by

$$\mu_t = 3.2 \times 10^{-3} \, \rho r_J \, \Delta V_1, \qquad (4-34)$$

where ΔV_1 was the velocity difference between the jet exit velocity and the minimum velocity and the freestream velocity and the minimum velocity in the inner and outer initial boundary layers, respectively. The initial grid values of $\bar{V}_1$, k and $\bar{\varepsilon}$ are shown in Figure 4.55. Using these starting conditions the distribution of mean parameters in the jet was calculated. The centerline velocity decay of the mean velocity and the mass concentration of helium is shown in Figure 4.56. The agreement between the predictions and the measurements of Forstall (ref. 109) was good.

The second test case used starting conditions taken from the current measurements for $M_J = .47$ and $\lambda = .382$. In order to examine the effect of initial grid spacing on the solutions, two sets of starting conditions were used. The turbulence kinetic energy and energy dissipation rate were calculated from the initial mean velocity profile in the same manner described above for the first case. The initial mean velocity profile for a 20-point grid and a 27-point grid are shown in Figure 4.57. The extra 7 points have given greater definition to the region of rapid velocity variation. The predicted variation of jet centerline velocity is shown in Figure 4.58. It can be seen that the decay is over-predicted by the finer initial grid whereas the agreement between the 20-point grid calculation and the measurements is good. Similar trends are shown in Figures 4.59 and 4.60 for radial mean velocity profiles at $\bar{x} = 18$ and 32, respectively. The agreement between the measurements and the more widely spaced finite difference grid is quite good in all cases. The variation of the turbulence kinetic energy along the jet centerline is shown in figure 4.61. The prediction has been compared with the measured values of $3\,\bar{v}_1^2/2$, the turbulence kinetic energy for isotropic turbulence. Agreement between the absolute magnitudes cannot be expected because of the known anisotropy of the flow; however, the prediction of the axial location of the peak turbulence kinetic energy is seen to agree well.

In this section it has been shown that the prediction of the time-averaged properties of a round jet in a moving stream may be numerically predicted using the method of Spalding and Patankar. However, it is clear that considerable expertise is required in the choice of initial boundary conditions if a good prediction is to be obtained.
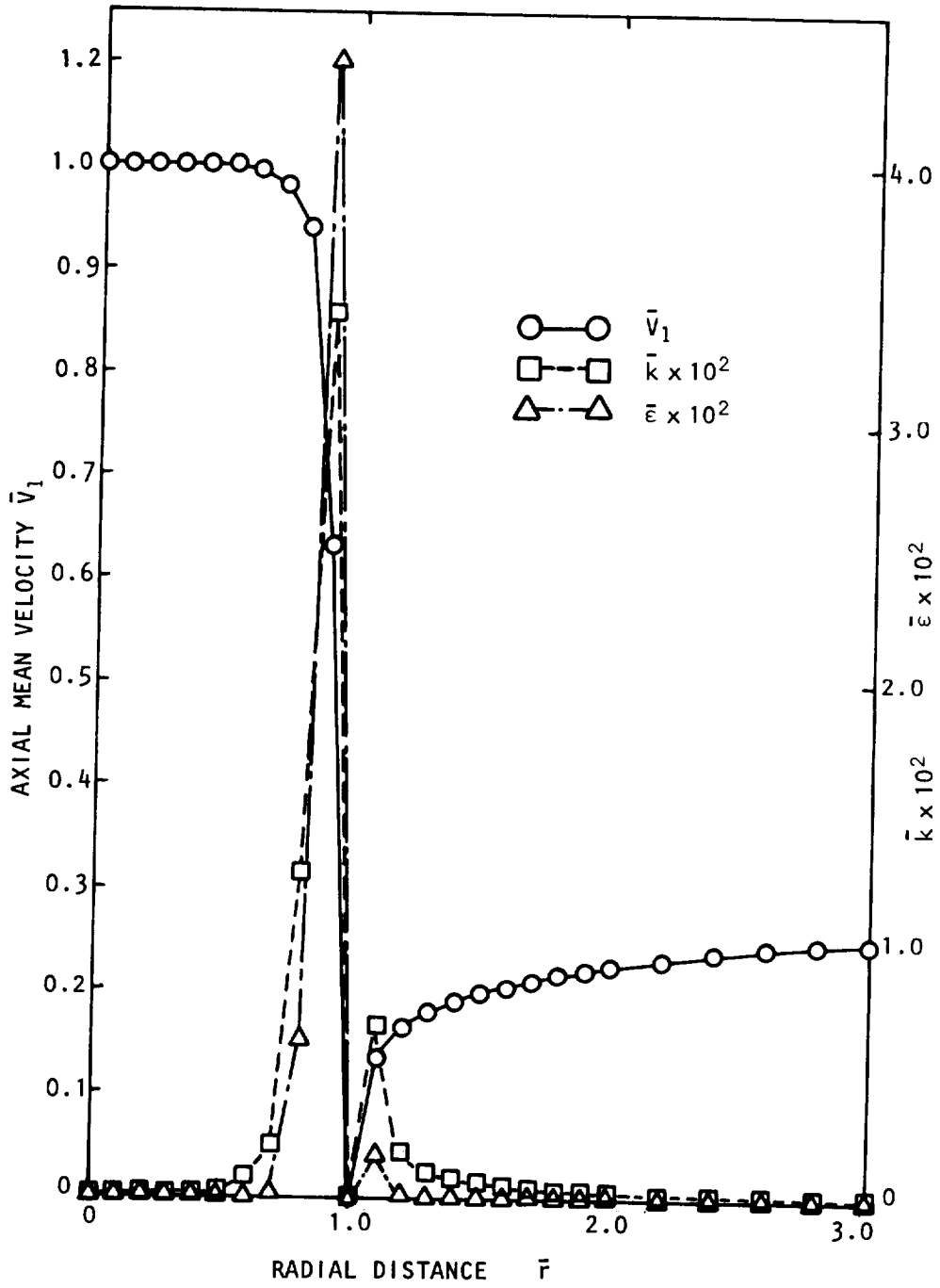
Figure 4.55 Initial profiles of $\bar{V}_1$, $\bar{k}$ and $\bar{\epsilon}$ showing grid points.
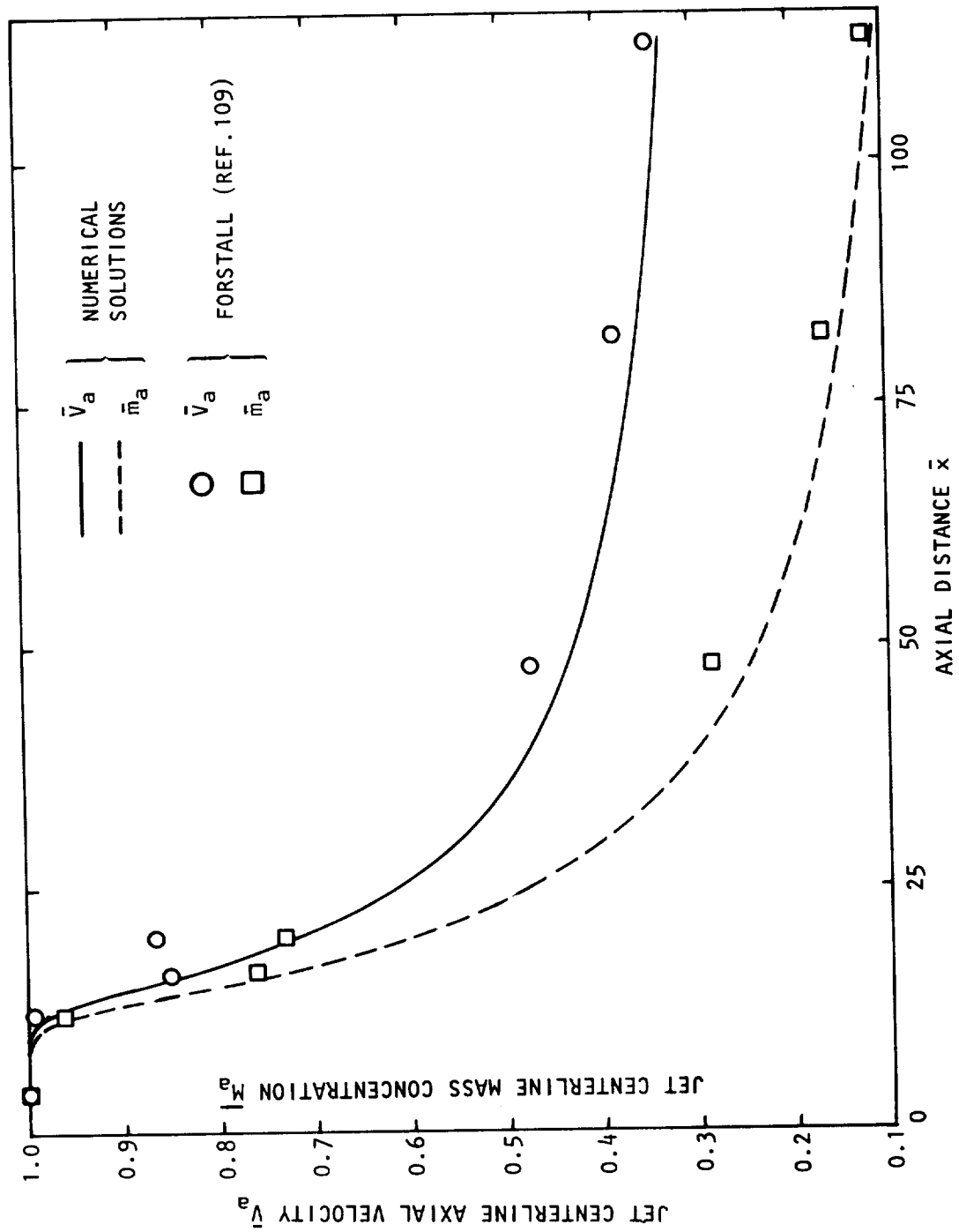
Figure 4.56 Centerline decay of axial mean velocity and mass concentration of helium.

182
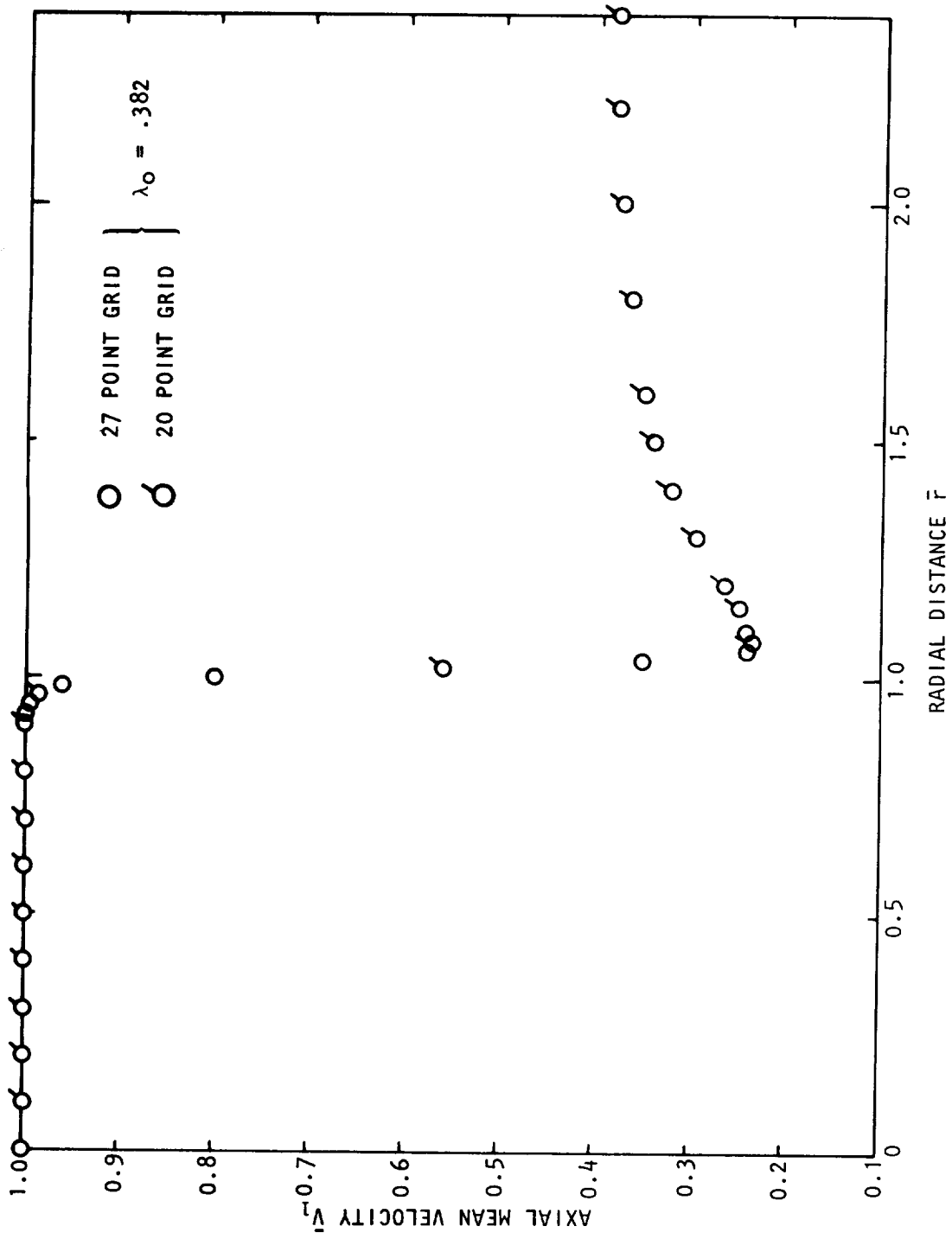
Figure 4.57 Initial mean velocity profiles, $\lambda = .382$.

183
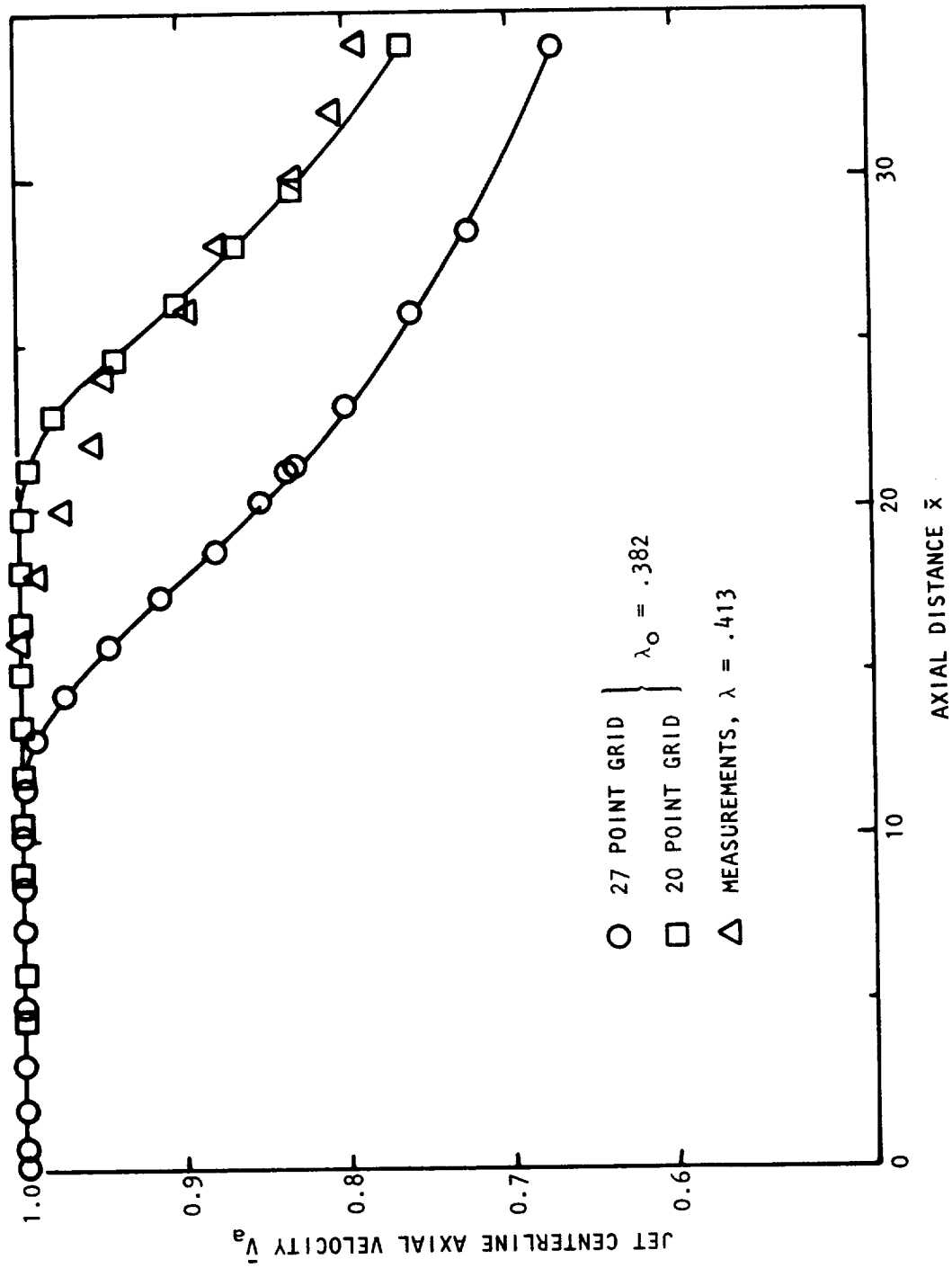
Figure 4.58 Numerical calculation of centerline axial mean velocity.

184
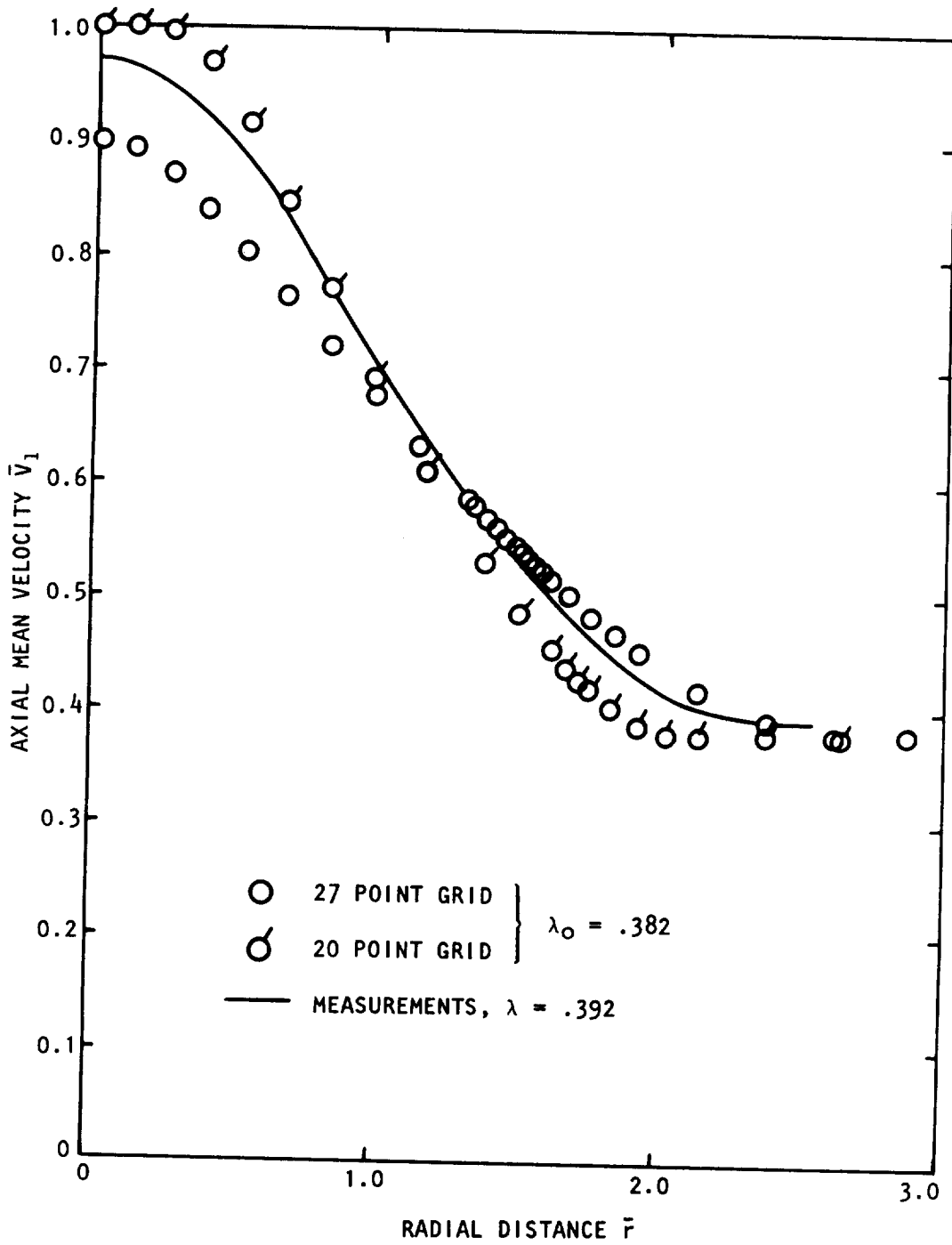
Figure 4.59   Radial velocity profiles at $\bar{x} = 18$.
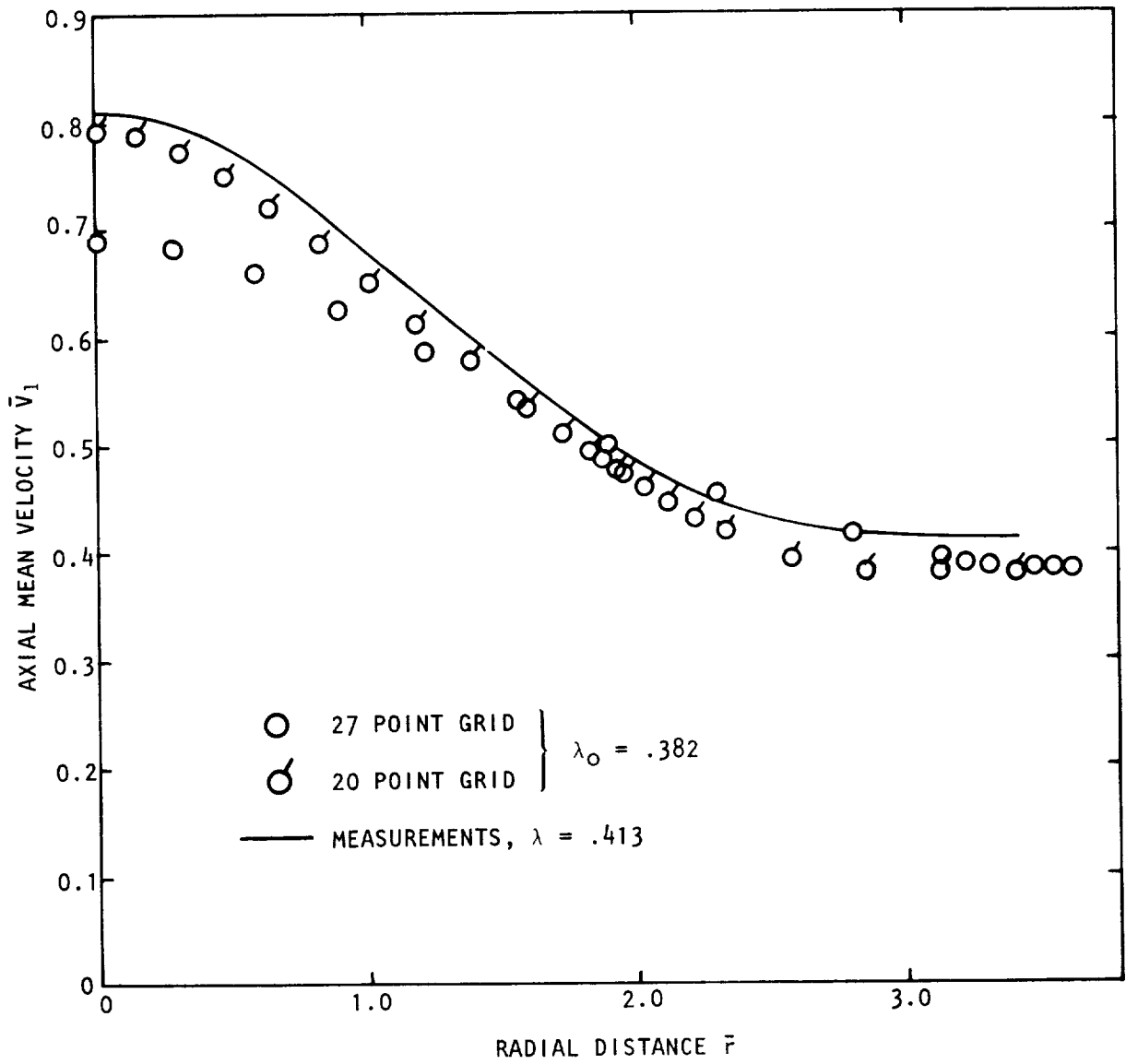
Figure 4.60 Radial velocity profiles at $\bar{x} = 32$.
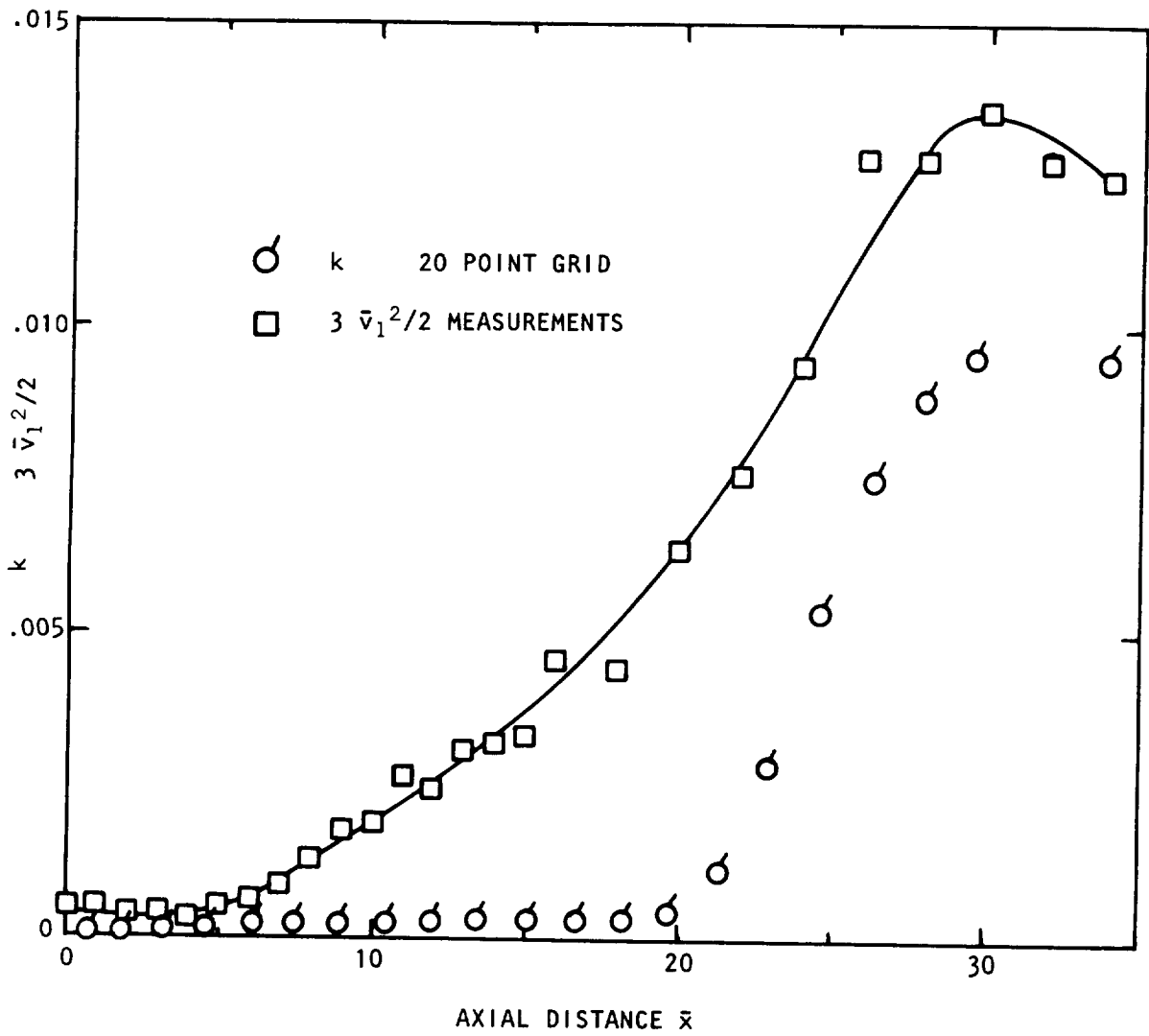
Figure 4.61   Jet centerline variation of turbulent kinetic energy.

4.4 ACOUSTIC SCALING LAWS

In this section the relationships between the flow parameters and the velocity ratio derived in section 4.2.4 will be used to estimate the variation of the radiated noise due to alteration in the noise source magnitude and distribution. In Appendix 4C another model of this kind has been developed based on the properties of the dividing streamline. In this section attention will be paid to the more usually used scale of the velocity difference. One major objection to attempts to scale the measurements with the difference between the jet centerline velocity and the freestream velocity has been the apparent unrealistic prediction of zero turbulence level and spreading for zero velocity difference. The existence of a mixing process for equal freestream and jet velocities in a realistic situation is due to the boundary layers on the inner and outer surfaces of the jet nozzle and the finite thickness of the jet lip. In the absence of these real phenomena, there would be no mixing for zero velocity difference. Thus, in theory, the turbulence level in the jet and the spreading rate could be related to the velocity difference between idealized freestream and jet velocities. In section 4.2.4 it is shown that for zero velocity difference a finite turbulence level and a finite rate of spread are predicted from data for lower velocity ratios. However, when dealing with a mean velocity profile where the minimum mean velocity is less than the freestream velocity such as that which exists in the vicinity of the jet exit, the real velocity difference, which governs the mean shear and hence the vorticity in the inner and outer flow regions, is not $\bar{V}_J - \bar{V}_T$ but the difference between the maximum and minimum velocities. From the initial velocity profiles shown in Figures 4.24 and 4.25, values of $\bar{v}_{1max}$ of .144 and .154 are found for maximum velocity differences of .76 and .83, respectively. Using equation (4-30) values of $\bar{v}_{1max}$ of .144 and .154 exactly are fortuitously predicted. If the prediction had been made on the basis of the velocity difference between the jet and the freestream values of $\bar{v}_{1max}$ of .125 and .111 would have been obtained. Clearly the use of the maximum velocity difference $\bar{V}_J - \bar{V}_{min}$ is more appropriate.

The method to be used for noise estimation is based on the original dimensional analysis of Lighthill (ref. 110) and follows the same lines as that used by Cocking and Bryce (ref. 23) though the scaling laws for the flow variables will be those derived in section 4.2.4. It will be assumed that the effect of freestream velocity on the radiated noise will be typified by its effect on the initial development of the jet not too far downstream of the potential cone. This limitation, which may still be representative of conditions further downstream, should include the major noise source region.

The noise per unit volume of the jet is given by

$$\text{noise/unit volume} \sim \frac{T^2 \, \omega^4 \, V_e}{\rho_o \, a_o^5} \, ,$$

(4-35)

188

where ω is a typical sound frequency, and V_e is the volume of an assumed eddy. The stress term T can be related to the total turbulence level by

$$T \sim \rho_o \, q_{max}^2.$$

(4-36)

Assuming that the velocity difference is not too small so that $\bar{v}_{1_{max}}$ is given by equation (4-26), equation (4-29) can be used to give

$$q_{max}^2 \sim \left\{ 1 + \frac{(1-\lambda)^{.6}}{(1+\lambda)^2} \right\} (1-\lambda)^{1.4} \, v_J^2$$

(4-37)

The volume of a typical eddy will be assumed to be related to the local thickness of the shear layer so that

$$V_e \sim \delta_\omega^3.$$

(4-38)

It will also be assumed that the characteristic frequency of an eddy noise source is given by,

$$\omega \sim \frac{v_{1_{max}}}{\delta_\omega} \sim \frac{(1-\lambda)^{.7}}{\delta_\omega} v_J.$$

(4-39)

Substitution of these relationships into equation (4-35) leads to

$$\text{noise/unit volume} \sim \rho_o \left\{ 1 + \frac{(1-\lambda)^{.6}}{(1+\lambda)^2} \right\}^2 \frac{(1-\lambda)^{5.6}}{\delta_\omega} \frac{v_J^8}{a_o^5}.$$

(4-40)

The cross-sectional area of the mixing region will be approximated by $2\pi r_J \delta_\omega$ so that the noise per unit length of the jet is given by

$$\text{noise/unit length} \sim \rho_o r_J \left\{ 1 + \frac{(1-\lambda)^{.6}}{(1+\lambda)^2} \right\}^2 \frac{(1-\lambda)^{5.6}}{a_o^5} v_J^8.$$

(4-41)

If the total noise producing length of the jet is characterized by the potential core length, then the total noise radiated is given by

$$\text{total noise} \sim \rho_o r_J^2 \left\{ 1 + \frac{(1-\lambda)^{.6}}{(1+\lambda)^2} \right\}^2 \frac{(1-\lambda)^{5.6}}{a_o^5} v_J^8 \, \bar{x}_c.$$

(4-42)

Equation (4-3) can be used to obtain

$$\text{total noise} \sim \frac{\rho_o r_J^2}{a_o^5} \left\{ 1 + \frac{(1-\lambda)^{.6}}{(1+\lambda)^2} \right\}^2 \frac{(1-\lambda)^{5.6}}{(1 - .92\lambda)} v_J^8.$$

(4-43)

Since the noise measurements at 90° to an isothermal jet are practically free from any convective or refractive effects, the predicted variation of total noise with velocity ratio can be compared with the measurements at this location. The change of the noise level relative to the level when $\lambda = 0$ is

plotted as a function of velocity difference in Figure 4.62. The prediction given by equation (4-43) tends to slightly over predict the effect of velocity difference on the radiated noise at small velocity differences. The exponent of the velocity difference from the noise measurements was 5.5. The exponent given by equation (4-43) is readily calculated from equation (4-43) and is shown in Figure 4-63. The exponent rapidly approaches the measured value of 5.5 from its value at $\lambda = 0$ of 7.28. The difference between the prediction and the measurements never exceeds 1.5 dB and, since the exponent is less than 5.5, the measured value for values of λ greater than one half, the difference becomes smaller at higher velocity ratios. However, since the relative velocity effect is only of the order of a few dB, the prediction could be improved.

The most probable cause of the inaccurate prediction is the form chosen for the variation of the turbulence level with velocity ratio. More specifically, the estimated variation of the radial and azimuthal turbulence intensities with velocity ratio appears to be too great at small values of λ. These variations are the only ones for which adequate experimental information was not available. It is of interest to note that if variation of spreading rate, and hence radial velocity fluctuation, of the form suggested by Yule (ref. 38) is used, namely,

$$\delta_\omega' \sim \frac{(1 - \lambda)}{(1 + \lambda)^{\frac{1}{2}}} \tag{4-44}$$

a better fit to the data is obtained. Use of equation (4-44) results in a noise prediction of the form,

$$\text{total noise} \sim \frac{\rho_o r_J^2}{a_o^5} \left[1 + \frac{(1 - \lambda)^{.6}}{(1 + \lambda)} \right]^2 \frac{(1 - \lambda)^{5.6}}{(1 - .92\,\lambda)} \; V_J^8. \tag{4-45}$$

The result for this prediction is also shown in Figure 4.62. The variation of the corresponding velocity difference exponent with velocity difference is shown in Figure 4.63. The small change in the expression for the variation of the spreading rate clearly has a significant effect on the resulting noise prediction. The variation of spreading rate and radial and azimuthal turbulence levels with velocity ratio for small values of velocity ratio is thus seen to be very important.

4.5 SUMMARY AND CONCLUSIONS

An experimental investigation of the effect of a secondary stream on the turbulent structure of a round jet, and the noise radiated by the jet, has been performed. The major highlights and conclusions are given below.

(1) A two-inch diameter jet was mounted on an aerodynamically faired plenum and support in a 0.76 m x 1.09 m low-speed wind tunnel. Tunnel velocities of up to 76.2 m/s could be achieved. Static pressure

190
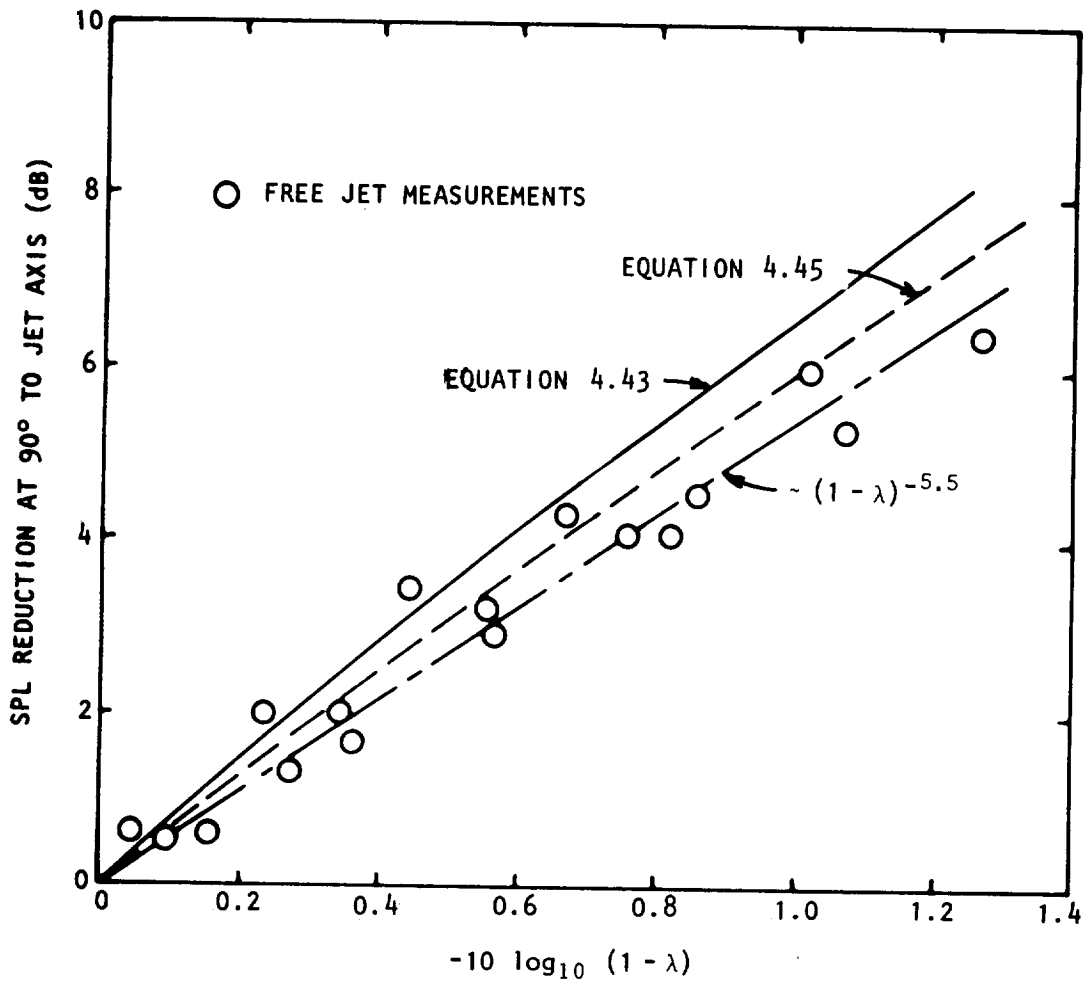
Figure 4.62   Predicted variation of radiated noise with
velocity difference.
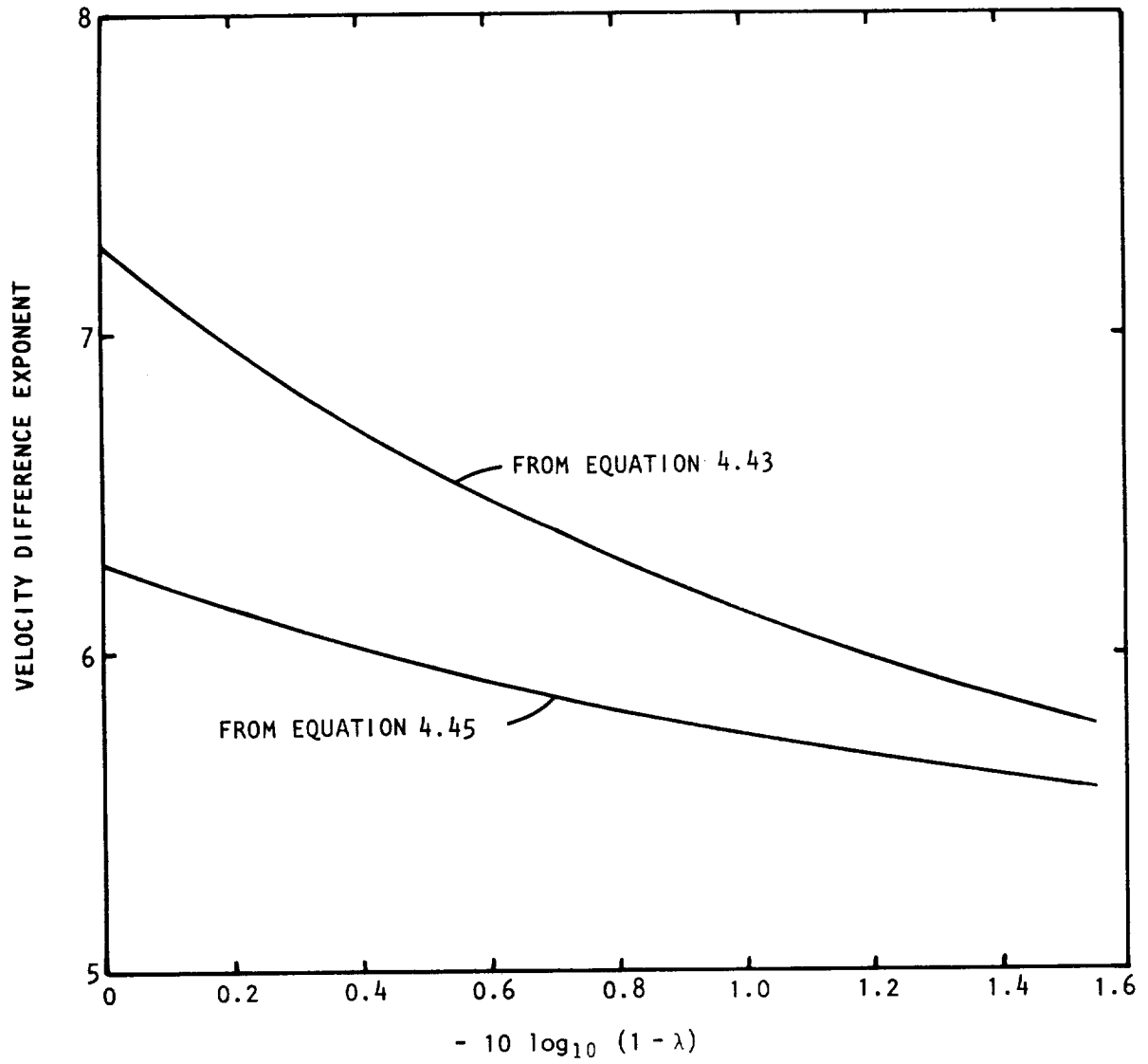
Figure 4.63   Variation of velocity difference exponent with velocity difference.

tappings were located along one wall of the working section. A window in the opposite working section wall allowed observation of the jet flow up to 0.86 m from the jet exit. The static pressure in the tunnel was controlled by a door in the tunnel return section.

(2)   Wall static pressure measurements indicated a maximum variation of two per cent in the working section tunnel velocity.

(3)   A laser velocimeter system was used to perform the velocity measurements. The velocimeter optics were mounted on two lathe guides and a hydraulic table which allowed traversing in three directions. The system operated in single-channel back-scatter mode enabling measurements of instantaneous axial velocity to be made. The jet supply air was seeded with one micron aluminum oxide particles and the wind tunnel air was seeded with a hydraulic oil aerosol.

(4)   Two series of test points were considered. The first were for fixed jet exit Mach number of .47 and velocity ratios of .1, .2, .3, .4, and .5. The second series were for a fixed velocity ratio of .1 and jet exit Mach numbers of .47, .9, 1.37, and 1.67. All experiments used unheated air.

(5)   For the fixed jet exit Mach number measurement series, radial velocity traverses were performed at axial locations of $x_c/4$, $x_c/2$, x_c and $x/r_J = 32$, the potential core length being determined by a centerline axial traverse. In the second measurement series for variable Mach number, radial traverses were performed at $x/r_J = 4$, 8, 16, and 32.

(6)   The jet centerline velocity was found to decay as,

$$\frac{(\bar{V}_a - \lambda)}{(1 - \lambda)} = 1 - \exp\left[\frac{-1}{.08 \ (1 - .92\lambda)\bar{x} - .7}\right],$$

downstream of the end of the potential core.

(7)   The potential core length for $M = .47$ is given as a function of λ as,

$$\bar{x}_c = 8.77/(1 - .92\lambda).$$

(8)   For fixed velocity ratio, .1, and variable jet Mach number, the potential core length followed the same variation as a jet exhausting into stationary air, being almost constant for $M_J < 1$.

(9)   In the annular mixing region of the jet, the rate of spread of the mixing layer agreed closely with that of a two-dimensional shear layer.

(10)   For supersonic jet exit velocities, the rate of spread was inversely proportional to the Mach number.

(11) The axial mean velocity radial profiles in the annular mixing region could be described by a shape function whose dimensions were fixed by the half-velocity radius and the vorticity thickness. This only applied after the region of flow establishment where the effects of the initial boundary layers and the finite jet lip thickness were no longer present.

(12) The radial distribution of axial mean velocity downstream of the potential core could also be described by a shape function and the local vorticity thickness and centerline velocity.

(13) The growth of the jet downstream of the potential core region was related to the centerline velocity decay through the momentum integral equation. The resulting relationship showed that the width of the jet was linearly proportional to axial distance for $\lambda = 0$ and large values of $\bar{x}$, but was proportional to $x^{\frac{1}{2}}$ for λ not equal to zero. It was noted that in reality the asymptotic limit would give an $x^{1/3}$ relationship.

(14) It was observed that the mixing characteristics of locally supersonic flow were different from that for locally subsonic flow. This was evident from axial and radial mean velocity profiles.

(15) The peak axial turbulence intensity at any axial location was found to be given by,

$$\bar{v}_{1_{max}} \sim (\bar{V}_a - \lambda)^{.7},$$

except at small values of $(\bar{V}_a - \lambda)$ where the peak intensity was linearly proportional to the relative velocity.

(16) The axial turbulence intensity was found to be independent of the jet exit Mach number.

(17) Using a simplified model of the noise generation mechanism, the radiated noise at $90°$ to the jet axis was found to be given by,

$$\text{Radiated noise at } 90° \sim \left[1 + \frac{(1 - \lambda)^{.6}}{(1 + \lambda)} \right]^2 \frac{(1 - \lambda)^{5.6}}{(1 - .92\lambda)} V_J^8 \, r_J^2 \, .$$

This agreed closely with the acoustic measurements obtained in the anechoic free-jet facility.

(18) The relative velocity exponent at $90°$ predicted by the expression above rapidly approached the measured value of 5.5 from a value of 6.3 at $\lambda = 0$.

(19) The turbulence measurements indicated that the measured relative velocity reduction in noise at $90°$ to the jet axis, which is observed in free-jet and wind tunnel measurements, may be attributed to changes in the source level due to alteration of the turbulence structure by the secondary stream.

194

5. SYNOPSIS OF TECHNICAL WORK

5.1 INFLIGHT SIMULATION EXPERIMENTS ON JET NOISE

5.1.1 Anechoic Free-Jet Facility

A new anechoic free-jet facility, funded by Lockheed, has been designed and constructed for investigating forward motion effects on jet noise. The facility was subjected to rigorous aerodynamic and acoustic performance evaluation tests prior to the inflight simulation experiments on jet noise.

The facility was powered by a jet ejector and was capable of providing tunnel velocities up to 75 m/s with a test section of .76 m by 1.07 m. Prior to the construction of the full-scale facility, an exact one-fifth scale model was built to confirm various aerodynamic performance concepts and to aid in the design of the free-jet working section as well as the shape of the collector. A planview schematic of the complete facility is shown in Figure 5.1. In order to provide low background noise levels, the tunnel ducting between the anechoic room and the jet ejector incorporated several sound absorbent sections. For minimum blockage (and therefore minimum flow disturbance) in the working section, the air supply ducting for the primary jet was installed axially in the intake/contraction section. The ducting was carefully designed to avoid any flow separation within the accelerating free-jet flow in the contraction section. The upstream internal noise levels were minimized by the two mufflers connected in series. The microphone arc was at 54 nozzle diameters, and was placed outside the free-jet flow. Noise data were normally taken in the range $30° \leq \theta_m \leq 90°$, but forward arc measurements could be accomplished by moving the primary jet downstream.

In order to confirm the design criteria and to ensure the accuracy of the subsequent jet noise measurements, the facility was subjected to rigorous performance evaluation tests, and the major findings were as follows:

Flow visualization tests using a smoke generator established that the free jet was stable throughout its length, and the air-flow circulation velocities in the anechoic room were negligible. The mean flow properties of the free-jet working section were examined quantitatively by using a specially designed pressure probe rake. The mean velocity profiles were mapped in detail, and the tunnel calibration was derived from these tests.

The acoustic performance tests were designed to examine the anechoic quality of the facility, the background noise levels, and the rig internal noise levels. It was established that (1) the facility was anechoic down to 200 Hz, (2) the facility background noise in the measurement arena was low (see Figure 5.2), and (3) the jet noise results would not be contaminated by internal noise at least down to $V_J/a_0 = 0.32$. (All symbols are defined in Appendix 5.)

Limited calibration experiments using a point source established that in the frequency range from 1 KHz to 5 KHz, no detectable internal reflections in the free-jet test section were observed for tunnel velocities up to 60 m/s. It was also confirmed that at these frequencies, the effect of turbulence scattering in the facility was not significant.
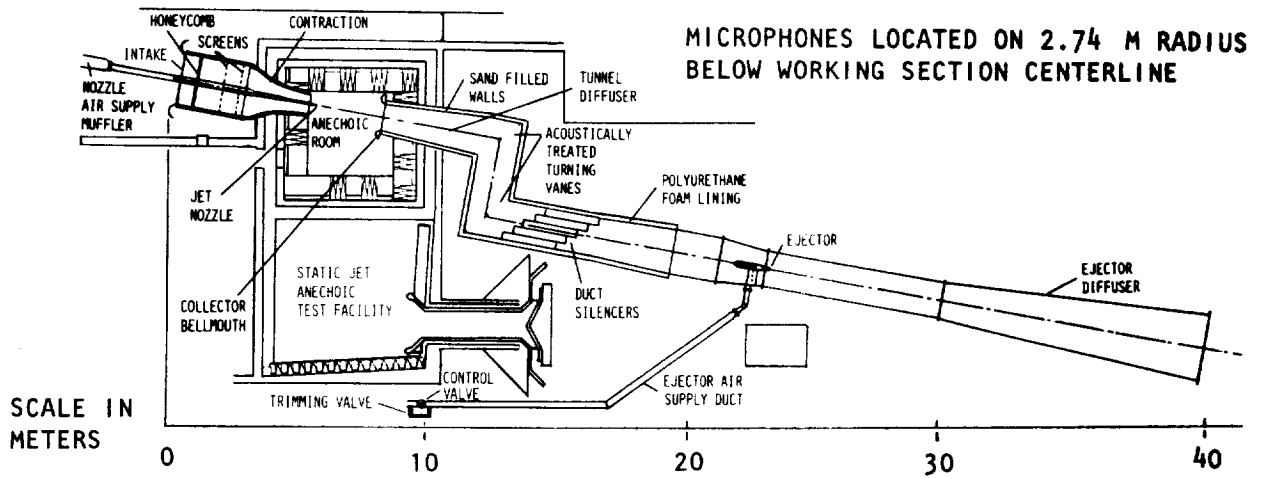
Figure 5.1 Planview schematic of Lockheed anechoic free-jet facility.
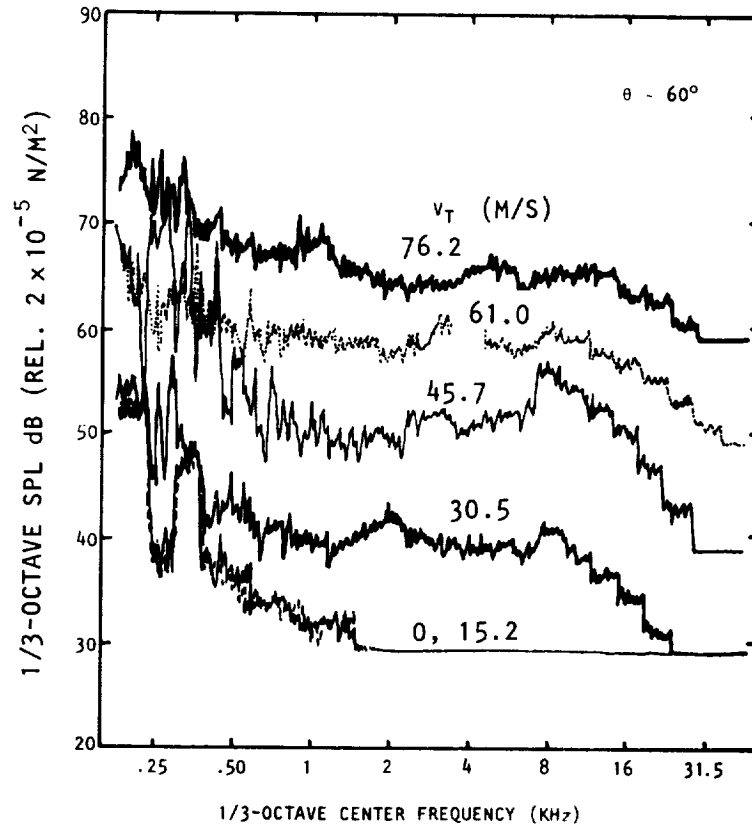
Figure 5.2 Background noise spectra at various
tunnel velocities.

5.1.2 Jet Noise Experiments

The effects of forward motion on the characteristics (both directivity and spectral) of turbulent mixing noise from jet exhausts were examined by conducting inflight simulation experiments in the anechoic free-jet facility. The resulting scaling laws, after applying facility corrections, were found to be in close agreement with the scaling laws derived from theoretical and semi-empirical considerations.

In the jet noise experimental program, the free-jet to nozzle area ratio was 400. The nozzles (d = 5.08 cm.) employed were a convergent nozzle, and M = 1.4 and 1.7 convergent-divergent nozzles. Acoustic measurements were conducted at forty different test conditions (combinations of V_J/a_0 and V_T/a_0); eight values of jet exit velocity were chosen in the range $0.4 \leq V_J/a_0 \leq 1.345$, and the tunnel velocity was varied up to $V_T/a_0 = 0.2$. All acoustic data were carefully scrutinized prior to detailed analysis, and all data likely to be contaminated by extraneous noise sources (background/instrumentation/shock noise) were not utilized.

The uncorrected results (i.e. data to which no facility corrections were applied) were found to be in good agreement with the results from published free-jet experiments.

The measured results were subjected to a systematic data correction procedure, which was derived in the present program, and which converted results from a free-jet facility to the corresponding results that would be obtained in a large-scale wind tunnel simulation. In essence, the correction procedure took proper account of source distribution effects in a jet flow, the downstream convection of sound waves by the tunnel flow, and the refraction of sound caused by the free-jet shear layer. Using the measured results at fixed measurement angles, θ_m, it finally yielded results corrected to constant emission angles, θ_e, for an observer moving with the nozzle. In general, the magnitudes of the facility corrections were small at 90° to the jet axis, but produced a significant effect at lower angles in the rearward arc.

At $\theta_e = 90°$, the effect of tunnel velocity on the corrected spectra was virtually independent of frequency, and the spectra at various tunnel velocities were nearly parallel. This implied constant reduction in equivalent source strength at all frequencies. A typical example for $V_J/a_0 = 0.9$ is presented in Figure 5.3.

The corrected overall SPL results indicate that the magnitudes of the inflight noise reductions increase as the observer moves from $\theta_e = 90°$ toward the downstream jet axis (Figure 5.4). The reductions at all emission angles were scaled on the relative velocity basis. At $\theta_e = 90°$, the OASPL is found to be proportional to 5.5 powers of the relative velocity, a result which agrees closely with the theoretical and semi-empirical scaling laws, derived purely from source alteration considerations.
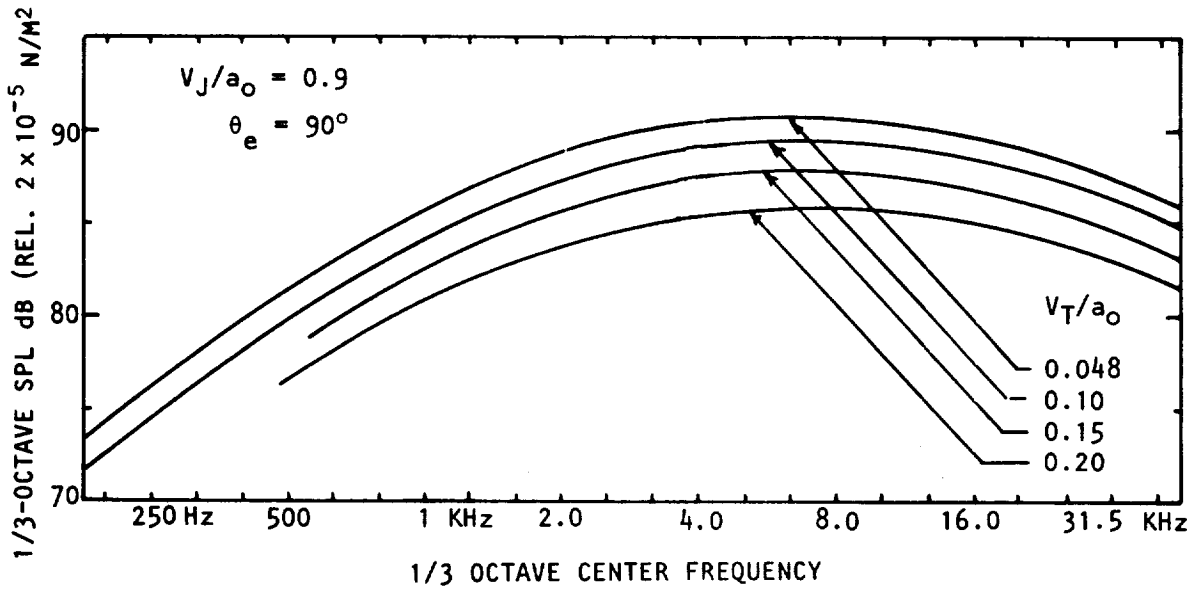
Figure 5.3 Effect of tunnel velocity on corrected spectra:
$V_J/a_o = 0.9$, $\theta_e = 90°$.
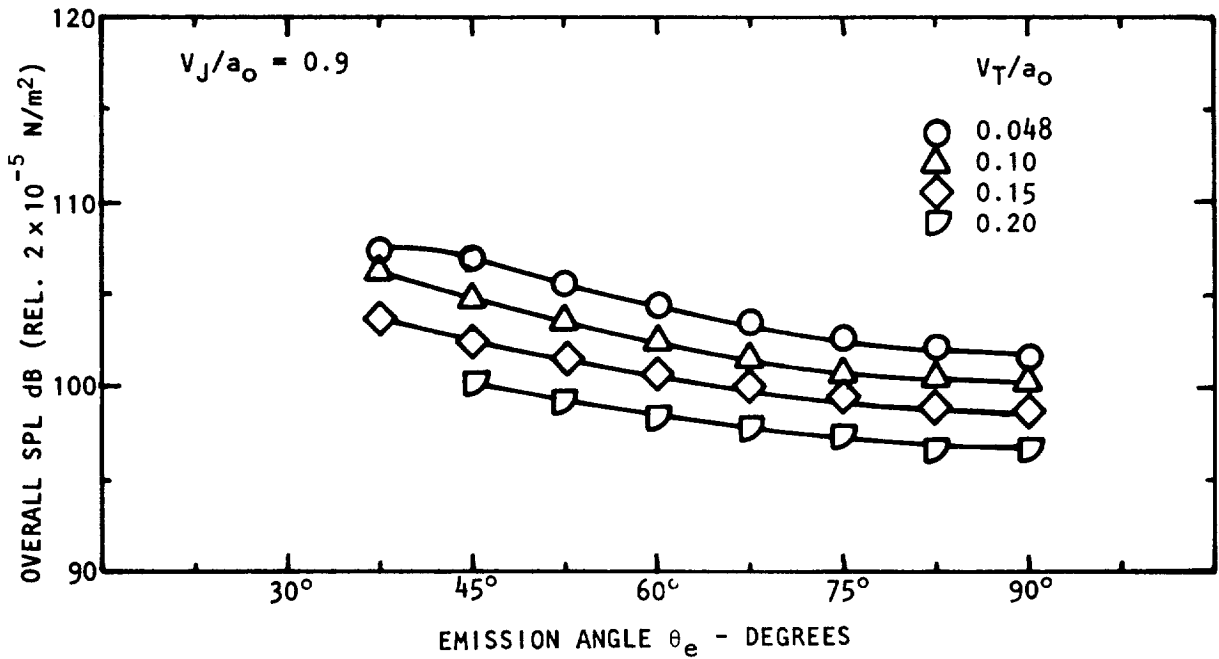
Figure 5.4 Effect of tunnel velocity on the directivity of
corrected overall SPL at $V_J/a_o = 0.9$.

*The results from the present free-jet experiments are in very good agreement
with published wind tunnel results. However, there are large differences
between the inflight effects as observed from model simulation experiments
and full-scale flight tests. These discrepancies are tentatively attributed
to the doubtful validity and accuracy of the flight data.*

The relative velocity exponents, obtained from the present corrected
results, are compared with the exponent values obtained in the NGTE wind
tunnel experiments (where the test section to nozzle area ratio was 5000) in
Figure 5.5. The agreement is good at all emission angles. From this compari-
son it is concluded that (1) the effect of scattering caused by turbulence
in the free-jet mixing layer does not appear to be significant; (2) the free
jet to nozzle area ratio of 400 used in the present experiments was adequate
for accurate evaluation of inflight effects on jet noise; and (3) a free-jet
facility is capable of simulating many of the inflight effects on jet noise
providing adequate and accurate facility corrections are applied to the
measured results.

The comparison of results from inflight simulation experiments with
full-scale flight results (Figure 5.5) shows that although the agreement is
reasonable at low angles to the jet exhaust, there are significant discrep-
ancies at larger angles. At $\theta_e = 90°$, there is little or no change in the
flyover noise levels, whereas the simulation experiments indicate significant
noise reductions. All attempts to explain this discrepancy in terms of source
motion (relative to a fixed observer) effects lead to the conclusion that the
flyover results at 90° will not be affected. It is therefore concluded that
the flight results considered here may not represent pure turbulent mixing
noise. It is recommended that the "acoustic cleanliness" and the measurement
accuracy of all flight results be examined thoroughly, both for existing
flight data as well as any future flight test results.

Finally, a theoretical formula for the prediction of inflight noise
reductions at emission angles outside the so-called zone of silence has been
derived, and the correlation between calculated and measured OASPL reductions
is obtained to an accuracy of $\pm 1/2$ dB, as shown in Figure 5.6.
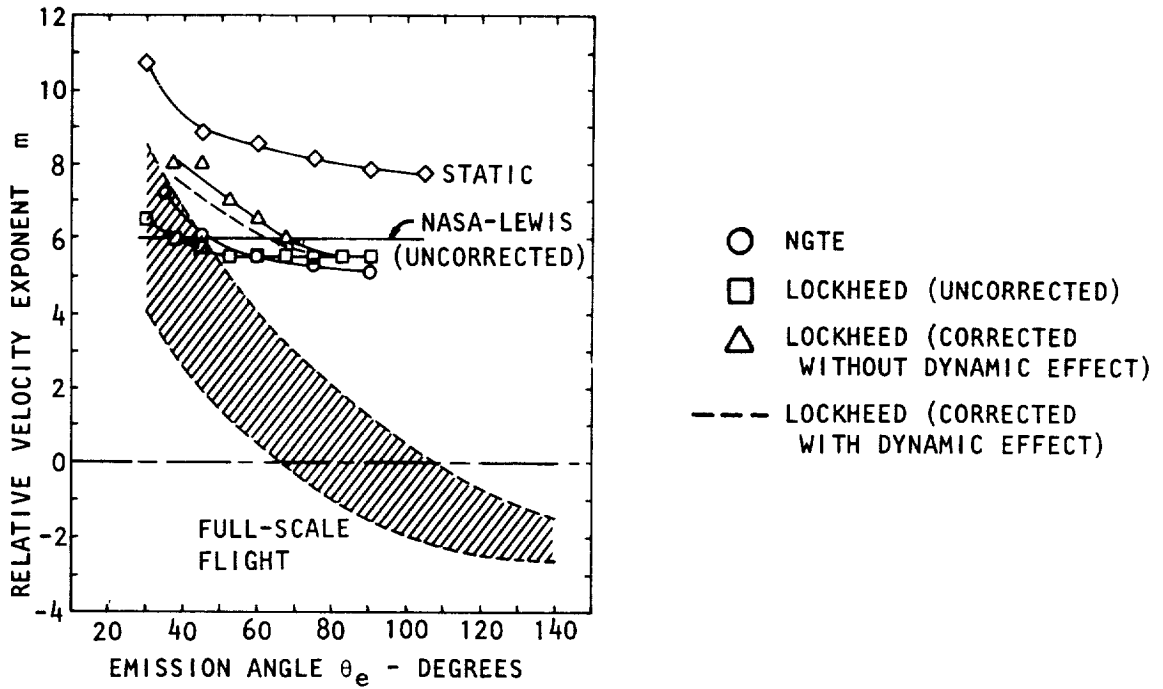
Figure 5.5 Comparison of relative velocity exponents from various inflight simulation experiments and flight tests.
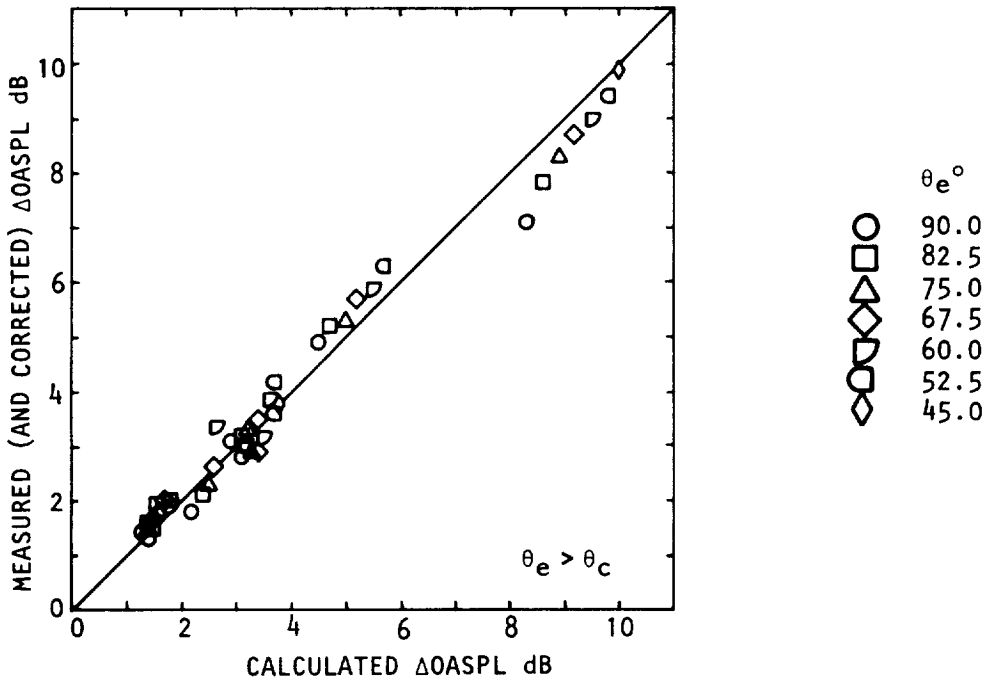
Figure 5.6 Comparison of measured (and corrected) OASPL reductions with calculated OASPL reductions.

5.2 ACOUSTIC PROPAGATION THEORY

5.2.1 An Acoustic Model of the Free-Jet Flight Simulation Facility

A geometric acoustics model of sound propagation through the free-jet shear layer has been evaluated. The model yields analytic formulae for angle and amplitude corrections that convert the measured free-jet data to estimated flight data. The recommended correction procedure takes into account the axial distribution of the jet mixing noise source as a function of Strouhal number.

In the Lockheed flight simulation facility, sound waves radiated from the primary jet are convected and refracted by the mean flow in the potential core and in the shear layer of the free-jet. The change in angle and amplitude of the direct radiation across the shear layer must be measured or calculated in order to convert the free-jet measured data to estimated flight data. A theoretical approach has been chosen, based upon Geometric Acoustics (GA) or "ray-tracing." The GA model has been partially justified with an order of magnitude study of the terms in the homogeneous Lilley equation which are neglected in the geometric approximation.

Results from the GA model indicate that axial variations and axial gradients of the mean flow velocity in the free-jet shear layer have a negligible effect on sound refraction and that the change in angle can be calculated with the analytic, stratified flow equation to a very good approximation (better than $1°$ accuracy). Examples of ray paths on the x-r plane (cylindrical coordinates, origin at free-jet nozzle) are shown in Figure 5.7, before and after propagation through the free-jet shear layer; θ_T is the wavenormal angle within the uniform flow and corresponds to the flight emission angle θ_e. The angle θ_m is the measured polar angle based on a microphone arc of radius $54\,d$ centered on the primary jet nozzle at $x = 6\,d$ (d is the primary nozzle diameter). The ray origin or source location $(X = X_s)$ is determined from an empirical model in which the effective center of the turbulent mixing noise source in the primary jet flow can be calculated as a function of the modified Strouhal number, S_m. In Figure 5.7 the source location corresponds to $S_m \doteq 1$. Ray paths inside the shear layer, although calculated, have been replaced by an extrapolation to the "lip-line" of the entry and exit ray paths. In general extrapolated ray paths, as in Figure 5.7, intersect the "lip-line" at almost exactly the same point and therefore, to a good approximation, ray paths can be drawn as if the shear layer were replaced by a vortex sheet at the "lip-line" as indicated in Figure 5.8.

However, this vortex sheet model is *not* used to calculate *amplitude* changes across the shear layer, only ray paths and changes in angle. The sound amplitude, according to GA, varies smoothly through the real shear layer and the total change in amplitude is calculated from an analytic expression based upon (i) the law of energy conservation in a ray tube and (ii) the change in ray-tube cross section across the shear layer which is defined by the ray paths as shown in Figure 5.8.

203
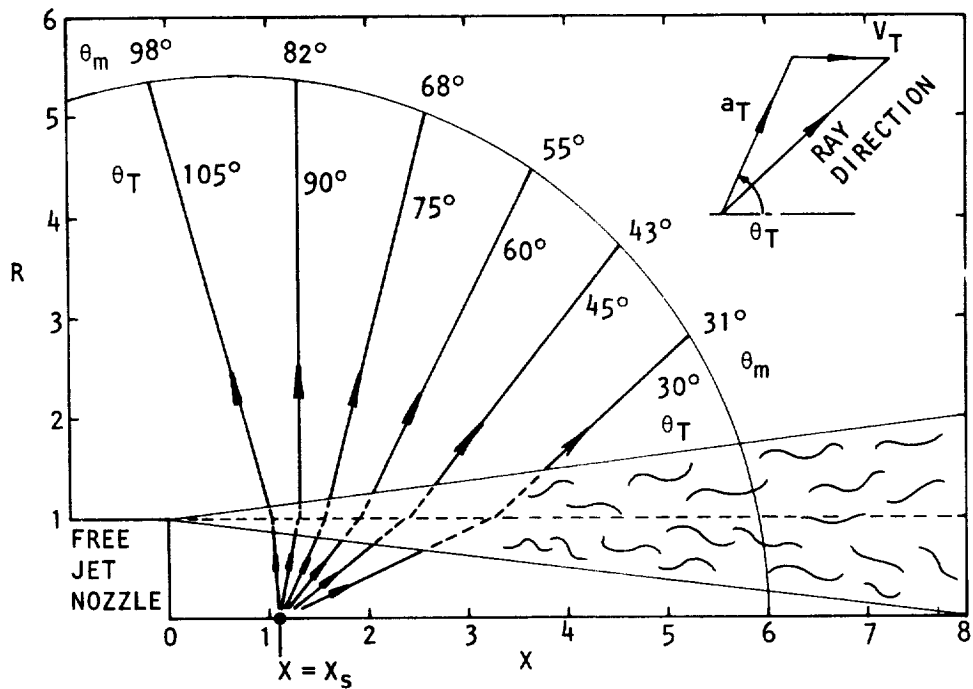
Figure 5.7 Ray paths in the free-jet facility X-R plane;
$X = x/r_T$, $R = r/r_T$, where r_T (= 10 d) is the effective
free-jet nozzle radius. Code: ►— calculated ray
path; — — — extrapolated ray path (from entry or exit
ray). Angles θ_T, θ_m and origin of rays, $X = X_s$, are
defined in the text; origin of microphone arc is at
$X = 0.6$.
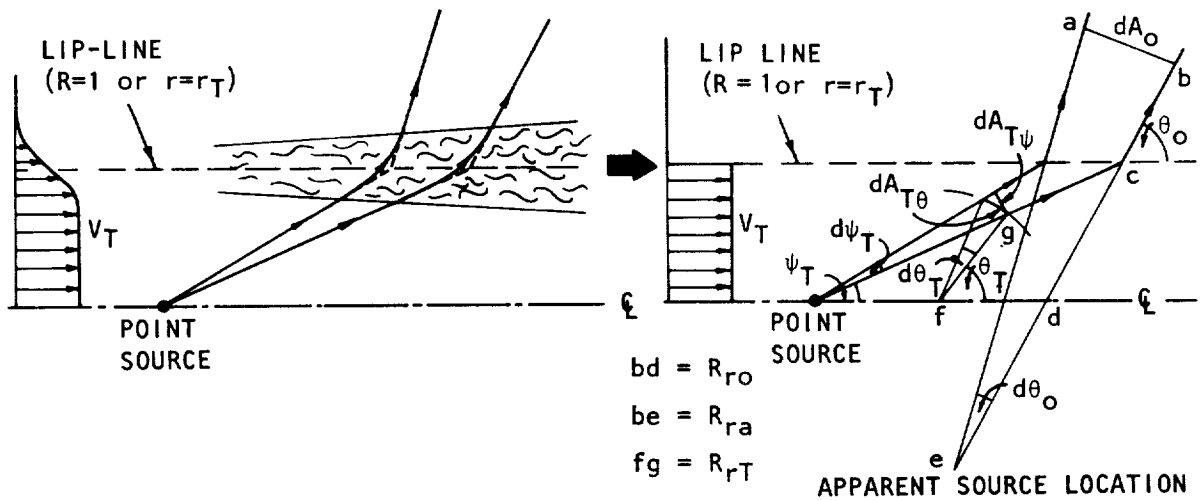
Figure 5.8 Free-jet shear layer can be replaced by a vortex sheet
at the "lip-line," $R = 1$, for ray tracing purposes. Ray
tube cross-section changes from $dA_{T\psi}$ to dA_0 across
shear layer; wavenormal angle from θ_T to θ_0.

204

5.2.2 The Influence of Forward Motion on Flow-Acoustic Interactions as Described by the Lilley Equation

---

The influence of forward motion on flow-acoustic interactions has been examined through a re-interpretation of the "static" numerical solutions to the Lilley equation. Outside the cone of silence, the Lilley equation radiation levels change with forward motion in a way that can be calculated, to a good approximation, with the geometric acoustics analytic result.

The influence of forward motion (simulated or actual) on the theoretical directivity of isothermal jet mixing noise can be summarized as follows. The expression for the proportional bandwidth mean square pressure in the static case is a product of two factors

$$\text{(Flow-acoustic interactions: } V_a) \quad \times \quad \text{(Eddy convective amplification: } V_c)$$

and, in the flight case, three factors

$$\text{(Flow-acoustic interactions: } V_a - V_A) \quad \times \quad \text{(Eddy convective amplification: } V_c - V_A) \quad \times \quad \text{(Dynamic effect: } V_A),$$

where V_A is the (uniform) aircraft flight speed. The eddy convection velocity, V_c, controls the static convective amplification (e.g. $|1 - V_c \cos\theta_e/a_0|^{-5}$); in the flight case it is the eddy convection velocity relative to the observer, $V_c - V_A$, that determines the amplification (e.g. $|1 - (V_c - V_A)\cos\theta_e/a_0|^{-5}$). Both this effect and the dynamic effect are well established results.

Similarly, the static flow-acoustic interaction effects are described by Lilley equation solutions based upon a mean velocity profile with a center-line velocity V_a and that is reduced to $V_{a,rel} = V_a - V_A$ for the flight case although it is still a "static" profile. Hence, forward motion effects can be examined through a re-interpretation of the "static" numerical solutions to the Lilley equation. Some typical numerical results outside the cone of silence for the variation of the flow-acoustic interactions factor, F_{rel}, with $V_{a,rel}$ are shown in Figure 5.9; the Strouhal number, S_m, takes two values that are appropriate for the four diameter axial station profile used in this example. This emission angle θ_e varies with $V_{a,rel}$ in these results since a source emission angle, θ_s, is held constant; θ_e lies between 50° and 60° over the range $0.75 \le V_{a,rel}/a_0 \le 1.25$.

The geometric acoustics analytic result is also shown for comparison in Figure 5.9. While there are significant absolute differences between it and the Lilley equation numerical results, the slopes are very similar. Therefore, outside the cone of silence, the Lilley equation flow factor variation with forward motion can be calculated, to a good approximation, with the geometric acoustics analytic result.

205
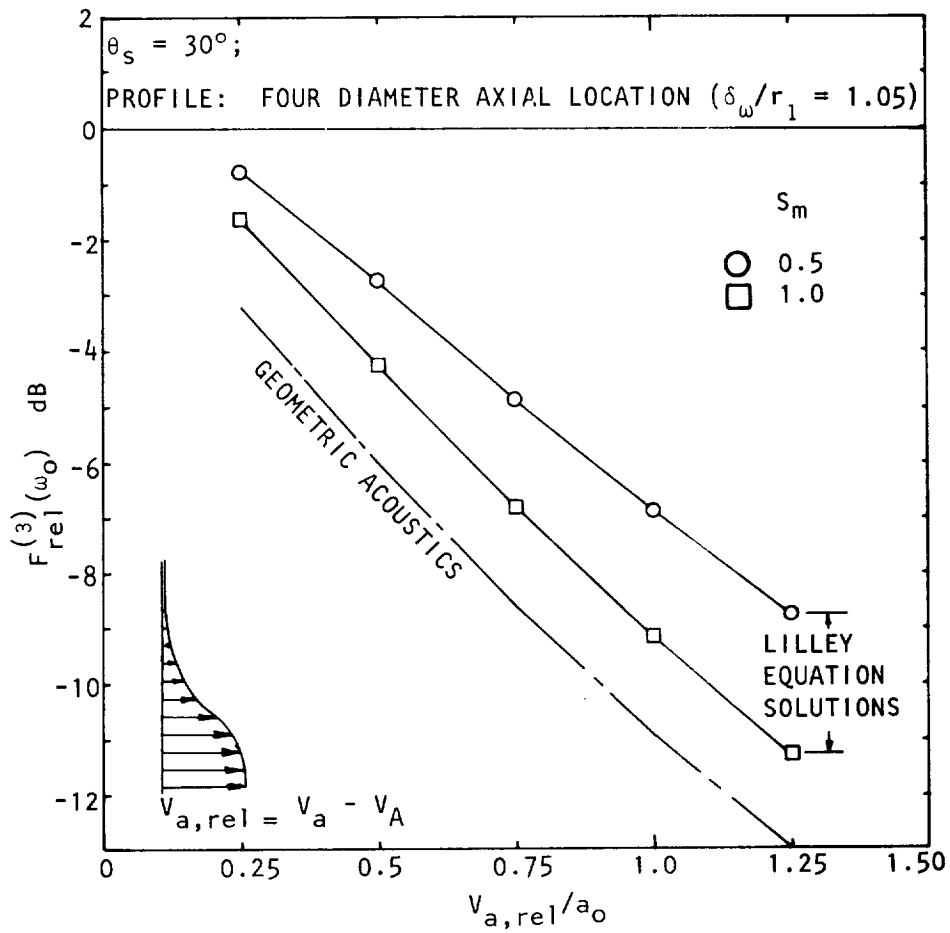
Figure 5.9 Variation of the flow-acoustic interactions factor, F_{rel}, (for the primary jet) with relative centerline jet velocity $V_{a,rel}$, from Lilley equation solutions. Geometric acoustics limit is shown for comparison. Source emission angle, θ_s, is held constant at $30°$. ($V_a \equiv V_J$).

5.3 EFFECT OF FORWARD VELOCITY ON THE
STRUCTURE OF A TURBULENT JET

5.3.1 Turbulence Measurements

Velocity measurements are made in a jet in a wind tunnel, with a laser velocimeter, to describe the effect of velocity ratio and jet exit Mach number on the development of a jet in a moving stream.

The aim of this work has been to describe the structure of a turbulent jet, in the presence of a secondary stream, in relation to the noise-producing properties of the jet.

A 5.08 cm. diameter jet was mounted on an aerodynamically faired plenum and support in a .76 m x 1.09 m low-speed wind tunnel. The experiments were conducted for a range of wind tunnel and jet exit velocities shown in Figure 5.10. One series of measurements, at fixed jet exit Mach number, examined the effect of velocity ratio on the jet development and the second series, at fixed velocity ratio examined the effect of jet exit Mach number on the jet structure.

Measurements of wall static pressure in the tunnel working section showed the axial pressure gradient to be less than an equivalent freestream velocity change of 2% at the highest tunnel velocity. Measurements of the instantaneous velocities in the jet were made with a laser velocimeter system mounted outside the tunnel working section.

The variation of jet width with axial distance in the annular mixing region of the jet was found to agree with the variation in a two-dimensional mixing layer. The variation of potential core length with velocity ratio was found to be given by, $\bar{x}_c = 8.77/(1 - .92 \, \lambda)$. This variation is shown in Figure 5.11, where it is compared to the linear variation of potential core length with velocity ratio proposed by Forstall and Shapiro (ref. 2). The method used by Forstall and Shapiro to determine the potential core length variation was applied to the present measurements and was found to overestimate the potential core length. The variation of potential core length with jet exit Mach number for a velocity ratio of 0.1 was found to be in agreement with the two region model prediction of Witze (ref. 3) for free jets. The radial mean velocity profiles in the annular mixing region of the jet and downstream of the end of the potential core were found to be represented well by shape functions using the half velocity radius and vorticity thickness and the jet centerline velocity as the characteristic properties of the flow. The collapse of the radial mean velocity profiles in the annular mixing region is shown in Figure 5.12.

For the most velocity ratios of practical interest the axial turbulence intensity was found to follow a relationship of the form, axial turbulence ~ (relative velocity)$^{0.7}$. This is shown in Figure 5.13. For small velocity differences the turbulence level is expected to be proportional to the relative velocity. The axial turbulence intensity was found to be independent of the jet exit Mach number.
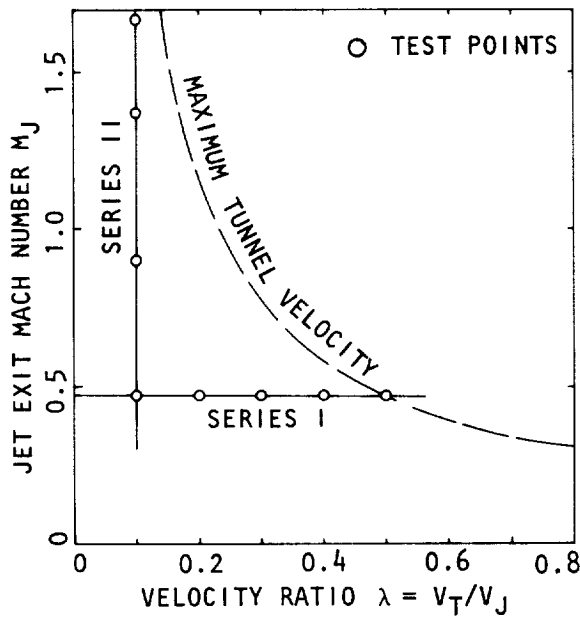
Figure 5.10 Turbulence test program.
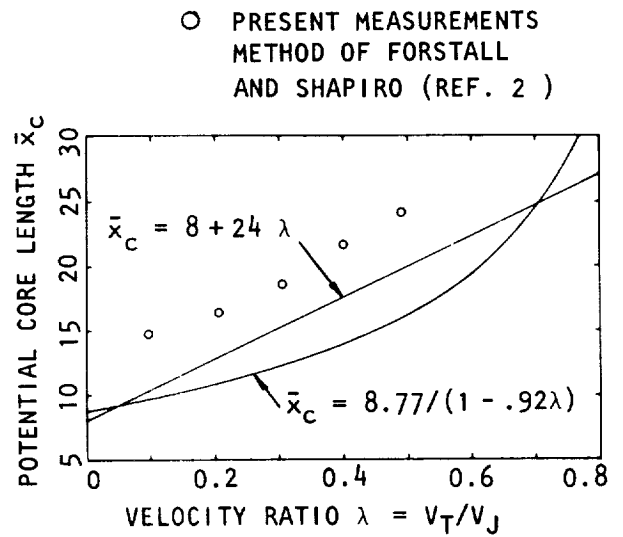
Figure 5.11 Variation of potential core length with velocity ratio.
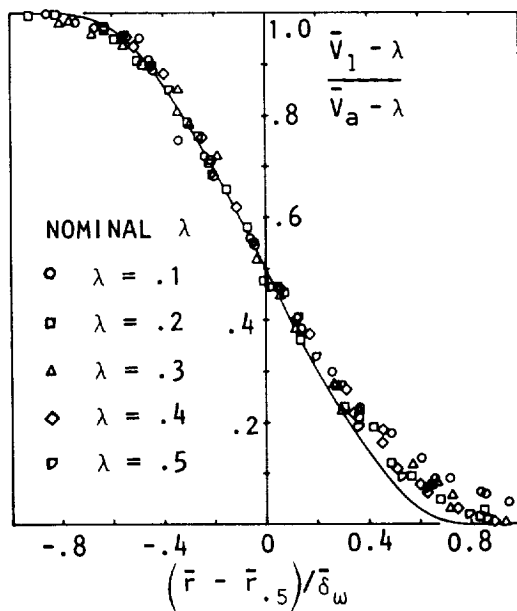
Figure 5.12 Radial distribution of axial velocity in the mixing region, $M_J = 0.47$.
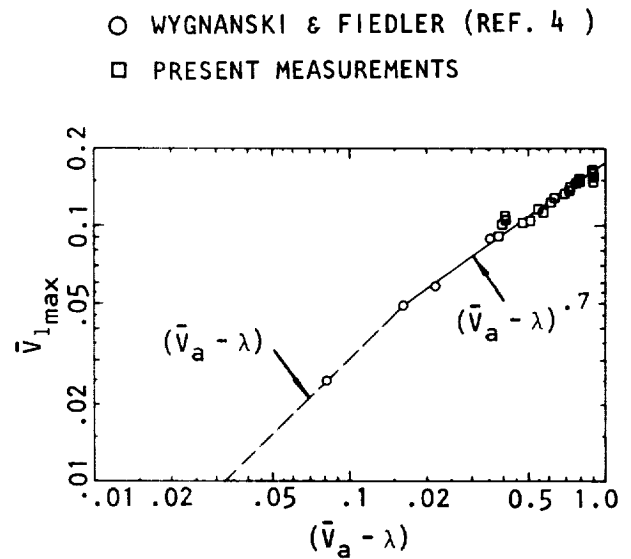
Figure 5.13 Variation of maximum turbulence intensity with velocity difference.

208

5.3.2 Jet Noise Scaling

The variation in radiated noise, at 90° to the jet axis, with velocity ratio is predicted using turbulence measurements and a simplified Lighthill noise radiation model.

The measurements of jet turbulence made in the subsonic wind tunnel experiments may be used to estimate changes in the radiated noise with velocity ratio.

The Reynolds stress sources in a subsonic jet are assumed to be proportional to the ambient density and the total turbulence intensity. In order to calculate the total turbulence level, three components of velocity fluctuations are required. The axial turbulence intensity is obtained directly from the measurements. The radial velocity fluctuations are assumed to be proportional to the rate of spread of the jet and the azimuthal velocity fluctuation is assumed to be the average of the other two components. The source frequency is related to the axial velocity fluctuation and the local shear layer thickness. The eddy volume is taken as proportional to the cube of the local thickness. The variation in the noise producing volume is considered to be described by variations in the mixing layer thickness and the potential core length.

Two prediction formulae are obtained depending on the description of the variation of local thickness with velocity ratio. Best agreement is obtained if the spreading rate of the mixing layer is assumed to be proportional to $(1 - \lambda)/1 + \lambda)^{\frac{1}{2}}$. In this case the radiated noise at 90° to the jet axis, where convection and refraction effects are at a minimum and changes reflect source alterations, is given by

$$\text{Radiated noise at } 90° \sim \frac{\rho_o \; r_J^2 \; V_J^8}{a_o^5} \left\{ 1 + \frac{(1 - \lambda)^{.6}}{(1 + \lambda)} \right\}^2 \frac{(1 - \lambda)^{5.6}}{(1 - .92 \; \lambda)} \; .$$

This prediction is compared with the free-jet noise measurements in Figure 5.14. The predicted variation of relative velocity exponent is shown in Figure 5.15. It can be seen that, except at small values of velocity ratio, the agreement between the predicted exponent and the measured value of 5.5 is good.
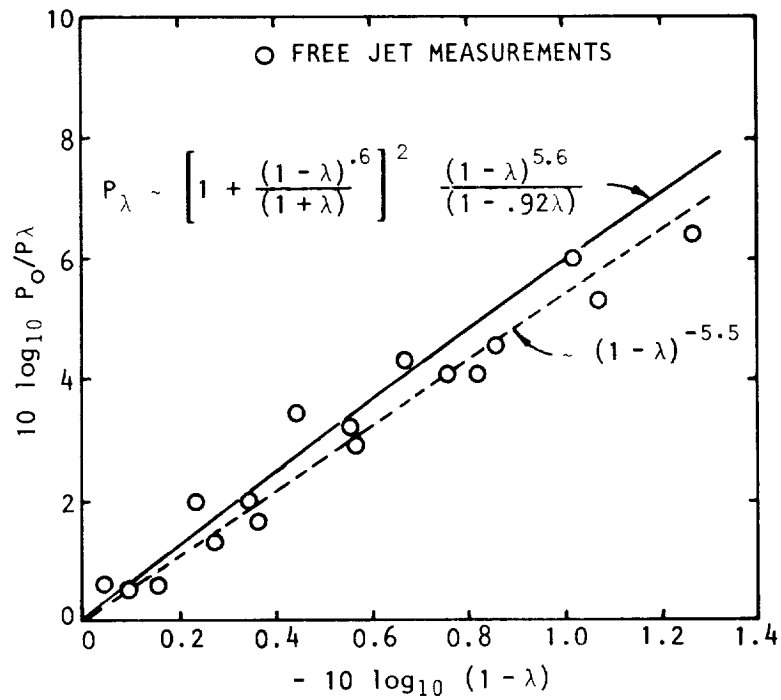
Figure 5.14 Predicted variation of radiated noise with velocity difference.

$$P_\lambda \sim \left[1 + \frac{(1-\lambda)^{.6}}{(1+\lambda)} \right]^2 \frac{(1-\lambda)^{5.6}}{(1-.92\lambda)}$$

$\sim (1-\lambda)^{-5.5}$

$$\text{SPREADING ANGLE} \sim \frac{(1-\lambda)}{(1+\lambda)^{\frac{1}{2}}}$$
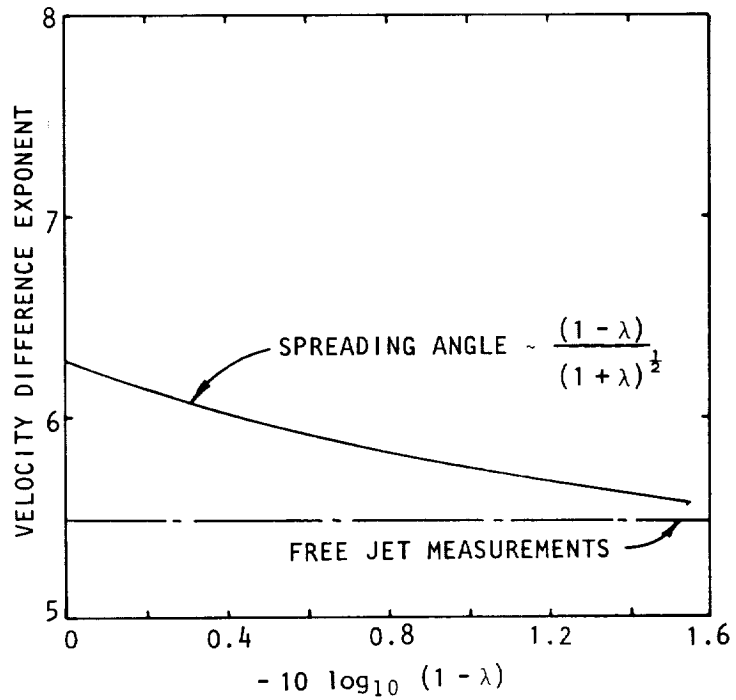
Figure 5.15 Variation of velocity difference exponent with velocity difference.

210

6. RECOMMENDATIONS FOR FUTURE WORK

The work conducted during the present program has examined many important aspects of forward velocity effects on turbulent jet mixing noise from a fundamental viewpoint. Several important recommendations for future work, necessary to achieve the ultimate goal of this research program (described in Section 1), have emerged during the course of this study. These recommendations are now discussed in detail.

The recommendations, essentially fall into two categories. The first category is centered on the problem that significant differences exist between the inflight effects as observed from the full-scale flight tests and those obtained from model-scale inflight simulation experiments conducted in static facilities like a wind tunnel or a free-jet facility. These discrepancies need to be resolved in a systematic manner, since the basic concept of predicting inflight noise levels from flight simulation tests becomes meaningful only when there is a good correlation between the flyover results and the corresponding forward velocity simulation results. The second category or set of recommendations form the continuation of the fundamental study that has been conducted in the present phase. These fundamental studies on the effects of forward velocity on jet noise are considered to be vital in achieving the long-term goal of being able to predict the sound field of a jet exhaust in flight without actually flying the jet configuration.

It is strongly recommended that in order to reach the ultimate objective of this research effort in an efficient manner, the two categories of recommendations described above should be implemented with *equal* emphasis. That is, both sets of recommendations should be followed concurrently if possible, and it could be detrimental if one set of recommendations is executed at the expense of the other.

6.1 FIRST CATEGORY RECOMMENDATIONS

The recommendations necessary to reconcile the differences between flight results and model simulation results are discussed first. From the present study, it can be concluded that the observed discrepancies may have arisen due to one of the following two reasons: (1) a relative source motion effect, which is present in the flyover tests, but which is absent in the simulation tests where the observer is effectively moving with the jet nozzle; (2) the doubtful validity of the cleanliness of flight data, which may give rise to inflight effects that may differ considerably from those that are associated with pure turbulent mixing noise. The basic philosophy behind future work on this aspect lies in the assessment of the relative roles played by these two possible reasons in producing the currently observed differences. This can be achieved by conducting a carefully controlled experiment where the two phenomena can be isolated. To do this, it is recommended that an experiment involving the measurement of the noise field, by stationary microphones, from a moving jet should be conducted.

The jet configuration to be used in this experiment should be free from internal noise, and the experiment should be conducted at model scale in a carefully controlled environment where the measurements and corrections can be obtained accurately. The same jet configuration should then be tested in a flight simulation facility, for example, in an anechoic free-jet facility, and the results from the two sets of experiments should be compared in detail.

The outcome of this comparison will establish the exact nature of subsequent research as follows: (1) If the results from the moving jet experiment agree with the corresponding results from the flight simulation experiment, then it can be concluded once and for all that the currently observed discrepancies arise due to some problems associated with a full-scale engine (e.g. internal noise, measurement problem, propagation effects), and are not related to any relative source motion phenomenon. (2) On the other hand, if the results from the simple moving jet experiment do not agree with the simulation data, but are found to be in reasonable agreement with the trends observed from existing full-scale flight data, then it will become clear that the currently observed differences are associated with some relative motion effects which have not been accounted for correctly in translating static simulation data to the flight results. Subsequent research can therefore be directed towards a re-examination of various phenomena associated with source motion relative to a fixed observer. In this manner, it will be possible to define the most fruitful avenues of approach for reconciling the flight data with model simulation results in the long-term research efforts.

6.2 SECOND CATEGORY RECOMMENDATIONS

Regardless of the outcome of the fundamental investigation, described above, of the noise of a pure jet in flight and in the flight simulation facility, it is necessary to continue the basic work of defining the effects of forward velocity on jet mixing and shock-associated noise, especially for heated jets. Preliminary aspects of this work have been completed during the current contract; however, considerably more detail must be obtained in all aspects of the work recommended below.

The specific technical objectives of the proposed fundamental study of flight effects on jet noise should be:

(1) to define the limitations of the anechoic free-jet facility technique for measuring flight effects on jet noise, using experimental information from current facilities in conjunction with appropriate theory;

(2) to further develop a methodology for using such facilities, in particular, to determine theoretically the proper transformation for converting facility data to the corresponding in-flight case;

(3) to measure the appropriate jet flow quantities for the in-flight condition, such as mean and turbulence velocity distributions, convection speeds and turbulence spectra, for input to a jet noise source alteration

212

model, and to define, by utilizing the data and available theoretical techniques, jet noise source alterations resulting from aircraft forward motion;

(4) to extend the acoustic inflight simulation experiments on turbulent mixing noise and shock-associated noise, in particular, to examine and quantify the effects of forward velocity on heated jets; and

(5) to calculate the noise field of a jet in flight and compare with experimental results.

The following recommendations are designed to meet the specific technical objectives.

6.2.1 Phase I - Methodology and Corrections for Transformation of Free-Jet Data to the Equivalent In-flight Condition

This phase of the program should be directed toward further development of the appropriate corrections and calibrations to convert noise measurements from a free-jet anechoic facility to equivalent linear measurements (parallel to direction of flight) for a jet in flight. The effort should use a combination of theoretical and experimental approaches as outlined below.

6.2.1.1 Theoretical program. Effects of the free-jet on the sound field of the model jet should be studied with the aid of appropriate flow-acoustic interaction models. Charts and calculation procedures should be produced which relate free-jet facility results to the corresponding in-flight noise levels.

(i) The effect of transmission through the mean flow field of the combined primary and secondary jets should be calculated by numerically solving the Lilley equation. This will provide a standard of comparison for the approximations below (ii, iii).

(ii) The effect of transmission through the outer mean shear layer alone should also be studied using the Lilley equation. In this way the effect of neglecting the primary jet flow field can be assessed.

(iii) The applicability of the geometric acoustics (GA) approximation for transmission through the combined (primary + free-jet) jet flow field should be assessed by comparing GA results with the full Lilley equation results, for realistic mean flow profiles.

(iv) The above calculations could be performed using a mean flow model which neglects spreading of the inner and outer shear layers. Growth of the outer free-jet shear layer in the downstream direction may significantly affect the interpretation of free-jet facility data. This possibility should be assessed using a geometric acoustics model of the acoustic-mean flow interaction process.

(v) The items listed above refer to interaction of sound with the mean flow field in a free-jet facility. The effect of turbulent scattering in the outer free-jet shear layer should also be examined in order to determine its importance.

(vi) Based on the results of the above studies, charts and calculation procedures should be developed and presented for converting jet noise measurements obtained in an anechoic free-jet facility to the corresponding in-flight situation.

6.2.1.2 Experimental program. Experiments should be performed in an anechoic free-jet facility to investigate the following aspects of its acoustic performance.

(i) Prior to any other testing, azimuthal symmetry of the jet noise field, after transmission through the rectangular free-jet boundary, should be experimentally investigated. If the jet noise field proves to be azimuthally asymmetric, the free-jet exit shape should be modified so as to give azimuthal symmetry for the jet noise field.

(ii) Refraction of sound by the mean flow field of the free-jet should be studied, using a single-frequency source placed in the jet flow. Phase measurements should be used to determine the orientation of the refracted waves.

(iii) Scattering of sound by turbulence in the free-jet shear layer should also be studied in more detail using a single-frequency source placed at various locations in the jet. Information in this case can be obtained by measuring the frequency spreading effect at different angles outside the free-jet.

(iv) The validity of in-flight jet noise data obtained from the free-jet facility should be checked empirically by means of a scaling test, in which results are compared from different primary nozzle sizes under the same test conditions. This will reveal the limitations imposed by having a finite area ratio (secondary/primary jet exit area).

6.2.2 Phase II - Mean Flow and Source Alteration Effects

This effort should be primarily experimental but should utilize previously developed theoretical results in conjunction with experimental results obtained under the current program to develop a source alteration model.

6.2.2.1 Experiment. Using a four-channel, two-point laser velocimeter system (or other acceptable instrumentation), extensive measurements should be made in the jet mixing and fully-developed regions for a cold jet mounted in a low-speed wind tunnel. The range of test parameters should be $0.45 \leq M_J \leq 2$ and $0.05 \leq V_T/V_J \leq 0.5$. In the supersonic experiments both conical and convergent-divergent nozzles should be tested so that the effect of shock containing flows can be determined. The following quantities should be determined.

(i) Mean velocity and turbulence intensity distributions for both the axial and radial components should be measured throughout the jet.

(ii) Spectra, cross-spectra and phase speeds (comparable to convection speed) should be determined from the two-point measurements for u', v' and u' - v' combinations.

(iii) Fourth-order cross-correlations and cross-spectra should be determined for the equivalent source function $(v_i \, v_j)$. This will provide all the information necessary to substantiate and/or empirically modify the source alteration model.

6.2.2.2 Theory. Theoretical programs are required to provide prediction of (a) the mean velocity and turbulence intensity distribution, (b) the turbulence jet noise source function distribution, and (c) the large-scale coherent turbulence structure source function (or more appropriately, the noise radiated from the large-scale turbulence structure in the presence of a relative velocity).

6.2.3 Phase III - Determination of Relative Velocity Effects on Jet Noise

In this phase, the effort should be primarily experimental, but should utilize previously developed theory to obtain a method of calculating the noise field of a jet in the forward flight condition.

6.2.3.1 Experimental program. An extensive set of noise measurements for both hot and cold jets should be made as follows:

(i) In the current exploratory program, cold jet noise measurements were taken at forty test conditions which consisted of combinations of five free-jet velocities and eight jet exit velocities. The range of this test program should be extended, including forward arc measurements if feasible in the available facility.

(ii) Shock associated noise measurements should be made over a range of free-jet and jet-exit velocity conditions.

(iii) The free-jet anechoic facility model jet air supply should be capable of delivering heated air up to 800°C. In this series of tests, approximately 200 combinations of jet velocity, jet temperature and free-jet velocity should be tested. The data should be examined in conjunction with the cold jet data to determine the appropriate scaling parameters.

(iv) Limited shock-associated noise measurements should be made for the heated jet case to validate the results on temperature effects from static jet tests.

6.2.3.2 Calculation of forward motion effects on jet noise from source alteration data. The information on source alteration effects associated with jet mixing in flight obtained from the Phase II program could be used to predict forward motion effects on far-field jet noise. For this purpose

the source alteration data should be combined with the jet noise radiation model, based on Lilley's equation, which has already been developed for static jets under Air Force/DOT contract (Contract F33615-C-2032).

6.2.3.3 Comparison of theory and experiment. The experimental jet noise data acquired under 6.2.3.1 should be corrected by the techniques developed under 6.2.1 and should be compared with the calculated result of 6.2.3.2 and with available full-scale in-flight data, as appropriate.

APPENDIX 2A

FLYOVER DATA ACQUISITION CONSIDERATIONS

The measurement of noise received on the ground from flying aircraft is very complicated and expensive. In order to ensure the accuracy of the measured data, and the subsequent comparison with static results, it is necessary to examine various aspects of data acquisition and correction procedures. In particular, detailed consideration should be given to the following five aspects of flyover noise tests:

(1) acquisition and analysis of non-stationary data,
(2) aircraft position and attitude,
(3) ground reflection effects,
(4) atmospheric attenuation corrections, and
(5) real atmosphere effects.

Furthermore, a study of each of the above aspects should consider (a) the procedure to be adopted, (b) the instrumentation requirements, and finally (c) the statistical accuracy of the measured data.

The problems associated with the acquisition and analysis of non-stationary flyover noise data are discussed in this Appendix.

ACQUISITION AND ANALYSIS OF NON-STATIONARY DATA

The acoustic signal received by a fixed far-field microphone from a static jet exhaust is random, but with stationary properties in the statistical sense. The accuracy of the measured data can therefore be increased to any desired level, simply by increasing the length (or time) of the data record. In contrast, in the case of a flying aircraft, the sound emission angle seen by a fixed ground-based observer is constantly changing with time. The sound pressure signal recorded by the microphone is thus non-stationary in nature, and the statistical accuracy of the measurements is limited.

To illustrate this feature, consider the sketch shown in Figure 2A.1, which shows the relationship between the sound reception time, t, and the reception angle ψ (i.e. the source-to-observer angle relative to the downstream jet axis at the time of reception). If the reception time is referenced to the time when the aircraft is directly above the microphone ($t = 0$ when $\psi = 90°$), then this relationship is

$$\tan \psi = \frac{H}{V_A t},$$
(2A-1)

where H is the normal height or distance of the flight path from the microphone, and V_A is the aircraft velocity. A sketch showing the variation of reception angle ψ with reception time t is also included in Figure 2A.1.
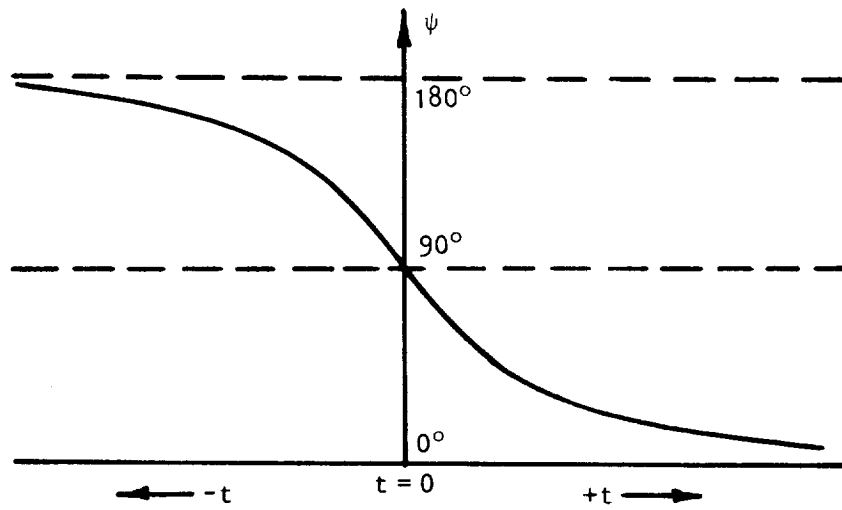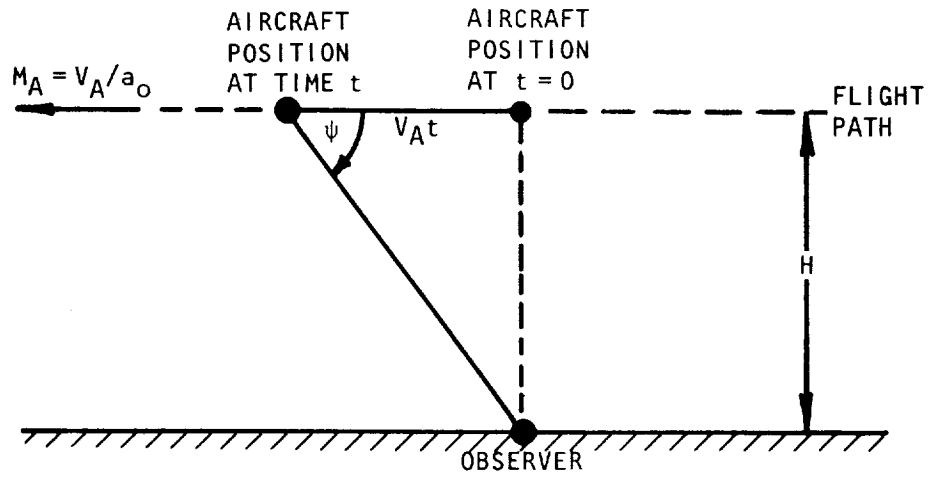
Figure 2A.1   Relationship between reception time (t) and reception angle (ψ).

From data acquisition considerations, the quantity of interest is the rate of change of angle ψ. Differentiation of equation (2A-1) with respect to time gives

$$\frac{d\psi}{dt} = -\frac{(H/V_A)}{(H/V_A)^2 + t^2} .$$

(2A-2)

Clearly, for fixed values of H and V_A, the rate of change of angle is maximum when $t = 0$. That is, the worst case is presented when the aircraft is directly above the microphone location.

In the study of inflight effects on jet noise, however, the comparison between static and flight results must be conducted at constant emission angles. It is therefore necessary to establish the relationship between the emission angle, θ_e, and the reception time, t. This can be obtained by deriving an expression which gives reception angle ψ as a function of emission angle θ_e. With reference to the geometry between these two angles defined in Figure 2A.2, the required result is obtained as

$$\tan \psi = \frac{\sin\theta_e}{M_A + \cos\theta_e} .$$

(2A-3)

Combining equations (2A-1) and (2A-3), for a pressure-time history recorded by a microphone, the time scale is related to the sound emission angle θ_e by

$$t = \frac{H}{V_A} (M_A \cosec \theta_e + \cot \theta_e).$$

(2A-4)

In order to obtain the inflight result at a specified emission angle θ_e from the non-stationary pressure-time history recorded by the microphone during a flyover test, the result has to be extracted from the continuous record. This is done by dividing the complete record into several smaller records, and the time-dependent pressure fluctuations within each of these records are assumed to possess locally stationary statistical properties. The length (or time Δt) of each of these records is clearly governed by the angular resolution (tolerable range of angular variation about a fixed value of θ_e under consideration) specified; as the resolution is increased, the available record length reduces.

Let us consider some typical examples. For an aircraft flying overhead at a height of $H = 152.4$ m and at a Mach number of 0.2 ($V_A = 68.6$ m/s) simple arithmetic, using the above equations, shows that in the worst cases, the record lengths (Δt) for various angular resolutions ($\Delta\theta_e$) are

$\Delta\theta_e$:	$4°$ ($\pm 2°$)	$6°$ ($\pm 3°$)	$10°$ ($\pm 5°$)
Δt:	0.155 sec.	0.25 sec.	0.4 sec.
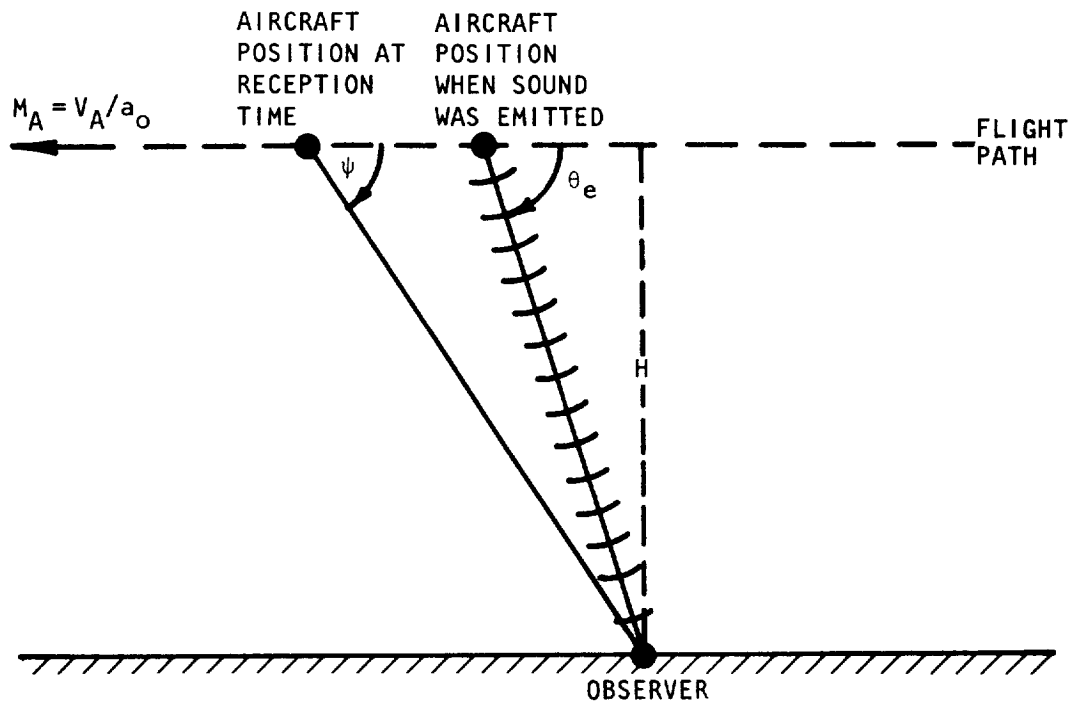
Figure 2A.2 Relationship between reception angle (ψ) and emission angle (θ_e).

It is clear that for tolerable angular resolution, the typical record length is rather small, usually of the order of 1/4 second. The accuracy of the frequency analysis of such small records is now examined.

The statistical quality of the data can be evaluated, at first in a preliminary manner, by examining the mean square error. For frequency analysis in constant percentage bands (for example, one-third octave analysis), the mean square error ϵ^2, where

$$\epsilon^2 = \frac{\text{mean square error}}{\text{true mean square value}} ,$$

can be expressed by the well-known result

$$\epsilon^2 \simeq \frac{1}{BT} . \tag{2A-5}$$

In the above equation, B is the bandwidth of the ideal filter under consideration, and T is the record length in seconds. For one-third octave analysis, the result can be written as

$$\epsilon^2 = \frac{1}{0.23\ T\ f_c} , \tag{2A-6}$$

where f_c is the center frequency of the one-third octave band. It is clear that for a fixed record length of time T, the mean square error increases as the frequency decreases. For a typical flyover test (T = 0.25 second), the mean square percentage errors are

$$f_c = 50\ \text{Hz}, \qquad \epsilon^2 \sim 35\%$$

$$f_c = 10\ \text{KHz}, \qquad \epsilon^2 \sim 0.2\%.$$

The statistical accuracy can further be expressed in terms of the confidence limits as determined from standard Chi-square distributions. The results can be obtained from any standard textbook on statistical analysis of stationary data.

For samples with n equivalent number of statistical degrees of freedom, where n = 2 BT, the measured mean square value s^2 and the true mean square value σ^2 are related by

$$\frac{s^2}{\sigma^2} = \frac{\chi^2}{n} \tag{2A-7}$$

where the value of χ^2 (Chi-square) for various confidence intervals may be obtained from standard statistical tables.

For the typical flyover test considered previously, the number of degrees of freedom at the lowest and highest one-third octave bands of interest are

$$f_c = 50 \text{ Hz}, \qquad B = 11.5 \text{ Hz}, \qquad n \sim 6$$
$$f_c = 10 \text{ KHz}, \qquad B = 2300 \text{ Hz}, \qquad n \sim 1150$$

for $T = 0.25$ second

The value of n at low frequencies is therefore rather small, and examination of statistical tables for chi-square distributions shows that the confidence level in the measured values of mean-square sound pressure at low frequencies is not high.

The statistical accuracy of the analysis at low frequencies can be improved by increasing the number of samples, and computing the arithmetic mean after analyzing all samples (record lengths). A description of the improvement in the statistical accuracy of the results derived from N samples can be obtained from any standard textbook on statistics, and the final result is that the standard deviation is inversely proportional to $N^{\frac{1}{2}}$. Thus, for large N, the measured (or sample) mean value approaches the true mean value.

In a flyover test, the required number of samples, for some specified statistical accuracy, can be obtained during a single aircraft flyover by utilizing a line of microphones set in the direction of the flight path. If the microphones are sufficiently far apart from each other to record uncorrelated (and hence necessarily independent) signals, and if each is analyzed and compared with the others after suitable time delays, a significant improvement in measurement accuracy can be achieved.

APPENDIX 2B

CALCULATIONS OF JET OPERATING CONDITIONS

In the experiments performed in the free jet facility and the low-speed wind tunnel, two factors alter the operating conditions from those used in a normal static jet test facility. Firstly, due to aerodynamic considerations, the plenum-to-jet area ratio is not large so that there is a finite velocity in the plenum or reservoir. Secondly, the jet is exhausting into a non-stationary stream so that the total pressure in the surrounding air does not equal the static pressure. The following analysis has been used to calculate the jet operating conditions. It is assumed that the static pressure in the plane of the primary jet exit is constant and, since the jet is unheated, the total temperature is also assumed to be constant. A sketch of the typical test setup is shown in Figure 2B.1, From the energy equation it is found that,

$$C_p T_R + \frac{V_R^2}{2} = C_p T_J + \frac{V_J^2}{2} = C_p T_T + \frac{V_T^2}{2} \qquad (2B-1)$$

so that,

$$\frac{T_J}{T_T} = 1 + \frac{(\gamma-1)}{2} \frac{V_J^2}{a_T^2} (\lambda^2 - 1), \qquad (2B-2)$$

where $\lambda = V_T/V_J$.

From the assumption of constant total temperature,

$$\frac{T_J}{T_T} = \frac{1 + (\gamma-1) V_J^2 \lambda^2 / 2 a_T^2}{1 + (\gamma-1) M_J^2 / 2}. \qquad (2B-3)$$

Combining equations 2.B.2 and 2.B.3, we get

$$M_J^2 = \frac{V_J^2/a_T^2}{1 + (\gamma-1) V_J^2 (\lambda^2 - 1)/2a_T^2} \qquad (2B-4a)$$

or

$$\frac{V_J^2}{a_T^2} = \frac{M_J^2}{1 + (\gamma-1) M_J^2 (1-\lambda^2)/2}. \qquad (2B-4b)$$

In order to calculate the velocity in the reservoir, the continuity of mass flow condition is used to give

$$\rho_R V_R A_R = \rho_J V_J A_J .$$

Letting the area ratio $A_J/A_R = \alpha$ $(\alpha \leq 1)$ then

V_T, p_T, T_T

V_R, p_R, T_R → V_J, p_T, T_J
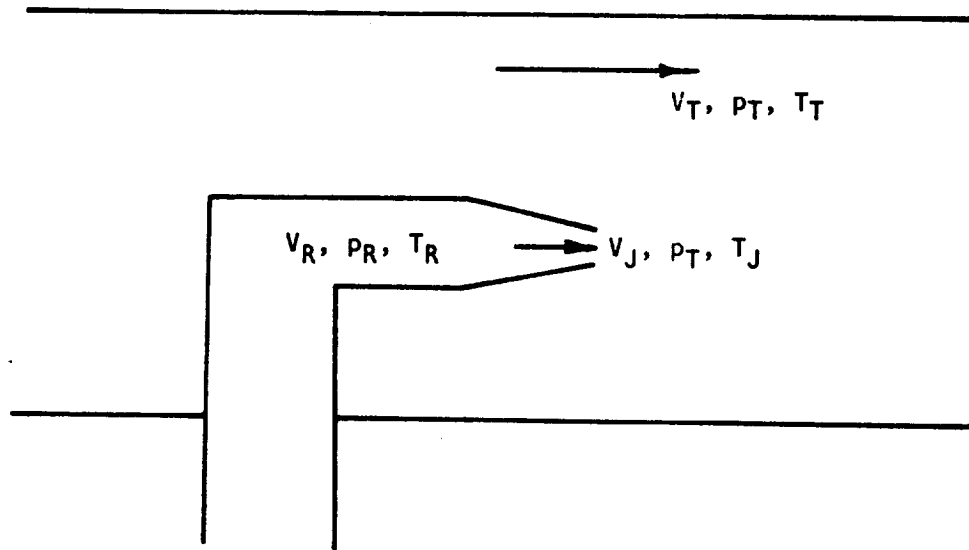
Figure 2B.1 Diagram of typical free-jet or wind tunnel facility.

228

$$\left(\frac{V_R}{a_R}\right)^2 = M_R^2 = \alpha^2 M_J^2 \left(\frac{T_J}{T_R}\right)^{\frac{(\gamma+1)}{(\gamma-1)}} \qquad (2B-5)$$

Since the total temperature is constant, the jet and reservoir temperatures are related by,

$$\frac{T_J}{T_R} = \frac{2 + (\gamma-1) M_R^2}{2 + (\gamma-1) M_J^2} \qquad (2B-6)$$

so that from (2B-6) and (2B-5) we obtain

$$\left(\frac{T_J}{T_R}\right)\left\{1 + \frac{(\gamma-1)}{2} M_J^2\right\} - 1 - \alpha^2 \frac{(\gamma-1)}{2} M_J^2 \left(\frac{T_J}{T_R}\right)^{\frac{(\gamma+1)}{(\gamma-1)}} = 0. \qquad (2B-7)$$

For a given value of M_J (or V_J/a_T from equation (2B-4)), the value of (T_J/T_R) can be calculated from equation (2B-7) by an iterative technique.

The static pressure ratio is given by

$$p_R/p_T = (T_R/T_J)^{\gamma/(\gamma-1)} \qquad (2B-8)$$

and the total pressure ratio is given by,

$$\frac{P_R}{P_T} = \frac{p_R}{p_T} \times \left| \frac{2 + (\gamma-1)M_R^2}{2 + (\gamma-1)\lambda^2 V_J^2/a_T^2} \right|^{\gamma/(\gamma-1)} \qquad (2B-9)$$

Consider the following example. We need to find the static and total pressure ratios for the following conditions,

$$\lambda = .25, \quad \alpha = .25 \quad \text{and} \quad M_J = .9.$$

From equation (2B-4b) $(V_J/a_T) = .838157$.

Iteration of equation (2B-7) using Newton-Raphson two times gives $(T_J/T_R) = .86334$, so that $M_R = .14518$ from equation (2B-5)

Thus, finally: $p_R/p_T = 1.667921$

and $P_R/P_T = 1.641591$.

Clearly the required jet operating conditions can be set using a measurement of either total or static pressure, whichever is experimentally more convenient.

APPENDIX 2C

TEST CONDITIONS AND MEASURED
(UNCORRECTED) TURBULENT MIXING NOISE DATA

TEST CONDITIONS

M = 1.0, CONVERGENT NOZZLE

Run Number	$\dfrac{V_J}{a_o}$	$\dfrac{V_T}{a_o}$	$\lambda \left(= \dfrac{V_T}{V_J}\right)$	$M_J \left(= \dfrac{V_J}{a_J}\right)$	$\dfrac{T_J}{T_T} \left(= \dfrac{T_J}{T_R}\right)$	$\dfrac{P_R}{P_T}$
7	0.400	0.019	0.047	0.407	0.969	1.1143
8	0.400	0.051	0.127	0.406	0.970	1.1139
9	0.400	0.100	0.251	0.406	0.970	1.1139
10	0.400	0.150	0.376	0.405	0.970	1.1135
11	0.400	0.200	0.500	0.404	0.970	1.1128
12	0.500	0.025	0.049	0.513	0.952	1.1870
13	0.500	0.051	0.101	0.513	0.952	1.1867
14	0.500	0.100	0.200	0.513	0.952	1.1865
15	0.500	0.150	0.300	0.512	0.952	1.1860
16	0.500	0.200	0.399	0.511	0.952	1.1855
17	0.600	0.030	0.050	0.623	0.930	1.2858
18	0.600	0.051	0.085	0.623	0.931	1.2851
19	0.600	0.100	0.167	0.622	0.931	1.2847
20	0.600	0.150	0.250	0.621	0.931	1.2837
21	0.600	0.200	0.333	0.620	0.931	1.2823
22	0.700	0.036	0.052	0.738	0.905	1.4176
23	0.700	0.051	0.072	0.737	0.905	1.4173
24	0.700	0.100	0.143	0.737	0.905	1.4163
25	0.700	0.150	0.215	0.736	0.905	1.4151
26	0.700	0.200	0.285	0.734	0.905	1.4134
27	0.801	0.042	0.052	0.858	0.875	1.5951
28	0.800	0.051	0.063	0.857	0.875	1.5934
29	0.800	0.100	0.125	0.856	0.875	1.5921
30	0.800	0.150	0.188	0.855	0.875	1.5903
31	0.800	0.200	0.250	0.853	0.876	1.5873
32	0.901	0.048	0.054	0.985	0.840	1.8344
33	0.900	0.051	0.056	0.984	0.841	1.8313
34	0.900	0.100	0.111	0.983	0.841	1.8291
35	0.900	0.150	0.167	0.981	0.841	1.8259
36	0.900	0.200	0.222	0.980	0.842	1.8216

233

M = 1.4, CONVERGENT-DIVERGENT NOZZLE

Run Number	$\dfrac{V_J}{a_o}$	$\dfrac{V_T}{a_o}$	$\lambda\left(=\dfrac{V_T}{V_J}\right)$	$M_J\left(=\dfrac{V_J}{a_J}\right)$	$\dfrac{T_J}{T_T}\left(=\dfrac{T_J}{T_R}\right)$	$\dfrac{P_R}{P_T}$
37	1.174	0.063	0.054	1.380	0.725	3.0610
38	1.175	0.100	0.085	1.381	0.725	3.0640
39	1.176	0.150	0.128	1.380	0.725	3.0611
40	1.178	0.200	0.170	1.380	0.725	3.0596

M = 1.7, CONVERGENT-DIVERGENT NOZZLE

Run Number	$\dfrac{V_J}{a_o}$	$\dfrac{V_T}{a_o}$	$\lambda\left(=\dfrac{V_T}{V_J}\right)$	$M_J\left(=\dfrac{V_J}{a_J}\right)$	$\dfrac{T_J}{T_T}\left(=\dfrac{T_J}{T_R}\right)$	$\dfrac{P_R}{P_T}$
42	1.343	0.077	0.057	1.683	0.638	4.7725
43	1.344	0.100	0.075	1.682	0.638	4.7709
44	1.346	0.150	0.112	1.683	0.638	4.7764
45	1.348	0.200	0.148	1.683	0.638	4.7760

234

RUN NUMBER 7

1/3 OCTAVE CENTER FREQ. HZ	MICRO PHONE NO. 1 ANGLE 30.0	MICRO PHONE NO. 2 ANGLE 37.5	MICRO PHONE NO. 3 ANGLE 45.0	MICRO PHONE NO. 4 ANGLE 52.5	MICRO PHONE NO. 5 ANGLE 60.0	MICRO PHONE NO. 6 ANGLE 67.5	MICRO PHONE NO. 7 ANGLE 75.0	MICRO PHONE NO. 8 ANGLE 82.5	MICRO PHONE NO. 9 ANGLE 90.0
200.0	60.9	56.0	56.5	55.0	55.4	57.2	54.4	55.7	52.9
250.0	61.8	58.6	59.0	56.8	56.7	56.6	55.4	56.5	54.2
315.2	64.0	61.5	60.0	59.0	58.2	58.2	57.5	58.7	56.9
400.0	65.1	63.4	61.2	60.5	58.9	59.6	59.6	59.3	57.8
500.0	66.1	63.9	62.1	61.2	60.3	60.8	60.5	59.9	60.4
630.0	67.7	65.8	63.4	62.5	61.9	62.0	61.6	60.7	61.6
800.0	68.1	66.5	63.8	64.1	63.4	63.1	61.7	61.0	61.7
1000.0	69.0	67.6	64.7	64.4	64.2	63.8	63.4	62.0	61.8
1250.0	69.8	68.6	65.8	66.1	64.7	64.4	64.2	63.4	63.0
1600.0	69.6	68.2	65.6	65.0	64.7	64.2	64.2	63.3	62.8
2000.0	69.2	68.4	66.0	66.2	65.5	64.6	64.8	63.4	62.7
2500.0	68.4	68.1	65.6	66.2	65.1	64.9	64.5	63.7	63.1
3150.0	67.5	68.0	65.6	66.1	65.1	65.2	64.3	63.7	63.6
4000.0	66.5	67.5	64.7	65.5	64.9	64.9	64.9	63.9	63.7
5000.0	65.8	66.6	64.4	65.1	64.6	64.5	64.6	63.4	63.1
6300.0	64.6	66.2	63.9	65.0	64.4	64.7	64.2	63.8	63.0
8000.0	63.2	64.7	62.7	63.4	63.7	63.8	62.1	63.4	62.8
10000.0	61.9	64.4	62.2	63.4	63.4	63.2	62.0	63.3	62.7
12500.0	60.7	63.6	61.3	62.6	63.0	62.8	62.8	63.0	62.5
16000.0	59.8	63.4	60.5	62.4	62.5	62.2	62.8	62.5	62.5
20000.0	58.7	62.0	59.2	61.5	61.9	61.4	61.4	61.9	61.5
25000.0	57.8	61.0	54.4	61.2	61.2	60.8	60.2	61.0	61.0
31500.0	56.8	59.9	57.2	60.3	60.3	59.7	59.7	60.0	60.0
40000.0	56.7	59.2	56.1	59.2	59.4	58.7	58.3	59.2	58.4
OVERALL SPL	79.6	79.2	76.8	77.4	76.8	76.6	76.2	75.8	75.5

RUN NUMBER 8

1/3 OCTAVE CENTER FREQ. HZ	MICROPHONE NO. 1 ANGLE 30.0	MICROPHONE NO. 2 ANGLE 37.5	MICROPHONE NO. 3 ANGLE 45.0	MICROPHONE NO. 4 ANGLE 52.5	MICROPHONE NO. 5 ANGLE 60.0	MICROPHONE NO. 6 ANGLE 67.5	MICROPHONE NO. 7 ANGLE 75.0	MICROPHONE NO. 8 ANGLE 82.5	MICROPHONE NO. 9 ANGLE 90.0
200.0	61.3	55.3	54.4	53.8	53.8	57.1	52.8	54.9	52.5
250.0	59.9	58.3	56.9	56.2	55.0	55.2	54.8	53.5	52.8
315.2	61.0	60.4	59.0	56.7	56.0	56.1	54.9	54.9	55.0
400.0	61.0	61.2	59.0	58.6	57.3	58.0	58.0	56.7	56.7
500.0	63.6	62.6	60.3	59.3	58.3	58.1	58.4	57.6	57.3
630.0	63.7	63.9	61.8	60.1	59.5	59.3	59.4	58.5	59.3
800.0	64.8	64.3	63.9	62.3	61.0	60.4	59.9	59.3	59.5
1000.0	65.6	65.5	63.6	62.2	62.1	61.8	61.2	60.0	59.5
1250.0	66.6	66.4	65.5	64.1	62.7	62.9	61.7	61.6	60.6
1600.0	65.8	65.8	65.6	64.3	62.8	62.4	61.6	61.0	60.3
2000.0	65.5	66.3	65.0	64.1	63.1	63.3	62.1	61.3	60.8
2500.0	65.6	66.0	65.1	64.1	63.3	62.9	62.2	61.9	61.4
3150.0	64.5	65.6	64.8	63.9	63.4	62.7	62.7	61.8	61.4
4000.0	63.7	65.6	64.6	63.5	62.9	62.5	63.1	61.8	61.5
5000.0	62.6	64.6	64.1	63.3	62.6	62.1	62.7	61.5	61.4
6300.0	61.6	64.5	63.8	62.4	62.5	62.4	62.5	61.8	61.4
8000.0	60.3	63.4	62.9	62.1	62.0	62.0	60.5	61.7	61.0
10000.0	59.4	62.7	62.4	61.6	61.6	62.1	60.6	61.4	61.4
12500.0	58.7	62.4	61.8	61.1	61.3	61.6	61.7	61.5	61.3
16000.0	59.6	62.3	61.3	60.9	60.9	61.2	61.7	61.3	61.3
20000.0	57.8	60.8	60.6	60.6	60.3	60.6	60.4	61.0	60.8
25000.0	56.4	60.1	60.3	60.4	59.7	60.1	59.4	60.4	60.5
31500.0	56.1	59.0	59.1	59.5	58.7	59.2	59.1	59.4	59.5
40000.0	57.2	58.4	57.9	59.0	58.5	58.2	57.7	58.5	57.9

| OVERALL SPL | 76.6 | 77.4 | 76.5 | 75.5 | 74.9 | 74.8 | 74.4 | 74.1 | 73.8 |

RUN NUMBER 9

1/3 OCTAVE CENTER FREQ. HZ	MICRO PHONE NO. 1 ANGLE 30.0	MICRO PHONE NO. 2 ANGLE 37.5	MICRO PHONE NO. 3 ANGLE 45.0	MICRO PHONE NO. 4 ANGLE 52.5	MICRO PHONE NO. 5 ANGLE 60.0	MICRO PHONE NO. 6 ANGLE 67.5	MICRO PHONE NO. 7 ANGLE 75.0	MICRO PHONE NO. 8 ANGLE 82.5	MICRO PHONE NO. 9 ANGLE 90.0
200.0	74.3	53.7	58.8	52.8	53.2	57.2	52.1	53.3	51.5
250.0	71.5	55.3	60.4	52.6	51.8	52.8	53.8	51.9	50.5
315.2	70.3	54.3	57.1	54.1	52.4	54.8	52.9	53.4	51.8
400.0	67.3	56.1	56.2	55.5	53.7	54.1	53.6	52.6	53.3
500.0	64.6	57.6	57.2	55.6	53.6	54.6	53.7	54.9	54.6
630.0	63.4	60.1	58.3	57.8	55.6	56.3	55.6	55.0	56.9
800.0	62.9	60.1	59.0	58.4	57.3	57.3	56.8	56.3	55.8
1000.0	62.0	61.0	60.5	59.4	58.5	58.4	57.8	57.0	55.1
1250.0	63.6	62.2	62.0	60.3	58.9	58.8	59.3	57.7	56.9
1600.0	62.8	62.1	61.7	60.7	58.9	59.3	58.7	56.9	57.4
2000.0	62.4	62.5	61.1	61.3	59.6	59.8	59.2	58.5	57.8
2500.0	62.1	62.3	61.0	60.7	59.2	59.6	58.6	59.1	57.7
3150.0	61.4	61.5	61.2	60.1	60.1	59.8	59.4	58.7	57.6
4000.0	60.9	61.3	61.3	60.3	60.1	60.0	60.0	58.6	58.1
5000.0	60.0	60.7	60.7	60.1	60.0	59.8	60.0	58.5	58.2
6300.0	59.5	60.8	60.5	60.2	60.1	60.3	59.8	59.4	58.4
8000.0	59.0	60.0	59.8	59.4	59.6	59.9	58.1	59.6	59.2
10000.0	58.0	59.9	59.2	58.9	59.3	59.8	58.1	59.7	59.7
12500.0	58.1	59.5	58.8	58.7	59.6	59.4	59.9	60.1	60.1
16000.0	59.5	59.7	58.2	58.4	59.6	59.3	60.7	60.7	60.9
20000.0	57.8	58.3	57.6	58.5	59.6	58.9	59.6	60.5	60.7
25000.0	56.6	57.3	56.9	58.3	59.0	58.6	58.6	60.0	60.7
31500.0	57.6	56.5	56.0	57.6	57.9	57.9	58.2	59.0	54.5
40000.0	60.5	56.2	55.2	56.9	57.7	57.2	56.7	58.1	57.8
OVERALL SPL	79.2	73.6	73.3	72.6	72.2	72.3	72.0	71.9	71.7

237

RUN NUMBER 10

1/3 OCTAVE CENTER FREQ. HZ	MICRO PHONE NO. 1 ANGLE 30.0	MICRO PHONE NO. 2 ANGLE 37.5	MICRO PHONE NO. 3 ANGLE 45.0	MICRO PHONE NO. 4 ANGLE 52.5	MICRO PHONE NO. 5 ANGLE 60.0	MICRO PHONE NO. 6 ANGLE 67.5	MICRO PHONE NO. 7 ANGLE 75.0	MICRO PHONE NO. 8 ANGLE 82.5	MICRO PHONE NO. 9 ANGLE 90.0
200.0	0.0	63.8	64.3	61.4	62.4	59.7	60.1	59.8	56.5
250.0	0.0	63.1	62.8	60.2	59.6	57.6	58.2	56.3	54.2
315.2	0.0	60.2	61.8	57.7	57.2	57.0	56.1	54.5	53.0
400.0	0.0	58.4	59.0	56.9	55.6	56.2	54.9	52.6	54.0
500.0	0.0	57.0	57.8	55.8	54.5	54.8	54.1	54.1	53.8
630.0	0.0	57.3	57.0	55.6	54.7	55.5	53.6	54.2	52.9
800.0	0.0	57.8	57.5	56.4	55.5	55.0	53.7	54.9	53.2
1000.0	0.0	58.3	58.1	57.2	55.9	55.8	54.3	54.1	53.7
1250.0	0.0	58.6	58.4	57.1	56.9	56.6	55.6	54.4	55.5
1600.0	0.0	58.5	58.3	57.5	56.2	56.3	55.0	55.1	54.1
2000.0	0.0	58.8	57.4	57.4	56.3	55.9	55.8	55.3	53.1
2500.0	0.0	58.3	58.0	57.7	56.8	56.2	56.1	55.4	55.0
3150.0	0.0	58.6	58.8	57.6	56.8	57.0	56.5	56.2	55.2
4000.0	0.0	58.9	57.9	57.5	57.1	56.4	56.5	55.8	55.8
5000.0	0.0	58.7	58.1	57.9	57.1	56.6	56.8	56.2	56.4
6300.0	0.0	59.6	58.3	58.1	58.0	57.9	57.6	57.3	57.8
8000.0	0.0	60.8	59.7	59.3	59.2	59.3	58.5	59.6	60.6
10000.0	0.0	60.3	59.3	58.9	59.4	59.2	58.5	59.7	60.9
12500.0	0.0	59.5	58.8	58.6	59.7	59.4	59.5	60.0	61.7
16000.0	0.0	59.2	60.0	59.8	60.5	60.0	60.7	60.4	61.9
20000.0	0.0	57.7	58.3	58.5	59.8	59.0	59.2	59.8	61.3
25000.0	0.0	56.3	56.5	57.6	59.3	58.6	57.3	59.1	61.4
31500.0	0.0	55.7	56.0	58.0	59.7	58.0	57.3	59.1	60.3
40000.0	0.0	56.1	57.8	59.3	60.7	58.4	57.2	59.4	58.8

| OVERALL SPL | 79.2 | 73.1 | 73.0 | 72.0 | 72.2 | 71.4 | 71.0 | 71.3 | 71.7 |

238

RUN NUMBER 11

1/3 OCTAVE CENTER FREQ. HZ	MICRO PHONE NO. 1 ANGLE 30.0	MICRO PHONE NO. 2 ANGLE 37.5	MICRO PHONE NO. 3 ANGLE 45.0	MICRO PHONE NO. 4 ANGLE 52.5	MICRO PHONE NO. 5 ANGLE 60.0	MICRO PHONE NO. 6 ANGLE 67.5	MICRO PHONE NO. 7 ANGLE 75.0	MICRO PHONE NO. 8 ANGLE 82.5	MICRO PHONE NO. 9 ANGLE 90.0
200.0	0.0	74.2	71.8	72.3	69.3	68.9	67.3	67.8	64.2
250.0	0.0	70.9	69.2	70.7	67.9	68.7	66.1	66.5	64.4
315.2	0.0	68.4	67.9	66.9	65.4	65.7	64.4	63.6	63.2
400.0	0.0	65.5	64.3	65.2	63.8	63.4	61.9	62.8	61.0
500.0	0.0	64.8	64.2	64.6	62.2	62.0	60.8	61.0	59.4
630.0	0.0	63.3	61.9	62.1	61.7	61.3	60.2	60.4	58.9
800.0	0.0	62.5	62.5	62.1	60.1	59.7	58.9	59.0	58.8
1000.0	0.0	62.4	62.2	60.9	60.5	59.7	59.5	59.4	58.2
1250.0	0.0	61.4	61.8	61.6	60.9	59.6	58.8	59.5	58.5
1600.0	0.0	61.6	61.0	61.0	60.2	59.5	59.3	58.4	57.8
2000.0	0.0	60.8	60.8	60.0	59.0	59.2	58.6	58.8	57.2
2500.0	0.0	60.5	60.2	59.9	59.2	58.1	58.2	58.3	57.0
3150.0	0.0	60.8	60.7	60.3	59.3	59.5	59.8	58.8	58.3
4000.0	0.0	60.6	60.0	60.3	59.8	60.2	60.9	60.4	59.5
5000.0	0.0	59.7	61.0	58.9	59.1	57.9	58.4	57.7	57.8
6300.0	0.0	59.3	59.3	58.7	58.8	58.4	58.6	58.3	58.6
8000.0	0.0	60.3	59.9	59.4	60.0	59.7	59.3	60.8	61.3
10000.0	0.0	60.2	59.9	59.3	60.1	60.1	59.0	61.0	61.6
12500.0	0.0	59.8	59.7	59.7	60.5	60.5	60.3	61.9	62.6
16000.0	0.0	59.5	60.2	60.5	61.4	60.8	61.6	61.8	63.1
20000.0	0.0	57.8	58.5	59.8	60.7	60.0	59.9	60.7	61.7
25000.0	0.0	56.5	57.0	59.5	60.3	58.9	57.7	59.8	60.6
31500.0	0.0	56.2	56.4	59.2	59.7	58.3	57.0	58.7	59.4
40000.0	0.0	56.3	56.9	59.7	60.1	58.3	57.1	59.7	59.9

| OVERALL SPL | 79.2 | 78.6 | 77.6 | 77.8 | 76.2 | 76.0 | 74.9 | 75.3 | 74.7 |

239

RUN NUMBER 12

1/3 OCTAVE CENTER FREQ. HZ	MICRO PHONE NO. 1 ANGLE 30.0	MICRO PHONE NO. 2 ANGLE 37.5	MICRO PHONE NO. 3 ANGLE 45.0	MICRO PHONE NO. 4 ANGLE 52.5	MICRO PHONE NO. 5 ANGLE 60.0	MICRO PHONE NO. 6 ANGLE 67.5	MICRO PHONE NO. 7 ANGLE 75.0	MICRO PHONE NO. 8 ANGLE 82.5	MICRO PHONE NO. 9 ANGLE 90.0
200.0	66.6	61.8	61.3	60.2	59.9	60.1	59.7	58.3	57.4
250.0	69.3	64.8	65.0	63.3	62.2	62.1	62.2	60.1	59.8
315.2	70.7	67.1	67.8	64.8	64.6	64.1	63.4	64.2	62.4
400.0	73.5	69.2	67.9	65.9	65.5	65.3	64.4	64.5	64.2
500.0	73.6	70.1	70.2	67.8	66.5	66.4	66.1	66.0	65.5
630.0	73.4	72.6	70.7	69.0	67.2	67.7	67.0	66.8	67.0
800.0	75.8	74.1	72.4	70.9	69.0	69.0	68.8	67.7	67.7
1000.0	77.4	74.7	73.4	71.6	70.2	70.0	69.7	68.9	68.3
1250.0	78.2	76.0	74.6	73.5	71.7	71.6	71.0	70.1	70.2
1600.0	77.7	76.1	74.6	73.6	71.9	71.2	70.6	70.1	69.4
2000.0	77.3	76.3	75.0	73.9	72.5	72.3	71.6	70.8	70.1
2500.0	77.1	76.4	75.4	74.3	72.7	72.3	72.3	71.1	70.6
3150.0	76.1	76.4	75.2	74.0	72.8	72.6	72.6	71.2	71.0
4000.0	74.7	76.1	74.9	73.5	72.6	72.5	72.5	70.9	70.9
5000.0	73.3	74.9	74.1	73.1	72.4	72.3	72.4	71.2	70.4
6300.0	72.2	74.8	73.9	73.3	72.2	72.5	72.1	71.3	70.7
8000.0	71.2	73.0	72.7	72.0	71.7	71.4	69.9	71.0	70.3
10000.0	70.0	72.1	71.9	71.5	71.8	70.9	69.6	70.1	69.4
12500.0	68.5	71.5	70.8	70.6	70.7	70.3	70.3	70.0	69.1
16000.0	67.4	71.1	70.0	70.1	70.0	69.7	70.0	69.5	68.7
20000.0	66.2	69.6	68.8	69.4	69.3	68.6	68.5	68.3	67.8
25000.0	64.9	68.6	68.4	69.0	68.7	67.8	67.1	67.4	67.1
31500.0	63.5	67.4	67.0	67.4	67.4	66.8	66.7	66.7	64.1
40000.0	62.5	66.7	65.6	66.5	66.2	65.9	65.4	66.1	65.1
OVERALL SPL	87.6	87.0	86.0	85.0	84.0	83.8	83.4	82.8	82.3

240

RUN NUMBER 13

1/3 OCTAVE CENTER FREQ. HZ	MICRO PHONE NO. 1 ANGLE 30.0	MICRO PHONE NO. 2 ANGLE 37.5	MICRO PHONE NO. 3 ANGLE 45.0	MICRO PHONE NO. 4 ANGLE 52.5	MICRO PHONE NO. 5 ANGLE 60.0	MICRO PHONE NO. 6 ANGLE 67.5	MICRO PHONE NO. 7 ANGLE 75.0	MICRO PHONE NO. 8 ANGLE 82.5	MICRO PHONE NO. 9 ANGLE 90.0
200.0	66.8	62.2	61.5	57.9	58.3	59.6	57.4	56.6	55.4
250.0	66.6	64.3	63.7	61.2	61.2	60.2	60.5	61.0	57.6
315.2	68.3	67.3	64.2	64.4	63.0	62.9	60.3	61.2	60.5
400.0	69.2	68.7	66.0	64.7	64.0	63.3	64.2	62.8	62.2
500.0	70.5	69.2	67.6	65.8	65.4	65.0	65.2	64.3	63.5
630.0	72.1	71.2	69.5	68.3	67.2	66.1	65.0	64.9	65.0
800.0	72.5	72.0	70.5	70.1	68.3	67.2	66.8	66.0	65.6
1000.0	74.5	73.4	71.5	70.6	69.4	68.7	66.3	66.9	66.4
1250.0	75.6	74.0	72.5	71.4	70.4	70.7	69.4	68.8	67.5
1600.0	76.1	74.4	73.1	71.8	70.1	70.3	69.2	69.3	67.7
2000.0	75.0	74.4	73.9	72.6	71.4	70.5	70.2	69.3	67.7
2500.0	74.7	74.4	74.0	72.6	71.1	71.0	70.1	69.6	68.4
3150.0	74.2	74.6	73.8	72.8	71.5	71.3	70.2	70.3	68.8
4000.0	72.9	74.4	73.5	72.3	71.3	71.5	70.8	70.1	68.9
5000.0	71.7	73.6	72.6	71.9	71.1	70.9	70.8	69.7	68.6
6300.0	70.8	73.4	72.8	72.1	71.0	71.3	70.5	70.0	68.4
8000.0	69.0	71.8	71.7	71.0	70.5	70.7	68.3	69.7	68.2
10000.0	68.0	71.7	71.2	70.4	70.3	70.6	68.3	69.3	67.3
12500.0	66.7	70.2	70.2	69.8	69.9	69.9	69.0	68.8	67.5
16000.0	65.5	69.9	69.8	69.5	68.8	69.2	68.8	68.4	67.2
20000.0	63.9	68.2	68.7	68.7	68.2	68.2	67.0	67.3	66.2
25000.0	62.7	67.3	68.1	68.2	67.4	67.5	66.1	66.6	65.8
31500.0	61.7	66.3	67.0	67.1	66.3	66.5	65.7	66.2	64.7
40000.0	61.2	65.4	65.4	66.0	65.0	65.7	64.5	65.6	63.7
OVERALL SPL	85.3	85.5	84.7	83.8	82.8	82.7	81.8	81.6	80.3

241

RUN NUMBER 14

1/3 OCTAVE CENTER FREQ. HZ	MICRO PHONE NO. 1 ANGLE 30.0	MICRO PHONE NO. 2 ANGLE 37.5	MICRO PHONE NO. 3 ANGLE 45.0	MICRO PHONE NO. 4 ANGLE 52.5	MICRO PHONE NO. 5 ANGLE 60.0	MICRO PHONE NO. 6 ANGLE 67.5	MICRO PHONE NO. 7 ANGLE 75.0	MICRO PHONE NO. 8 ANGLE 82.5	MICRO PHONE NO. 9 ANGLE 90.0
200.0	80.7	64.5	59.7	58.1	59.0	57.4	57.9	57.1	55.3
250.0	80.1	66.5	66.0	65.2	65.6	63.8	67.4	64.7	63.3
315.2	75.9	65.2	61.5	61.2	58.6	59.4	61.3	59.4	58.6
400.0	75.0	66.4	63.2	62.9	60.4	61.6	64.2	60.9	61.4
500.0	73.2	66.3	64.6	63.4	63.0	62.2	62.5	61.2	60.8
630.0	72.5	67.8	66.3	65.5	64.4	63.5	62.9	61.7	62.8
800.0	71.8	69.8	67.5	66.2	65.7	64.7	65.6	62.9	63.0
1000.0	72.6	71.0	68.7	68.1	66.2	65.7	66.3	64.1	63.5
1250.0	72.9	71.6	70.1	68.6	67.3	66.9	66.6	65.8	65.4
1600.0	72.2	72.0	70.5	69.0	68.1	67.1	67.3	65.8	65.4
2000.0	73.1	71.8	70.1	69.5	68.1	68.1	67.9	66.0	65.6
2500.0	72.6	72.0	70.4	69.6	68.2	68.3	67.6	66.3	65.8
3150.0	71.7	71.9	70.4	69.8	69.0	68.8	68.0	66.8	66.3
4000.0	70.7	72.1	70.2	69.7	68.9	68.6	68.3	66.7	66.5
5000.0	69.5	70.9	70.6	69.2	68.9	68.3	68.6	66.4	66.1
6300.0	68.6	70.7	69.6	69.6	68.5	68.7	67.6	66.6	66.1
8000.0	67.8	69.2	69.0	68.4	68.2	67.7	65.9	66.8	65.8
10000.0	66.7	68.4	68.3	67.4	67.8	67.5	65.6	66.4	65.7
12500.0	66.6	68.0	67.9	67.4	67.3	67.0	66.7	65.9	65.5
16000.0	66.1	67.5	67.3	67.1	67.0	66.4	66.3	65.8	65.4
20000.0	64.9	66.2	66.4	66.4	66.3	65.6	64.9	64.8	64.5
25000.0	64.1	65.2	65.6	66.0	65.7	64.8	64.0	64.3	64.1
31500.0	63.4	64.3	64.9	65.1	65.0	64.0	64.0	63.5	63.1
40000.0	64.6	64.2	64.0	64.5	64.2	63.1	62.8	63.4	62.3
OVERALL SPL	87.1	83.1	81.8	81.1	80.5	80.0	79.8	78.7	78.2

RUN NUMBER 15

1/3 OCTAVE CENTER FREQ. HZ	MICRO PHONE NO. 1 ANGLE 30.0	MICRO PHONE NO. 2 ANGLE 37.5	MICRO PHONE NO. 3 ANGLE 45.0	MICRO PHONE NO. 4 ANGLE 52.5	MICRO PHONE NO. 5 ANGLE 60.0	MICRO PHONE NO. 6 ANGLE 67.5	MICRO PHONE NO. 7 ANGLE 75.0	MICRO PHONE NO. 8 ANGLE 82.5	MICRO PHONE NO. 9 ANGLE 90.0
200.0	0.0	-4.7	-5.1	-4.6	-5.9	-5.6	-5.2	-4.1	-5.6
250.0	0.0	4.2	3.1	3.6	3.2	3.8	3.8	4.2	3.7
315.2	0.0	-6.7	-5.4	-5.5	-6.4	-7.4	-7.7	-7.2	-6.7
400.0	0.0	-5.2	-5.0	-5.0	-7.0	-7.1	-5.5	-6.5	-7.0
500.0	0.0	-4.6	-4.5	-5.2	-6.3	-6.2	-5.3	-5.6	-5.9
630.0	0.0	3.6	3.2	2.8	2.5	2.6	2.1	2.7	2.6
800.0	0.0	6.7	6.4	6.3	5.5	5.7	5.3	6.0	5.6
1000.0	0.0	5.0	3.9	2.8	2.0	1.9	1.0	0.8	-0.2
1250.0	0.0	9.3	7.6	6.9	6.0	6.0	4.4	4.8	4.2
1600.0	0.0	10.7	10.1	9.0	8.0	7.5	6.5	6.1	5.9
2000.0	0.0	13.3	12.0	11.4	10.2	9.9	9.3	8.7	8.6
2500.0	0.0	14.4	13.8	12.6	11.7	11.1	10.5	10.1	9.9
3150.0	0.0	16.3	15.5	14.7	13.9	12.9	12.6	11.9	12.0
4000.0	0.0	17.6	16.7	16.3	15.5	15.1	15.1	14.0	13.5
5000.0	0.0	18.9	18.9	17.8	17.1	16.6	16.5	15.5	15.2
6300.0	0.0	20.4	20.2	19.2	18.5	18.0	17.6	17.5	16.6
8000.0	0.0	20.7	21.0	19.9	19.5	18.8	17.2	18.8	18.4
10000.0	0.0	21.6	21.5	20.2	20.1	19.6	18.2	19.4	19.7
12500.0	0.0	21.9	21.4	20.7	21.0	20.2	20.1	20.4	20.5
16000.0	0.0	22.1	21.7	21.2	21.5	20.5	21.2	21.0	21.3
20000.0	0.0	20.9	20.9	20.8	20.9	20.2	20.0	20.3	20.6
25000.0	0.0	20.3	20.4	20.8	20.7	19.8	19.1	20.1	20.4
31500.0	0.0	19.7	20.0	20.6	20.6	19.4	19.2	20.0	20.1
40000.0	0.0	19.4	19.7	20.8	20.9	19.5	16.6	20.3	20.0
OVERALL SPL	87.1	31.3	31.2	30.8	30.7	29.8	29.4	29.9	29.9

RUN NUMBER 16

1/3 OCTAVE CENTER FREQ. HZ	MICRO PHONE NO. 1 ANGLE 30.0	MICRO PHONE NO. 2 ANGLE 37.5	MICRO PHONE NO. 3 ANGLE 45.0	MICRO PHONE NO. 4 ANGLE 52.5	MICRO PHONE NO. 5 ANGLE 60.0	MICRO PHONE NO. 6 ANGLE 67.5	MICRO PHONE NO. 7 ANGLE 75.0	MICRO PHONE NO. 8 ANGLE 82.5	MICRO PHONE NO. 9 ANGLE 90.0
200.0	0.0	73.8	72.4	71.0	77.0	72.5	70.4	70.1	64.6
250.0	0.0	71.6	70.9	70.1	72.1	70.4	68.8	65.3	63.4
315.2	0.0	70.1	68.4	67.3	68.9	68.9	67.1	64.7	62.5
400.0	0.0	68.1	66.3	65.9	66.6	66.2	64.1	63.8	61.5
500.0	0.0	66.7	65.4	65.6	65.4	63.0	63.4	60.9	60.6
630.0	0.0	66.2	64.6	64.2	61.6	63.0	62.7	62.2	61.7
800.0	0.0	65.7	64.2	64.1	62.9	62.1	62.7	62.1	61.7
1000.0	0.0	65.9	64.7	63.5	62.1	62.3	62.1	62.2	61.4
1250.0	0.0	66.6	64.9	63.7	63.2	63.0	63.6	62.1	61.0
1600.0	0.0	66.1	64.4	64.1	62.5	63.6	62.9	62.3	61.7
2000.0	0.0	66.3	64.2	63.6	62.7	63.4	63.1	62.5	62.1
2500.0	0.0	66.3	65.3	64.1	62.6	62.5	63.1	62.1	61.7
3150.0	0.0	66.7	65.4	64.1	63.2	63.8	63.7	63.0	62.7
4000.0	0.0	66.3	65.7	64.4	63.2	64.3	64.5	64.0	63.1
5000.0	0.0	65.9	64.9	63.7	62.7	62.6	64.2	62.5	62.4
6300.0	0.0	66.1	64.4	63.9	63.1	63.3	63.8	63.2	62.8
8000.0	0.0	65.6	64.1	63.5	63.2	63.5	62.7	64.0	63.8
10000.0	0.0	65.3	63.7	63.5	63.2	63.3	62.4	63.9	64.1
12500.0	0.0	64.8	63.3	63.3	62.9	63.7	63.7	64.2	64.8
16000.0	0.0	64.7	63.6	63.6	63.1	63.3	64.4	64.2	65.1
20000.0	0.0	63.3	62.5	63.0	62.8	62.8	62.8	63.4	64.1
25000.0	0.0	62.6	61.4	62.8	62.6	62.2	61.8	62.9	63.7
31500.0	0.0	61.9	61.3	62.9	62.7	61.9	62.0	62.9	63.4
40000.0	0.0	62.0	61.7	62.8	63.4	61.8	61.7	63.1	63.7

| OVERALL SPL | 87.1 | 81.0 | 79.7 | 79.0 | 80.7 | 79.1 | 78.3 | 77.7 | 76.9 |

244

RUN NUMBER 17

1/3 OCTAVE CENTER FREQ. HZ	MICRO PHONE NO. 1 ANGLE 30.0	MICRO PHONE NO. 2 ANGLE 37.5	MICRO PHONE NO. 3 ANGLE 45.0	MICRO PHONE NO. 4 ANGLE 52.5	MICRO PHONE NO. 5 ANGLE 60.0	MICRO PHONE NO. 6 ANGLE 67.5	MICRO PHONE NO. 7 ANGLE 75.0	MICRO PHONE NO. 8 ANGLE 82.5	MICRO PHONE NO. 9 ANGLE 90.0
200.0	72.9	68.0	66.2	65.5	64.2	62.6	61.1	63.4	61.5
250.0	74.4	70.1	69.0	67.8	67.0	67.0	66.4	66.4	64.2
315.2	75.4	72.3	70.6	68.8	69.0	67.7	66.8	67.2	66.7
400.0	77.5	74.7	72.9	71.2	70.0	69.4	69.2	68.4	68.6
500.0	79.5	76.4	74.1	72.5	70.9	70.5	71.0	69.6	71.0
630.0	80.2	77.7	75.7	74.8	73.1	72.7	72.2	71.0	71.5
800.0	81.8	79.7	77.4	76.0	75.3	74.5	73.4	72.8	72.7
1000.0	83.2	80.8	78.6	77.4	76.4	75.6	74.5	73.5	73.6
1250.0	84.1	82.1	80.5	78.8	77.2	76.8	76.6	76.2	75.0
1600.0	83.7	82.8	81.4	79.4	77.7	77.6	76.8	76.4	74.8
2000.0	84.0	83.3	81.9	80.1	78.6	78.4	78.0	76.5	75.4
2500.0	83.4	82.6	81.6	79.9	78.8	78.3	77.7	77.0	76.1
3150.0	82.8	83.0	81.5	80.1	78.8	78.5	78.3	77.3	76.7
4000.0	81.7	82.9	81.4	80.1	79.2	78.6	78.5	77.1	77.1
5000.0	80.4	81.8	80.6	79.9	79.2	78.2	78.8	77.3	76.8
6300.0	79.6	81.7	80.6	79.8	79.2	78.9	78.6	77.3	76.5
8000.0	77.7	80.0	79.5	78.8	78.7	77.9	76.0	77.0	76.2
10000.0	76.3	79.1	78.7	78.1	78.2	77.4	75.7	76.4	76.0
12500.0	74.8	78.3	77.6	77.4	77.9	76.8	76.3	75.9	75.5
16000.0	73.3	77.8	76.8	77.0	77.1	75.9	76.1	75.4	74.9
20000.0	71.4	76.0	75.8	75.8	76.4	75.0	74.2	74.1	73.6
25000.0	70.2	74.6	75.0	75.1	75.8	74.1	73.1	73.3	73.0
31500.0	68.7	73.3	73.7	73.9	74.4	72.9	72.8	72.4	71.9
40000.0	67.6	72.1	72.0	72.6	72.9	71.9	71.1	71.9	71.0

| OVERALL SPL | 93.8 | 93.5 | 92.2 | 91.1 | 90.4 | 89.7 | 89.2 | 88.6 | 88.0 |

RUN NUMBER 18

1/3 OCTAVE CENTER FREQ. HZ	MICRO PHONE NO. 1 ANGLE 30.0	MICRO PHONE NO. 2 ANGLE 37.5	MICRO PHONE NO. 3 ANGLE 45.0	MICRO PHONE NO. 4 ANGLE 52.5	MICRO PHONE NO. 5 ANGLE 60.0	MICRO PHONE NO. 6 ANGLE 67.5	MICRO PHONE NO. 7 ANGLE 75.0	MICRO PHONE NO. 8 ANGLE 82.5	MICRO PHONE NO. 9 ANGLE 90.0
200.0	75.0	67.2	64.0	65.0	64.1	63.2	62.9	61.4	60.8
250.0	73.9	70.3	68.4	66.6	65.4	66.1	65.7	64.7	63.5
315.2	74.2	72.3	69.4	68.8	67.5	67.7	66.4	67.0	66.8
400.0	76.5	74.1	71.6	69.6	68.4	69.6	68.3	69.8	68.5
500.0	78.1	75.6	73.2	71.3	70.2	70.7	69.8	69.9	69.7
630.0	79.0	77.3	74.6	73.1	71.9	72.3	71.7	71.2	71.2
800.0	80.3	79.0	77.2	75.2	73.8	74.0	72.9	72.1	72.0
1000.0	82.3	80.4	78.2	76.4	75.3	74.6	74.8	73.5	72.7
1250.0	82.8	82.0	79.6	77.7	76.7	76.3	75.6	75.2	74.1
1600.0	82.3	82.3	80.3	78.9	77.4	76.7	76.2	75.4	74.1
2000.0	82.4	82.4	80.8	79.2	77.5	77.3	76.9	76.0	74.9
2500.0	82.2	82.4	80.7	79.2	78.0	77.8	77.0	76.3	75.5
3150.0	81.7	82.7	80.7	79.6	78.7	78.4	77.6	76.5	76.2
4000.0	81.1	82.3	80.7	79.6	78.6	78.3	78.3	76.7	76.3
5000.0	79.5	81.5	80.3	79.4	78.4	78.3	78.5	76.5	76.0
6300.0	78.4	81.8	80.7	79.6	78.5	78.2	77.9	76.8	76.2
8000.0	76.7	80.2	79.5	78.4	78.2	77.8	75.7	76.6	75.8
10000.0	74.8	79.2	74.7	77.9	77.5	77.0	75.5	75.9	75.4
12500.0	73.2	78.4	77.7	77.1	77.3	76.8	76.3	75.7	75.0
16000.0	71.8	77.5	76.9	76.5	76.4	76.0	75.9	75.1	74.2
20000.0	70.0	75.8	75.7	75.6	75.5	74.9	74.3	74.0	73.2
25000.0	68.7	74.3	75.0	74.9	74.6	73.9	73.1	73.1	72.4
31500.0	67.2	72.7	73.6	73.5	73.4	72.8	72.6	72.1	71.4
40000.0	66.3	71.7	72.2	72.3	72.0	71.9	71.3	71.7	70.5
OVERALL SPL	92.6	93.2	91.7	90.5	89.7	89.4	88.8	88.1	87.4

RUN NUMBER 19

1/3 OCTAVE CENTER FREQ. HZ	MICROPHONE NO. 1 ANGLE 30.0	MICROPHONE NO. 2 ANGLE 37.5	MICROPHONE NO. 3 ANGLE 45.0	MICROPHONE NO. 4 ANGLE 52.5	MICROPHONE NO. 5 ANGLE 60.0	MICROPHONE NO. 6 ANGLE 67.5	MICROPHONE NO. 7 ANGLE 75.0	MICROPHONE NO. 8 ANGLE 82.5	MICROPHONE NO. 9 ANGLE 90.0
200.0	73.8	63.8	63.5	62.1	61.4	60.8	61.2	60.7	57.7
250.0	73.5	66.6	66.5	64.7	64.6	63.4	63.0	62.8	61.3
315.2	74.1	69.0	68.0	65.7	65.4	66.2	64.2	65.0	63.3
400.0	74.3	71.4	68.4	67.8	67.4	68.0	66.0	67.0	65.4
500.0	75.0	72.1	71.6	69.4	68.4	68.5	66.6	67.9	67.5
630.0	74.6	73.8	72.1	70.7	70.0	69.6	69.0	68.8	68.2
800.0	75.8	75.7	75.0	72.8	71.8	71.0	70.4	70.3	69.7
1000.0	77.1	77.0	75.7	74.0	73.3	73.6	71.9	71.7	70.3
1250.0	78.5	79.0	77.4	75.6	74.5	74.0	73.3	72.8	72.1
1600.0	77.8	79.3	77.6	76.1	75.0	74.4	73.4	73.2	72.0
2000.0	77.8	79.6	78.2	76.7	76.4	75.2	74.3	73.5	72.9
2500.0	78.1	79.7	78.7	77.0	76.4	75.6	74.2	73.9	73.2
3150.0	77.7	79.4	78.5	77.2	76.4	75.9	74.7	73.9	74.1
4000.0	77.4	79.4	78.4	77.3	76.9	76.1	75.8	74.1	73.8
5000.0	76.3	78.4	78.1	77.2	76.4	75.9	75.6	74.2	73.8
6300.0	75.1	78.3	77.7	76.3	76.7	76.1	75.0	74.6	73.9
8000.0	73.7	76.7	76.9	76.1	76.3	75.5	73.3	74.4	73.4
10000.0	72.5	76.3	76.1	74.8	76.0	75.0	73.0	73.9	73.0
12500.0	71.7	75.3	75.5	75.1	75.5	74.5	74.0	73.5	72.5
16000.0	70.4	74.7	74.7	74.6	74.7	73.9	73.8	72.9	71.9
20000.0	68.8	73.0	73.6	73.6	74.0	72.9	72.3	72.0	70.9
25000.0	67.1	72.0	72.8	73.0	73.0	72.1	71.2	71.1	70.3
31500.0	65.7	70.8	71.7	72.0	71.9	70.9	71.2	70.4	69.2
40000.0	65.0	69.9	71.0	71.1	71.0	70.3	71.0	70.2	68.3
OVERALL SPL	86.9	90.1	89.3	88.2	87.9	87.2	86.3	85.9	85.1

247

RUN NUMBER 20

1/3 OCTAVE CENTER FREQ. HZ	MICRO PHONE NO. 1 ANGLE 30.0	MICRO PHONE NO. 2 ANGLE 37.5	MICRO PHONE NO. 3 ANGLE 45.0	MICRO PHONE NO. 4 ANGLE 52.5	MICRO PHONE NO. 5 ANGLE 60.0	MICRO PHONE NO. 6 ANGLE 67.5	MICRO PHONE NO. 7 ANGLE 75.0	MICRO PHONE NO. 8 ANGLE 82.5	MICRO PHONE NO. 9 ANGLE 90.0
200.0	85.5	76.6	66.6	63.4	63.4	62.8	64.1	61.0	58.4
250.0	86.2	73.6	65.5	64.2	64.7	62.6	63.5	61.9	59.0
315.2	85.7	72.8	66.3	64.4	64.6	63.6	64.0	62.0	62.4
400.0	79.0	70.8	66.9	65.0	64.4	64.4	63.2	64.0	63.0
500.0	78.0	70.5	68.0	65.8	65.2	66.3	64.4	64.4	64.9
630.0	77.6	71.7	69.6	67.6	66.9	67.6	66.1	65.5	65.8
800.0	77.6	73.0	71.0	70.8	68.6	68.7	68.4	66.3	66.2
1000.0	76.7	74.1	72.7	72.4	69.6	69.9	69.3	68.0	67.5
1250.0	76.8	75.8	75.0	73.4	70.8	71.4	70.5	69.8	69.5
1600.0	76.7	76.0	75.0	73.5	72.3	71.7	70.6	70.1	69.0
2000.0	76.6	77.2	75.2	73.9	73.0	72.5	71.8	70.6	69.6
2500.0	76.5	76.7	75.7	74.8	73.1	72.4	71.9	70.8	70.1
3150.0	76.0	76.2	76.0	74.8	73.8	73.1	72.3	71.6	71.0
4000.0	75.3	76.5	76.0	74.8	73.8	73.2	73.1	71.7	70.8
5000.0	74.2	76.2	75.5	74.4	74.0	73.1	72.9	71.4	70.9
6300.0	73.1	75.8	75.3	73.7	74.1	73.2	72.8	72.0	71.2
8000.0	72.5	74.6	74.7	73.6	73.6	72.9	70.6	71.8	71.3
10000.0	71.4	74.2	73.8	72.6	73.3	72.4	70.4	71.3	70.9
12500.0	70.4	74.0	73.3	72.1	72.9	72.1	71.5	71.0	70.7
16000.0	70.1	73.3	72.7	71.2	72.2	71.5	71.6	70.6	70.5
20000.0	68.4	71.9	71.7	71.2	71.4	70.5	69.7	69.8	69.2
25000.0	66.8	70.6	70.8	70.7	70.8	69.9	68.4	69.0	68.8
31500.0	66.8	70.0	69.8	70.0	69.9	68.9	68.0	68.5	68.1
40000.0	67.8	69.1	68.9	69.2	69.2	68.2	66.9	68.3	67.7
OVERALL SPL	92.6	88.2	86.8	85.9	85.2	84.5	83.8	83.2	82.7

248

RUN NUMBER 21

1/3 OCTAVE CENTER FREQ. HZ	MICRO PHONE NO. 1 ANGLE 30.0	MICRO PHONE NO. 2 ANGLE 37.5	MICRO PHONE NO. 3 ANGLE 45.0	MICRO PHONE NO. 4 ANGLE 52.5	MICRO PHONE NO. 5 ANGLE 60.0	MICRO PHONE NO. 6 ANGLE 67.5	MICRO PHONE NO. 7 ANGLE 75.0	MICRO PHONE NO. 8 ANGLE 82.5	MICRO PHONE NO. 9 ANGLE 90.0
200.0	0.0	75.0	73.1	70.5	68.2	70.4	71.2	68.3	65.6
250.0	0.0	73.7	71.2	69.2	68.4	70.4	69.0	66.8	65.6
315.2	0.0	71.4	69.6	67.3	66.8	68.4	68.7	64.3	63.7
400.0	0.0	69.9	67.9	66.6	65.3	65.8	66.1	64.4	64.3
500.0	0.0	69.5	68.2	67.6	65.5	65.6	65.0	65.2	64.2
630.0	0.0	69.9	68.6	67.2	65.5	65.4	64.8	65.6	64.6
800.0	0.0	71.4	69.3	68.3	67.0	67.0	66.4	65.0	65.3
1000.0	0.0	72.2	70.2	69.5	68.3	67.1	67.5	66.7	65.0
1250.0	0.0	73.9	71.7	70.6	69.3	68.8	68.6	67.9	66.9
1600.0	0.0	73.8	72.5	71.0	69.9	69.0	68.3	68.3	66.8
2000.0	0.0	74.6	72.9	71.3	69.7	69.7	68.4	68.3	67.6
2500.0	0.0	74.5	72.8	71.7	70.0	69.9	69.2	68.8	68.2
3150.0	0.0	74.7	73.0	71.7	71.2	70.3	70.1	69.6	68.5
4000.0	0.0	74.6	72.9	71.9	71.1	70.4	70.7	69.6	68.9
5000.0	0.0	74.2	72.4	71.7	71.1	70.1	71.1	69.2	68.7
6300.0	0.0	73.9	72.2	71.9	71.4	70.2	70.5	69.8	69.1
8000.0	0.0	72.7	71.7	71.0	70.9	70.1	68.9	70.0	69.3
10000.0	0.0	72.2	71.0	70.7	70.8	69.9	68.5	69.4	69.1
12500.0	0.0	72.0	70.7	70.5	70.7	69.8	69.6	69.4	69.1
16000.0	0.0	71.6	70.1	70.2	70.2	69.4	09.6	68.8	68.8
20000.0	0.0	70.2	69.1	69.4	69.5	68.4	67.9	68.1	67.8
25000.0	0.0	69.2	68.2	68.9	68.8	67.7	66.9	67.3	67.3
31500.0	0.0	68.5	67.2	68.1	68.0	66.8	67.0	66.9	66.8
40000.0	0.0	68.3	66.6	67.9	67.4	66.5	66.9	67.1	66.7
OVERALL SPL	92.6	86.4	84.7	83.9	83.1	82.7	82.5	81.8	81.1

249

RUN NUMBER 22

1/3 OCTAVE CENTER FREQ. HZ	MICRO PHONE NO. 1 ANGLE 30.0	MICRO PHONE NO. 2 ANGLE 37.5	MICRO PHONE NO. 3 ANGLE 45.0	MICRO PHONE NO. 4 ANGLE 52.5	MICRO PHONE NO. 5 ANGLE 60.0	MICRO PHONE NO. 6 ANGLE 67.5	MICRO PHONE NO. 7 ANGLE 75.0	MICRO PHONE NO. 8 ANGLE 82.5	MICRO PHONE NO. 9 ANGLE 90.0
200.0	76.2	70.9	69.4	69.5	68.3	67.9	67.4	66.9	63.5
250.0	76.6	74.9	73.8	71.5	69.6	70.7	71.8	70.1	66.9
315.2	80.2	78.1	74.6	72.6	71.5	72.4	71.7	71.7	70.7
400.0	82.7	79.4	77.2	75.2	74.6	74.0	74.5	73.8	72.5
500.0	84.7	81.0	79.2	77.3	75.8	76.0	75.5	74.8	73.7
630.0	85.5	83.7	80.4	79.0	77.8	76.6	76.4	75.4	75.0
800.0	88.0	84.2	82.3	80.7	79.3	78.6	78.2	76.8	76.9
1000.0	88.9	86.9	83.9	83.0	80.5	80.3	79.5	78.9	77.2
1250.0	89.8	88.0	85.4	83.6	82.1	81.8	81.0	80.6	78.8
1600.0	89.8	88.7	86.5	84.4	82.5	82.2	82.0	81.0	79.4
2000.0	89.6	89.2	87.3	85.4	83.4	83.7	82.5	81.3	80.1
2500.0	89.4	88.7	87.4	85.4	83.9	83.9	82.5	81.9	80.4
3150.0	88.3	89.0	87.1	86.0	84.4	84.0	83.7	82.6	81.0
4000.0	87.5	88.8	87.2	86.0	84.4	84.3	83.9	82.8	81.8
5000.0	86.2	87.8	87.2	86.2	84.9	84.2	83.9	82.5	81.6
6300.0	84.7	87.8	86.6	86.2	85.2	84.4	83.8	82.7	81.9
8000.0	83.4	85.9	85.8	85.2	84.5	84.0	81.8	82.8	81.4
10000.0	81.9	85.5	85.2	84.4	94.0	83.5	81.6	82.5	81.4
12500.0	80.5	84.4	84.4	84.0	83.9	82.8	82.4	81.9	80.8
16000.0	79.2	84.0	83.4	83.5	83.2	82.3	82.1	81.3	80.2
20000.0	77.5	82.2	82.2	82.5	82.3	81.3	80.6	80.1	78.9
25000.0	76.1	80.6	81.6	82.2	81.6	80.3	79.4	79.3	78.2
31500.0	74.2	79.2	80.0	80.7	80.4	79.3	79.0	78.2	77.1
40000.0	72.8	78.1	78.2	79.3	78.9	78.1	77.6	77.7	76.0
OVERALL SPL	99.4	99.4	98.0	97.0	95.8	95.3	94.6	93.9	92.7

RUN NUMBER 23

1/3 OCTAVE CENTER FREQ. HZ	MICROPHONE NO. 1 ANGLE 30.0	MICROPHONE NO. 2 ANGLE 37.5	MICROPHONE NO. 3 ANGLE 45.0	MICROPHONE NO. 4 ANGLE 52.5	MICROPHONE NO. 5 ANGLE 60.0	MICROPHONE NO. 6 ANGLE 67.5	MICROPHONE NO. 7 ANGLE 75.0	MICROPHONE NO. 8 ANGLE 82.5	MICROPHONE NO. 9 ANGLE 90.0
200.0	78.1	70.8	68.8	69.6	68.7	66.6	65.4	65.3	64.1
250.0	79.0	74.1	72.4	71.6	70.2	70.7	70.0	69.6	68.1
315.0	79.7	75.8	75.2	73.0	72.1	72.2	71.6	71.4	70.1
400.0	82.0	78.5	75.9	75.5	72.9	72.9	74.0	71.9	72.1
500.0	83.6	80.2	78.4	77.0	74.5	74.9	74.5	74.0	73.6
630.0	85.5	83.1	79.7	78.2	76.1	76.6	75.8	74.6	75.0
800.0	87.0	84.3	82.0	80.2	78.0	78.6	78.0	76.1	75.2
1000.0	89.0	85.7	83.6	81.3	80.1	79.8	79.0	77.7	76.6
1250.0	89.5	87.5	85.4	82.9	81.8	81.6	80.2	80.1	78.6
1600.0	89.0	87.8	85.5	84.0	82.2	81.9	80.9	80.1	78.9
2000.0	89.6	88.7	86.2	85.2	83.0	82.8	82.0	80.6	79.6
2500.0	88.6	88.0	86.7	85.1	83.4	83.1	81.9	81.1	80.0
3150.0	87.6	88.3	87.0	85.3	84.4	83.8	82.7	82.1	80.6
4000.0	86.8	88.7	87.1	85.7	84.3	83.7	83.4	81.7	81.2
5000.0	85.4	87.8	86.6	85.9	84.2	83.7	83.3	81.5	81.1
6300.0	84.6	87.6	86.8	86.2	84.8	84.5	83.6	82.1	81.3
8000.0	82.9	85.7	85.7	85.0	84.1	83.5	81.4	82.1	80.8
10000.0	81.7	85.1	85.1	84.8	84.0	83.3	81.1	81.3	80.9
12500.0	80.3	84.4	84.1	84.0	83.4	82.8	82.0	81.2	80.1
16000.0	78.8	83.8	83.5	83.7	82.6	82.1	81.5	80.7	79.6
20000.0	77.1	81.9	82.1	82.5	81.8	80.9	80.1	79.6	78.3
25000.0	75.7	80.8	81.4	82.1	81.0	80.1	78.7	78.8	77.6
31500.0	73.6	79.4	80.0	80.8	79.8	78.9	78.5	77.8	76.5
40000.0	72.2	78.5	78.5	79.3	78.5	77.9	77.1	77.4	75.6
OVERALL SPL	99.0	99.0	97.7	96.7	95.4	95.0	94.0	93.2	92.2

RUN NUMBER 24

1/3 OCTAVE CENTER FREQ. HZ	MICROPHONE NO. 1 ANGLE 30.0	MICROPHONE NO. 2 ANGLE 37.5	MICROPHONE NO. 3 ANGLE 45.0	MICROPHONE NO. 4 ANGLE 52.5	MICROPHONE NO. 5 ANGLE 60.0	MICROPHONE NO. 6 ANGLE 67.5	MICROPHONE NO. 7 ANGLE 75.0	MICROPHONE NO. 8 ANGLE 82.5	MICROPHONE NO. 9 ANGLE 90.0
200.0	74.8	68.8	66.6	65.4	65.3	65.2	63.7	63.0	61.0
250.0	75.9	71.2	69.9	68.4	68.2	68.1	66.8	66.1	65.0
315.2	76.1	73.6	72.3	70.8	69.5	69.6	67.7	67.8	67.7
400.0	80.6	75.0	73.4	73.3	71.0	71.2	70.5	70.0	69.3
500.0	81.7	77.4	75.1	73.8	72.1	72.7	72.0	71.2	70.8
630.0	82.9	78.8	77.0	75.8	74.2	74.1	73.5	72.6	72.4
800.0	85.0	80.6	79.0	77.2	75.8	75.6	74.0	73.9	72.6
1000.0	86.1	82.3	80.1	79.4	77.5	77.5	76.4	75.5	73.4
1250.0	87.3	83.5	82.5	81.2	79.0	79.5	77.9	77.6	75.8
1600.0	87.5	84.2	83.2	82.4	80.0	79.6	78.3	77.8	75.6
2000.0	80.7	85.4	83.6	82.8	80.7	80.1	79.5	78.4	76.5
2500.0	82.3	85.1	83.9	83.5	80.7	80.5	79.5	78.5	77.3
3150.0	86.0	85.4	84.3	83.4	81.6	81.5	80.0	79.2	77.8
4000.0	85.1	85.6	84.4	83.8	82.1	81.7	80.9	79.3	78.3
5000.0	84.0	85.2	84.4	83.5	82.0	81.8	81.2	79.3	78.2
6300.0	82.6	85.0	85.2	83.8	82.0	82.1	80.6	79.1	77.6
8000.0	81.4	83.6	83.9	82.8	81.9	81.5	79.0	79.5	78.0
10000.0	80.1	83.2	83.6	82.2	81.7	81.3	78.8	78.8	77.1
12500.0	79.4	82.8	82.7	81.4	81.2	80.8	79.9	78.8	77.3
16000.0	77.7	82.0	81.9	81.3	80.5	80.1	79.7	78.3	76.8
20000.0	76.1	80.6	80.5	80.4	80.0	79.2	78.2	77.1	75.5
25000.0	74.3	79.4	79.8	79.9	79.2	78.3	77.0	76.2	74.8
31500.0	72.5	78.1	78.3	78.5	78.3	77.1	76.7	75.0	73.7
40000.0	71.6	77.7	77.3	77.5	77.5	76.3	76.1	74.6	72.8
OVERALL SPL	96.9	96.1	95.4	94.6	93.1	92.8	91.6	90.7	89.2

252

RUN NUMBER 25

1/3 OCTAVE CENTER FREQ. HZ	MICRO PHONE NO. 1 ANGLE 30.0	MICRO PHONE NO. 2 ANGLE 37.5	MICRO PHONE NO. 3 ANGLE 45.0	MICRO PHONE NO. 4 ANGLE 52.5	MICRO PHONE NO. 5 ANGLE 60.0	MICRO PHONE NO. 6 ANGLE 67.5	MICRO PHONE NO. 7 ANGLE 75.0	MICRO PHONE NO. 8 ANGLE 82.5	MICRO PHONE NO. 9 ANGLE 90.0
200.0	93.8	70.3	67.8	66.2	66.1	66.5	62.7	64.1	61.0
250.0	93.7	71.4	69.8	67.9	66.2	67.7	66.2	66.2	65.0
315.2	92.9	72.5	69.7	68.6	67.0	68.2	68.1	67.0	66.1
400.0	92.8	74.1	72.2	69.7	68.2	69.8	69.2	68.3	68.5
500.0	90.4	75.0	73.1	72.0	69.8	71.2	70.2	70.0	70.1
630.0	86.6	78.0	74.6	73.1	71.6	72.3	71.0	70.6	71.4
800.0	85.4	78.8	76.9	75.0	74.0	74.1	72.8	71.8	71.7
1000.0	86.6	80.7	78.8	76.6	75.2	75.4	74.5	73.4	72.6
1250.0	86.5	82.1	80.6	79.0	76.7	77.1	75.8	75.3	74.8
1600.0	85.0	83.0	81.3	79.7	77.5	77.2	76.1	75.9	75.2
2000.0	85.4	83.6	81.7	79.9	78.4	78.3	77.5	76.5	75.7
2500.0	84.8	83.5	82.5	80.6	78.8	78.5	76.0	77.2	76.3
3150.0	84.7	83.5	82.4	80.8	79.5	79.6	78.8	77.5	77.1
4000.0	84.0	83.8	82.5	81.2	79.7	79.7	79.6	77.8	77.4
5000.0	83.5	83.2	82.3	81.1	79.7	79.4	79.6	77.7	77.6
6300.0	82.6	83.3	82.3	81.0	79.9	79.9	79.3	78.3	77.4
8000.0	81.8	81.9	81.5	80.6	79.7	79.6	77.5	78.0	77.5
10000.0	80.7	81.5	80.5	80.8	79.2	79.1	77.1	77.6	77.1
12500.0	79.7	80.8	80.1	80.0	79.2	78.6	78.2	77.6	76.8
16000.0	78.6	80.4	79.2	79.3	78.5	77.6	77.8	76.9	76.2
20000.0	76.4	78.7	78.0	78.5	77.6	76.6	76.1	75.9	74.9
25000.0	75.0	77.2	77.1	77.7	76.6	75.8	74.5	75.0	74.2
31500.0	73.8	75.7	75.9	76.5	75.4	74.7	73.9	73.7	73.0
40000.0	73.5	74.6	74.7	75.3	74.2	73.9	72.6	73.4	72.3
OVERALL SPL	101.4	94.4	93.2	92.3	90.9	90.7	89.9	89.2	8A.6

253

RUN NUMBER 26

1/3 OCTAVE CENTER FREQ. HZ	MICRO PHONE NO. 1 ANGLE 30.0	MICRO PHONE NO. 2 ANGLE 37.5	MICRO PHONE NO. 3 ANGLE 45.0	MICRO PHONE NO. 4 ANGLE 52.5	MICRO PHONE NO. 5 ANGLE 60.0	MICRO PHONE NO. 6 ANGLE 67.5	MICRO PHONE NO. 7 ANGLE 75.0	MICRO PHONE NO. 8 ANGLE 82.5	MICRO PHONE NO. 9 ANGLE 90.0
200.0	0.0	73.6	73.6	72.1	71.7	70.3	71.6	68.2	64.7
250.0	0.0	72.8	71.9	72.2	68.9	69.5	70.0	68.1	65.0
315.2	0.0	71.6	70.4	70.9	68.6	67.9	68.1	67.8	66.4
400.0	0.0	72.1	70.5	70.8	68.1	68.1	66.5	67.8	66.4
500.0	0.0	72.4	70.5	70.2	69.0	68.7	67.6	67.9	68.1
630.0	0.0	74.2	72.1	71.3	70.1	70.2	68.4	68.4	68.4
800.0	0.0	76.2	74.2	73.7	72.1	72.9	70.7	70.3	69.2
1000.0	0.0	77.4	75.5	75.0	73.2	74.1	72.8	71.0	70.0
1250.0	0.0	79.4	77.7	76.5	74.5	75.3	73.8	73.2	71.8
1600.0	0.0	79.9	78.3	77.0	76.5	75.7	74.4	73.3	72.5
2000.0	0.0	81.1	79.2	78.0	77.0	76.3	75.2	73.9	73.1
2500.0	0.0	80.5	79.8	78.8	77.2	76.4	75.6	74.6	74.2
3150.0	0.0	80.4	79.9	79.3	78.1	77.6	76.8	75.0	74.4
4000.0	0.0	81.1	80.0	79.5	78.3	78.1	77.3	75.2	74.9
5000.0	0.0	80.3	79.9	79.3	78.3	77.7	77.4	75.5	75.2
6300.0	0.0	80.4	79.9	79.2	78.4	78.2	77.5	75.6	75.0
8000.0	0.0	79.4	79.2	78.9	78.2	77.8	75.2	75.8	75.0
10000.0	0.0	79.2	78.8	78.2	78.1	77.3	75.1	75.3	74.8
12500.0	0.0	78.4	78.0	77.9	78.0	76.8	76.2	75.1	74.5
16000.0	0.0	77.8	77.2	77.8	77.4	76.2	76.0	74.5	74.0
20000.0	0.0	76.3	76.3	76.7	76.4	75.5	74.3	73.3	72.9
25000.0	0.0	75.4	75.2	76.3	75.8	74.7	72.9	72.7	72.3
31500.0	0.0	74.1	74.0	75.2	74.5	73.3	72.4	71.7	71.3
40000.0	0.0	73.4	72.9	74.7	73.5	72.7	71.1	71.6	70.5
OVERALL SPL	101.4	91.8	90.9	90.5	89.6	89.1	88.0	86.9	86.3

254

RUN NUMBER 27

1/3 OCTAVE CENTER FREQ. HZ	MICRO PHONE NO. 1 ANGLE 30.0	MICRO PHONE NO. 2 ANGLE 37.5	MICRO PHONE NO. 3 ANGLE 45.0	MICRO PHONE NO. 4 ANGLE 52.5	MICRO PHONE NO. 5 ANGLE 60.0	MICRO PHONE NO. 6 ANGLE 67.5	MICRO PHONE NO. 7 ANGLE 75.0	MICRO PHONE NO. 8 ANGLE 82.5	MICRO PHONE NO. 9 ANGLE 90.0
200.0	80.0	73.4	72.9	72.1	71.2	70.1	69.0	69.7	68.2
250.0	81.8	78.6	76.4	74.4	74.4	74.5	73.6	73.8	71.9
315.2	83.9	81.7	79.2	76.1	76.6	76.3	74.6	75.0	74.8
400.0	86.9	83.5	81.4	77.9	78.3	77.7	77.3	76.5	77.5
500.0	89.3	85.8	82.2	80.1	79.6	79.4	78.1	77.7	78.4
630.0	90.7	87.8	84.2	82.1	81.5	81.0	79.6	79.5	79.5
800.0	93.3	89.2	86.1	84.4	83.1	82.5	81.4	80.7	80.4
1000.0	95.0	90.9	88.1	85.7	84.3	83.7	82.7	82.3	81.6
1250.0	95.6	92.4	90.0	87.3	85.9	85.4	84.1	83.9	83.5
1600.0	95.0	92.6	90.6	88.0	86.7	86.6	84.8	84.7	83.8
2000.0	94.8	93.6	91.5	89.1	87.5	87.6	86.3	85.4	84.8
2500.0	94.7	94.1	92.1	89.6	88.3	88.1	86.8	85.8	85.5
3150.0	93.4	93.8	92.0	90.2	88.7	88.5	87.3	86.6	86.1
4000.0	92.4	93.6	92.1	90.1	89.1	88.8	88.1	86.8	86.4
5000.0	91.2	92.7	92.2	90.1	89.2	88.8	88.3	86.9	86.3
6300.0	89.9	92.3	91.7	90.4	89.5	89.1	88.6	86.8	86.5
8000.0	86.4	90.9	91.0	89.8	89.2	88.9	86.4	87.1	86.3
10000.0	87.1	89.9	89.9	89.3	88.8	88.7	86.2	86.9	86.4
12500.0	85.7	89.4	89.5	89.0	88.8	88.4	87.5	86.8	86.1
16000.0	84.1	88.7	88.4	88.6	88.0	87.6	87.3	86.2	85.6
20000.0	82.2	86.7	87.1	87.4	87.4	86.7	85.7	85.1	84.4
25000.0	80.6	85.2	86.1	87.0	86.7	85.9	84.4	84.4	83.8
31500.0	78.8	83.7	84.3	85.6	85.4	84.8	84.0	83.3	82.6
40000.0	77.1	82.6	82.5	84.5	84.3	83.9	82.9	82.9	81.7
OVERALL SPL	104.7	104.0	102.7	101.2	100.4	100.0	96.9	98.2	97.7

255

RUN NUMBER 28

1/3 OCTAVE CENTER FREQ. HZ	MICRO PHONE NO. 1 ANGLE 30.0	MICRO PHONE NO. 2 ANGLE 37.5	MICRO PHONE NO. 3 ANGLE 45.0	MICRO PHONE NO. 4 ANGLE 52.5	MICRO PHONE NO. 5 ANGLE 60.0	MICRO PHONE NO. 6 ANGLE 67.5	MICRO PHONE NO. 7 ANGLE 75.0	MICRO PHONE NO. 8 ANGLE 82.5	MICRO PHONE NO. 9 ANGLE 90.0
200.0	80.5	74.4	72.5	73.5	71.2	70.5	70.1	69.0	67.4
250.0	81.4	78.2	74.4	73.8	73.4	74.4	73.5	73.2	71.2
315.2	84.0	80.2	77.6	75.8	76.1	76.2	73.2	75.0	73.5
400.0	86.4	82.2	79.5	78.3	76.9	76.6	75.0	75.6	75.5
500.0	86.1	84.0	81.2	80.1	78.9	79.2	77.3	77.8	77.5
630.0	90.3	86.7	82.9	81.2	80.7	80.3	77.9	78.9	78.2
800.0	92.4	89.4	84.9	83.1	82.1	82.0	80.2	80.1	79.8
1000.0	94.3	90.6	87.5	85.0	83.8	83.8	82.1	81.9	81.4
1250.0	95.0	92.8	89.6	86.8	84.6	85.2	83.8	83.4	83.1
1600.0	94.8	92.6	90.6	88.1	86.1	86.1	83.9	84.1	83.3
2000.0	95.2	93.2	91.6	89.2	86.8	87.1	85.1	85.0	83.7
2500.0	94.6	93.6	91.4	89.2	87.3	87.6	85.4	85.8	84.6
3150.0	93.4	93.4	91.6	89.9	88.2	87.7	86.3	86.2	85.5
4000.0	92.7	93.4	92.1	90.2	88.5	88.0	87.2	86.4	85.7
5000.0	91.2	93.0	91.5	90.1	88.4	88.2	87.5	86.7	86.0
6300.0	90.0	92.7	91.4	90.3	88.6	88.8	87.2	87.0	86.2
8000.0	88.4	91.0	90.2	89.6	88.6	88.5	85.8	87.2	86.0
10000.0	87.0	90.7	89.7	89.4	88.5	88.4	85.7	86.8	85.8
12500.0	85.4	89.6	89.2	88.8	88.3	87.9	86.6	86.5	85.6
16000.0	83.9	89.1	88.2	88.5	87.7	87.4	86.5	86.2	85.2
20000.0	82.4	87.3	87.2	87.7	87.0	86.2	85.0	85.0	84.0
25000.0	81.0	86.0	86.4	87.2	86.5	85.6	84.2	84.3	83.3
31500.0	79.1	84.5	84.9	86.0	85.5	84.6	83.8	83.4	82.2
40000.0	77.4	83.3	83.2	85.0	84.3	83.9	83.0	82.8	81.4
OVERALL SPL	104.5	104.0	102.3	101.1	99.8	99.6	98.0	98.0	97.1

256

RUN NUMBER 29

1/3 OCTAVE CENTER FREQ. HZ	MICROPHONE NO. 1 ANGLE 30.0	MICROPHONE NO. 2 ANGLE 37.5	MICROPHONE NO. 3 ANGLE 45.0	MICROPHONE NO. 4 ANGLE 52.5	MICROPHONE NO. 5 ANGLE 60.0	MICROPHONE NO. 6 ANGLE 67.5	MICROPHONE NO. 7 ANGLE 75.0	MICROPHONE NO. 8 ANGLE 82.5	MICROPHONE NO. 9 ANGLE 90.0
200.0	85.4	73.0	72.4	70.7	70.6	69.0	69.9	69.2	67.3
250.0	87.7	77.2	77.3	77.2	76.6	74.1	74.5	75.2	74.6
315.2	86.2	79.9	76.4	75.5	75.8	74.2	72.2	73.2	72.4
400.0	86.0	81.0	78.6	76.8	76.1	76.1	76.1	74.6	74.4
500.0	87.1	83.6	81.0	77.6	78.5	77.0	76.3	75.2	75.7
630.0	88.3	84.4	82.1	80.0	79.3	78.5	78.9	76.7	77.2
800.0	91.0	86.8	84.8	82.3	80.2	79.9	79.6	78.3	78.3
1000.0	92.7	88.5	86.2	84.1	82.4	80.9	80.5	80.3	79.3
1250.0	93.9	90.7	87.7	86.1	84.4	83.1	82.4	81.4	80.9
1600.0	93.0	90.5	88.5	86.7	85.7	84.0	83.2	82.2	81.7
2000.0	93.6	91.6	89.7	87.7	86.3	85.1	83.9	82.7	82.2
2500.0	93.2	91.9	89.7	88.0	86.6	85.3	84.8	83.5	83.3
3150.0	92.4	92.2	90.2	88.8	87.3	86.2	85.6	84.2	83.9
4000.0	91.9	92.0	90.1	89.1	87.5	86.3	86.2	84.6	84.3
5000.0	90.4	91.1	90.0	88.9	87.6	86.3	86.5	84.5	84.2
6300.0	89.2	90.7	89.7	89.0	87.7	86.7	86.3	85.0	84.5
8000.0	88.3	89.8	88.9	88.5	87.7	86.3	84.2	85.2	84.8
10000.0	86.8	89.3	88.1	87.8	87.5	85.9	84.2	84.7	84.4
12500.0	85.4	88.4	87.6	87.6	87.1	85.7	85.4	84.6	84.4
16000.0	84.2	87.7	86.5	87.3	86.4	85.0	85.4	84.3	83.8
20000.0	82.7	86.0	85.4	86.4	85.7	83.9	83.7	83.3	82.8
25000.0	81.1	84.7	84.5	86.0	84.9	82.9	82.4	82.5	82.0
31500.0	79.5	82.9	83.0	84.8	83.8	81.5	82.0	81.2	80.8
40000.0	78.6	81.8	81.7	84.1	82.6	80.8	80.8	81.1	80.4
OVERALL SPL	103.5	102.3	100.7	99.9	98.8	97.4	96.9	96.1	95.7

257

RUN NUMBER 30

1/3 OCTAVE CENTER FREQ. HZ	MICRO PHONE NO. 1 ANGLE 30.0	MICRO PHONE NO. 2 ANGLE 37.5	MICRO PHONE NO. 3 ANGLE 45.0	MICRO PHONE NO. 4 ANGLE 52.5	MICRO PHONE NO. 5 ANGLE 60.0	MICRO PHONE NO. 6 ANGLE 67.5	MICRO PHONE NO. 7 ANGLE 75.0	MICRO PHONE NO. 8 ANGLE 82.5	MICRO PHONE NO. 9 ANGLE 90.0
200.0	82.1	71.3	70.2	70.3	68.1	68.0	65.9	66.8	64.6
250.0	82.4	74.5	73.7	72.2	69.0	69.3	68.8	70.2	68.0
315.2	82.0	76.5	75.2	72.5	71.3	71.9	71.6	71.2	71.0
400.0	83.0	78.9	76.0	74.7	73.0	74.9	73.0	72.0	73.2
500.0	83.3	80.0	78.1	77.2	75.2	74.9	74.6	73.1	74.3
630.0	85.2	82.3	80.0	77.9	76.7	76.7	76.1	74.6	74.7
800.0	87.8	84.1	82.1	80.3	78.4	78.3	77.0	76.4	76.6
1000.0	86.8	85.8	83.8	81.6	80.7	80.0	78.8	78.4	76.7
1250.0	90.9	88.4	85.9	83.6	82.2	81.6	80.2	79.8	78.9
1600.0	90.8	88.4	87.0	84.4	82.8	82.1	81.0	80.3	79.7
2000.0	90.4	89.4	87.6	85.2	83.8	83.1	82.2	81.1	80.3
2500.0	90.2	89.3	87.9	85.8	84.3	83.3	82.6	81.7	80.8
3150.0	90.4	89.8	88.3	86.4	85.1	84.2	83.5	82.6	81.6
4000.0	89.3	90.0	88.5	86.7	85.2	84.6	84.3	82.7	81.8
5000.0	88.9	89.1	88.2	86.6	85.5	84.6	84.6	82.8	82.3
6300.0	87.8	89.1	88.2	86.4	85.8	85.1	84.1	83.4	82.5
8000.0	86.4	88.1	87.3	86.4	85.5	84.8	82.2	83.6	82.4
10000.0	85.8	87.3	86.8	85.9	85.5	84.5	82.0	83.2	82.1
12500.0	84.6	87.0	86.3	85.7	85.3	84.3	83.2	82.8	81.9
16000.0	83.8	86.2	85.6	85.4	84.4	83.9	82.8	82.2	81.4
20000.0	82.3	84.2	84.3	84.3	83.6	82.8	81.2	81.3	80.1
25000.0	80.9	82.9	83.4	83.6	82.8	82.0	79.9	80.5	79.4
31500.0	79.4	81.4	82.0	82.4	81.6	80.8	79.3	79.6	78.4
40000.0	78.4	80.3	80.7	81.3	80.1	80.0	78.0	79.1	77.4
OVERALL SPL	100.9	100.2	99.0	97.7	96.6	95.9	94.7	94.3	93.4

258

RUN NUMBER 31

1/3 OCTAVE CENTER FREQ. HZ	MICRO PHONE NO. 1 ANGLE 30.0	MICRO PHONE NO. 2 ANGLE 37.5	MICRO PHONE NO. 3 ANGLE 45.0	MICRO PHONE NO. 4 ANGLE 52.5	MICRO PHONE NO. 5 ANGLE 60.0	MICRO PHONE NO. 6 ANGLE 67.5	MICRO PHONE NO. 7 ANGLE 75.0	MICRO PHONE NO. 8 ANGLE 82.5	MICRO PHONE NO. 9 ANGLE 90.0
200.0	103.3	78.5	74.4	73.6	72.4	70.5	70.8	68.2	68.1
250.0	101.5	77.8	74.9	73.5	71.6	71.3	71.5	69.9	70.1
315.2	100.3	77.3	74.2	72.1	70.8	71.3	70.1	69.7	70.1
400.0	97.6	77.6	74.5	73.7	72.2	71.9	71.6	70.8	70.6
500.0	95.0	77.8	75.3	74.6	72.8	73.6	72.3	71.7	71.0
630.0	93.8	80.0	77.2	76.3	74.4	75.2	73.8	73.0	72.8
800.0	92.1	82.0	79.3	79.0	76.9	77.0	75.6	74.7	73.6
1000.0	89.9	83.6	80.8	79.9	78.2	77.8	77.0	75.9	74.6
1250.0	89.0	85.3	83.4	81.4	79.9	80.2	76.4	78.3	74.8
1600.0	89.0	86.2	84.0	82.0	80.6	80.2	79.0	78.8	77.5
2000.0	89.2	87.1	85.0	84.0	81.7	81.2	80.4	79.7	77.4
2500.0	88.8	87.4	85.7	84.7	81.7	81.5	86.4	80.0	77.5
3150.0	87.5	87.9	85.6	84.4	82.4	82.4	81.4	80.7	79.4
4000.0	87.1	87.9	86.0	85.4	82.9	82.5	82.4	80.9	79.9
5000.0	86.5	87.2	86.1	85.2	83.1	83.1	82.5	81.3	80.0
6300.0	85.2	87.2	85.9	85.4	83.3	83.9	82.5	82.0	80.4
8000.0	84.0	85.7	85.6	85.0	83.1	83.1	80.6	81.8	80.9
10000.0	82.7	85.4	85.4	84.5	83.3	83.1	80.4	81.4	80.3
12500.0	82.1	84.7	84.6	83.9	83.0	82.7	81.7	81.1	80.4
16000.0	81.7	84.3	83.6	83.7	82.3	82.2	81.6	80.8	80.0
20000.0	80.1	82.7	82.4	82.6	81.5	81.3	80.0	80.0	79.1
25000.0	78.8	81.5	81.6	82.1	81.0	80.3	76.9	79.1	78.6
31500.0	77.9	80.4	80.5	81.1	80.1	79.3	78.5	78.3	77.8
40000.0	76.0	79.6	79.5	80.3	78.8	78.5	77.6	78.0	77.3
OVERALL SPL	108.2	98.3	96.9	96.3	94.4	94.3	93.1	92.7	91.7

259

RUN NUMBER 32

1/3 OCTAVE CENTER FREQ. HZ	MICRO PHONE NO. 1 ANGLE 30.0	MICRO PHONE NO. 2 ANGLE 37.5	MICRO PHONE NO. 3 ANGLE 45.0	MICRO PHONE NO. 4 ANGLE 52.5	MICRO PHONE NO. 5 ANGLE 60.0	MICRO PHONE NO. 6 ANGLE 67.5	MICRO PHONE NO. 7 ANGLE 75.0	MICRO PHONE NO. 8 ANGLE 82.5	MICRO PHONE NO. 9 ANGLE 90.0
200.0	83.7	78.2	76.3	76.2	76.8	74.4	75.0	72.8	70.0
250.0	85.8	81.0	80.2	78.6	77.8	77.4	77.5	77.4	75.0
315.2	87.8	84.3	82.8	79.6	79.4	78.9	78.2	76.6	77.0
400.0	90.6	87.0	84.0	81.0	81.2	81.0	80.6	78.9	79.0
500.0	92.9	89.6	85.8	83.6	82.4	81.7	81.8	80.4	80.6
630.0	95.7	92.2	87.8	85.7	84.6	84.1	82.9	81.9	83.0
800.0	97.9	93.6	90.1	87.9	86.7	86.0	84.6	83.7	84.2
1000.0	100.0	96.1	91.5	89.5	87.8	87.5	86.8	85.2	85.2
1250.0	101.3	97.0	93.3	91.6	90.2	89.4	87.9	87.4	87.3
1600.0	100.5	97.8	94.9	92.1	90.9	90.3	89.0	87.7	86.9
2000.0	100.2	99.1	94.6	93.5	92.1	91.3	89.9	89.3	88.2
2500.0	99.5	99.2	96.2	94.1	92.3	91.3	90.5	89.9	88.8
3150.0	98.5	99.2	96.6	94.4	93.1	91.9	91.6	90.4	89.6
4000.0	97.4	98.8	96.8	94.9	93.3	92.5	91.8	90.4	90.1
5000.0	96.0	97.5	96.5	95.1	93.6	92.5	92.0	90.6	90.0
6300.0	94.8	97.2	96.4	95.2	93.7	93.3	92.2	91.2	90.3
8000.0	93.4	95.8	95.8	94.6	93.4	92.6	90.1	91.2	90.2
10000.0	92.0	95.0	95.0	94.5	93.4	92.6	89.9	90.8	90.1
12500.0	90.6	94.1	94.2	93.9	93.1	92.4	91.5	90.7	90.1
16000.0	89.0	93.5	93.2	93.5	92.3	91.7	91.3	90.2	89.7
20000.0	87.1	91.4	91.9	92.6	91.6	90.7	89.7	89.3	88.8
25000.0	85.9	90.1	90.8	92.0	90.8	90.0	88.3	88.8	88.6
31500.0	84.0	88.4	89.4	90.4	89.5	88.9	87.9	87.7	87.1
40000.0	82.7	87.3	87.6	89.1	88.0	87.9	86.4	87.1	85.9
OVERALL SPL	109.8	109.0	107.1	105.9	104.6	103.8	102.7	102.1	101.4

260

RUN NUMBER 33

1/3 OCTAVE CENTER FREQ. HZ	MICRO PHONE NO. 1 ANGLE 30.0	MICRO PHONE NO. 2 ANGLE 37.5	MICRO PHONE NO. 3 ANGLE 45.0	MICRO PHONE NO. 4 ANGLE 52.5	MICRO PHONE NO. 5 ANGLE 60.0	MICRO PHONE NO. 6 ANGLE 67.5	MICRO PHONE NO. 7 ANGLE 75.0	MICRO PHONE NO. 8 ANGLE 82.5	MICRO PHONE NO. 9 ANGLE 90.0
200.0	82.6	77.2	77.2	77.4	75.9	74.1	71.4	72.4	70.8
250.0	85.0	81.8	79.8	79.0	77.7	76.7	76.5	78.0	74.7
315.2	87.7	84.2	82.9	80.7	80.4	79.0	77.3	78.5	77.8
400.0	89.8	87.4	83.5	82.7	81.4	79.8	78.7	79.9	78.2
500.0	92.7	89.5	85.5	84.2	83.3	82.5	80.8	80.8	80.7
630.0	95.0	91.8	88.0	86.2	84.4	83.8	83.2	82.5	82.5
800.0	97.6	92.8	91.0	87.9	86.3	85.7	84.6	83.7	84.1
1000.0	99.8	95.0	91.9	89.4	88.6	86.7	86.6	85.0	84.3
1250.0	101.0	97.5	94.2	91.9	89.8	88.9	87.9	87.7	87.2
1600.0	100.6	98.2	95.5	92.7	90.9	90.0	88.6	88.2	87.3
2000.0	100.5	98.8	95.9	93.9	92.1	90.2	89.8	88.8	87.8
2500.0	99.7	98.7	96.7	94.6	92.0	90.8	90.6	89.9	88.8
3150.0	98.4	98.7	97.0	94.7	93.1	91.9	91.3	90.3	88.9
4000.0	97.5	98.9	96.9	94.9	93.3	92.3	91.8	90.8	90.2
5000.0	96.3	98.0	96.7	95.2	93.6	92.5	92.4	90.5	90.1
6300.0	95.3	97.3	96.4	95.2	93.7	92.8	92.2	91.0	90.2
8000.0	93.5	95.9	95.8	94.6	93.7	92.8	90.6	91.0	90.4
10000.0	92.2	95.0	95.1	94.3	93.2	92.4	90.4	90.8	90.4
12500.0	91.0	94.3	94.6	93.9	93.3	92.1	91.4	90.8	90.2
16000.0	89.6	93.5	93.5	93.6	92.7	91.4	91.3	90.4	89.8
20000.0	88.0	91.6	92.0	92.7	91.8	90.4	89.7	89.4	88.5
25000.0	86.4	90.3	91.0	92.0	91.0	89.7	88.4	88.8	88.0
31500.0	84.4	88.8	89.5	90.7	89.9	88.9	88.1	87.8	86.6
40000.0	82.9	87.8	87.8	89.5	88.4	87.8	86.6	87.3	85.7
OVERALL SPL	109.8	108.9	107.4	106.0	104.6	103.5	102.7	102.1	101.4

261

RUN NUMBER 34

1/3 OCTAVE CENTER FREQ. HZ	MICRO PHONE NO. 1 ANGLE 30.0	MICRO PHONE NO. 2 ANGLE 37.5	MICRO PHONE NO. 3 ANGLE 45.0	MICRO PHONE NO. 4 ANGLE 52.5	MICRO PHONE NO. 5 ANGLE 60.0	MICRO PHONE NO. 6 ANGLE 67.5	MICRO PHONE NO. 7 ANGLE 75.0	MICRO PHONE NO. 8 ANGLE 82.5	MICRO PHONE NO. 9 ANGLE 90.0
200.0	90.7	75.7	73.9	75.4	74.7	72.4	71.6	70.6	68.8
250.0	90.1	79.2	78.6	77.7	77.2	75.4	75.4	74.6	73.6
315.2	87.9	82.7	79.5	79.0	78.1	77.9	76.9	76.8	76.3
400.0	89.7	84.0	82.0	80.8	79.3	79.4	79.4	78.7	77.3
500.0	91.0	85.9	83.6	82.1	81.6	80.2	80.3	80.0	79.4
630.0	93.0	90.1	86.3	84.3	82.8	82.1	81.7	80.5	80.8
800.0	95.9	91.5	89.0	86.6	85.6	84.2	83.5	82.3	82.2
1000.0	98.0	94.0	90.0	87.6	86.5	86.0	84.7	84.1	82.8
1250.0	99.5	95.6	92.2	90.0	88.2	87.7	87.1	85.7	85.5
1600.0	99.9	96.2	93.0	91.6	89.8	88.5	87.3	86.3	85.6
2000.0	99.6	97.2	94.3	92.1	90.1	89.4	88.2	87.6	86.8
2500.0	98.8	97.2	94.8	92.5	90.8	89.8	88.7	88.3	87.4
3150.0	98.0	97.4	95.0	93.4	91.6	90.5	89.3	89.0	88.0
4000.0	97.1	97.5	95.2	93.7	91.9	90.6	90.6	89.2	88.9
5000.0	96.0	96.7	94.5	93.4	92.1	90.9	90.8	89.1	88.9
6300.0	94.8	96.1	94.5	93.6	92.2	91.2	90.8	89.8	89.1
8000.0	93.5	94.9	94.1	93.1	92.0	90.8	88.7	89.8	89.0
10000.0	92.3	94.2	93.4	92.7	91.5	90.4	88.6	89.6	88.8
12500.0	90.8	93.5	93.0	92.3	91.6	90.4	89.9	89.5	88.8
16000.0	89.5	92.8	92.0	92.1	91.0	89.9	89.9	88.8	88.3
20000.0	87.6	90.9	90.6	90.9	90.2	88.9	87.9	88.0	87.5
25000.0	86.1	89.8	89.6	90.3	89.6	88.0	86.8	87.6	87.2
31500.0	84.3	88.3	88.1	88.8	88.2	86.9	86.5	86.8	86.2
40000.0	82.9	87.1	86.7	87.5	86.5	85.9	85.1	86.1	85.0

| OVERALL SPL | 108.9 | 107.6 | 105.6 | 104.4 | 103.1 | 102.0 | 101.2 | 100.7 | 100.1 |

RUN NUMBER 35

1/3 OCTAVE CENTER FREQ. HZ	MICRO PHONE NO. 1 ANGLE 30.0	MICRO PHONE NO. 2 ANGLE 37.5	MICRO PHONE NO. 3 ANGLE 45.0	MICRO PHONE NO. 4 ANGLE 52.5	MICRO PHONE NO. 5 ANGLE 60.0	MICRO PHONE NO. 6 ANGLE 67.5	MICRO PHONE NO. 7 ANGLE 75.0	MICRO PHONE NO. 8 ANGLE 82.5	MICRO PHONE NO. 9 ANGLE 90.0
200.0	100.2	79.5	73.7	74.7	73.7	72.6	70.7	68.9	67.8
250.0	95.4	80.7	76.8	75.4	74.8	75.0	74.7	74.3	72.5
315.2	96.6	82.6	77.5	77.7	77.3	76.7	76.0	74.0	74.6
400.0	94.5	83.3	80.6	79.0	78.3	78.2	77.3	75.8	76.3
500.0	93.5	84.2	81.0	81.0	80.3	78.7	76.7	77.2	77.4
630.0	93.8	87.3	84.1	82.1	82.2	81.0	79.7	78.6	79.6
800.0	94.0	89.4	86.3	84.6	83.6	82.7	81.5	80.9	80.2
1000.0	94.9	91.3	88.2	86.2	85.2	84.8	83.0	82.6	81.4
1250.0	97.1	93.8	90.0	88.2	87.0	86.1	84.7	84.2	83.9
1600.0	97.5	93.8	91.2	89.2	88.1	87.0	85.5	84.4	83.8
2000.0	96.9	95.0	92.2	90.0	88.8	87.9	86.8	85.6	85.1
2500.0	96.5	94.8	92.8	90.7	89.3	88.4	87.2	86.3	85.8
3150.0	95.6	95.1	93.1	91.1	90.0	88.8	88.2	86.8	86.2
4000.0	95.1	95.3	93.4	91.8	90.5	89.7	89.1	87.5	86.7
5000.0	94.0	94.4	93.5	91.7	90.5	89.8	89.3	87.6	86.7
6300.0	93.0	94.4	93.3	92.0	90.5	90.0	88.8	88.0	87.0
8000.0	92.0	93.3	92.5	91.6	90.4	89.8	87.2	87.9	87.2
10000.0	90.7	92.7	91.9	90.8	90.2	89.6	86.9	87.5	86.9
12500.0	89.4	92.1	91.2	90.6	90.2	89.5	88.5	87.7	87.0
16000.0	88.1	91.6	90.4	90.6	89.4	89.0	88.1	87.2	86.4
20000.0	86.4	89.8	89.3	89.7	88.6	88.2	86.4	86.3	85.6
25000.0	85.1	88.4	88.4	89.1	87.9	87.3	85.1	85.6	85.2
31500.0	83.4	86.8	87.0	87.9	86.7	86.0	84.5	84.8	84.3
40000.0	82.5	85.6	86.6	86.7	85.1	85.3	83.1	84.2	83.0
OVERALL SPL	108.4	105.6	103.9	102.7	101.6	100.9	99.5	98.9	98.2

263

RUN NUMBER 36

1/3 OCTAVE CENTER FREQ. HZ	MICRO PHONE NO. 1 ANGLE 30.0	MICRO PHONE NO. 2 ANGLE 37.5	MICRO PHONE NO. 3 ANGLE 45.0	MICRO PHONE NO. 4 ANGLE 52.5	MICRO PHONE NO. 5 ANGLE 60.0	MICRO PHONE NO. 6 ANGLE 67.5	MICRO PHONE NO. 7 ANGLE 75.0	MICRO PHONE NO. 8 ANGLE 82.5	MICRO PHONE NO. 9 ANGLE 90.0
200.0	109.6	79.8	75.3	74.8	73.8	72.9	72.7	70.0	69.3
250.0	109.7	80.9	76.2	75.9	74.0	73.8	74.1	72.5	71.4
315.2	107.4	79.9	78.4	75.4	75.9	76.0	73.2	72.5	73.0
400.0	105.6	81.0	79.2	76.7	76.6	77.0	75.6	74.7	75.4
500.0	104.5	84.4	80.3	78.6	77.4	77.9	76.8	76.3	76.5
630.0	103.7	85.4	82.3	81.0	79.4	79.3	78.4	77.2	77.6
800.0	99.5	87.2	84.9	82.2	81.6	81.2	80.1	79.0	78.2
1000.0	96.8	89.6	86.1	83.9	83.0	82.3	82.2	80.8	79.4
1250.0	96.6	91.7	88.8	86.8	84.4	84.1	82.9	82.3	82.2
1600.0	95.7	92.2	89.4	87.4	85.8	84.8	83.7	82.8	82.1
2000.0	95.3	92.8	90.2	88.4	86.9	85.8	84.8	83.7	83.4
2500.0	94.4	93.6	90.8	88.8	87.2	86.8	85.2	83.9	83.6
3150.0	94.0	93.5	91.8	89.5	87.9	87.0	86.1	85.0	84.4
4000.0	93.5	93.7	91.5	89.8	88.6	87.7	87.1	85.4	84.9
5000.0	92.2	92.9	91.7	90.1	88.6	87.7	87.2	85.2	84.5
6300.0	91.2	92.8	91.5	90.2	88.8	88.0	87.2	85.9	85.5
8000.0	90.3	91.4	90.8	89.8	88.9	87.9	85.4	86.1	85.6
10000.0	88.8	91.1	89.9	89.2	88.4	87.7	85.1	85.5	85.6
12500.0	88.2	90.6	89.5	89.2	88.6	87.6	86.5	85.7	85.6
16000.0	86.6	89.9	88.7	88.7	87.8	87.1	86.5	85.2	85.2
20000.0	85.2	88.6	87.6	87.9	87.2	86.2	84.9	84.4	84.2
25000.0	83.7	87.4	86.7	87.2	86.8	85.4	83.6	83.5	83.5
31500.0	82.5	86.1	85.4	86.2	85.7	84.1	83.2	82.6	82.5
40000.0	82.2	84.9	84.3	85.2	84.6	83.4	82.3	82.4	81.9

| OVERALL SPL | 115.6 | 104.0 | 102.1 | 100.9 | 99.8 | 98.9 | 97.8 | 96.9 | 96.7 |

264

RUN NUMBER 37

1/3 OCTAVE CENTER FREQ. HZ	MICROPHONE NO. 1 ANGLE 30.0	MICROPHONE NO. 2 ANGLE 37.5	MICROPHONE NO. 3 ANGLE 45.0	MICROPHONE NO. 4 ANGLE 52.5	MICROPHONE NO. 5 ANGLE 60.0	MICROPHONE NO. 6 ANGLE 67.5	MICROPHONE NO. 7 ANGLE 75.0	MICROPHONE NO. 8 ANGLE 82.5	MICROPHONE NO. 9 ANGLE 90.0
200.0	93.6	85.0	81.6	83.2	82.1	82.1	80.2	79.3	78.4
250.0	94.1	89.3	87.4	85.6	84.8	84.4	84.9	83.7	82.6
315.2	95.5	91.6	88.6	87.1	87.3	86.7	85.9	84.2	84.4
400.0	96.5	94.7	90.5	89.5	88.8	88.2	87.6	86.3	85.2
500.0	100.8	96.0	93.5	91.2	90.9	89.5	88.7	88.3	87.6
630.0	103.6	99.0	95.2	93.2	92.9	91.0	90.9	89.4	89.3
800.0	107.0	101.9	98.3	96.0	93.8	93.4	92.2	90.7	90.9
1000.0	109.8	104.7	100.1	97.1	96.3	94.7	94.1	92.7	92.4
1250.0	111.9	107.3	102.5	99.4	97.4	96.8	95.9	94.4	94.5
1600.0	112.5	108.2	103.4	99.9	98.7	97.4	96.4	95.7	95.4
2000.0	113.3	109.2	104.8	101.2	99.9	98.5	97.4	96.8	95.7
2500.0	112.0	109.1	105.5	102.2	100.4	99.5	98.1	97.4	96.8
3150.0	110.5	109.1	106.1	103.2	101.1	100.0	98.7	98.1	97.5
4000.0	108.9	109.1	106.3	103.6	102.1	100.6	99.3	98.8	97.6
5000.0	106.8	108.1	106.4	103.8	102.5	100.9	99.6	98.7	98.3
6300.0	105.8	107.7	106.5	104.1	102.6	101.6	100.4	99.8	99.2
8000.0	104.4	106.8	105.9	104.0	103.0	101.8	100.5	100.2	99.8
10000.0	103.5	106.1	105.4	103.9	102.9	101.6	100.8	100.9	102.5
12500.0	101.9	104.9	104.7	103.6	103.1	102.1	101.9	104.3	105.9
16000.0	100.1	103.9	103.5	103.3	102.9	102.8	103.7	105.6	104.9
20000.0	98.5	102.3	102.6	103.2	103.7	103.7	103.7	104.8	104.8
25000.0	97.0	101.5	102.0	103.4	104.2	103.4	103.0	103.7	103.4
31500.0	95.6	100.2	101.2	103.2	103.4	102.2	101.8	102.6	102.6
40000.0	94.4	99.5	99.8	101.9	101.8	101.3	100.9	102.1	101.4
OVERALL SPL	121.0	119.2	116.9	115.2	114.4	113.5	112.9	113.6	113.7

RUN NUMBER 38

1/3 OCTAVE CENTER FREQ. HZ	MICRO PHONE NO. 1 ANGLE 30.0	MICRO PHONE NO. 2 ANGLE 37.5	MICRO PHONE NO. 3 ANGLE 45.0	MICRO PHONE NO. 4 ANGLE 52.5	MICRO PHONE NO. 5 ANGLE 60.0	MICRO PHONE NO. 6 ANGLE 67.5	MICRO PHONE NO. 7 ANGLE 75.0	MICRO PHONE NO. 8 ANGLE 82.5	MICRO PHONE NO. 9 ANGLE 90.0
200.0	95.6	84.9	81.2	83.3	82.2	80.3	78.4	78.3	75.7
250.0	95.4	87.3	86.5	85.8	83.0	83.3	83.6	82.9	81.6
315.2	95.7	90.5	88.2	87.3	86.1	85.4	85.4	83.9	83.6
400.0	97.6	93.3	90.1	88.4	88.2	87.6	86.2	85.5	85.4
500.0	100.6	95.6	92.2	90.9	89.7	88.5	87.2	86.7	86.7
630.0	101.6	98.8	94.4	93.6	92.3	90.2	89.3	88.9	88.1
800.0	105.6	101.0	96.9	94.6	93.8	92.6	91.0	90.4	89.8
1000.0	108.5	103.5	99.0	96.4	94.8	94.0	93.6	91.9	90.7
1250.0	110.8	106.3	101.3	98.4	96.5	95.6	94.9	93.7	93.6
1600.0	111.4	107.0	102.7	99.4	97.3	96.6	95.5	94.8	94.2
2000.0	111.6	108.3	103.5	100.2	99.0	97.8	96.2	95.5	94.6
2500.0	110.8	108.0	104.4	101.4	99.7	98.3	97.0	96.4	95.7
3150.0	109.1	108.2	104.8	102.5	100.3	99.1	97.7	97.1	96.3
4000.0	108.0	108.4	105.3	103.1	100.9	99.7	98.4	97.4	96.6
5000.0	106.3	107.8	105.6	103.1	101.5	100.0	98.7	97.9	97.4
6300.0	105.3	107.6	105.9	103.4	102.1	100.7	99.5	99.0	98.2
8000.0	103.9	106.8	105.8	103.5	102.1	101.0	99.6	99.3	98.8
10000.0	102.6	106.2	105.0	103.0	101.8	100.7	100.0	100.3	101.9
12500.0	101.6	105.1	104.4	102.9	102.0	101.4	101.6	104.2	105.4
16000.0	100.0	104.2	103.5	102.5	101.8	102.4	103.6	105.3	105.2
20000.0	98.3	102.8	102.9	102.6	102.8	103.3	103.7	104.5	104.1
25000.0	96.7	101.9	102.5	103.0	103.3	102.9	102.8	103.1	102.6
31500.0	95.4	100.8	101.9	102.8	102.4	101.8	101.3	102.2	101.7
40000.0	94.4	100.1	100.8	101.6	100.6	100.8	100.4	101.8	100.5
OVERALL SPL	119.9	118.6	116.3	114.6	113.5	112.8	112.4	113.1	112.9

266

RUN NUMBER 39

1/3 OCTAVE CENTER FREQ. HZ	MICROPHONE NO. 1 ANGLE 30.0	MICROPHONE NO. 2 ANGLE 37.5	MICROPHONE NO. 3 ANGLE 45.0	MICROPHONE NO. 4 ANGLE 52.5	MICROPHONE NO. 5 ANGLE 60.0	MICROPHONE NO. 6 ANGLE 67.5	MICROPHONE NO. 7 ANGLE 75.0	MICROPHONE NO. 8 ANGLE 82.5	MICROPHONE NO. 9 ANGLE 90.0
200.0	101.7	82.6	82.2	82.1	82.2	79.9	78.8	76.2	73.6
250.0	101.7	86.2	86.2	84.6	82.3	82.5	82.0	81.2	80.8
315.2	100.9	89.0	86.5	85.8	85.4	83.5	83.8	81.8	81.8
400.0	99.9	91.3	89.3	87.6	87.2	86.7	84.3	83.8	85.0
500.0	100.2	92.9	91.0	89.0	88.7	87.1	86.8	85.4	85.7
630.0	101.3	96.6	92.4	91.9	91.2	89.7	87.9	87.5	86.8
800.0	103.6	99.0	95.8	93.3	91.8	91.4	89.5	89.5	88.4
1000.0	106.4	101.6	97.6	95.0	93.9	92.2	91.9	90.7	89.6
1250.0	106.8	104.5	100.5	97.3	95.5	94.7	93.3	92.5	92.0
1600.0	109.6	105.4	101.5	98.6	96.5	95.6	94.4	92.9	92.7
2000.0	109.3	106.1	102.5	99.4	98.0	96.2	95.1	94.6	93.6
2500.0	108.7	106.2	103.3	100.0	98.8	97.3	95.9	95.3	94.1
3150.0	107.4	106.0	103.8	101.1	99.5	98.1	96.8	96.1	95.2
4000.0	106.0	106.5	104.1	101.5	99.9	98.8	97.4	96.7	95.7
5000.0	104.6	106.1	104.1	101.9	100.5	98.9	97.6	96.5	96.2
6300.0	103.9	106.2	105.0	103.0	101.6	99.9	98.6	97.8	96.9
8000.0	103.4	106.0	104.6	103.2	101.4	100.1	98.6	98.0	97.8
10000.0	102.4	105.4	103.8	102.3	101.2	100.0	98.9	99.2	101.6
12500.0	100.5	103.8	103.1	102.1	101.2	100.8	100.8	103.6	105.6
16000.0	98.9	102.8	101.9	102.0	101.2	102.1	103.0	104.5	105.5
20000.0	97.5	101.5	101.1	102.3	102.5	103.2	103.0	103.7	104.2
25000.0	96.1	100.7	100.7	103.0	103.3	102.7	101.9	102.3	102.6
31500.0	94.7	99.8	100.6	102.9	102.2	101.5	100.6	101.5	101.8
40000.0	93.6	99.0	99.5	101.6	100.6	100.7	99.5	100.9	100.5
OVERALL SPL	118.4	117.0	115.0	113.9	112.9	112.2	111.5	112.2	112.8

RUN NUMBER 40

1/3 OCTAVE CENTER FREQ. HZ	MICRO PHONE NO. 1 ANGLE 30.0	MICRO PHONE NO. 2 ANGLE 37.5	MICRO PHONE NO. 3 ANGLE 45.0	MICRO PHONE NO. 4 ANGLE 52.5	MICRO PHONE NO. 5 ANGLE 60.0	MICRO PHONE NO. 6 ANGLE 67.5	MICRO PHONE NO. 7 ANGLE 75.0	MICRO PHONE NO. 8 ANGLE 82.5	MICRO PHONE NO. 9 ANGLE 90.0
200.0	106.8	83.7	81.6	80.4	80.4	79.6	79.5	76.3	74.0
250.0	106.5	86.8	84.2	82.9	82.9	81.4	80.9	81.0	79.3
315.2	105.1	87.5	86.3	85.0	83.9	82.7	82.2	80.9	80.6
400.0	103.6	89.0	88.4	86.4	85.4	85.8	84.0	83.2	83.0
500.0	102.1	91.0	90.0	88.3	87.0	86.7	84.8	83.8	85.3
630.0	101.7	94.8	91.4	90.5	89.0	88.2	86.6	86.5	86.5
800.0	102.7	97.7	94.3	92.1	90.5	90.5	86.6	87.5	86.7
1000.0	104.6	99.5	96.4	94.1	92.4	92.0	90.5	89.5	88.6
1250.0	106.9	102.4	99.0	96.2	94.3	93.2	92.6	91.4	91.0
1600.0	107.7	102.9	94.6	97.1	95.6	94.4	92.8	91.8	91.4
2000.0	107.3	103.8	100.7	98.4	96.7	95.8	94.1	93.3	92.3
2500.0	106.5	104.4	101.7	99.2	97.4	96.7	94.8	94.2	93.1
3150.0	105.6	104.2	102.3	100.4	98.2	97.2	95.3	94.8	93.9
4000.0	104.9	105.1	102.6	100.0	98.9	98.0	96.0	95.2	94.3
5000.0	103.5	104.6	103.0	101.3	99.6	97.9	96.5	95.2	95.0
6300.0	103.7	104.4	103.7	102.3	100.3	99.0	97.7	96.7	96.1
8000.0	103.8	104.1	102.9	102.2	100.2	99.0	97.6	97.5	97.0
10000.0	102.3	103.0	102.0	101.5	100.3	99.5	98.1	99.1	101.4
12500.0	100.1	102.3	101.6	101.3	100.6	100.2	100.4	103.4	105.2
16000.0	98.5	101.6	100.9	101.2	100.9	102.0	102.9	104.5	104.7
20000.0	97.4	100.6	100.4	101.7	102.2	103.2	102.6	103.7	103.5
25000.0	96.0	100.0	100.5	102.6	102.8	102.5	101.4	102.4	102.0
31500.0	94.8	99.4	100.4	102.5	101.7	101.3	100.1	101.3	101.1
40000.0	93.8	98.8	99.4	101.2	100.2	100.2	99.1	100.9	99.9
OVERALL SPL	117.9	115.3	113.7	113.2	112.1	111.7	110.9	111.9	112.1

268

RUN NUMBER 42

1/3 OCTAVE CENTER FREQ. HZ	MICROPHONE NO. 1 ANGLE 30.0	MICROPHONE NO. 2 ANGLE 37.5	MICROPHONE NO. 3 ANGLE 45.0	MICROPHONE NO. 4 ANGLE 52.5	MICROPHONE NO. 5 ANGLE 60.0	MICROPHONE NO. 6 ANGLE 67.5	MICROPHONE NO. 7 ANGLE 75.0	MICROPHONE NO. 8 ANGLE 82.5	MICROPHONE NO. 9 ANGLE 90.0
200.0	94.7	88.4	86.5	89.3	87.1	86.3	83.8	82.1	80.4
250.0	97.5	92.6	91.8	90.9	90.4	88.9	87.8	88.8	87.7
315.2	99.5	94.4	93.5	92.8	91.6	91.3	90.1	88.8	84.4
400.0	103.4	98.2	95.4	94.6	93.3	92.5	91.0	90.8	90.4
500.0	106.2	101.0	97.4	95.3	95.0	93.0	93.1	91.5	91.8
630.0	109.0	103.5	99.7	98.5	98.2	96.2	94.8	93.9	93.9
800.0	112.4	106.2	102.8	99.7	99.0	97.7	96.9	96.1	96.1
1000.0	115.3	109.4	104.8	101.9	100.2	99.4	99.3	97.4	96.8
1250.0	118.1	112.9	107.6	103.7	101.8	101.4	100.0	99.3	99.0
1600.0	119.6	113.5	107.9	104.8	103.2	102.1	101.0	100.4	99.9
2000.0	120.4	115.2	109.7	105.9	103.9	102.8	101.7	101.2	99.9
2500.0	121.1	115.7	110.8	107.0	104.7	103.6	102.8	102.0	100.6
3150.0	120.8	115.4	111.1	108.1	105.9	104.6	103.6	102.7	101.9
4000.0	120.3	115.8	111.5	108.7	106.9	105.1	103.7	103.7	103.8
5000.0	118.6	114.7	111.8	108.9	106.9	105.7	104.7	104.9	104.9
6300.0	117.6	114.2	112.0	109.4	107.8	107.0	106.2	105.3	104.4
8000.0	115.8	112.9	111.2	109.5	107.7	106.8	105.2	104.8	104.5
10000.0	114.3	111.8	110.7	109.8	107.7	106.2	105.3	105.4	105.6
12500.0	113.0	111.6	110.3	109.6	107.6	106.5	106.0	105.8	105.0
16000.0	111.2	110.7	109.7	108.9	107.2	106.2	105.4	105.0	104.4
20000.0	109.8	109.4	103.4	108.2	107.1	105.5	104.3	104.0	103.4
25000.0	108.2	108.4	107.2	107.5	106.5	104.8	103.7	103.3	102.6
31500.0	106.6	106.8	104.9	106.7	105.4	103.9	102.7	102.5	101.7
40000.0	104.7	105.7	104.3	105.3	103.9	103.1	101.8	102.2	101.0
OVERALL SPL	129.7	125.4	122.1	120.2	118.5	117.3	116.2	115.9	115.4

269

RUN NUMBER 43

1/3 OCTAVE CENTER FREQ. HZ	MICROPHONE NO. 1 ANGLE 30.0	MICROPHONE NO. 2 ANGLE 37.5	MICROPHONE NO. 3 ANGLE 45.0	MICROPHONE NO. 4 ANGLE 52.5	MICROPHONE NO. 5 ANGLE 60.0	MICROPHONE NO. 6 ANGLE 67.5	MICROPHONE NO. 7 ANGLE 75.0	MICROPHONE NO. 8 ANGLE 82.5	MICROPHONE NO. 9 ANGLE 90.0
200.0	96.4	89.0	8n.0	88.5	87.8	85.8	84.8	82.7	8n.7
250.0	97.4	91.5	91.2	90.6	89.9	87.2	87.9	87.4	86.6
315.2	98.7	94.6	93.1	92.1	91.3	89.2	88.9	87.6	8A.3
400.0	101.7	97.6	94.1	94.2	92.5	91.9	90.2	88.9	90.2
500.0	105.0	99.9	97.3	95.2	94.7	93.3	91.6	90.8	91.3
630.0	107.9	102.8	9A.8	98.6	97.2	96.4	95.6	93.1	93.3
800.0	111.5	105.3	101.9	100.0	99.0	97.4	96.1	95.3	94.6
1000.0	114.5	108.4	104.3	101.4	100.1	98.8	97.7	96.5	96.4
1250.0	117.5	112.6	106.7	103.3	101.4	100.9	99.7	99.0	99.0
1600.0	116.9	113.6	107.4	104.3	103.2	101.6	100.7	99.2	99.5
2000.0	119.9	114.8	109.5	105.5	104.1	102.3	101.8	100.5	94.6
2500.0	120.1	115.0	110.2	106.5	104.7	102.8	102.0	101.0	100.7
3150.0	119.9	115.1	110.8	107.7	105.3	104.1	102.8	101.9	101.5
4000.0	119.3	114.9	111.3	108.4	106.0	104.6	103.8	103.2	104.0
5000.0	117.7	114.7	111.7	108.6	106.9	105.2	104.9	104.8	104.6
6300.0	116.0	114.1	111.9	108.8	107.4	106.5	105.8	104.8	104.1
8000.0	114.5	113.0	111.0	109.0	107.7	106.3	104.9	104.2	104.4
10000.0	113.3	111.5	110.7	109.3	107.6	105.8	105.2	105.1	105.3
12500.0	111.5	111.3	110.3	109.0	107.5	106.1	105.8	105.2	105.0
16000.0	109.7	110.3	109.3	108.1	106.9	106.0	105.0	104.3	104.2
20000.0	108.3	109.2	108.1	107.6	106.7	105.1	104.0	103.5	103.2
25000.0	106.5	107.8	106.9	107.0	106.1	104.4	103.2	102.7	102.2
31500.0	104.6	106.2	105.7	106.0	105.1	103.5	102.2	101.9	101.6
40000.0	102.9	105.2	104.4	104.7	103.3	102.7	101.4	101.6	10n.9
OVERALL SPL	126.8	125.0	121.8	119.7	118.2	116.8	115.9	115.3	115.2

270

RUN NUMBER 44

1/3 OCTAVE CENTER FREQ. HZ	MICROPHONE NO. 1 ANGLE 30.0	MICROPHONE NO. 2 ANGLE 37.5	MICROPHONE NO. 3 ANGLE 45.0	MICROPHONE NO. 4 ANGLE 52.5	MICROPHONE NO. 5 ANGLE 60.0	MICROPHONE NO. 6 ANGLE 67.5	MICROPHONE NO. 7 ANGLE 75.0	MICROPHONE NO. 8 ANGLE 82.5	MICROPHONE NO. 9 ANGLE 90.0
200.0	97.4	87.6	86.2	86.3	87.4	87.8	84.3	81.0	80.1
250.0	97.4	90.4	90.6	90.1	87.2	87.3	87.2	85.5	85.6
315.2	97.6	94.3	91.0	90.2	90.1	88.7	88.0	86.4	87.2
400.0	101.8	95.7	93.8	93.6	91.5	90.9	90.1	88.5	88.9
500.0	103.7	98.2	96.2	94.1	92.9	92.6	90.4	90.2	90.0
630.0	107.1	101.6	97.0	97.3	95.9	94.2	93.3	92.4	92.5
800.0	110.0	104.6	100.6	98.9	97.8	96.8	95.5	93.6	93.7
1000.0	111.8	106.4	102.8	100.1	98.8	97.9	96.3	95.4	95.5
1250.0	115.7	110.2	104.9	102.3	100.4	100.2	98.6	97.8	97.9
1600.0	116.1	111.0	106.4	103.2	101.9	100.8	99.8	98.5	96.6
2000.0	117.9	113.3	107.7	104.4	102.8	101.6	100.2	98.8	99.1
2500.0	118.4	113.4	108.6	105.6	103.7	102.4	100.8	99.5	99.8
3150.0	117.5	112.9	109.3	106.2	104.2	103.2	101.4	100.5	100.7
4000.0	116.4	113.5	110.0	107.1	105.0	104.1	102.6	103.2	103.6
5000.0	115.4	113.2	110.6	107.4	105.7	104.5	104.1	103.6	103.7
6300.0	113.8	113.0	111.4	108.2	106.5	106.1	104.9	102.6	103.0
8000.0	112.4	111.9	109.7	108.2	107.0	105.6	103.7	103.6	103.6
10000.0	110.4	110.5	109.3	108.6	106.9	104.9	103.9	104.4	105.1
12500.0	109.0	110.2	109.0	108.1	106.7	105.5	104.6	104.1	104.3
16000.0	107.3	109.4	104.1	107.3	106.0	105.5	104.0	103.3	103.5
20000.0	106.1	108.0	106.9	106.6	105.7	104.6	103.0	102.3	102.4
25000.0	104.3	106.6	106.0	106.2	105.1	103.7	102.1	101.2	101.5
31500.0	102.4	104.9	104.8	105.3	104.1	102.6	101.2	100.8	101.1
40000.0	100.8	104.0	103.4	104.0	102.7	101.8	100.1	99.9	100.2
OVERALL SPL	126.6	123.5	120.5	118.7	117.3	116.2	114.8	114.2	114.5

271

RUN NUMBER 45

1/3 OCTAVE CENTER FREQ. HZ	MICROPHONE NO. 1 ANGLE 30.0	MICROPHONE NO. 2 ANGLE 37.5	MICROPHONE NO. 3 ANGLE 45.0	MICROPHONE NO. 4 ANGLE 52.5	MICROPHONE NO. 5 ANGLE 60.0	MICROPHONE NO. 6 ANGLE 67.5	MICROPHONE NO. 7 ANGLE 75.0	MICROPHONE NO. 8 ANGLE 82.5	MICROPHONE NO. 9 ANGLE 90.0
200.0	99.7	86.5	84.3	86.7	85.4	84.0	84.1	81.0	79.5
250.0	98.4	90.6	90.2	89.4	88.2	86.6	86.4	86.1	84.6
315.2	97.3	92.6	91.3	89.6	89.4	88.5	88.7	85.8	85.0
400.0	100.1	94.4	93.6	91.2	90.6	89.0	89.3	88.6	88.3
500.0	101.8	97.0	95.0	94.0	92.2	91.5	90.4	89.8	90.2
630.0	104.5	100.0	97.4	96.1	94.1	93.6	92.3	91.4	91.0
800.0	106.7	103.9	99.6	97.0	96.2	95.0	94.0	93.4	92.6
1000.0	110.8	105.5	101.3	99.6	98.1	96.8	96.5	94.6	93.9
1250.0	113.6	108.8	103.8	101.3	99.8	99.0	97.9	97.2	96.1
1600.0	115.4	110.1	104.6	102.2	100.9	100.2	99.0	97.8	96.9
2000.0	116.7	110.6	106.2	103.0	101.9	101.4	99.8	98.8	98.0
2500.0	116.1	111.3	107.2	104.3	102.7	101.5	100.6	99.6	98.8
3150.0	116.4	111.5	107.7	105.0	103.8	102.1	101.0	100.3	99.9
4000.0	114.9	111.9	108.5	105.4	104.4	102.9	102.0	102.3	103.1
5000.0	113.6	111.4	108.6	106.2	104.7	103.8	103.7	104.1	102.9
6300.0	112.5	111.0	109.0	106.8	105.8	105.5	104.3	102.7	101.9
8000.0	110.4	110.4	108.6	106.9	106.2	104.8	102.9	102.6	103.3
10000.0	108.6	109.9	108.3	107.0	106.0	104.4	103.4	104.2	104.3
12500.0	107.1	109.5	108.4	106.8	105.9	104.9	104.4	103.9	103.6
16000.0	105.1	108.5	107.5	106.2	105.6	104.9	103.2	103.1	102.6
20000.0	103.6	107.2	106.1	105.7	105.4	104.0	102.3	102.1	101.6
25000.0	102.1	106.0	105.0	105.3	104.7	102.9	101.5	101.2	100.8
31500.0	100.5	104.2	103.9	104.2	103.4	101.9	100.6	100.4	100.2
40000.0	99.2	103.3	102.6	102.8	102.1	101.2	99.9	100.2	99.4
OVERALL SPL	125.0	122.0	119.3	117.5	116.6	115.4	114.3	114.0	113.6

272

APPENDIX 3A

GEOMETRICAL ACOUSTICS FOR PARALLEL, SHEARED FLOW

The notes in this Appendix describe the derivation of analytic, geometric acoustics results for the radiation from various types of acoustic source distribution surrounded by a parallel sheared flow.

The notation in this Appendix and Appendix 3B differs in some respects from that used elsewhere in the report. The main difference is that here the external flow speed or flight speed is $'V_0'$ as opposed to $'V_T'$ or $'V_A'$ used elsewhere; in general, external flow conditions are referred to here by subscript '0'. This means that θ_0 here is equivalent to θ_T in, for example, Appendix 3C and *not* θ_0. Notation in general is explained with the aid of Figure 3A.1.

3A.1   SOURCE IN SHEAR FLOW — GA LIMIT
(FIXED FRAME ANALYSIS)

The stationary-fluid result, in terms of the $(\underline{k}, \omega)$ cross power spectral density (cpsd) of the acoustic source distribution $\tilde{q}(\underline{x}, t)$, would be (with $\underline{V}_s = 0$)

$$R_r^2 \; P(\omega) \big|_s = \frac{\pi}{2} \, \rho_s^2 \; \Phi \; (\omega \underline{\alpha}_s/a_s, \; \omega) \qquad (3A\text{-}1)$$

where $P(\omega)$ is the psd of the far-field pressure in the source-region fluid, ω is the fixed-frame frequency, and the functional form of the source $(\underline{k}, \omega)$ cpsd is $Q(\underline{k}, \omega) = \rho_s^2 \, \Phi \, (\underline{k}, \omega)$.

Provided q contains no $\partial/\partial t$ operators, the Doppler transformation gives the corresponding moving-fluid result — in terms of fixed-frame frequencies — as

$$R_r^2 \; P(\omega) \big|_s = \frac{\pi}{2} \, \rho_s^2 \; \Phi \; (\omega_s \underline{\alpha}_s/a_s, \; \omega) \; D_s^2 \qquad (3A\text{-}2)$$

where

$$\omega_s/\omega = D_s = \{1 + \underline{\alpha}_s \cdot \underline{V}_s/a_s\}^{-1}$$

$$= \{1 + V_s \cos\theta_s/a_s\}^{-1} \qquad (3A\text{-}3)$$

and $\omega_s \underline{\alpha}_s/a_s$ is the radiation wavenumber in the source-region fluid. In equation (3A-2) and elsewhere, R_r denotes the distance travelled by the wavefronts in the wavenormal direction.

To go from the source region to far outside the jet, we assume that the external radiation pattern is axisymmetric. It then follows from energy conservation that
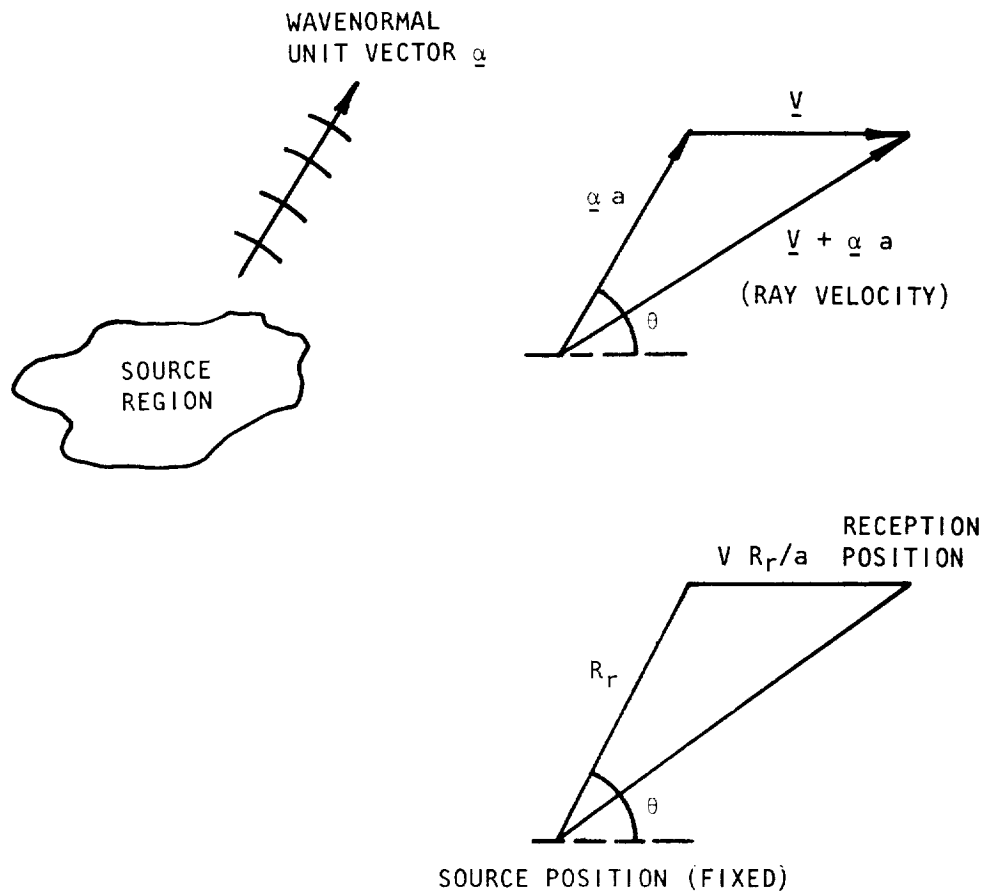
Figure 3A.1 Definition sketch.

$$\frac{\{R_r^2\, P(\omega)\}_o}{\{R_r^2\, P(\omega)\}_s} = \frac{\rho_o D_o{}^4}{\rho_s D_s{}^4} \tag{3A-4}$$

where

$$D_o = \{1 + \underline{a}_o \cdot \underline{V}_o/a_o\}^{-1} = \{1 + V_o\cos\theta_o/a_o\}^{-1} = \omega_o/\omega \tag{3A-5}$$

is the Doppler factor ω_o/ω relating frequencies relative to the external flow to frequencies in the fixed frame.

Combining equations (3A-2) and (3A-4) gives the radiation psd in the external flow as

$$\{R_r^2\ P(\omega)\}_o = \rho_o\, \rho_s\, \frac{\pi}{2}\, \Phi(\omega_s\underline{a}_s/a_s,\ \omega)\, D_o^4\ D_s^{-2} \ . \tag{3A-6}$$

3A.1.1 Compact Volume Acceleration Source at Rest

If we put $Q(\underline{k},\ \omega) = \rho_s^2\ \Phi(\underline{k},\ \omega)$ and assume Φ compact, we get

$$\{R_r^2\, P(\omega)\}_o \doteq \rho_o\, \rho_s\, \frac{\pi}{2}\, \Phi(0,\ \omega)\, D_o^4\ D_s^{-2} \tag{3A-7}$$

compared with

$$\{R_r^2\ P_o(\omega)\}_o = \rho_o^2\, \frac{\pi}{2}\, \Phi(0,\ \omega) \tag{3A-8}$$

if the entire flow field were replaced by fluid $(\rho_o,\ a_o)$ at rest.

Thus for the same emission direction and distance, the effect of the *flow field* on the radiation from a specified compact volume acceleration distribution at rest is given by

$$\frac{P(\omega)}{P_o(\omega)} = \frac{\rho_s}{\rho_o}\, D_o^4\ D_s^{-2} \quad \text{(stationary point volume-} \tag{3A-9}$$
$$\text{acceleration source)} .$$

This result is not to be confused with any effects which arise from having a convected *source* pattern; only the *fluid* is moving here.

3A.1.2 Compact Volume-Acceleration Quadrupole at Rest

If $q = \rho_s\ (\partial^2 S_{ij}/\partial x_i \partial x_j)$, so that

$$Q(\underline{k},\ \omega) = \rho_s^2\, k_i\, k_j\, k_\ell\, k_m\, \Phi_{ij\ell m}(\underline{k},\ \omega) \tag{3A-10}$$

is the functional form of the source $(\underline{k}, \omega)$ cpsd, then (3A-6) is replaced by

$$R_r^2 \left. P(\omega) \right|_o = \frac{\rho_o \rho_s}{a_s^4} \frac{\pi}{2} \, \alpha_{si} \, \alpha_{sj} \, \alpha_{s\ell} \, \alpha_{sm} \, \Phi_{ij\ell m}(\omega_s \underline{\alpha}_s / a_s, \, \omega)$$

$$\times \, \omega_s^4 \, D_o^4 \, D_s^{-2},$$

and if Φ is compact, we get (using $\omega_s = \omega D_s$)

$$R_r^2 \left. P(\omega) \right|_o = \frac{\rho_o \rho_s}{a_s^4} \frac{\pi}{2} \cdot \alpha_{si} \, \alpha_{sj} \, \alpha_{s\ell} \, \alpha_{sm} \, \Phi_{ij\ell m}(0, \, \omega)$$

$$\times \, \omega^4 \, D_o^4 \, D_s^2 \, . \tag{3A-11}$$

For a given emission direction $\underline{\alpha}_s$ and distance R_r, the effect of the *flow field* on the radiation from a specified $S_{ij}(\underline{x}, t)$ compact distribution is

$$\frac{P(\omega)}{P_o(\omega)} = \frac{\rho_s}{\rho_o} \left(\frac{a_s}{a_o} \right)^{-4} D_o^4 \, D_s^2 \quad \begin{array}{l}\text{(stationary point volume-} \\ \text{acceleration quadrupole).}\end{array} \tag{3A-12}$$

3A.1.3 Compact Volume-Displacement Quadrupole at Rest

If $q = \rho_s (\partial^2/\partial t^2)(\partial^2 B_{ij}/\partial x_i \partial x_j)$ relative to the flow, so that

$$Q(\underline{k}, \omega) = \rho_s^2 \, \omega^4 \, k_i \, k_j \, k_\ell \, k_m \, \Phi_{ij\ell m} \, (\underline{k}, \, \omega)$$

is the functional form of the source $(\underline{k}, \omega)$ cpsd, then the compact-source result is (in the GA limit)

$$R_r^2 \left. P(\omega) \right|_o = \frac{\rho_o \rho_s}{a_s^4} \frac{\pi}{2} \cdot \alpha_{si} \, \alpha_{sj} \, \alpha_{s\ell} \, \alpha_{sm} \, \Phi_{ij\ell m} \, (0, \, \omega)$$

$$\times \, \omega^8 \, D_o^4 \, D_s^6 \, .$$

Thus, the effect of the *flow field*, for a given $B_{ij}(\underline{x}, t)$ distribution, is given by

$$\frac{P(\omega)}{P_o(\omega)} = \frac{\rho_s}{\rho_o} \left(\frac{a_s}{a_o} \right)^{-4} D_o^4 \, D_s^6 \quad \begin{array}{l}\text{(stationary point volume} \\ \text{displacement quadrupole),}\end{array}$$

if $\underline{\alpha}_s$ and R_r are held constant.

278

3A.2 NON-COMPACTNESS EFFECTS AND SOURCE CONVECTION

The simplest estimate of non-compactness effects in aerodynamic noise is obtained by assuming isotropy of Φ (or $\Phi_{ij\ell m}$) with respect to the direction of the vector argument ($k_1 V_{e1}$, $k_2 V_{e2}$, $k_3 V_{e3}$, $\omega - k_1 V_{c1}$). (For convenience a convection velocity (V_{c1}, 0, 0) is assumed, i.e. parallel to the mean flow velocity). Thus, we put

$$Q(\underline{k}, \omega) = \rho_s^2 \Phi(\underline{k}, \omega') \quad (\omega' = \omega - k_1 V_{c1}$$
$$= \text{convected frame}$$
$$\text{frequency)};$$

$$\Phi(\underline{k}, \omega') = \Phi(0, \{(k_1 V_{e1})^2 + (k_2 V_{e2})^2 + (k_3 V_{e3})^2 + \omega'^2\}^{\frac{1}{2}})$$

$$(\text{isotropic function assumption}) . \qquad (3A-13)$$

Putting $\underline{k} = \omega_s \underline{\alpha}_s / a_s$ in (3A-13) gives the required value of Φ as

$$\Phi(\omega_s \underline{\alpha}_s / a_s, \omega - \omega_s \alpha_{s1} V_{c1} / a_s) = \Phi(0, \omega_m), \quad \text{say,} \qquad (3A-14)$$

which defines the *modified frequency* ω_m and the *modified Doppler factor* $D_m = \omega_m/\omega$. Note that $\omega_s \alpha_{s1}/a_s = \omega_0 \alpha_{o1}/a_o$ (for k_1 matching).

Thus, the stationary compact-source result (3A-11) is modified to

$$R_r^2 P(\omega)\big|_0 = \frac{\rho_o \rho_s}{a_s^4} \frac{\pi}{2} \{\alpha_{si} \alpha_{sj} \alpha_{s\ell} \alpha_{sm} \Phi_{ij\ell m}^{(1)} (0, \omega_m)\omega_m^4\}$$

$$\times D_o^4 D_s^2/D_m^4$$

$$(\text{non-compact convected volume-acceleration quadrupole}) . \qquad (3A-15a)$$

Also,

$$R_r^2 P(\omega)\big|_0 = \frac{\rho_o \rho_s}{a_s^4} \frac{\pi}{2} \{\alpha_{si} \alpha_{sj} \alpha_{s\ell} \alpha_{sm} \Phi_{ij\ell m}^{(3)}(0, \omega_m)\omega_m^8\} \frac{D_o^4 D_s^6}{D_m^8}$$

$$(\text{non-compact convected volume-displacement quadrupole}) . \qquad (3A-15b)$$

Note that in (3A-15), $\Phi_{ij\ell m}^{(\nu)}$ is a kinematic quantity, i.e. it contains no density factors.

3A.2.1 Recovery of Lighthill Radiation Model

In the Lighthill radiation model, the sources radiate directly into the surrounding fluid (density ρ_0, sound speed, a_0, velocity $\underline{V}_0$). The foregoing results may be converted to the Lighthill radiation model by simply putting

$$\rho_s \rightarrow \rho_0$$
$$a_s \rightarrow a_0$$
$$V_s \rightarrow V_0 \tag{3A-16}$$
$$\alpha_s \rightarrow \alpha_0$$

and

$$D_s \rightarrow D_0$$

Further details are given below, in sections 3A.2.2 and 3A.2.3.

3A.2.2 Evaluation of D_m (GA Limit)

From (3A-13) and (3A-14),

$$\omega_m^2 = (\omega_0 \alpha_{01}/a_0)^2 \, V_{e1}^2 + k_2^2 \, V_{e2}^2 + k_3^2 \, V_{e3}^2$$

$$+ [\omega - (\omega_0 \alpha_{01}/a_0) \, V_{c1}]^2, \tag{3A-17}$$

where

$$k_2^2 + k_3^2 = (\omega_s/a_s)^2 - k_1^2$$

$$= (\omega/a_s)^2 \, D_s^2 - (\omega_0 \alpha_{01}/a_0)^2$$

$$= (\omega/a_s)^2 \, D_s^2 - (\omega/a_0)^2 \, D_0^2 \cos^2\theta_0$$

$$(\alpha_{01} = \cos\theta_0) \, . \tag{3A-18}$$

Thus if we make the simplifying assumption that $V_{e2} = V_{e3} = V_{et}$, say, the modified Doppler factor follows from (3A-17) and (3A-18) as

$$D_m = \omega_m/\omega = \left\{ D_0^2 \cos^2\theta_0 \left(\frac{V_{e1}^2 - V_{et}^2}{a_0^2} \right) + D_s^2 \left(\frac{V_{et}}{a_s} \right)^2 \right.$$

$$\left. + (1 - D_0 \frac{V_{c1}}{a_0} \cos\theta_0)^2 \right\}^{\frac{1}{2}} \tag{3A-19}$$

The following special cases of (3A-19) are of interest.

(a) $\underline{V}_0 = 0$ (source region at rest relative to external fluid): then $D_0 = 1$. Also,

280

$$D_s = (1 + V_s\cos\theta_s/a_s)^{-1} = (1 - V_s\cos\theta_0/a_0) \tag{3A-20}$$

from consideration of phase speeds in the axial direction.

(b) Lighthill radiation model: all s subscripts in (3A-19) are changed to 0. Thus,

$$D_m = D_0 \left\{ \left(\frac{V_{e1}}{a_0}\right)^2 \cos^2\theta_0 + \left(\frac{V_{et}}{a_0}\right)^2 \sin^2\theta_0 + \left(D_0^{-1} - \frac{V_{c1}}{a_0}\cos\theta_0\right)^2 \right\}^{\frac{1}{2}}; \tag{3A-21}$$

Note that

$$D_0^{-1} - \frac{V_{c1}}{a_0}\cos\theta_0 = 1 - \left(\frac{V_{c1} - V_0}{a_0}\right)\cos\theta_0 \tag{3A-22}$$

from the definition of D_0 in equation (3A-5).

(c) General GA modified Doppler factor with $V_{c1} = V_s$: If the convection velocity is set equal to the local flow velocity in the shear layer, equation (3A-19) simplifies to

$$D_m = D_0 \left\{ \cos^2\theta_0 \left(\frac{V_{e1}^2 - V_{et}^2}{a_0^2}\right) + D_{s,rel}^2 \left(\frac{V_{et}^2}{a_s^2} + 1\right) \right\}^{\frac{1}{2}}, \tag{3A-23}$$

where the relative motion Doppler factor is defined by

$$D_{s,rel} = 1 - \left(\frac{V_s - V_0}{a_0}\right)\cos\theta_0 \tag{3A-24}$$

$$= \left\{ 1 + \frac{V_s - V_0}{a_s}\cos\theta_s \right\}^{-1} \tag{3A-25}$$

$$= \frac{\omega_s}{\omega_0} = \frac{D_s}{D_0}. \tag{3A-26}$$

Equations (3A-25) and (3A-26) follow from the phase-speed relationship across the shear layer, $V_s + a_s/\cos\theta_s = V_0 + a_0/\cos\theta_0$.

3A.2.3 Check on the Ffowcs Williams (ref. 7) result obtained using
         Lighthill radiation model

Changing all s subscripts to 0 in equation (3A-15) gives the radiation from a Lighthill-type convected quadrupole distributon in a completely uniform moving medium (velocity V_0 parallel to the convection direction). Thus, in proportional bandwidth form,

$$\{R_r^2 \ P(\omega)\omega\}_0 = \frac{\rho_0^2}{a_0^4} \ \{\alpha_{0i} \ \alpha_{0j} \ \alpha_{0l} \ \alpha_{0m} \ \phi_{ijlm}^{(1)}(0,\omega_m)\omega_m^5\} \ \times \ \frac{D_0^6}{D_m^5} \tag{3A-27}$$

To convert from source-region frequency ω to the frequency ω_0 relative to the uniform flow, *no change* in the proportional-bandwidth mean square pressure is involved, but simply a frequency shift by a factor $\omega_0/\omega = D_0$, as given by equation (3A-5). The frequency ω_0 corresponds to the frequency heard by an observer on the ground, as the source region is moved past with velocity $-V_0$ (assuming the atmosphere is at rest).

The factor D_0^6/D_m^5 follows from (3A-21) and (3A-22) above as

$$(1 + \frac{V_0}{a_0} \cos\theta_0)^{-1} \left\{ \left[1 - \left(\frac{V_{c1} - V_0}{a_0} \right) \cos\theta_0 \right]^2 + \left(\frac{V_{e1}}{a_0} \right)^2 \cos^2\theta_0 \right.$$

$$\left. + \left(\frac{V_{et}}{a_0} \right)^2 \sin^2\theta_0 \right\}^{-5/2} , \tag{3A-28}$$

which is the same as the factor obtained by Ffowcs Williams (ref. 7) for a homogeneous source model with a Gaussian space-time correlation function. The Ffowcs Williams form of source distribution is a special case of the more general form assumed in (3A-13), which was first proposed by Crighton (ref. 111).

282

APPENDIX 3B

GENERAL RESULTS FOR PARALLEL SHEAR FLOWS
(SOURCE DISTRIBUTIONS WITH AXIAL COHERENCE ONLY)

These notes describe the framework in which the Lilley equation flow factor solution can be used to estimate flow-acoustic alteration effects due to forward motion.

The notation used here and in Appendix 3A differs in some respects from that used elsewhere in the report. The main differences are described in the introduction to Appendix 3A.

3B.1 THE MODIFIED DOPPLER FACTOR

When only axial source coherence effects are retained, the modified frequency, ω_m, defined in section 2 of Appendix 3A, reduces to

$$\omega_m^2 = \left(\frac{\omega_0}{a_0} \cos\theta_0 \, V_{e1} \right)^2 + \left(\omega - \frac{\omega_0}{a_0} \cos\theta_0 \, V_{c1} \right)^2$$

i.e.

$$\omega_m = \omega \left\{ \left(1 - D_0 \frac{V_{c1}}{a_0} \cos\theta_0 \right)^2 + D_0^2 \left(\frac{V_{e1}}{a_0} \cos\theta_0 \right)^2 \right\}^{\frac{1}{2}}$$

$$= \omega D_m, \text{ say} \tag{3B-1}$$

In (3B.1),

$$D_0 = \left(1 + \frac{V_0}{a_0} \cos\theta_0 \right)^{-1} = \frac{\omega_0}{\omega} \tag{3B-2}$$

3B.2 EQUIVALENT STATIONARY POINT VOLUME-ACCELERATION OR VOLUME-DISPLACEMENT QUADRUPOLE

The quadrupole cross-power spectral density in axial wavenumber and frequency, evaluated at the *actual frequency* ω[†] and the *actual wavenumber* $k_1 = (\omega/a_0)D_0\cos\theta_0$ required for radiation at θ_0 to the x_1 axis, is assumed to be the same as the cross-power spectral density at the *modified frequency* ω_m and at *zero wavenumber*, $k_1 = 0$. Coherence of the quadrupole distribution in the transverse plane (x_2, x_3) is assumed to be negligible

Thus, if $\hat{P}(\omega)$ is the far-field pressure psd[‡] radiated by a *stationary point* volume acceleration/displacement quadrupole of the *same instantaneous total strength*, the radiation at the same distance from the *actual non-compact* quadrupole distribution is given by

---

[†]*Relative to coordinates fixed in the source region, i.e. fixed with respect to the nozzle.*

[‡]*Azimuthally averaged.*

$$P(\omega) = \hat{P}(\omega_m) \, D_m^{-4} \qquad (\nu = 1)$$

or

$$P(\omega) = \hat{P}(\omega_m) \, D_m^{-8} \qquad (\nu = 3) \qquad\qquad \text{(3B-3)}$$

The D_m^{-4} or D_m^{-8} factor arises from the ω^4 or ω^8 frequency dependence of $\hat{P}(\omega)$. If proportional frequency-bandwidth values are required, the factor becomes D_m^{-5} or D_m^{-9}; thus,

$$P(\omega)\omega = \hat{P}(\omega_m)\omega_m \, D_m^{-5} \qquad (\nu = 1)$$

or

$$P(\omega)\omega = \hat{P}(\omega_m)\omega_m \, D_m^{-9} \qquad (\nu = 3) \qquad\qquad \text{(3B-4)}$$

which is a more convenient form for scaling purposes.

3B.3   SCALING OF RADIATED PRESSURE
POWER SPECTRAL DENSITY

In a *uniform fluid at rest*, the radiation from the stationary point quadrupole described above would be given by

$$R_r^2 \, \hat{P}(\omega)\omega = \frac{\pi}{2} \frac{\rho_o^2}{a_o^4} \, \alpha_{oi} \, \alpha_{oj} \, \alpha_{o\ell} \, \alpha_{om} \Phi_{ij\ell m}^{(\nu)}(0,\omega) \, \omega^{2\nu+3} \qquad\qquad \text{(3B-5)}^\dagger$$

Here, for example,

$$\Phi_{ij\ell m}^{(1)}(0,\omega)\omega \propto (V_J^2 \, d^3)^2$$

$$\Phi_{ij\ell m}^{(3)}(0,\omega)\omega \propto d^{10} \qquad\qquad \text{(3B-6)}$$

since $\Phi_{ij\ell m}^{(\nu)}(0,\omega)$ is the cross-power spectral density (in ω) of the total integrated quadrupole strength, $\int v_i{}'v_j{}'d\underline{x}$ or $\int \xi_i{}'\xi_j{}'d\underline{x}$, and it is assumed in this example that $v_i{}'$ scales on V_J or that $\xi_i{}'$ scales on $V_J(V_J/d)^{-1} = d$, the nozzle diameter. Also,

$$\omega \propto V_J/d; \qquad\qquad \text{(3B-7)}$$

so

$$\frac{R_r^2 \, \hat{P}(\omega)\omega}{d^2 \rho_o^2 \, a_o^4} \propto \left(\frac{V_J}{a_o}\right)^8 \qquad\qquad \text{(3B-8)}$$

---

†*Note $\Phi_{ij\ell m}^{(\nu)}(0,\omega)$ is the ω-spectral density of the quadrupole strength.*

286

Thus if $F^{(\nu)}$ is the factor by which the point volume-acceleration/displacement quadrupole radiation intensity is multiplied, due both to finite Mach numbers in the flow and to departures of (ρ, a) from (ρ_0, a_0), the scaling law derived from (3B-4) and (3B-8) is

$$\frac{R_r^2 \, P(\omega)\omega}{d^2 \rho_0^2 a_0^4} \propto \left(\frac{V_J}{a_0}\right)^8 F^{(\nu)}(\omega) \, D_m^{-(2\nu+3)}$$

$$\text{(for given } \omega_m d/V_J) \tag{3B-9}$$

3B.4 EFFECT OF EXTERNAL STREAM, OF SPEED V_0, ON FLOW RADIATION FACTOR $F(\omega)$

The flow factor $F^{(\nu)}(\omega)$ refers to the situation (a) sketched in Figure 3B.1 in which a stationary point quadrupole is placed in a shear layer with (in general) a non-zero external velocity.

If the flow factor in the situation (b) sketched in Figure 3B.1 is denoted by $F_{rel}^{(\nu)}(\omega)$, where the flow velocities are reduced everywhere by V_0 to bring the external stream to rest, then $F^{(\nu)}(\omega)$ is given by

$$F^{(\nu)}(\omega) = F_{rel}^{(\nu)}(\omega D_0) \, D_0^{2\nu+4} \quad \text{(for same } \alpha_{01}) \tag{3B-10}$$

since (a) is equivalent to having a convected point quadrupole of frequency ω moving upstream at V_0 as in (c). The fixed-frame frequency corresponding to (c) is $\omega_0 = \omega D_0$, since (c) is simply (a) with a velocity $-V_0$ superimposed; this is the reason for having ωD_0 as the argument of $F_{rel}^{(\nu)}$.

The factor $D_0^{2\nu+4}$ in (3B-10) represents the basic effect of a completely uniform flow of velocity V_0 on the point quadrupole radiation[†]; once this has been allowed for the $F_{rel}^{(\nu)}(\omega D_0)$ factor accounts for departures from this uniform flow as described above.

Note that the combination $D_0^{2\nu+4} \, D_m^{-(2\nu+3)}$ which appears in the *radiation scaling law* when (3B-10) is substituted into (3B-9), may be written as

$$D_0 (D_m/D_0)^{-(2\nu+3)} = D_0 \, D_{m,rel}^{-(2\nu+3)} \tag{3B-11}$$

where $D_{m,rel}$ is the modified Doppler factor as in equation (3B-1), but with V_{c1} replaced by $V_{c1} - V_0$. Thus, the scaling law may be written in the more useful form

---

[†]*As follows from the Doppler transformation.*

POINT
QUADRUPOLE ☆
(ω)

V_O

V_J

(a)

POINT
QUADRUPOLE ☆
(ω)

$V_J - V_O$

(b)

POINT
QUADRUPOLE

(ω)

⟵ ☆

V_O

$V_J - V_O$

(c)
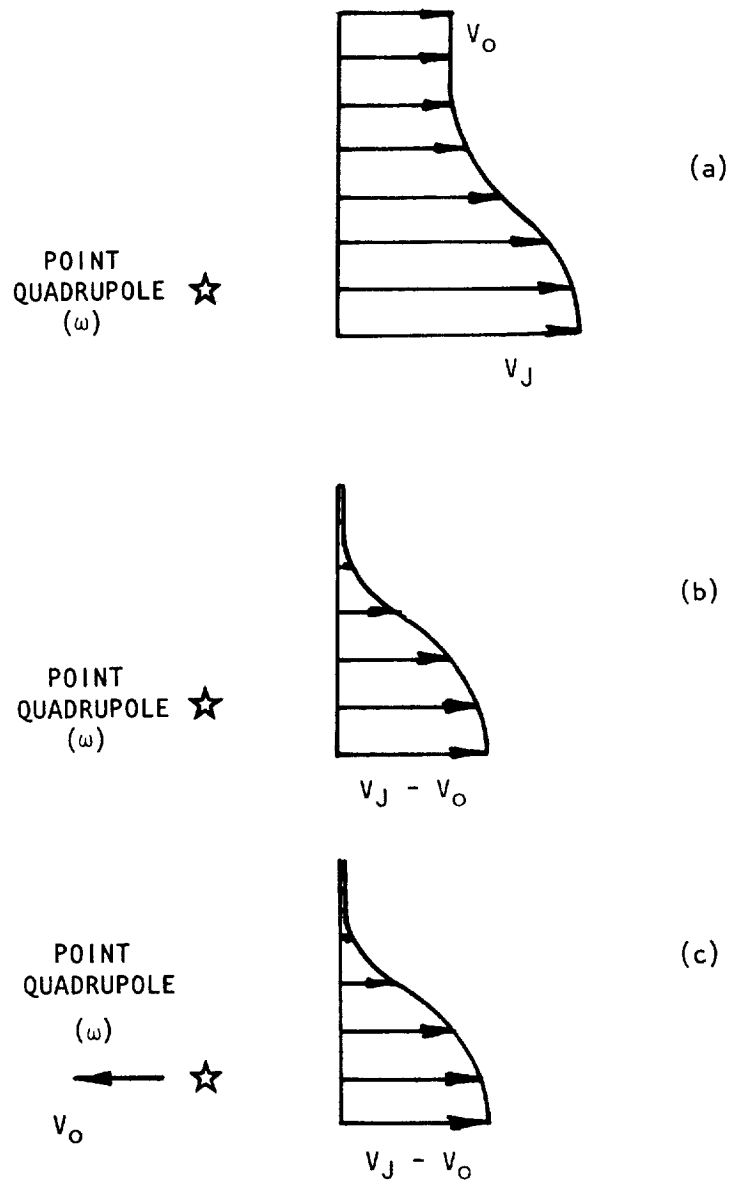
Figure 3B.1   Flow factor — velocity profile situations.

$$\frac{R_r^2 \; P(\omega)\omega}{d^2 \; \rho_o^2 \; a_o^4} \; \left(\frac{V_J}{a_o}\right)^8 \; \propto \; F_{rel}^{(\nu)}(\omega D_o) \; \frac{D_o}{D_{m,rel}^{2\nu+3}} \qquad\qquad (3B-12)$$

289

APPENDIX 3C

A GEOMETRIC ACOUSTICS INVESTIGATION INTO THE
INFLUENCE OF FREE-JET MEAN VELOCITY AXIAL VARIATIONS
(NON-STRATIFIED FLOW) ON SOUND REFRACTION BY THE
SHEAR LAYER (RELATIVE TO THE STRATIFIED FLOW CASE).

The simple, analytic relationships used elsewhere in this report, between ray and/or wavenormal angles inside and outside an axisymmetric cylindrical sheared flow field are results which are valid only for the special case of a parallel or unidirectional, stratified[†] mean flow field. These terms are used occasionally to mean that such properties persist at all locations upstream and downstream of the local flow region under consideration. Here that unrealistic flow field model would be referred to as an *infinite* stratified, parallel flow field model and is thereby distinguished from the more realistic *(locally)* parallel, stratified flow field model. The latter is a fairly realistic model of the initial mixing region of an axisymmetric jet flow, since the mean velocity vector varies in direction by only 2 or 3° from the axial direction and its magnitude is only a weak function of the axial coordinate compared with its strong dependence on the transverse or radial coordinate

Here the restriction that the flow be stratified is removed so that the magnitude of the axial mean velocity vector is allowed to vary with axial position in a realistic way. With that dependence specified, the refraction or bending of sound rays as they propagate through a parallel, but non-stratified, shear layer is examined and emerging ray angle results are compared with those calculated for the parallel stratified shear layer case; ray displacement effects are also studied.

In a sense this non-stratified flow model may be more unrealistic than the stratified one; for example, if the flow is incompressible, then the continuity equation can be written as

$$\frac{\partial V_r}{\partial x} = - \frac{1}{r} \frac{\partial (r\, V_t)}{\partial r} - \frac{1}{r} \frac{\partial V_\phi}{\partial \phi} \qquad (3C-1)$$

where V_t, V_ϕ are the mean velocity components in the radial (r) and azimuthal (ϕ) directions. Thus, when $V_x = V_x(x,r)$, the continuity equation requires, in general, a non-zero radial mean velocity V_t, i.e. the flow is non-parallel which is in conflict with the flow model as specified. In principle then, when the stratified flow restriction is removed, non-axial mean velocity components should be included in the mean flow model, in particular (for non-swirling flows) the component $V_t = V_t(x,r)$ with $V_\phi = 0$. This would be a useful extension of the present work.

3C.1 A JUSTIFICATION FOR UTILIZATION OF THE GEOMETRIC ACOUSTICS EQUATIONS TO DESCRIBE SOUND PROPAGATION THROUGH THE FREE-JET SHEAR LAYER

According to Morse and Ingard (ref. 112) the geometric approximation is "...appropriate when a and $\underline{V}$ vary slowly and 'smoothly' (i.e. when the

---

[†]*Defined as the flow properties being a function of the transverse coordinate only.*

293

wavelength times the Laplacian of a and $\underline{V}$ are negligible compared to their gradients) ...." The geometric acoustics equations used below are obtained by assuming a solution for the acoustic pressure, p', of the form

$$p'(\underline{x},t) = A(\underline{x},\omega) \exp[-jk\Phi(\underline{x}) + j\omega t] \tag{3C-2}$$

to the convected wave equation

$$\frac{1}{a^2} \frac{\bar{D}^2 p'}{Dt^2} = \nabla^2 p' \tag{3C-3}$$

$$(\bar{D}/Dt \equiv \partial/\partial t + V_i \; \partial/\partial x_i).$$

Φ is the so-called eikonal function which defines the surfaces of equal phases and A($\underline{x}$) is the amplitude function. The eikonal equation

$$|\text{grad}\Phi| = \frac{a_0}{a + \underline{V} \cdot \hat{n}} \tag{3C-4}$$

$$(\hat{n} = \text{grad}\Phi/|\text{grad}\Phi|) \tag{3C-5}$$

is derived by substituting the solution (3C-2) into equation (3C-3) and neglecting all but the highest powers of k $(=\omega/a_0)$. However apart from the trivial case of a completely uniform flow, $\underline{V}(\underline{x})$ = constant, equation (3C-3) is itself an approximation: if $\underline{V} = (V_x(r),0,0)$, a = a(r), $\rho = \rho(r)$, then the exact equation is simply the left hand side of the Lilley equation set equal to zero (since sources within the free-jet shear layer are not considered here, only sound propagation through it), that is,

$$\frac{\bar{D}}{Dt}\left|\frac{1}{a^2}\frac{\bar{D}^2 p'}{Dt^2} - \nabla^2 p'\right| + \frac{1}{\rho}\frac{d\rho}{dr}\frac{\bar{D}}{Dt}\left|\frac{\partial p'}{\partial r}\right| + 2\left(\frac{dV_x}{dr}\right)\frac{\partial^2 p'}{\partial x \partial r} = 0 . \tag{3C-6}$$

In this particular kind of flow field, an infinite, parallel, stratified flow, the geometric approximation is valid, in the first instance, when the last two terms can be neglected in equation (3C-6) thereby reducing it to a form closely resembling that of equation (3C-3); clearly, the geometric acoustic solutions of equation (3C-3) also satisfy this reduced form of the Lilley equation.

By considering the solution of equation (3C-6) at a particular frequency and for a certain radiation angle, it is not difficult to show that the mean velocity gradient term is of order $1/S_{\delta T}$ relative to the two leading terms, for a given mean velocity profile shape. The Strouhal number $S_{\delta T}$ is based upon the vorticity thickness of the free-jet shear layer, $\delta_{\omega T}$, and the centerline or exit mean velocity, V_T.

In the free-jet configuration $\delta_{\omega T}$ will be typically an order of magnitude larger than that in the primary jet for a given "ray path" at 90° or in the rear arc. The ratio of the tunnel or free-jet exit velocity, V_T, to the primary jet centerline velocity varies over a wide range of values (for

a given ray path) but is less than unity so that

$$S_{\delta T} \geq 10 \ S_{\delta P}$$

where $S_{\delta P}$ is the Strouhal number based on primary jet quantities. It can be evaluated by linking it with the axial location of maximum radiation in the primary jet and is found to be (empirically) of order unity. Hence, in the present problem, the gradient term in the homogeneous Lilley equation is at least an order of magnitude smaller than the two leading terms that form the basis for the geometric approximation.

The Lilley equation solutions presented in section 3.2 for sound radiation from the primary jet alone *do* exhibit significant deviations from the geometric acoustic solutions but that represents, in principle, a combination of source-flow interactions and propagation effects. That is, sources are located within the shear layer and the sheared flow modifies the emission process as well as that of propagation. In any case the corresponding free-jet Strouhal numbers would be an order of magnitude larger than the values adopted there and the trends in those results indicates a rapid approach to geometric acoustics with increasing Strouhal number.

3C.2 BASIC EQUATIONS FOR A GEOMETRIC ACOUSTICS STUDY OF REFRACTION IN A PARALLEL NON-STRATIFIED MEAN FLOW MODEL OF THE FREE-JET

The equations governing the propagation and refraction of acoustic rays in an otherwise time independent mean flow field can be written as three second order, ordinary differential equations [Ugincius (ref. 113)]:

$$\frac{d}{ds}\left(N \frac{d\underline{r}}{ds}\right) + \frac{d\underline{r}}{ds} \times (\underline{\nabla} \times \underline{W}) = \underline{\nabla} N \tag{3C-7}$$

Later Ugincius (ref. 114) corrected these to

$$\frac{d}{ds}\left(N \frac{d\underline{r}}{ds}\right) - \left(\frac{d^2\underline{r}}{ds^2} \cdot \underline{\nabla}'\right) \underline{W} + \frac{d\underline{r}}{ds} \times (\underline{\nabla} \times \underline{W}) = \underline{\nabla} N \tag{3C-8}$$

where $\underline{r} = \underline{r}(s)$ is the position vector of the ray as a function of arc length s and

$$\underline{W} = \mu \ \frac{\underline{V}}{a} \tag{3C-9}$$

$$\mu = \frac{a_0}{a + \underline{V} \cdot \hat{\underline{n}}} \tag{3C-10}$$

$$N = \mu \ V_r/a \tag{3C-11}$$

295

$$\frac{V_r}{a} = 1 + \left| \frac{|\underline{V}|}{a} \right|^2 + 2 \left| \frac{|\underline{V}|}{a} \right| \cos\theta. \tag{3C-12}$$

$\underline{V} \equiv \hat{\underline{e}}_i \, \partial/\partial x_i$ and $\underline{\nabla}' \equiv \hat{\underline{e}}_i \partial/\partial x_i'$ where

$$x_i' = d\underline{r}/ds. \tag{3C-13}$$

The speed of sound $a(\underline{r})$ and velocity vector $\underline{V}(\underline{r})$ are arbitrary, well-behaved functions of the position vector, $\underline{r}$; the speed of sound a_0 is a reference value. The relationship between $\underline{V}$, $\underline{n}$, a, V_r and θ is indicated in Figure 3C.1. The vector $\hat{\underline{n}}$ is the unit normal to the wavefront (a surface of constant phase); it is the direction of the sound ray only if there is no flow, $\underline{V} \equiv 0$. With flow the ray direction is given by the vector $\underline{V}_r$ where

$$\underline{V}_r = a\hat{\underline{n}} + \underline{V} \tag{3C-14}$$

i.e. the direction of the ray, $d\underline{r}/ds$, is given by

$$d\underline{r}/ds = \hat{\underline{V}}_r = \underline{V}_r/V_r \, .$$

The angle between the wavefront normal direction and that of the mean flow velocity is designated θ and that between the ray direction and the mean flow direction, ψ.

Equations (3C-7) and (3C-8) differ by the term

$$-\left(\frac{d^2\underline{r}}{ds^2} \cdot \underline{\nabla}' \right) \underline{W}$$

which Ugincius (ref. 114) argues is negligible for low Mach number flows. The present investigation is based on equation (3C-7), since typical Mach numbers of the jet flows of interest are less than 0.25. However, the influence of that extra term should be considered in future work [by solving equation (3C-8)].

Equation (3C-7) simplifies considerably when the mean velocity vector is defined to be every where parallel to the x axis and axisymmetric, i.e.

$$\underline{V} = \{V_x(x,r), \, 0, \, 0\} \tag{3C-16a}$$

with
$$a = a(x,r) \tag{3C-16b}$$

so that

$$\underline{W} = \{\mu V_x/a, \, 0, \, 0\} \tag{3C-17}$$

$$\mu = \frac{a_0}{a + V_x \cos\theta} \tag{3C-18}$$

$$\frac{V_r}{a} = 1 + (V_x/a)^2 + 2(V_x/a) \cos\theta \, . \tag{3C-19}$$

296

$$\underline{V}_r = a\underline{\hat{n}} + \underline{V}$$

$$= V_r \ \frac{d\underline{r}}{ds}$$
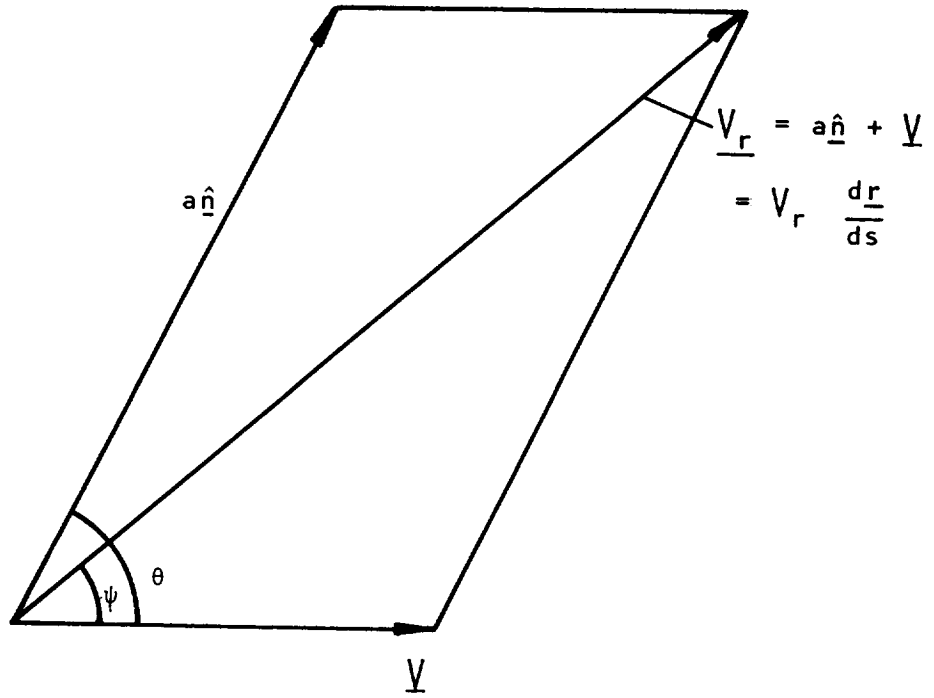
Figure 3C.1 Definition sketch.

$$\underline{V}_r = \left| V_x + \cos\theta, \ a \sin\theta, \ 0 \right| \tag{3C-20}$$

$$\frac{d\underline{r}}{ds} = \left| \frac{V_x + a \cos\theta}{V_r}, \ \frac{a \sin\theta}{V_r}, \ 0 \right| \tag{3C-21}$$

With equations (3C-16) through (3C-21) the x component of equation (3C-7) reduces to

$$\frac{d}{ds} \left| \frac{\cos\theta}{a + V_x \cos\theta} \right| = - \frac{1}{V_r(a + V_x \cos\theta)} \left| \frac{\partial a}{\partial x} + \cos\theta \ \frac{\partial V_x}{\partial x} \right| . \tag{3C-22}$$

When a *stratified flow field* is assumed $[V_x = V_x(r), \ a = a(r)]$, equation (3C-22) can be solved immediately to give

$$\frac{\cos\theta}{a + V_x \cos\theta} = \text{constant}.$$

It follows that if (i) $\theta = \theta_T$, $V_x = V_T$, $a = a_T$ and (ii) $\theta = \theta_o$, $V_x = 0$, $a = a_o$ at two points on the ray path then

$$\frac{a_T}{\cos\theta_T} + V_T = \frac{a_o}{\cos\theta_o}$$

a relation that also can be obtained by "matching axial phase velocities" on both sides of a stratified shear layer (a vortex sheet being a special case).

Equation (3C-22) was adopted by Schubert (ref. 115) for his "Numerical Study of Sound Refraction by a Jet Flow," based on ray or geometric acoustics

With the following relations

$$\frac{d}{ds} \equiv \cos\psi \ \frac{\partial}{\partial x} + \sin\psi \ \frac{\partial}{\partial r} \tag{3C-24}$$

$$\cos\psi = \frac{V_x + a \cos\theta}{V_r}; \quad \sin\psi = \frac{a \cos\theta}{V_r}. \tag{3C-25}$$

Schubert (ref. 115) reduces equation (3C-22) to

$$\frac{d\theta}{ds} = \frac{1}{V_r} \left| \sin\theta \ \frac{\partial a}{\partial x} - \cos\theta \ \frac{\partial a}{\partial r} + \cos\theta \left(\sin\theta \ \frac{\partial V_x}{\partial x} - \cos\theta \ \frac{\partial V_x}{\partial r} \right) \right| \tag{3C-26}$$

and then by differentiating

$$\tan\psi = a \sin\theta / (V_x + a \cos\theta) \tag{3C-27}$$

to obtain

$$\frac{d\tilde{\psi}}{ds} = \frac{a^2}{V_r^2} \left[(1 + V_x/a \cdot \cos\theta) \frac{d\theta}{ds} - \sin\theta \frac{d}{ds} (V_x/a) \right] \qquad (3C\text{-}28)$$

Schubert (ref. 115) finally obtains the following equation for the ray curvature $d\psi/ds$

$$\frac{d\psi}{ds} = \frac{1}{V_r} \left| \frac{V_r}{a} \sin\psi \frac{\partial a}{\partial x} + \left(2 \, M \sin^2\psi - \frac{a}{V_r} \cos\psi \right) \frac{\partial a}{\partial r} - \frac{V_r}{a} M \sin^3\psi \frac{\partial V_x}{\partial x} \right.$$

$$\left. - \frac{a^2}{V_r^2} \left[1 + M \left(\frac{V_r}{a} \cos\psi - M \right)^3 \right] \frac{\partial V_x}{\partial r} \right| \qquad (3C\text{-}29)$$

where $M = V_x/a$. The ray speed can be expressed in terms of

$$V_r/a = M\cos\psi + (1 - M^2\sin^2\psi)^{\frac{1}{2}} \qquad (3C\text{-}30)$$

so that the right-hand side of equation (3C-29) is a function of the mean flow properties and is only an algebraic function of the angle between the ray and mean velocity vectors, ψ.

In order to solve equation (3C-29) numerically, the following identities are substituted

$$\frac{d\psi}{ds} \equiv \frac{- \, d^2x/dr^2}{[1 + (dx/dr)^2]^{3/2}} \qquad (3C\text{-}31)$$

$$\sin\psi \equiv \frac{1}{[1 + (dx/dr)^2]^{\frac{1}{2}}} \qquad (3C\text{-}32)$$

$$\cos\psi \equiv \frac{dx/dr}{[1 + (dx/dr)^2]^{\frac{1}{2}}} \qquad (3C\text{-}33)$$

$$(\cot\psi \equiv dx/dr)$$

so that equation (3C-29) is a nonlinear, second-order, ordinary differential equation of the form

$$\frac{d^2x}{dr^2} = f\left(\frac{dx}{dr}, \, x, \, r \right) \qquad (3C\text{-}34)$$

Equation (3C-34) is reduced to two first order equations, in the usual way, by denoting dx/dr by Y_1:

$$\frac{dY_1}{dr} = f_1(Y_1, \, x, \, r) \qquad$$

$$\frac{dx}{dr} = f_2(Y_1, \, x, \, r) = Y_1 \qquad (3C\text{-}35)$$

The mean flow model described below is isothermal ($a = \text{constant} = a_0$) and the mean velocity gradients are specified with respect to coordinates non-dimensionalized by r_T — an effective free-jet nozzle radius. In these coordinates the equations to be solved are

$$\frac{dY_1}{dR} = F_1 \; (Y_1, \; X, \; R) \; \frac{\partial \bar{V}_x}{\partial R} + F_2(X, \; R) \; \frac{\partial \bar{V}_x}{\partial X} \qquad (3C\text{-}36a)$$

$$\frac{dX}{dR} = Y_1 \qquad (3C\text{-}36b)$$

where $X = x/r_T$, $R = r/r_T$,

$$F_1(Y_1, \; X, \; R) = \{1 + Y_1{}^2\}^{3/2} \; x \left| \left(\frac{V_T}{a_0}\right)\left(\frac{a_0}{V_r}\right)^3 \left[1 + \frac{V_T}{a_0} \, \bar{V}_x \left(\frac{V_r}{a_0} \cos\psi - \frac{V_T}{a_0} \, \bar{V}_x\right)^3\right]\right| \qquad .$$

and

$$F_2(X, \; R) = \left(\frac{V_T}{a_0}\right)^2 \bar{V}_x \; . \qquad (3C\text{-}37)$$

The trigonometric functions have been retained here, although they are evaluated with

$$\sin\psi = [1 + Y_1{}^2]^{-\frac{1}{2}} \qquad (3C\text{-}38)$$

$$\cos\psi = Y_1 \cdot \sin\psi; \qquad (3C\text{-}39)$$

the ray speed, V_r, is evaluated with equation (3C-30).

3C.3 MEAN FLOW FIELD MODEL

The free-jet is assumed to be isothermal and axisymmetric with an effective nozzle radius, r_T. The axial mean velocity profile, $\bar{V}_x$, is given by

$$\bar{V}_x \equiv \frac{V_x}{V_T} = \frac{1}{2} \{1 - \text{erf} \; (\chi)\} \qquad (3C\text{-}40)$$

where

$$\chi = \sigma \left(\frac{r - r_T}{x}\right) - b_T \qquad (3C\text{-}41)$$

The constant $b_T = .297$ is chosen to yield a $\bar{V}_x$ value of 0.663 at $r = r_T$; that is, at the "lip-line" the mean velocity is chosen to be 66.3% of the center-line value. A nominal value of the spreading parameter, σ, is 13.5. Rewriting equation (3C-41) in terms of nondimensional coordinates

300

$$X = \frac{\sigma(R-1)}{X} - b_T \qquad (3C\text{-}42)$$

the required radial and axial derivatives with respect to R and X can both be expressed in terms of $d\bar{V}_X/d\chi$:

$$\frac{\partial \bar{V}_X}{\partial R} = \frac{\partial V_X}{d\chi} \frac{\partial \chi}{\partial R}, \qquad (3C\text{-}43)$$

$$\frac{\partial \bar{V}_X}{\partial X} = \frac{d\bar{V}_X}{d\chi} \frac{\partial \chi}{\partial X}, \qquad (3C\text{-}44)$$

and from equation (3C-40)

$$\frac{d\bar{V}_X}{d\chi} = -\frac{1}{\pi^{\frac{1}{2}}} e^{-\chi^2}, \qquad (3C\text{-}45)$$

and equation (3C-42),

$$\frac{\partial \chi}{\partial R} = \frac{\sigma}{X} ; \qquad \frac{\partial \chi}{\partial X} = -\frac{(X + b_T)}{X} . \qquad (3C\text{-}46)$$

The mean velocity gradients can be written as

$$\frac{\partial \bar{V}_X}{\partial R} = -\frac{\sigma}{X} \cdot \pi^{-\frac{1}{2}} e^{-\chi^2}, \qquad (3C\text{-}47)$$

$$\frac{\partial \bar{V}_X}{\partial X} = -\frac{(R-1)}{X} \frac{d\bar{V}_X}{dR} = -\frac{(X + bT)}{\sigma} \frac{d \bar{V}_X}{dR} \qquad (3C\text{-}48)$$

3C.4 ACOUSTIC MODEL AND SOLUTION METHOD

The flow-acoustic model is sketched in Figure 3C.2. A point source is located on the free-jet centerline, at an axial position, X_s (X has its origin at the free-jet nozzle exit). This idealized point source representation of the turbulence noise source distribution within the primary jet is discussed in Appendix 3D. An acoustic ray radiated from the point source intercepts the inner edge of the free-jet shear layer at a point (X_1, R_1). The angle between the ray and the downstream jet axis, ψ_T, is related to its wavenormal angle, θ_T, by

$$\cot \theta_T = \frac{\cos \theta_T + V_T/a_o}{\sin \theta_T} = \frac{X_1 - X_s}{R_1} . \qquad (3C\text{-}49)$$
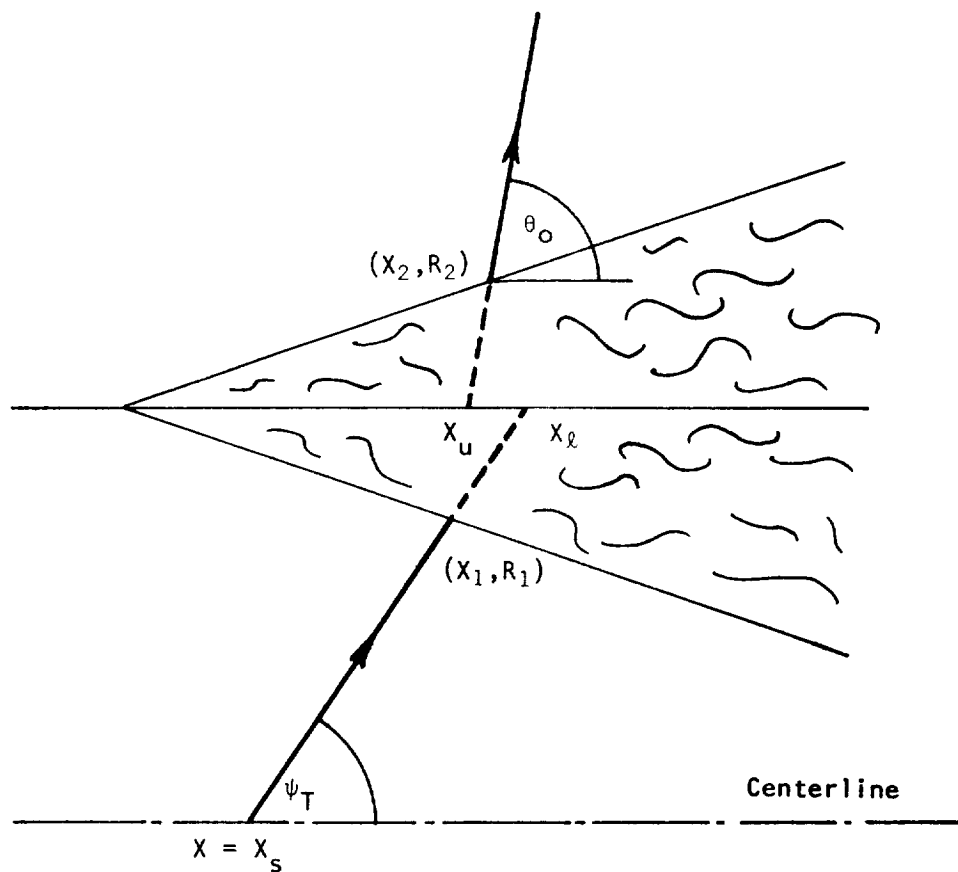
Figure 3C.2   The flow-acoustic propagation model showing a typical
ray path on the X-R plane before and after refraction
through the free-jet shear layer $(X = x/r_T, \ R = r/r_T)$.
Code: → ray path; --- extrapolated ray path (from
entry or exit ray).

302

The ray path through the parallel but non-stratified shear layer is determined from a numerical solution of equations (3C-36) with the initial conditions

$$Y_1(R_1) = \frac{dX}{dR} = \cot\psi_T \tag{3C-50}$$

and

$$X(R_1) = X_1 \tag{3C-51}$$

Numerical integration of equations (3C-36) from $R = R_1$ to $R = R_2$ (the outer edge of the shear layer) then gives the ray angle ψ_0 or θ_0 as it enters the ambient medium

$$Y_2(R_2) = \cot\psi_0 = \cot\theta_0 \tag{3C-52}$$

and its axial position

$$X(R_2) = X_2. \tag{3C-53}$$

The initial and final values $R = R_1$, R_2 are determined from values of X that define the inner and outer edges of the shear layer, i.e.

$$(1 - \bar{V}_x) < \Delta V \quad \text{when} \quad X \leq X_1$$

$$\bar{V}_x < \Delta V \quad \text{when} \quad X \geq X_2 \tag{3C-54}$$

where ΔV is a small number, e.g. 10^{-4}.

3C.5 SUMMARY OF RESULTS: COMPARISON OF NUMERICAL SOLUTIONS TO THE GEOMETRIC ACOUSTIC EQUATIONS WITH STRATIFIED FLOW RESULTS

Numerical results are presented for four axial source locations $X_s = 0.6$, 1.1, 1.6 and 2.1 for six ray paths corresponding to the wavenormal angles (within the uniform flow) $\theta_T = 30°$, $45°$, $60°$, $75°$, $90°$ and $105°$. The numerical solutions are compared with the analytic, stratified flow results.

The isothermal, axisymmetric mean flow model of the free-jet is characterized by the jet exit velocity, V_T, or the Mach number, V_T/a_0, and the spreading parameter, σ. In view of the Mach number limitation in the basic equations [according to Ugincius (ref. 114)], the value of V_T/a_0 in the following results is limited to values less than or equal to 0.2, which is the highest value of immediate interest in the present investigation. Further work is required to determine the significance of this Mach number limitation, but it is not expected to have any serious bearing on the Mach 0.2

results given below. The spreading parameter is not varied here but is held constant and equal to a nominal value of 13.5. Preliminary results, not included here, indicate that variations in the value of this parameter (which encompass effective values for the free-jet) have little or no effect on the numerical solutions.

The solution method was partially verified by solving equations (3C-36) with axial variations suppressed and the axial gradient term omitted; the numerical solutions for say, θ_0, should agree with values calculated from the equation based on a stratified flow model, that is, from equation (3C-23)

$$\theta_0 = \cot^{-1} \{\cos\theta_T [(a_T/a_0 + V_T/a_0 \cos\theta_T)^2 - \cos^2\theta_T]^{-\frac{1}{2}}\} \qquad (3C-55)$$

or since $a_T = a_0$,

$$\theta_0 = \cot^{-1} \{\cos\theta_T [(1 + M_T \cos\theta_T)^2 - \cos^2\theta_T]^{-\frac{1}{2}}\}. \qquad (3C-56)$$

A set of θ_0 results are shown for comparison in Table 3C.I; the numerical and analytic results agree to four significant figures. For reference purposes ψ_T values are included in Table 3C.I.

θ_T°	θ_0° (NUMERICAL)	θ_0° (ANALYTIC)	ψ_T°
105	105.84	105.84	93.48
90	90.00	90.00	78.69
75	75.75	75.75	64.59
60	62.96	62.96	51.05
45	51.72	51.72	37.94
30	42.42	42.42	25.13

Table 3C.I. Verification of Numerical Solution Method: Comparison of stratified flow θ_0 values given by numerical solution with values given by equation (3C-56); $V_T/a_0 = 0.2$, $\sigma = 13.5$.

When equations (3C-36) are solved *with* axial variations and the axial gradient of $\bar{V}_x$ is included, the resulting θ_0 values for this non-stratified case (N.S.) differ by less than $\frac{1}{2}^\circ$ from the corresponding stratified flow (S.) values, as shown in Table 3C.II.

With reference to equations (3C-36) and (3C-37) the superficial reasons for the almost negligible influence of axial variations in $\bar{V}_x$ are that (i) the axial gradient term is of order V_T/a_0 smaller than the (leading) shear gradient term and (ii) it changes sign at the lip-line, making a positive contribution to $d(\cot\psi)/dR$ in the first half of the interval $R_1 \leq R \leq 1$ and a negative contribution in the remaining interval $1 \leq R \leq R_2$. These observations do not concern axial variations in $\bar{V}_x$ which are present in the

$\theta_T{}^\circ$	$\theta_o{}^\circ$ (N.S.)	$\theta_o{}^\circ$ (S.)	$\Delta\theta_o{}^\circ$
105	105.76	105.84	-.08
90	89.99	90.00	-.01
75	75.82	75.75	.07
60	63.12	62.96	.16
45	52.00	51.72	.28
30	42.88	42.42	.46

Table 3C.11. Comparison of Non-Stratified and Stratified Flow
θ_o Values: $V_T/a_o = 0.2$, $\sigma = 13.5$.

leading term as well. It follows from (i) that the non-stratified flow effects at Mach numbers lower than $V_T/a_o = 0.2$ can be also safely ignored.

In the results so far, no mention has been made of the influence of X_s the point source or ray origin position on the jet centerline. Its value determines, with the ray angle ψ_T, the point at which the ray enters the shear layer (X_1, R_1). However, it can be shown that this has no influence on the magnitude of the refraction $(\theta_o - \psi_T)$, as follows.

Equation (3C-36) may also be expressed in terms of χ (in place of R):

$$\frac{d(\cot\psi)}{d\chi} = F(\cot\psi, \chi) \frac{d\bar{V}_x}{d\chi} \qquad (3C\text{-}57a)$$

$$\frac{dX}{d\chi} = \frac{(\cot\psi)X}{\sigma} \qquad (3C\text{-}57b)$$

where

$$F(\cot\psi, \chi) = F_1(\cot\psi, \chi) + F_2(\chi)\left\{ -\frac{(\chi + b_T)}{\sigma} \right\} \qquad (3C\text{-}58)$$

Hence the equations are decoupled; that is, equation (3C-57a) could be integrated separately between $X = X_1$ and X_2, given the initial value $\cot\psi$, to yield local ray angles and the emerging ray angle, θ_o, at $X = X_2$; since the limits $X = X_1$, X_2 define the inner and outer edges of the shear layer at any axial location, $\theta_o - \psi_T$ is independent of X_s. The ray displacment information is contained in the solution to the second equation.

Equation (3C-57) demonstrates that the refraction or bending of acoustic rays by the shear layer is independent of axial location in the present flow model and depends only upon the initial ray angle, ψ_T, the profile shape, $\bar{V}_x$, expressed in terms of the similarity coordinate, χ, and V_T/a_o.

It follows that results such as those given in Table 3C.11 are valid for any axial source position.

Finally, solutions for the *axial displacement* of the refracted ray, $X_2 - X_1$, (see Figure 3C.2) are considered in the following way. The ray paths within the uniform flow and ambient medium are extrapolated without change in direction to the "lip-line," $R = 1$, as shown, for example in Figure 3C.2, the axial intercepts being denoted respectively by X_ℓ, X_u. The numerical results for X_u, X_ℓ indicate that, to a very good approximation, these points are coincident. A set of results is given in Table 3C.III for the four source positions. These numerical results are consistent with the analytical result indicated by equation (3C-57b) that the ratio X_2/X_1 is independent of axial location and, in particular, of the source position X_s.

To summarize, numerical solutions to the geometric acoustic equations indicate that to a good approximation two simple rules govern sound refraction by a parallel, non-stratified free-jet mixing region.

Rule (a)   The sound ray refraction (or angle change) can be calculated to a good approximation with the analytic formulae for refraction by stratified flow, and

Rule (b)   the ray path (or axial displacement) can be calculated as if the stratified flow refraction all takes place abruptly at the "lip-line."

	$X_s = 0.6$				$X_s = 1.1$	
θ_T	X_ℓ	X_u	ΔX	X_ℓ	X_u	ΔX
105	0.54	0.54	.00	1.04	1.04	.00
90	0.80	0.80	.00	1.30	1.31	.01
75	1.08	1.08	.00	1.58	1.58	.00
60	1.41	1.42	.01	1.91	1.92	.01
45	1.88	1.90	.02	2.38	2.41	.03
30	2.73	2.77	.04	3.23	3.28	.05

	$X_s = 1.6$				$X_s = 2.1$	
θ_T	X_ℓ	X_u	ΔX	X_ℓ	X_u	ΔX
105	1.54	1.55	.01	2.04	2.05	.01
90	1.80	1.81	.01	2.30	2.31	.01
75	2.80	2.09	.01	2.58	2.59	.01
60	2.41	2.43	.02	2.91	2.93	.02
45	2.88	2.91	.03	3.38	3.42	.04
30	3.73	3.79	.06	4.23	4.30	.07

Table 3C.III. Axial displacement of acoustic rays: "lip-line" intercepts X_ℓ, X_u of extrapolated ray paths for axial source positions X_s = 0.6, 1.1, 1.6 and 2.1. (V_T/a_0 = 0.2, σ = 13.5).

Rule (a) is not an unexpected result; it justifies the utilization of results from Appendices 3A and 3B which are based upon a parallel stratified flow for free-jet model calculations. It is also an encouraging indication that *wave acoustic* models based upon infinite, parallel stratified flow models, such as Lilley's equation, may be good approximations, particularly as they are often utilized for conditions approaching the GA limit. Finally, Rule (a) justifies the use of the vortex sheet model for sound refraction calculation since there is no distinction between the model and one consisting of a finite thickness stratified shear layer in this immediate context.

Rule (b) is consistent with and provides the justification for models developed and used elsewhere (ref. 116 and 117) in which the free-jet shear layer is replaced by a vortex sheet. However, in those models both the ray paths and shear layer transmission effects on the sound amplitude are calculated on the basis that the shear layer is replaced by a vortex sheet. Rule (b) only confirms that *ray paths* can be calculated on that basis. Transmission effects on the sound amplitude are analyzed in Appendix 3E.

The application of these two rules to the calculation of the angle θ_m in the present free-jet configuration (θ_m is the polar angle based upon an origin at $X_s = 0.6$) yields results which are in very close agreement with those calculated with axial variations and gradients of $\bar{V}_x$ included in the basic GA equations. In Figures 3C.3 through 3C.6, the ray paths *outside* the free-jet shear layer are shown for the four source positions; these have been derived from the full numerical solution to the axial variation/gradient equations. Inside the shear layer rather than show the exact ray paths, the rays have been extrapolated to the "lip-line" to illustrate the magnitude of the error involved if Rule (b) is applied. Also, in Figures 3C.3 through 3C.6, values of θ_m are shown; values from a calculation based on rules (a) and (b) give results that agree with those to the nearest degree. Exact figures are given in Table 3C.IV.

307

Figure 3C.3 Ray paths on the X-R plane for wavenormal (≡ emission) angles
$\theta_T = 30°$ (15°) 105°, with resultant microphone angles, θ_m.
$V_T/a_o = 0.2$, $X_s = 0.6$ ($x_s'/d = 0$). Code: as in Figure 3C.2.

Figure 3C.4 Ray paths on the X-R plane for wavenormal (≡ emission) angles
$\theta_T = 30°$ (15°) 105°, with resultant microphone angles, θ_m.
$V_T/a_o = 0.2$, $X_s = 1.1$ ($x_s'/d = 5$). Code as in Figure 3C.2.

Figure 3C.5 Ray paths on the X-R plane for wavenormal (≡ emission) angles $\theta_T = 30°$ (15°) 105°, with resultant microphone angles, θ_m. $V_T/a_o = 0.2$, $X_s = 1.6$ ($x_s'/d = 10$). Code: as in Figure 3C.2.

Figure 3C.6 Ray paths on the X-R plane for wavenormal ($\equiv$ emission) angles $\theta_T = 30°$ (15°) 105°, with resultant microphone angles, θ_m. $V_T/a_o = 0.2$, $X_s = 2.1$ ($x_s'/d = 15$). Code as in Figure 3C.2.

311

	$X_s = 0.6$		$X_s = 1.1$	
θ_T°	θ_m°	θ_{mab}°	θ_m°	θ_{mab}°
105	103.47	103.56	98.32	98.44
90	87.83	87.88	82.48	82.55
75	73.47	73.48	68.28	68.32
60	60.17	60.15	55.38	55.40
45	47.63	47.60	43.37	43.42
30	34.93	34.97	31.20	31.35

	$X_s = 1.6$		$X_s = 2.1$	
θ_T°	θ_m°	θ_{mab}°	θ_m°	θ_{mab}°
105	93.11	93.26	87.79	87.97
90	77.07	77.16	71.53	71.65
75	63.03	63.09	57.66	57.76
60	50.54	50.60	45.60	45.71
45	39.07	39.18	34.69	34.87
30	27.43	27.68	23.59	23.94

Table 3C.IV. Comparison of values of θ_m° calculated from numerical solutions to axial variation/gradient GA equations with values θ_{mab}° calculated by Rules (a) and (b): $V_T/a_o = 0.2$, $\sigma = 13.5$.

APPENDIX 3D

A MODEL FOR THE EFFECTIVE POINT SOURCE — AXIAL
LOCATIONS OF PRIMARY JET TURBULENCE MIXING NOISE
AS A FUNCTION OF STROUHAL NUMBER

The recent measurements by Grosche (ref. 118) and Laufer *et al* (ref. 119) provide quantitative information on apparent or effective axial distributions of the turbulence mixing noise source in subsonic and supersonic jets as a function of the Strouhal number, fd/V_J.

The utilization of this information is necessary in the present problem because measurements in Flight Simulation Facilities are usually taken relatively close to the jet, as close as 20 jet nozzle diameters (see Figure 3D.1), while flight data is usually acquired at much larger distances of the order of a hundred jet nozzle diameters or more. Suppose it is assumed that radiation at a particular Strouhal number originates mainly from a region 10 diameters downstream of the jet nozzle and the radiation level at a particular polar angl θ_m is under investigation. Then with the origin at the jet nozzle, flight data (i.e. $R_m > 100\,d$) at angle θ_m will be a good measure of the radiation from the source region at angle θ_m. If the distance is reduced to $R_m = 80$ diameters, then in the example shown in Figure 3D.1, the measured data would correspond to radiation at an angle $\theta_m + 6°$, while at a distance of $R_m = 20$ diameters it corresponds to $\theta_m + 30°$. Furthermore, the ray path length, the distance between the measurement point and the effective point source location, differs, in general, from the "measured radius" R_m. Clearly, a correction procedure is required if "near-field" flight simulation data is to be extrapolated and compared with true far-field flight data.

Morfey (ref. 120) has proposed a simple model in which the real axial source distribution for each Strouhal number is replaced by a point source located at the axial position x_s'[†] where the apparent distribution reaches a maximum. An empirical law for the variation of the point source axial position, x_s'/d, with Strouhal number is derived from the Grosche and Laufer (ref. 118, 119) data on the following basis. The radiation at a particular frequency is associated with a shear layer thickness and a centerline velocity. In the initial mixing region the centerline velocity is a constant and equal to the jet exit velocity, V_J, whereas the shear layer thickness is proportional to the distance from the jet exit. Consequently, the empirical law for the initial mixing region is of the form

$$x_s'/d \ \alpha \ \frac{1}{S}.$$

In the fully developed region the reciprocal of the centerline velocity is also proportional to the distance from the jet exit (at large distances) and hence the law takes the form

$$x_s'/d \ \alpha \ \frac{1}{S^{\frac{1}{2}}}.$$

The Strouhal number, S, is now replaced by the modified Strouhal number (to allow for the convected nature of the source), S_m, which is defined below.

[†] *The prime is used to distinguish this x coordinate, which has its origin at the primary jet exit plane, from that used elsewhere within Chapter 3 which has its origin at the free-jet exit plane.*
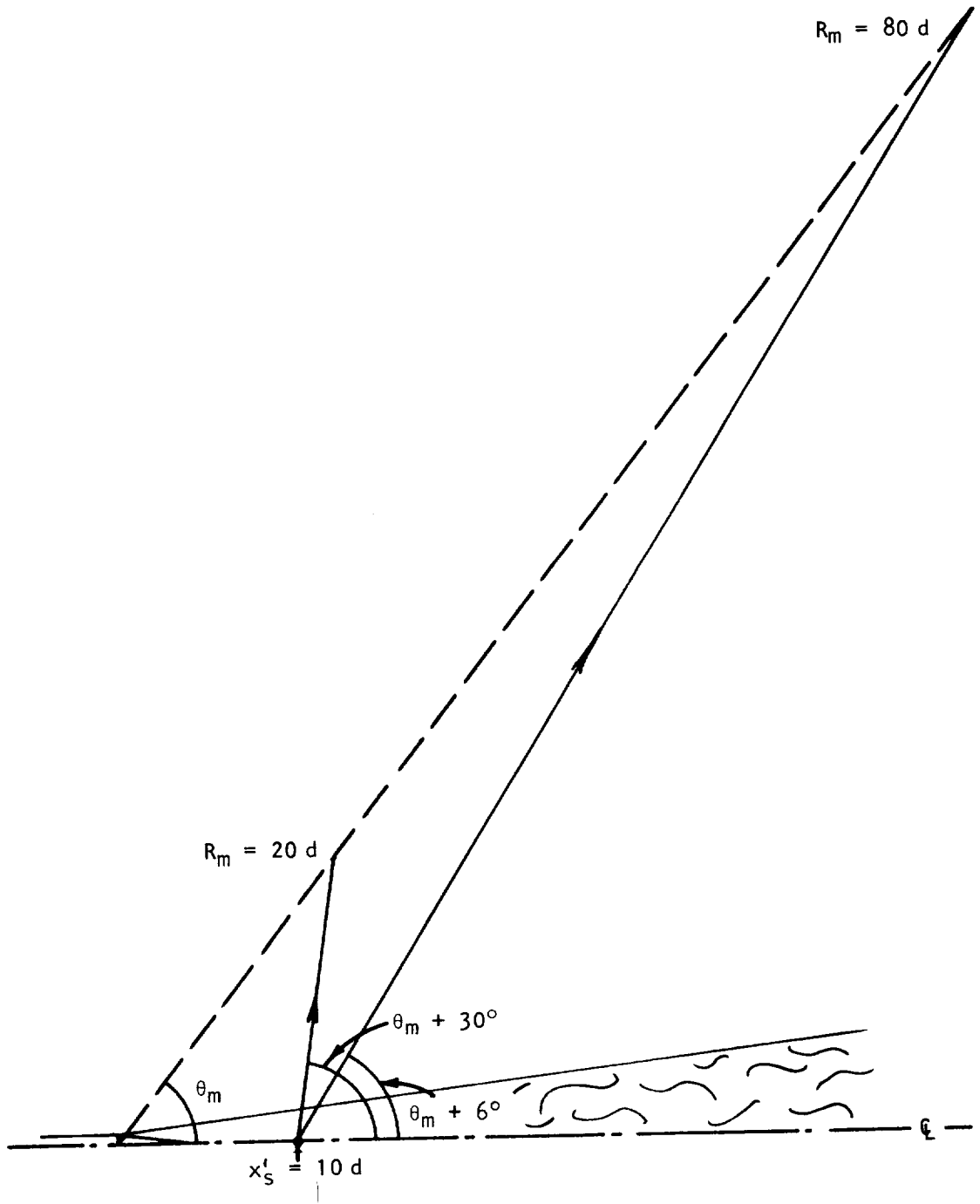
Figure 3D.1   Illustration of near and "almost far-field" measurement locations (R_m = 20d and 80d) with effective source location at x_s'/d = 10.

Morfey (ref. 120) obtains the constants of proportionality from the Grosche and Laufer data (ref. 118, 119) and finds that, to a good approximation,

$$x_s'/d = \frac{5}{S_m}$$

for the initial mixing region and

$$x_s'/d = \frac{4}{S_m^{\frac{1}{2}}}$$

for the fully developed region. In Figure 3D.2 those empirical expressions are compared with some of Laufer's (ref. 119) data. The agreement is particularly good in the important low Strouhal number range, $.15 \le S_m \le .6$, (leading to the largest angle corrections) whereas the discrepancies at high Strouhal number are of little significance for the present application. The "cross-over" point between the two empirical laws should be, according to the physical basis for these laws (ref. 120), in the region of $x_s'/d \sim 4$-5. Here it is chosen to be the point $S_m = 1.5$, i.e. $x_s/d \doteq 3.3$ to achieve a smooth "transition."

The modified Strouhal number is defined in this exercise as

$$(S_m = S\ D_m).$$

$$D_m = \{(1 - M_c\cos\theta_T)^2 + \alpha^2 M_c^2\}^{\frac{1}{2}}$$

$$(M_c = 0.67\ V_J/a_0,\ \alpha = 0.3)$$

Therefore, given d, f and V_J in consistent units, and θ_T, the axial source location, x_s'/d, is calculated *via* the following steps:

$$S = fd/V_J$$

$$D_m = \{(1 - M_c\cos\theta_T)^2 + \alpha^2 M_c^2\}^{\frac{1}{2}}$$

$$(M_c = 0.67\ V_J/a_0,\ \alpha = 0.3)$$

$$S_m = S\ D_m$$

$$S_m \ge 1.5:\quad x_s'/d = 5/S_m$$

$$S_m < 1.5\quad x_s'/d = 4/S_m^{\frac{1}{2}}$$

In the Lockheed free-jet facility the measurement radius, R_m, is 54d, where d is the primary nozzle diameter (d = 2") or 5.4 r_T where r_T is the effective free-jet nozzle radius (to a good approximation $r_T = 20$"). The primary jet nozzle protrusion beyond the free-jet exit plane, x_n, is 6 d or
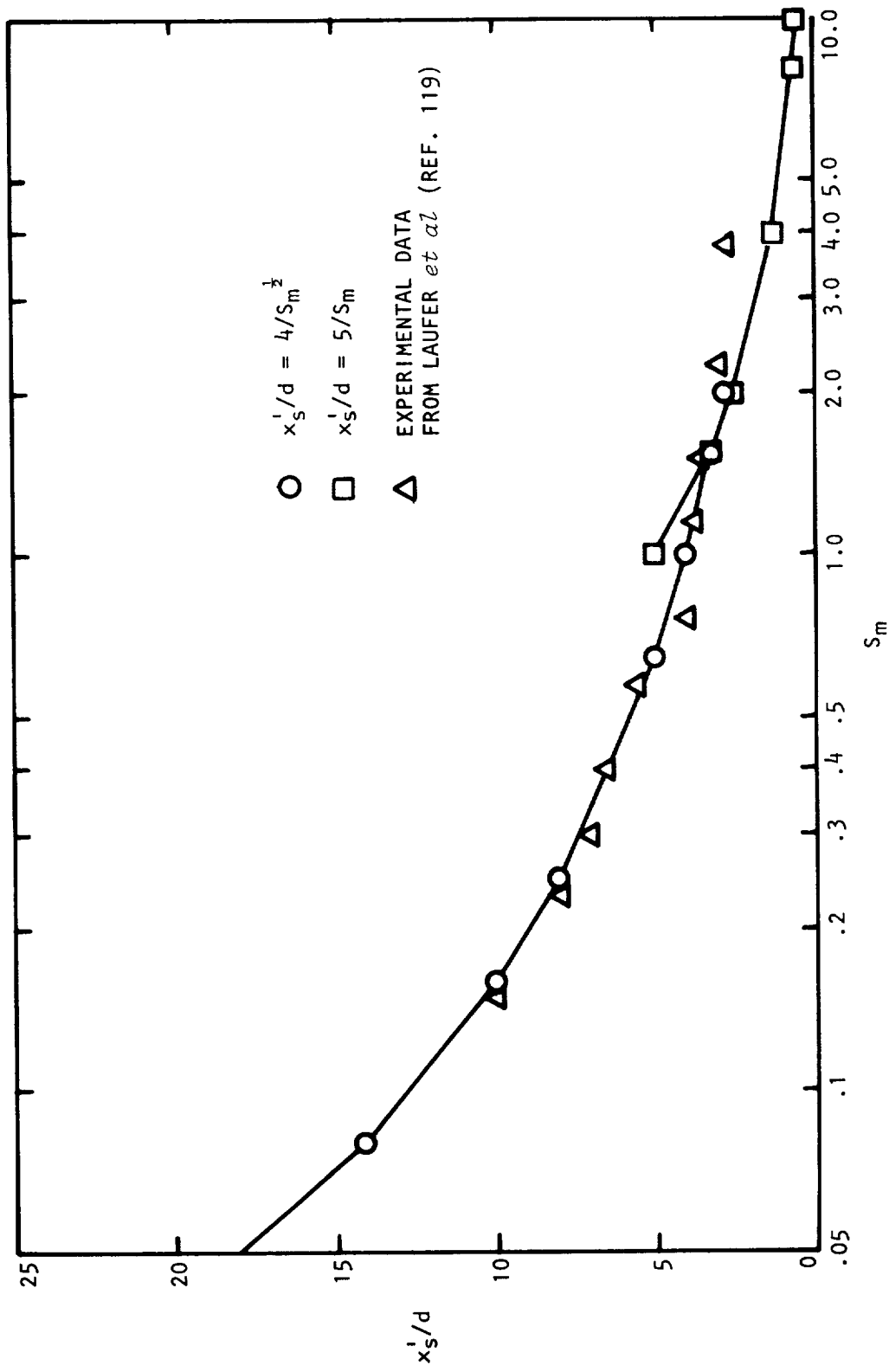
Figure 3D.2 Variation of effective point source axial location, x_s'/d, with modified Strouhal number, S_m. Code: $\bigcirc$, $\square$ semi-empirical model; $\triangle$ experimental data.

318

0.6 r_T. The effect of the extended axial source distribution on the values of the measurement polar angle, θ_m, which correspond to specified polar radiation angles, θ_T, is illustrated in Figures 3D.3 through 3D.6 for the case of zero free-jet velocity, V_T. That is, X_S has its origin at the free-jet exit plane so that the first value of X_S corresponds to a source location at the primary jet nozzle, succeeding values correspond to 5d increments. The first value (Figure 3D.3) represents the ideal case where the measured and actual polar radiation angles θ_m, θ_T and distances R_m, R_r coincide. A source location of 5d downstream (Figure 3D.4) gives rise to angle differences of up to 5°, of 10 d to 11° and of 15 d to 16°. The effect of forward motion on the co-flowing stream (the uniform potential core of the free-jet) is *not* included in this source location model. A preliminary study has indicated that this effect is unlikely to be important in the present correction procedure.
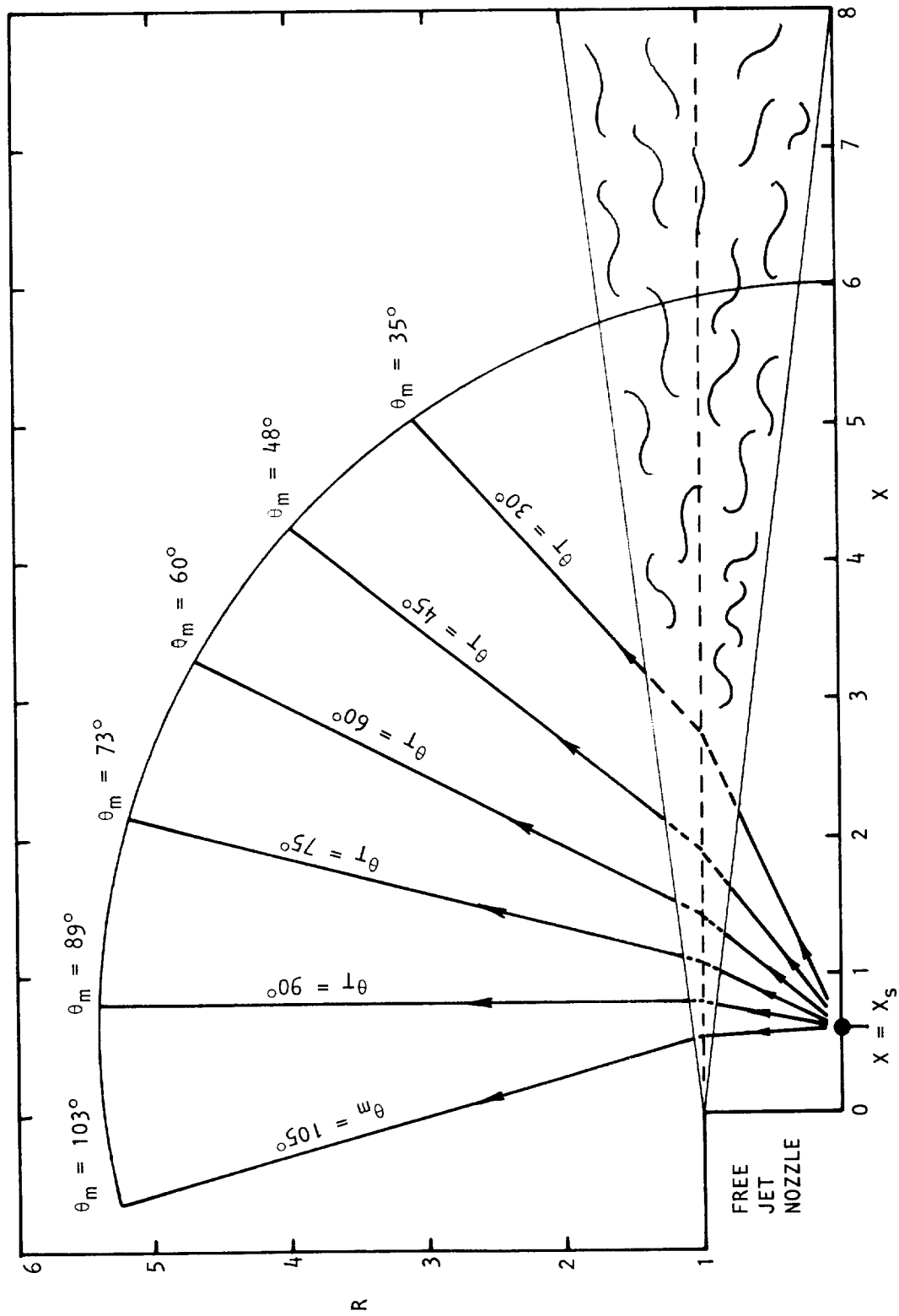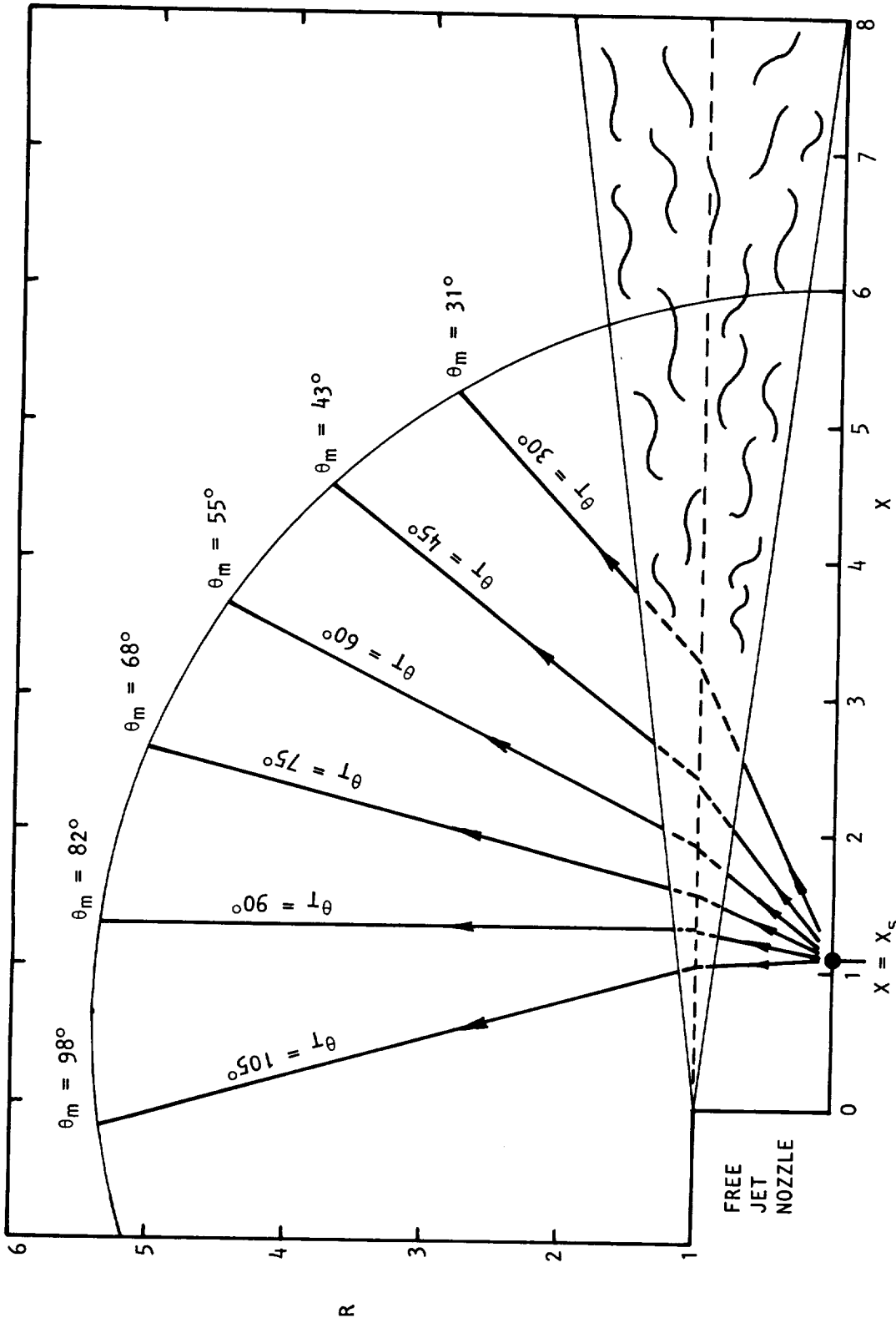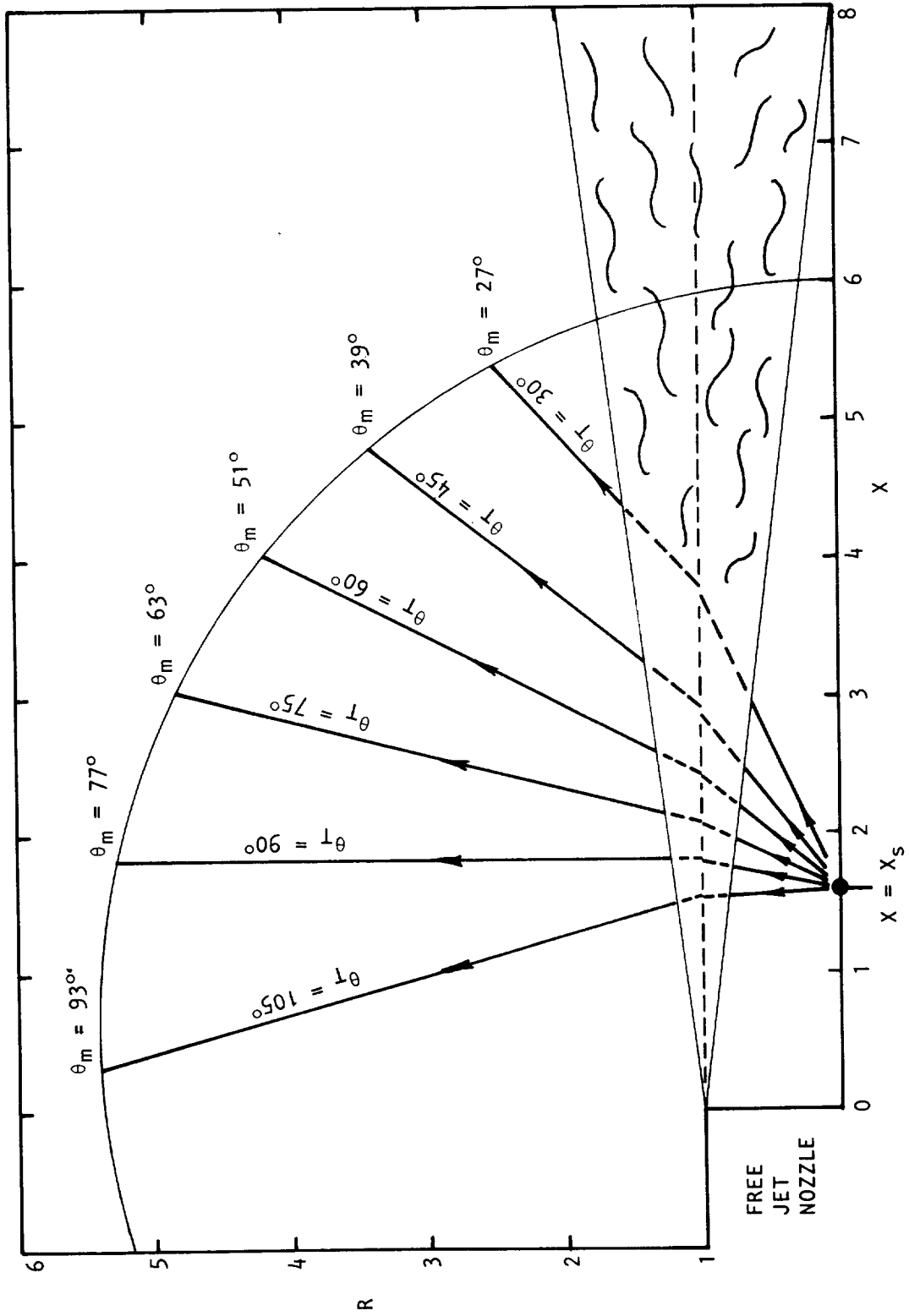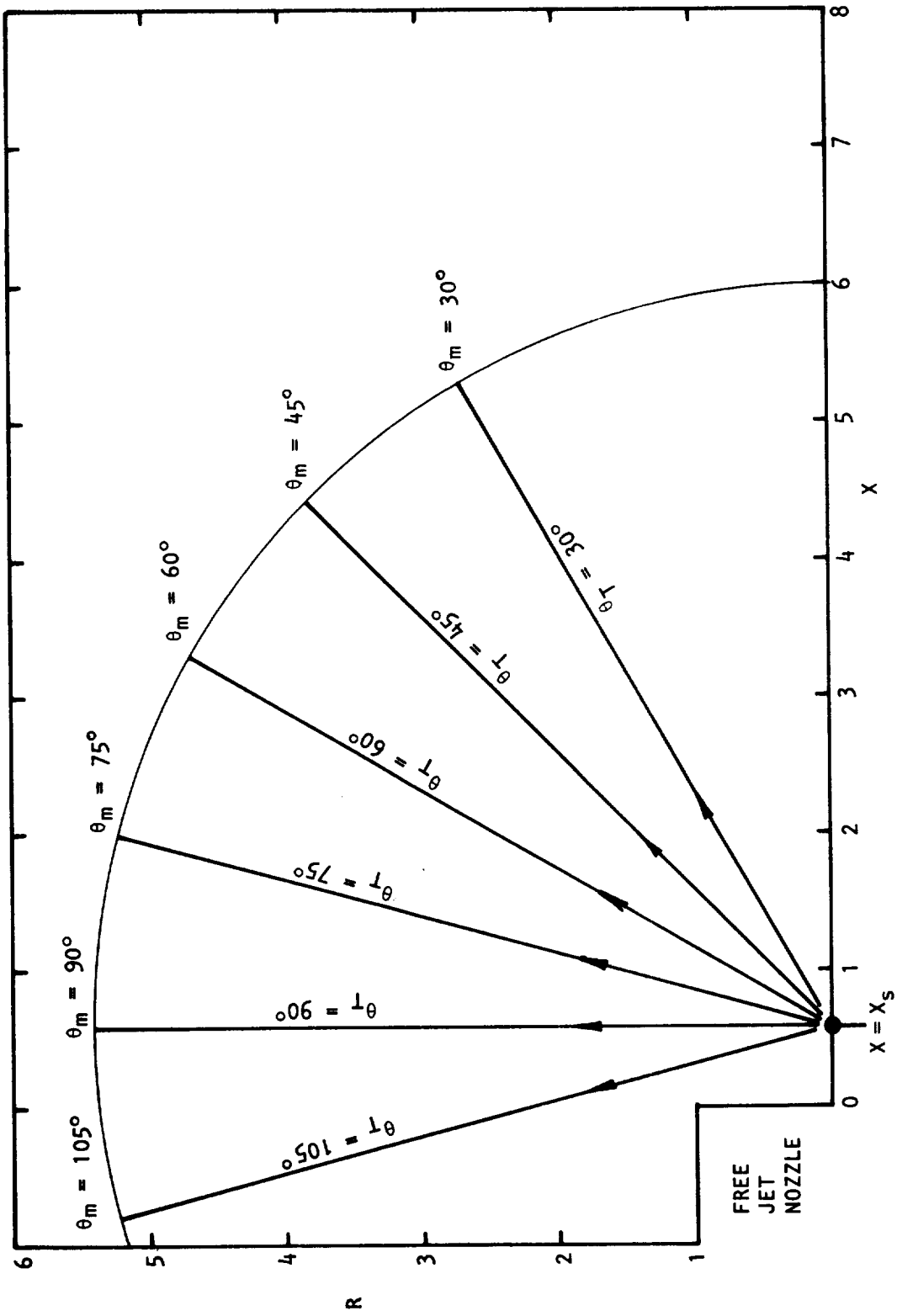
Figure 3D.3 Ray paths on the X-R plane for wavenormal ($\equiv$ emission) angles $\theta_T = 30°$ (15°) 105°, with resultant microphone angles, θ_m. $V_T/a_o = 0.0$, $X_s = 0.6$ ($x_s'/d = 0$). Code: $\rightarrow$ Ray path.

320
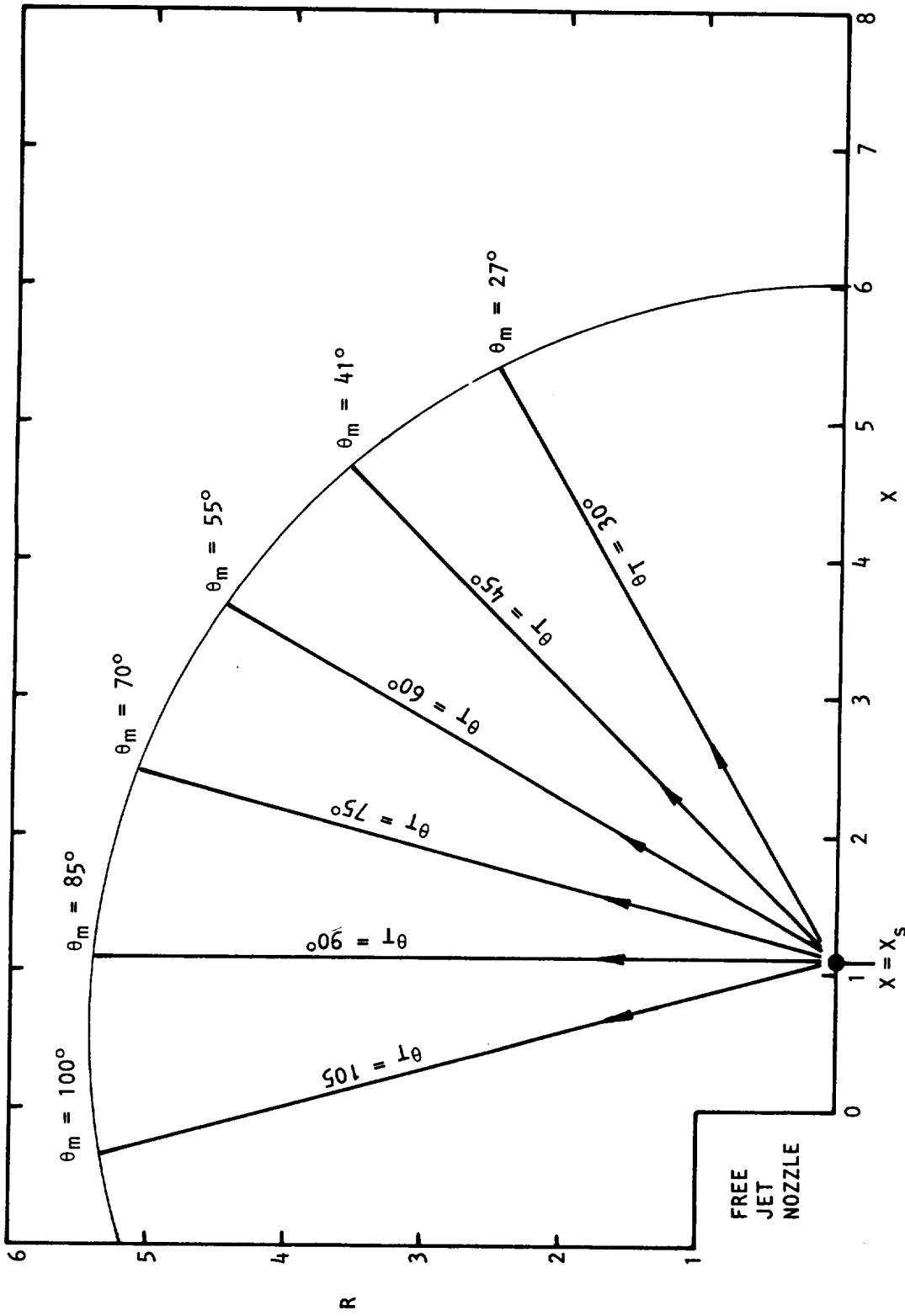
Figure 3D.4 Ray paths on the X-R plane for wavenormal (≡ emission) angles
$\theta_T = 30°$ (15°) 105°, with resultant microphone angles, θ_m.
$V_T/a_0 = 0.0$, $X_s = 1.1$ ($x_s'/d = 5$). Code: → Ray path.

321
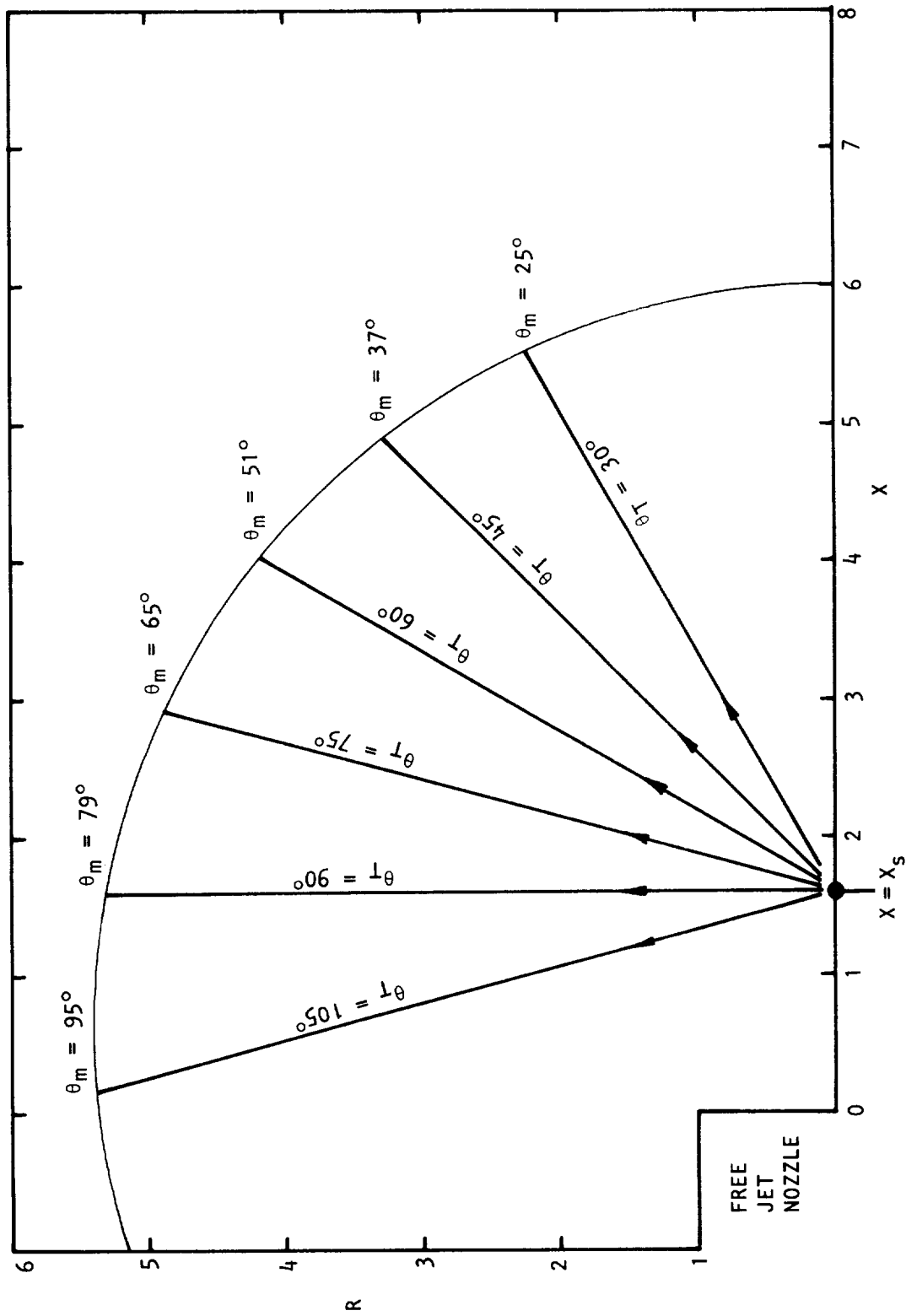
Figure 3D.5 Ray paths on the X-R plane for wavenormal ($\equiv$ emission) angles $\theta_T = 30°$ (15°) 105°, with resultant microphone angles, θ_m. $V_T/a_o = 0.0$, $x_s = 1.6$ ($x_s'/d = 10$). Code: $\rightarrow$ Ray path.
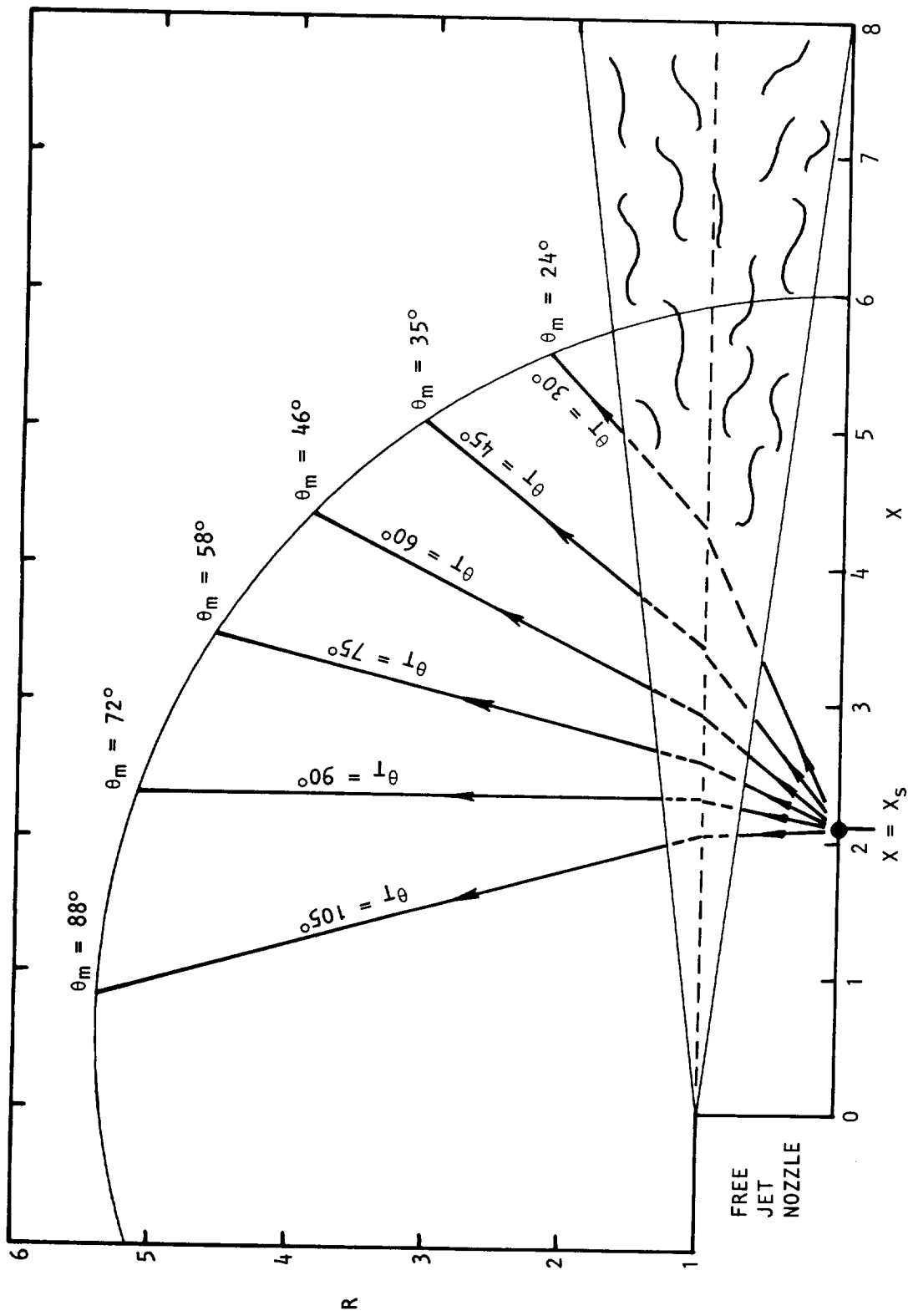
322
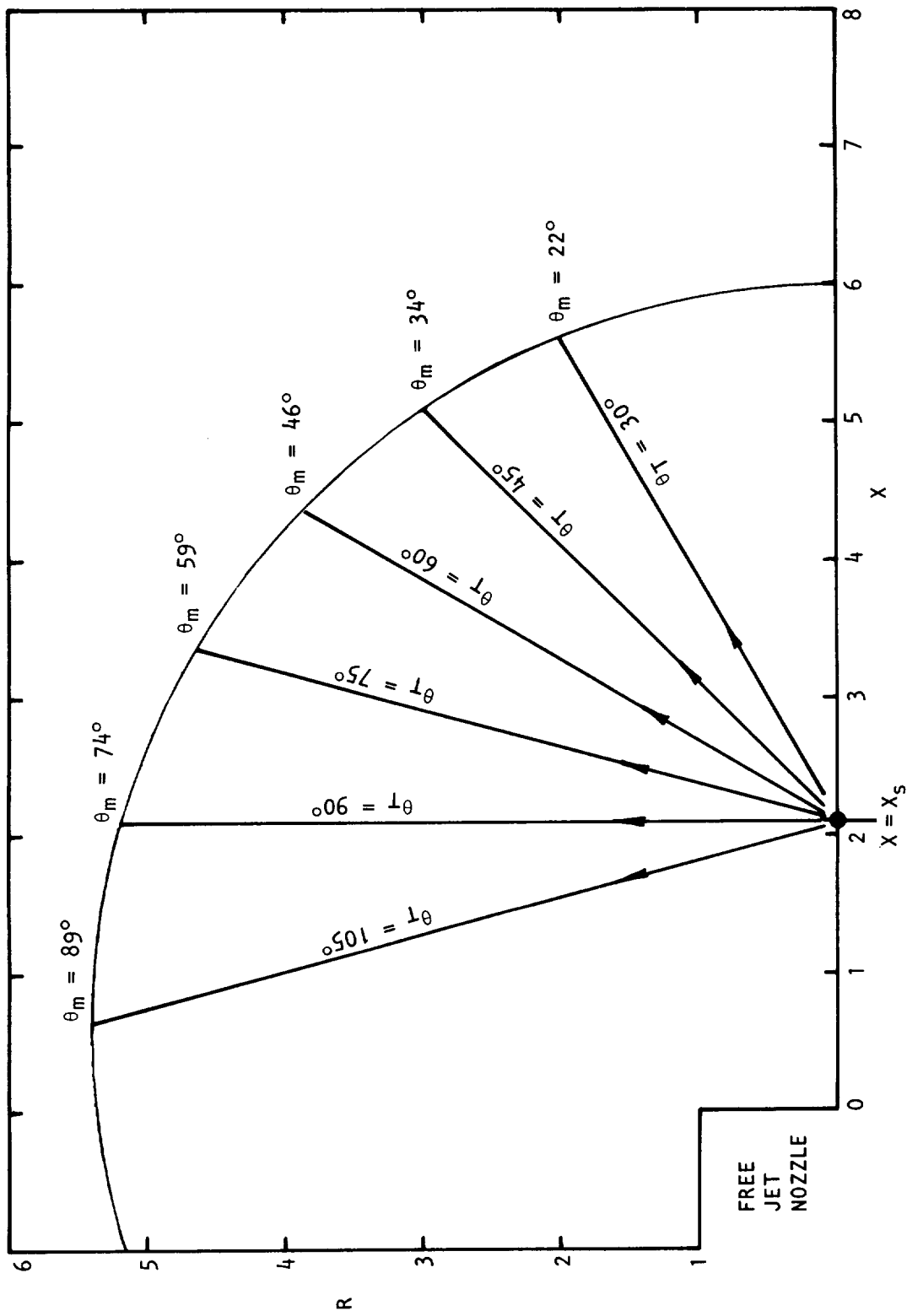
Figure 3D.6 Ray paths on the X-R plane for wavenormal ($\equiv$ emission) angles $\theta_T = 30^\circ$ (15°) 105°, with resultant microphone angles, θ_m. $V_T/a_O = 0.0$, $X_s = 2.1$ ($x_s'/d = 15$). Code: $\rightarrow$ Ray path.

323
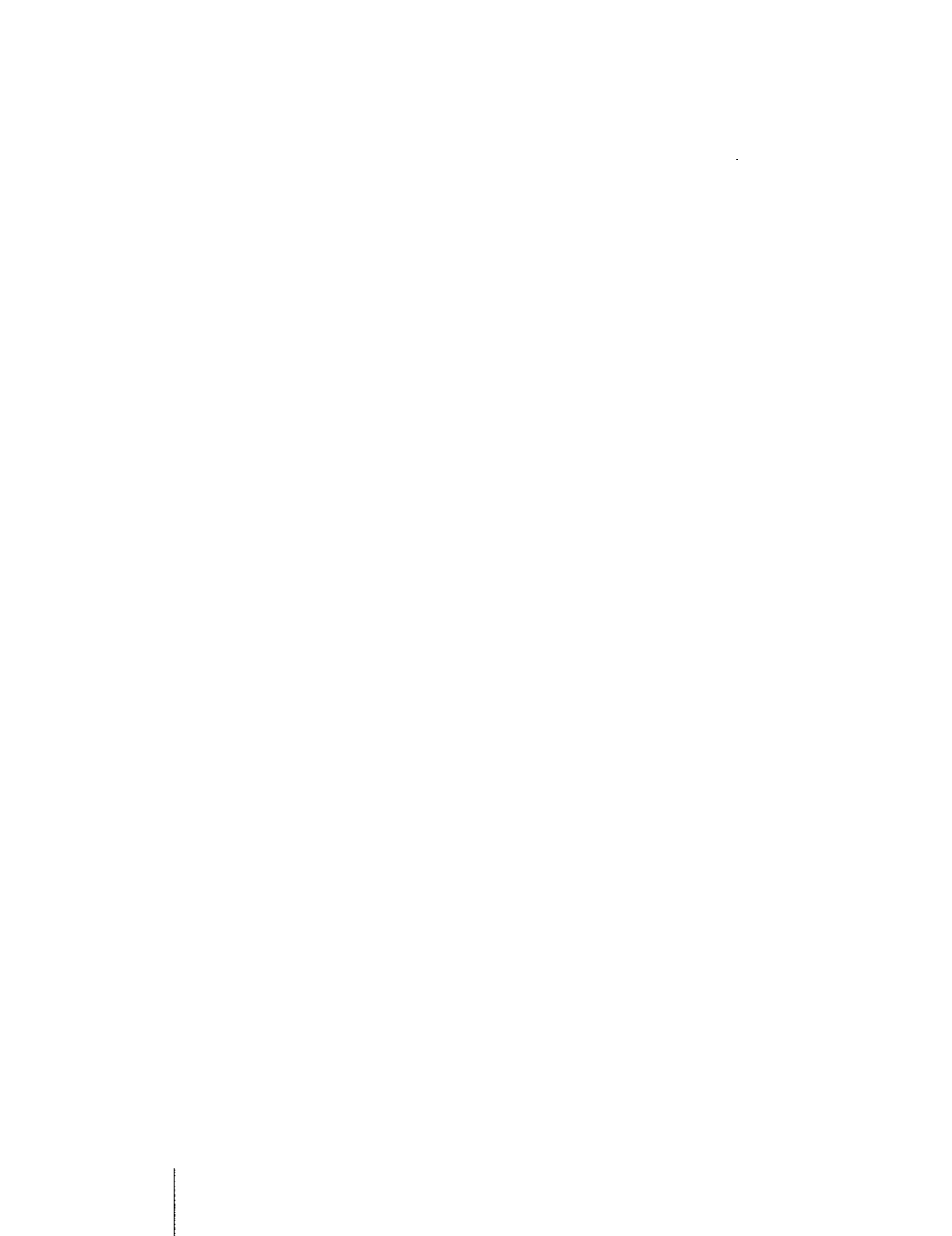
APPENDIX 3E

FREE-JET-TO-IWT TRANSMISSION AMPLITUDE CORRECTIONS
FROM A STRATIFIED FLOW — GEOMETRICAL ACOUSTICS MODEL

The main result of the investigation described in Appendix 3C is that (in the geometric acoustics limit) the direction and position of rays emerging from a parallel non-stratified model of the free-jet shear layer can be accurately calculated with the stratified flow analytic expressions together with the condition that the rays are refracted abruptly at the lip-line. The result is illustrated by Figure 3E.1; for ray path calculation purposes the realistic situation depicted in (a) can be replaced by the *conceptual* model shown in (b).

Clearly the flow model is now a cylindrical region of uniform flow bounded by a vortex sheet. However, emphasis on this aspect of the result has been deliberately avoided since in one other important respect the vortex sheet feature is *not* utilized. In the analysis given below, the finite width stratified shear layer *is* retained for the purposes of deriving a relation between the amplitude of the direct radiation from the primary jet inside the free-jet uniform flow region and the radiation amplitude outside the free-jet in the ambient medium.

The basis for this relation is the law of energy conservation in a ray tube. This law applies to the geometric acoustics limit; in the same limit the energy flux associated with a particular ray in the uniform flow region is completely determined by the amplitude of the direct radiation, since, by definition there are no reflections, single or multiple, *from* the shear layer. In a vortex sheet model [for example, see Amiet (ref. 116)], there are reflections and the corresponding relation between the transmitted and incident pressure amplitudes at the vortex sheet, in effect, replaces the energy conservation law that will be used here. While the results from each method may not differ drastically, the arguments presented in Appendix 3C in support of a GA model apply equally well here and therefore this approach will be used in preference to that associated with a vortex sheet flow model.

The principles employed and the end result are identical to those described by Schubert (ref. 115) — see his Appendix B: "Ray acoustics for nonspreading jet" — although with the results of Appendix 3C it will be argued that the result *is* also valid for the real, spreading, free jet.

In the geometric acoustics limit the law of energy conservation in a ray tube holds, however complex the mean flow field within the free-jet shear layer. On the other hand the analytic relations between angles and distances used below rest upon the stratified flow assumption. Conceivably, a more realistic flow model than that investigated in Appendix 3C might lead to results that are significantly different from those given by the stratified flow expressions. For the present, this possibility is set aside, pending further work in that direction.

With reference to sketch (b) in Figure 3E.1, the law of energy conservation along a ray tube, given by Blokhintsev (ref. 121) is

$$I \, dA = \text{constant} \tag{3E-1}$$

or

$$I_{T\psi} \, dA_{T\psi} = I_o \, dA_o \, ,$$
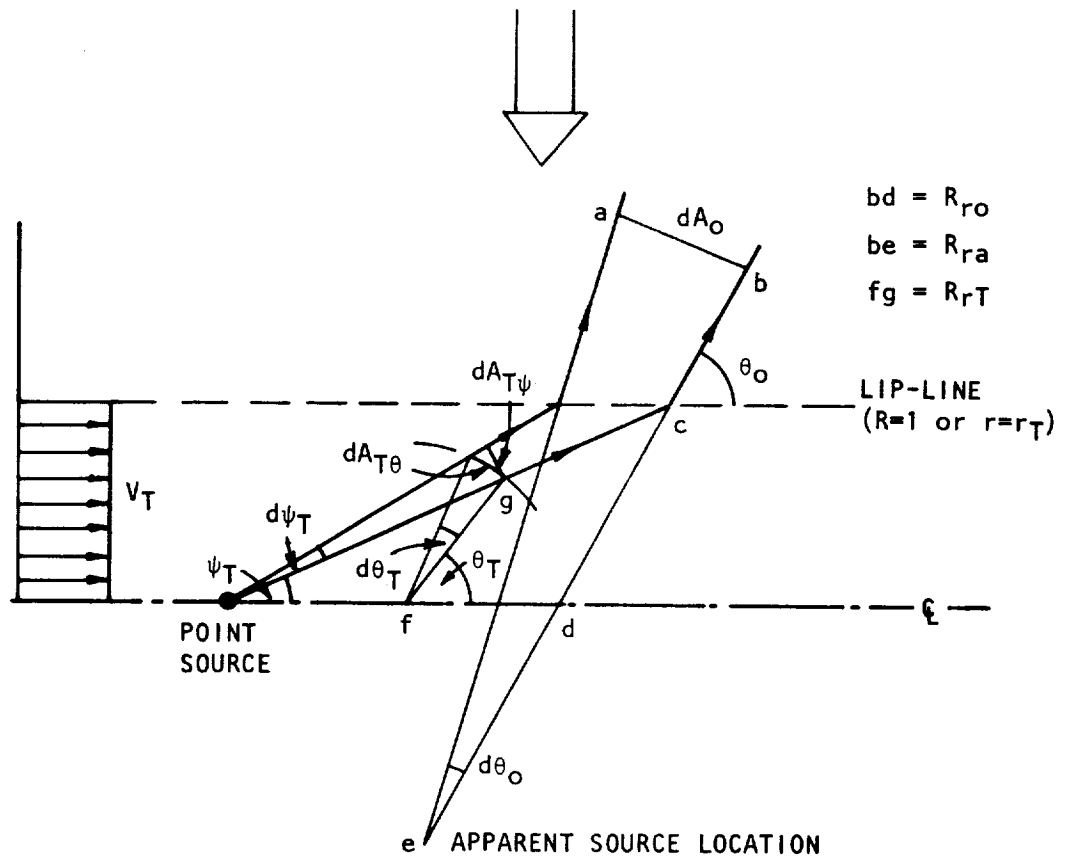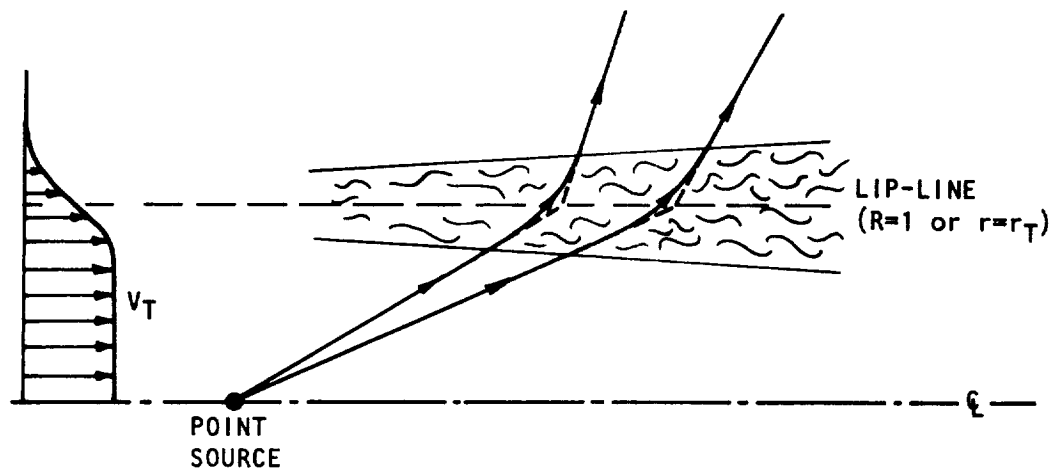
Figure 3E.1 Free-jet shear layer can be replaced by a vortex sheet at the "lip-line," R = 1, for ray tracing purposes. Ray tube cross-section changes from $dA_{T\psi}$ to dA_O across shear layer; wavenormal angle from θ_T to θ_O.

328

where I is acoustic intensity and dA the cross section area element of the ray tube or conical sector (the direction of the intensity, I, is identical to the ray direction). The subscript "T" denotes evaluation at some point along the ray tube in the uniform free-jet flow and subscript "ψ" denotes the conical sector (ψ_T, $\psi_T + d\psi_T$); subscript "0" denotes, as usual, evaluation in the ambient medium. It is preferable to rewrite the equation as

$$I_{T\psi} \; dA_T = I_{T\theta} \; dA_{T\theta} = I_o \; dA_o \tag{3E-3}$$

where $I_{T\theta}$ is the intensity component normal to the wavefront; $dA_{T\theta}$ is the elemental wavefront cross section area element formed by the intersection of the ray tube and the wavefront.

Morfey (ref. 122) has expressed Blokhintsev's (ref. 121) acoustic intensity definition in terms of the wavenormal component, I_n:

$$I_n = \overline{p'u_n} + (V_n/\rho a^2) \; \overline{p'^2} + (V_n/a)^2 \; \overline{p'u_n} + \rho V_n \; \overline{u_n^2} \tag{3E-4}$$

where overbar denotes time average, ρ, a are the local density and speed of sound and u_n, V_n denote the components of the fluctuating and mean velocity normal to the wavefront. With the GA relation

$$p' = \rho a \; u_n \tag{3E-5}$$

the expression reduces to

$$I_n = \frac{\overline{p'^2}}{\rho a} \left| 1 + \frac{V_n}{a} \right|^2. \tag{3E-6}$$

Thus, in the present problem the intensities $I_{T\theta}$, I_o are given by

$$I_{T\theta} = \frac{\overline{p'_T{}^2}}{\rho_T \; a_T} \{1 + (V_T/a_T) \; \cos\theta_T\}^2, \tag{3E-7}$$

$$I_o = \frac{\overline{p'_o{}^2}}{\rho_o \; a_o}. \tag{3E-8}$$

The corresponding area elements (see figure 3E.1b) are

$$dA_{T\theta} = (2\pi R_{rT} \; \sin\theta_T) \; R_{rT} \; d\theta_T, \tag{3E-9}$$

$$dA_o = (2\pi R_{ro} \; \sin\theta_o) \; R_{ra} \; d\theta_o. \tag{3E-10}$$

where R_{ra}, the distance from the apparent source location, is derived as follows.

329

Writing R_{ra} as the sum (see Figure 3E.1b)

$$R_{ra} = bc + ce$$

$$= (bd - cd) + ce$$

$$= (R_{ro} - cosec\theta_o) + ce \qquad (3E-11)$$

and noting that

$$ce = - sin\theta_o \frac{dX_c}{d\theta_o} = - sin\theta_o \frac{d}{d\theta_o} (cot\psi_T) \qquad (3E-12)$$

where X_c is the axial location of the point c, an analytic expression for R_{ra} can be found if the stratified flow relation

$$cot\psi_T = \{(V_T/a_T)(a_o/a_T) + \beta^2 cos\theta_o\}/\kappa_T \qquad (3E-13)$$

$$\left(\beta^2 = 1 - (V_T/a_T)^2\right)$$

is used to determine the derivative $d(cot\psi_T)/d\theta_o$. Equation (3E-13) has been derived from the definition

$$cot\psi_T = \frac{V_T + a_T cos\theta_T}{a_T sin\theta_T} \qquad (3E-14)$$

and the stratified flow relations (from "phase velocity matching")

$$cos\theta_T = (a_T/a_o) cos\theta_o/D_T \qquad (3E-15)$$

and

$$sin\theta_T = (a_T/a_o) \kappa_T/D_T \qquad (3E-16)$$

where

$$D_T = 1 - (V_T/a_o) cos\theta_o = \frac{1}{1 + (V_T/a_T) cos\theta_T} \qquad (3E-17)$$

and

$$\kappa_T = \{(a_o/a_T)^2 D_T^2 - cos^2\theta_o\}^{\frac{1}{2}} . \qquad (3E-18)$$

Differentiating equation (3E-13) with respect to θ_o gives

$$\frac{d cot \psi_T}{d\theta_o} = - sin\theta_o (a_o/a_T)^2/\kappa_T^3 \qquad (3E-19)$$

330

so that from equation (3E-12)

$$ce = \sin^2\theta_o \, (a_o/a_T)^2/\kappa_T^3 \tag{3E-20}$$

and hence

$$R_{ra} = R_{ro} + \mathrm{cosec}\,\theta_o \, \{(\sin\theta_o/\kappa_T)^3 \, (a_o/a_T)^2 - 1\}. \tag{3E-21}$$

Substituting the intensity expressions, given by equations (3E-7) and (3E-8), into the energy conservation law, equation (3E-3), leads to an expression relating the pressure amplitudes $p_T{}'$ and $p_o{}'$:

$$\overline{p_T{}'^2}/\overline{p_o{}'^2} = \frac{(\rho_T \, a_T)/(\rho_o \, a_o)}{\{1 + (V_T/a_T)\cos\theta_T\}^2} \, \frac{dA_o}{dA_{T\theta}} \tag{3E-22}$$

From equations (3E-9) and (3E-10) the last factor can be written as

$$\frac{dA_o}{dA_{T\theta}} = \frac{R_{ro} \, R_{ra}}{R_{rT}^2} \, \frac{d(\cos\theta_o)}{d(\cos\theta_T)} = \frac{R_{ro} \, R_{ra}}{R_{rT}^2} \, (a_o/a_T) \, D_T^2 \,; \tag{3E-23}$$

equations (3E-15) and (3E-17) have been used to evaluate $d(\cos\theta_o)/d(\cos\theta_T)$. Combining equations (3E-22) and (3E-23) the final result is

$$\overline{p_T{}'^2}/\overline{p_o{}'^2} = (\rho_T \, D_T^4/\rho_o) \, (R_{ro} \, R_{ra}/R_{rT}^2). \tag{3E-24}$$

The isothermal forms $(\rho_T = \rho_o, \, a_T = a_o)$ of equations (3E-21) and (3E-24) are used in Appendix 3F to correct free-jet measured data to that which would be measured under IWT conditions. There the distance R_{rT} is replaced by $\bar{R}_r$, a specified "emission radius" at which $\overline{p_T{}'^2}$ is required. This may take any value, that is, an estimate of $\overline{p_T{}'^2}$ can be made at any distance, since it simply varies as R_{rT}^{-2} under IWT conditions [as indicated by equation (3E-24)].

APPENDIX 3F

FREE-JET-TO-IWT DATA CORRECTION PROCEDURE

The free-jet SPL measurements are taken at a number of evenly spaced polar angles θ_{mi}, $i = 1, 2 \ldots$ on an arc of radius R_m centered at the primary jet nozzle (see Figure 3F.1). The primary objective of the correction procedure outlined below is to convert free-jet data to that which would be measured under IWT conditions for any value of the emission radius, R_r, and at specified emission angles θ_{ei}, $i = 1, 2 \ldots$.

As a secondary objective, corrections are included to allow for the finite distance between the effective center of the turbulent mixing noise source distribution and the nozzle exit. This minimizes the errors involved in the extrapolation of small R_m flight simulation data to a large R_m or R_r IWT conditions.

PROCEDURE OUTLINE: FREE-JET TO IWT CONDITIONS

Step

1. Given $\theta_{ei} = \theta_T$, V_T/a_0, calculate ψ_T, θ_0:

$$\cot\psi_T = \frac{\cos\psi_T + V_T/a_0}{\sin\theta_T}$$

$$\cot\theta_0 = \cos\theta_T/\{(1 + V_T/a_0 \cos\theta_T)^2 - \cos^2\theta_T\}^{\frac{1}{2}}.$$

2. Given $f*$, $d*$, V_J^*, M_c and x, calculate x_s'/d with procedure given in Appendix 3D.

3. Given R_m/d, r_T/d, x_n/d calculate X_s, X_ℓ and hence R_{ro}, θ_m:

$$X_n = (x_n/d)/(r_T/d)$$

$$X_s = X + (x_s'/d)/(r_T/d)$$

$$X_\ell = X_s + \cot\psi_T$$

$$R_{ro} = \{\bar{R}_m^2 - \ell^2\sin^2\theta_0\}^{\frac{1}{2}} - \ell \cos\theta_0$$

$$\cos\theta_m = (\bar{R}_m^2 + \ell^2 - R_{ro}^2)/2\ell\bar{R}_m$$

Consistent units.
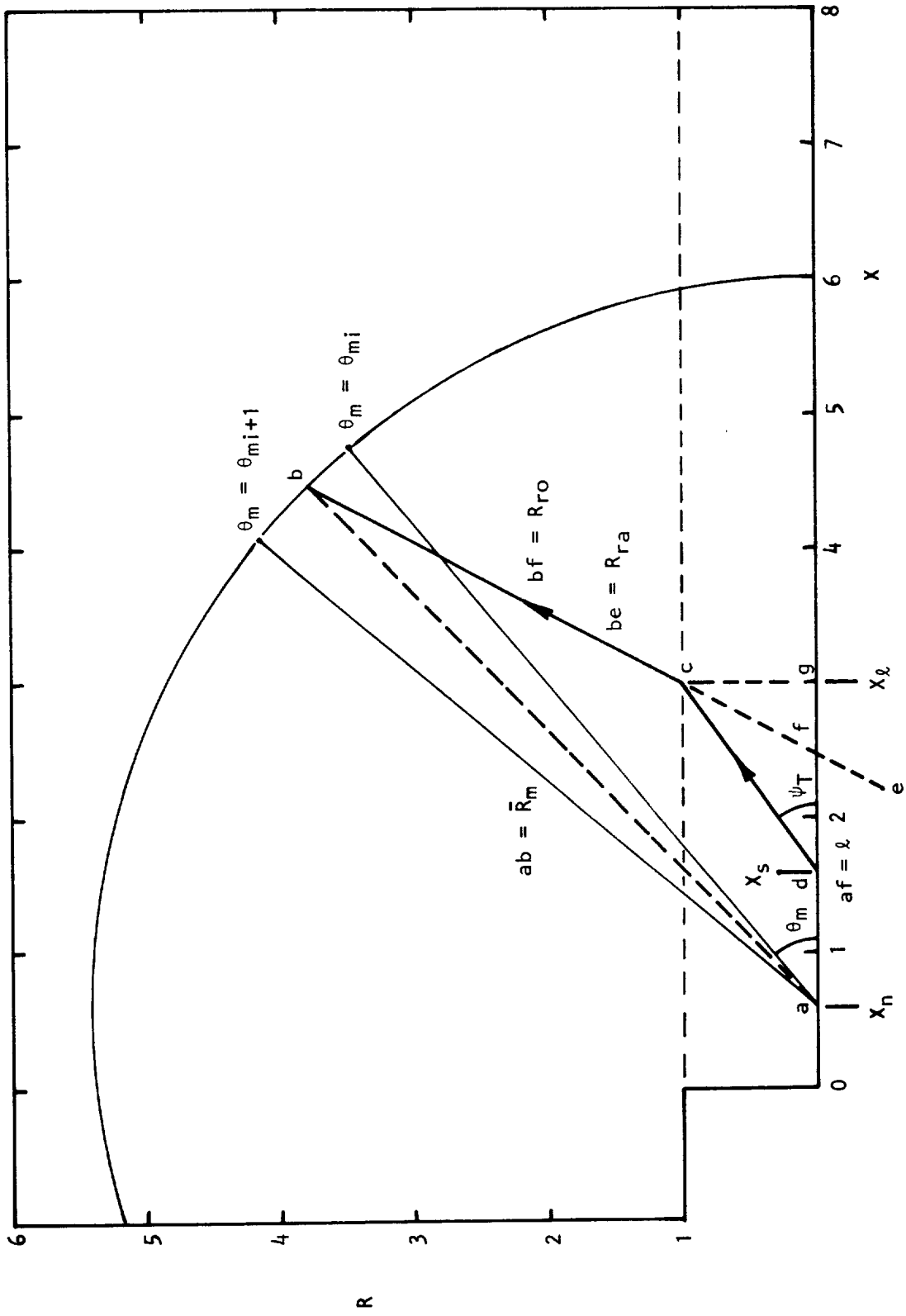
Figure 3F.1 Definition sketch for free-jet-to-IWT data correction procedure.

336

where
$$\bar{R}_m = \frac{(R_m/d)}{(r_T/d)}$$

$$\ell = (X_\ell - X_n) - \cot\theta_0.$$

4.   Interpolate for $SPLI(\theta_m)$ at frequency f:

$$SPLI(\theta_m) = (1-h)\ SPLM(\theta_{mi}) + h\ SPLM(\theta_{mi+1})$$

where
$$\theta_{mi} \leq \theta_m \leq \theta_{mi+1}$$

$$h = \frac{\theta_m - \theta_{mi}}{\theta_{mi+1} - \theta_{mi}} \ .$$

5.   Given R_r/d calculate R_{ra} and apply amplitude correction given in Appendix 3E:

$$R_{ra} = R_{ro} + \mathrm{cosec}\,\theta_0\ \{(\sin\theta_0/\kappa_T)^3 - 1\}$$

$$SPLC(R_r,\ \theta_T) = SPLI(\theta_m) + 10\log_{10} C_F\ C_R\ ,$$

where

$$\kappa_T = \{(1 - V_T/a_0\ \cos\theta_0)^2 - \cos^2\theta_0\}^{\frac{1}{2}}$$

$$C_F = D_T^4$$

$$D_T = \frac{1}{1 + (V_T/a_0)\cos\theta_T} = 1 - (V_T/a_0)\ \cos\theta_0$$

$$C_R = R_{ro}\ R_{ra}/\bar{R}_r^2$$

$$\bar{R}_r = (R_r/d)/(r_T/d)\ .$$
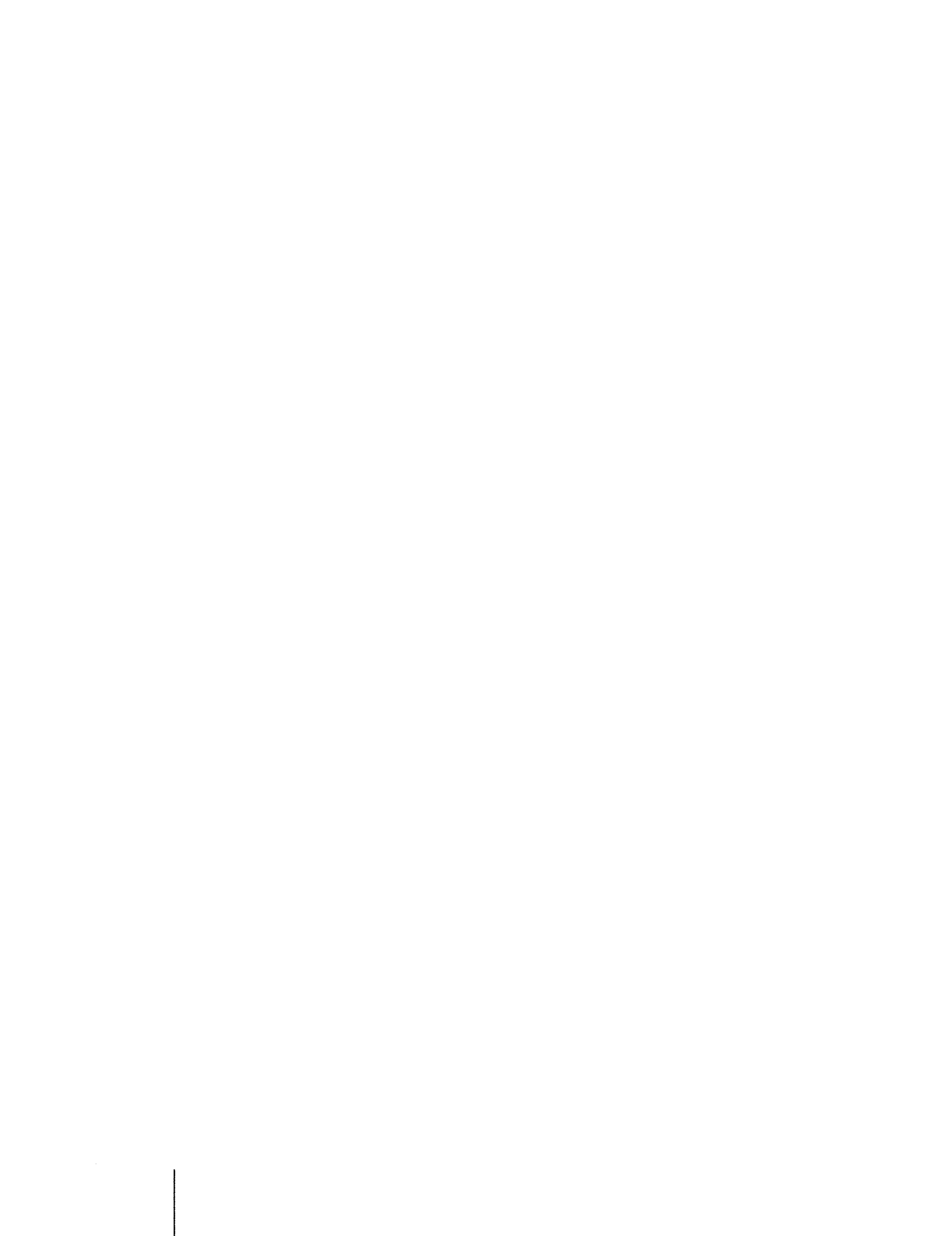
APPENDIX 4A

TABULATED VELOCITY MEASUREMENTS

AXIAL TRAVERSES

IX	M_J = .47, λ = .096, F̄ = 0 $\bar{v}_1$	$\bar{v}_1$	M_J = .47, λ = .206, F̄ = 0 $\bar{v}_1$	$\bar{v}_1$	M_J = .47, λ = .305, F̄ = 0 $\bar{v}_1$	$\bar{v}_1$	M_J = .47, λ = .413, F̄ = 0 $\bar{v}_1$	$\bar{v}_1$	M_J = .47, λ = .497, F̄ = 0 $\bar{v}_1$	$\bar{v}_1$
1.00	0.992	0.019	0.991	0.016	0.990	0.016	0.987	0.016	0.975	0.017
2.00	0.989	0.018	0.988	0.017	0.991	0.014	0.991	0.016	0.980	0.019
3.00	0.976	0.020	0.978	0.017	0.997	0.016	0.970	0.016	0.971	0.018
4.00	0.990	0.028	0.999	0.023	0.997	0.017	0.999	0.014	0.993	0.019
5.00	1.000	0.037	0.998	0.030	1.000	0.021	1.000	0.018	1.004	0.017
6.00	0.998	0.046	0.995	0.032	0.997	0.028	0.997	0.020	0.999	0.021
7.00	0.989	0.056	0.988	0.043	0.993	0.034	0.991	0.024	0.990	0.022
8.00	0.993	0.062	0.986	0.048	0.993	0.042	0.995	0.029	0.989	0.025
9.00	0.987	0.067	0.981	0.054	0.989	0.044	0.993	0.034	0.988	0.030
10.00	0.977	0.068	0.983	0.056	0.984	0.048	0.983	0.035	0.980	0.034
11.00	0.979	0.073	0.987	0.055	0.988	0.051	0.985	0.042	0.982	0.034
12.00	0.984	0.079	0.980	0.060	0.993	0.053	0.994	0.040	0.992	0.039
13.00	0.958	0.085	0.974	0.064	0.986	0.052	0.986	0.045	0.985	0.041
14.00	0.957	0.089	0.960	0.070	0.991	0.058	0.995	0.046	0.999	0.045
15.00	0.930	0.106	0.928	0.081	0.981	0.060	0.992	0.047	0.991	0.047
16.00	0.896	0.113	0.895	0.097	0.977	0.068	0.988	0.055	0.981	0.047
18.00	0.837	0.132	0.827	0.114	0.957	0.077	0.972	0.054	0.997	0.047
20.00	0.766	0.132	0.794	0.126	0.920	0.088	0.952	0.065	0.948	0.046
22.00	0.716	0.129	0.743	0.124	0.884	0.102	0.942	0.071	0.983	0.050
24.00	0.648	0.132	0.706	0.126	0.843	0.111	0.895	0.079	0.980	0.060
26.00	0.609	0.127	0.672	0.121	0.787	0.112	0.876	0.092	0.950	0.068
28.00	0.578	0.119	0.639	0.114	0.771	0.108	0.839	0.092	0.927	0.074
30.00	0.550	0.113	0.611	0.111	0.742	0.103	0.807	0.095	0.898	0.076
32.00	0.501	0.108	0.590	0.105	0.713	0.098	0.790	0.092	0.879	0.080
34.00	0.478	0.101		0.101	0.688	0.096		0.091	0.860	0.083

341

AXIAL TRAVERSES

$\bar{x}$	$M_J = .90$ $\lambda = .102$ $\bar{r} = 0$		$M_J = 1.37$ $\lambda = .098$ $\bar{r} = 0$		$M_J = 1.67$ $\lambda = .098$ $\bar{r} = 0$	
	$\bar{V}_1$	$\tilde{v}_1$	$\bar{V}_1$	$\tilde{v}_1$	$\bar{V}_1$	$\tilde{v}_1$
2.00	0.996	0.013	0.973	0.012	1.002	0.014
4.00	1.000	0.016	1.007	0.014	1.002	0.015
6.00	1.000	0.019	1.001	0.013	0.993	0.015
8.00	0.999	0.026	0.985	0.015	0.993	0.016
10.00	0.986	0.033	0.994	0.016	0.985	0.019
12.00	1.005	0.038	0.989	0.016	0.983	0.018
14.00	1.004	0.045	1.003	0.021	1.007	0.022
16.00	0.970	0.075	0.995	0.023	0.994	0.027
18.00	0.914	0.113	0.982	0.026	0.992	0.033
20.00			0.988	0.031	0.980	0.040
21.00	0.840	0.135	0.981	0.036	0.967	0.049
22.00	0.773	0.136			0.952	0.063
23.00			0.971	0.046		
24.00	0.727	0.132				
25.00						
26.00	0.673	0.124	0.946	0.057	0.918	0.081
28.00	0.643	0.121	0.917	0.073	0.881	0.094
30.00	0.614	0.114	0.895	0.084	0.833	0.107
32.00	0.591	0.112	0.846	0.096	0.774	0.114
34.00			0.819	0.104	0.734	0.114

342

RADIAL TRAVERSES

M_J = .47 λ = .1 $\bar{x}$ = 3.25			M_J = .47 λ = .101 $\bar{x}$ = 6.5		
$\bar{r}$	$\bar{V}_1$	$\bar{v}_1$	$\bar{r}$	$\bar{V}_1$	$\bar{v}_1$
0.48	1.000	0.034	0.02	1.000	0.047
0.62	0.997	0.039	0.23	1.002	0.049
0.68	0.980	0.090	0.43	0.976	0.077
0.82	0.922	0.125	0.57	0.958	0.092
0.88	0.779	0.155	0.63	0.902	0.122
0.93	0.751	0.154	0.82	0.709	0.152
1.02	0.601	0.149	1.12	0.441	0.142
1.03	0.588	0.151	1.23	0.374	0.136
1.08	0.516	0.146	1.32	0.309	0.117
1.28	0.241	0.094	1.43	0.262	0.106
1.38	0.182	0.063	1.52	0.221	0.087
1.48	0.153	0.047	1.62	0.178	0.067
1.58	0.135	0.037	1.73	0.158	0.062
			1.82	0.139	0.043
			2.02	0.109	0.026
			2.52	0.101	0.008

M_J = .47 λ = .102 $\bar{x}$ = 15			M_J = .47 λ = .096 $\bar{x}$ = 32		
$\bar{r}$	$\bar{V}_1$	$\bar{v}_1$	$\bar{r}$	$\bar{V}_1$	$\bar{v}_1$
0.00	0.904	0.120	0.04	0.501	0.104
0.20	0.891	0.121	0.21	0.495	0.105
0.40	0.839	0.144	0.46	0.482	0.105
0.50	0.786	0.152	0.54	0.479	0.108
0.60	0.758	0.160	0.71	0.469	0.105
0.80	0.681	0.162	0.96	0.445	0.105
1.00	0.562	0.165	1.04	0.425	0.110
1.00	0.545	0.162	1.46	0.381	0.107
1.20	0.465	0.156	1.54	0.368	0.108
1.40	0.365	0.137	1.96	0.321	0.104
1.50	0.306	0.124	2.04	0.316	0.103
1.80	0.241	0.104	2.46	0.268	0.094
2.00	0.204	0.085	2.96	0.214	0.072
2.20	0.166	0.065	3.46	0.185	0.060
2.40	0.142	0.052	3.96	0.158	0.052
2.60	0.120	0.035	4.46	0.131	0.043
2.80	0.105	0.011	4.96	0.109	0.026
3.00	0.102	0.007	5.96	0.096	0.004
3.20	0.100	0.005			
3.40	0.099	0.005			
3.60	0.102	0.004			

RADIAL TRAVERSES

$M_J = .47$, $\lambda = .2$, $\bar{x} = 3.5$			$M_J = .47$, $\lambda = .201$, $\bar{x} = 7$		
$\bar{r}$	$\bar{V}_1$	$\bar{v}_1$	$\bar{r}$	$\bar{V}_1$	$\bar{v}_1$
0.00	0.996	0.020	0.00	0.995	0.046
0.20	0.998	0.020	0.15	0.999	0.050
0.20	0.997	0.020	0.30	0.997	0.049
0.40	0.998	0.022	0.30	1.000	0.050
0.40	0.997	0.023	0.45	0.996	0.055
0.50	0.999	0.026	0.60	0.975	0.070
0.60	1.000	0.031	0.60	0.977	0.070
0.60	0.997	0.031	0.75	0.923	0.096
0.70	0.994	0.038	0.90	0.809	0.126
0.80	0.981	0.052	0.90	0.813	0.123
0.80	0.975	0.057	1.05	0.664	0.144
0.90	0.919	0.089	1.20	0.522	0.152
1.00	0.764	0.133	1.20	0.511	0.153
1.10	0.572	0.150	1.35	0.381	0.130
1.20	0.377	0.136	1.50	0.294	0.098
1.30	0.275	0.087	1.50	0.295	0.095
1.40	0.211	0.029	1.65	0.239	0.068
			1.80	0.205	0.020
			1.95	0.201	0.015
			2.10	0.201	0.012

$M_J = .47$, $\lambda = .193$, $\bar{x} = 14$			$M_J = .47$, $\lambda = .206$, $\bar{x} = 32$		
$\bar{r}$	$\bar{V}_1$	$\bar{v}_1$	$\bar{r}$	$\bar{V}_1$	$\bar{v}_1$
0.24	0.959	0.085	0.08	0.612	0.106
0.36	0.925	0.100	0.42	0.600	0.108
0.44	0.913	0.107	0.92	0.547	0.108
0.64	0.829	0.135	1.08	0.513	0.108
0.76	0.767	0.138	1.42	0.483	0.104
0.84	0.721	0.147	1.92	0.412	0.098
1.04	0.579	0.144	2.08	0.383	0.095
1.16	0.561	0.147	2.42	0.347	0.089
1.24	0.486	0.129	2.92	0.287	0.073
1.44	0.414	0.117	3.42	0.243	0.052
1.56	0.366	0.110	3.92	0.215	0.021
1.64	0.350	0.106	4.42	0.208	0.010
1.84	0.295	0.089	4.92	0.206	0.006
1.96	0.260	0.073	5.42	0.206	0.004
2.04	0.250	0.068			
2.24	0.221	0.044			
2.44	0.205	0.026			
2.64	0.197	0.014			
2.84	0.194	0.008			
3.24	0.193	0.005			

RADIAL TRAVERSES

$M_J = .47$, $\lambda = .286$, $\bar{x} = 15$			$M_J = .47$, $\lambda = .279$, $\bar{x} = 7.5$		
$\bar{r}$	$\bar{V}_1$	$\bar{v}_1$	$\bar{r}$	$\bar{V}_1$	$\bar{v}_1$
0.04	0.984	0.060	0.06	1.002	0.035
0.24	0.971	0.069	0.24	1.002	0.040
0.36	0.953	0.075	0.36	0.995	0.042
0.44	0.936	0.088	0.51	0.987	0.050
0.64	0.862	0.115	0.66	0.962	0.063
0.76	0.801	0.124	0.81	0.893	0.103
0.84	0.754	0.133	0.84	0.846	0.116
1.04	0.652	0.132	1.11	0.600	0.136
1.16	0.604	0.129	1.14	0.548	0.135
1.24	0.559	0.125	1.26	0.440	0.109
1.44	0.483	0.112	1.41	0.358	0.089
1.56	0.448	0.104	1.44	0.355	0.089
1.64	0.421	0.101	1.56	0.301	0.052
1.84	0.370	0.086	1.71	0.279	0.025
1.96	0.346	0.074	1.86	0.279	0.017
2.04	0.327	0.067			
2.24	0.290	0.025			
2.44	0.286	0.013			
2.64	0.286	0.009			

$M_J = .47$, $\lambda = .283$, $\bar{x} = 3.75$			$M_J = .47$, $\lambda = .305$, $\bar{x} = 32$		
$\bar{r}$	$\bar{V}_1$	$\bar{v}_1$	$\bar{r}$	$\bar{V}_1$	$\bar{v}_1$
0.04	0.998	0.019	0.08	0.713	0.098
0.16	0.997	0.019	0.42	0.681	0.100
0.24	1.001	0.022	1.08	0.594	0.108
0.34	1.001	0.022	1.42	0.530	0.098
0.36	0.998	0.021	1.92	0.447	0.087
0.44	1.003	0.022	2.08	0.421	0.082
0.54	1.003	0.024	2.42	0.379	0.068
0.56	0.994	0.027	2.92	0.328	0.041
0.64	0.999	0.032	3.42	0.307	0.014
0.74	0.995	0.041	3.92	0.305	0.007
0.76	0.982	0.041			
0.84	0.947	0.064			
0.94	0.824	0.116			
0.96	0.815	0.113			
1.04	0.644	0.141			
1.14	0.450	0.137			
1.24	0.314	0.074			
1.34	0.275	0.035			
1.44	0.273	0.024			
1.54	0.276	0.017			
1.96	0.292	0.011			
2.04	0.293	0.009			

RADIAL TRAVERSES

$M_J = .47$, $\lambda = .383$, $\bar{x} = 4.5$			$M_J = .47$, $\lambda = .389$, $\bar{x} = 9$		
$\bar{r}$	$\bar{V}_1$	$\bar{v}_1$	$\bar{r}$	$\bar{V}_1$	$\bar{v}_1$
0.02	1.002	0.017	0.03	0.999	0.043
0.12	1.002	0.017	0.18	0.998	0.041
0.18	0.999	0.017	0.27	0.996	0.043
0.32	1.001	0.018	0.33	0.996	0.045
0.38	1.001	0.019	0.48	0.991	0.051
0.52	0.998	0.022	0.57	0.978	0.056
0.58	0.998	0.023	0.63	0.967	0.065
0.72	0.995	0.032	0.78	0.907	0.087
0.78	0.986	0.039	0.87	0.848	0.105
0.87	0.947	0.070	0.93	0.801	0.111
0.92	0.876	0.102	1.08	0.681	0.124
0.97	0.818	0.109	1.17	0.608	0.122
1.02	0.734	0.118	1.23	0.562	0.114
1.07	0.642	0.128	1.38	0.483	0.090
1.12	0.562	0.122	1.47	0.432	0.078
1.17	0.485	0.104	1.53	0.404	0.046
1.22	0.429	0.084	1.68	0.397	0.028
11.27	0.393	0.059	1.83	0.385	0.018
1.32	0.369	0.040	2.03	0.388	0.012
1.42	0.366	0.029	2.23	0.389	0.009
1.52	0.372	0.023	3.03	0.389	0.005
1.77	0.382	0.012			
2.02	0.383	0.008			

$M_J = .47$, $\lambda = .392$, $\bar{x} = 18$			$M_J = .47$, $\lambda = .413$, $\bar{x} = 32$		
$\bar{r}$	$\bar{V}_1$	$\bar{v}_1$	$\bar{r}$	$\bar{V}_1$	$\bar{v}_1$
0.08	0.970	0.065	0.08	0.807	0.092
0.28	0.914	0.081	0.42	0.790	0.091
0.32	0.931	0.083	0.67	0.742	0.095
0.48	0.902	0.099	1.08	0.682	0.101
0.68	0.830	0.108	1.17	0.642	0.095
0.72	0.793	0.112	1.42	0.598	0.092
0.88	0.751	0.111	1.67	0.547	0.081
1.08	0.672	0.111	2.08	0.469	0.066
1.12	0.641	0.112	2.17	0.466	0.060
1.28	0.607	0.106	2.42	0.441	0.044
1.48	0.546	0.096	2.67	0.421	0.025
1.52	0.517	0.091	2.92	0.413	0.013
1.68	0.498	0.083	3.42	0.413	0.008
1.88	0.437	0.060			
1.92	0.428	0.062			
2.08	0.408	0.039			
2.28	0.395	0.020			
2.48	0.392	0.012			
3.08	0.392	0.007			

346

RADIAL TRAVERSES

$M_J = .47$, $\lambda = .481$, $\bar{x} = 5.25$			$M_J = .47$, $\lambda = .479$, $\bar{x} = 10.5$		
$\bar{r}$	$\bar{V}_1$	$\bar{v}_1$	$\bar{r}$	$\bar{V}_1$	$\bar{v}_1$
0.40	1.000	0.021	0.06	0.988	0.034
0.60	0.999	0.028	0.14	0.990	0.036
0.70	0.998	0.035	0.26	0.989	0.037
0.80	0.981	0.050	0.34	0.988	0.040
0.85	0.956	0.071	0.35	0.990	0.040
0.90	0.904	0.097	0.46	0.987	0.044
0.95	0.840	0.112	0.56	0.977	0.047
1.00	0.788	0.112	0.66	0.961	0.057
1.05	0.712	0.116	0.74	0.934	0.075
1.10	0.636	0.111	0.76	0.923	0.075
1.15	0.589	0.106	0.84	0.853	0.094
1.20	0.533	0.087	0.94	0.800	0.105
1.25	0.491	0.069	0.96	0.787	0.103
1.30	0.470	0.060	1.06	0.715	0.103
1.35	0.455	0.047	1.14	0.654	0.105
1.40	0.454	0.038	1.16	0.638	0.099
1.50	0.456	0.031	1.26	0.587	0.092
1.75	0.472	0.019	1.34	0.538	0.079
2.00	0.477	0.013	1.36	0.534	0.072
2.25	0.481	0.009	1.46	0.504	0.058
2.50	0.481	0.009	1.54	0.477	0.039
			1.56	0.482	0.046
			1.66	0.474	0.034
			1.86	0.475	0.018
			2.06	0.479	0.013

$M_J = .47$, $\lambda = .496$, $\bar{x} = 21$			$M_J = .47$, $\lambda = .497$, $\bar{x} = 32$		
$\bar{r}$	$\bar{V}_1$	$\bar{v}_1$	$\bar{r}$	$\bar{V}_1$	$\bar{v}_1$
0.11	0.975	0.057	0.10	0.879	0.080
0.19	0.976	0.056	0.15	0.864	0.083
0.31	0.955	0.064	0.40	0.836	0.088
0.39	0.952	0.072	0.65	0.792	0.091
0.51	0.905	0.088	0.90	0.737	0.089
0.59	0.880	0.091	1.10	0.700	0.086
0.71	0.825	0.100	1.15	0.685	0.086
0.79	0.790	0.103	1.40	0.637	0.079
0.91	0.756	0.097	1.65	0.589	0.071
0.99	0.721	0.092	1.90	0.548	0.058
1.11	0.690	0.090	2.10	0.527	0.043
1.19	0.655	0.088	2.15	0.529	0.043
1.31	0.629	0.086	2.40	0.499	0.015
1.39	0.588	0.076	2.55	0.498	0.012
1.51	0.576	0.074	2.90	0.497	0.009
1.59	0.541	0.054	3.15	0.498	0.009
1.71	0.529	0.051	3.40	0.497	0.008
1.91	0.506	0.030			
2.11	0.497	0.019			
2.31	0.495	0.013			
2.51	0.496	0.011			
2.71	0.496	0.010			
2.91	0.496	0.009			

RADIAL TRAVERSES

$M_J = .90$			$M_J = .90$		
$\lambda = .104$			$\lambda = .104$		
$\bar{x} = 4$			$\bar{x} = 8$		
$\bar{r}$	$\bar{V}_1$	$\bar{v}_1$	$\bar{r}$	$\bar{V}_1$	$\bar{v}_1$
0.03	0.998	0.014	0.04	1.000	0.025
0.23	0.999	0.014	0.24	0.998	0.027
0.43	0.996	0.016	0.26	0.999	0.029
0.57	0.999	0.020	0.44	0.995	0.037
0.63	0.996	0.026	0.46	0.999	0.037
0.73	0.985	0.057	0.54	0.999	0.044
0.77	0.953	0.093	0.54	0.922	0.113
0.78	0.940	0.104	0.66	0.907	0.124
0.83	0.874	0.140	0.74	0.817	0.147
0.87	0.798	0.152	0.84	0.766	0.154
0.88	0.772	0.162	0.86	0.734	0.150
0.93	0.697	0.159	1.04	0.557	0.142
0.97	0.625	0.149	1.06	0.547	0.145
0.98	0.580	0.150	1.14	0.482	0.136
1.03	0.513	0.148	1.24	0.384	0.130
1.08	0.448	0.138	1.34	0.321	0.118
1.13	0.395	0.131	1.44	0.260	0.106
1.18	0.312	0.116	1.54	0.212	0.095
1.23	0.263	0.105	1.64	0.147	0.058
1.28	0.208	0.092	1.84	0.113	0.019
1.33	0.148	0.054	2.04	0.105	0.009
1.43	0.117	0.021	2.24	0.104	0.007
1.53	0.108	0.012			
1.73	0.105	0.007			
1.83	0.104	0.005			

$M_J = .90$			$M_J = .90$		
$\lambda = .102$			$\lambda = .102$		
$\bar{x} = 16$			$\bar{x} = 32$		
$\bar{r}$	$\bar{V}_1$	$\bar{v}_1$	$\bar{r}$	$\bar{V}_1$	$\bar{v}_1$
0.06	0.957	0.087	0.04	0.629	0.119
0.24	0.931	0.109	0.21	0.625	0.119
0.26	0.926	0.110	0.46	0.595	0.122
0.44	0.866	0.135	0.54	0.578	0.127
0.46	0.842	0.141	0.71	0.562	0.123
0.64	0.753	0.152	0.96	0.497	0.125
0.66	0.744	0.151	1.04	0.468	0.123
0.84	0.635	0.147	1.46	0.395	0.118
0.86	0.620	0.148	1.54	0.384	0.121
1.04	0.551	0.143	1.96	0.321	0.104
1.06	0.549	0.144	2.04	0.305	0.106
1.26	0.476	0.135	2.46	0.260	0.091
1.46	0.377	0.122	2.96	0.204	0.077
1.66	0.311	0.111	3.46	0.138	0.047
1.86	0.262	0.100	3.96	0.114	0.020
2.06	0.179	0.076	4.46	0.106	0.011
2.26	0.147	0.058	4.96	0.103	0.007
2.46	0.124	0.035	5.46	0.103	0.004
2.66	0.112	0.020	5.96	0.102	0.003
2.86	0.106	0.011			
3.05	0.103	0.008			
3.26	0.103	0.006			
3.46	0.102	0.005			
3.66	0.102	0.004			

RADIAL TRAVERSES

$M_J = 1.37$, $\lambda = .100$, $\bar{x} = 4$			$M_J = 1.37$, $\lambda = .101$, $\bar{x} = 8$		
$\bar{r}$	$\bar{V}_1$	$\bar{v}_1$	$\bar{r}$	$\bar{V}_1$	$\bar{v}_1$
0.06	0.998	0.013	0.04	1.004	0.015
0.26	0.998	0.014	0.24	1.001	0.016
0.34	0.991	0.013	0.36	1.003	0.017
0.46	1.000	0.015	0.44	0.997	0.022
0.54	0.994	0.014	0.54	0.995	0.027
0.56	0.998	0.015	0.64	0.979	0.041
0.66	0.997	0.017	0.74	0.941	0.066
0.74	0.993	0.019	0.84	0.861	0.122
0.76	0.996	0.024	0.89	0.770	0.163
0.81	0.974	0.055	0.94	0.672	0.160
0.83	0.949	0.086	0.99	0.565	0.160
0.86	0.876	0.134	1.04	0.501	0.150
0.88	0.818	0.155	1.09	0.450	0.122
0.94	0.608	0.169	1.14	0.360	0.104
0.94	0.614	0.158	1.19	0.344	0.103
0.96	0.545	0.154	1.24	0.304	0.092
1.01	0.446	0.125	1.44	0.150	0.051
1.03	0.412	0.120	1.54	0.121	0.035
1.06	0.348	0.107	1.64	0.106	0.020
1.09	0.317	0.106	1.74	0.101	0.012
1.11	0.291	0.102			
1.16	0.239	0.089			
1.21	0.186	0.075			
1.26	0.127	0.037			
1.36	0.104	0.015			
1.46	0.100	0.009			
1.66	0.100	0.005			
1.86	0.100	0.003			

$M_J = 1.37$, $\lambda = .099$, $\bar{x} = 16$			$M_J = 1.37$, $\lambda = .098$, $\bar{x} = 32$		
$\bar{r}$	$\bar{V}_1$	$\bar{v}_1$	$\bar{r}$	$\bar{V}_1$	$\bar{v}_1$
0.00	0.994	0.027	0.00	0.775	0.111
0.20	0.989	0.030	0.25	0.725	0.119
0.40	0.974	0.045	0.50	0.690	0.126
0.60	0.944	0.061	0.75	0.593	0.137
0.80	0.882	0.094	1.00	0.527	0.134
0.90	0.835	0.117	1.50	0.429	0.116
1.00	0.740	0.155	2.00	0.322	0.091
1.10	0.674	0.147	2.00	0.314	0.094
1.20	0.532	0.150	2.50	0.225	0.076
1.30	0.449	0.125	3.00	0.154	0.053
1.40	0.368	0.112	3.50	0.122	0.038
1.60	0.279	0.095	4.00	0.103	0.018
1.80	0.224	0.084	4.50	0.098	0.009
2.20	0.126	0.042			
2.40	0.108	0.024			
2.60	0.101	0.103			
2.80	0.099	0.009			

RADIAL TRAVERSES

$M_J = 1.67$, $\lambda = .096$, $\bar{x} = 4$			$M_J = 1.67$, $\lambda = .099$, $\bar{x} = 8$		
$\bar{r}$	$\bar{V}_1$	$\bar{v}_1$	$\bar{r}$	$\bar{V}_1$	$\bar{v}_1$
0.03	1.007	0.013	0.05	0.987	0.014
0.13	1.006	0.015	0.25	0.987	0.015
0.23	1.001	0.013	0.35	0.990	0.014
0.33	0.998	0.013	0.45	0.990	0.017
0.37	0.994	0.015	0.55	0.991	0.019
0.43	0.995	0.013	0.55	0.994	0.019
0.53	0.992	0.015	0.65	0.989	0.025
0.57	0.989	0.014	0.75	0.967	0.045
0.63	0.989	0.014	0.75	0.979	0.034
0.73	0.986	0.017	0.80	0.942	0.063
0.77	0.984	0.015	0.85	0.912	0.083
0.83	0.978	0.025	0.90	0.862	0.109
0.86	0.962	0.042	0.95	0.765	0.153
0.88	0.953	0.048	1.00	0.623	0.162
0.90	0.928	0.064	1.05	0.484	0.135
0.93	0.871	0.116	1.05	0.499	0.138
0.95	0.771	0.158	1.10	0.444	0.129
0.97	0.742	0.173	1.15	0.360	0.106
0.98	0.644	0.177	1.20	0.332	0.099
1.01	0.475	0.142	1.25	0.239	0.084
1.03	0.428	0.121	1.35	0.208	0.072
1.06	0.334	0.102	1.45	0.160	0.058
1.08	0.301	0.098	1.55	0.126	0.039
1.13	0.247	0.083	1.65	0.107	0.021
1.18	0.163	0.058	1.75	0.100	0.012
1.23	0.127	0.040	1.85	0.099	0.009
1.28	0.101	0.018			
1.33	0.096	0.013			
1.43	0.096	0.009			

$M_J = 1.67$, $\lambda = .099$, $\bar{x} = 16$			$M_J = 1.67$, $\lambda = .098$, $\bar{x} = 32$		
$\bar{r}$	$\bar{V}_1$	$\bar{v}_1$	$\bar{r}$	$\bar{V}_1$	$\bar{v}_1$
0.06	1.000	0.024	0.10	0.834	0.102
0.26	0.995	0.028	0.40	0.802	0.114
0.44	0.985	0.041	0.60	0.734	0.136
0.46	0.978	0.042	0.90	0.648	0.139
0.66	0.920	0.087	1.60	0.350	0.107
0.76	0.863	0.123	2.10	0.284	0.090
0.86	0.789	0.149	2.10	0.269	0.085
0.94	0.667	0.169	2.60	0.189	0.068
0.96	0.649	0.164	3.10	0.140	0.049
1.06	0.540	0.148	3.50	0.108	0.025
1.16	0.478	0.133	4.10	0.098	0.012
1.26	0.377	0.110			
1.46	0.270	0.083			
1.66	0.218	0.073			
2.06	0.126	0.037			
2.26	0.107	0.023			
2.56	0.099	0.010			

RADIAL TRAVERSES

	MJ = .47 λ = .384 x̄ = .2			MJ = .47 λ = .480 x̄ = .2	
$\bar{r}$	$\bar{V}_1$	$\bar{v}_1$	$\bar{r}$	$\bar{V}_1$	$\bar{v}_1$
0.94	0.991	0.017	0.91	1.000	0.027
0.94	0.991	0.025	0.93	1.000	0.025
0.96	0.981	0.032	0.94	1.004	0.023
0.96	0.995	0.029	0.95	0.904	0.025
0.98	0.958	0.052	0.97	0.973	0.039
1.00	0.838	0.107	0.98	0.940	0.067
1.01	0.568	0.144	0.99	0.876	0.083
1.02	0.507	0.144	1.01	0.315	0.138
1.03	0.414	0.107	1.02	0.376	0.114
1.04	0.331	0.094	1.02	0.330	0.154
1.05	0.277	0.072	1.03	0.236	0.083
1.05	0.237	0.044	1.03	0.312	0.076
1.06	0.243	0.047	1.04	0.216	0.070
1.07	0.236	0.040	1.06	0.173	0.078
1.09	0.239	0.032	1.09	0.277	0.039
1.11	0.235	0.030	1.19	0.322	0.041
1.14	0.258	0.031	1.29	0.360	0.039
1.16	0.246	0.029	1.39	0.391	0.040
1.24	0.288	0.032	1.59	0.437	0.033
1.26	0.270	0.029	1.79	0.462	0.021
1.36	0.295	0.031	1.99	0.471	0.014
1.56	0.337	0.027	2.19	0.476	0.009
1.76	0.360	0.020	2.39	0.479	0.007
1.96	0.374	0.012	2.59	0.480	0.006
2.16	0.381	0.008			
2.36	0.383	0.006			
2.56	0.384	0.005			

APPENDIX 4B

MEAN VELOCITY DECAY ANALYSIS

The analysis of this section is based on that by Kleinstein (ref. 123) who obtained solutions for mixing the turbulent axisymmetric free jets using the "modified Oseen method." In this method the conservation equations are linearized in the plane of the von Mises variables resulting in a system of equations of the heat-conduction type.

The equations of continuity, momentum and energy are, neglecting the axial pressure gradient (though the experiments to be considered were performed in a wind tunnel, the axial pressure gradient was small since the ratio of tunnel area to jet exit area was large):

$$\frac{\partial(\rho V_1 r)}{\partial x} + \frac{\partial(\rho V_2 r)}{\partial r} = 0, \tag{4B-1}$$

$$\rho V_1 \frac{\partial V_1}{\partial x} + \rho V_2 \frac{\partial V_1}{\partial r} = \frac{1}{r} \frac{\partial}{\partial r} \left\{ (\rho\epsilon) r \frac{\partial V_1}{\partial r} \right\}, \quad \text{and} \tag{4B-2}$$

$$\rho V_1 \frac{\partial H}{\partial x} + \rho V_2 \frac{\partial H}{\partial r} = \frac{1}{r} \frac{\partial}{\partial r} \left\{ \frac{(\rho\epsilon)}{P_r} r \frac{\partial H}{\partial r} \right\} \tag{4B-3}$$

Equations (4B-2) and (4B-3) have an identical form, as would the equation for conservation of chemical species in a nonreacting turbulent fluid. This general form may be written,

$$\rho V_1 \frac{\partial P_k}{\partial x} + \rho V_2 \frac{\partial P_k}{\partial r} = \frac{1}{r} \frac{\partial}{\partial r} \left\{ A_k (\rho\epsilon) r \frac{\partial P_k}{\partial r} \right\}. \tag{4B-4}$$

A dimensionless stream function ψ is introduced in the form

$$\frac{\partial(\Psi/2)^2}{\partial \bar{r}} = \bar{\rho}\bar{V}_1\bar{r}, \frac{\partial(\Psi/2)^2}{\partial \bar{x}} = -\bar{\rho}\bar{V}_2\bar{r} \tag{4B-5a}$$

where $$\psi = (\Psi/2)^2, \tag{4B-5b}$$

and overbars indicate dimensionless variables.

The von Mises transformation with independent variables Ψ and $\bar{x}$ is applied to equation (4B-4) giving,

$$\frac{\partial P_k}{\partial \bar{x}} = \frac{4}{\Psi} \frac{\partial}{\partial \Psi} \left\{ A_k \overline{\rho\epsilon} \, \bar{\rho}\bar{V}_1 \frac{\bar{r}^2}{\Psi} \frac{\partial P_k}{\partial \Psi} \right\} \tag{4B-6}$$

The term $[A_k(\rho\epsilon)\bar{\rho} \, \bar{V}_1\bar{r}^2]$ is written in a series expansion in Ψ^2 about a point $\bar{x}$ on the axis yielding:

$$[A_k(\rho\epsilon)\bar{\rho} \, \bar{V}_1\bar{r}^2]_{\bar{x},\Psi} = [A_k(\rho\epsilon)]_{\bar{x},o} \, \Psi^2/2 + O(\Psi^4). \tag{4B-7}$$

Neglecting terms of fourth order and higher in this expression and substituting into equation (4B-6) yields

$$\frac{\partial P_k}{\partial \bar{x}} = \frac{2}{\Psi} \frac{\partial}{\partial \Psi} \left\{ [A_k \overline{(\rho \varepsilon)}]_{\bar{n},o} \Psi \frac{\partial P_k}{\partial \Psi} \right\} . \tag{4B-8}$$

Finally, equation (4B-8) may be written

$$\frac{\partial P_k}{\partial \xi_k} = \frac{1}{\Psi} \frac{\partial}{\partial \Psi} \left\{ \Psi \frac{\partial P_k}{\partial \Psi} \right\} \tag{4B-9}$$

where,

$$\xi_k = 2 \int_0^{\bar{x}} [A_k \overline{\rho \varepsilon}]_{Y,o} \, d\bar{x} . \tag{4B-10}$$

Equation (4B-9) is the well-known heat conduction equation and solutions to this equation are available. We note that in the form of equation (4B-9) a constant shift of the dependent variables P_k does not effect the solution in the ξ_k, Ψ plane. Thus, a step function boundary condition in velocity equal to the velocity difference for $\bar{r} \leq 1$ and zero for $\bar{r} < 1$ is permissible. The boundary conditions on P_k are, $P_k(\Psi,o) = g_k(\Psi)$ and $P_k(\infty, \xi_k) = 0$ with $g_k(\Psi)$ by,

$$g_k(\Psi) = \begin{cases} P_{kJ} - P_{ko} & 0 \leq \Psi \leq \Psi_J \\ \\ 0 & \Psi_J < \Psi \end{cases} .$$

Subject to these conditions, the solution to equation (4B-9) is equivalent to the heat conduction equation solution for an instantaneous cylindrical source of heat at $t = 0$, Carslaw and Jaeger (ref. 124), and is

$$P_k = \frac{P_k - P_{ko}}{P_{kJ} - P_{ko}} = \frac{1}{2\xi_k} \exp \left\{ - \frac{\Psi^2}{4\xi_k} \right\} \times$$

$$\int_0^{\Psi_J} \exp \left\{ - \frac{\psi'^2}{4\xi_k} \right\} I_o \left\{ \frac{\Psi\psi'}{2\xi_k} \right\} \psi' \, d\psi' \tag{4B-11a}$$

and along the axis

$$P_{ka} = 1 - \exp \left(- \Psi_J^2 / 4\xi_k \right) \tag{4B-11b}$$

where the subscript 'a' refers to jet centerline conditions.

356

Clearly, from equation (4B-11b) the variation of ξ_k with $\bar{x}$ is given by

$$\xi_k(\bar{x}) = - \Psi_J^2/4 \; \ln[1 - P_{ka}(\bar{x})], \qquad (4B\text{-}12)$$

and experimentally obtained centerline distributions of the function P can be used to determine ξ_k.

We will seek a form for $\overline{\rho\epsilon}$ which will be regarded as a function of $\bar{x}$ and λ only. To this end $\overline{\rho\epsilon}$ is assumed to take the form

$$\overline{\rho\epsilon} = k_1 \; \bar{r}_{.5} \; [(\bar{\rho} \; \bar{V}_1)_a - (\bar{\rho} \; \bar{V}_1)_o] \qquad (4B\text{-}13)$$

in a manner analogous to the formulation due to Ferri, Libby and Zakkay (ref. 90) for $\bar{V}_J = 0$. $\bar{r}_{.5}$ is the half-width of the jet, given by the point at which the momentum is given by

$$\bar{\rho} \; \bar{V}_1 \; \bar{\rho u} = \tfrac{1}{2} \; [(\bar{\rho} \; \bar{V}_1)_a + (\bar{\rho} \; \bar{V}_1)_o]. \qquad (4B\text{-}14)$$

In order to obtain the form of $\overline{\rho\epsilon}$ the behavior of the variables as $\xi_v \to \infty$ is examined.

The solution, $P(\Psi, \xi_k)$, given by equation (4B-11a) is conveniently divided into an axial variation and a radiation variation viz.

$$P(\Psi, \xi_k) = P_a[\Psi_J/(2\xi_k)^{\frac{1}{2}};0]P^* \; [\Psi_J/(2\xi_k)^{\frac{1}{2}}; \; \Psi/(2\xi_k)^{\frac{1}{2}}].$$

Now as $\xi_k \to \infty$

$$P_a[\Psi_J/(2\xi_k)^{\frac{1}{2}},0] = \Psi_J^2/4\xi_k \qquad (4B\text{-}15a)$$

and $\qquad P^* \; [\Psi_J/(2\xi_k)^{\frac{1}{2}}; \; \Psi/(2\xi_k)^{\frac{1}{2}}] = \exp \; (- \Psi^2/4\xi_k) \qquad (4B\text{-}15b)$

Also the density at large axial distances becomes uniform so that from equation (4B-14)

$$\bar{V}_1(\Psi_{.5}, \xi_v) = \tfrac{1}{2} \; [\bar{V}_a + \bar{V}_o]$$

or $\qquad\qquad\qquad P_a \; P^*_{.5} = \tfrac{1}{2} \; P_a,$

thus $\qquad P^*[\Psi_J/(2\xi_v)^{\frac{1}{2}}, \; \Psi_{.5}/(2\xi_v)^{\frac{1}{2}}] = \tfrac{1}{2} \; . \qquad (4B\text{-}16)$

The form of $\bar{r}_{.5}$ as $\xi_v \to \infty$ is thus given by

$$\bar{r}_{.5}^2 = \int_0^{\Psi_{.5}} \frac{\Psi \, d\Psi}{\bar{\rho} \bar{V}_1} = \frac{1}{\bar{\rho}_0} \int_0^{\Psi_{.5}} \frac{\Psi \, d\Psi}{P_a P \ast (\bar{V}_J - \bar{V}_0) + \bar{V}_0} .$$

For convenience in this case all quantities are nondimensionalized with respect to jet exit conditions, so that $\bar{V}_J = 1$, $\bar{\rho}_J = 1$, etc. and more importantly,

$$\Psi_J^2/4 = \tfrac{1}{2}.$$

Denoting $\bar{V}_0 = V_0/V_J$ by λ the expression for $\bar{r}_{.5}$ becomes:

$$\bar{r}_{.5}^2 = \frac{1}{\bar{\rho}_0} \int_0^{\Psi_2} \frac{\Psi \, d\Psi}{\tfrac{1}{2}\xi_v \exp(-\Psi^2/4\xi_v)(1-\lambda) + \lambda}$$

$$= \frac{2\xi_v}{\lambda\bar{\rho}_0} \ln \frac{[(1-\lambda) + 2\xi_v \exp(\Psi_{.5}^2/4\xi_v)]}{[(1-\lambda) + 2\xi_v\lambda]}$$

and finally using equations (4B-15b) and (4B-16) this becomes:

$$\bar{r}_{.5}^2 = \frac{2\xi_v}{\lambda\bar{\rho}_0} \ln \frac{[(1-\lambda) + 4\xi_v\lambda]}{[(1-\lambda) + 2\xi_v\lambda]} \qquad (4B-17a)$$

Using L'Hopital's rule, it can be shown that

$$\lim_{\lambda \to 0} (\bar{r}_{.5}^2) = \frac{4\xi_v^2}{\bar{\rho}_0}, \qquad (4B-17b)$$

which is the expression obtained by Kleinstein (ref. 123) for $\lambda = 0$. Thus, the expression for $\overline{\rho\varepsilon}$, equation (4B-13), becomes,

$$\overline{\rho\varepsilon} = k_1\bar{\rho}_0 \sqrt{\frac{2\xi_v}{\lambda\bar{\rho}_0} \ln \left|\frac{\cdot(1-\lambda) + 4\xi_v\lambda}{\cdot(1-\lambda) + 2\xi_v\lambda}\right|} \cdot \frac{(1-\lambda)}{2\xi_v}$$

$$= k_1\bar{\rho}_0^{\frac{1}{2}} (1-\lambda) \sqrt{\frac{1}{2\xi_v\lambda} \ln\left|\frac{(1-\lambda) + 4\xi_v\lambda}{(1-\lambda) + 2\xi_v\lambda}\right|} \qquad (4B-18a)$$

as $\lambda \to 0$, $\overline{\rho\varepsilon} = k_1\bar{\rho}_0^{\frac{1}{2}}$. $\qquad (4B-18b)$

The variation of ξ_v with $\bar{x}$ can be found from equation 12. The values of ξ_v as a function of $\bar{x}$ are tabulated in Tables 4B-I and 4B-II and ξ_v is plotted as a function of $\bar{x}$ in Figures 4B-1 and 4B-2. The straight lines in

358

$\bar{x}$	$\lambda = .096$ $M_J = .47$	$\lambda = .206$ $M_J = .47$	$\lambda = .305$ $M_J = .47$	$\lambda = .413$ $M_J = .47$	$\lambda = .497$ $M_J = .47$
16	.2312	---	---	---	---
18	.2916	.2460	---	---	---
20	.3701	.3263	.2312	---	---
21	---	---	---	---	---
22	.4317	.3680	.2793	.1999	---
23	---	---	---	---	---
24	.5296	.4400	.3361	.3162	.1553
25	---	---	---	---	---
26	.5973	.4989	---	---	---
28	.6596	.5608	.4498	.3213	.2589
30	.7172	.6279	.5043	.3862	.3136
32	.8414	.6948	.5655	.4498	.3514
34	.9093	.7469	.6244	.4868	.3906

$$\xi_{.096} = - .35 + .0362\,\bar{x}$$

$$\xi_{.206} = - .35 + .0328\,\bar{x}$$

$$\xi_{.305} = - .35 + .0287\,\bar{x}$$

$$\xi_{.413} = - .35 + .0245\,\bar{x}$$

$$\xi_{.491} = - .35 + .0217\,\bar{x}$$

Table 4B.1 Variation of ξ_v with velocity ratio for $M_J = .47$.

$\bar{x}$	$\lambda = .096$ $M_J = .47$	$\lambda = .102$ $M_J = .9$	$\lambda = .098$ $M_J = 1.37$	$\lambda = .098$ $M_J = 1.67$
16	.2312	---	---	---
18	.2916	.2133	---	---
20	.3701	---	---	---
21	---	.2897	---	---
22	.4317	---	---	---
23	---	.3638	---	---
24	.5296	---	.1702	---
25	---	.4199	---	---
26	.5973	---	.2086	.1777
28	.6596	.4948	.2469	.2096
30	.7172	.5427	.2963	.2321
32	.8414	.5924	.3617	.2831
34	.9093	.6350	.4096	.3116

$$\xi_{.47} = -.35 + .0362 \, \bar{x}$$

$$\xi_{.9} = -.35 + .0302 \, \bar{x}$$

$$\xi_{1.37} = -.35 + .0218 \, \bar{x}$$

$$\xi_{1.67} = -.35 + .0198 \, \bar{x}$$

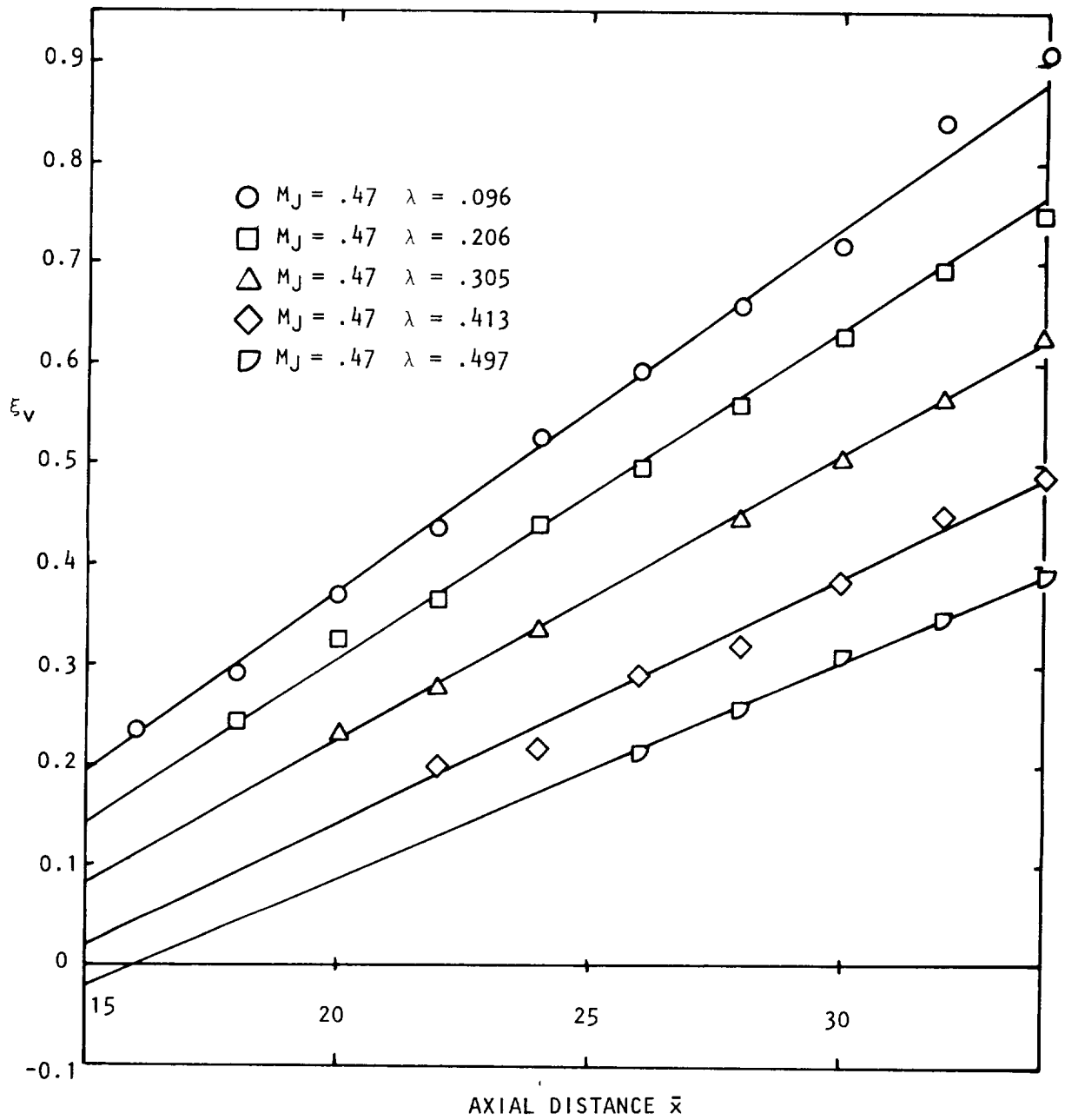Table 4B.11   Variation of ξ_V with Mach number for $\lambda = .1$.

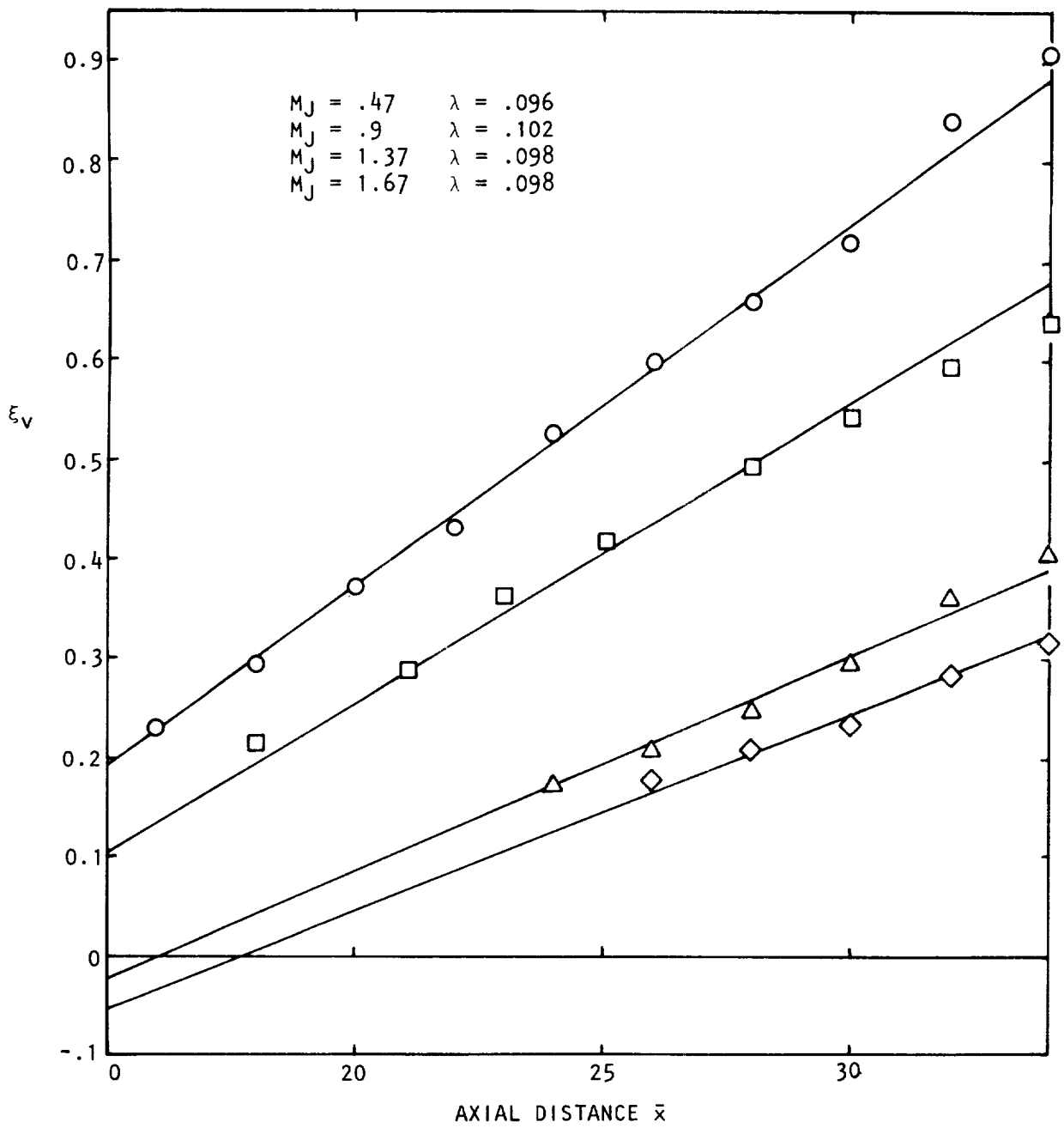Figure 4B.1 Variation of ξ_v with axial distance $M_J = .47$.

Figure 4B.2   Variation of ξ_v with axial distance, $\lambda = .1$.

362

Figure 4B-1, which are seen to fit the data well, are given by the equation,

$$\xi_v = f(\lambda)\bar{x} - .35, \qquad (4B-19)$$

where $f(\lambda)$ is the slope of the straight lines for each value of λ. The slope of $f(\lambda)$ is plotted as a function of λ in figure 4B-3, for $M_J = .47$. A good fit to the measurements is given by

$$f(\lambda) = .0399 \, (1 - .9223\lambda). \qquad (4B-20)$$

It is interesting to note that the value of $f(\lambda)$ for $\lambda = 1$, that is equal jet exit and moving stream velocities, is non-zero. This implies that a mixing process is taking place for equal velocities and the turbulent shear stresses produced give rise to a finite eddy viscosity. This mixing is due to the boundary layers which exist on the inner and outer surfaces of the jet nozzle upstream of the jet exit. If no such boundary layers existed and the jet lip was of zero thickness, then the form of equations (4B-18) and (4B-20) would suggest that $f(\lambda)$ be given by

$$f(\lambda)/f(0) = (1 - \lambda). \qquad (4B-21)$$

It is also of interest to note that in spite of the dependence of the term under the square root sign in equation (4B-18) on both λ, $\bar{\rho}_0$, and $\bar{x}$ the eddy viscosity $\overline{\rho\varepsilon}$ is independent of $\bar{x}$ for the developed region of the jet flow. However, the eddy viscosity is clearly a function of velocity ratio and density ratio.

Since the exact value of the constants in the expression for $f(\lambda)$ will have a direct dependence on the jet and free stream initial profiles, a more general form is given by equation (4B-21) and this form will be used. Making use of this expression in equation (4B-16) leads to:

$$\frac{(\bar{V}_a - \lambda)}{(1 - \lambda)} = 1 - \exp\left\{- \frac{1}{\kappa(1-\lambda)\bar{x} - X_c}\right\} \qquad (4B-22)$$

where κ is a function of $\bar{\rho}_0$ and λ and, from equation (4B-19), $X_c = .70$. This equation is identical to that given by Witze (ref. 3) for $\lambda = 0$ except that no $\bar{\rho}_0$ dependence has been given in equation (4B-22). For the case of $\lambda = 0$ Witze correlated a large amount of experimental data and was able to derive expressions for the dependence of κ on M_J and $\bar{\rho}_0$. Since the current measurements only considered three cases at a fixed velocity ratio for different Mach numbers, there is insufficient data to provide the variation of κ with λ, M_J and $\bar{\rho}_0$. The values of K calculated from the present measurements are listed in Table 4B.III.

The value of κ for $M_J = .47$ in Table 4B.III is taken from the analysis by Witze (ref. 3) for $\lambda = 0$ and $M_J = .47$. Using this set of values for K the measured centerline velocities were plotted as a function of $\kappa(1-\lambda)\bar{x}$ in Figure 4B-4. The general agreement is fairly good since the experiments were carried out in a wind tunnel with a small, but finite, pressure gradient and there existed boundary layers at the jet exit.

$$f(\lambda) = \frac{d\xi v}{dx}$$

$$f(\lambda) = .0399 \ (1 - .9223 \ \lambda)$$

EQUATION 20
$f(0) = .0375$
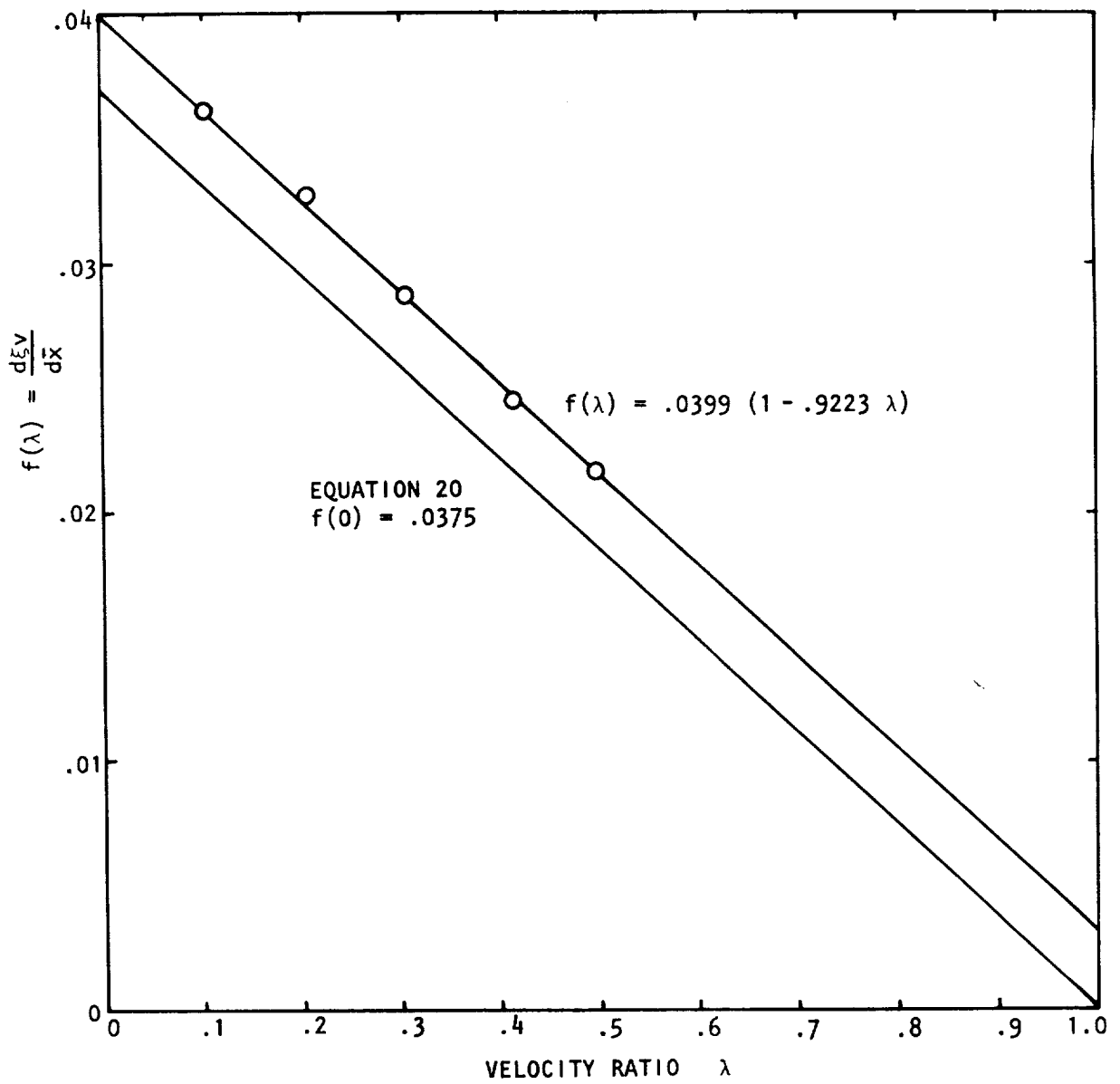
VELOCITY RATIO λ

Figure 4B.3 Variation of dξv/dx with velocity ratio, M$_J$ = .47.

364

M_J	λ	$\bar{\rho}_0$	κ
.47	.096, .206, .305, .413, .497	1.045	.075
.9	.102	1.163	.0673
1.37	.098	1.378	.0483
1.67	.098	1.562	.0439

Table 4B.III Variation of decay coefficient x with λ and M_J.
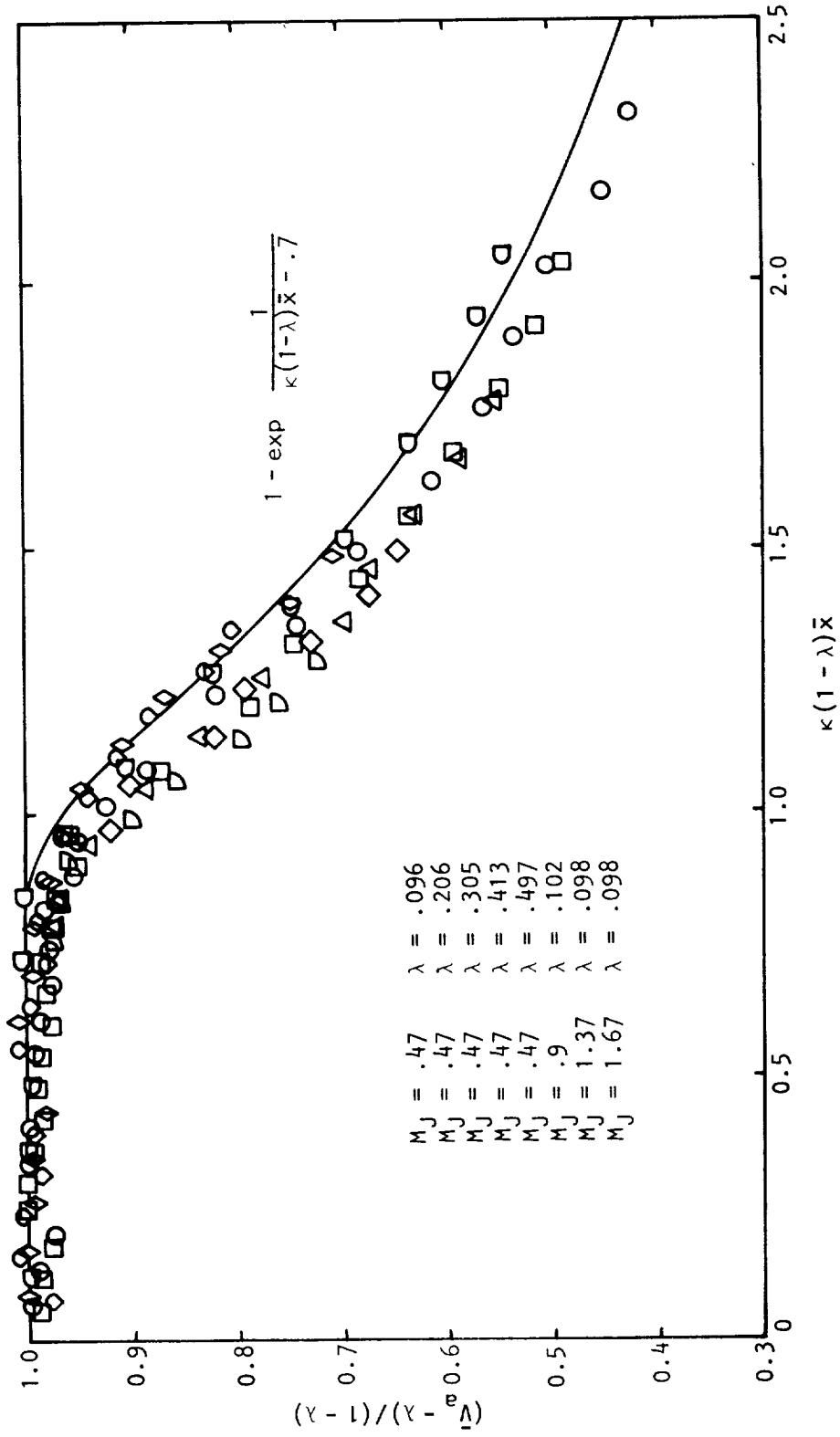
Figure 4B.4 Jet centerline velocity decay.

$$1 - \exp \frac{1}{\kappa(1-\lambda)\bar{x} - .7}$$

$\kappa(1-\lambda)\bar{x}$

$(\bar{V}_a - \lambda)/(1-\lambda)$

$M_J = .47$	$\lambda = .096$
$M_J = .47$	$\lambda = .206$
$M_J = .47$	$\lambda = .305$
$M_J = .47$	$\lambda = .413$
$M_J = .47$	$\lambda = .497$
$M_J = .9$	$\lambda = .102$
$M_J = 1.37$	$\lambda = .098$
$M_J = 1.67$	$\lambda = .098$

366

APPENDIX 4C

JET NOISE IN FORWARD FLIGHT — SOURCE ALTERATION EFFECTS

INTRODUCTION: LIGHTHILL'S MODEL FOR
JET NOISE SOURCE SCALING

The basic source of jet noise is taken to be the volume-acceleration quadrupole density $v_i'v_j'$. In the *absence* of the flow-acoustic interaction (i.e. for radiation in a uniform medium of density ρ_0 and sound speed c_0), the acoustic intensity per unit volume of turbulent flow is predicted [Lighthill (ref. 110) equation 13] to scale according to

$$I_{vol} \propto \frac{V_e}{\tau_e^4} q^4 .$$

(4C-1)

Here V_e is the correlation volume for $v_i'v_j'$ fluctuations; τ_e is a characteristic time scale, and the covariance of $v_i'v_j'$ has been assumed proportional to the fourth power of the rms turbulent velocity q ($= <v_i^2>^{\frac{1}{2}}$). Source non-compactness and convection effects are disregarded for the time being; they will be discussed later, when the source alteration effects implied by equation (4C-1) have been studied.

QUADRUPOLE CORRELATION VOLUME AND TIME SCALE

The quantities V_e and τ_e are assumed to scale on the local shear layer thickness δ and the local rms velocity fluctuation q. Thus

$$V_e \propto \delta^3 ,$$

(4C-2)

$$\tau_e \propto \delta/q$$

(4C-3)

and hence from equation (4C-1)

$$I_{vol} \propto q^8 \delta^{-1} .$$

(4C-4)

Alternatively, the intensity radiated per unit area of shear layer is independent of δ (and hence streamwise position), and proportional simply to q_{max}^8.

INTENSITY RADIATED BY THE ENTIRE JET

The quantity of interest is not I_{vol}, but the intensity radiated by the whole volume of turbulent flow. We introduce for this purpose the axial scale parameter σ (as used to scale mixing layer profiles, where the transverse coordinate is written as $\sigma y/x$). The parameter σ is used to indicate the axial extent of the initial region of the jet; thus the total intensity contributed by this region (up to the end of the potential core) is expected to scale according to

$$I \propto q_{max}^8 \, \sigma, \tag{4C-5}$$

where q_{max} is the maximum value of q across the shear layer.

FREQUENCY SCALING

In a truly two-dimensional mixing layer, the relation (4C-5) would apply not only to the overall intensity but to the proportional-band intensity at any frequency, since the radiation at any frequency f would be associated with a typical shear layer thickness q_{max}/f. However, the jet exit diameter d sets an upper limit to the value of δ for which the shear layer can be modelled as two-dimensional. The corresponding frequency scale q_{max}/d sets a lower limit to f, if (4C.5) is to remain valid.

For this reason, the intensity scaling prediction (4C-5) should be applied to corresponding frequency bands on the non-dimensional frequency scale

$$S_t = \frac{fd}{q_{max}}, \tag{4C-6}$$

with a lower limit on S_t set by the end of the jet potential core. Sound radiated predominantly from the region *downstream* of the potential core is expected to scale differently (but is not considered here).

FLOW PARAMETERS

In order to predict forward flight effects on jet noise at various temperatures on the basis of (4C-5), we require the variation of $q_{max}^8 \sigma$ with the following parameters.

(a) Shear layer velocity ratio, λ

(b) Shear layer density ratio, ρ_o/ρ_i

(c) Mach number (in case compressibility effects are important).

Subscripts (i,o) refer to the inner (or high-speed) and outer (or low-speed) sides of a two-dimensional shear layer. For the case of a round jet in forward flight, V_i is identified with the jet exit velocity V_J, and V_o with the forward flight velocity.

370

EMPIRICAL CORRELATIONS FOR (q, σ)

Reliable measurements of q over a combined range of λ and ρ_0/ρ_i are not available, although LV measurements may provide the missing information before long. For constant-density mixing, however, the data of Yule (refs. 125, 126) are sufficient to show that the simple scaling law $q \propto (V_i - V_0)$ is inadequate; an alternative relation is proposed below.

For the axial scale parameter σ, a limited amount of data — not entirely self-consistent — does exist on the combined effects of λ and ρ_0/ρ_i variations, but there is no generally accepted prediction method. The situation is summarized in a useful review by Birch and Eggers (ref. 70).

The following empirical relations are offered as a provisional fit to the published data; they make use of the dividing-streamline velocity V_{ds} as a correlating parameter (see following section).

(a) For the *rms velocity fluctuation*, the relation

$$q_{max} \propto (V_i - V_{ds}) \tag{4C-7}$$

is proposed. The actual profile of q across the shear layer is assumed to be a universal function of the mean-velocity profile variable $(V_1 - V_0)/(V_i - V_0)$.

(b) For the *axial scale parameter*, a simple relation which roughly predicts the observed trends with all three flow parameters listed above (velocity ratio, density ratio and Mach number) is

$$\sigma \propto \left(\frac{V_{ds}}{V_i - V_{ds}} \right)^2 . \tag{4C-8}$$

A somewhat better fit to the published data is given by

$$\sigma \propto \left(\frac{V_{ds}}{V_i - V_{ds}} \right)^{4/3} \left(\frac{\rho_i}{\rho_{ds}} \right)^{1/3} , \tag{4C-9}$$

but the simpler relation (4C-8) has been used for preliminary prediction purposes.

Note that the predicted intensity given by (4C-5) is much more sensitive to q_{max} variations than to σ variations.

CALCULATION OF DIVIDING STREAMLINE

In a self-preserving two-dimensional free shear layer between two parallel streams, the dividing streamline is defined by the property that

there is no mass transport across it, on average. Thus, the dividing streamline separates the mass flows of the two streams; it also locates the position of maximum turbulent shear stress, and thus has a physical significance which makes the choice of (V_{ds}, ρ_{ds}) for correlation purposes appear somewhat less arbitrary.

The position of the dividing streamline, in terms of the mean velocity ratio $V_{ds}/V_i = \lambda_{ds}$, can be deduced from the mean profiles of density and velocity in the shear layer. Values of λ_{ds}, for various combinations $(\lambda, \rho_o/\rho_i)$, have been calculated by Korst and Chow (ref. 67) using the following assumptions.

(a) For incompressible mixing, the mean profiles of specific volume $\rho^{-1}(y)$ and velocity $V(y)$ are the same shape.

(b) For compressible gas mixing with γ constant across the shear layer, the mean profiles of stagnation temperature $T_{tot}(y)$ and velocity $V(y)$ are the same shape.

(c) The profile shapes in each case are represented by an error-function curve.

Values of λ_{ds} obtained in this way were used in equations (4C-7) and (4C-8) to predict (q_{max}, σ) variations relating to the standard case ($\lambda = 0$, $\rho_i/\rho_o = 1$, incompressible flow), and the results are shown in Figures 4C.1 and 4C.2. Figure 4C.1 shows reasonable agreement between the predicted q_{max} variation (for constant-density mixing) and the measurements of Yule (refs. 125, 126). In Figure 4C.2 experimental spreading-rate ratios σ_o/σ (where σ_o refers to the standard case above) are shown from the results of Sabin (ref. 37), Baker and Weinstein (ref. 127), Abramovich $et~al$) (ref. 128), Johnson (ref. 129), and Brown and Roshko (ref. 41). The scatter is considerable, but the predicted σ variation is roughly consistent with the observed trends.

JET NOISE PREDICTION

Combining (4C-7) and (4C-8) with (4C-5) gives the prediction that

$$I \propto (V_i - V_{ds})^6 ~ V_{ds}^2 ,$$

i.e.

$$I \propto V_i^8 ~ (1 - \lambda_{ds})^6 ~ \lambda_{ds}^2 . \tag{4C-10}$$

The frequency parameter S_t defined by (4C-6) may be replaced, in view of (4C-7), by

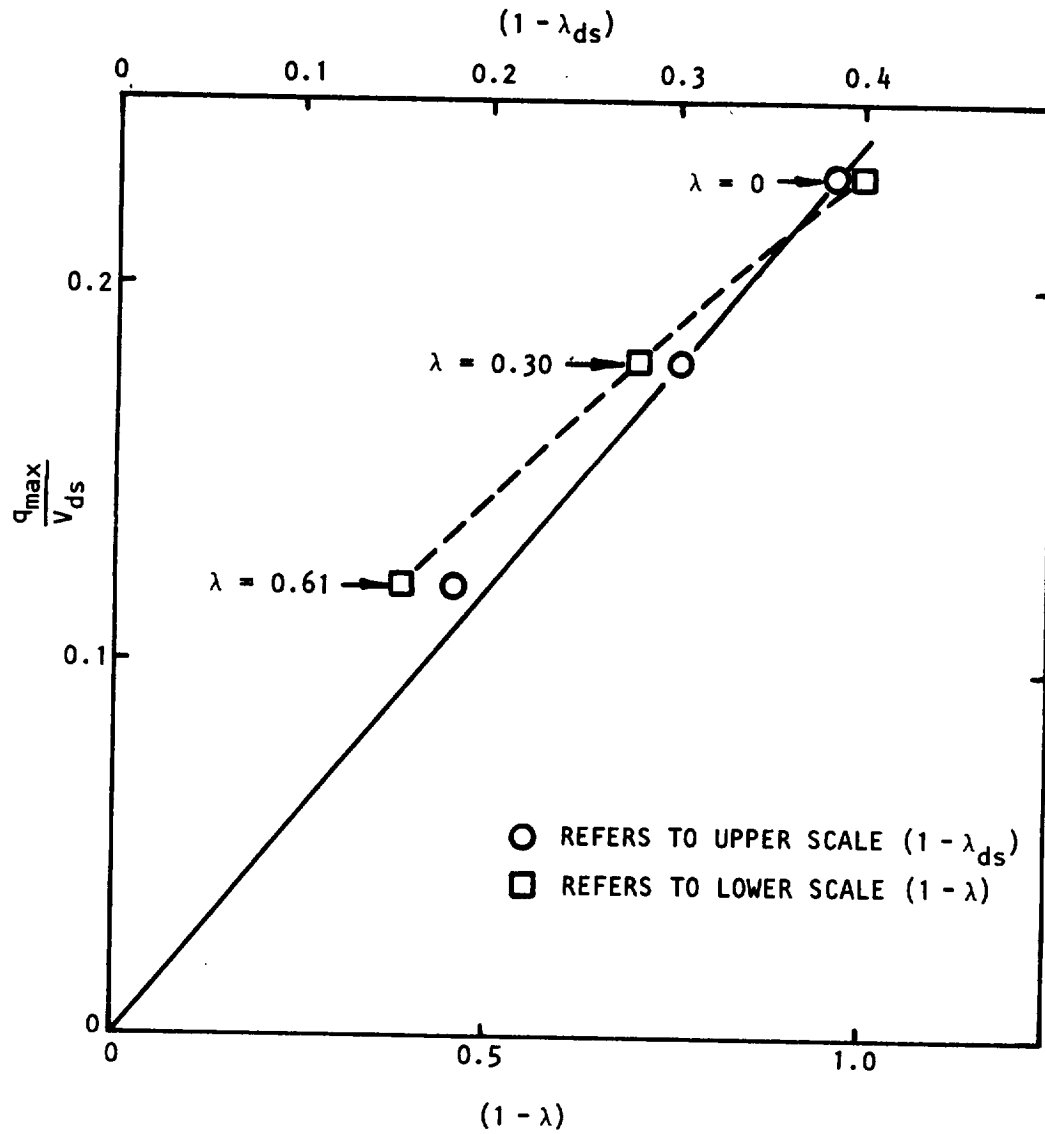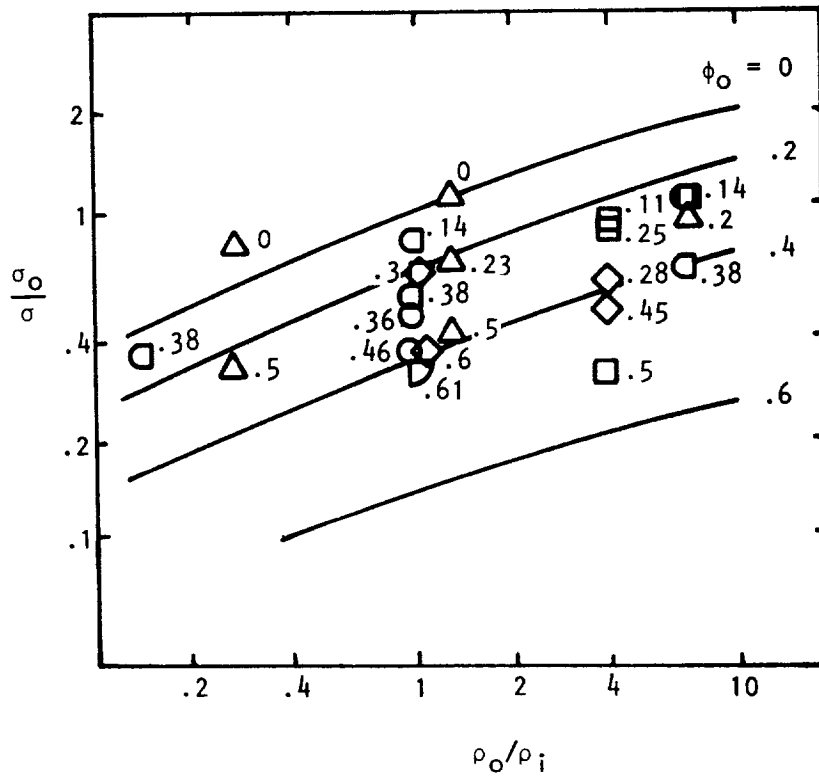$$S_{ds} = \frac{fd}{V_i(1 - \lambda_{ds})} . \tag{4C-11}$$

372

Figure 4C.1 Variation of turbulence intensity with velocity ratio in two-stream mixing (low Mach no., $\rho_o/\rho_i = 1$). Data from Yule (ref. 125, 126).

Figure 4C.2 Spreading rate variation with velocity and density ratio, in incompressible two-stream mixing

EFFECT OF INCREASING JET TEMPERATURE
AT ZERO VELOCITY RATIO

The effect on jet noise intensity of raising the jet temperature can be predicted from (4C-10); as noted at the outset, what is being predicted is a source alteration effect, and any flow-acoustic interaction effects must be allowed for subsequently. We denote the isothermal-jet intensity at the same jet velocity by I_o (in the corresponding normalized frequency band). Then (4C-10) gives

$$\frac{I}{I_o} = \frac{\{(1 - \lambda_{ds})^6 \; \lambda_{ds}^2\}_{hot}}{\{(1 - \lambda_{ds})^6 \; \lambda_{ds}^2\}_{isothermal}} , \qquad (4C-12)$$

e.g.   for $T_J/T_o = 2$, $I/I_o = 1.5$ dB;

   for $T_J/T_o = 10$, $I/I_o = 3.8$ dB.[†]

These increases in effective source strength are in fact small compared with the reductions in intensity expected from flow acoustic interaction effects.

EFFECT OF INCREASING VELOCITY RATIO
FOR GIVEN JET CONDITIONS

The intensity radiated from a jet in a surrounding stream can be related, using (4C-10) to the intensity radiated by a jet of the same exit velocity and temperature mixing with fluid at rest. The result, shown in Figure 4C.3, is a prediction of the forward flight effect on jet noise, purely from the source alteration viewpoint. It should be noted that Figure 4C.3 is calculated for jet exit Mach numbers of order 1, but by specifying the remaining parameters as λ and $T_{tot,J}/T_o$ the effect of Mach number variations is kept small. Moreover, inclusion of flow-acoustic interaction effects at $90°$ to the jet axis [by inserting a factor $(T_o/T_J)^3$ on the radiated intensity] makes a negligible difference (less than $\frac{1}{2}$ dB) to the predicted intensity reduction factor, over the range of parameters covered by Figure 4C.3.

[†]*Calculated from the λ_{ds} values of Korst and Chow (ref. 67), using a mainstream Crocco number $C_i = 0$. There is no significant change in these figures if $C_i^2 = 0.2$ is used.*
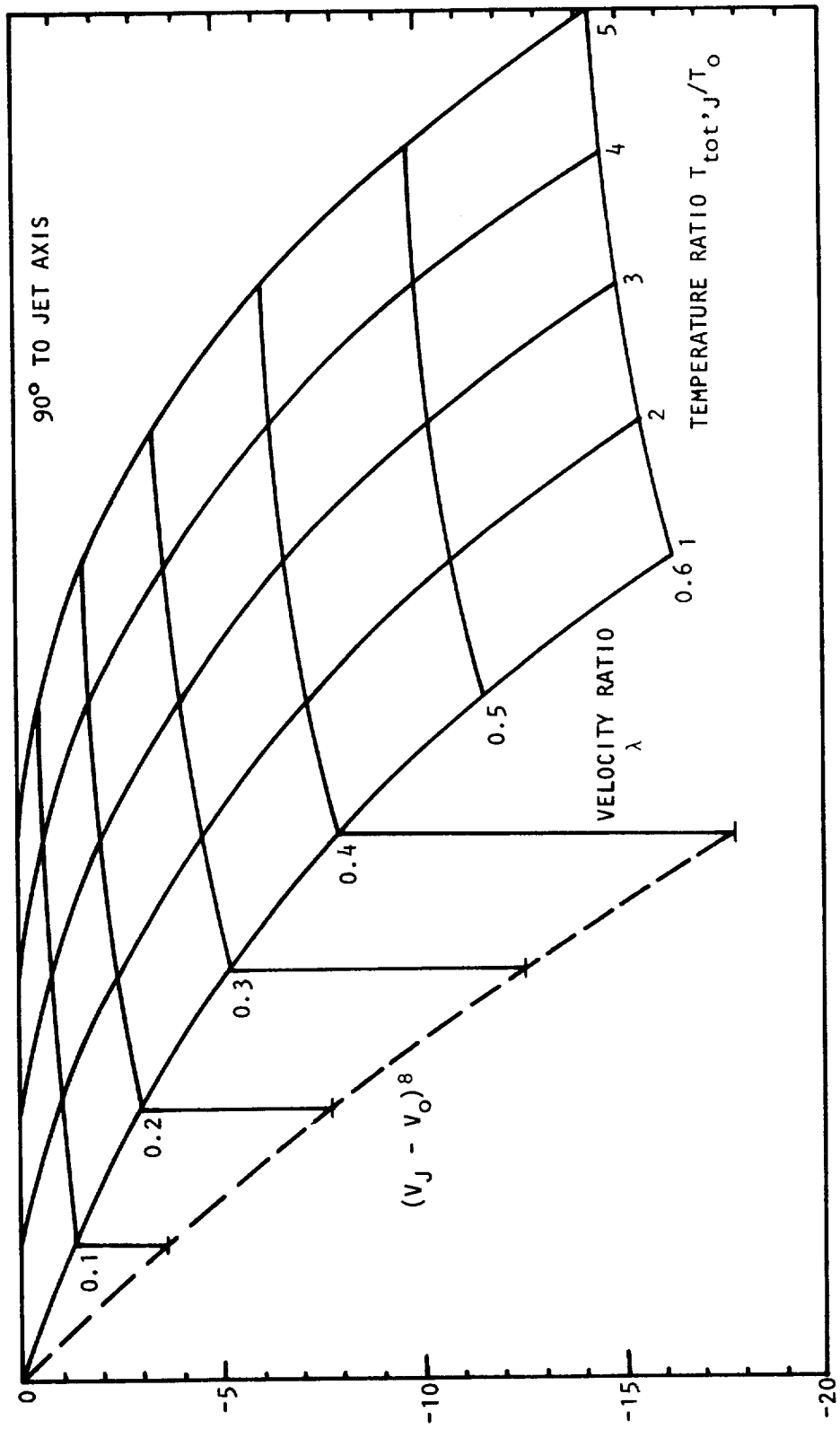
Figure 4C.3 Predicted effect of forward flight on jet mixing noise at 90°

SOURCE NON-COMPACTNESS AND CONVECTION EFFECTS

A reasonable hypothesis for the source convection velocity under various conditions of jet density and velocity ratio would be to assume

$$V_c = V_{ds} \tag{4C-13}$$

For the standard jet ($\lambda = 0$, $\rho_o/\rho_i = 1$), for example, this gives $V = 0.62 \, V_i$ using Korst and Chow's value for λ_{ds}.

The scaling velocities V_{ei} which appear in the source wavenumber-frequency spectrum model may be taken as proportional to q_{max}, and hence to $(V_i - V_{ds})$.

APPENDIX 4D

VELOCITY SAMPLING CALCULATION
AND LV PROCESSING EXAMPLE

In reference 1 it is argued that if there is no dependence of particle number on particle velocity, that is, there is no uniform particle distribution in the flow, then the true mean velocity is given by the reciprocal of the arithmetic mean of the particle periods (the time taken for the particle to cross a fixed number of fringes), multiplied by a proportionality constant.

If the particle velocity sample V_i is related to the period sample T_i by $V_i = K/T_i$, then the true mean velocity $\bar{V}$ is given by

$$\bar{V} = KN / \sum_{i=1}^{N} T_i .$$

This is equivalent to the harmonic mean of the velocity samples since that is given by

$$\frac{1}{\bar{V}} = \frac{1}{N} \sum_{i=1}^{N} \frac{1}{V_i} .$$

It can also be shown that the biasing effect leads to a weighting of the velocity probability density function by a factor proportional to the velocity. Thus, by dividing the measured probability density function by the velocity and normalizing, the true velocity probability density function can be obtained. The measured velocity p.d.f. is denoted by P_{V_s}, in a discrete form. The mean value of V_s is given by

$$\bar{V}_V = \sum_s V_s P_{V_s} .$$

If a new p.d.f. is generated in the manner outlined above, the new p.d.f. can be given by

$$P_s = \frac{P_{V_s}}{V_s \sum_n \frac{P_{V_n}}{V_n}} ,$$

and the mean value is

$$\bar{V} = \frac{1}{\sum_n \frac{P_{V_n}}{V_n}} \cdot \sum_s \frac{V_s P_{V_s}}{V_s} .$$

This last term is unity and the remaining expression represents the harmonic mean of V, the true velocity. A simple example will now be given to demonstrate this equivalence.

Consider the following samples of velocity; 11, 10, 12, 15, 11, 12, 13, 13, 12, 13, 14, 14, 15, 14, 14, 16, 14, 15, 13, 17. The arithmetic mean is found to be 13.40 and the harmonic mean is 13.18. The discrete probability density function is,

V_s	10	11	12	13	14	15	16	17
p_{V_s}	.05	.1	.15	.2	.25	.15	.05	.05

Then following the analysis above:

V_s	10	11	12	13	14	15	16	17
p_s	.0659	.1198	.1647	.2027	.2353	.1318	.0412	.0388

Using the modified probability density function, the mean value of V_s is given by

$$\bar{V} = \sum_s V_s p_s$$

and is found to be $\bar{V} = 13.18$.

The procedure for processing the recorded LV data will not be given. The unprocessed data is printed out in the form shown in Figure 4D.1. The histogram, taken from the computer print out, is shown in Figure 4D.2. The validated points for axial velocities of 225.4 m/s and 709.3 m/s have a considerable effect on the higher order moments. In view of their high values, the jet exit velocity being 161.5 m/s, they may be justifiably regarded as incorrectly validated noise. The velocity data is therefore limited to the range 45.7 - 173.7 m/s. Having bounded the data in this manner, it is reprocessed and weighted by the inverse of the velocity. The resulting histogram is shown in Figure 4D.2 with the corresponding computer printout given in Figure 4D.3. It can be seen that the true velocity distribution found in this manner is very nearly Gaussian, having a skewness of -.0101 and kurtosis of 2.7956. (The Gaussian distribution has corresponding values of 0 and 3.)

If the flow velocity changes very rapidly the particles may lag behind the flow. This would lead to low instantaneous velocity reading for rapid flow acceleration and a high reading for rapid flow deceleration. Some slight particle lag was expected and observed close to the jet exit at the highest Mach numbers where the flow has been rapidly accelerated. For a particle already accelerated to the local mean flow velocity, the frequency of fluctuations in flow velocity it observes will be lower, in its moving frame, than that seen by the stationary observer, such as at the measurement volume. For the particle size distribution used in the present measurements, there is no observable amplitude or phase lag for frequencies in the moving frame less than 1 KHz (ref. 58). Since the expected dominant observed frequencies at the stationary frame were never more than an order of magnitude greater than this particle size distribution was expected to have a negligible effect on the measurements. Thus, no correction for particle size was applied to the data.

```
         4562        PJM  3  12
           22     ST 310 280 500K 100 CLO
 X MEAN =         117.9 M/S   XSTD =     18.0 M/S

 NO BLK =      178


 JET POSITION:   AXIAL=      61 CM.
                 HORIZ=      00
                 VERT=       00


              AXIAL
    VEL (M/S)      COUNT        PERCENT

        46.2          2          0.02
        52.2          3          0.03
        58.2          4          0.04
        64.1         24          0.27
        70.1         74          0.83
        76.1        132          1.48
        82.1        284          3.19
        88.0        346          3.89
        94.0        485          5.45
       100.0        749          8.42
       106.0        973         10.93
       111.9       1498         16.83
       117.9       1271         14.28
       123.9        946         10.63
       129.8        585          6.57
       135.8        537          6.03
       141.8        466          5.24
       147.8        354          3.98
       153.7        124          1.39
       159.7         30          0.34
       165.7          8          0.09
       171.8          3          0.03
       225.4          1          0.01
       709.3          1          0.01


 AXIAL MEAN VEL=        117.95 M/S
        TURB INT=        19.55 M/S
        SKEWNESS=         4.1861
        KURTOSIS=       130.1180


 MEAN RATE            184. PPS
          1      1500      5700
```

Figure 4D.1   Unprocessed velocity data.
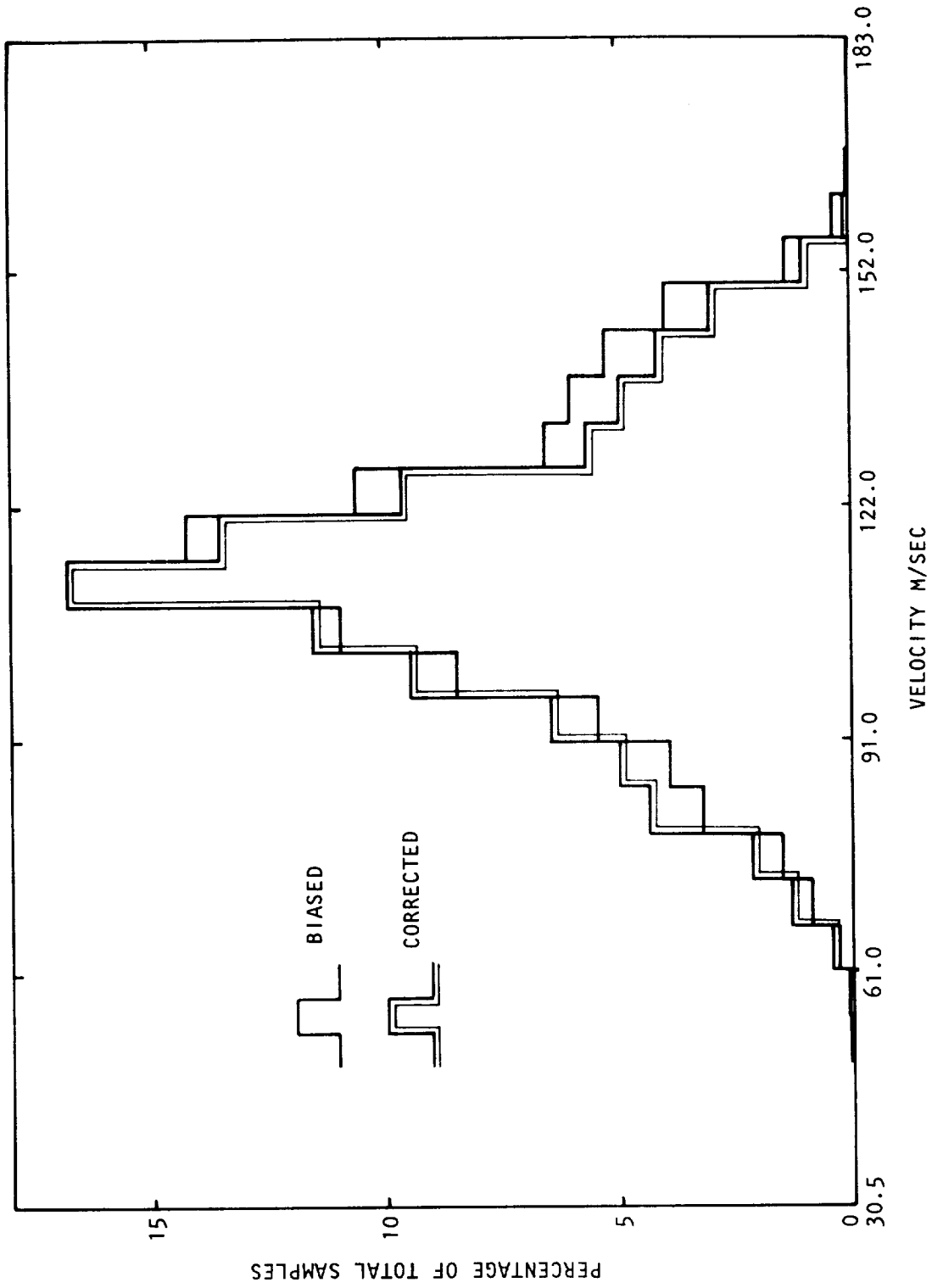
Figure 4D.2 Example of LV data processing.

CORRECTED HISTOGRAMS

	AXIAL	
VEL (M/S)	COUNT	PERCENT
46.2	5	0.05
52.2	6	0.06
58.2	8	0.09
64.1	44	0.47
70.1	124	1.32
76.1	204	2.18
82.1	408	4.35
88.0	463	4.94
94.0	608	6.49
100.0	883	9.42
106.0	1082	11.55
111.9	1577	16.83
117.9	1271	13.56
123.9	900	9.60
129.8	531	5.67
135.8	466	4.97
141.8	387	4.13
147.8	282	3.01
153.7	95	1.01
159.7	22	0.23
165.7	5	0.05
171.8	1	0.01

```
AXIAL MEAN VEL =    114.7 M/S
       TURB INT =     18.9 M/S
      SKEWNESS =    -0.0101
      KURTOSIS =     2.7956
```

Figure 4D.3   Processed velocity data.

APPENDIX 5
LIST OF SYMBOLS

a, a_0	local, ambient speed of sound
a_J, a_T	speed of sound in primary jet, tunnel flow
A_J, A_R	primary jet, plenum cross-sectional area
b_T	velocity profile constant
B	filter bandwidth
B_{ij}	volume displacement quadrupole source strength
C_n	effective nozzle coefficient
C_p	specific heat at constant pressure
C_F	free-jet data correction factor for flow effects
C_R	free-jet data correction factor for distance effects
CA	eddy convective amplification
d	primary jet nozzle diameter
dA	. area of ray tube cross-section
D	Doppler factor
D_m	modified Doppler factor
f	frequency
f_c	center frequency of one-third octave filter
$F^{(\nu)}$	flow factor
H	stagnation enthalpy; or normal height or distance of aircraft flight path from microphone
I	acoustic intensity
k	turbulent kinetic energy
$\underline{k}$	wavenumber vector
m	exponent of relative velocity; or total mass flow per unit area [Hill (ref. 47)]

m_a	mass concentration on jet centerline
M	nozzle Mach number; or axial flow Mach number, V_x/a; or twice the average sum of momentum and pressure forces per unit area [Hill (ref. 47)]
M_c	axial eddy convection Mach number, V_c/a_o
M_A	aircraft Mach number, V_A/a_o
M_J	jet Mach number, V_J/a_J
M_R	reservoir or plenum airflow Mach number
M_T	tunnel or free-jet Mach number, V_T/a_o
M_{TO}	minimum tunnel or free-jet Mach number
$\hat{n}$	wavenormal unit vector
OASPL	overall sound pressure level
p	static pressure
p'	acoustic pressure
p_o	ambient pressure in anechoic room
p_1	free-jet intake static pressure
p_R	reservoir or plenum static pressure
p_T	tunnel or free-jet test section static pressure
P	total pressure
$P(\omega)$	power spectral density of acoustic pressure
P_r	Prandtl number
P_R	reservoir or plenum total pressure
P_T	tunnel or free-jet test section total pressure
q	total turbulence intensity
$q(\underline{x}, t)$	acoustic source distribution

LIST OF SYMBOLS (Cont'd)

$Q(\underline{k}, \omega)$	cross-power spectral density of source distribution
r	radial distance; or (cylindrical) radial coordinate
$\underline{r}$	ray path position vector
r_1	(cylindrical) radius at which axial mean velocity is 66.3% of centerline value
$r_{.5}$	half-velocity radius
r_c	potential core radius
r_J	primary jet nozzle radius
r_T	tunnel equivalent radius
R	normalized (cylindrical) radial coordinate, r/r_T
R, R_m	microphone, measurement radius (spherical)
R_r	(spherical) radial coordinate
R_ψ	source-observer separation at reception time
R_T	radius of duct
RN	run number in free-jet experimental program
s	distance along ray path
S	Strouhal number
S_m	modified Strouhal number
S_{ij}	volume acceleration quadrupole source strength
SPL	sound pressure level
t	time
$\hat{t}$	pulse travel time, R_r/a_0
T	temperature; or flyover noise record length
T_0	free-jet intake temperature
T_a	temperature on jet centerline

LIST OF SYMBOLS (Cont'd)

T_J primary jet exit temperature

T_R reservoir or plenum flow temperature

T_T tunnel or free-jet test section temperature

v acoustic particle velocity

v_1, v_2, v_3 axial, radial, azimuthal velocity fluctuation

$\underline{V}$ mean flow velocity vector

V_1, V_2 axial, radial mean velocity

V_a axial mean velocity on jet centerline; or lower stream velocity in 2-D mixing layer

V_b upper stream velocity in 2-D mixing layer

V_c, V_{c1} eddy convection axial mean velocity

V_{ds} dividing streamline velocity

V_e eddy volume

V_{e1}, V_{e2}, V_{e3} wavenumber scaling velocity components

V_{et} transverse wavenumber scaling velocity, $= V_{e2} = V_{e3}$

V_r ray propagation speed

V_s axial mean velocity of fluid at source position

V_x, V_t, V_ϕ mean flow velocity components in x, r, ϕ directions

$\bar{V}_x$ velocity profile, e.g. V_x/V_T

V_A aircraft speed

V_J primary jet exit axial mean velocity

V_{REL} relative velocity, $(V_J - V_T)$ or $(V_J - V_A)$

V_T tunnel or free-jet velocity

V_{TO} minimum tunnel or free-jet velocity

x axial distance or axial coordinate

LIST OF SYMBOLS (Cont'd)

x_o virtual origin of mixing

x_c potential core length

x_n axial protrusion of primary nozzle downstream of free-jet exit plane

x_s' axial distance between effective source location and primary nozzle

X normalized axial coordinate, x/r_T

α scaling parameter in a modified Doppler factor

$\underline{\alpha}$ wavenormal unit vector

α_1 axial wavenumber scaling velocity constant, $\alpha_1 V_{a,rel} = V_{e1}$

β_1 transverse wavenumber scaling velocity constant, $\beta_1 V_{a,rel} = V_{et}$

γ ratio of specific heats

δ_ω vorticity thickness of shear layer, $V_{a,rel}/|dV_x/dr|_{max}$

δ_ω' axial derivative of vorticity thickness, spreading rate

$\Delta\theta_e$ angular resolution in aircraft flyover tests

Δt noise record length corresponding to $\Delta\theta_e$

ε turbulence energy dissipation rate; or kinematic eddy viscosity (Appendix 4B)

θ wavenormal angle (except θ_m) relative to downstream jet axis

θ_c cone of silence angle

θ_e polar angle, relative to downstream jet axis, at emission time

θ_m measured polar angle

κ radial wavenumber

λ velocity ratio, V_T/V_J

μ index of refraction

390

LIST OF SYMBOLS (Cont'd)

μ_t	eddy viscosity
ρ	fluid mean density
ρ_o	density in surrounding flow
ρ_J	primary jet exit density
σ	jet flow spreading parameter; or spread rate defined by Görtler [ref. (69)] such that similarity of mean profiles were obtained by plotting against $(\sigma y/x)$
σ_o	σ for $\lambda = 0$
ϕ	(cylindrical) azimuthal coordinate
Φ	eikonal function
$\Phi(\underline{k}, \omega)$	source function cross power spectral density
χ	similarity coordinate for velocity profile
ψ	ray angle relative to downstream jet axis; or polar angle, relative to downstream jet axis, at reception time; or stream function
ω	source frequency; or radian frequency

Subscripts

a	jet centerline value
e	at emission time
i, j	denote Cartesian coordinate directions (i, j = 1, 2, 3)
J	primary jet exit value
m	measured value; or modified value
rel, REL	relative to velocity V_A or V_T
R	reservoir or plenum value
s	refers to source conditions within the primary jet flow
T	wind tunnel or free-jet uniform test section value

o   ambient value; or stationary observer reference frame in flyover case; or external flow conditions (Appendices 3A and 3B)

Overbars   denote non-dimensionalized quantities

REFERENCES

1. Bushell, K. W.: Measurement and Prediction of Jet Noise in Flight. AIAA Paper No. 75-461, March 1975.

2. Forstall, W.; and Shapiro, A. H.; Momentum and Mass Transfer in Coaxial Gas Jets. *J. Appl. Mech.*, vol. 17, 1951, pp. 399-408.

3. Witze, P. O.: Centerline Velocity Decay of Compressible Free Jets. *AIAA Journal*, vol. 12, no. 4, April 1974, pp. 417-418.

4. Wygnanski, I.; and Fiedler, H.: Some Measurements in the Self-Preserving Jet. *J. Fluid Mech.*, vol. 38, no. 3, 1969, pp. 577-612.

5. Greatrex, F. G.: Bypass Engine Noise. Society of Automotive Engineers, National Aeronautics Meeting, New York, Oral Presentation, 1960.

6. Coles, G. M.: Estimating Jet Noise. *Aeronautical Quarterly*, vol. 14, 1963.

7. Ffowcs Williams, J. E.: The Noise from Turbulence Convected at High Speed. *Philosophical Transactions of the Royal Society*, vol. A255, 1963, pp. 469-503.

8. Mangiarotty, R. A.; and Turner, B. A.: Wave Radiation Doppler Effect Correction for Motion of a Source, Observer and Surrounding Medium. *Journal of Sound and Vibration*, vol. 6, 1967, pp. 110-116.

9. Anon.: Jet Noise Prediction. Society of Automotive Engineers, AIR 876, 1965.

10. Coles, W. D.; Mihaloew, J. A.; and Swann, W. H.: Ground and In-flight Acoustic Performance Characteristics of Jet Aircraft Exhaust Noise Suppressors. NASA TN D-874, 1961.

11. Brausch, J. F.: Flight Velocity Influence on Jet Noise Conical Ejector, Annular Plug, and Segmented Suppressor Nozzle. NASA CR-230961, 1972.

12. Burley, R. R.; and Karabinus, R. J.: Flyover and Static Tests to Investigate External Flow Effect on Jet Noise for Non-suppressor and Suppressor Exhaust Nozzles. NASA TM X-68161, 1973.

13. Hoch, R.; and Hawkins, R.: Recent Studies into Concorde Noise Reduction. Proceedings of the AGARD Conference on Noise Mechanisms, Brussels, Belgium. 1973.

14. Von Glahn, U.; Goodykoontz, J.; and Wagner, J.: Nozzle Geometry and Forward Velocity Effects on Noise for CTOL Engine-over-the-Wing Concept. NASA TM X-71453, 1973.

15. Burley, R. R.; and Johns, A. L.: Flight Velocity Effects on Jet Noise of Several Variations of a Twelve-Chute Suppressor Installed on a Plug Nozzle. NASA TM X-2918, 1974.

16. Burley, R. R.; Karabinus, R. J.; and Freedman, R. J.: Flight Investigation of Acoustic and Thrust Characteristics of Several Exhaust Nozzles Installed on Under-Wing Nacelles on an F106 Aircraft. NASA TM X-2854, 1973.

17. Chamberlain, R.: Flyover and Static Tests to Study Flight Velocity Effects on Jet Noise of Suppressed and Unsuppressed Plug Nozzle Configurations. NASA TM X-2856, 1973.

18. Von Glahn, U.; and Goodykoontz, J.: Forward Velocity Effects on Jet Noise with Dominant Internal Noise. NASA TM X-71438, 1973.

19. Burley, R. R.; and Head, V. L.: Flight Velocity Effects on Jet Noise of Several Variations of 48-Tube Suppressor Installed on a Plug Nozzle. NASA TM X-2919, 1974.

20. Gubkina, G. I.; and Mel'nikov, B. N.: Effects of Air Speed on the Flight Noise of Airliners and of Noise Duration on its Subjective Rating. *Soviet Physics - Acoustics*, vol. 16, 1968.

21. Von Glahn, U.; Groesbeck, D.; and Goodykoontz, J.: Velocity Decay and Acoustic Characteristics of Various Nozzle Geometries in Forward Flight. AIAA Paper No. 73-629, July 1973.

22. Brooks, J. R.; and Woodrow, R. J.: The Effects of Forward Speed on a Number of Turbojet Exhaust Silencers. AIAA Paper No. 75-506, March 1975.

23. Cocking, B. J.; and Bryce, W. D.: Subsonic Jet Noise in Flight Based on Some Recent Wind Tunnel Results. AIAA Paper No. 75-462, March 1975.

24. Anon.: A Review of Current Research Aimed at the Design and Operation of Large Wind Tunnels. Report of the Mini-Laws Working Group, AGARD-AR-68, 1974.

25. Williams, J.; and Holbeche, A.: Acoustic Considerations for Noise Experiments at Model Scale in Subsonic Wind Tunnels. AGARD Report No. 601, 1973. Also, Royal Aircraft Establishment Report TR-72155, 1972.

26. Timme, A.: Effect of Turbulence and Noise on Wind Tunnel Measurements at Transonic Speeds. AGARD Report R-602, 1973.

27. Mani, R.: Diffusion of Radiation Patterns Due to Scattering by Random Inhomogeneities. *Journal of Sound and Vibration*, vol. 17, 1971, pp. 95-104.

28. Rudd, M. J.: A Note on the Scattering of Sound in Jets and the Wind. *Journal of Sound and Vibration*, vol. 26, 1973, pp. 551-560.

29. Brown, E. H.; and Clifford, S. F.: Spectral Broadening of an Acoustic Pulse Propagating through Turbulence. *Journal of the Acoustical Society of America*, vol. 54, 1973, pp. 36-39.

30. Foley, W. M.; and Paterson, R. W.: Development of the United Technologies Research Center Acoustic Research Tunnel and Associated Test Techniques. Paper presented at AGARD Flight Mechanics Panel Symposium on Flight/Ground Testing Facilities Correlation, Valloire, Savoie, France, June 1975.

31. Ribner, H. S.: The Generation of Sound in Turbulent Jets. *Advances in Applied Mechanics*, vol. 8, 1964, pp. 103-182.

32. Tester, B. J.; and Morfey, C. L.: Developments in Jet Noise Modeling — Theoretical Predictions and Comparisons with Measured Data. Submitted to Journal of Sound and Vibration.

33. Tester, B. J.; and Morfey, C. L.: Developments in Jet Noise Modeling — Theoretical Predictions and Comparisons with Measured Data. AIAA Paper No. 75-477, March 1975.

34. Szewczyk, V. M.; and Morfey, C. L.: (Institute of Sound and Vibration Research, The University, Southampton, England). Personal Communication.

35. Tanna, H. K.; Fisher, M. J.; and Dean, P. D.: Effect of temperature on supersonic jet noise. AIAA Paper No. 73-991, October 1973.

36. Tanna, H. K.; and Dean, P. D.: An Experimental Study of Shock-Free Supersonic Jet Noise. AIAA Paper No. 75-480, March 1975.

37. Sabin, C. M.: An Analytical and Experimental Study of the Plane, Incompressible, Turbulent Free Shear Layer with Arbitrary Velocity Ratio and Pressure Gradient. Report MD-9 (AFOSR-TN-5443), Mech. Eng. Dept. Stanford Univ., October 1963.

38. Yule, A. J.: On the Mixing of Two Parallel Streams. Ph.D. Thesis, Univ. of Manchester, 1970.

39. Miles, J. B.; and Shih, J.-S.: Similarity Parameter for Two-Stream Turbulent Jet-Mixing Region. *AIAA Journal*, vol. 6, no. 7, July 1968, pp. 1429-1430.

40. Jones, B. G.; Planchon, H. P.; and Hammersley, R. T.: Turbulent Correlation Measurements in a Two-Stream Mixing Layer. *AIAA Journal*, vol. 11, no. 8, 1973, pp. 1146-1150.

41. Brown, G. L.; and Roshko, A.: On Density Effects and Large Structure in Turbulent Mixing Layers. *J. Fluid Mech.*, vol. 64, no. 4, 1974, pp. 775-816.

42. Bradbury, L. J. S.: The Structure of a Self-Preserving Turbulent Plane Jet, *J. Fluid Mech.*, vol. 23, no. 1, 1965, pp. 31-64.

43. Bradbury, L. J. S.; and Riley, J.: The Spread of a Turbulent Plane Jet Issuing into a Parallel Moving Airstream. *J. Fluid Mech.*, vol. 27, no. 2, pp. 381-394.

44. Weinstein, A. S.; Osterle, J. F.; and Forstall, W.: Momentum Diffusion from a Slot Jet into a Moving Secondary. *J. Appl. Mech.*, vol. 23, 1956, p. 437.

45. Curtet, R.; and Ricou, F. P.: On the Tendency to Self-Preservation in Axisymmetric Ducted Jets. *J. Basic Eng.*, Trans. ASME, Series D, vol. 86, 1964, pp. 765,776.

46. Antonia, R. A.; and Bilger, R. W.: An Experimental Investigation of an Axisymmetric Jet in a Co-Flowing Air Stream. *J. Fluid Mech.*, vol. 61, no. 4, 1973, pp. 805-822.

47. Hill, P. G.: Turbulent Jets in Ducted Streams. *J. Fluid Mech.*, vol. 22, no. 1, 1965, pp. 161-186.

48. Landis, F.; and Shapiro, A. H.: The Turbulent Mixing of Coaxial Gas Jets. *Proc. of the Heat Trans. and Fluid Mech. Inst.*, Stanford Univ. Press, 1951.

49. Pabst, O.: Die Ausbreitung Heisser Gasstrahlen in Bewegter Luft. Focke-Wulf Flugzengbau, Untersuchungen und Mitteilungen 8007, 1944.

50. Szablewski, W.: The Diffusion of a Hot Air Jet in Air in Motion. NACA TM 1288, 1950.

51. Von Glahn, U.; Sekas, N.; Groesbeck, D.; and Huff, R.: Forward Flight Effects on Mixer Nozzle Design and Noise Considerations for STOL Externally Blown Flap Systems. NASA TM X-68102, 1972.

52. Alpinieri, L. J.: Turbulent Mixing of Coaxial Jets. *AIAA Journal*, vol. 2, 1964, pp. 1560-1568.

53. Peters, C. E.; Chriss, D. E.; and Paulk, R. A.: Turbulent Transport Properties in Subsonic Coaxial Free-Mixing Systems. AIAA Paper No. 69-681, 1969.

54. Fricke, H. D.; and Schorr, C. J.: Measurement of Gaseous Mixing Downstream of Coaxial and Adjacent Orifices. *J. Spacecraft Rockets*, vol. 9, 1972, pp. 563-564.

55. Zawacki, T. S.; and Weinstein, H.: Experimental Investigation of Turbulence in the Mixing Region between Coaxial Streams. NASA CR-959, 1968.

56. Eggers, J. M.; and Torrence, M. G.: An Experimental Investigation of the Mixing of Compressible Air Jets in a Coaxial Configuration. NASA TN D-5315, July 1969.

57. Stevenson, W. H.; Redijo, M. K.; and Zammitt, R. E.: Bibliography on Laser Doppler Velocimeters: Theory, Design and Applications. Paper presented at the Laser Doppler Velocimeter Workshop, Purdue University, March 1972.

58. Whiffen, M. C.; and Meadows, D. M.: Two Axis, Single Particle Laser Velocimeter System for Turbulence Spectral Analysis. Paper presented at the Laser Doppler Velocimeter Workshop, Purdue University, March 1972.

59. Smith, D. M.; and Meadows, D. M.: Power Spectra from Random-Time Samples for Turbulence Measurements with a Laser Velocimeter. Paper presented at the Laser Doppler Velocimeter Workshop, Purdue University, March 1972.

60. Echols, W. H.; and Young, J. A.: Studies of Portable Air-Operated Aerosol Generators. NRL Report 5929, U. S. Naval Research Laboratory, July 1963.

61. Cline, V. A.; and Bentley, H. T.: Application of a Dual Beam Laser Velocimeter to Turbulent Flow Measurements. AEDC-TR-74-56, Arnold Engineering Development Center, Tennessee, Sept. 1974.

62. Patel, R. P.: An Experimental Study of a Plane Mixing Layer. *AIAA Journal*, vol. 11, 1973, p. 67.

63. Reichardt, H.: Gesetz mässigkeiten der Freien Turbulenz. VDI-Forschungsch. 414, 1942.

64. Spencer, B. W.; and Jones, B. G.: Statistical Investigation of Pressure and Velocity Fields in the Turbulent Two-Stream Mixing Layer. AIAA Paper No. 71-613, June 1971.

65. Mills, R. D.: Numerical and Experimental Investigations of the Shear Layer Between Two Parallel Streams. *J. Fluid Mech.*, vol. 33, pt. 3, 1968, pp. 591-616.

66. Pui, N. K.: The Plane Mixing Layer Between Parallel Streams. M.A. Sc. Thesis, Univ. of British Columbia, 1969.

67. Korst, H. H.; and Chow, W. L.: Non-Isoenergetic Turbulent ($Pr_t = 1$) Jet Mixing Between Two Compressible Streams at Constant Pressure. NASA CR-419, April 1966.

68. Squire, H. B.; and Trouncer, J.: Round Jets in a General Stream. R&M No. 1974, British A.R.C., 1944.

69. Görtler, H.: Berechnung von Aufgaben der Freien Turbulenz auf Grund eines Neuen Naherungsansatzes. ZAMM, vol. 22, pt. 5, 1942, pp. 244-254.

70. Birch, S. F.; and Eggers, J. M.: A Critical Review of the Experimental Data for Developed Turbulent Free Shear Layers. Proceedings of the NASA Conference on Free Turbulent Shear Flows, Vol. 1, NASA SP-321, 1972, pp. 11-37.

71. Maydew, R. C.; and Reed, J. F.: Turbulent Mixing of Compressible Free Jets. *AIAA Journal*, vol. 1, 1963, p. 1443.

72. Eggers, J. M.: Velocity Profiles and Eddy Viscosity Distributions Downstream of a Mach 2.22 Nozzle Exhausting to Quiescent Air. NASA TN D-3601, 1966.

73. Ikawa, H.: Turbulent Mixing Layer in Supersonic Flow. Ph.D. Thesis, California Institute of Technology, 1973.

74. Sirieix, M.; and Solignac, J.-L.: Contributions a l'Étude Experimentale de la Couche de Mélange Turbulent Isobare d um Écoulement Supersonique. Symposium on Separated Flows, AGARD Conference Proceedings, 1966, p. 4.

75. Anderson, A. R.; and Johns, F. R.: Characteristics of Free Supersonic Jets Exhausting into Quiescent Air. *Jet Propulsion*, vol. 25, no. 1, Jan. 1955, pp. 13-15.

76. Townsend, A. A.: *The Structure of Turbulent Shear Flow*. Cambridge University Press, 1956.

77. Abramovich, G. N.: *The Theory of Turbulent Jets*. MIT Press, 1963.

78. Pai, S. I.: *Fluid Dynamics of Jets*. Von Norstrand, 1954.

79. Schlichting, H.: *Boundary Layer Theory*. Sixth Ed., McGraw-Hill Book Co., Inc., 1968.

80. Patel, R.; and Newman, B. G.: Self-Preserving, Two-Dimensional Turbulent Jets and Wall Jets in a Moving Stream. Report Ae5, Mech. Eng. Dept., McGill Univ., 1961.

81. Gartshore, I. S.: The Streamwise Development of Certain Two-Dimensional Shear Flows, Report 65-3, Mech. Eng. Dept., McGill Univ., 1965.

82. Vogel, W. M.: Exact Solution of Growth Parameters for Two-Dimensional and Axisymmetric, Self-Preserving Turbulent Jets and Wakes. Report 68-5, Mech. Eng. Dept., McGill Univ., 1968.

83. Peters, C. E.; and Phares, W. J.: An Integral Turbulent Kinetic Energy Analysis of Free Shear Flows. Proceedings of the NASA Conference on Free Turbulent Shear Flows, Vol. 1, NASA SP-321, 1972, pp. 577-624.

84. Boussinesq, J.: Théorie de l'Écoulement Tourbillant. Mémoirs Presentes par Divers Savants a`l'Acadamic des Sciences Paris, vol. 23, 1877, p. 46.

85. Prandtl, L.: Über die Ausgebildete Turbulenz. ZAMM, vol. 5, 1925, pp. 136-139.

86. Prandtl, L.: Bermerkungen zur Theorie der Freien Turbulenz. ZAMM, vol. 22, 1942, pp. 241-243.

87. Kleinstein, G.: On the Mixing of Laminar and Turbulent Axially Symmetric Compressible Flows. PIBAL Report 756, Polytechnic Institute of Brooklyn, 1963.

88. Warren, W. R.: An Analytical and Experimental Study of Compressible Free Jets. Report 381, Princeton University Aero. Eng. Lab., 1957.

89. Alpinieri, L. J.: An Experimental Investigation of the Turbulent Mixing of Non-Homogeneous Coaxial Jets. PIBAL Report 789, Polytechnic Institute of Brooklyn, 1963.

90. Ferri, A.; Libby, P. A.; and Zakkay, V.: Theoretical and Experimental Investigation of Supersonic Combustion. ARL 62-467, Aeronautical Research Laboratories, Wright-Patterson AFB, 1962.

91. Zelazny, S. W.; Morgenthaler, J. H.; and Herendeen, D. L.: Shear Stress and Turbulence Intensity Models for Co-Flowing Axisymmetric Streams. *AIAA Journal*, vol. 11, 1973, pp. 1165-1173.

92. Glushko, G. S.: Turbulent Boundary Layer on a Flat Plate in an Incompressible Fluid. NASA TT F-10, 1965.

93. Harlow, F. H.; and Nakayama, P. L.: Turbulence Transport Equations. Phys. Fluids, vol. 10, 1967, pp. 2323-2332.

94. Beckwith, E.; and Bushnell, D. M.: Calculation of Mean and Fluctuating Properties of the Incompressible Turbulent Boundary Layer. Computation of Turbulent Boundary Layers - 1968 AFOSR-IFP - Stanford Conference, vol. I, S. J. Kline, M. V. Morkovin, G. Sovran, and D. J. Cockrell, eds., Stanford Univ., 1968.

95. Mellor, G. L.; and Herring, H. J.: Two Methods of Calculating Turbulent Boundary Layer Behavior Based on Numerical Solutions of the Equations of Motion. Computation of Turbulent Boundary Layers - 1968 AFOSR-IFP - Stanford Conference, vol. I, S. J. Kline, M. V. Morkovin, G. Sovran, and D. J. Cockrell, eds., Stanford Univ., 1968.

96. Spalding, D. B.: Turbulent Mixing in Combustion Chambers. Report 118-1, Northern Research and Engineering Corporation, 1966.

97. Bradshaw, P.; Ferriss, D. H.; and Atwell, N. P.: Calculation of Boundary Layer Development Using the Turbulent Energy Equation. *J. Fluid Mech.*, vol. 28, 1967, pp. 593-616.

98. Nash, J. F.; and Patel, V. C.: *Three-Dimensional Turbulent Boundary Layers*. SBC Technical Books, Atlanta, 1972.

99. Harsha, P. T.; and Lee, S. C.: Correlation Between Turbulent Shear Stress and Turbulent Kinetic Energy. *AIAA Journal*, vol. 8, 1970, pp. 1508-1510.

100. Lee, S. C.; and Harsha, P. T.: Use of Turbulent Kinetic Energy in Free Mixing Studies. *AIAA Journal*, vol. 8, 1970, pp. 1026-1032.

101. Heck. P. H.; and Ferguson, D. R.: Analytical Solution for Free Turbulent Mixing in Compressible Flows. AIAA Paper 71-4, 1971.

102. Heck, P. H.; and Merkle, C. L. : Analytical Flow Field Analysis for Compressible Turbulent Jets. Chap. 1. Supersonic Jet Exhaust Noise. M. J. Benzakein, and P. R. Knott, eds., AFAPL-TR-72-52, AFAPL, Wright-Patterson AFB, 1972.

103. Patankar, S. V.; and Spalding, D. B.: *Heat and Mass Transfer in Boundary Layers*. Second Ed., Int. Textbook Co. Ltd. (London), 1970.

104. Rotta, J.: Statistical Theory of Non-Homogeneous Turbulence. Part I: Z. Physik, Bd. 129, 1951, pp. 547-572.

105. Jones, W. P.; and Launder, B. E.: The Prediction of Laminarization with a Two-Equation Model of Turbulence, *Int. J. Heat & Mass Transfer*, vol. 15, no. 2, Feb. 1972, pp. 301-314.

106. Rodi, W.; and Spalding, D. B.: A Two-Parameter Model of Turbulence, and Its Application to Free Jets. Wärme-und Stoffübertragung, vol. 3, no. 2, 1970, pp. 85-95.

107. Launder, B. E.; Morse, A.; Rodi, W.; and Spalding, D. B.: Prediction of Free Shear Flows. A Comparison of the Performance of Six Turbulence Models. Proceedings of the NASA Conference on Free Turbulent Shear Flows, vol. I, NASA SP-321, 1972, pp. 361-422.

108. Proceedings of the NASA Conference on Free Turbulent Shear Flows, vol. II, NASA SP-321, 1972, pp. 36-39.

109. Forstall, W.: Material and Momentum Transfer in Coaxial Gas Streams. Sc.D. Thesis, Masachusetts Inst. Technology, June 1949.

110. Lighthill, M. J.: Jet Noise. *AIAA Journal*, vol. 1, 1963, pp. 1507-1517.

111. Crighton, D. G.: Basic Principles of Aerodynamic Noise Generation. Progress in Aerospace Sciences, vol. 16, 1975.

112. Morse, P. M.; Ingard, K. U.: Linear Acoustic Theory. vol. XI/1 of *Encyclopedia of Physics*, S. Flügge, ed., Springer-Verlag (Berlin), 1961, pp. 1-128.

113. Ugincius, P.: Acoustic-Ray Equations for a Moving, Inhomogeneous Medium. *Journal of the Acoustical Society of America*, vol. 37, 1965, pp. 476-479.

114. Ugincius, P.: Ray Acoustics and Fermat's Principle in a Moving Inhomogeneous Medium. *Journal of the Acoustical Society of America*, vol. 51, 1972, pp. 1759-1763.

115. Schubert, L. K.: Numerical Study of Sound Refraction by a Jet Flow. I. Ray Acoustics. *Journal of the Acoustical Society of America*, vol. 51, 1972, pp. 439-446.

116. Amiet, R. K.: Correlation of Open Jet Wind Tunnel Measurements for Shear Layer Refraction. AIAA Paper No. 75-532, March 1975.

117. Packman, A. B.; Ng, K. W.; and Paterson, R. W.: Effect of Simulated Forward Flight on Subsonic Jet Exhaust Noise. AIAA Paper No. 75-869, June 1975.

118. Grosche, F.-R.: Distributions of Sound Source Intensities in Subsonic and Supersonic Jets. AGARD CP-131, 1973.

119. Laufer, R. E.; Kaplan, R. E.; and Chu, W. T.: On noise produced by subsonic jets. Proceedings of the Second Interagency Symposium on University Research in Transportation Noise, vol. I, June 1974, pp. 50-58.

120. Morfey, C. L.: Personal Communication, 1974.

121. Blokhintsev, D. I.: Acoustics of a Nonhomogeneous Moving Medium. NACA TM 1399, 1956.

122. Morfey, C. L.: Acoustic Energy in Non-Uniform Flows. *Journal of Sound and Vibration*, vol. 14, no. 2, 1971, pp. 159-170.

123. Kleinstein, Gdalia: Mixing in Turbulent Axially Symmetric Free Jets. *J. Spacecraft*, vol. 1, no. 4, July-August 1964, pp. 403-408.

124. Carslaw, H. S.; and Jaeger, J. C.: Conduction of Heat in Solids. Second ed., Oxford University Press, 1959.

125. Yule, A. J.: Two-Dimensional Self-Preserving Turbulent Mixing Layers at Different Free Stream Velocity Ratios. R&M No. 3683, British A.R.C., 1972.

126. Yule, A. J.: Spreading of Turbulent Mixing Layers. *AIAA Journal*, vol. 10, 1972, pp. 686-687.

127. Baker, R. L.; and Weinstein, W.: Experimental Investigation of the Mixing of Two Parallel Streams of Dissimilar Fluids. NASA CR-957, 1968.

128. Abramovich, G. N.; Yakovlevsky, O. V.; Smirnova, I. P.; Secundov, A. N.; and Yu Krasheninnikov, S.: An Investigation of the Turbulent Jets of Different Gases in a General Stream. *Astronaut. Acta.*, vol. 14, 1969, pp. 229-240.

129. Johnson, D. A.: An Investigation of the Turbulent Mixing Between Two Parallel Gas Streams of Different Composition and Density with a Laser Doppler Velocimeter. Ph.D. Thesis, Univ. of Missouri, 1971.